World Scientific Series on Carbon Nanoscience

Handbook of Carbon Nano Materials

Volume 5

Graphene — Fundamental Properties

Editors

Francis D'Souza

Karl M. Kadish

World Scientific

Handbook of Carbon Nano Materials

Volume 5

Graphene — Fundamental Properties

This page intentionally left blank

World Scientific Series on Carbon Nanoscience

Handbook of Carbon Nano Materials

Volume 5
Graphene — Fundamental Properties

Editors

Francis D'Souza
University of North Texas, USA

Karl M. Kadish
University of Houston, USA

World Scientific

NEW JERSEY • LONDON • SINGAPORE • BEIJING • SHANGHAI • HONG KONG • TAIPEI • CHENNAI

Published by

World Scientific Publishing Co. Pte. Ltd.
5 Toh Tuck Link, Singapore 596224
USA office: 27 Warren Street, Suite 401-402, Hackensack, NJ 07601
UK office: 57 Shelton Street, Covent Garden, London WC2H 9HE

Library of Congress Control Number: 2012470297

British Library Cataloguing-in-Publication Data
A catalogue record for this book is available from the British Library.

HANDBOOK OF CARBON NANO MATERIALS
(In 2 Volumes)
Volume 5: Graphene — Fundamental Properties

Copyright © 2014 by World Scientific Publishing Co. Pte. Ltd.

All rights reserved. This book, or parts thereof, may not be reproduced in any form or by any means, electronic or mechanical, including photocopying, recording or any information storage and retrieval system now known or to be invented, without written permission from the Publisher.

For photocopying of material in this volume, please pay a copying fee through the Copyright Clearance Center, Inc., 222 Rosewood Drive, Danvers, MA 01923, USA. In this case permission to photocopy is not required from the publisher.

ISBN 978-981-4566-69-8 (Set)
ISBN 978-981-4566-72-8 (Vol. 5)

Typeset by Stallion Press
Email: enquiries@stallionpress.com

Printed in Singapore.

Contents

Preface xi

List of Contributors xiii

Chapter 1 Fundamental Properties of Graphene 1
Henry P. Pinto and Jerzy Leszczynski 1

1. Introduction 1
2. Electronic Properties of Pristine Graphene 5
   - 2.1. Band structure 5
     - 2.1.1. Few-layered graphene 8
   - 2.2. Chirality and quantum hall effect 10
   - 2.3. The Klein tunneling in graphene 11
   - 2.4. Atomic collapse on graphene 14
3. Elastic Properties of Graphene 16
4. Structural Defects in Graphene 19
   - 4.1. Stone–Wales defects 21
   - 4.2. Carbon vacancies 21
   - 4.3. Carbon adatoms 23
   - 4.4. Grain boundary loops 24
   - 4.5. Noncarbon adatoms and substitutional impurities 25
   - 4.6. Grain boundaries 26
   - 4.7. Effect of defects on the properties of graphene 27
5. Summary 30

Acknowledgments 31
References 32

Chapter 2 Adsorption on and Reactivity of Carbon Nanotubes and Graphene.....39
M. Rosa Axet, Revathi R. Bacsa, Bruno F. Machado and Philippe Serp

1. Introduction 40
2. Structure and Adsorption Sites..... 42
   2.1. Structure and adsorption sites of graphene and FLG 42
      2.1.1. Presence of defects 45
   2.2. Structure and adsorption sites of carbon nanotubes..... 49
      2.2.1. Presence of defects 51
3. Physisorption on CNTs and Graphene 54
   3.1. Physisorption of gases on CNTs and graphene 55
      3.1.1. Physisorption on individual CNTs 55
      3.1.2. Physisorption on CNT bundles 59
      3.1.3. Physisorption on graphene 62
   3.2. Physisorption of liquids on CNTs and graphene..... 66
      3.2.1. Adsorption of water on CNTs and graphene 68
      3.2.2. Physisorption of ionic liquids on graphene and CNTs 71
      3.2.3. Physisorption on CNTs and graphene of ions and molecules from solution 73
      3.2.4. Physisorption of liquids on doped CNTs and graphene 77
   3.3. Physisorption of solids on CNTs and graphene 77
      3.3.1. Metals and semiconductors 77
      3.3.2. Physisorption of metals and semiconductors on doped CNTs or graphene..... 80
      3.3.3. Physisorption of polymers 81
      3.3.4. Polymer adsorption on doped graphene or CNTs..... 82
4. Chemisorption on CNTs and Graphene 83
   4.1. Chemisorption of gases on CNTs and graphene 83
      4.1.1. Gas chemisorption on CNTs 83
      4.1.2. Effect of dopants on gas chemisorption with CNTs..... 84
      4.1.3. Gas chemisorption on graphene 87
      4.1.4. Effect of dopants on gas chemisorption with graphene 93
   4.2. Chemisorption of liquids on CNTs and graphene..... 97
   4.3. Chemisorption of solids on CNTs and graphene 99
      4.3.1. Alkali metals..... 99
      4.3.2. Alkaline-earth metals 102
      4.3.3. d-metals 102
      4.3.4. Adsorption of other metals, metalloids, and non-metals.. 115
      4.3.5. Polymers 116

5. Reactivity on CNTs and Graphene 122
5.1. Surface chemistry of nanostructured carbon materials 124
5.2. Catalysis 128
5.2.1. CNTs, CNFs, and FLG as metal-free catalyst 129
5.2.2. Hydrogenation 136
5.2.3. Oxidation and environmental catalysis 140
5.2.4. Fuel cell catalysis 144
5.3. Gas sensors 150
5.4. Bioreactivity and degradability of CNTs and graphene 153
5.4.1. Biosensors 155
5.4.2. Drug delivery 156
5.4.3. Biodegradability and toxicity 158
References 160

Chapter 3 Chemical Manipulation of Graphene in Dispersions 185
Jesús Iván Tapia and Mildred Quintana

1. Introduction 186

2. Liquid-Phase Exfoliated Graphene 187
2.1. Ultrasonication of graphite 187
2.1.1. Graphene dispersions in organic solvents 188
2.1.2. Graphene dispersions in surfactant solutions 190
2.2. Non-ultrasonication techniques 190
2.2.1. Intercalation compounds 190
2.2.2. Ionics compounds 191
2.2.3. Ball-milling production 193
2.2.4. Supercritical fluids 194
2.2.5. Unzipping of carbon nanotubes 194
3. Other Nanostructures from Liquid-Phase Exfoliated Graphene 195
3.1. Deformation, folding, and stabilization 196
3.2. Ultrasonication of graphite 196
3.2.1. Tiopronin as antioxidant molecule 196
3.2.2. Transformation of few-layer graphene into MWNTs 197
4. Covalent Functionalization of Graphene in Dispersions 199
4.1. Free radical addition 201
4.2. Dienophiles addition 201
5. Graphene Composites 204
5.1. Graphene/polymer composites 206
5.2. Synthesis of graphene/polymer composites 207

5.3. Graphene/inorganic material composites 208
5.4. Synthesis of graphene–inorganic nanocomposites 209
5.5. Miscellaneous applications of graphene 210
6. Conclusions 212
Acknowledgments..... 212
References 212

Chapter 4 On Thermodynamic Characteristics of the Thermal Desorption of Hydrogen from Hydrogenated Graphene Layers 219
Yury S. Nechaev and T. Nejat Veziroglu

1. Introduction 220

2. Analysis and Comparison of Data..... 223
2.1. Consideration of data on theoretical graphanes (CH)..... 223
2.2. Consideration of data on hydrogen thermal desorption from theoretical and experimental graphanes..... 226
2.3. Consideration of a thermodynamic probability of existence of hydrogenated graphenes–graphanes possessing of a very high binding energy..... 228
2.4. Consideration of data on hydrogen desorption in the hydrogenated mono- and bilayer epitaxial graphene samples 230
3. Analysis and Comparison of Data..... 235
3.1. Analysis of the Raman spectroscopy data on thermal desorption of hydrogen from hydrogenated graphene flakes..... 235
3.2. Analysis of the STM and STS data on reversible hydrogenation of epitaxial graphene and graphite surfaces..... 237
3.3. Analysis of the HREELS/LEED data on thermal desorption of hydrogen from hydrogenated graphene on SiC substrate..... 239
3.4. Analysis of the Raman spectroscopy data on thermal desorption of hydrogen from hydrogenated graphene layers on SiO_2 substrate..... 242
3.5. Analysis of TDS and STM data on HOPG treated by deuterium 244
3.6. Analysis of PES and ARPES data on dehydrogenation of graphene/SiC samples 245
3.7. Analysis of TDS and STM data on HOPG treated by hydrogen..... 246

4. A Possibility of Intercalation of Solid H_2 into Hydrogenated Graphite Nanofibers, Relevance to the Hydrogen On-Board Storage Problem 250
5. Conclusions 253
Acknowledgments 254
References 255

Cumulative Index of Volumes 5 and 6 259

This page intentionally left blank

Preface

We are pleased to present the third two-volume set of *The Handbook of Carbon Nanomaterials*. What started out to be a one-time publication of a "*Handbook*" set to mark the 25th anniversary of the discovery of Fullerenes in 2011, now appears to be a successful publication series. This is primarily due to the multiple new discoveries which continue to be published on the basic properties and applications of fullerenes, carbon nanotubes and graphene materials.

The first published set of volumes in the *Handbook of Carbon Nanomaterials* comprised 23 chapters in two volumes which summarized research developments in the field of carbon nanomaterials as seen through the eyes of more than three dozen leading researchers from around the world. The topics covered four general areas. The first part of the book dealt with the chemistry of fullerenes and carbon nanotubes, including organic functionalization, reactivity, perfluoroalkylation, and fullerenes linked to photosensitizers. The second part covered the chemistry and physics of endohedral fullerenes. The third part of the book covered the molecular and supramolecular chemistry of fullerenes and carbon nanotubes while the fourth described topics related to photoinduced energy and electron transfer. Finally, applications of fullerenes, carbon nanotubes and graphenes as applied to organic molecular electronics, polymers composites, thermal conductive materials, photovoltaics and sensing were presented.

The second published set of volumes in the *Handbook of Carbon Nanomaterials* (Volumes 3 and 4) contained material from leading authors on medicinal and bio-related applications and on topics ranging from materials to fundamental applications. Specific topics covered in Volume 3 were fullerenes in biology and medicine, the current state of the art of toxicity studies of fullerenes and carbon nanotubes, methods of detection of carbon nanotubes in living cells, carbon nanotechnology in regenerative medicine, chemical and biochemical sensors based on carbon nanotubes, molecular recognition

approach for separating left- and right-handed structures of single wall carbon nanotubes and open cage fullerene. The specific topics covered in Volume 4 were functionalization of graphene, electrochemical conversion and storage of energy, nanocarbon based molecular architectures for light energy conversion, electrochemistry of fullerenes as applicable for functional devices, fullerenes as self-assembled morphological materials, semiconductor carbon nanotube optics, near-filed optics of nanotubes and energy transfer at the nanoscale level, understanding the role of metal catalysts in chiral selective growth of carbon nanotubes, and finally, computational studies on the stability of fullerenes and metallofullerenes.

The current two volume set (Volumes 5 and 6) is dedicated in large part to recent discoveries on graphene. There are nine chapters in this set; the first four chapters (Volume 5) summarize the basic science of graphene. Specific topics include fundamental properties of graphene, adsorption and reactivity of graphene, chemical manipulation of graphene in dispersions, and thermodynamic characterization of thermal desorption of hydrogen from hydrogenated graphene layers. The next five chapters (Volume 6) provide an up-to-date summary of energy and sensor applications of graphene. The topics covered in this volume include graphene materials for energy conversion and storage applications, graphene for biosensor and electrochemical biosensor applications, and finally, carbon nanomaterials in biomedical and energy research.

Like the previous four volumes, the current two-volume set of the Handbook has been written as a hands-on reference guide for scientists working in the fields of biology, medicine, chemistry, physics, materials science, solid-state physics and nanotechnology. The coverage of topics presented is both in-depth and comprehensive. When combined with the perspectives for future research given by the contributing authors, this series makes an invaluable reference source that should be considered essential reading for both students and advanced researchers in the field.

The editors would like to acknowledge the contributors for their timely submission of the state-of-the-art reviews. Last, but not least, the staff of World Scientific Publishing Co. is acknowledged for their immense help in bringing out this publication in a timely manner.

Francis D'Souza
Denton, TX, USA

Karl M. Kadish
Houston, TX, USA
August 7, 2013

List of Contributors

M. Rosa Axet
Laboratoire de Chimie de Coordination
UPR CNRS 8241
Composante ENSIACET
Université de Toulouse
UPS/INP/LCC
4 allée Emile Monso, BP 44362
31432 Toulouse Cedex 4, France
Chapter 2 (Vol. 5)

Revathi R. Bacsa
Laboratoire de Chimie de Coordination
UPR CNRS 8241
Composante ENSIACET
Université de Toulouse
UPS/INP/LCC
4 allée Emile Monso, BP 44362
31432 Toulouse Cedex 4, France
Chapter 2 (Vol. 5)

Thomas Hirsch
Institute of Analytical Chemistry, Chemo- and Biosensors
University of Regensburg
93053 Regensburg, Germany
thomas.hirsch@ur.de
Chapter 3 (Vol. 6)

Yanglong Hou
Department of Materials Science and Engineering
College of Engineering
Peking University
Beijing 100871, China
hou@pku.edu.cn
Chapter 2 (Vol. 6)

Partha Khanra
Advanced Wind Power System Research Center
Department of BIN Fusion Technology
Chonbuk National University
Jeonju, Jeonbuk 561-756, Korea
Chapter 1 (Vol. 6)

Nam Hoon Kim
Advanced Wind Power System Research Center
Department of BIN Fusion Technology
Chonbuk National University
Jeonju, Jeonbuk 561-756, Korea
Chapter 1 (Vol. 6)

Tapas Kuila
Surface Engineering and Tribology Division
CSIR-Central Mechanical Engineering Research Institute
Council of Scientific and Industrial Research (CSIR)
Mahatma Gandhi Avenue
Durgapur — 713209, India
Chapter 1 (Vol. 6)

Hemant Kumar
Centre for Condensed Matter Theory
Department of Physics
Indian Institute of Science
Bangalore 560012, India
Chapter 5 (Vol. 6)

Joong Hee Lee
Advanced Wind Power System Research Center
Department of BIN Fusion Technology
and Department of Polymer and Nano Science and Technology
Chonbuk National University
Jeonju, Jeonbuk 561-756, Korea
jhl@chonbuk.ac.kr
Chapter 1 (Vol. 6)

Jerzy Leszczynski
Interdisciplinary Center for Nanotoxicity
Department of Chemistry and Biochemistry
Jackson State University
Jackson, MS 39217, USA
jerzy@icnanotox.org
Chapter 1 (Vol. 5)

Jinghong Li
Department of Chemistry
Beijing Key Laboratory for Analytical Methods and Instrumentation
Tsinghua University
Beijing 100084, China
jhli@mail.tsinghua.edu.cn
Chapter 4 (Vol. 6)

Yang Liu
Department of Chemistry
Beijing Key Laboratory for Analytical Methods and Instrumentation
Tsinghua University
Beijing 100084, China
Chapter 4 (Vol. 6)

Bruno F. Machado
Laboratoire de Chimie de Coordination
UPR CNRS 8241
Composante ENSIACET
Université de Toulouse
UPS/INP/LCC
4 allée Emile Monso, BP 44362
31432 Toulouse Cedex 4, France
Chapter 2 (Vol. 5)

Nasir Mahmood
Department of Materials Science and Engineering
College of Engineering
Peking University
Beijing 100871, China
Chapter 2 (Vol. 6)

Prabal K. Maiti
Centre for Condensed Matter Theory
Department of Physics
Indian Institute of Science
Bangalore 560012, India
maiti@physics.iisc.ernet.in
Chapter 5 (Vol. 6)

Santosh Mogurampelly
Centre for Condensed Matter Theory
Department of Physics
Indian Institute of Science
Bangalore 560012, India
Present address: Department of Physics, University of Rome "La Sapienza", Ple A. Moro 2, 00185, Rome, Italy.
Chapter 5 (Vol. 6)

Bidisha Nandy
Centre for Condensed Matter Theory
Department of Physics
Indian Institute of Science
Bangalore 560012, India
Chapter 5 (Vol. 6)

Yury S. Nechaev
Bardin Institute for Ferrous Metallurgy
Kurdjumov Institute of Metals Science and Physics
Vtoraya Baumanskaya St., 9/23
Moscow 105005, Russia
Yuri1939@inbox.ru
Chapter 4 (Vol. 5)

Wendy Patterson
Institute of Analytical Chemistry, Chemo- and Biosensors
University of Regensburg
93053 Regensburg, Germany
Chapter 3 (Vol. 6)

Henry P. Pinto
Interdisciplinary Center for Nanotoxicity
Department of Chemistry and Biochemistry
Jackson State University
Jackson, MS 39217, USA
Chapter 1 (Vol. 5)

Debabrata Pramanik
Centre for Condensed Matter Theory
Department of Physics
Indian Institute of Science
Bangalore 560012, India
Chapter 5 (Vol. 6)

Mildred Quintana
Instituto de Física
Universidad Autónoma de San Luis Potosí
77290 SLP, México
mildred@ifisica.uaslp.mx
Chapter 3 (Vol. 5)

Philippe Serp
Laboratoire de Chimie de Coordination
UPR CNRS 8241
Composante ENSIACET
Université de Toulouse
UPS/INP/LCC

4 allée Emile Monso, BP 44362
31432 Toulouse Cedex 4, France
philippe.serp@ensiacet.fr
Chapter 2 (Vol. 5)

Jesús Iván Tapia
Instituto de Física
Universidad Autónoma de San Luis Potosí
77290 SLP, México
Chapter 3 (Vol. 5)

V. Vasumathi
REQUIMTE, Department of Chemistry
University of Porto
Rua do Campo Alegre 687
4168–007 Porto, Portugal
Chapter 5 (Vol. 6)

T. Nejat Veziroglu
International Association for Hydrogen Energy
5794 SW 40 St. # 303
Miami, FL 33155, USA
Chapter 4 (Vol. 5)

Han Yin
Department of Materials Science and Engineering
College of Engineering
Peking University
Beijing 100871, China
Chapter 2 (Vol. 6)

Chenzhen Zhang
Department of Materials Science and Engineering
College of Engineering
Peking University
Beijing 100871, China
Chapter 2 (Vol. 6)

Ling Zhang
College of Chemistry and Life Science
Shenyang Normal University
Shenyang 110034, China
Chapter 4 (Vol. 6)

Qian Zhang
College of Chemistry
Liaoning University
Shenyang 110036, China
Chapter 4 (Vol. 6)

Alexander Zöpfl
Institute of Analytical Chemistry, Chemo- and Biosensors
University of Regensburg
93053 Regensburg, Germany
Chapter 3 (Vol. 6)

Contents of Volumes 5 and 6

Volume 5 Graphene — Fundamental Properties

1. Fundamental Properties of Graphene
   Henry P. Pinto and Jerzy Leszczynski
2. Adsorption on and Reactivity of Carbon Nanotubes and Graphene
   M. Rosa Axet, Revathi R. Bacsa, Bruno F. Machado and Philippe Serp
3. Chemical Manipulation of Graphene in Dispersions
   Jesús Iván Tapia and Mildred Quintana
4. On Thermodynamic Characteristics of the Thermal Desorption of Hydrogen from Hydrogenated Graphene Layers
   Yury S. Nechaev and T. Nejat Veziroglu

Volume 6 Graphene — Energy and Sensor Applications

1. Graphene-Based Materials for Energy Storage Applications
   Tapas Kuila, Partha Khanra, Nam Hoon Kim and Joong Hee Lee
2. Graphene-Based Nanomaterials for Energy Conversion and Storage
   Chenzhen Zhang, Nasir Mahmood, Han Yin and Yanglong Hou
3. Graphene for Biosensor Applications
   Alexander Zöpfl, Wendy Patterson and Thomas Hirsch
4. Graphene-Based Electrochemical Biosensor
   Qian Zhang, Ling Zhang, Yang Liu and Jinghong Li
5. Graphene and Carbon Nanotube-Based Nanomaterial: Application in Biomedical and Energy Research
   Hemant Kumar, Debabrata Pramanik, Santosh Mogurampelly, V. Vasumathi, Bidisha Nandy and Prabal K. Maiti

This page intentionally left blank

Chapter 1

Fundamental Properties of Graphene

*Henry P. Pinto and Jerzy Leszczynski**

Interdisciplinary Center for Nanotoxicity
Department of Chemistry and Biochemistry
Jackson State University, Jackson, MS 39217, USA

1. Introduction 1
2. Electronic Properties of Pristine Graphene 5
   2.1. Band structure 5
      2.1.1. Few-layered graphene 8
   2.2. Chirality and quantum hall effect 10
   2.3. The Klein tunneling in graphene 11
   2.4. Atomic collapse on graphene 14
3. Elastic Properties of Graphene 16
4. Structural Defects in Graphene 19
   4.1. Stone–Wales defects 21
   4.2. Carbon vacancies 21
   4.3. Carbon adatoms 23
   4.4. Grain boundary loops 24
   4.5. Noncarbon adatoms and substitutional impurities 25
   4.6. Grain boundaries 26
   4.7. Effect of defects on the properties of graphene 27
5. Summary 30
Acknowledgments 31
References 32

* Corresponding author. E-mail: jerzy@icnanotox.org.

1. Introduction

Graphene and its variations is becoming the most influential material in science and technology due to its fascinating properties. From an historical perspective, graphene has actually been in use since the invention of the pencil as a writing tool from *ca.* 1589.[1] Basically, when someone writes with a pencil, what is actually happening is stacks of graphene are depositing as the graphite is pressed against a writable surface. Graphite has a layered structure of graphene glued together by van der Waals forces. These forces are weak compared to the covalent bonds between the carbon atoms lying on a graphene sheet; this fact makes it possible to write with a pencil. Nonetheless, the scientific community was unaware of the existence of freestanding 2D crystals until 2004 when Andre Geim and Kostya Novoselov reported the successful isolation of one-atom thick graphite (graphene).[2] The ingenuity of Geim and Novoselov allows to isolate graphene by using *micromechanical cleavage*: this technique basically pulls out a graphene layer from graphite using a thin SiO_2 substrate; the one-atom thick layer is observable by an optical microscope, thanks to optical effect that graphene creates on the SiO_2 substrate.[2] This discovery resulted in both scientists, Geim and Novoselov being awarded the Nobel Prize in Physics in October 2010.

The remarkable physical properties of graphene lay on its honeycomb structure made out of hexagons (see Figure 1). Each carbon atom is bonded to three others making an angle of 120° and a bonding length of 1.42 Å. The stability of this lattice is given by the sp^2 hybridization between one *s* orbital with two *p* orbitals that leads to the formation of σ bonds between C atoms. The corresponding σ band is closed-shell and gives the robustness to the lattice. The remaining *p* orbital is oriented perpendicularly to the planar structure and can interact and form covalent bonds with the adjacent C atoms forming a π band. This band is half-filled since each *p* orbital has one extra electron.

Graphene could be seen as an universal carbon material. It can be wrapped up into 0D fullerenes, rolled into 1D nanotubes, or stacked into 3D graphite crystal (see Figure 2). From a theoretical perspective, graphene has been under study for 60 years and it is used for describing properties of related carbon-based materials.[3–5] Before 2004, graphene was considered a purely academic material. Within the scientific community, there was a consensus that graphene should be an unstable structure with respect to carbon nanotubes, fullerenes, and powder-like form of amorphous carbon; and therefore 2D carbon crystals could not exist.[6] In fact, it was commonly accepted for a long time that any 2D crystal would be structurally unstable because of long

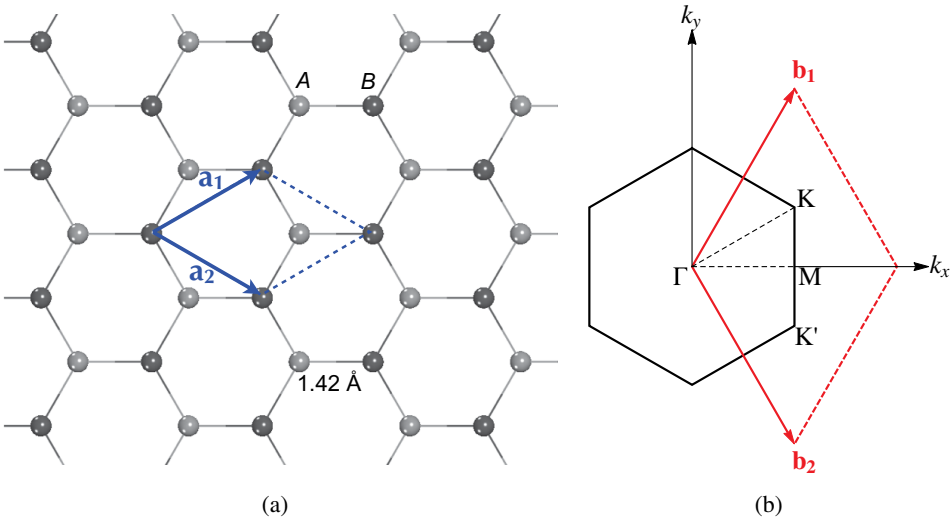

Figure 1. (a) Atomic structure of graphene showing its honeycomb arrangement, the dotted blue lines denote the two-atom primitive cell with lattice vectors $\mathbf{a}_1$ and $\mathbf{a}_2$; the carbon atoms are represented by gray spheres. The lattice can be also represented by two interpenetrated carbon triangular sublattices *A* (light gray) and *B* (dark gray). (b) The corresponding reciprocal lattice denoted by the red dotted lines with lattice vectors $\mathbf{b}_1$ and $\mathbf{b}_2$; the first Brillouin zone (BZ) is denoted by the hexagon with the high symmetry points **Γ**, **M**, and **K** (Dirac-point).

wavelength fluctuations according to Mermin–Wagner theorem.[7] After the development of the *micromechanical cleavage* methodology, that allowed Geim and Novoselov to isolate monolayers of graphene, triggered the discovery and realization of free-standing atomic 2D crystals like boron nitride (BN), several dichalcogenides, and complex oxides;[8] that might find interesting technological applications.

The discovery of graphene triggered the quest for new 2D carbon structures with sp^2-hybridized carbon sheets containing heptagons and pentagons only (pentaheptite)[9] or 2D crystals containing pentagons, heptagons, and/or hexagons (Haeckelites)[10] (see Figure 3). These are predicted to have a metallic character but they are still waiting for experimental confirmation.

Due to graphene's exceptional properties, it might revolutionize a wide range of fields.[11] Graphene-based electronics "graphenium" is an active field of application. This material has already shown its potential as IBM scientists have developed a graphene field-effect transistors with an operation frequency of 26 GHz.[12] A likely candidate to substitute the silicon-based technology is the development of graphenium technology.[9] Another field that is growing

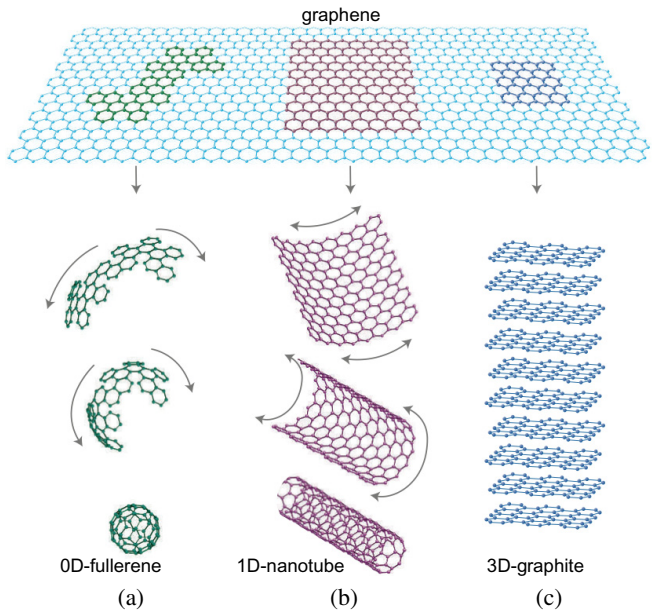

Figure 2. Graphene and its descendants, (a) wrapped graphene=fullerenes; (b) rolled graphene=nanotubes; and (c) staked graphene=graphite. Adapted from Ref. 9.

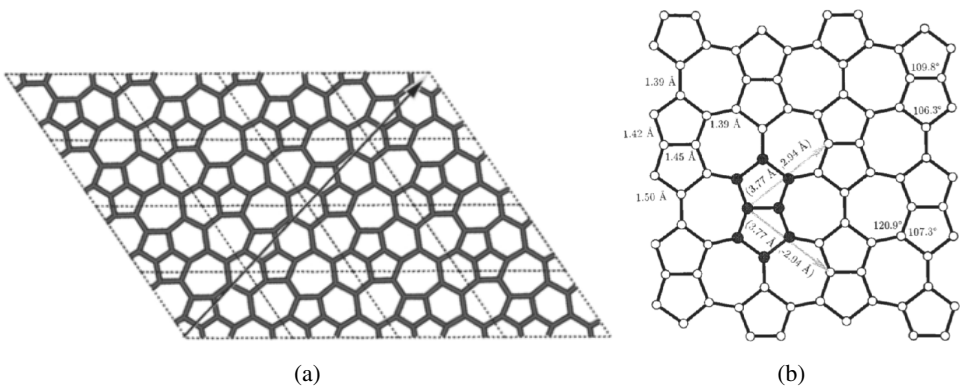

Figure 3. Theoretically predicted 2D atomic structures with sp^2-like hybridized carbon nanostructures: (a) Haeckelite carbon sheets with hexagonal unit cell. (b) Pentaheptite. Adapted from Refs. 10 and 11.

by the graphene discovery and the 2D crystals in general is the area of ultrathin and flexible devices applied to electronics. Indeed, the practical isolation of 2D crystals and the subsequent staking forming composed ultra thin films has opened a new kind of materials: heterostructures composed by 2D crystals.[13] Recent studies on a specific class of heterostructure thin film

formed by semiconducting transition metal (TM) dichalcogenides (TMDC)/graphene stacks has shown exceptional performance in flexible photovoltaic devices with photoresponsivity above 0.1 A/W.[13] Moreover, the unique 2D properties of graphene where the conductive electrons to behave as massless Dirac fermions[14,15] allows graphene to be a fertile playground for testing exotic predictions of quantum electrodynamics (QED).[16–19]

2. Electronic Properties of Pristine Graphene

2.1. Band structure

The band structure of graphene was first published by Wallace in 1946.[3] At that time, graphene was only considered a theoretical system, and his studies were the basis for understanding graphite. His work already showed the unique semimetallic characteristic of graphene. Figure 1 depicts the atomic structure of graphene and its corresponding reciprocal space lattice and BZ. The lattice vectors of the graphene unit cell are defined by (see Figure 1a):

$$\boldsymbol{a}_1 = \frac{a}{2}\begin{pmatrix} 3 \\ \sqrt{3} \end{pmatrix} \qquad \boldsymbol{a}_2 = \frac{a}{2}\begin{pmatrix} 3 \\ -\sqrt{3} \end{pmatrix}, \tag{1}$$

where the C–C distance is $a \sim 1.42$ Å; the corresponding reciprocal cell is defined like

$$\boldsymbol{b}_1 = \frac{2\pi}{3a}\begin{pmatrix} 1 \\ \sqrt{3} \end{pmatrix} \qquad \boldsymbol{b}_2 = \frac{2\pi}{3a}\begin{pmatrix} 1 \\ -\sqrt{3} \end{pmatrix}. \tag{2}$$

The most remarkable feature of graphene lattice is the so-called Dirac points $\boldsymbol{K}$ and $\boldsymbol{K}'$ located at the vertices of the BZ with coordinates (see Figure 1(b)):

$$\boldsymbol{K} = \frac{2\pi}{3a}\begin{pmatrix} 1 \\ \frac{1}{\sqrt{3}} \end{pmatrix} \qquad \boldsymbol{K}' = \frac{2\pi}{3a}\begin{pmatrix} 1 \\ -\frac{1}{\sqrt{3}} \end{pmatrix}, \tag{3}$$

The electronic structure of graphene can be solved using *e.g.*, tight-binding theory (used by Wallace[3]) or *ab initio* calculations. Figure 4 shows the computed electronic structure of graphene using density-functional theory (DFT) implemented by the plane-wave code VASP[20,21] with the PBEsol functional[22] that replicates the *ab initio* calculations by Reich *et al.*[23] Furthermore, the electronic properties of graphene can be acceded directly

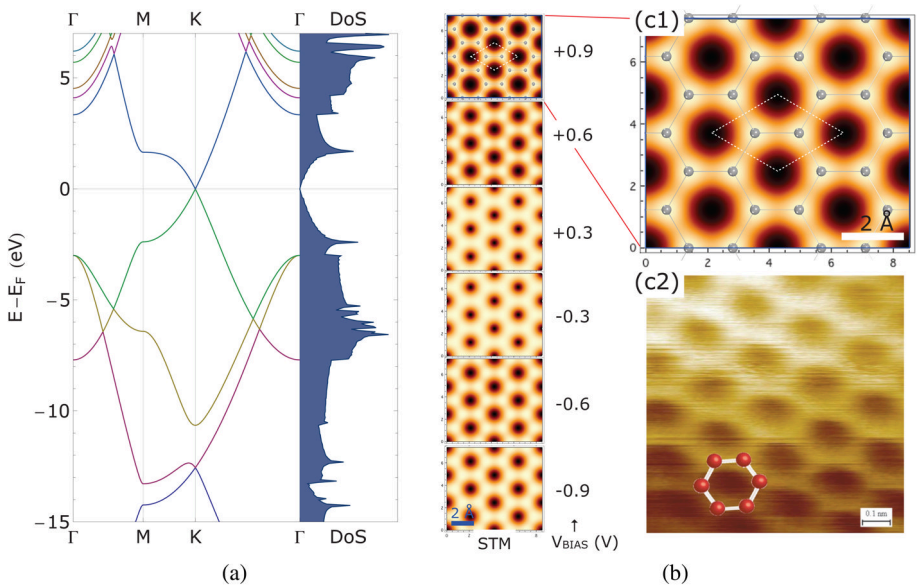

Figure 4. PBEsol computed electronic structure of pristine graphene. (a) Band structure along the symmetry points: Γ(0, 0, 0), $M(\frac{1}{2},0)$, and $K(\frac{1}{3},\frac{1}{3})$, here E_F denotes the Fermi level. Notice the linear dispersion of the bands around the $\boldsymbol{K}$ point (Dirac point). The plot also includes the DoS. (b) Simulated constant-current STM images for V_{BIAS} = ±0.9, ±0.6, and ±0.6 V: the bright protrusions are above the C atoms. (c1) Close-up of the STM image for V_{BIAS} = +0.9 V superimposed the graphene lattice. (c2) Experimental constant-current STM image for single-layer graphene with V_{BIAS} = +1 *V* and tunneling current of 1 nA. Adapted from Ref. 24. Notice that STM with positive (negative) V_{BIAS} is mapping the empty (occupied) states at the Fermi level.

by scanning probe microscopies in contrast to semiconductors where the electronic states can be lying deep under the surface. The displayed electronic structure on Figure 4 is complemented by the computed constant-current scanning tunneling microscopy (STM) topologies and compared with the observed STM images for single-layer grapheme.[24] The energy dispersion $E(\boldsymbol{k})$ around the $\boldsymbol{K}$ point can also be found using tight-binding approximation on the π orbitals. Considering the result by Sato,[25] we have

$$E^{\pm}(k) = \frac{\varepsilon_{2p} \mp \gamma_0 \sqrt{f(k)}}{1 \mp s_0 \sqrt{f(k)}}, \tag{4}$$

with

$$f(\boldsymbol{k}) = 3 + 2\cos(\boldsymbol{k}\cdot\boldsymbol{a}_1) + \cos(\boldsymbol{k}\cdot\boldsymbol{a}_2) + 2\cos(\boldsymbol{k}\cdot(\boldsymbol{a}_1 - \boldsymbol{a}_2)), \tag{5}$$

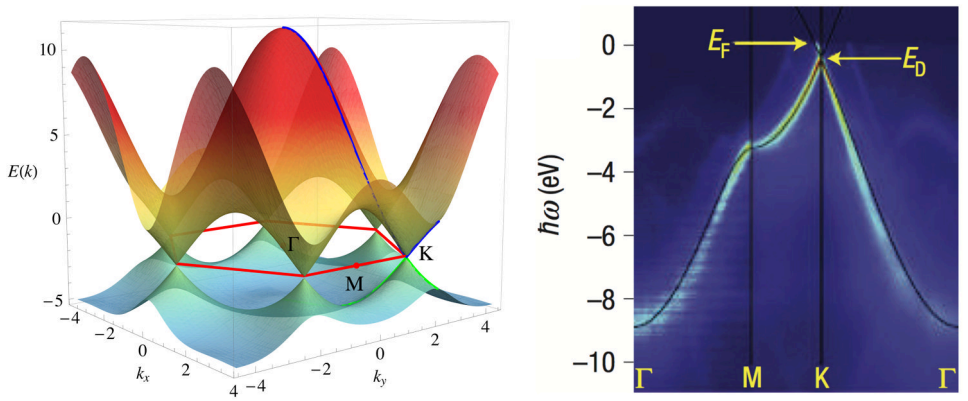

Figure 5. (a) Electronic dispersion $E^{\pm}(\boldsymbol{k})$ obtained with tight-binding approximation. The blue and green lines are the dispersion along $\Gamma-\boldsymbol{K}$ path where a linear dispersion appears around $\boldsymbol{K}$ (or $\boldsymbol{K}'$) point: the Dirac point. The red hexagon denotes the first BZ. (b) ARPES measurements applied to a single layer of graphene, grown on the (0001) surface of SiC. Adapted from Ref. 27.

where ε_{2p}, γ_0, and s_0 are parameters fitted to reproduce experimental or *ab initio* data around the $\boldsymbol{K}$ point. The accepted values are $\varepsilon_{2p} = 0$ $_e$V, γ_0 between –3 and –2.5 eV, and s_0 below 0.1 eV. Figure 5 depicts the electronic dispersion $E^{\pm}(\boldsymbol{k})$ showing the so-called Dirac points as well as the observed angle-resolved photoemission spectroscopy (ARPES) of a single layer of grapheme.[26,27] The linear dispersion at the Dirac point is more evident if $E^{\pm}(\boldsymbol{k})$ is expanded around the $\boldsymbol{K}$ point for $\boldsymbol{k} = \boldsymbol{K}+\boldsymbol{q}$ with $|\boldsymbol{q}| \ll |\boldsymbol{K}|$ yielding

$$E^{\pm}(q) \approx \pm v_F |q| + O[(q/K)^2], \tag{6}$$

where v_F is the Fermi velocity of $\sim 1\times10^6$ m s^{-1} or $\sim c/300$ (c as the speed of light).[3] This remarkable property of graphene contrast with the usual dispersion observed in solids where $E(\boldsymbol{q}) = q^2/(2m^*)$ with m^* as the effective mass of the electron moving with a speed $v = k/m\sqrt{2E/m}$ — *i.e.*, the speed changes with the energy. In graphene, the fact that there is a linear dispersion of $E(\boldsymbol{q})$, means the electrons are massless. This feature resembles "relativistic" particles (like photons traveling in free space at the speed of light with energy $E = \hbar kc$) but replacing the speed of light c by v_F. Relativistic particles are quantum mechanically described by the massless Dirac equations (for a more detailed description see Ref. 28). These equations are used in QED. Indeed,

the electronic properties of graphene near the ***K*** point can be described as a 2D zero-gap semiconductor described by the Dirac-like Hamiltonian:[5,16,18]

$$\widehat{\mathcal{H}}_K = -i\hbar v_F \boldsymbol{\sigma} \cdot \nabla, \tag{7}$$

where $\boldsymbol{\sigma} = (\sigma_x, \sigma_y)$ are the Pauli matrices; neglecting the many-body effects, this description is accurate theoretically.[5,16,18] The fact that electrons in graphene behaves like relativistic particles has open-up an unique opportunity to probe QED phenomena.

2.1.1. Few-layered graphene

The electronic properties of graphene depends on the number of layers and the staking order. The bilayer graphene can have a staking order AA where each atom is on top of another atom or, AB where the atom on the first layer is on top of the center of the hexagon of the layer beneath. Increasing the number of layers yields more complex ordering; in the case of graphite, there are three common types of staking: (i) AB or Bernal stacking, (ii) the AA staking, and (iii) no defined stacking or turbostratic stacking (see Figure 6). The energetically most favorable stacking configuration is AB but the other configurations are also likely to exist specially in few-layer graphenes. Indeed, the AA staking has been already experimentally observed in a bilayer-graphene.[29]

The increase of graphene layers has a direct impact on its electronic structure approaching the 3D limit of graphite at 10 layers.[30] The Dirac point observed in single-layered graphene (Figure 7a) disappears in bilayer

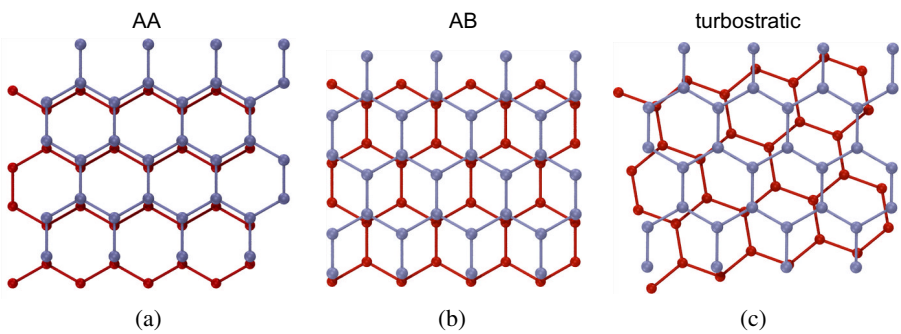

Figure 6. Staking order in graphite (a) AA, (b) AB, and (c) turbostratic staking. These figures show only the 1st and 2nd layers of graphite where the carbon atoms are represented by blue (red) spheres at the top (bottom).

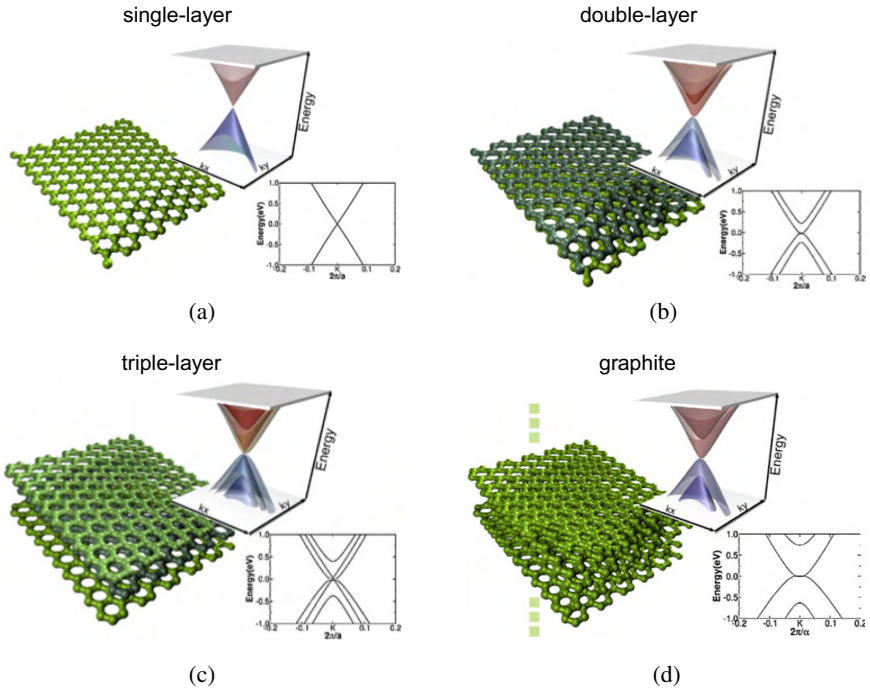

Figure 7. Effect of staking on graphenes on the electronic structure around the ***K*** point. (a) Typical linear dispersion observed in (single-layer) graphene. (b) The AB staking double-layer graphene shows no linear dispersion is observed and instead a parabolic dispersion appears. (c) The AB staking triple-layer graphene reestablish the linear dispersion, (d) The band structure for graphite that has parabolic dispersion. Adapted from Ref. 36.

(AB stack) graphene where the linear dispersion is no longer observable and instead appear parabolic bands with zero value at the Fermi level (Figure 7b). Interestingly, the band gap of this bilayer graphene can be opened by an external electric field, property that could have technological applications.[31] Adding a third layer allows the system to recover its linear dispersion but the electronic structure has more complexity being a combination of a monolayer and a bilayer graphene (Figure 7b). The trend observed for AB staking for additional layers ($N < 10$) suggest that for N-layered graphene, if N is odd, then the electronic structure will have linear dispersion[32] (Figure 7c). The effect of having more than two layers yields an electronic structure with several carriers and the conduction and valence bands increments its overlapping.[2,30,33] Considering this, the 2D-graphenes are classified into three classes: single-, double-, and few-($N < 10$) layer graphene. Thicker graphenes

can be considered thin films or slabs of graphite.[9] Finally, it is important to mention that the staking order or disorder has dramatic effect on the electronic properties of multilayer graphene where Dirac fermions can appear as a consequence of symmetry breaking.[34,35]

2.2. Chirality and quantum hall effect

Chirality[18] is another important quantity that appears as a consequence of QED in graphene. Basically, this quantity is related to the fact that k electrons and $-k$ holes (lack of electrons) states are connected because they originate from the same carbon sublattices. Several experiments on graphene monolayers have already observed the exotic behavior of Dirac fermions. The conductivity (σ) increases linearly with the gate voltage (V_g) (see Figure 8a). Interestingly, the conductivity does not becomes zero when the concentration of carriers n tend to zero ($n \approx \alpha V_g$, $\alpha \approx 7.3\times10^{10}$ cm^{-2} V^{-1}),[37] the minimum for $\sigma_{min} = 4e^2/h$. This quantized minimum of conductance has also been observed in two-and three-layered graphene.[37] The theoretical prediction for σ_{min} is $4e^2/h\pi$ being π times smaller than the observed value.[38–41] This discrepancy is

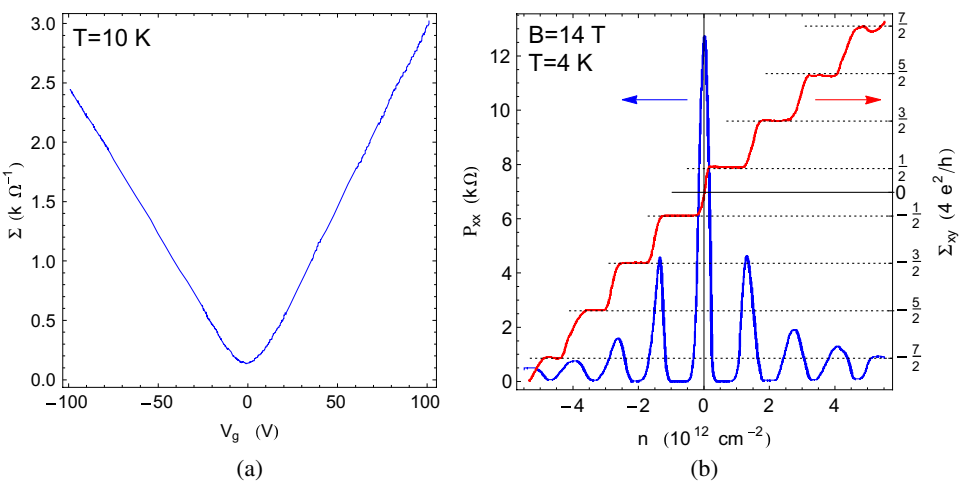

Figure 8. Experimental evidence of Dirac fermions in graphene. (a) Change of the conductivity σ as a function of voltage gate V_g at 10 K. Extrapolating $\sigma(V_g)$ for electron and holes yields a non-zero conductivity. (b) Half-integer QHE in graphene as a function of carrier concentration n at $B = 14$T and $T = 4$K; the red line depicts the Hall conductivity σ_{xy} where the horizontal dotted lines show the plateaux at half-integer of $4e^2/h$. The blue line shows the SdH oscillations observed in the longitudinal resistivity p_{xx}, the peak at the Dirac point ($n = 0$) is due to a Landau level at zero energy. Adapted from Ref. 37.

known as the *mystery of the missing pie*.[9] Some suggest that this difference is an experimental limitation but it could also be a consequence of the theoretical approximation of the electron scattering in graphene. Geim and Novoselov have suggested that this difference could be solved considering that at the neutrality point, the graphene conducts as a random network of electron and hole puddles that is related to the inherently graphene sheets warping/rippling.[9]

Anomalous quantum hall effect (QHE) is another important property observed in graphene. The observed Hall conductivity of pristine graphene σ_{xy} and its resistivity ρ_{xx} as a function of the electron and hole concentration n at constant magnetic field and low temperature is displayed in Figure 8b. The conductivity shows a ladder feature with a series of plateaux distributed equidistantly at $4e^2/h\nu$, where ν takes values of $N+1/2$, N is the Landau level index.[14,42] Interestingly, σ_{xy} does not become zero at the Dirac point where $n = 0$; furthermore, the fact that ν is not integer makes it a non-standard QHE and it is commonly known as half-integer QHE. In addition, the Shubnikov-de Haas (SdH) oscillations observed in the longitudinal resistivity ρ_{xx}, each peak corresponds to a Landau level. Notice the peak at the Dirac point ($n = 0$) that is responsible of the anomalous QHE. The explanation of this behavior lies in QED-like quantization of the electronic levels of graphene in the presence of a magnetic field B and expressed like $E_N = \pm v_F\sqrt{2e\hbar BN}$, where ± stands for electrons and holes.[43–45] The existence of a quantized level at zero E is the key to understand the anomalous QHE.[44,45]

2.3. The Klein tunneling in graphene

The implications of the behavior of electrons in graphene as massless Dirac fermions have opened the possibilities of making tabletop experiments on QED. The Klein paradox[46,47] is an exotic consequence of massless Dirac fermions when tunneling through an arbitrarily high potential barrier. The QED predicts that carriers in graphene hitting a potential step transmit with probability one, independently of the width and height of the step. The fundamental explanation suggests that a strong enough repulsive potential for the electrons is attractive to the holes that results in hole states within the barrier which align with the continuum electron states outside the barrier. Correspondence between the wavefunctions of those holes with the electrons on the other side of the barrier yields the high tunneling transmission.[28,47] This is in contrast with normal electrons crossing a potential where its amplitude decays exponentially. The Klein paradox in graphene can be shown theoretically considering potential barrier V_0 with a rectangular shape and width D along the x axis (see Figure 9).

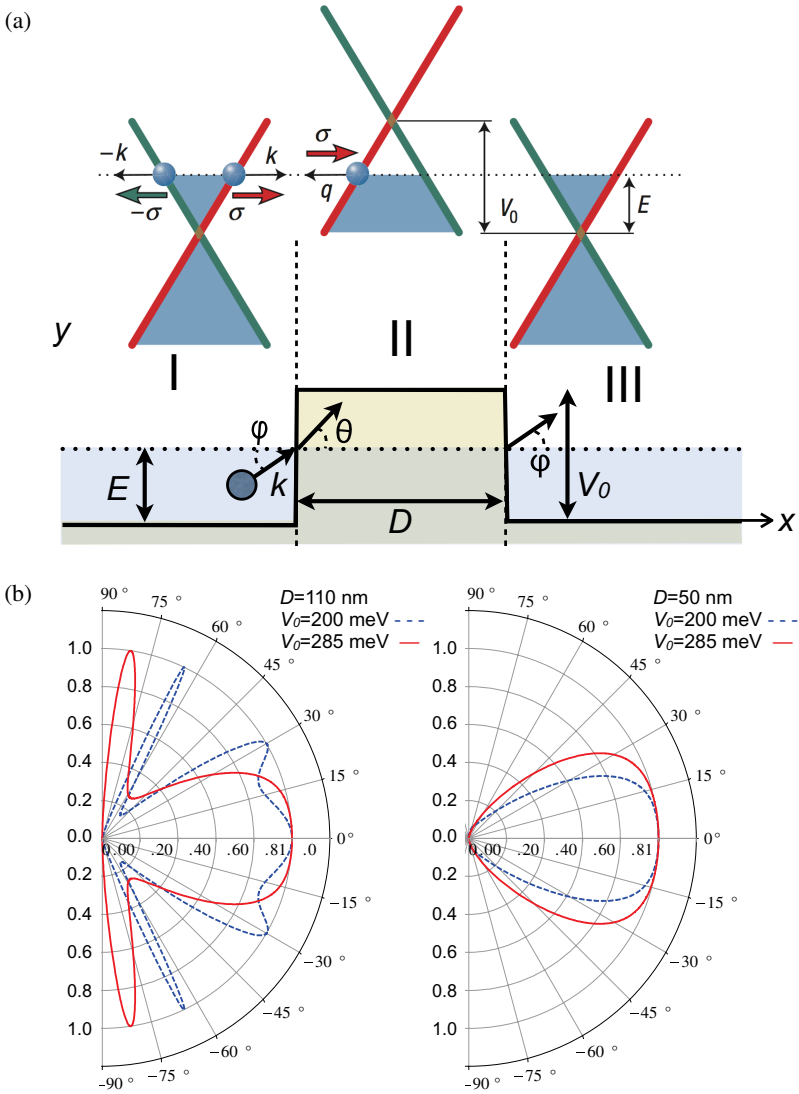

Figure 9. Klein tunneling in graphene. (a) Top: sketch of the graphene band structure around ***K*** point. The linear dispersion is a sign of relativistic carriers where the blue and green lines originate from the *A* and *B* sublattices, respectively. Bottom: Diagram of the square potential barrier V_0 and width D; it also displays the definition of the angles θ and ϕ used to define wavefunctions in regions I, II, and III. In both sketches, the position of the Fermi level E is denoted by the horizontal dotted line and the blue filled areas indicate occupied states. The pseudo spin denoted by vector σ conserves its direction along the green and red branches of the electronic spectrum. Adapted from Ref. 47. (b) Transmission probability $T(\phi)$ as solved in Eq. (12) with $E = 80$ meV, $v_F = 10^6$ ms^{-1}, $k_F = 2\pi/\lambda$, $\lambda = 50$ nm. Left: $D = 110$ nm and $V_0 = 200$ meV (dotted blue line) and 285 meV (red line). Right: $D = 50$ nm and $V_0 = 200$ meV (dotted blue line) and 285 meV (red line).

The Hamiltonian that describes this system can be approximated by $\widehat{\mathcal{H}} = \widehat{\mathcal{H}}_K + V(x)$, described by Eq. (7). Thus, the wavefunction around $\boldsymbol{K}$ can be expressed like[28]

$$\psi_{\kappa}(\boldsymbol{\kappa}) = \frac{1}{\sqrt{2}}\begin{pmatrix} 1 \\ \pm e^{i\phi k} \end{pmatrix}. \tag{8}$$

This wavefunction can be expressed as a combination of incident and reflecting wave depending on the region (I, II, and III; as depicted in Figure 9). For region I, we have:

$$\psi_{\mathrm{I}}(r) = \frac{1}{\sqrt{2}}\begin{pmatrix} 1 \\ se^{i\phi} \end{pmatrix} e^{i(k_x x + k_y y)} + \frac{r}{\sqrt{2}}\begin{pmatrix} 1 \\ se^{i(\pi-\phi)} \end{pmatrix} e^{i(-k_x x + k_y y)}, \tag{9}$$

with $\phi = \arctan(k_y/k_x)$, $k_x = k_F \cos\phi$, $k_y = k_F \sin\phi$, where k_F is the Fermi momentum. Region II, ψ becomes:

$$\psi_{\mathrm{I}}(r) = \frac{1}{\sqrt{2}}\begin{pmatrix} 1 \\ s'e^{i\phi} \end{pmatrix} e^{i(k_x x + k_y y)} + \frac{r}{\sqrt{2}}\begin{pmatrix} 1 \\ s'e^{i(\pi-\phi)} \end{pmatrix} e^{i(-k_x x + k_y y)}, \tag{10}$$

with $\theta = \tan^{-1}(k_y/q_x)$ and $q_x = \sqrt{(V_0 - E)^2/(\hbar^2 v_F^2) - k_y^2}$; in addition, $s = \mathrm{sgn}(E)$ and $s' = \mathrm{sgn}(E - V_0)$. Finally, in region III, there is only a transmitted wave

$$\psi_{\mathrm{III}}(r) = \frac{t}{\sqrt{2}}\begin{pmatrix} 1 \\ se^{i\phi} \end{pmatrix} e^{i(k_x x + k_y y)}. \tag{11}$$

In these equations, r, a, b, and t are coefficients that can be solved considering that the wavefunctions only need to be continue on the boundaries of the barrier, but in contrast to the Schrödinger equation, the continuity of the derivative is not necessary.[28] After doing some algebra, one can arrive to a solution for the transmission as a function of the angle ϕ:

$$T(\phi) = \frac{\cos^2\theta\cos^2\phi}{[\cos(Dq_x)\cos\phi\cos\theta]^{2+}\sin^2(Dq_x)(1 - ss'\sin\phi\sin\theta)^2}. \tag{12}$$

Figure 9b shows the change of the transmission probability T with the angle ϕ as expressed by Eq. (12). The plots clearly show preferable directions for which the transmission becomes 1. The asymptotic form of $T(\phi)$, in the limit when $|V_o| \gg E$, can be expanded to a simplified form that yields:

$$T(\phi) \simeq \frac{\cos^2\phi}{1 - \cos^2(Dq_x)\sin^2\phi}. \tag{13}$$

Notice that for Eqs. (12) and (13), $T(\phi)=1$ in the following conditions: (i) $Dq_x=n\pi$, with $n=0, \pm1, \cdots$; (ii) normal incidence — *i.e.*, θ and ϕ is 0 with any value of Dq_x. In those cases, the barrier becomes totally transparent. These results encompass what is known as the Klein paradox in QED.[28,47]

2.4. Atomic collapse on graphene

How big can a nucleus be? Fundamental limits are imposed when the number of protons Z within a nucleus pass a critical value $Z_c \sim 170$.[48–51] QED predicts that under such critical conditions, an electron–positron can be generated from the vacuum. The electron will collapse in the super-heavy nucleus discharging it and the positron will diffuse away from it;[52] this process is called atomic collapse. Experimental observation of atomic collapse is challenging. Superheavy nuclei is needed to be produced. Furthermore, the most heavy nucleus observed so far is $Z=118$ with a short lifetime.

Graphene provides the basic elements needed for the realization of atomic collapse.[28,37,42] Relativistic charge carriers (electrons and holes) in graphene mimics the virtual particles present in the vacuum in QED; impurity atoms that are attached to the graphene and gaining charge (Coulomb impurity) can be considered as atomic nuclei. Moreover, the large fine-structure constant value allows the occurrence of atomic collapse for $Z_c \simeq 1$.[53–55] Theoretical calculation predicts that in graphene, the atomic collapse state will appear as a spatially extended electronic resonance which quasi-bonded electronic state energy is just below the Dirac point. This prediction has been experimentally observed by the aid of precise atom manipulation on graphene using STM[19] (see Figures 10a and 10b). It is important to mention that STM has a unique advantage to probe locally the electronic properties of conductive surfaces.

The experimental realization is challenging (see Figure 10c). A particular STM setup is needed to successfully produce atomic collapse. A graphene layer is mechanically placed over a BN flake set upon a SiO_2 substrate, this arrangement allows uniform background charge distribution.[56] The electronic structure at the surface can be probed measuring the changes of the tunneling current with the applied bias voltage V_{BIAS} and the distance between the sample and the STM tip. Moreover, a backgate voltage V_G is applied to the doped Si electrode that allows to change the charge-carrier doping of graphene. Atomic manipulation of Ca atoms on the graphene/BN/Si_2 can arrange calcium dimers with $+e$ charge. The experimental results shows that a cluster formation of five of such charged Ca-dimers (that mimics the charge of a boron nucleus) on graphene is enough to produce atomic collapse observed by STM. Figure 10a displays the observed change of the

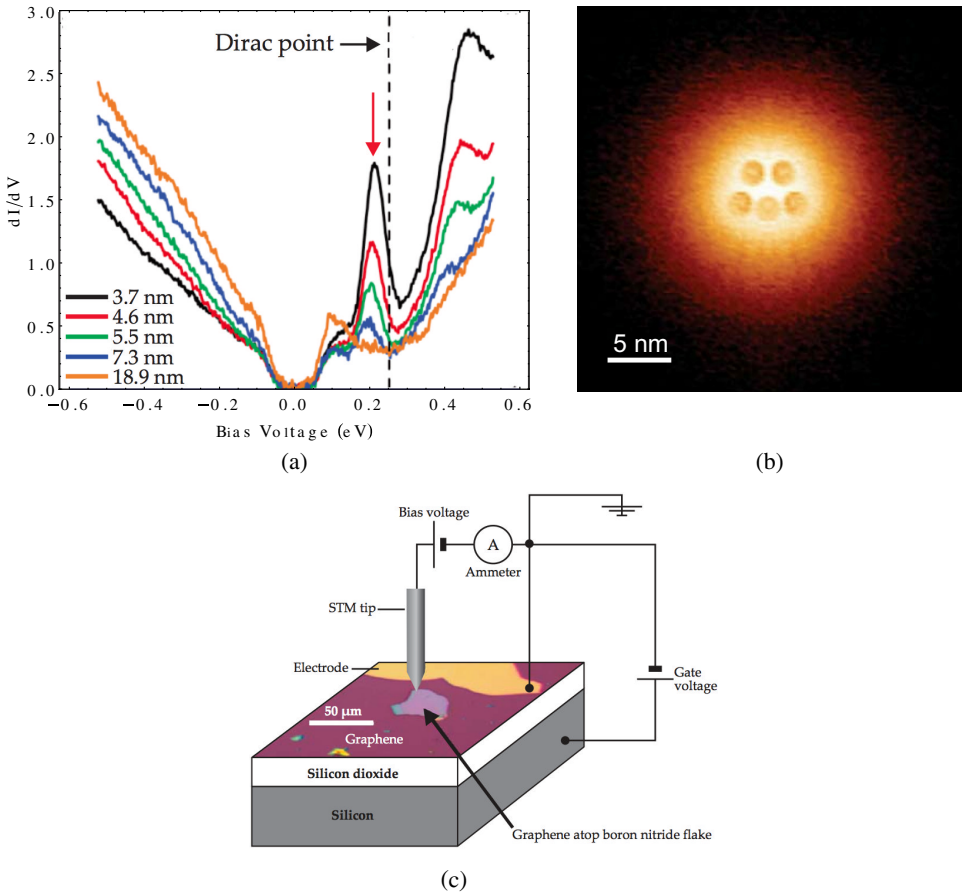

Figure 10. Atomic collapse observed in graphene. (a) dV/dI variation with the V_{BIAS} and fixed $V_G = -30$ V, for a series of tip–cluster distances going from 3.7 to 18.9 nm. The tip is located just above the center of the five Ca-dimer cluster. The Dirac point is pointed by the dotted vertical line at ~0.25 eV and the red arrow indicates atomic collapse state. (b) dV/dI map at the Ca-dimer cluster for $V_{BIAS} = +0.2$ eV that corresponds to the resonant state; tunneling parameters: $I = 15$ pA, $V_G = -30$ V. Adapted from Ref. 19. (c) Experimental STM setup to measure the local electronic properties of Ca-dimer cluster deposited on the graphene/BN/SiO_2. Adapted from Ref. 56.

tunneling current I with V_{BIAS}, dV/dI, for a series of tip–sample distances. Mind that dV/dI is directly related to the local density of states (LDOS) at the surface. The spectra shows the Dirac point at ~0.2 eV instead of 0 eV. This shift is explained by the effect of an applied gate voltage that prepopulates the sample with holes. Moreover, the apparent gap of ~0.2 eV around $V_{BIAS} = 0$ is a consequence of phonon-assisted tunneling. The signature of the

atomic collapse appears as the peak just below the Dirac point for tip-sample distance of less than 18 nm (Figure 10a). Above that distance, the spectrum is similar to the one without Ca-dimers. The observed peak is a direct demonstration of the predicted quasi-bonded electronic. The spatia distribution of that state is clearly observed in the dV/dI map (see Figure 10b) as the halo around the Ca-dimer cluster. The implications of this experiment are relevant for miniaturization of graphene-based electronics and leads to fundamental open questions such as what new properties could be observed for a periodic arrange of such Ca-dimer cluster?[19]

3. Elastic Properties of Graphene

The outstanding mechanical properties of graphene is also another feature of this material that could find important technological applications.[9,57] The ultrastrength observed not only on graphene but also in carbon nanotubes is a direct consequence of the covalent sp^2 hybridization between carbon atoms. Strength and stiffness are essential for the stability and durability of many devices.[58] The state-of-the-art measurements on the elastic properties of pristine graphene yields a Young's modulus (Y) of ~1000 GPa and a tensile strength (σ_T) of ~130 GPa[59] — *i.e.*, it is around 200 times stronger than structural steel (A36). To illustrate the magnitude of graphene's σ_T, this material could sustain a weight of 13 tons suspended in 1 mm^2 surface area. A fundamental study of Griffith[60] suggest that the actual breaking strength of a brittle material is governed by the sizes of defects and flaws within the material, rather than the intrinsic strength of its atomic bonds. Nevertheless, when the characteristic size of the system becomes around or less than $L_C \sim 10^2$nm, the population dynamics of defects is fundamentally different from that in the macro-system.[61] Table 1 lists the elastic properties of graphene and other allotropes of carbon.

Measuring the intrinsic strength of graphene or carbon nanotubes is challenging due to the uncertainty of the geometry of the sample, defects, and grain boundaries. Experimental sophistication allowed Lee *et al.* to accurately measure the mechanical properties of graphene.[59] The experimental setup includes atomic force microscope (AFM) nanoindentation to measure the elastic properties of monolayer graphene membranes suspended over open holes (diameters 1.5 μm and 1 μm, depth 500 nm) formed in a Si substrate with a 300 nm SiO_2 epilayer by nanoimprint lithography and reactive ion etching (see Figure 11a). The force–displacement response by a AFM tip on monolayer graphene can be described by[59,68]

Table 1. Elastic properties of several allotropes of carbon. The experimental values of the Young's moduli Y and the tensile strength σ_T are listed. SWCNT (MWCNT) denotes single-wall (multi-wall) carbon nanotubes. The values within parenthesis are the density-functional theory within the local density approximation (DFT-LDA) predicted values.

Material	**Y (GPa)**	σ_T **(GPa)**
Graphene[a,f]	1000 ± 100 (1050)	130 ± 10 (121)
SWCNT[b]	320–1470	13–52
MWCNT[c]	200–950	11–150
Diamond[d]	1063	—
	1020*	—
Graphite[e]	36.5†	—

[a] Ref. 59.
[b] Ref. 62.
[c] Refs. 63 and 64.
[d] Ref. 65: along the cubic axis.
[e] Refs. 66 and 67: *in the basal plane and †along the *c* axis.
[f] Ref. 61.

$$F = \sigma_0^{2D}(\pi a)\left(\frac{\delta}{a}\right) + E^{2D}(q^3 a)\left(\frac{\delta}{a}\right)^3, \tag{14}$$

where F is the applied force, a and δ are the diameter and the deflection at the center point of the membrane, respectively; σ_0^{2D} is the pretension on the film, $E^{2D} = d_0 Y$ is an elastic constant in units of force/length which is directly proportional to its Young's modulus by the interlayer spacing in graphite (d_0 = 3.35Å[69]). Finally, $q = 1/(1.050.15\nu 0.16\nu^2) = 1.02$ is a dimensional parameter expressed in terms of the Poisson's ratio for graphite in the basal plane (ν = 0.165).[66] The fit of this equation to the experimental data displayed in Figure 11a yields a mean E^{2D} of 342 Nm^{-1} and a standard deviation of 30 Nm^{-1}.[59] Figure 11b shows the experimental stress–strain curve where the maximum stress (or tensile strength) is ~130 GPa.

Theoretical simulations using *ab initio* DFT already predicted the ultrastrength of grapheme.[61,70] Figure 11b shows the predicted stress–strain curve; here, the strain is defined like $\varepsilon = L/L_0 - 1$. From these results, DFT predicts that for small strains ($\varepsilon \lesssim 0.1$), graphene is isotropic with a Young's modulus y = 1050 GPa and Poisson's ratio ν = 0.186. These simulations used a four-atom cell as depicted in the inset of Figure 11b. When $\varepsilon > 0.1$, the lattice

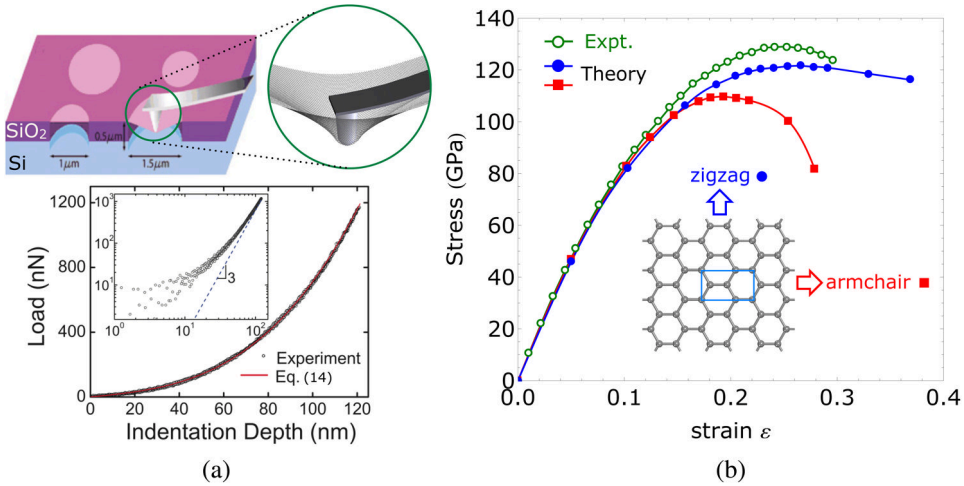

Figure 11. (a) Top panel: AFM nanoindentation of a monolayer graphene membrane deposited onto a Si/SiO_2 substrate with an array of circular wells 500 nm depth and diameters of 1.5 μm and 1 μm; the close up shows the AFM cantilever with diamond tip. Bottom panel: measured loading/unloading data, the red line is the fitting using Eq. (14); notice the asymptotic cubic behavior for high loads depicted in the inset. (b) Elastic properties of monolayer graphene: experiment vs theory. The strain–stress curves shows the non-linear elastic behavior of graphene. The green lines is the experimental result from AFM nanoindentation measurements[59] and the blue (red) line is the result from DFT simulations along the zigzag (armchair) direction.[61] The inset displays the graphene lattice where the light-blue line delimits the four-atom cell used for the simulations. Adapted from Refs. 59 and 61.

symmetry is broken and the stress response becomes anisotropic as it depends on the strain direction. The predicted maximum strain (or tensile strength) along the zigzag (armchair) direction in graphene yields 121 (110) GPa at ε of 0.266 (0.194) (see Figure 11b).[61] The computed values are in good agreement with the experimental values. Figure 12 shows the computed zero-stress phonon dispersion along the Γ-M-K-Γ using DFT. The lowest branch at Γ point, the frequency $\omega = kK^2$ and it describes free bending wave of the graphene sheet at zero stress, here κ is proportional to the bending modulus of the sheet; this allows graphene to have a finite density of states at zero frequency.[61]

It is important to stress the fact that the reported values of elasticity for graphene applies if no defects are present. In general, graphene materials have always some structural defects.[9,74,75] It is well reported that defects such as monovacancies and Stone–Wales (SW) dislocations,[76] slits, and holes,[77,78]

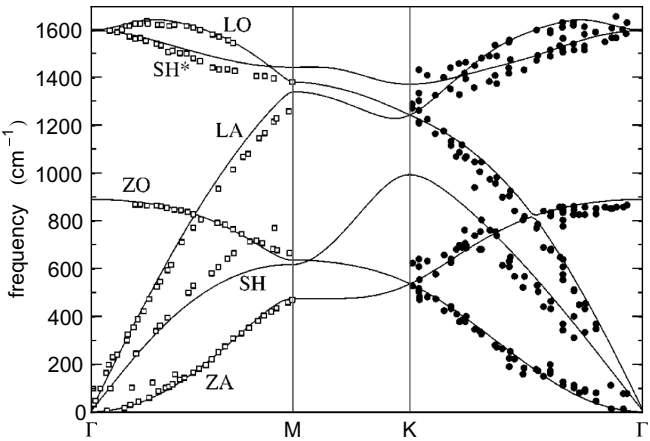

Figure 12. Phonon dispersion of graphene at zero stress: theory vs experiment. The DFT computed dispersion by Dubay *et al.*[71] is displayed with solid lines. The empty squares are the experimental reflection electron-energy-loss spectroscopy data from Oshima *et al.*[72] The full circles corresponds to the high-resolution electron-energy-loss spectroscopy data of Siebentritt *et al.*[73] Adapted from Ref. 71.

affect the mechanical properties of graphene. For instance, the inclusion of large slits or holes drastically reduces the fracture strength of graphene sheets to 30–40 GPa.[77,78]

4. Structural Defects in Graphene

Crystal disorder in a material is a fundamental consequence of the second law of thermodynamics. In addition, imperfection in material production processes yields, as a result, impurities and defects in actual crystalline materials. Lattice defects play a relevant role in the mechanical, electronic, optic, and thermal properties of any material. It is well documented that properties of technologically important materials like the mechanical strength and ductility or the conductivity of semiconductors are controlled by defects.[79]

Theoretical studies have already predicted outstanding properties of pristine graphene. The experimental confirmation of the theoretical predictions triggered the need for graphene samples that in turn motivated the development of large-scale synthesis methods like chemical vapor-deposition[80,81] and epitaxial growth on metal and SiC substrates.[82,83] The experimental observation of some graphene properties as predicted, is only realizable when it has ultra-low defect concentration. Fortunately, the formation energy of points defects in graphene is high (*cf.* Table 2) allowing to keep graphene samples as pristine as possible. Nevertheless, defects are present in graphene and have a

Table 2. Compendium of the formation and migration energies (points defects only) of defects in graphene based on DFT predictions.

Defect type	Configuration	Formation energy (eV)	Migration energy (eV)	Figure	Ref.
Stone–Wales	55–77	4.5–5.3	10	13(a)	92, 93
Single vacancy	5–9	7.3–7.5	1.2–1.4	13(b)	95
Double vacancy	5–8-5	7.2–7.9	7	13(c)	95, 97
	555–777	6.4–7.5	6	13(d)	96, 104
	555–6-777	7	6	13(e)	94
Adatom	—	6–7	0.4	14	98, 99
Inverse SW	57–57	5.8	—	15(a)	101
Inverse SW+SW	—	6.1	—	15(b)	101
Adatom-SV pair	—	14	—	—	101
GBL (13 atom core)	C_3	9.3	—	16(a)	103
GBL (24 atom core)	C_6(1,1)	7.0	—	16(b)	103
GBL (54 atom core)	C_6(2,1)	19.9	—	16(c)	103

Part of this table was adapted from Ref. 75.

dramatic impact on its properties. In addition, defects can also be induced, for instance, by chemical treatment and radiation. The effects observed in 3D-crystals also applies in graphene. The scattering of the electron waves at the defects has important impacts on the electron conductivity. The mechanical strength and thermal conductivity are also affected by the weakening of the bonds around the defect. The stability of carbon allotropes lies on the capacity to form different hybridization depending on the coordination: sp, sp^2, and sp^3. The sp^2-hybridization of carbon, where graphene constitutes its most stable configuration with hexagonal arrangement, is not the only possibility as in general sp^2-hybridization can form different polygons, including hexagons. The flexibility of 2D-carbon structures to form non-hexagonal structures with no dangling bonds and with no under-coordinated carbons, can effectively change the local electronic structure that increases the reactivity of the structure allowing the possibility to absorb other atoms.[75] Since graphene is truly a 2D-crystal, real space spectroscopies are best suitable to observe defects. Indeed, STM[84,85] and transmission electron microscopy (TEM)[86–90] have been able to observe defects in graphene.

Despite the outstanding properties of graphene, technological applications are not straightforward. For instance, practical applications of graphene in electronics imply a modification of its electronic structure; pristine

graphene has zero band gap and it does not allow switching of grapheme-based transistors with a high enough on–off ratio. Graphene needs to be modified for practical applications in electronics.

In general, defects are classified considering if the lattice order is altered with (without) external atoms, it is denominated extrinsic (intrinsic) defects. In addition, defects have dimensionality that in the case of 2D-crystals, the defects could be zero- or one-dimensional. Moreover, defects can migrate producing effects on the defective lattice. Graphene could have defects where mobility along the plane could be high like the observed adatoms in pristine graphene or quite low like the observed in extended vacancies complexes. The mechanisms of migration are related to the activation barriers depending on the defect and increases exponentially with the temperature.[75]

4.1. Stone–Wales defects

The most simple point-defect (zero-dimensional) is where the defect is formed by a local lattice reconstruction in graphene that conserves both the density and the number of C atoms and there are no dangling bonds. This defect called SW[91] has one C–C bond that rotates 90° causing the reconfiguration of graphene lattice where four hexagons are transformed into two pentagons and two heptagons: SW(55-77) (Figure 13a). DFT calculations predict a high formation energy of ~5 eV.[92] The inplane rotation of the two C atoms involved have a kinetic energy barrier of ~10 eV while the reverse process involves a barrier of ~5 eV.[93] The high energy barriers suggest that SW(55-77) formation is negligible for temperatures below 1000°C. However, this defect can be formed under radiation and its high reverse barrier of 5 eV allows the SW(55-77) to be stable at room temperature.

4.2. Carbon vacancies

A missing C atom in graphene forms a *single vacancy* (SV) defect which is the most simple defect. It has been experimentally observed with TEM[88] and STM.[85] The atomic structure of this defect has been computed using *ab initio* DFT[95] and is shown in Figure 13b. An unrelaxed carbon vacancy site has three dangling bonds but after a Jahn–Teller distortion, the structure becomes stable saturating two dangling bonds forming a pentagon and leaving the remaining dangling bond unsaturated that forms a nine-carbon ring V_1(5–9). The DFT calculations suggest a high formation energy of ~7.5 eV, this high value can be justified by the presence of an undercoordinated C atom. The local electronic structure has been probed by

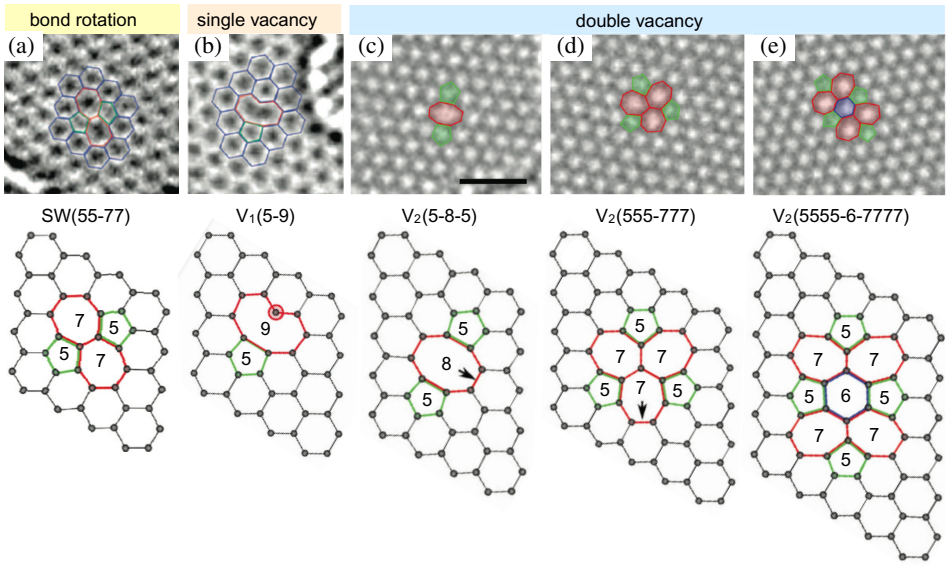

Figure 13. Intrinsic defects in graphene induced by irradiation and observed with high-resolution TEM. The creation of defects involves atom ejection and/or bond rotation. (a) 90° C–C bond rotation, SW. (b) Single vacancy V_1(5-9), (c) V_2 (5-8-5) divacancy, (d) V_2 (555-777) divacancy, and (e) V_2 (5555-6-7777) divacancy. The experimental TEM images in the top depict the superimposed bonds around the defect; the atomic structures in the bottom correspond to the DFT optimized coordinates by Banhart *et al.*[75] The ↘ points the C–C bonds that undergo a 90° rotation. Adapted from Refs. 75 and 94.

STM which shows a high electronic localization around the dangling bond (*cf.* Figures 19c and 19d). The computed energy migration barrier for SV in graphene is ~1.3 eV.[95]

Double vacancies can also form in graphene with different likely configurations and no dangling bonds, then it is expected to be more energetically stable than SVs. Figures 13c–13e depict three observed configurations. The V_2 (5-8-5) formed by two pentagons joined by one octagon has a DFT computed formation energy of ~8 eV[95] — *i.e.*, 4 eV per vacancy, thus this defect is thermodynamically more stable than SVs. The V_2 (555-777) is the more stable divacancy configuration (Figure 13d), it can be generated from V_2 (5-8-5) after rotating a C–C bond from the octagon (pointed by ↘ in Figure 13c). The energy formation of this divacancy defect is ~7 eV.[96] The configuration V_2 (5555-6-7777) has been also observed (Figure 13e) that can be formed from V_2 (555-777) with an additional C–C bond rotation

(pointed by ↘ win Figure 13d). The corresponding formation energy of this divacancy defect is between V_2 (5-8-5) and V_2 (555-777).[94] The migration energies of these divacancy defects are computed to be ~7 eV;[97] therefore, these defects are practically static at room temperature but they can start to migrate at high enough temperature.

4.3. Carbon adatoms

Contrary to carbon vacancies, adding extra C atoms in graphene can only happen as *adatoms*. This is because it is highly unstable to incorporate a carbon within the in-plane honeycomb lattice. The carbon is adsorbed on the graphene lattice forming a stable configuration with some sp^3 hybridization. The most likely adsorbed configuration is for the adatom in bridge site (Figure 14a) with a formation energy of ~7 eV (this corresponds to an absorption energy of ~2 eV).[98,99] The computed migration barrier of 0.4 eV suggests the easy mobility of C adatoms on graphene.[99] The metastable dumbbell configuration (Figure 14b) is another defective configuration and relevant in bilayer graphene, it has an energy 0.5 eV higher than the bridge configuration and its energy barrier migration is computed to be ~0.9 eV.[100]

The high mobility of carbon adatoms could allow the formation of a carbon dimer adsorbed on the graphene lattice (Figure 15a) This defect reaches stability by deforming the planar graphene lattice with some local curvature. This defect is known as inverse Stone–Wales (ISW) defect[101,102] formed by two pentagons and two heptagons, ISW(55-77). The computed formation energy is ~5.8 eV higher than two SW defects, thus it is unlikely to be seen but this defect could be used for tailoring the electronic properties of

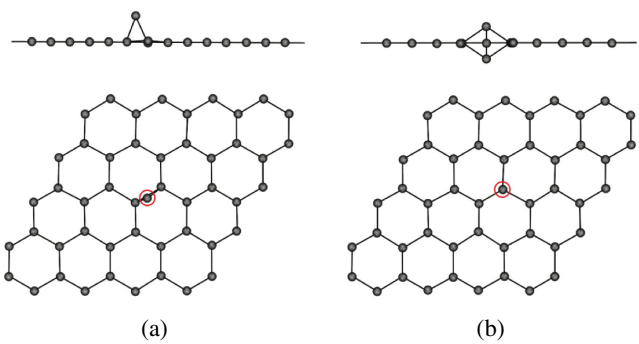

Figure 14. Single carbon adatom on graphene in (a) bridge and (b) dumbbell configurations. Adapted from Ref. 75.

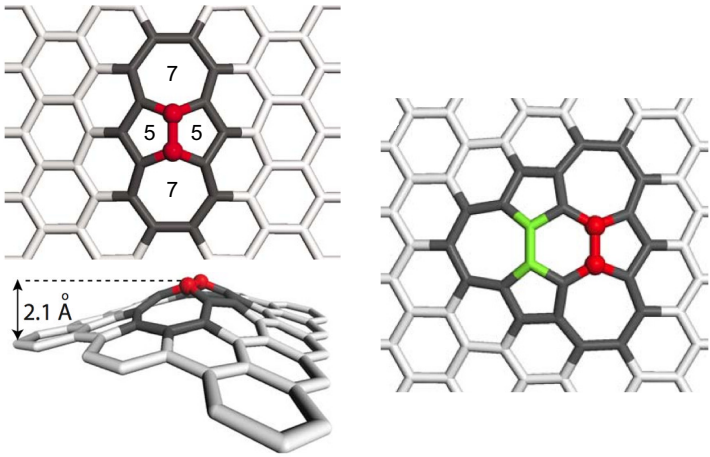

Figure 15. Defects with two carbon adatoms. (a) Computed structure of the ISW defect (55-77); bottom: notice the locally induced curvature; the two adatoms are in red. (b) Predicted structure of the ISW+SW defect formed by a ISW (red) and a SW (green) defects. Adapted from Ref. 102.

graphene.[101] There is another interesting configuration with three pentagons and three heptagons alternated around a hexagon. This defect can be considered as a combination of an ISW with a SW defect and is called as ISW+SW defect. The computed formation energy is ~6.1 eV[101] that is 0.3 eV higher than an ISW defect. A periodic arrangement of this defect yields the theoretically predicted Haeckelite structure that is 229 meV/atom less stable than graphene[101] but to the best of our knowledge has not yet been made experimentally.

4.4. Grain boundary loops

There are other type of structural defects that also keep the graphene density and the coordination. The grain boundary loops (GBL) are a family of defects that can be formed by extracting certain part of the graphene lattice and reinserting it after rotating certain angle.[103] Depending on the number of atoms of the rotated section (core atoms), the boundary of the defect is formed by pentagons, hexagons, and heptagons. The SW defect can be considered a member of this GBL family as it is formed by a 90° rotation of two core atoms. Figure 16 displays a family of possible GBL with C_3 and C_6 symmetry. STM experiments have already observed one of such GBL defects, the C_6 (1, 1) has a core of 24 atoms rotated 30° (Figure 16b), the DFT computed

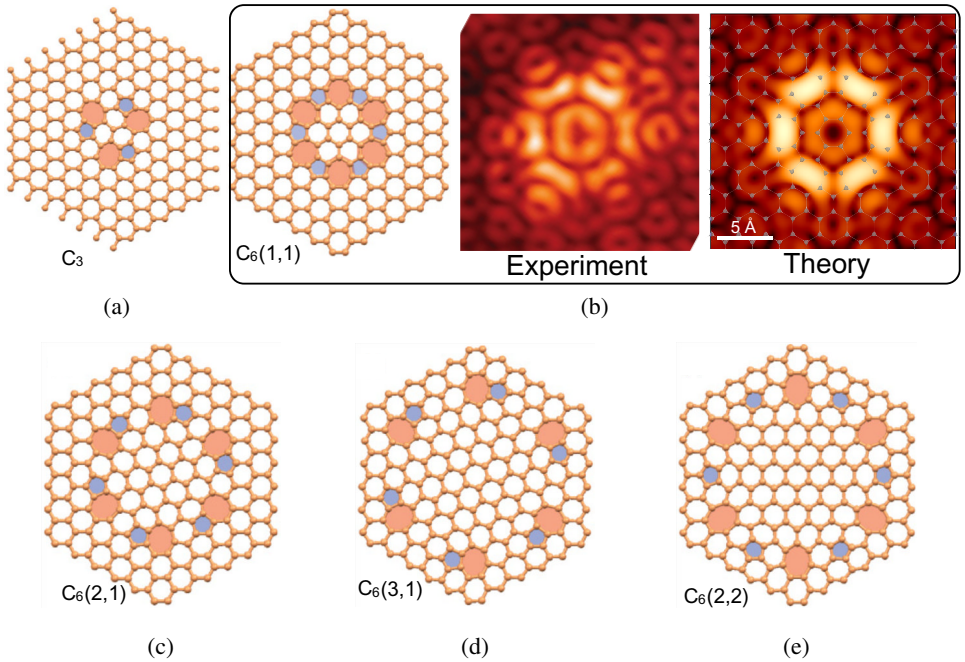

Figure 16. Atomic configurations of some GBLs with different number of core atoms. (a) The 13 atom core with C_3 symmetry. (b) The $C_6(1, 1)$ with 24 atom core, the center panel shows the experimental STM image in topographic mode with tunneling current of 100 pA and bias voltage of 0.3 V (empty states) at $T = 4.3$ K; the right panel is the DFT computed STM image for the same bias voltage, the corresponding lattice is superimposed in the image. (c) The $C_6(2, 1)$ with 54 atom core. (d) $C_6(3, 1)$ and (e) $C_6(2, 2)$. In all the figures, the pentagons and heptagons are highlighted by pink and blue colors, respectively. Adapted from Ref. 103.

formation energy is ~7 eV — *i.e.*, ~1.2 eV per pentagon–heptagon pair;[103] this is lower than for SW defects that have ~2.5 eV per pentagon–heptagon pair. The computed formation energies for C_3 (Figure 16a) and $C_6(2, 1)$ (Figure 16c) are 9.3 and 19.9 eV, respectively; this means that $C_6(1, 1)$ is the most stable of the GBL defect family. The $C_6(1, 1)$ has also been observed using TEM for graphene grown in Ni substrate. Given the size of these defects, it could be infered that the energy migration would be high but to the best of our knowledge, there is no calculation of energy barriers for these defects.

4.5. Noncarbon adatoms and substitutional impurities

The iteration between TM adatoms and pristine graphene has been computed to be weak with activation energies of 0.14–0.8 eV.[105–107] In general, the

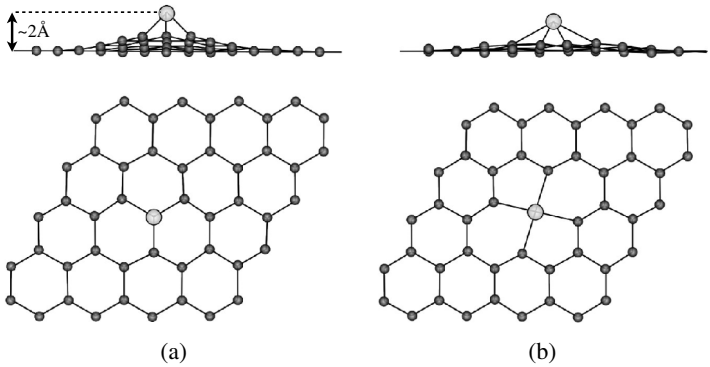

Figure 17. Typical structure of TM adatoms interacting with (a) SV and (b) double vacancy sites. On the top (bottom) is the top (side) view of the structure. These structures are non-planar. In this figure, the carbon (metal) atoms are represented by small (big) circles. Adapted from Ref. 75.

strength of the interaction of noncarbon atoms with graphene could be weak, where no actual bonding is formed and van der Waals interactions are important, or strong with covalent character. Defects like V_2(555-777) and ISW(57-57) introduce reactive sites on inert graphene.

Substitutional atoms are also likely to happen in graphene. The most common are boron or nitrogen because of their similar atomic radii with carbon. These atoms can efficiently affect the electronic structure of graphene introducing reactive sites into the lattice thus allowing some functionalization of graphene.[108,109] TM atoms can effectively interact with under-coordinated carbon atoms forming strong covalent bonds that is reflected in the computed binding energies of 2–8 eV.[106,110] In addition, the stable configuration of such defects is non-planar due to the perturbation of the TM adatom that has bigger atomic radii than carbon. Figure 17 depicts typical atomic configurations of TM with single and double vacancies.

4.6. Grain boundaries

These one-dimensional defects have been observed in graphene with STM[111] and high-resolution TEM.[112] It is known that these defects are likely to happen when graphene is grown by chemical deposition on metal surfaces with hexagonal symmetry; usually on (0001) surfaces of hexagonal or (111) of cubic crystals.[113,114] On weakly interacting metals, simultaneous nucleation of different rotational-domain can grow, the intersection of two grains with different orientation can form a line defect. Understanding of grain

boundaries defects requires the definition of Burgers vector and a dislocation line. Similar as in bulk materials, these boundaries can be described by a linear array of edge dislocations. Figures 18a–18e depict some elements of a single dislocation: it can be seen as an alternate arrangement of pentagons and heptagons pairs to obtain zigzag or armchair-oriented tilt grain boundaries. The orientation and position of these pairs determine the Burgers vector and the separation of these dislocations determines the tilt angle in a grain boundary. These defects have a non-planar structure predicted by DFT calculations (see Figure 18a).

4.7. Effect of defects on the properties of graphene

The effect of defects in graphene is still not well understood despite the considerable number of available experimental observations and the vast theoretical work. One of the limitations is the lack of reproducible experimental results. Nevertheless, defects play a key role in tailoring graphene properties for specific proposes. This section only presents selected examples as this chapter is not intended to cover all the predicted properties due to defects in graphene.

From a *chemical perspective*, DFT simulations have already predicted that the induced dangling bonds by vacancies in graphene will increase the reactivity of graphene: hydroxyl, carboxyl, or other groups can be easily absorbed in those sites.[108] Local reactivity is also enhanced by defects with no dangling bonds like SW or reconstructed vacancies, this effect is explained by changes in the local distribution of the π-electron density on those sites.[108,115]

From an *electronic perspective*, defects can dramatically change the electronic properties of graphene. One of the most impressive examples is the atomic collapse observed in graphene. This effect was observed by clustering charged Ca-dimers on graphene.[19] In general, the electronic properties of graphene are determined by the overlap of p_z orbitals that are perturbed around the defect. Several factors induced by defect-like changes in the bond length or induced local curvature lead to rehybridization of the σ- and π-orbitals that in turn have a direct effect on the electronic structure of graphene. SV defects can induce localized states the Fermi level; the band gap of graphene can be manipulated by certain vacancy-defects[116] and SW defects,[117] this can be important for future applications of graphene in electronics. Furthermore, points defects in graphene have shown exceptional optical properties. This defect is observed to convert light into an electronic signal and vice versa, making it a nanoantenna in the petahertz frequency range that leads to surface plasmon resonances at the subnanometer scale[118] (see Figure 19).

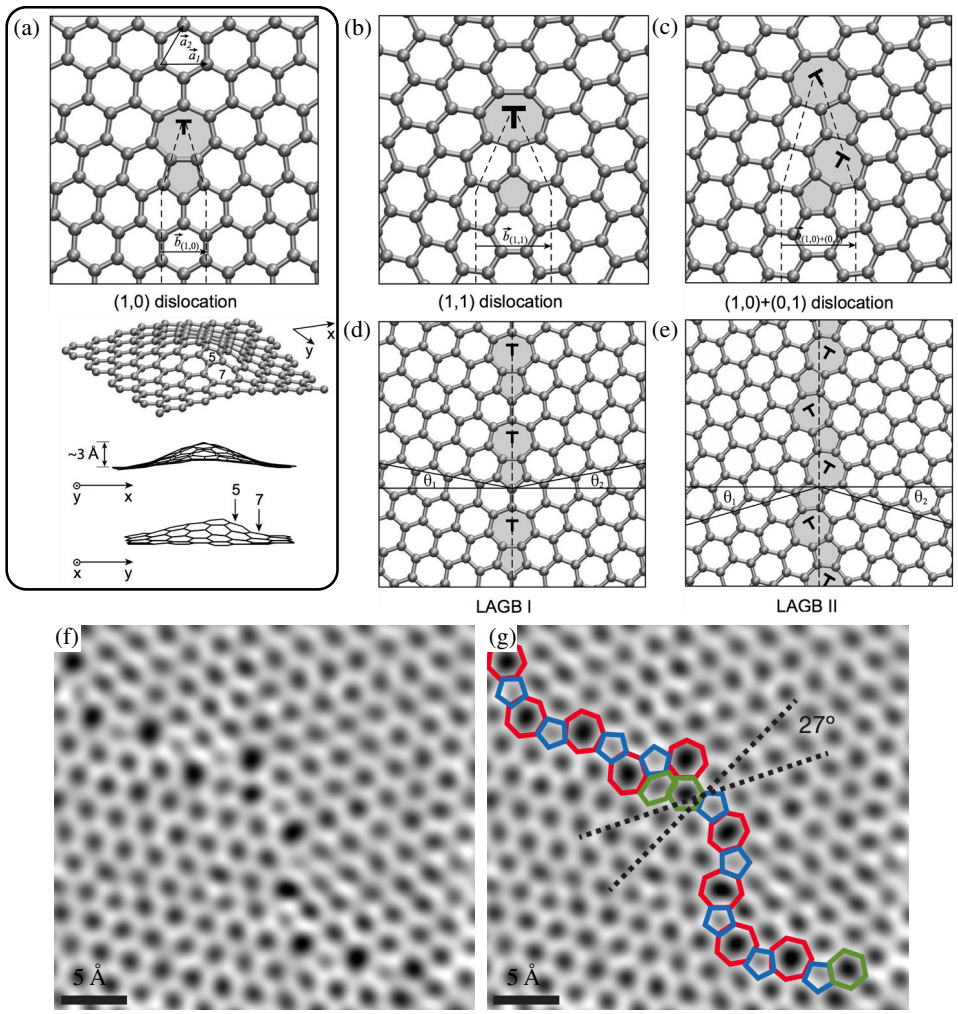

Figure 18. Atomic structure of grain boundaries in graphene. (a) Top and perspective views of a (1, 0) dislocation; notice the induced buckling due to the dislocation. (b) The (1, 1) dislocation. (c) Dislocation pair (1, 0) + (1, 1). (d) and (e) structure of the $\theta = 21.8°$ and the $\theta = 32.2°$ symmetric large-angle grain boundaries, respectively. The dashed lines denote the boundary lines. Adapted from Ref. 114. (f) Atomic resolution TEM image of two grains intersecting with a 27° relative rotation. (g) Same image where is highlighted the elements of the dislocation: pentagons (blue), heptagons (red), and distorted hexagons (green). Adapted from Ref. 112.

Doping of graphene by defects can be a consequence of intrinsic or extrinsic defects that modifies the π-electron system. Intrinsic defects modify the electronic defect locally due to the defect-induced electron-hole asymmetry, this effect is also known as "self-doping".[28] Extrinsic defects like metal

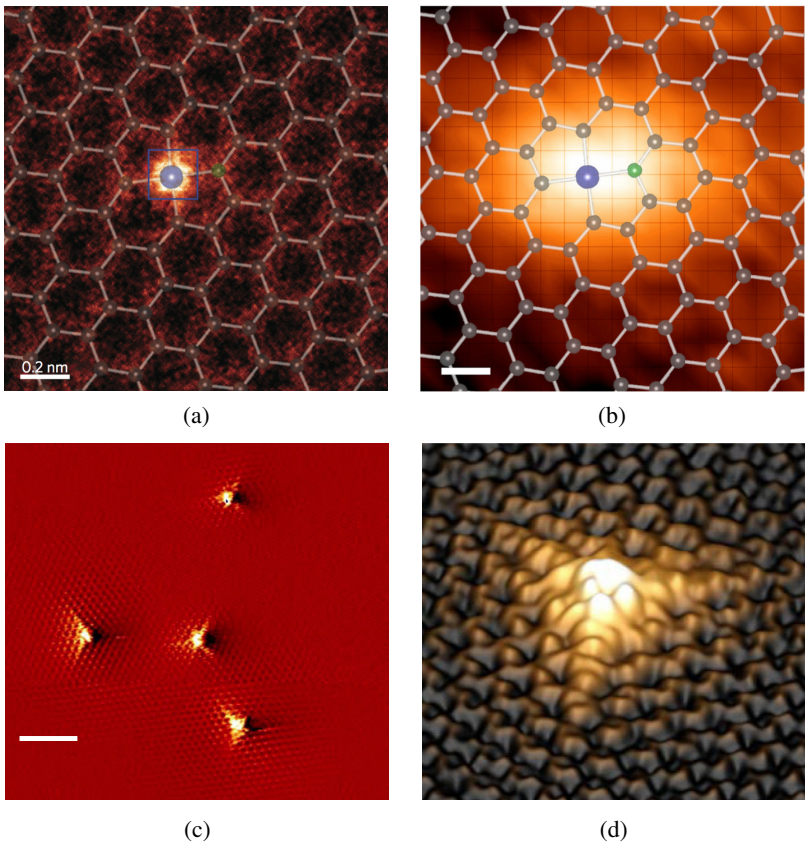

Figure 19. Atomic scale properties of defective graphene. Localized plasmons at defect sites: (a) high-resolution TEM of a complex defect site with superimposed lattice showing the atoms carbon (gray), nitrogen (green), and silicon (blue), the (b) Plasmon map of the same structure showing localized enhancement of the plasmon at the silicon atom. Adapted from Ref. 118. Magnetism in graphene: (c) low temperature STM image of graphene with four carbon vacancy sites. Sample bias: +270 mV and tunneling current: 1 nA. (d) Perspective view of a STM image of a single carbon vacancy site. Sample bias: +150 mV and tunneling current: 0.5 nA. The protrusion in the image reveals a localized electronic resonance at the Fermi level that is associated with the formation of a local magnetic moment. Adapted from Ref. 85.

adatoms or attaching organic molecules can inject carriers to the system, but they introduce strong scattering affecting negatively the conductivity of graphene for the first case or the defect is unstable with the temperature for the last case.[28,119] It is suggested that a more efficient doping could be obtained with adatoms attached to defective sites which increases effectively its stability preserving the coherence of the graphene lattice.[104]

Grain boundaries in graphene can be considered as a way to create metallic wires within a graphene wafer. Indeed, theoretical calculations have shown that one-dimensional defects composed of an array of nonhexagonal rings have enhanced conductivity[120] where the electronic states are localized across the line and extended along the line. On the other hand, ISW defects can be arranged linearly to form extended ridges that may be useful in directing charge transport in graphene electronics applications.[102]

Magnetism in graphene is a field of intensive research[121] motivated by the search of light non-metallic magnets that are stable well above room temperature. Experimental evidence of magnetism in graphene has been already reported.[122] Theoretical calculations predict the possibility of magnetic solutions by vacancies, carbon adatoms, interstitials, and graphene nanoribbons.[99,123–125] Interestingly, non-magnetic impurity atoms like hydrogen or nitrogen appear to originate magnetism in grapheme.[122]

The effect of defects on the *mechanical properties* of graphene has not been experimentally explored yet but theoretical simulations on the impact of one-dimensional defects suggest that the strength of graphene is only reduced for small-angle tilt boundaries while large angle boundaries exhibit practically the same strengths as pristine grapheme.[126] On the other hand, point defects are expected to decrease the Young's modulus and tensile strength of graphene but either theoretical or experimental proof is needed.

5. Summary

Graphene, the one-atom thick carbon crystal, was considered experimentally unthinkable until 2004 when Andre Geim and Kostya Novoselov reported the successful isolation of graphene from which work they were awarded the Nobel Prize in Physics in 2010. Graphene is the first material reported to have charge carriers that behave like massless Dirac fermions and has inspired the quest for *graphene cousins* with similar properties (*cf.* Ref. 127). In this chapter, we have presented fundamental aspects of the electronic properties of graphene. The electronic spectra shows a linear dispersion near the so-called Dirac point, this feature resembles relativistic massless particles but traveling at speed of v_F instead of c and its behavior are governed by the Dirac equations. For this reason, graphene offers a unique "scientific playground" for testing QED phenomena using available experimental surface science facilities. Since graphene's charge carriers (electrons and holes) can be described within the framework of quantum electrodynamics, chirality and pseudospin can be assigned; the conservation of such quantities can explain many electronic properties. QHE observed in graphene is a non-standard

integer QHE and is explained by a quantized level at zero E which is shared by electrons and holes. The zero-field conductivity has a non-zero value when the carriers concentration vanish. QED predicts for graphene a conductivity minimum that is π times smaller than the experimentally measured. The explanation of this difference is still under debate and is referred as the mystery of the missing pie. The counterintuitive tunneling of relativistic particles through a potential barrier with a transmission of 1 is one of the most exotic properties predicted to occur in graphene. This effect, so-called the Klein paradox, is explained by solving the Dirac equations for a potential barrier. The relevance of this process in graphene relies on the actual realization of such QED effects under normal conditions. This effect has been already experimentally confirmed by observing the conductance oscillations in extremely narrow graphene heterostructures where a resonant cavity is formed between two electrostatically created bipolar junctions.[128] Atomic collapse is the most recent process observed in graphene. QED predicts that a nucleus with more than 170 protons will perturb the vacuum generating electron–positron pairs. The electron will collapse into the nucleus discharging it and the positron will diffuse away. Due to graphene's relativistic-like charges (electrons and holes that play the role of the virtual particles in QED) and the fact that charge impurities can act like atomic nuclei, a direct observation of atomic collapse has been observed with the aid of STM. This process appears as a spatially extended electronic resonance where the quasi-bonded electronic state energy is just below the Dirac point, this is seen in STM images as a halo around the impurities cluster. Topological defects in graphene, dislocations, and grain boundaries are the key to tailor graphene with desired properties. The study of defects in graphene is still in its infancy and is still not well understood despite the considerable number of experimental work that lacks reproducibility despite the large amount of theoretical work available.

Acknowledgments

The authors would like to thank for support from the National Science Foundation: the HRD-0833178 CREST and HRD-0833178 CREST supplement, and DMR-1205194 PREM grants. This work was also supported by the Office of Naval Research (ONR) grant 08PRO2615-00/N00014-08-1-0324.

References

1. Petroski, H. *The Pencil: A History of Design and Circumstance*, New York: Knopf, **1989**.
2. Novoselov, K. S.; Geim, A. K.; Morozov, S. V.; Jiang, D.; Zhang, Y.; Dubonos, S. V.; Grigorieva, I. V.; Firsov, A. A. *Science* **2004**, *306*, 666–669.
3. Wallace, P. R. *Phys. Rev.* **1947**, *71*, 622–634.
4. McClure, J. W. *Phys. Rev.* **1956**, *104*, 666–671.
5. Slonczewski, J. C.; Weiss, P. R. *Phys. Rev.* **1958**, *109*, 272–279.
6. Peierls, R. E. *Ann. I. H. Poincare.* **1935**, *5*, 177–222.
7. Mermin, N. D. *Phys. Rev.* **1968**, *176*, 250–254.
8. Novoselov, K. S.; Jiang, D.; Schedin, F.; Booth, T. J.; Khotkevich, V. V.; Morozov, S. V.; Geim, A. K. *Proc. Nat. Acad. Sci. USA* **2005**, *102*, 10451–10453.
9. Crespi, V. H.; Benedict, L. X.; Cohen, M. L.; Louie, S. G. *Phys. Rev. B* **1996**, *53*, R13303–R13305.
10. Terrones, H.; Terrones, M.; Hernández, E.; Grobert, N.; Charlier, J.-C.; Ajayan, P. M. *Phys. Rev. Lett.* **2000**, *84*, 1716–1719.
11. Geim, A. K.; Novoselov, K. S. *Nat. Mater.* **2007**, *6*, 183–191.
12. Lin, Y.-M.; Jenkins, K. A.; Valdes-Garcia, A.; Small, J. P.; Farmer, D. B.; Avouris, P. *Nano Lett.* **2009**, *9*, 422–426.
13. Britnell, L.; Ribeiro, R. M.; Eckmann, A.; Jalil, R.; Belle, B. D.; Mishchenko, A.; Kim, Y.-J.; Gorbachev, R. V.; Georgiou, T.; Morozov, S. V.; Grigorenko, A. N.; Geim, A. K.; Casiraghi, C.; Neto, A. H. C.; Novoselov, K. S. *Science* **2013**, 340, 1311–1314.
14. Novoselov, K. S.; Geim, A. K.; Morozov, S. V.; Jiang, D.; Katsnelson, M. I.; Grigorieva, I. V.; Dubonos, S. V.; Firsov, A. A.; *Nature* **2005**, *438*, 197–200.
15. Zhang, Y.; Tan, Y.-W.; Stormer, H. L.; Kim, P. *Nature* **2005**, *438*, 201–204.
16. Semenoff, G. W. *Phys. Rev. Lett.* **1984**, *53*, 2449–2452.
17. Fradkin, E. *Phys. Rev. B* **1986**, *33*, 3263–3268.
18. Haldane, F. D. M. *Phys. Rev. Lett.* **1988**, *61*, 2015–2018.
19. Wang, Y.; Wong, D.; Shytov, A. V.; Brar, V. W.; Choi, S.; Wu, Q.; Tsai, H.-Z.; Regan, W.; Zettl, A.; Kawakami, R. K.; Louie, S. G.; Levitov, L. S.; Crommie, M. F. *Science* **2013**, *340*, 734–737.
20. Kresse, G.; Furthmüller, J.; *Phys. Rev. B* **1996**, *54*, 11169–11186.
21. Kresse, G.; Furthmüller, J. *Comput. Mater. Sci.* **1996**, *6*, 15–50.
22. Perdew, J. P.; Ruzsinszky, A.; Csonka, G. I.; Vydrov, O. A.; Scuseria, G. E.; Constantin, L. A.; Zhou, X.; Burke, K. *Phys. Rev. Lett.* **2008**, *100*, 136406–136409.
23. Reich, S.; Maultzsch, J.; Thomsen, C.; Ordejón, P. *Phys. Rev. B* **2002**, *66*, 035412–035416.

24. Stolyarova, E.; Rim, K. T.; Ryu, S.; Maultzsch, J.; Kim, P.; Brus, L. E.; Heinz, T. F.; Hybertsen, M. S.; Flynn, G. W. *Proc. Nat. Acad. Sci. USA* **2007**, *104*, 9209–9212.
25. Saito, R.; Dresselhaus, G.; Dresselhaus M. S.; *Physical Properties of Carbon Nanotubes*, London: Imperial College Press, **1998**.
26. Zhou, S. Y.; Gweon, G. H.; Graf, J.; Fedorov, A. V.; Spataru, C. D.; Diehl, R. D.; Kopelevich, Y.; Lee, D. H.; Louie, S. G.; Lanzara, A. *Nat. Phys.* **2006**, *2*, 595–599.
27. Bostwick, A.; Ohta, T.; Seyller, T.; Horn, K.; Rotenberg, E.; *Nat. Phys.* **2006**, *3*, 36–40.
28. Castro Neto, A. H.; Peres, N. M. R.; Novoselov, K. S.; Geim, A. K. *Rev. Mod. Phys.* **2009**, *81*, 109–162.
29. Liu, Z.; Suenaga, K.; Harris, P. J. F.; Iijima, S. *Phys. Rev. Lett.* **2009**, *102*, 015501.
30. Partoens, B.; Peeters, F. M. *Phys. Rev. B* **2006**, *74*, 075404.
31. Zhang, Y.; Tang, T.-T.; Girit, C.; Hao, Z.; Martin, M. C.; Zettl, A.; Crommie, M. F.; Shen, Y. R.; Wang, F. *Nature* **2009**, 459, 820–823.
32. Partoens, B.; Peeters, F. M. *Phys. Rev. B* **2007**, *75*, 193402.
33. Morozov, S. V.; Novoselov, K. S.; Schedin, F.; Jiang, D.; Firsov, A. A.; Geim, A. K. *Phys. Rev. B* **2005**, *72*, 201401.
34. Luk'yanchuk, I. A.; Kopelevich, Y. *Phys. Rev. Lett.* **2006**, *97*, 256801.
35. Latil, S.; Meunier, V.; Henrard, L. *Phys. Rev. B* **2007**, *76*, 201402.
36. Terrones, M.; Botello-Méndez, A. R.; Campos-Delgado, J.; López-Uras, F.; Vega-Cantú, Y. I.; Rodríguez-Mac´ıas, F. J.; Elías, A. L.; Muñoz-Sandoval, E.; Cano-Márquez, A. G.; Charlier, J.-C.; Terrones, H. *Nano Today* **2010**, 5, 351–372.
37. Novoselov, K. S.; Geim, A. K.; Morozov, S. V.; Jiang, D.; Katsnelson, M. I.; Grigorieva, I. V.; Dubonos, S. V.; Firsov, A. A. *Nature* **2005**, *438*, 197–200.
38. Abergel, D. S. L.; Russell, A.; Fal'ko, V. I. *Appl. Phys. Lett.* **2007**, *91*, 063125–063127.
39. Bhattacharjee, S.; Sengupta, K. *Phys. Rev. Lett.* **2006**, *97*, 217001–217004.
40. Biswas, R. R.; Sachdev, S.; Son, D. T. *Phys. Rev. B* **2007**, *76*, 205122–205126.
41. Bunch, J. S.; van der Zande, A. M.; Verbridge, S. S.; Frank, I. W.; Tanenbaum, D. M.; Parpia, J. M.; Craighead, H. G.; McEuen, P. L. *Science* **2007**, *315*, 490–493.
42. Zhang, Y.; Tan, Y.-W.; Stormer, H. L.; Kim, P. *Nature* **2005**, *438*, 201–204.
43. Gorbar, E. V.; Gusynin, V. P.; Miransky, V. A.; Shovkovy, I. A. *Phys. Rev. B* **2002**, *66*, 045108–045129.
44. Zheng, Y.; Ando, T. *Phys. Rev. B* **2002,** *65*, 245420–245430.

45. Peres, N. M. R.; Guinea, F.; Castro Neto, A. H. *Phys. Rev. B* **2006**, *73*, 125411–125433.
46. Klein, O. *Z. Phys.* **1929**, *53*, 157–165.
47. Katsnelson, M. I.; Novoselov, K. S.; Geim, A. K. *Nat. Phys.* **2006**, *2*, 620–625.
48. Greiner, W.; Muller, B.; Rafelski, J. *Quantum Electrodynamics of Strong Fields*, Berlin: Springer, **1985**.
49. Pomeranchuk, I.; Smorodinsky, Y. *J. Phys. USSR* **1945**, *9*, 97.
50. Cowan, T.; Backe, H.; Begemann, M.; Bethge, K.; Bokemeyer, H.; Folger, H.; Greenberg, J. S.; Grein, H.; Gruppe, A.; Kido, Y.; Klüver, M.; Schwalm, D.; Schweppe, J.; Stiebing, K. E.; Trautmann, N.; Vincent, P. *Phys. Rev. Lett.* **1985**, *54*, 1761–1764.
51. Schweppe, J.; Gruppe, A.; Bethge, K.; Bokemeyer, H.; Cowan, T.; Folger, H.; Greenberg, J. S.; Grein, H.; Ito, S.; Schule, R.; Schwalm, D.; Stiebing, K. E.; Trautmann, N.; Vincent, P.; Waldschmidt, M. *Phys. Rev. Lett.* **1983**, *51*, 2261–2264.
52. Smart, A. G. *Phys. Today* **2013**, *66*, 12–13.
53. Pereira, V. M.; Nilsson, J.; Castro Neto, A. H. *Phys. Rev. Lett.* **2007**, *99*, 166802–166805.
54. Shytov, A. V.; Katsnelson, M. I.; Levitov, L. S. *Phys. Rev. Lett.* **2007**, *99*, 246802–246805.
55. Shytov, A. V.; Katsnelson, M. I.; Levitov, L. S. *Phys. Rev. Lett.* **2007**, *99*, 236801–236804.
56. Decker, R.; Wang, Y.; Brar, V. W.; Regan, W.; Tsai, H.-Z.; Wu, Q.; Gannett, W.; Zettl, A.; Crommie, M. F. *Nano. Lett.* **2011**, *11*, 2291–2295.
57. Geim, A. K. *Science* **2009**, *324*, 1530–1534.
58. Zhang, J.; Zhao, J.; Lu, J. *ACS Nano* **2012**, *6*, 2704–2711.
59. Lee, C.; Wei, X.; Kysar, J. W.; Hone, J. *Science* **2008**, *321*, 385–388.
60. Griffith, A. A. *Philos. Trans. R. Soc. London Ser. A* **1921**, *221*, 163.
61. Liu, F.; Ming, P.; Li, J. *Phys. Rev. B* **2007**, *76*, 064120.
62. Yu, M.-F.; Files, B. S.; Arepalli, S.; Ruoff, R. S. *Phys. Rev. Lett.* **2000**, *84*, 5552–5555.
63. Yu, M.-F.; Lourie, O.; Dyer, M. J.; Moloni, K.; Kelly, T. F.; Ruoff, R. S. *Science* **2000**, *287*, 637–640.
64. Demczyk, B.; Wang, Y.; Cumings, J.; Hetman, M.; Han, W.; Zettl, A.; Ritchie, R. *Mater. Sci. Eng. A* **2002**, *334*, 173–178.
65. Huntington, J. B. In *Solid State Physics*; Vol. 7; Seitz, F.; Turnbull, D., Eds.; New York: Academic, **1958**.
66. Blakslee, O. L.; Proctor, D. G.; Seldin, E. J.; Spence, G. B.; Weng, T.; *J. Appl. Phys.* **1970**, *41*, 3373–3382.
67. Seldin, E. J.; Nezbeda, C. W. *J. Appl. Phys.* **1970**, *41*, 3389–3400.

68. Wan, K.-T.; Guo, S.; Dillard, D. A. *Thin Solid Films* **2003**, *425*, 150–162.
69. Huang, Y.; Wu, J.; Hwang, K. C. *Phys. Rev. B* **2006**, *74*, 245413.
70. Kudin, K. N.; Scuseria, G. E.; Yakobson, B. I. *Phys. Rev. B* **2001**, *64*, 235406.
71. Dubay, O.; Kresse, G. *Phys. Rev. B* **2003**, *67*, 035401.
72. Oshima, C., Aizawa, T.; Souda, R.; Ishizawa, Y.; Sumiyoshi, Y. *Solid State Commun*. **1988**, *65*, 1601–1604.
73. Siebentritt, S., Pues, R.; Rieder, K.-H.; Shikin, A. M. *Phys. Rev. B* **1997**, *55*, 7927–7934.
74. Hashimoto, A.; Suenaga, K.; Gloter, A.; Urita, K.; Iijima, S. *Nature* **2004**, *430*, 870–873.
75. Banhart, F.; Kotakoski, J.; Krasheninnikov, A. V. *ACS Nano* **2011**, *5*, 26–41.
76. Hao, F.; Fang, D.; Xu, Z. *Appl. Phys. Lett*. **2011**, *99*, 041901.
77. Zhao, H.; Aluru, N. R. *J. Appl. Phys*. **2010**, *108*, 064321.
78. Khare, R.; Mielke, S. L.; Paci, J. T.; Zhang, S.; Ballarini, R.; Schatz, G. C.; Belytschko, T. *Phys. Rev. B* **2007**, *75*, 075412.
79. Kittel, C. *Introduction to Solid State Physics*, New York: John Wiley & Sons, **2005**.
80. Bae, S.; Kim, H.; Lee, Y.; Xu, X.; Park, J.-S.; Zheng, Y.; Balakrishnan, J.; Lei, T.; Ri Kim, H.; Song, Y. I.; Kim, Y.-J.; Kim, K. S.; Ö zyilmaz, B.; Ahn, J.-H.; Hong, B. H.; Iijima, S. *Nat. Nanotechnol*. **2010**, *5*, 574–578.
81. Kim, K. S.; Zhao, Y.; Jang, H.; Lee, S. Y.; Kim, J. M.; Kim, K. S.; Ahn, J.-H.; Kim, P.; Choi, J.-Y.; Hong, B. H. *Nature* **2009**, *457*, 706–710.
82. Berger, C.; Song, Z.; Li, X.; Wu, X.; Brown, N.; Naud, C.; Mayou, D.; Li, T.; Hass, J.; Marchenkov, A. N.; Conrad, E. H.; First, P. N.; de Heer, W. A. *Science* **2006**, *312*, 1191–1196.
83. Berger, C.; Song, Z.; Li, T.; Li, X.; Ogbazghi, A. Y.; Feng, R.; Dai, Z.; Marchenkov, A. N.; Conrad, E. H.; First, P. N.; de Heer, W. A. *J. Phys. Chem. B* **2004**, *108*, 19912–19916.
84. Tapasztó, L.; Dobrik, G.; Nemes-Incze, P.; Vertesy, G.; Lambin, P.; Biró, L. P. *Phys. Rev. B* **2008**, *78*, 233407.
85. Ugeda, M. M.; Brihuega, I.; Guinea, F.; Gómez-Rodriguez, J. M. *Phys. Rev. Lett*. **2010**, *104*, 096804.
86. Hashimoto, A.; Suenaga, K.; Gloter, A.; Urita, K.; Iijima, S. *Nature* **2004**, *430*, 870–873.
87. Gass, M. H.; Bangert, U.; Bleloch, A. L.; Wang, P.; Nair, R. R.; Geim, A. K. *Nat. Nanotechnol*. **2008**, *3*, 676–681.
88. Meyer, J. C.; Kisielowski, C.; Erni, R.; Rossell, M. D.; Crommie, M. F.; Zettl, A. *Nano Lett*. **2008**, *8*, 3582–3586.
89. Warner, J. H.; Rümmeli, M. H.; Ge, L.; Gemming, T.; Montanari, B.; Harrison, N. M.; Bu¨chner, B.; Briggs, G. A. D. *Nat. Nanotechnol* **2009**, *4*, 500–504.

90. Girit, C¸. O.; Meyer, J. C.; Erni, R.; Rossell, M. D.; Kisielowski, C.; Yang, L.; Park, C.-H.; Crommie, M. F.; Cohen, M. L.; Louie, S. G.; Zettl, A. *Science* **2009**, *323*, 1705–1708.
91. Stone, A.; Wales, D. *Chem. Phys. Lett.* **1986**, *128*, 501–503.
92. Ma, J.; Alfè, D.; Michaelides, A.; Wang, E. *Phys. Rev. B* **2009**, *80*, 033407.
93. Li, L.; Reich, S.; Robertson, J. *Phys. Rev. B* **2005**, *72*, 184109.
94. Kotakoski, J.; Krasheninnikov, A. V.; Kaiser, U.; Meyer, J. C. *Phys. Rev. Lett.* **2011**, *106*, 105505.
95. Krasheninnikov, A.; Lehtinen, P.; Foster, A.; Nieminen, R. *Chem. Phys. Lett.* **2006**, *418*, 132–136.
96. Lee, G.-D.; Wang, C. Z.; Yoon, E.; Hwang, N.-M.; Kim, D.-Y.; Ho, K. M. *Phys. Rev. Lett.* **2005**, *95*, 205501.
97. El-Barbary, A. A.; Telling, R. H.; Ewels, C. P.; Heggie, M. I.; Briddon, P. R. *Phys. Rev. B* **2003**, *68*, 144107.
98. Lee, Y. H.; Kim, S. G.; Tománek, D. *Phys. Rev. Lett.* **1997**, *78*, 2393–2396.
99. Lehtinen, P. O.; Foster, A. S.; Ayuela, A.; Krasheninnikov, A.; Nordlund, K.; Nieminen, R. M. *Phys. Rev. Lett.* **2003**, *91*, 017202.
100. Ma, Y. *Phys. Rev. B* **2007**, *76*, 075419.
101. Lusk, M. T.; Carr, L. D. *Phys. Rev. Lett.* **2008**, *100*, 175503.
102. Lusk, M. T.; Wu, D. T.; Carr, L. D. *Phys. Rev. B* **2010**, *81*, 155444.
103. Cockayne, E.; Rutter, G. M.; Guisinger, N. P.; Crain, J. N.; First, P. N.; Stroscio, J. A. *Phys. Rev. B* **2011**, *83*, 195425.
104. Cretu, O.; Krasheninnikov, A. V.; Rodríguez-Manzo, J. A.; Sun, L.; Nieminen, R. M.; Banhart, F. *Phys. Rev. Lett.* **105**, 196102 (2010).
105. Chan, K. T.; Neaton, J. B.; Cohen, M. L. *Phys. Rev. B* **2008**, *77*, 235430.
106. Krasheninnikov, A. V.; Lehtinen, P. O.; Foster, A. S.; Pyykkö, P.; Nieminen, R. M. *Phys. Rev. Lett.* **2009**, *102*, 126807.
107. Wehling, T. O.; Balatsky, A. V.; Katsnelson, M. I.; Lichtenstein, A. I.; Rosch, A. *Phys. Rev. B* **2010**, *81*, 115427.
108. Boukhvalov, D. W.; Katsnelson, M. I. *Nano Lett.* **2008**, *8*, 4373–4379.
109. Nevidomskyy, A. H.; Csányi, G.; Payne, M. C. *Phys. Rev. Lett.* **2003**, *91*, 105502.
110. Santos, E. J. G., Ayuela, A.; Sánchez-Portal, D. *New J. Phys.* **2010**, *12*, 053012.
111. Simonis, P.; Goffaux, C.; Thiry, P.; Biro, L.; Lambin, P.; Meunier, V. *Surf. Sci.* **2002**, *511*, 319–322.
112. Huang, P. Y.; Ruiz-Vargas, C. S.; van der Zande, A. M.; Whitney, W. S.; Levendorf, M. P.; Kevek, J. W.; Garg, S.; Alden, J. S.; Hustedt, C. J.; Zhu, Y.; Park, J.; McEuen, P. L.; Muller, D. A. *Nature* **2012**, *469*, 389–392.
113. Coraux, J.; N Diaye, A. T.; Busse, C.; Michely, T. *Nano Lett.* **2008**, *8*, 565–570.

114. Yazyev, O. V.; Louie, S. G. *Phys. Rev. B* **2010**, *81*, 195420.
115. Duplock, E. J.; Scheffler, M.; Lindan, P. J. D. *Phys. Rev. Lett.* **2004**, *92*, 225502.
116. Appelhans, D. J.; Carr, L. D.; Lusk, M. T. *New J. Phys.* **2010**, *12*, 125006.
117. Peng, X.; Ahuja, R. *Nano Lett.* **2008**, *8*, 4464–4468.
118. Zhou, W.; Lee, J.; Nanda, J.; Pantelides, S. T.; Pennycook, S. J.; Idrobo, J.-C. *Nat. Nanotechnol.* **2012**, *7*, 161–165.
119. Coletti, C.; Riedl, C.; Lee, D. S.; Krauss, B.; Patthey, L.; von Klitzing, K.; Smet, J. H.; Starke, U. *Phys. Rev. B* **2010**, *81*, 235401.
120. Lahiri, J.; Lin, Y.; Bozkurt, P.; Oleynik, I. I.; Batzill, M. *Nat. Nanotechnol.* **2010**, *5*, 326–329.
121. Yazyev, O. V. *Rep. Progr. Phys.* **2010**, *73*, 056501.
122. Wang, Y.; Huang, Y.; Song, Y.; Zhang, X.; Ma, Y.; Liang, J.; Chen, Y. *Nano Lett.* **2009**, *9*, 220–224.
123. Andriotis, A. N.; Menon, M.; Sheetz, R. M.; Chernozatonskii, L. *Phys. Rev. Lett.* **2003**, *90*, 026801.
124. Yazyev, O. V. *Phys. Rev. Lett.* **2008**, *101*, 037203.
125. Son, Y.-W.; Cohen, M. L.; Louie, S. G. *Nature* **2006**, *444*, 347–349.
126. Grantab, R.; Shenoy, V. B.; Ruoff, R. S. *Science* **2010**, *330*, 946–948.
127. Lebégue, S.; Björkman, T.; Klintenberg, M.; Nieminen, R. M.; Eriksson, O. *Phys. Rev. X.* **2013**, *3*, 031002 .
128. Young, A. F.; Kim, P. *Nat. Phys.* **2009**, *5*, 222–226.

This page intentionally left blank

Chapter 2

Adsorption on and Reactivity of Carbon Nanotubes and Graphene

*M. Rosa Axet, Revathi R. Bacsa, Bruno F. Machado and Philippe Serp**

Laboratoire de Chimie de Coordination, UPR CNRS 8241
Composante ENSIACET, Université de Toulouse UPS/INP/LCC
4 allée Emile Monso, BP 44362, 31432 Toulouse Cedex 4, France

1. Introduction 40
2. Structure and Adsorption Sites 42
   2.1. Structure and adsorption sites of graphene and FLG 42
      2.1.1. Presence of defects 45
   2.2. Structure and adsorption sites of carbon nanotubes 49
      2.2.1. Presence of defects 51
3. Physisorption on CNTs and Graphene 54
   3.1. Physisorption of gases on CNTs and graphene 55
      3.1.1. Physisorption on individual CNTs 55
      3.1.2. Physisorption on CNT bundles 59
      3.1.3. Physisorption on graphene 62
   3.2. Physisorption of liquids on CNTs and graphene 66
      3.2.1. Adsorption of water on CNTs and graphene 68
      3.2.2. Physisorption of ionic liquids on graphene and CNTs 71
      3.2.3. Physisorption on CNTs and graphene of ions and molecules from solution 73
      3.2.4. Physisorption of liquids on doped CNTs and graphene 77
   3.3. Physisorption of solids on CNTs and graphene 77
      3.3.1. Metals and semiconductors 77
      3.3.2. Physisorption of metals and semiconductors on doped CNTs or graphene 80
      3.3.3. Physisorption of polymers 81
      3.3.4. Polymer adsorption on doped graphene or CNTs 82

* Corresponding author. E-mail: philippe.serp@ensiacet.fr

4. Chemisorption on CNTs and Graphene 83
4.1. Chemisorption of gases on CNTs and graphene 83
4.1.1. Gas chemisorption on CNTs 83
4.1.2. Effect of dopants on gas chemisorption with CNTs 84
4.1.3. Gas chemisorption on graphene 87
4.1.4. Effect of dopants on gas chemisorption with graphene 93
4.2. Chemisorption of liquids on CNTs and graphene 97
4.3. Chemisorption of solids on CNTs and graphene 99
4.3.1. Alkali metals 99
4.3.2. Alkaline-earth metals 102
4.3.3. d-metals 102
4.3.4. Adsorption of other metals, metalloids, and non-metals 115
4.3.5. Polymers 116
5. Reactivity on CNTs and Graphene 122
5.1. Surface chemistry of nanostructured carbon materials 124
5.2. Catalysis 128
5.2.1. CNTs, CNFs, and FLG as metal-free catalyst 129
5.2.2. Hydrogenation 136
5.2.3. Oxidation and environmental catalysis 140
5.2.4. Fuel cell catalysis 144
5.3. Gas sensors 150
5.4. Bioreactivity and degradability of CNTs and graphene 153
5.4.1. Biosensors 155
5.4.2. Drug delivery 156
5.4.3. Biodegradability and toxicity 158
References 160

1. Introduction

Graphene and carbon nanotubes (CNTs) are among the most prominent nanoscale materials currently studied. The confinement to one or two dimensions and the high symmetry of these materials lead to interesting new physics and many potential applications, including adsorption and reactivity. One-dimensional (1D) CNTs can be metallic or semiconducting, depending on chirality, and can act as quantum wires with minimal scattering. Two-dimensional (2D) graphene has rather unique sublattice symmetry and is a zero-gap semiconductor with a point-like Fermi surface and a linear dispersion at the Fermi level.

The hollow 1D structure of CNTs and the ultimate 2D structure of graphene are especially attractive for adsorption-related applications. The use of

CNTs or graphene for developing catalysts,[1–5] sensors of pollutant gases, [6–8] storage of alternative fuels,[9–12] and removal of hazardous pollutants from gas or aqueous[13–15] streams is being studied extensively, for which the characterization of their adsorption properties (both physical and chemical) is important. The interaction of graphene or CNTs with their environment and in particular with gases or dopant adsorbed either on their internal (CNTs) or external surface also attracts increasing attention due to the possible influence of the adsorption on some of the properties of these materials.[16–18] Additionally, the adsorption of biomolecules on CNTs or graphene is critical for biosensors,[19,20] CNT and graphene biocompatibility,[21–23] and for nanomedicine.[24,25] Finally, the possibility to adsorb and/or transport species in the inner cavity of CNTs, where confinement effects are expected, opens an entirely new field of research.[26–28]

As for any materials, adsorption on graphene or CNTs is related to their surface physical and chemical properties. Surface area and porosity are important physical properties that influence the quality, utility, and handling of graphene or CNTs, which often must be carefully engineered to perform specific functions. Differences in the surface area and porosity of graphene and CNTs, which otherwise may have the same physical dimensions, can greatly influence their adsorption performances and therefore have a pronounced impact on their applications. Therefore, it is critically important that these characteristics be accurately determined and controlled.[29] The surface chemistry of graphene or CNTs is governed by basal and edge carbon atoms,[30,31] as well as by the presence of defects (*i.e.*, structural carbon vacancies, non-aromatic rings).[32] These imperfections and defects along the edges of graphene layers are the most active sites owing to high densities of unpaired electrons. Indeed, the zigzag sites are carbene-like, and the armchair sites are carbyne-like.[32] Heteroatoms, such as oxygen, hydrogen, nitrogen, and sulfur can be chemisorbed, leading to stable surface compounds, and resulting in a complex surface chemistry, if compared to classical oxides (Al_2O_3, SiO_2, TiO_2). If most of the adsorption sites for chemisorption are on the basal planes (inner or outer surface in the case of CNTs), the much higher activity of the heterogeneous groups can result in significant effects on the overall adsorption capacity. The exact mechanism by which the heterogeneous surface affects the adsorption is of great current interest. Among the heteroatoms that can be voluntarily introduced, nitrogen has been particularly studied since it provides basicity to the surface.[33,34]

In this chapter, we will focus our attention on (i) the description of the different types of sites for both physi- and chemisorption, (ii) the adsorption on/in individual perfect CNTs and graphene, (iii) the importance of defects

on the adsorption, and (iv) the role of intertube voids on the porosity of these materials.

2. Structure and Adsorption Sites

The interaction of graphene and CNTs with their environment, and in particular with gases or liquids adsorbed either on their internal (CNTs) or external surfaces, is attracting increasing attention. Many of the intriguing properties of graphene are a consequence of its 2D electronic band structure. Electrons in a single-layer graphene exhibit a characteristic linear dispersion relationship between energy and momentum near the K point of the Brillouin zone. Interlayer coupling in few-layer graphene (FLG) leads to a dramatic change of this electronic structure, with the emergence of hyperbolically dispersing bands.[35] Further, the electronic properties of FLG are predicted to be highly sensitive to crystallographic stacking sequence. Thus, even though several physical properties are shared between graphene and its few-layers, recent theoretical and experimental advances demonstrate that each specific thickness of FLG is a material with unique physical properties.[36] To date the role of stacking has, however, been overlooked in experimental studies dealing with adsorption on FLG with crystalline order. CNTs are usually associated with other nanotubes in bundles, fibers, films, papers, and so on, rather than as a single entity. Each of these associations has a specific range of porosities that determines its adsorption properties.

2.1. Structure and adsorption sites of graphene and FLG

The single-layer graphene is a one-atom thick sheet of hexagonally arranged sp^2-bonded carbon atoms. With the impressive progress in research on graphene mono- and bilayers, recent attention has also turned to graphene few-layer counterparts. In FLG, the crystallographic stacking of the individual graphene sheets provides an additional degree of freedom. The distinct lattice symmetries associated with different stacking orders of FLG have been predicted to strongly influence the electronic properties of FLG, including the band structure, interlayer screening, magnetic state, and spin–orbit coupling.[37] For graphene trilayers, two stable crystallographic configurations are predicted: ABA and ABC stacking order (Figure 1). In the absence of direct evidence of ABC stacking order in trilayers, ABA stacking order has generally been presumed in most studies of exfoliated materials, as this structure is believed to be slightly more thermodynamically stable than the other. Recent studies, however, indicate distinct properties for these two types of graphene

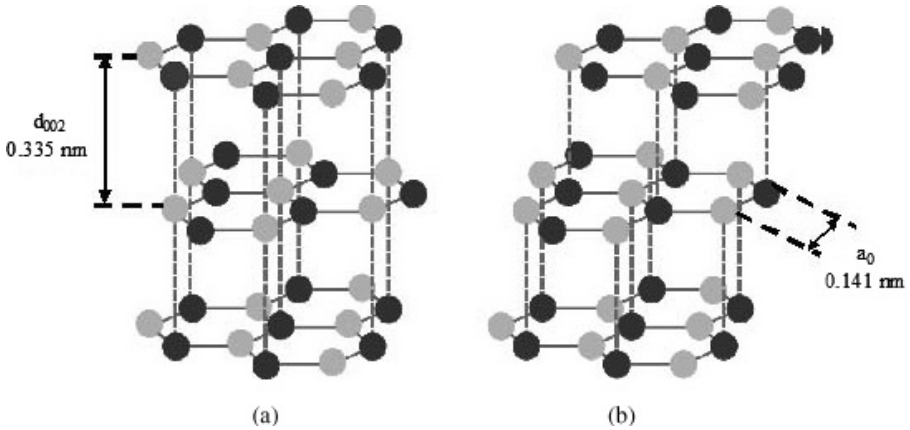

Figure 1. Lattice structure of trilayer graphene with (a) ABA and (b) ABC stacking sequence. The grey and black dots represent carbon atoms in the A and B sublattices of the graphene honeycomb structure.

trilayers. ABA-stacked trilayers are semimetals with an electrically tunable band overlap, while ABC-stacked trilayers are predicted to be semiconductors with an electrically tunable band gap.[37] Graphene sheets can fold/scroll back with an arbitrary folding direction leading to rotational stacking faults that produce Moiré interference.

The edge shape of graphene is also of great interest for adsorption, since chirality and morphology of the edges are known to determine the electronic properties.[31] The edge morphology affects significantly not only the chemical reactivity but also the edge stability, which determine the band gap properties, magnetic and optical behavior of graphene. Graphene edges could be configured as either zigzag or armchair based on morphology, open or closed depending on whether decorated with fully coordinated bonds or not, or folded/unfolded upon edge terminations.

Graphene, with its sp^2-hybridized carbon atoms packed in a hexagonal lattice, has edges that consist of two different configurations referred to as "armchair" and "zigzag" (Figure 2). An edge may also be comprised of a combination of both configurations. Carbon atoms of the zigzag edge have an unpaired electron, which is active to combine with other reactants (carbene-like chemistry). The carbon atoms of the armchair edge side are less reactive because of a triple covalent bond between the two open edge carbon atoms of each edge hexagonal ring. Therefore, the chemically reactive sites in carbon materials, rather than being (as is too often assumed) either the very unstable unadulterated radicals formed by H removal from graphene edges or the very stable hydrogen-saturated graphene edges, are proposed to be an

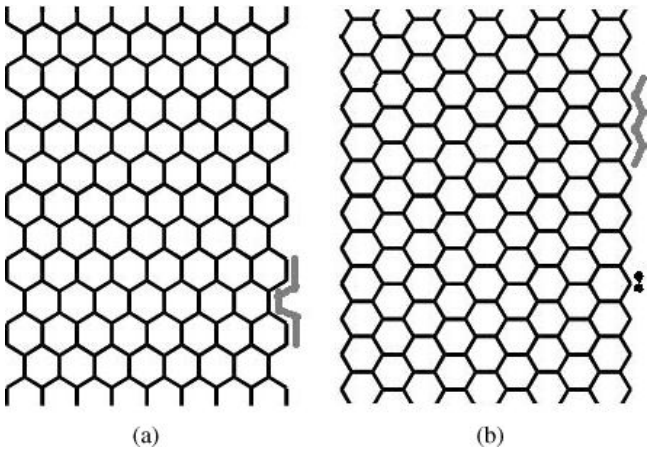

Figure 2. Graphene structures with (a) armchair and (b) zigzag edges.

isolated carbene-type zigzag carbon atom and a carbyne-type armchair pair of carbon atoms.[38] Energetically, these zigzag edges are more stable than armchair edges. Therefore, the interconversion of zigzag edges to the armchair configuration is difficult due to their greater stability, which requires migration of the edge atoms to be transformed. Therefore, the reactivity sequence of the edge carbon atoms should be carbene zigzag carbon > armchair carbon > zigzag carbon. The concentration of the edge sites at the periphery of graphene nanodomains is significant compared to the basal plane sites.

Even though many studies claim that the zigzag edges are the most stable configuration, there are some studies contradicting this fact. Indeed, edge configuration can strongly be altered by the chemical environment, which varies the edge energies and the edge forces. Edge-to-edge forces therefore become a dominant effect once the edges are terminated with functional groups involving oxygen, hydrogen, nitrogen, and boron using oxygen gas plasma, hydrogenation, and doping with either nitrogen or boron. In principle, the impact of the chemical functionalization determines the edge states, which can be easily tailored through either covalent or noncovalent bonding. Consequently, structural edge modification or reconstruction is likely to occur upon either edge passivation or termination. More interestingly, etched defective sites as well as etched holes behave as hosts for molecules to adsorb especially for gas species, which alter the electronic and electrical properties of graphene. Although much progress has been made in understanding and distinguishing the edge configuration and types of edge

defects and their locations, there is significantly more to be explored given the highly facile properties of the material. This area still remains challenging due to the limitations of characterization techniques for such atomic-scale understanding and thus requires more involvement of researchers for further investigations.

2.1.1. Presence of defects

It is intuitively clear that defects associated with dangling bonds should enhance the reactivity of graphene. A specificity of graphene, besides being truly 2D, is that it can host lattice defects in reconstructed atom arrangements. This is partly due to different possible hybridizations of carbon that allow different numbers of nearest neighbors and lead to the occurrence of different stable structures. Perhaps even more importantly, sp^2-hybridized carbon atoms arrange themselves into a variety of different polygons, not only hexagons, to form different structures. The non-hexagonal rings may either introduce curvature in the sheet or leave it flat when the arrangement of polygons satisfies certain symmetry rules. The reconstructions in the atomic network permit a coherent defective lattice without undercoordinated atoms. Although they have no dangling bonds, these reconstructed defects locally increase the reactivity of the structure and allow adsorption of other atoms on graphene.[32]

Defects in three-dimensional (3D) crystals are referred to as *intrinsic* when the crystalline order is perturbed without the presence of foreign atoms. The latter are denoted as impurities and constitute *extrinsic* defects. In macroscopic crystalline materials, intrinsic defects have different dimensionalities. Point defects, typically vacancies or interstitial atoms, are zero-dimensional (0D), whereas the concept of dislocations is based on 1D line of defects. Grain boundaries or stacking faults extend in two dimensions, while inclusions and voids have a finite size in all three dimensions. Foreign atoms may exist as 0D defects when they substitute individual atoms of the crystal or are located on interstitial sites. Agglomerations of foreign atoms can extend to more dimensions. The reduced dimensionality of graphene itself decreases the number of possible defect types. Therefore, in graphene, the concept of 0D point defects is quite similar to bulk crystals, but line defects already play a different role. Truly 3D defects do not exist in graphene. It is well-known that defects are not always stationary and that their migration can have an important influence on the properties of a defective crystal. In graphene, each defect has certain mobility parallel to the graphene plane.

Point defects

Single and multiple vacancies. The simplest defect in any material is the missing lattice atom (Figure 3a). The calculated migration barrier for a single vacancy (SV) in graphene is about 1.3 eV. This already allows a measurable migration slightly above room temperature (373–473 K). Double vacancies (DV) can be created either by the coalescence of two SVs or by removing two neighboring carbon atoms. As shown in Figure 3b, no dangling bond is present in a fully reconstructed DV so that two pentagons and one octagon appear instead of four hexagons in perfect graphene.

Stone–Wales defect. As mentioned above, one of the unique properties of the graphene lattice is its ability to reconstruct by forming non-hexagonal rings. The simplest example is the Stone–Wales (SW) defect, which does not involve any removed or added atoms. Four hexagons are transformed into two pentagons and two heptagons [SW(5,5-7,7) defect] by rotating one of the C–C bonds by 90°, as shown in Figure 3c. Such rotation creates two pairs of pentagons and heptagons opposite to each other around the rotated C–C bond. For this reason, SW defects are also known as a 5-7-7-5 defects.

Carbon adatoms. Interstitial atoms, as they appear in 3D crystals, do not exist in graphene. This is because placing an atom to any in-plane position,

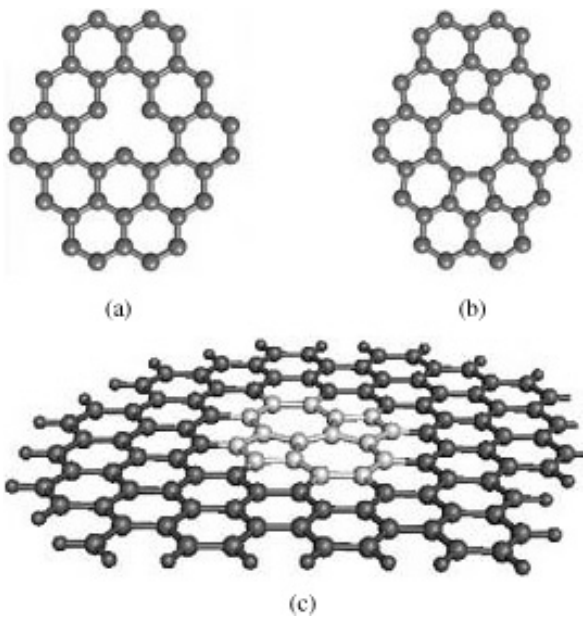

Figure 3. Point defects in the graphene system. Monovacancy (a), divacancy, (b) and (c) SW defect.

for example, in the center of a hexagon, would require a prohibitively high energy. Rather than straining the local structure in two dimensions, additional atoms use the third dimension. The energetically favored position is the bridge configuration (B-site, on top of a carbon–carbon bond, as shown in Figure 4).[39] When a carbon atom interacts with a perfect graphene layer, the hybridization of the carbon atoms in the layer changes. Some degree of sp^3 hybridization can appear locally so that two new covalent bonds can be formed between the adatom and the underlying atoms in the graphene plane. The binding energy of the carbon adatom is of the order of 1.5–2 eV. In addition to the bridge position, other metastable configurations are possible. The small energy difference of about 0.3 eV between the local and global minima indicates that adatoms migrate easily over the graphene surface. Indeed, calculations have given a migration barrier of about 0.4 eV. This means that carbon adatoms on flat graphene flakes migrate rapidly already at room temperature.

Foreign adatoms. The effect of a heteroatom on the properties of graphene depends on the bonding between the atom and graphene. If the bond is weak, only physisorption due to van der Waals interaction occurs. If the interaction is stronger, covalent bonding between the foreign atom and the nearest carbon atoms leads to chemisorption. Various bonding configurations, normally corresponding to high symmetry positions such as on top of a carbon atom (T-site, Figure 4), on top of the center of a hexagon (H6-site), or the bridge position (B-site) are possible.

Foreign atoms can also be incorporated into graphene as *substitutional* impurities. In this case, the impurity atom replaces one or two carbon atoms. Boron or nitrogen serve as the natural dopants in carbon structures since they have one electron less or more, respectively, and roughly the same atomic radius. Much larger atoms such as transition metal impurities have also

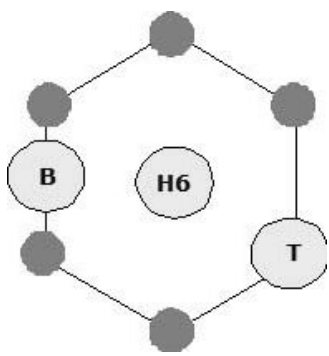

Figure 4. The three adsorption sites of graphene: hollow H6, bridge B, and top T.

received particular attention due to their ability to inject charge into the electron system of graphene.

Topology of defective graphene. Since the discovery of the fullerenes, it has been known that non-hexagonal rings induce local Gaussian curvature in a graphene sheet. Pentagons lead to positive and heptagons to negative curvature. In defective graphene, the arrangement of defects determines the local deviation from planarity.

One-dimensional defects

Dislocation-like defects. 1D defects have been observed in several experimental studies of graphene. Generally, these line defects are tilt boundaries separating two domains of different lattice orientations with the tilt axis normal to the plane. Graphene domain boundaries and the interconnection between FLG sheets are important considerations when working to optimize adsorption properties or reactivity. As shown schematically in Figure 5, there are two primary ways one can envisage two separate graphene domains being connected: either by direct atomic bonding at the interface of the two graphene sheets to create a discrete atomic domain boundary (Figures 5a and 5b) or by

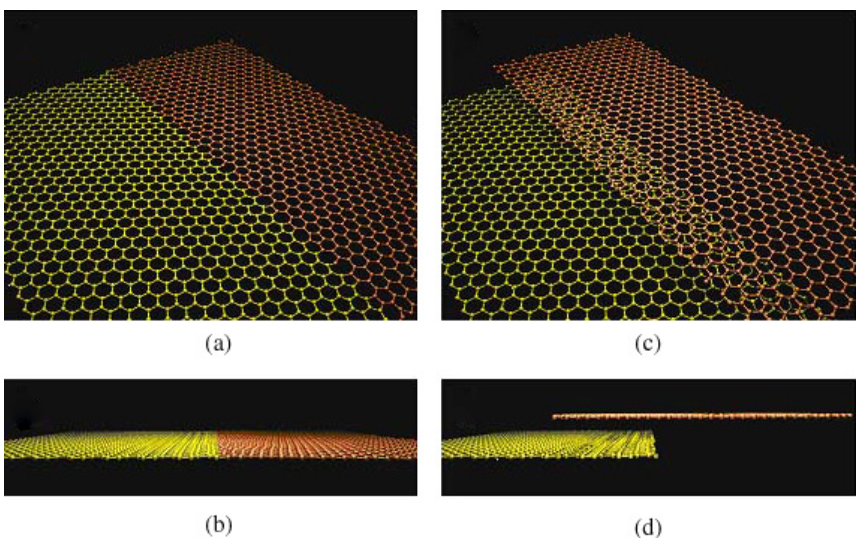

Figure 5. Schematic illustrations of the two primary ways of connecting graphene sheets. (a) 3D perspective view of atomic bonding at the interface. (b) Side view of the atomic interface. (c) 3D perspective view showing the graphene sheet on the right overlapping on top of the graphene sheet on the left (*i.e.*, overlap interface). (d) Side view of the overlapping interface. From Ref. 40 with permission.

one sheet overlapping another to form a bilayer boundary region that is not atomically discrete and relies on interlayer van der Waals forces to hold the two domains together (Figures 5c and 5d).[40] These shall be referred to as the atomic interface and the overlap interface, respectively. Recent investigations of monolayer graphene domain boundaries reported the existence of atomically bonded discrete interfaces. These domain boundaries were found to consist of pentagonal, hexagonal, and heptagonal carbon rings connected in a chain, allowing for two graphene domains of different lattice directions to bond together. These studies and observations illustrate the complexity of the FLG system, with both atomic domain boundaries and small regions of turbostratic graphene, originating from overlap at domain intersections, in an otherwise well-ordered AB Bernal-stacked graphitic system.

The behavior of intrinsic 0D or 1D defects in graphene such as vacancies or line defects is governed by the reconstruction of the graphenic lattice around defects. The high stability of the divacancy in its different configurations is of particular importance.

Defects at the edges of a graphene layer. Each graphene layer is terminated by edges with the edge atom being either free or passivated with hydrogen or oxygen atoms. The simplest edge structures are the armchair and the zigzag orientations. They can reconstruct and any other direction in between these two can be imagined. However, the zigzag and armchair orientations seem to be preferred, possibly because they minimize the number of dangling bonds at the edge. Defective edges can appear because of local changes in the reconstruction type or because of sustained removal of carbon atoms from the edges. Under these conditions, armchair edges can be transformed to zigzag edges. An intermediate structure can be considered as a defective edge. A simple example of an edge defect is the removal of one carbon atom from a zigzag edge. This leads to one pentagon in the middle of a row of hexagons at the edge. Other edge reconstructions result in different combinations of pentagons and heptagons at the edge.

2.2. Structure and adsorption sites of carbon nanotubes

Because the electronic structure of CNTs depends delicately on the nanotube parameters, such as tube diameter and helicity, it is expected that they will also affect strongly the adsorption. Additionally, the possibility to adsorb species on the convex (exohedral adsorption) or concave (endohedral adsorption) surface should be taken into account.

The nature and strength of the adsorption is directly correlated to carbon hybridization. In graphite, the four outer electrons of carbon form three

sp^2-hybridized σ bonds and one π-orbital, which gives the conduction band six Fermi points and a linear dispersion around each of them. If a graphene sheet is rolled up into a structure like a CNT, the orbital structure of carbon is altered, because the bond length between carbon atoms decreases and the bond angle changes. The σ- and π-orbitals are no longer perpendicular to each other. Overlap of the π-orbitals is introduced. As a consequence, the parts of the π-orbitals inside and outside of a nanotube rearrange, in a way that the outer contribution is larger than the inner one (see Figure 6a). The curvature induces a mixed state of σ- and π-orbitals, called rehybridization. Consequently, the π-orbital is always inclined by the hybridization angle $\delta = a/(2\sqrt{3}d)$ (a the length of the lattice unit vector and d the diameter) relative to the normal direction to the tube's surface.[41] This tilting angle is strongly dependent on CNT diameter and helicity.[42] Curvature in the nanotube introduces misalignment of π-orbitals within the graphene sheet (Figure 6b). The π-orbitals of a nanotube are not pointed directly toward the central axis of the nanotube, and some adjacent carbon π-orbitals have a misalignment angle, ϕ, between them. The π-orbitals of adjacent carbon atoms in a (10,10) and (5,5) nanotube have a π-orbital misalignments for the two different C–C bonds of $\phi = 0°$ and 10.4° for (10,10) and 0° and 21.3° for (5,5), respectively.

The rehybridization can also be explained by a mixture of sp^2 and sp^3 orbitals. While single sp^2 and sp^3 orbitals are saturated, the mixed state contains unsaturated orbitals. The mixing of a tetravalent sp^3 orbital to a trivalent sp^2 orbital leaves one hybrid orbital free for binding. The higher the ratio of the sp^3 contribution, the more free bonds exist and the higher the reactivity. As an index for local reactivity, the pyramidalization angle θ is used

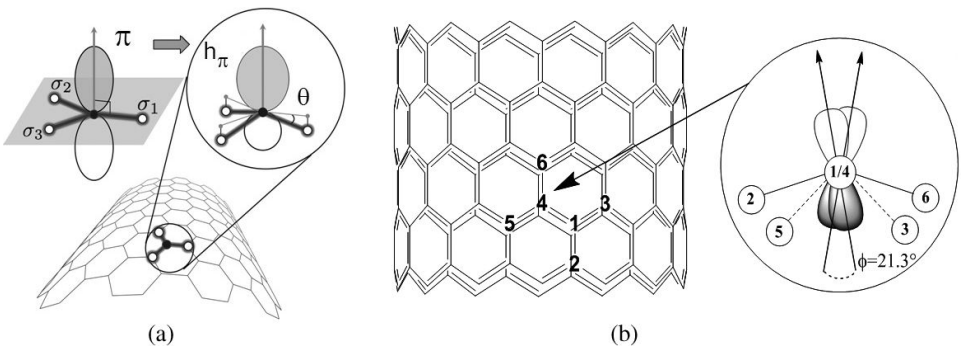

Figure 6. (a) Diagram showing the π-orbital in planar graphene and its change into h_π under bending together with the pyramidalization angle θ. (b) The π-orbital misalignment angles ϕ along the C_1–C_4.

(see Figure 6a), which is sufficient for describing the curvature-induced shift in sp^2 hybridization. θ is the angle between the σ- and π-orbitals minus 90° ($\theta = 0°$ for the sp^2 hybridization). The tetrahedral sp^3 orbital has a pyramidalization angle of 19.5°. This angle changes depending on the local mixture of sp^2 and sp^3 orbitals. The degree of hybridization $sp^{2+\eta}$ could be obtained, η being a number between 0 and 1. The comparison between different pyramidalization angles allows the comparison of reactivity, where a higher angle results in a larger reactivity. Thus, the degree of hybridization is highly curvature dependent, so that it is even possible to increase the reactivity alone by bending a CNT.

To summarize, strain in non-defective nanotube sidewalls is manifested in pyramidalization and π-orbital misalignment, which can be relieved by the addition of an atom or functional group to the CNT external surface. As the nanotube diameter increases, both the pyramidalization angle and π-orbital misalignment angle decrease, lowering the chemical reactivity of the C–C bonds, eventually approaching planar graphite for very large CNT diameters.

Finally, the CNT convex (outer) surface is chemically reactive because the convex arrangement of pyramidalized sp^2 carbon atoms is correctly disposed for the formation of chemical bonds with reagent species. For the same reason, the concave (inner) surface should be more inert and can withstand the presence of highly reactive species encapsulated within the nanotubes.

2.2.1. Presence of defects

The presence of defects in the CNT structure drastically affects all their properties such as transport, mechanical, magnetic, electronic, optical, or adsorptive.[43,44] These defects, which can be seen as islands with elevated reactivity, can be produced naturally during growth and purification processes, or can also be introduced intentionally to modify CNT properties. An interesting structural feature occurs near the ends of all CNTs from the closure of the graphene cylinders by the incorporation of topological defects such as pentagons in the hexagonal carbon lattice. Complex end structures can arise, for instance conical-shaped sharp tips, due to the way pentagons are distributed near the ends for full closure. It is predicted by theory that the ends of the tubes should have different electronic structure due to the presence of topological defects.[45] Under harsh conditions (purification and functionalization are commonly carried out with strong acids), the nanotubes are also attacked, resulting in the formation of defects on both the open-ended tips and sidewalls.[45–47] Among the most common defects are non-hexagonal rings, vacancies, and substitutional impurities (Figure 7).

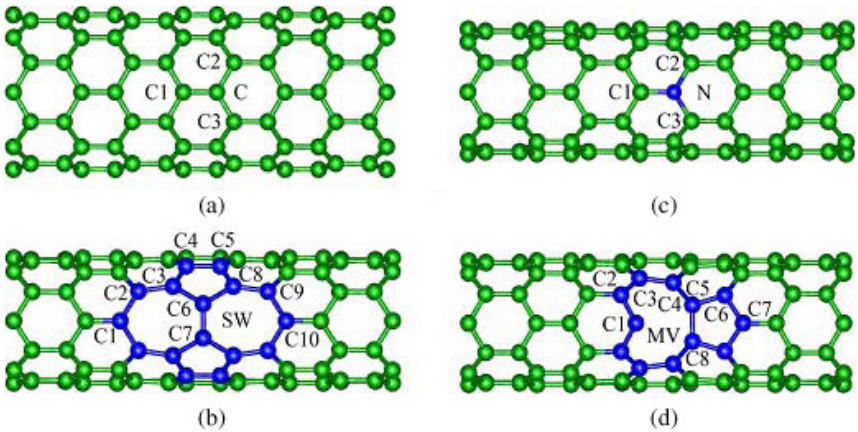

Figure 7. Side view of (8,0) nanotube structure (a) without deformation, (b) a SW defect, (c) nitrogen substitutional impurity, and (d) monovacancy. The labels identify atoms of the defective sites. Adapted from Ref. 53.

The most common type of defects in CNTs are non-hexagonal rings, namely pentagons and heptagons, where five- or seven-membered rings are present in the C framework, instead of the normal six-membered ring, which results in the bending of the nanotube. Other rings such as squares, octagons, nonagons, and decagons can also be observed at certain stages of the surface reconstruction, but they are found to rearrange by the SW mechanism, thus leading the structure to be mainly constituted of five-, six-, and seven-membered rings. When a pentagon is attached to a heptagon, it creates only topological changes (but no net disclination), which can be treated as a single local defect. A SW defect (Figure 7b) takes place in a carbon network when one C–C bond is rotated by 90°.[48] The pairs of pentagons and heptagons create a local disturbance (electrons are more concentrated around the double bonds involved in the defect instead of participating in the delocalized electron cloud above the graphene as usual), which serves as a reactive center for adsorption of various atoms, nanoparticles, or molecules.[49–51] Carbon atoms belonging to the tips are more reactive than those belonging to the sidewall of the nanotube, even in the presence of a SW defect.[52] Among the carbons making up the tips, the activity of each pyramidal structure is strongly correlated to its local curvature angle.

Another common type of defect is vacancies (Figure 7d). On such defects, the initial threefold symmetry is broken and a vacancy is formed. Removing a carbon atom leaves a vacant space with three dangling carbon bonds in the nanotube network.[54] The triplet state is slightly more stable than the singlet

state.[55] These three dangling bonds are unstable and undergo recombination to make a chemical bond between two of them, forming a pentagon ring and one remaining dangling bond — in a nonagon ring.[56] The related singly occupied molecular orbital (MO), given in Figure 8, clearly indicate the propensity of one carbon atom of the defect to be very reactive. Worthy of note is that such MOs and the singlet–triplet quasi-degeneracy point to the chemistry of carbenes. The formation of a vacancy and its orientation depends on the radius and chirality of nanotubes. Such a disturbance causes significant changes in their transport, magnetic, mechanical, and optical properties.[57,58] On the other hand, the dangling bond can also participate in the interaction with other molecules as well as it can be the center of functionalization of nanotubes.

Another well-known defect in CNTs is the presence of heteroatoms, which happen when a carbon atom is substituted by a foreign one (Figure 7c). CNT doping has drawn substantial interest due to the increased reactivity of doped nanotubes.[59] The most important and, at the same time, the most abundant heteroatom that affects the use of CNTs is oxygen. It is usually either chemisorbed on the surface or arranged in the form of functional groups analogous to those existing in organic chemistry. Since those groups increase the reactivity of the otherwise hydrophobic carbon surface, oxidation often opens the door to further modifications via interactions of specific chemicals with the groups and their reactions on the surface. Boron and nitrogen are the natural choices for doping CNTs since they differ only by one valence atom compared to carbon atoms. The boron and nitrogen serve as acceptors and donors of electrons in the CNTs, respectively, since boron has one electron less, and nitrogen has one electron more than the carbon

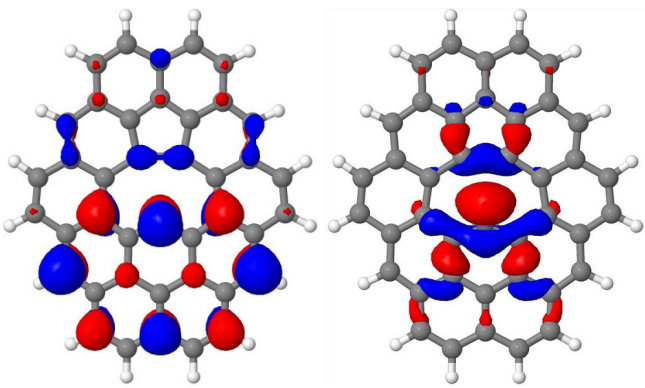

Figure 8. Singly occupied MOs in the lowest triplet state for a vacancy on a graphene sheet. From Ref. 55.

atom. Since the atomic radii are similar to the carbon atom, they create a small perturbation in the nanotube structure in comparison to the perfect one. The nitrogen in the nanotubes can be seen as regular defects, which change the chemical behavior of the tubes. The reactivity of these N-doped nanotubes can be estimated to be higher than undoped CNTs of same diameters. Theoretical calculations predict a localization of the unpaired electrons around the nitrogen defect in the semiconducting heteronanotubes.[59] Other heteroatoms such as hydrogen and sulfur can also be chemisorbed over a large number of imperfections and defects leading to stable surface compounds.[60]

Several studies have indicated that defective sites are of great importance to the adsorption process.[61–63] The presence of these defects in the nanotube structure creates highly reactive sites for the adsorption of various species. This means that the overall chemical reactivity of CNTs depends strongly on the number of surface defects present in the sample (sidewall and tips).

3. Physisorption on CNTs and Graphene

Depending on the intensity of the interaction between one or more adsorbates and a given substrate, a qualitative distinction can be usually made between *physisorption* and *chemisorption*. Physisorption results from the presence of van der Waals attractive forces due to fluctuating dipole moments between the adsorbate and the substrate (no charge transfer or electrons shared between atoms). Typically, this process involves energies in the order of 50–500 meV per atom. In the case of chemisorption, the adsorption energy (E_{ads}) of the adatom can rise to a few electron volt per atom, and a strong "chemical bond" is formed between the adsorbate and the substrate. The most common differences between these two adsorptive processes are shown in Table 1.

The adsorption of various gas molecules on graphitic surfaces is usually studied by first-principles calculations using density functional theory (DFT). The binding energy, tube/graphene–adsorbate distance, and charge transfers are generally obtained.[6,65] Atomistic modeling of gas adsorption should be treated differently depending on the specific phenomena involved, either physical adsorption or chemical bonding. Sometimes, however, the classification of the studied phenomena in terms of physical or chemical adsorption is quite difficult due to the occurrence of strong polar interactions or weak charge transfer that make uncertain the classification of the case under study. In these cases, the calculation of energetic quantities, such as the activation energy or the adsorption enthalpy, may help to get a clearer scenario, because

Table 1. Common features characterizing physisorption and chemisorption.[64]

Physisorption	Chemisorption
• Evidence for the perturbation of the electronic states of adsorbent and adsorbate is minimal.	• Changes in the electronic state.
• The chemical nature of the adsorptive is not altered by adsorption and subsequent desorption.	• The chemical nature of the adsorptive(s) may be altered, *i.e.*, the chemisorption may not be reversible.
• Energies are of order 50–500 meV/atom.	• The energy is of the same order of magnitude as the energy change in a chemical reaction between a solid and a fluid, eV/atom.
• The elementary step in physisorption from a gas phase does not involve activation energy.	• The elementary step in chemisorption often involves *activation energy* (*adsorption sites*).
• Multilayer adsorption or filling of micropores.	• One layer of chemisorbed molecules is formed.

it is expected that physical adsorption exhibits lower adsorption enthalpy values than the ones involved in chemical bonds.[66] The physical adsorption is believed to act as a step in the transition toward a chemisorption state. This transition usually results in the splitting of the molecule and adsorption of individual atoms, commonly identified as dissociative chemisorption.

3.1. Physisorption of gases on CNTs and graphene

In recent years, CNTs have been proposed as adsorbents for a wide variety of gases. The presence of structural defects plays a significant role in the adsorption over nanotubes and graphene. In general terms, a strong interaction is obtained whenever a gas molecule adsorbs over a defect on the nanotube surface (chemisorption), whereas a much weaker interaction (physisorption) is obtained when the same gas molecules interacts with a perfect surface.

3.1.1. Physisorption on individual CNTs

Although most of the studies deal with a perfect surface of individual CNTs, it is worth noting that some works have been devoted to the comparison of the reactivity of the tip of CNTs with the rest of its surface. Although the contribution of the tips to adsorption in terms of specific surface area (SSA) is negligible, it can be relevant at very low coverage or when studying field emission properties.[67]

The selected adsorption behavior of sulfur atoms on single-walled CNTs (SWCNTs) was studied by DFT in terms of adsorption energy and charge transfer.[68] It was found that the adsorption on the tips was energetically preferred in perfect SWCNTs; the adsorption energy and charge transfer on five-membered ring with one dangling bond defects were significantly larger with respect to perfect sites on SWCNTs, suggesting selective adsorption of sulfur on these defects. Importantly, adsorbed sulfur atoms can effectively stabilize these defects through the formation of S–C bond, which is not found in perfect SWCNTs. DFT calculations have also shown that O_2 and H_2O behave differently when they are adsorbed on a SWCNT tip.[69] The tip–molecule distance is 2.722 Å for O_2, and 2.488 Å for H_2O, and the binding energies are –0.51 eV and –0.12 eV, for O_2 and H_2O respectively, indicating that O_2 and H_2O are weakly adsorbed on the tip. H_2O molecules can be adsorbed on both closed and open-ended SWCNTs, and O_2 molecules can be adsorbed on a closed SWCNT. Quite differently, O_2 molecules are decomposed and chemisorbed on an open-ended zigzag SWCNT.

Considering gas adsorption over the CNT walls, there have been several attempts to explain the adsorption mechanism of different gases. In general terms, physisorption is believed to take place over a perfect surface. The presence of imperfections on the CNT walls, such as defects (see Section 2.2.1), often produces stronger interactions between the gas adsorbate and the surface, thus yielding a chemisorptive mechanism.

Given its potential in energy applications, the adsorption of hydrogen is perhaps one of the most debated in terms of mechanism, as different explanations have been proposed throughout the years. Based on first-principles theoretical calculations[70] and DFT calculations,[71] it has been reported that on pristine SWCNTs, the dissociative adsorption of H_2 molecules is improbable due to high energy barriers of about 2–3 eV. The dissociative chemisorption weakens carbon–carbon bonds, and the concerted effect of many incoming molecules with sufficient kinetic energies can lead to the scission of the nanotube. Thus, molecular physisorption is predicted to be the most stable adsorption state. The physisorption energies outside the CNTs are approximately 0.07 eV, and larger inside, reaching a value of 0.17 eV inside a (5,5) SWCNT. On the other side, H atoms have low-energy barriers, less than 0.3 eV. A DFT study of the interaction between atomic hydrogen and (5,5) and (10,0) SWCNT has shown a weak chemisorption on the outer wall.[72] A geometry relaxation produces a binding energy of about –1.5 eV. When SWCNTs are completely covered by hydrogen, the binding energy is enlarged by about 0.3 eV. From this study, a high sensitivity of the electronic structure to the presence of an H atom is reported.

Storage of fuels other than H_2 has also been studied in nanotubes. Natural gas (methane is the primary constituent) adsorbed on porous materials is a promising alternative to compressed natural gas as a clean vehicular fuel. Ganji *et al.* studied the role of defects on the interaction of methane with SWCNTs by using DFT-based calculations.[73] The energy values and H–C binding distances obtained from the *ab initio* calculations were typical of a physisorption process. The obtained results revealed a considerable increase in the adsorption binding energy of the order of 156% due to the presence of structural defects in CNTs, which affects the methane storage capacity in CNTs.

Physisorption of noble gases is widely employed to study the structural and theoretical aspects of surface adsorption because the inertness of the noble gases typically excludes the possibility of chemical and polar interactions with the surface. For helium, the difference of energy between the most favorable adsorption site (*H6-site*, see Figure 4) and the less favorable one (top site *T*) characterizes surface roughness; its value, of the order of 3.45 10^{-3} eV, is comparable to that on planar graphite.[74] The energy barriers for displacements of He atoms along the nanotube walls are of the order of 1.21 10^{-3} eV and the minimum energy of He–He interaction is –0.86 10^{-3} eV. Adsorption of other noble gases (Ar, Kr, Xe) on metallic and semiconducting CNTs was investigated using the van der Waals density functional.[75] It was found no difference in the adsorption between the metallic and semiconducting nanotubes, indicating that the adsorption energies for rare gases on CNTs are not strongly influenced by differences in the electronic structure of the nanotubes. Molecular dynamics simulation has been used to study the adsorption isotherms of noble gases on open-ended SWCNTs.[76] It was shown that adsorption occur both inside and outside an open-ended SWCNT in the pressure range (0.1–2.5 MPa). The interior coverage of 0.06 Xe–C and 0.08 Kr–C was reported at saturation conditions. The monolayer coverage on the exterior surface is 0.23 Xe–C and 0.25 Kr–C. Grand canonical Monte Carlo calculations performed on Xe adsorption on SWCNTs, at low pressure shows a similar tendency.[77] However, in that case and at very low pressure, simulations indicate that adsorption takes place primarily on the inside of the nanotubes. Interstitial and external adsorptions were found to be negligible in comparison with adsorption inside the nanotubes. The results also indicate that the curvature of the nanotube does not substantially perturb the adsorption potential from that of a graphene sheet.

Zhao *et al.* studied the adsorption of various gas molecules (NO_2, O_2, NH_3, CH_4, CO_2, H_2 and N_2) on SWCNTs using first-principles method.[78] The equilibrium tube–molecule distance, adsorption energy, and charge

transfer for various molecules on (10,0), (17,0), and (5,5) SWCNTs were calculated, as shown in Table 2. The results show that most of the studied molecules (except for NO_2 and O_2) are charge donors with small charge transfer (0.01–0.035 e) and weak binding (≤ 0.2 eV). For these molecules, the adsorption can be identified as physisorption. For O_2 and NO_2, it shows that they both are charge acceptors with large charge transfer and adsorption energies. It also demonstrated that there is no clear dependence of adsorption on the tube size and chirality.

Infrared (IR) spectroscopy has proved to be a very sensitive technique to study different adsorption sites on SWCNTs.[79] For gas molecules adsorbed onto SWCNT surfaces, there is a dispersive interaction that causes a softening of the bonds in the molecule, seen as a downshift in IR modes (Table 3). This effect has been well-documented and has been used to distinguish between exohedral and endohedral adsorption, by magnitude of the shift. This difference was shown with clarity and supported by calculations for CO adsorbed on SWCNTs. The ν(C–O) mode of endohedral CO showed a downshift Δ of 8 cm^{-1} and the exohedral CO showed a downshift of 3 cm^{-1}, compared to the gas phase. For physisorbed molecules, the higher coordination of

Table 2. Equilibrium tube–molecule distance (d), adsorption energy (E_{ads}), and charge transfer (Q) of various molecules on (10,0), (17,0), and (5,5) individual SWCNTs. Adapted from Ref. 78.

	NO_2	O_2	NH_3	CH_4	CO_2	H_2	N_2
(10,0) SWCNT							
d (Å)	1.93	2.32	2.99	3.17	3.20	2.81	3.32
E_a (meV)	797	509	149	190	97	113	164
Q (e)	–0.061	–0.128	0.031	0.027	0.016	0.014	0.008
Site	*T*	*A*	*T*	*H*	*H*	*H*	*H*
(5,5) SWCNT							
d (Å)	2.16	2.46	2.99	3.33	3.54	3.19	3.23
E_a (meV)	427	306	162	122	109	84	123
Q (eV)	–0.071	–0.142	0.033	0.022	0.014	0.016	0.011
Site	*T*	*A*	*T*	*H*	*H*	*H*	*H*
(17,0) SWCNT							
d (Å)	2.07	2.50	3.00	3.19	3.23	2.55	3.13
E_a (meV)	687	487	127	72	89	49	157
Q (eV)	–0.089	–0.096	0.027	0.025	0.015	0.012	0.006
Site	*T*	*A*	*T*	*H*	*H*	*H*	*H*

Table 3. Effects of interactions with nanotubes on IR spectra of small molecules.

Molecules	Non-interacting I/cm^{-1}	Endohedral I/cm^{-1}	Exohedral I/cm^{-1}	Endohedral shift I/cm^{-1}
CO	$\nu = 2143$ (gas)	$\nu = 2135$	$\nu = 2140$	$\Delta = -8$
NO_2	$\nu_1 = 1868$ (gas)	$\nu_1 = 1853$	—	$\Delta = -15$
NO_2	$\nu_{SS} = 1318$ (gas)	$\nu_{SS} = 1026$	$\nu_{SS} = 1026$	$\Delta = -292$
CO_2	$\nu = 2349$ (gas)	$\nu = 2329$	$\nu = 2342$	$\Delta = -20$
SF_6	$\nu_3 = 947$ (gas)	$\nu_3 = 927$	—	$\Delta = -20$
CF_4	$\nu_3 = 1282$ (gas)	$\nu_3 = 1247$	$\nu_3 = 1267$	$\Delta = -35$
NH_3	$\nu_1 = 3336$ (gas)	$\nu_1 = 3156$	$\nu_1 = 3205$	$\Delta = -180$

endohedral sites causes a greater downshift for endohedrally adsorbed gas molecules, compared to the surface of bundle (Table 3).

3.1.2. Physisorption on CNT bundles

During the growth process, SWCNTs usually aggregate into bundles because of van der Waals interactions. Thus, it is most appropriate to discuss adsorption on CNTs samples not in terms of adsorption on individual nanotubes but in terms of adsorption on the exterior or interior surfaces of such agglomerates. Most of the work on gas adsorption has been analyzed in terms of the homogeneous model of the bundle. This model considers that bundles are constituted by infinitely long nanotubes of the same diameter, packed into perfect arrays. An alternative model, the heterogeneous bundle, has tubes of different diameters constituting the bundles. Diameter mismatch leads to the appearance of packing defects in the bundles, which give rise to interstitial channels with diameters larger than those found in the homogeneous bundles. Theoretical calculations have predicted that the molecule adsorption on the surface or inside of the SWCNT bundle (Figure 9) is stronger than that on an individual tube.[78] A similar situation exists for multiwalled CNTs (MWCNTs), where adsorption could occur either on or inside the tube or between aggregated MWCNTs.[80]

It has also been shown that the curvature of the graphene sheets constituting the CNT walls can result in a lower heat of adsorption with respect to this on a planar graphitic surface due to rehybridization (see 2.2).[81] Additionally, DFT calculations have shown that nitrogen adsorption energies are stronger on armchair than on zigzag SWCNTs.[82] These considerations raise a number of questions with respect to the accessible sample surface area and pore size

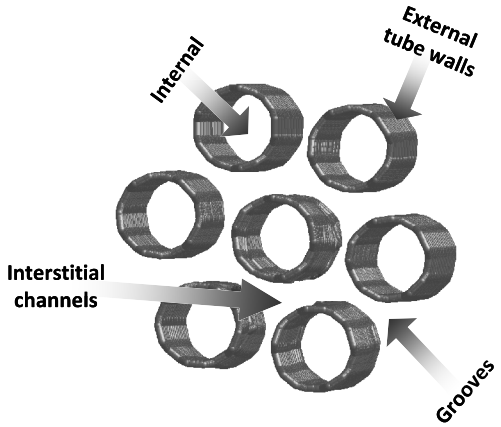

Figure 9. Schematic representation of a SWCNT bundle illustrative of the different adsorption sites.

distribution (PSD), the preferred binding sites, the uptake capacity as well as the strength (chemi- or physisorption) of the corresponding adsorbate–substrate interaction.

The structure of the pores and PSD of CNTs are largely dictated by the type of CNT. The pores in CNTs are scattered over a wide range of size and shape. The pores are classified by their sizes usually into three groups: (i) macropores having an average diameter of more than 50 nm, (ii) mesopores with a diameter of 2–50 nm, and (iii) micropores having an average diameter of less than 2 nm. The latter are further divided into supermicropores (0.7–2.0 nm) and ultramicropores of diameter less than 0.7 nm. For CNTs, which can be either microporous (SWCNTs) or mesoporous (MWCNTs), one should consider two types of pores: the well-defined inner cavity, cylindrical endocavities or α-pores[83] and the intertube voids, interstitial pores or β-pores[84] that will both contribute to the PSD. In addition to the well-known α and β pores, two types of newly defined pores with diameters of 2–10 and 8–100 nm have been evidenced for SWCNT arrays, interbundle (packing of bundles) pores and interarray (bundle arrays) pores.[85] For MWCNTs, it was shown that the aggregated (intertube) pores are much more important for adsorption than the endocavities.[80] It is worth noting that, since it is difficult to describe the complex secondary structures of such materials by the methods of Euclidean geometry, the method of fractal geometry has been applied.[86]

An important problem to solve when undertaking adsorption studies on nanotubes is the identification of the adsorption sites. Adsorption in a SWCNT bundle can occur inside the tubes, in the interstitial triangular

channels between the tubes, on the outer surface of the bundle, or in a groove formed at the contact between adjacent tubes on the outside of the bundle (Figure 9). For MWCNTs, adsorption can occur in the aggregated pores, inside the tube, or on the external walls, as already discussed; in this latter case, the presence of defects, as incomplete graphene layers, has to be taken into consideration. Although adsorption between the walls has been proposed in the case of hydrogen adsorption in herringbone-type graphite nanofibers, it is unlikely to occur in the case of MWCNTs due, for many molecules, to steric effect and should not prevail for small molecules due to long diffusion path. Finally, the tip of CNTs can also be considered as a specific adsorption site presenting pentagonal rings.[69,87]

Considering closed-end SWCNTs, simple molecules can be adsorbed onto the walls of the outer nanotubes of the bundle and preferably on the external grooves. In the first stages of adsorption (corresponding to the most reactive sites for adsorption), adsorption or condensation in the interstitial channels of the SWCNT bundles depends on the size of the molecule (and/or on the SWCNT diameters) and on their interaction energies.[88–91] Opening of the tubes favors gas adsorption of small molecules (including O_2, N_2, and H_2) within the inner walls.[92–94] It was found that the adsorption of nitrogen on open-ended SWCNT bundles is three times larger than that on closed-ended SWCNT bundles.[95] For hydrogen and other molecules such as CO, CH_4, or CF_4, computational methods have shown that, for open SWCNTs, groove sites are energetically more favorable than surface sites.[78,91,96–98]

Neutron diffraction experiments performed by Bienfait *et al.*[99] showed the adsorption of CO_2, and other gas molecules, on the groove sites of SWCNTs bundles. Yim and coworkers[100] combined IR spectra with local density approximation DFT to investigate CO_2 adsorption at different graphitic surfaces. They found that CO_2 adsorption was preferred on the grooves and interstitial sites of bundles of SWCNTs.

Zhao *et al.*[78] studied the adsorption of various gas molecules (Ar, N_2, H_2, O_2, H_2O, CO_2, CH_4, NO_2, and NH_3) in SWCNT bundles and on the bundle surface using first-principles methods. They found that the adsorption energy and charge transfer of the gases in the interstitial and groove sites of the tube bundle were considerably larger than those on the surface sites. The pore site was also energetically more favorable than the surface site. The enhancement of molecule adsorption on the groove and interstitial sites can be understood by the increased number of CNTs interacting with the molecule. Experimental results on the adsorption of NO_2 and NH_3 on SWCNTs were reported by Ellison *et al.*[97] Temperature-programmed desorption (TPD) data confirmed that NH_3 and NO_2 adsorbed molecularly and that

NO_2 was slightly more strongly bound than NH_3. In addition, the vibrational data were consistent with molecules that are adsorbed in interstitial channels in nanotube bundles. Rawat *et al.* measured the adsorption of xenon on purified SWCNTs for coverage in the first layer,[101] and found two rounded substeps adsorption data. This indicated the existence of at least two distinct groups of binding sites for adsorption in the monolayer: grooves and external surface. The binding energy on the strongest binding sites for Xe on the purified nanotubes was found to be 1.6 times greater than the corresponding value on planar graphite.

The trends observed in the binding energies of gases with different van der Waals radii suggest that the groove sites of SWCNTs are the preferred low-coverage adsorption sites, owing to their high binding energies. Furthermore, several studies have shown that at low coverage, the binding energy of the adsorbate on SWCNTs is between 25 and 75% higher than the monolayer binding energy on graphite. The changes observed in binding energy can be related to an increase in the coordination possibilities in binding sites, such as the groove sites in SWCNT bundles.[102,103]

There are not many studies addressing adsorption sites in MWCNTs. Hilding *et al.*[104] studied the adsorption of butane on MWCNTs at room temperature. They found that butane adsorbs on MWCNTs by two mechanisms: pore condensation and surface condensation. MWCNTs with smaller outside diameters adsorbed more butane, consistent with other findings that the strain in curved graphitic surfaces affects adsorption and reaction. Most of the butane adsorbs to the external surface of the MWCNTs, while only a small fraction of the gas condenses in the pores.[104]

3.1.3. Physisorption on graphene

The potential of hydrogen as a "green" fuel served as driving force to the development of novel materials capable of storing high amounts of this gas at ambient conditions. Due to its characteristics, CNTs and more recently graphene have been targeted as potential storage units. Hydrogen can be adsorbed on graphene sheets by two different ways: either by physisorption (interaction by van der Waals forces) or by chemisorption (forming a chemical bond with the C atoms). Physisorption usually happens with hydrogen in molecular form. The H_2 binding energy was theoretically evaluated in the range of 0.01–0.06 eV.[105,106] It is clear that the binding of molecular hydrogen is very weak and requires therefore low temperatures and high pressures to ensure reasonable storage stability. Chemisorption of molecular hydrogen on graphene presents rather high barriers estimated around ~1.5 eV,[107]

because it requires the dissociation of H_2 (dissociative adsorption). Conversely, the chemisorption of atomic hydrogen is a rather favorable process: commonly accepted values for H binding energy and chemisorption barriers are ~0.7 eV and ~0.3 eV, respectively. Theoretical studies have shown, in particular, that adsorption of the first H atom locally modifies the graphene structure favoring further H binding, with a collective stabilization effect.[108,109] The formation of a completely saturated graphene sheet, with 1:1 stoichiometry between C and H ("graphane"), would be able to store a maximum amount of 7.7 wt.% of H_2.[110] For those approaches that possess sufficiently large hydrogen storage capacity, desorption through heat is commonly used to release hydrogen. As an alternative to this process, Tozzini and Pellegrini[10] proposed an approach in which they take advantage of the variation of H binding energy with graphene curvature (Figure 10). The large variation of

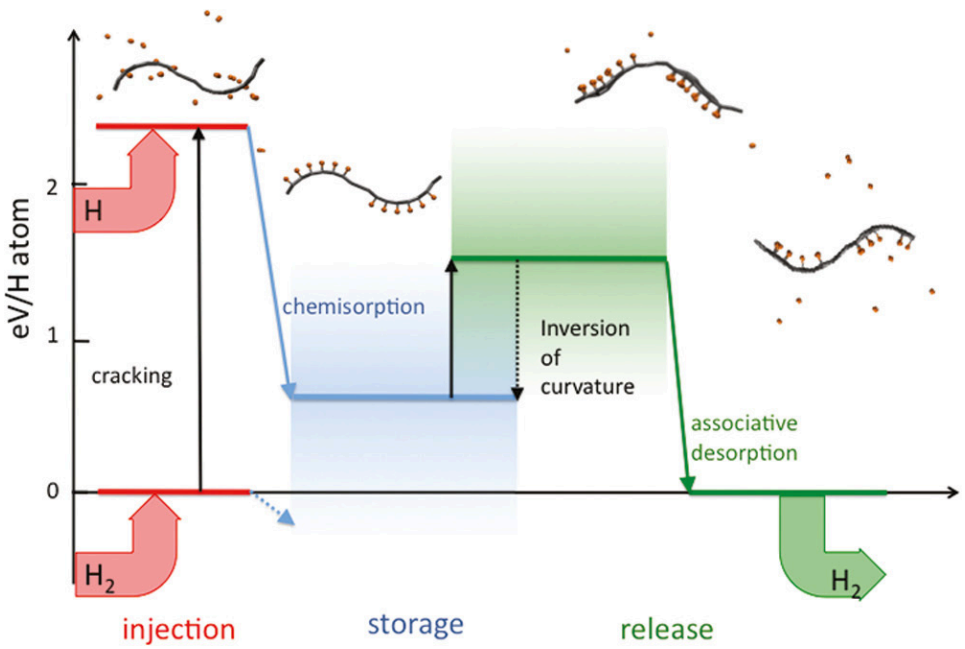

Figure 10. Working scheme of the proposed microscopic mechanism for hydrogen storage. Three phases can be distinguished: during the injection (red), the atomic hydrogen is cracked and introduced in the system. It will chemisorb on the convex regions during the storage phase (blue). The release phase (green) is activated by inversion of curvature, causing the associative desorption of H_2. The horizontal lines are placed according to the effective energies/H atom (shades represent range of energy variability). Graphene sheet is represented in gray and the hydrogen in orange. Reprinted from Ref. 106 with permission. Copyright © 2011 American Chemical Society.

H binding energy makes the chemisorption a favorable process on convex sites and hydrogen release a favorable process on graphene concave sites.

The adsorption and reactivity of CO_2 on carbonaceous surfaces is a subject of great interest in the technological and environmental fields. From an environmental protection point of view, the reduction of the greenhouse gas CO_2 concentration on the atmosphere is an urgent requirement, and various studies have focused on the potential capture and storage of CO_2.[111–113] Cabrera-Sanfelix studied the adsorption and reactivity of CO_2 on a vacancy defect of a graphene sheet, using DFT calculations.[112] A mechanism (Figure 11) to fix and remove gaseous CO_2 molecules was proposed to consist in (i) physisorption of CO_2 on the top of the vacancy defect, with the inner axis of the molecule parallel to the surface (strong physisorption with a binding energy of –0.136 eV); (ii) formation of a lactone group with the C atoms surrounding the vacancy through a chemisorptive state (after overcoming an energy barrier of ~1.2 eV and it involves an energy release of about 1.4 eV); (iii) the lactone chemisorbed state show dissociation of the CO_2 through the formation of epoxy groups (which is more stable than the preceding lactone group by ~0.614 eV); (iv) oxygen recombination from the epoxy groups and the desorption of O_2 as the global minimum (energy release of ~3.4 eV with respect to the gas phase and with an energy barrier of ~1.08 eV relative to the previous epoxy-complexes configuration), yielding a defect-free graphene sheet surface.

Leenaerts *et al.* investigated the adsorption of H_2O, NH_3, CO, NO_2, and NO on a graphene substrate using first-principles calculations.[114] They

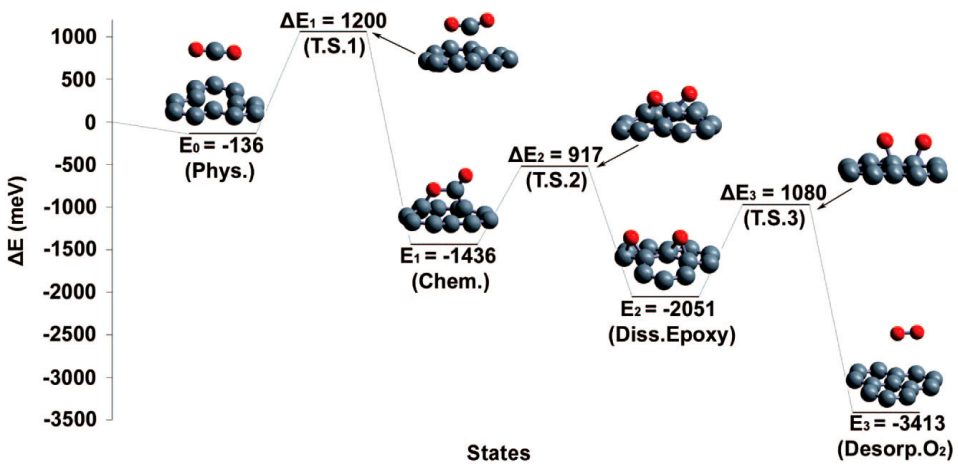

Figure 11. Structural and energetic scheme of the proposed global reaction path for the interaction of CO_2 with defective graphene layer. Reprinted from Ref. 112 with permission. Copyright © 2009 American Chemical Society.

found that the adsorbates were physically adsorbed on the pristine graphene and that the charge transfer between the adsorbates and graphene was almost independent on the adsorption site. However, charge transfer did strongly depend on the orientation of the adsorbate with respect to the graphene surface. In addition, charge transfer was interpreted in light of two different mechanisms: for NO_2 on graphene, it is mainly due to the position of the lowest unoccupied molecular orbital (LUMO) below the Dirac point, whereas for all the other adsorbates, it was caused by the mixing of the highest occupied molecular orbital (HOMO) or LUMO orbitals with the orbitals of graphene; the strength of the hybridization being deduced from the geometrical orientation of the HOMO and LUMO orbitals with respect to the graphene surface.

Daykova *et al.* used first-principles simulations to study the adsorption of methane on a perfect graphene sheet.[115] They found that CH_4 occupies the center of the hexagon and interaction between the methane molecule and graphene induces a dipole moment in methane. The dipole moment is *ca.* 1.5 Debye if only one bond of CH_4 faces toward the graphene surface, and it is much smaller, *i.e.*, *ca.* 0.5 Debye, if three bonds point at the surface.

The adsorption of Xe on graphene was systematically investigated by *ab initio* MP2 calculations using Dunning's correlation-consistent basis sets.[116] The polycyclic aromatic hydrocarbon (*i.e.*, coronene) was used to model the graphene surface. The equilibrium distance of Xe at the hollow site was calculated to be 3.56 Å, which was in excellent agreement with the available experimental value of 3.59 ± 0.05 Å. The corresponding binding energy at the hollow site was calculated as −142.9 meV, whereas the binding energies at the bridge and on-top sites were −130.8 and −127.4 meV, respectively.

From an experimental point of view, Kayhan *et al.* studied the gas-sensing properties toward low concentrations of CO and H_2, using a FLG film prepared by Ni-catalyzed chemical vapor deposition (CVD) synthesis.[117] They observed no resistance change of CVD-graphene at room temperature after exposure to CO. Coverage of graphene with H_2 gas at room temperature did induce a slight increase in the resistance, although no concentration dependency was found. This behavior indicated that both gases undergo only physical adsorption on graphene, due to rather weak van der Waals interactions between the graphene surface and the gas phase, thus corroborating theoretical studies previously discussed.

Yoon *et al.* reported a graphene-based CO_2 gas sensor fabricated by mechanical cleavage of highly ordered pyrolytic graphite (HOPG).[118] The sensor showed significant conductance changes when exposed to various concentrations of CO_2 in air. Because of the weak interaction between CO_2 and

graphene, the device response was rapid (response time of less than 10 s) and reproducible.

3.2. Physisorption of liquids on CNTs and graphene

Adsorption of liquids on carbon, though less studied than gas adsorption, is no less important due to the number of applications that these studies find in water purification, environmental protection, oil recovery, adhesion, and lubrication.[119] The liquid–solid surface interaction can be broadly divided into two topics, namely, (i) the study of the energetics of immersion of a solid in a liquid or wetting of a liquid on a solid surface, and (ii) adsorption on a solid surface by species present in solution. To understand these adsorption phenomena, it is necessary to not only characterize the surface structure of the solid but also the nature of the interaction between the liquid and the solid. Techniques such as immersion microcalorimetry have been used for the calculation of the heat of immersion of powders in several types of liquids. In parallel, microscopic methods have been used for determining the degree of wetting of a liquid on a solid surface. The principles of these experimental methods and the thermodynamic quantity determination there from have been detailed in several monographs.[120–122] The interactive forces between the solid surface and the liquid in which it is immersed play a key role in the phenomenon of "wetting" for the liquid and "wettability" for the solid phase. When a solid is immersed in a liquid, wetting can arise due to adhesional forces between a liquid film on the solid, spreading of a liquid drop on the solid, or condensation of a liquid from the vapor phase on the solid. The determination of the wettability Δ of a surface is often carried out microscopically by measuring the contact angle θ between the two surfaces that is related to the surface tension γ of the liquid by the simple relation: $\Delta = \gamma \cos\theta$. For contact angles less than 90°, the liquid is said to wet the solid surface and vice versa (Figure 12).

The process of wetting being an exothermic one, wettabilities of powders can also be determined by immersion calorimetry using the relationship between wettability and the heat of immersion. The advantage of this technique is that in addition to the wettability, an estimation of various other parameters such as surface polarity, porosity of the surface, and the surface area of the solid can also be obtained.[120] The determination of the wettability of carbonaceous substrates such as graphite or carbon black (CB) is routinely carried out in view of their application in industry for oil recovery and lubrication.

The second type of adsorption, namely, adsorption on carbon substrates from species present in solution is also of great importance and a wide

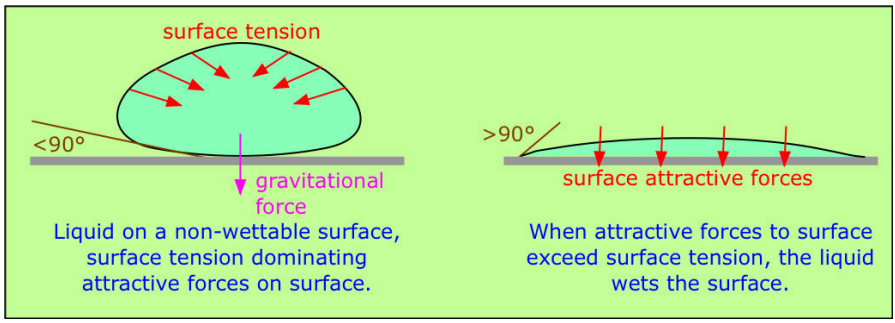

Figure 12. Illustration of surface wetting phenomenon.

spectrum of adsorbates, including organic molecules used in chemical and pharmaceutical industry, biomolecules, natural organic matter (NOM), and polymers, have been investigated.[123] These processes are completely different from those involving the adsorption of gases principally due to the presence of two adsorbing species present, namely, the solute and the solvent. The overall adsorption isotherm cannot be derived from the individual adsorption isotherms of the two components. The thermodynamics and the theoretical aspects of such composite isotherms have been treated in detail.[121,122] For all practical applications, only dilute solutions have been considered where one of the components, the solvent, is in excess. In such cases, a number of assumptions about the thickness (monolayer), composition, and structure of the adsorbed layer (no interaction between the adsorbed species on the substrate) can be made as a result of which an adsorption isotherm obtained by plotting the amount absorbed as a function of the concentration of the solute describes the phenomenon adequately.[120] Experimentally, this involves either the measurement of the enthalpy of adsorption of the solution by microcalorimetry or the concentration of the solution after adsorption followed by sedimentation and filtration. Factors such as the pH of the solution or the presence of surface charges on the adsorbent influence the shape of the isotherm and hence give valuable information about the adsorption process. For polymers and biomolecules, steric effects may also play a role in determining the concentration of the adsorbate on the surface.[124] Even so, the mechanistic aspects of such studies is still unclear mainly due to the innate complexity of liquid adsorption, namely, non-ideal behavior due to strong intermolecular interaction when compared to gases.[125] Unlike the case of gases, the sizes of the liquid adsorbates can vary greatly and the porosity of the carbon adsorbent surface needs to be suitably tailored. The fundamental aspects of liquid adsorption on carbon substrates highlighting the factors that control the adsorption process from aqueous phase have been treated in a

compact review article by Moreno-Castilla.[125] In the following paragraphs, the adsorption and wetting of CNTs and graphene surfaces by liquid adsorbates will be described highlighting the influence of the microstructure, the surface functionalization, and the presence of heteroatoms on the carbon substrate on the adsorption process. Some representative examples, including water, ionic liquids (ILs), and organic molecules, that are liquids at 298 K are outlined; following which adsorption of species present in dilute aqueous or organic solutions on the surface of CNTs and graphene is highlighted using selected examples.

3.2.1. Adsorption of water on CNTs and graphene

One of the most well-studied liquid adsorbed on CNTs and graphene is water. Water confined inside SWCNTs is of particular interest for understanding the wetting properties of the nanotubes surface that is important for many applications. In addition, water confined in the nanotube cavity gives interesting information on the structure, reactivity, and physical properties of confined fluids. Striolo *et al.* performed grand canonical Monte Carlo simulations on the water uptake by SWCNTs and found that the calculated adsorption isotherms depended on the diameter and chirality of the nanotubes.[126] Adsorption isotherms simulated for (10,10), (12,12) and (20,20) SWCNTs were found to be of type V in the IUPAC classification characterized by negligible water uptake at low pressures, sudden and complete pore filling once a threshold pressure is reached, and wide adsorption–desorption hysteresis loops. On the other hand, no hysteresis was observed for water adsorption in smaller tubes (6,6) and (8,8) and the amount of water adsorbed in SWCNTs increased with increasing pressure. The authors also studied the structure of the confined "water nanotubes" and reported that water confined in (6,6) SWCNT at 298 K forms 1D hydrogen-bonded chains, in which each water molecule receives one hydrogen from the preceding molecule and donates one hydrogen to the following molecule along the chain. For the larger tubes, 3D structures such as cubic or octagonal water were predicted (Figure 13).

Marti and Gordillo[127] studied the dynamics of liquid water and its isotopes when adsorbed inside CNTs of different diameters by means of molecular dynamics simulations and reported the presence of new bands in the vibrational spectra. The presence of liquid-like water at temperatures much lower than the freezing point of water was confirmed by Maniwa *et al.* using X-ray diffraction (XRD) where liquid-like water transformed into ice at 235 K.[128] It has been suggested that this anomalous fluid-like behavior of

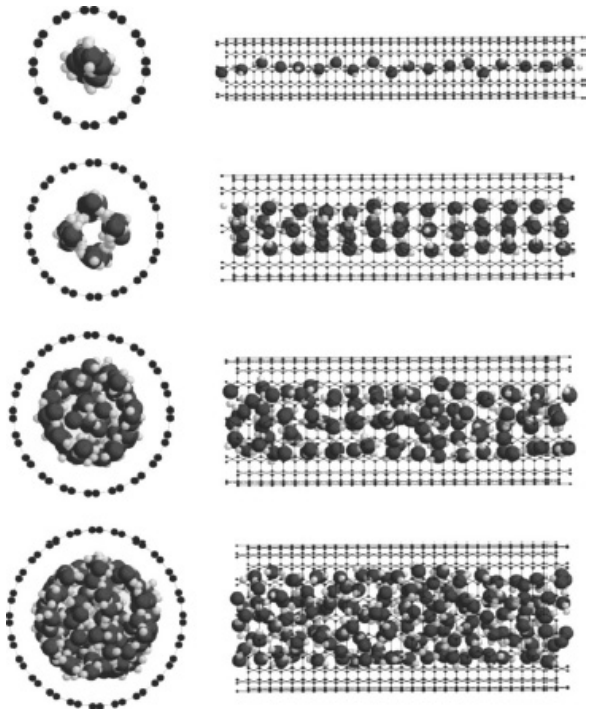

Figure 13. Front and lateral views of representative simulation snapshots for water adsorbed in SWCNTs at 298 K. From top to bottom figures are for water confined in (6,6), (8,8), (10,10), and (12,12) SWCNTs. Dark gray spheres represent oxygen atoms and light gray spheres represent hydrogen atoms. Reproduced from Ref. 126 with permission.

"water nanotube" may explain water transport mechanisms in nominally hydrophobic regions of transmembrane proteins.

The adsorption of water on the surface of graphene has been studied by several workers following the observation of Novoselov *et al.*,[129] who reported that traces of adsorbed water dramatically altered the mobility of FLG. Both experimental and theoretical work on graphene surfaces have been reported. Gordillo and Marti have reported interesting results about the behavior of water confined inside or close to different graphene surfaces by means of molecular dynamics simulations.[130] This allowed the calculation of the structural properties such as atomic density profiles, molecular orientation, and hydrogen bond distributions, showing a significant difference from bulk water. Important changes were also predicted for the dynamic properties such as IR spectra, translational and rotational diffusion coefficients of adsorbed water. At the carbon–water interface, dielectric properties such as permittivity were found to be up to five times compared to the bulk. These

changes are similar to those for water confined in CNTs.[131] As far as experimental data are concerned, Yavari *et al.* measured the sheet resistance of graphene prepared by CVD on copper foils transferred onto silicon substrate exposed to controlled humidity and found that the resistivity of the film as measured in a closed chamber changed with the amount of water present in the chamber[132] (Figure 14).

The resistivities returned to their original values if the films were annealed under vacuum. By varying the temperature of the film, the authors concluded that the presence of water vapor opened a band gap in graphene of 0.2 eV. However, this experimentally observed gap was one order of magnitude

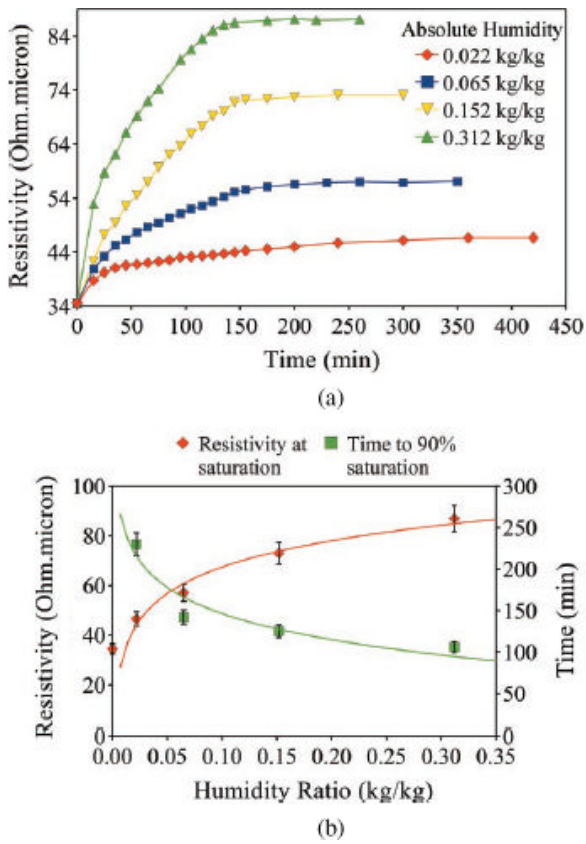

Figure 14. (a) Resistivity versus time characteristics of graphene film for different values of absolute humidity. (b) The values of maximum resistivity observed and the time taken to achieve 90% of the saturation value for different values of absolute humidity. The graphene film's resistivity is increased by increasing the absolute humidity while the time to saturation decreases with increasing humidity. Reproduced from Ref. 132 with permission.

lower than that predicted by spin-polarized DFT calculations by Berashevich and Chakraborty who predicted changes in band gap up to 2.0 eV.[133] This difference was explained to be due to the effect of the underlying substrate on the adhesion of water molecules on the graphene surface effects that influenced the experimental data. Rafiee *et al.* studied the wetting of graphene sheets by water and reported that graphene sonicated in water, acetone, or a combination of water and acetone showed different contact angles with water droplet ranging from superhydrophobic to superhydrophilic behavior.[134] The molecular arrangement of water on graphene surface has also been studied by Kimmel *et al.* who deposited thin films of H_2O or D_2O on graphene substrate grown on Pt crystal at temperatures ranging from 20 to 152 K. It was found that ice layers formed on the graphene surface showed significant wetting at 135 K.[135,136] At higher temperatures, these ice layers dewet the surface forming ice crystals. The presence of a vacancy of a defect changed the adsorption energy of water for graphene. DFT calculations have shown that on pristine graphene, water is physisorbed but on vacancy sites, the adsorption energy is increased so as to give a chemisorbed-physisorbed state.[137]

3.2.2. Physisorption of ionic liquids on graphene and CNTs

Over the past few years, ILs have gained considerable attention as "green media" for chemical reactions, owing to their unique characteristics such as low toxicity, low vapour pressure, high ionic conductivity, and good solvation properties. The adsorption of ILs on CNTs and graphene is of great interest in view of the potential applications of such hybrid systems in electrochemistry, composites, and catalysis. The synthesis, characterization, and applications of CNT-IL and graphene-IL composites have been reviewed recently.[138] IL-based surfactants adsorb on the CNT surface via their hydrophobic long alkyl chain orienting their hydrophilic cationic imidazolium groups toward the aqueous phase (Figure 15). Hence these have also been adsorbed on CNTs or graphene to achieve a homogeneous dispersion of the latter.[139] Several types of long- and short-chain ILs have been investigated to disperse CNTs in aqueous solvents. Surfactant-like long-chain ILs such as 1-alkyl-3-methylimidazolium bromides, butyl-*a*,*b*-bis(dodecylimidazolium bromide),[140] carbazole-tailed ILs (1-*n*-(*N*-carbazole)alkyl]-3-methylimidazolium bromide),[141] and imidazolium ion-based ILs with hexadecyl alkyl chain have been found to be quite effective in dispersing CNTs in water. While CNT-IL dispersions formed by non-covalent wrapping are relatively unstable, physisorbed polymerized ionic liquids (PILs) form stable dispersions with CNTs.[142]

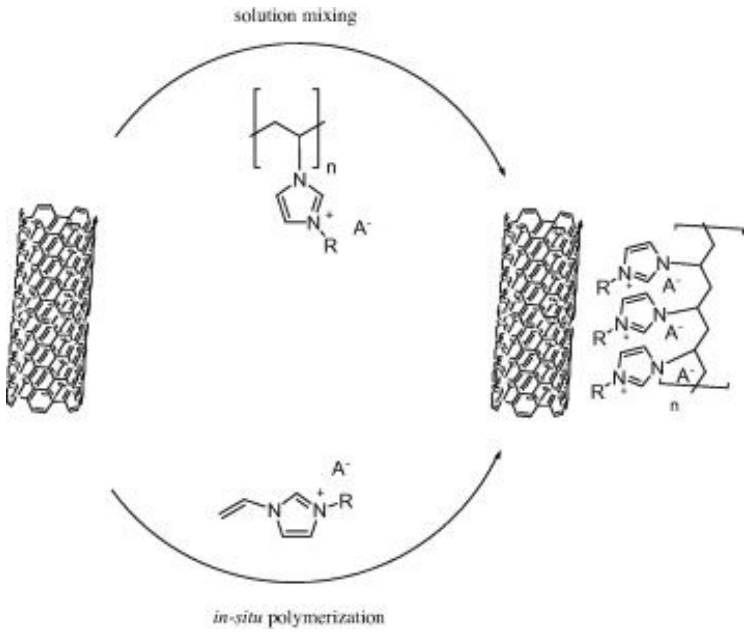

Figure 15. Schematic representation of the non-covalent functionalization of PILs on CNTs. Reproduced from Ref. 138 with permission.

Figure 15 shows the schematic diagram of CNTs and graphene surfaces non-covalently wrapped with PILs. Such dispersions may owe their stability to the larger size of the PILs that prevent the CNTs from agglomerating. Despite rapid advancement in applications, only few reports exist on the fundamental adsorption characteristics of these systems. Frolov *et al.* have studied the basic mechanisms of CNT interactions with several room temperature ILs by means of fully atomistic molecular simulations, and related these interactions to the length of the alkyl cation chain on the IL, the presence of solvents, and the charge on the CNT.[143] Microscopic adsorption structures of imidazolium-based ILs, [mmim]PF_6, [bmim]PF_6, [mmim]Cl, and [bmim]Cl, on the surfaces of graphene plates, coronene, and circumcoronene, were studied in detail by quantum chemical computation.[144] It was found that the adsorption process modifies the charges of carbon atoms of the graphite model involved in the interaction appreciably but does not modify those of adsorbed ILs. The type of imidazolium-based IL determines the extent of charge modification of graphite model atoms.

For graphene, the physisorption of IL can be used not only to disperse but also to exfoliate graphite to form FLG.[145] It has been found that ILs are ideal for exfoliating graphite since their surface tension values match the surface

energy of graphite and their ionicity helps to stabilize the exfoliated graphene sheets. ILs can adsorb on the graphene surface through non-covalent interactions of anion and/or cation with graphene. The preparation of FLG sheets, mostly with less than five layers, by direct exfoliation of pristine graphite in [bmim]NTf_2 and [bmpy]NTF_2 by sonication for 1 h has been reported.[146] In addition to dispersion in solvents, physisorption of ILs can also be achieved by direct grinding of graphene or CNT with ILs giving rise to what are known as bucky gels. These have gained a lot of importance due to the ease of handling and the unique combination of the mechanical properties of CNT or graphene with the ionic conductivity of the ILs. It appears that the molecular ordering of the non-volatile ILs and the networking of CNTs by weak physical bonds give rise to the formation of the gel. Using PILs, these gels can be used for preparing conducting polymer materials with enhanced mechanical properties.[147] Analogous to the other adsorbates, the adsorption of IL is also influenced by the presence of functional groups on the CNT or graphene. For graphene oxide (GO), the addition of a hydrophilic PIL followed by reduction, leads to the formation of highly dispersed graphene in the aqueous phase that can be transferred into an organic phase by anion exchange.[148] Furthermore, the reducing capability of imidazolium-based PIL leads to a more effective reduction of GO as confirmed by X-ray photoelectron spectroscopy (XPS).[149]

3.2.3. Physisorption on CNTs and graphene of ions and molecules from solution

The adsorption of organic molecules and inorganic ions from solution is of importance for applications in the preparation of CNT and graphene dispersions, in water purification and in environmental pollution control. CNTs have been particularly targeted due to their ability to remove inorganic pollutants, including heavy metal ions and radionuclides from large volumes of waste water.[150] The mechanisms of heavy metal ion adsorption on CNTs are very complicated and appear attributable to physical adsorption, electrostatic attraction, precipitation, and chemical interactions with the surface functional groups of CNTs. The most important factors influencing these adsorptions are the pH of the solution and the nature of the functional groups on the CNT surface. Among heavy metal ions, Pb^{2+}, Ni^{2+}, and Cd^{2+} have been the most studied.

Organic adsorbates have been commonly used for non-covalent functionalization of the CNT and graphene surface to achieve homogeneous dispersions with or without added surfactants. It is found that for CNTs, the adsorption of organic molecules such as benzene or toluene is enhanced in

the presence of surfactants.[151,152] In general, the physisorption of organic moieties on CNTs takes place through π–π interactions, hydrogen bonding, or through hydrophobic effects.[17] A highly heterogeneous adsorption profile has been observed for CNTs, the adsorption involving mainly defective sites, functional groups, and interstitial spaces between the grooves in bundles.[153] Various models have been proposed for the adsorption of organic molecules on CNTs.[154] For many organic molecules, multilayer adsorption followed by condensation, including condensation inside CNT cavities, has been observed. Concentration dependencies are generally not observed in aqueous solutions in contrast to that observed for organic vapors. Hysteresis is observed for several organic adsorbates that has been attributed to strong π–π coupling and capillary condensation.[155] In some cases, the adsorption of the organic molecule changes the secondary structure (for example, debundling of SWCNTs) resulting in different mechanisms for adsorption and desorption, thus giving rise to hysteresis.[156] The adsorption of organic molecules on CNTs usually shows a strong dependence on the morphology of the nanotubes and is not directly related to the surface area. Mezgebe *et al.* compared the adsorption of hexane, diiodomethane, water, and formamide on SWCNTs and MWCNTs using capillary rise methods and found that the former showed a higher adsorption of polar liquids whereas the latter showed a preference for nonpolar liquids[157] (Figure 16). Diiodomethane showed the maximum adsorption whereas hexane was the least adsorbed. It is also interesting to note that water-adsorption curves for SWCNTs showed two stages while for MWCNTs only one stage is visible, indicating that wettabilities of the two surfaces are different.

The pore size compatibility with the adsorbate was found to be important for adsorption on CNT walls, especially for natural organic matter (NOM). The amount of adsorbed NOM onto CNTs increased with a rise in initial NOM concentration and with the ionic strength of the solution but decreased with a rise in solution pH. A comparative analysis on the NOM adsorption between CNTs and granular activated carbon (GAC) has been reported. Under the same conditions, the acid-treated CNTs have the best NOM adsorption performance, followed by raw CNTs and then the GAC, suggesting that the CNTs are efficient NOM adsorbents.[158,159] On the other hand, in special cases, even large molecules such as enzymes were able to enter the inner pores of CNTs.[160] In some cases, larger molecules can show increased adsorption on CNTs due to curvature effect. It has been proposed that large molecules can assume twisted geometries to match the surface of CNTs.[161–163] Ji *et al.* studied SWCNTs and MWCNTs as potential effective adsorbents for removal of tetracycline from aqueous solution. After normalization for

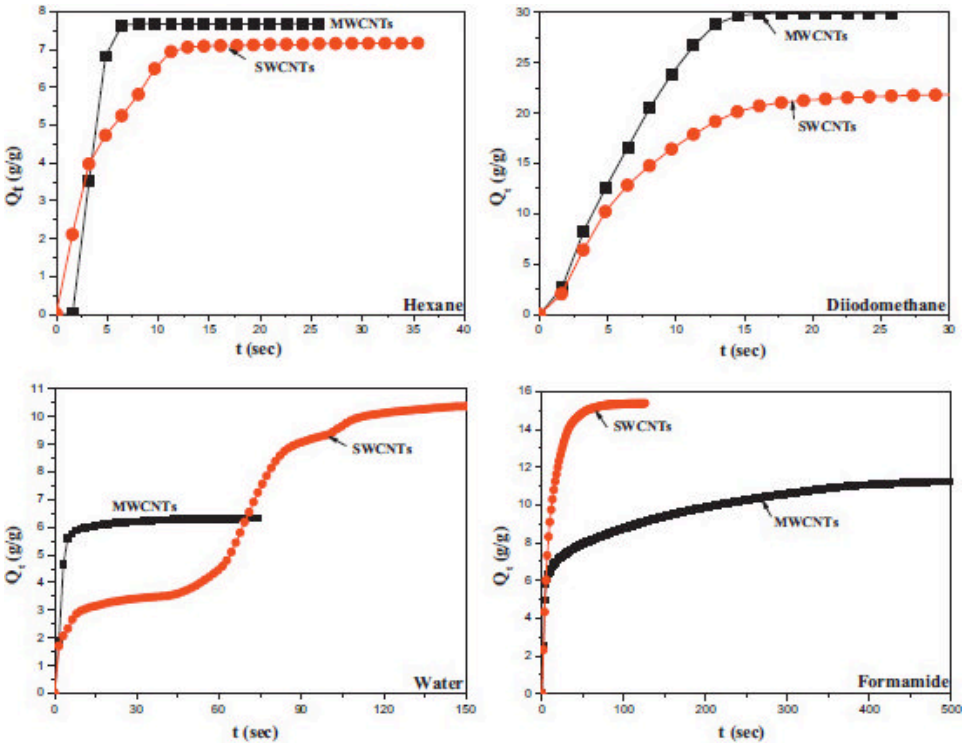

Figure 16. A comparison of the adsorption curves for SWCNTs and MWCNTs in relation with probe liquids. Reproduced from Ref. 157 with permission.

adsorbent surface area, the adsorption affinity of tetracycline decreased in the order of graphite/SWCNT > MWCNT > AC. The remarkably strong adsorption of tetracycline on CNTs and graphite can be attributed to the strong adsorptive interactions (van der Waals forces, π–π electron-donor–acceptor interactions, cation–π bonding) with the graphene surface.[164]

Relatively few studies are available for the adsorption of organic liquids on graphene. Using *ab initio* electronic structure calculations, Junkermeier *et al.* estimated the energy of adsorption of amine groups on graphene sheets. They found that amine is found to form a semi-ionic bond of 0.778 eV on pristine graphene. Its binding is found to be modified near other defects and substituent atoms.[165] The adsorption mechanisms of formaldehyde (H_2CO) on modified graphene, including aluminum doping, SW defects, and a combination of these two, were investigated via DFT. It was found that the graphene with SW defect is more sensitive than perfect graphene for detecting H_2CO molecules.[166] For graphene, π–π interactions were found to be the most important criterion for increased physisorption efficiency. The adsorption

characteristics of chemically reduced graphene toward acrylonitrile, *p*-toluenesulfonic acid, 1-naphthalenesulfonic acid, and methylene blue were evaluated. The results showed that organic chemicals with larger molecule size and more benzene rings possessed a higher adsorption rate and a higher maximum adsorption capacity on graphene and fluorescence spectra indicated that the adsorption of methylene blue on graphene was a π–π stacking adsorption process.[167] Similarly, graphene was found to be a good adsorbent for bisphenol A (Figure 17) with a maximum adsorption capacity for graphene as obtained from Langmuir adsorption isotherm that was reportedly the highest value ever observed for a carbonaceous substrate.[168] Results on the adsorption of thiophene and nitrate ions show that graphene, despite its lower SSA when compared to nanotubes and activated carbon, shows a high adsorption capacity.[169,170]

The presence of oxygenated functional groups drastically changes the adsorption properties of nanotubes and graphene. In some cases, the functional groups may increase the wettability for polar compounds while in other cases; they may block potential adsorption sites leading to reduced adsorption.[171] Hsu *et al.* have reported the adsorption and desorption of 2-propanol on oxidized CNTs. The adsorption mechanism is mainly attributable to physical forces from 278 to 298 K, but appears attributable to chemical forces from 298 to 308 K.[172] Liao *et al.*[173] discussed the sorption capacity of pristine and acid-treated MWCNTs and found that acid-treated MWCNTs become more hydrophilic due to the presence of carboxylic groups that give to the surface a negative charge. This negative charge reduced the adsorption of certain molecules such as resorcinol. A second effect was the surface deformation caused by functionalization that led to the decrease in pore volume and led to the decrease in adsorption capacity. In the case of graphene, many

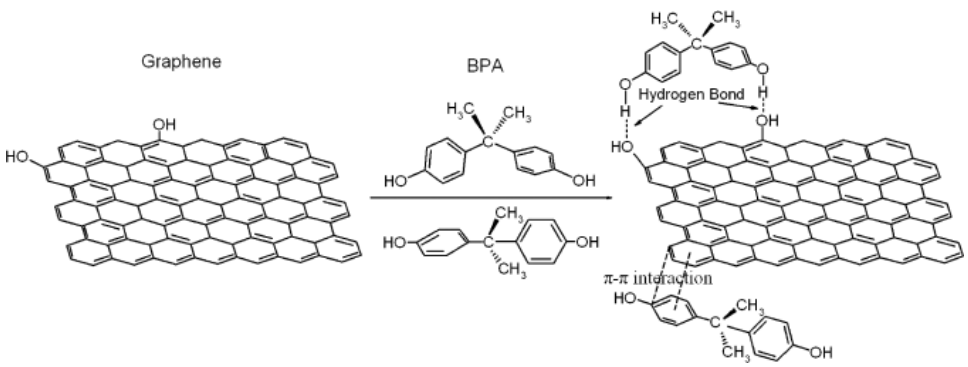

Figure 17. Schematic of π–π interactions and hydrogen bonding between bisphenol A and graphene. Reproduced from Ref. 168 with permission.

adsorption experiments have been carried out on GO dispersions and it was found that for methylene blue adsorption, GO was more efficient than activated carbon or CNTs despite the lower SSA. The increased activity was attributed to a combination of increased electrostatic π–π interactions between the graphene sheets and the adsorbate as well as the hydrogen bonding that anchors the organic adsorbate on to the graphene surface.[174]

3.2.4. Physisorption of liquids on doped CNTs and graphene

It has been found that doping CNTs and graphene by aliovalent atoms such as boron, nitrogen, and fluorine changes the electronic properties significantly and in turn modifies the acidity–basicity of the surface through charge transfer.[175] As already shown in the case of gases in Section 3.1.1, the adsorption energy for any adsorbent is modified by the presence of the defect and is proportional to the distance from the defect.[165,176] This effect is more pronounced for highly electronegative substituent atoms such as fluorine. Analogous to structural defects, it is found that the adsorption energy of adsorbates is increased in the presence of the dopant. Zhang *et al.* prepared non-symmetrically modified single-layer graphene (Janus graphene) by a two-step surface covalent functionalization assisted by a poly(methyl methacrylate) (PMMA)-mediated transfer approach.[177] Four types of Janus graphene were produced by the co-grafting of halogen and aryl/oxygen-functional groups on each side. The wettability of the doped graphene surfaces was estimated by measuring the contact angle between the graphene film and water droplets. Chemical decorations on one side are found to be capable of affecting both chemical reactivity and physical wettability of the opposite side, indicative of communication between the two grafted groups (Figure 18).

3.3. Physisorption of solids on CNTs and graphene

In this section, adsorption of metals, semiconductors, polymers, and other inorganic and organic materials that are solids at 298 K are considered. While adsorption of metals involving chemical bonding is discussed in Section 4.3, in this section, a few examples of physisorption of solids on CNTs and graphene will be given.

3.3.1. Metals and semiconductors

Due to the high surface area and pore volume of CNTs, colloidal particles can be anchored to the surface through electrostatic interaction between the

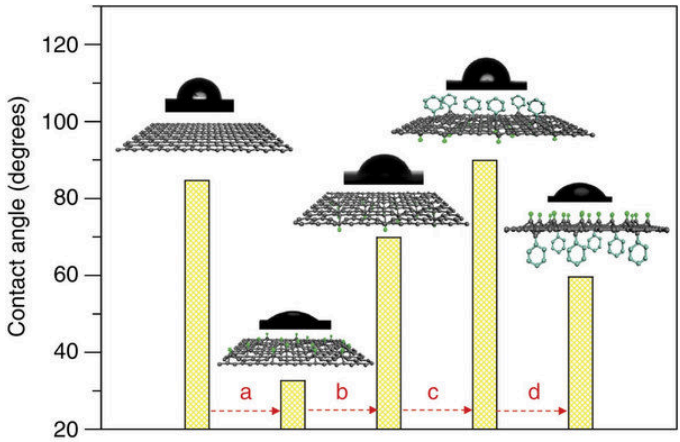

Figure 18. Static water contact angle measurements in the fabrication procedures of Janus graphene: (a) single-sided photochlorination; (b) exposure of graphene fresh side; (c) single-sided phenylation; (d) release of Janus graphene. The insets exhibit images of water droplets and schematic illustrations of the related surfaces. Reproduced from Ref. 177 with permission.

surface of the nanoparticle and the chemically functionalized sites present on the substrate, which in the case of a nanotube, are, the walls, the tips, and the cavity. For graphene, mainly defective sites, doping and edges function as active sites for adsorption. The coating of solids on CNTs by physisorption and the application of coated nanotubes have been treated in many reviews[4,178] and only a few results will be highlighted, mainly concerning the deposition of metal and semiconductor nanoparticles using self-assembly approach. The fundamentals of metal adsorption on CNTs and graphene have been treated in detail in a recent review by Machado and Serp.[3] It was found that the most stable adsorption configuration and binding energy of the adatoms on CNTs are sensitive to the type of metal element and nanotube curvature, while the electronic properties depend on the valence electronic configuration of the metal atoms. The metal–CNT interaction results in considerable charge transfer accompanied by a substantial modification of the electronic states of CNTs around the Fermi energy. Among metals, noble metals used in catalysis such as Au, Ag, Pt, Ru, Rh, Pd and metals used as electrodes for electronic applications such as Ti and In have been the most investigated. Nakada and Ishii calculated the adsorption and migration energy systematically for each adatom adsorbed using the band calculation with the Projector Augmented-Wave (PAW) method at the three adsorption sites on 3×3 graphene and have made general predictions on the preferential site for adsorption for the large

number of elements, including transition metals, alkaline earth metals, and halogens.[179] Following this study, it was reported that several transition metals such as Ti and Zr showed a high binding energy for adsorption on graphene and hence have the potential to form viable electrodes for graphene-based devices.

Metal particles and semiconductor quantum dots have been physisorbed on the nanotube surface using suitable capping agents to provide electrostatic bonding to specified sites on the nanotube surface. The nanoscale nature of the tube provides an excellent template for a bottom-up organization of a nanocomposite. Gold nanowires were formed by the templated self-assembly of gold nanoparticles surface coated with tetraoctylammonium bromide.[180] On heating the composite, the gold nanoparticles could be sintered to produce wires. The strong nanotube–gold interaction is attributed to electron transfer between the gold nanoparticles to the continuum of π^* states in the nanotubes. Surface modification by AEPA (2-aminoethylphosphonic acid) and APTES (3-aminopropyltriethoxysilane) was used for the coating of CNTs with TiO_2 and SiO_2 particles.[181]

In view of its application in electronics and energy storage, metal deposition on graphene has been studied using both theoretical and experimental approaches, the former adapting the results already obtained for CNT–metal systems.[182] While clusters of metals such as Au, Pt, and Pd have been adsorbed on graphene sheets and the energies of adsorption have been estimated,[183] experimental observation of such clusters have only been recently reported. For example, gold clusters on graphene have been imaged using aberration corrected High-Resolution Transmission Electron Microscopy (HRTEM) in the High-Angle Annular Dark-Field (HAADF) mode. It was observed that the gold clusters assumed a square planar arrangement and were mobile on the graphene surface.[184] Several research teams have studied the deposition of Pt nanoparticles on graphene for application in oxidation reduction reactions in electrochemical cells.[185,186] In all cases, it was observed that for efficient coating of Pt, the surface of graphene was modified to introduce oxygen-containing functional groups. Similar to the case of CNTs, the adsorption of oxides and sulfide colloids on graphene surface using π–π interactions has also been reported (*e.g.*, with TiO_2, Al_2O_3, SnO_2, and clay).[187–189] For example, TiO_2 particles and GO colloids have been mixed ultrasonically followed by the reduction of GO to yield TiO_2 graphene nanocomposites. Preformed SnO_2 nanoparticles have been chemically mixed with graphene to form composite materials. Figure 19 shows uniform FePt alloy nanoparticles self-assembled on graphene[190] that were found to be active catalysts for the oxygen reduction reaction (ORR) in 0.1 M $HClO_4$.

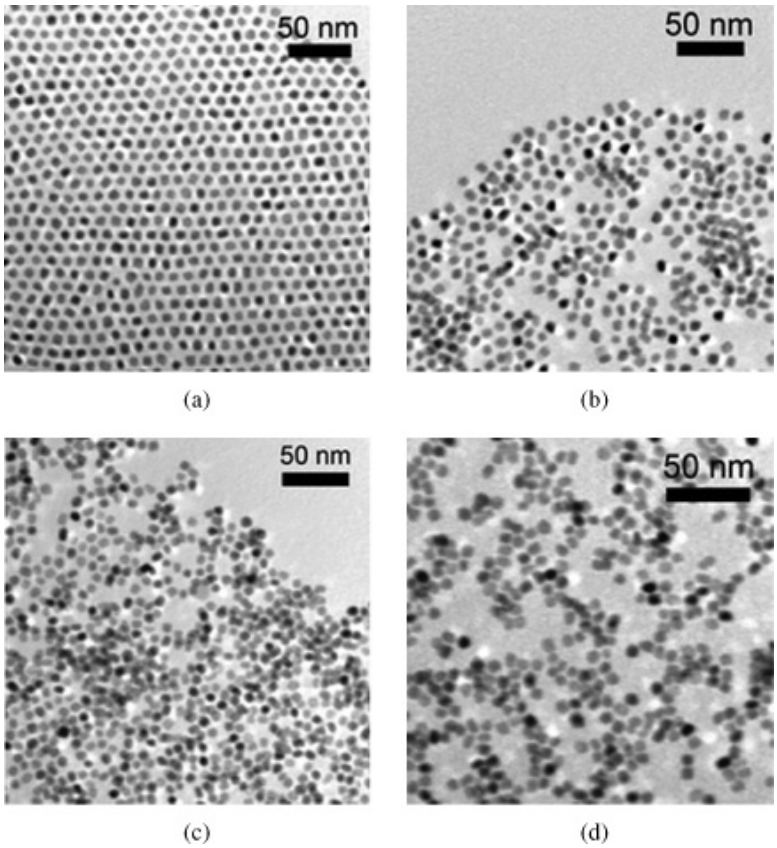

Figure 19. Transmission Electron Microscopy (TEM) images of (a) the 7 nm $Fe_{58}Pt_{42}$ NPs assembled on the amorphous carbon surface; (b) the $Fe_{58}Pt_{42}$ NPs assembled on G surface, giving G/$Fe_{58}Pt_{42}$ NPs; (c) the G/$Fe_{58}Pt_{42}$ NPs after acetic acid wash, resulting in G/$Fe_{22}Pt_{78}$ NPs; and (d) the G/$Fe_{22}Pt_{78}$ NPs annealed under Ar + 5% H_2 at 373 K for 1 h (G = graphene). Image reproduced from Ref. 190 with permission.

3.3.2. Physisorption of metals and semiconductors on doped CNTs or graphene

The presence of dopants on the CNT or graphene surface has a strong effect on the dispersion and density of the deposited metal particles. The sidewalls of acid-treated N-doped MWCNTs, coated with a cationic polyelectrolyte such as PDADMAC [poly (diallyldimethylammonium chloride)], were used as substrate to anchor 10 nm gold particles by dipping in a negatively charged gold colloid.[191] Well-dispersed gold particles decorated the walls of the nanotubes quite uniformly. The effect of doping on metal adsorption has been studied for graphene due the potential application of nitrogen-doped

graphene (N-graphene) in electrochemical applications. For Pt/N-graphene used for an oxidation reaction, it has been reported that Pt nanoparticles could disperse better on the surface of N-graphene when compared to undoped graphene.[192] Groves *et al.* have studied the interaction between Pt atom and N-graphene using DFT to calculate the binding energy of Pt atom to N-graphene[193] and have reported that the presence of nitrogen doping prevents the clustering of the Pt particles by aggregation.

3.3.3. Physisorption of polymers

Other solids physisorbed on CNTs and graphene are polymers. The physisorption of polymers on CNTs is a vast area of research and is of great importance in the field of polymer–nanotube composites since the interfacial energy between the polymer and the nanotubes is the key parameter for effecting optimum load transfer. The fundamental and application aspects have been reviewed extensively.[194,195] Physisorbed polymers are preferred in such applications since chemical attachment generally leads to loss of CNT mechanical properties. The polymer alters its lowest energy configuration (coil configuration in a solvent) in order to coat or wrap around the nanotube. In bundled nanotubes, this coiling may cause the "unzipping" where penetration of polymer segments into the spaces between CNTs leads to the debundling of CNT aggregates (Figure 20).[196] Due to the even charge distribution on the CNT surface, there is no electrostatic interaction between the polymer and the nanotubes and the physisorption takes place mainly through van der Waal's forces. The strength of this interaction depends on the functional groups on the polymer and more importantly, on the geometry of the wrapped polymer around the nanotubes.[197] The wrapping of the polymer around the nanotubes was found to be driven by thermodynamics to eliminate the hydrophobic interface between the tubes and their aqueous medium.[198] Using molecular dynamics simulation, it was found that CNT–polymer interactions are the strongest for conjugated polymers with aromatic rings on the polymer backbone, as these rings are able to align parallel to the nanotube surface and thereby provide strong interfacial adhesion.[197] Experimental studies by Steuerman *et al.* have confirmed this behavior.[199] Such interactions were obviously enhanced, even with a small number of functional groups or defects, on the CNT surface wherein the end-functional groups of the polymers underwent non-covalent grafting through zwitterionic interaction or hydrogen bonding.[200] For dendritic polymers,[201] if the branches contain certain types of groups such as aromatic, these have strong interactions with the CNT surface and it is observed that the branched architectures can

discriminate between different CNT diameters in contrast to their linear analogs (Figure 20).

For graphene, studies of polymer physisorption have been directed toward the exfoliation of FLG or graphite.[146,202,203] Several commonly available polymers such as polyvinylpyrolidone (PVP) and polyethylene glycol (PEG) have been used for the exfoliation of graphite. More detailed studies on the graphene–polymer interphases have been carried out with respect to electrical and mechanical property improvement in polymer graphene composites and these have been reviewed by Terrones *et al.*[204] As in the case of nanotubes, both theoretical and experimental studies have helped to determine the influence of chemical functionalization or the presence of dopants. The influence of the chemical functionalization of graphene on the interfacial bonding characteristics between graphene and polymers was investigated using molecular mechanics and molecular dynamics simulations. The simulations show that the bonding energy and shear stress between graphene and the polymer increase with increase of the concentration of functionalized groups.[205]

3.3.4. Polymer adsorption on doped graphene or CNTs

Relatively few studies are available on the physisorption of polymers on doped CNTs and graphene. In some cases, the adsorption of the polymer resulted in the formation of doped CNTs due to charge transfer and in the case of semiconducting SWCNTs, the electronic behavior changed from *n*- to *p*-type.[206,207] Adsorption of polymers on nitrogen-doped graphene has been reported wherein, it was found that the dispersion of polymers on fluorinated graphene was better than undoped graphene.[204] In many cases, doping

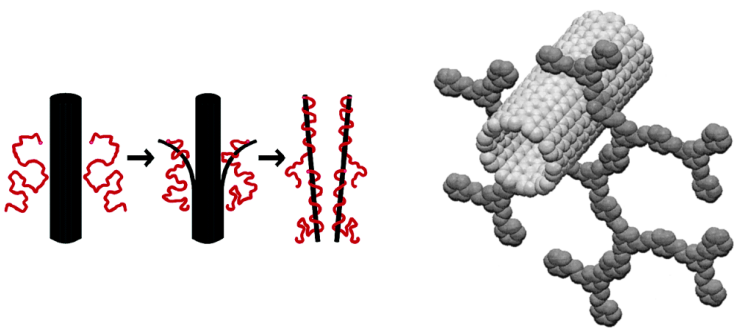

Figure 20. Left: Debundling of CNTs by physisorption of polymer. Reproduced with permission from Ref. 196. Right: Molecular modeling of an ideal stilbenoid dendrimer (without alkoxy substituents on phenylene rings) and (10,10)-SWCNT. Reproduced from Ref. 201 with permission.

changes the energy of adsorption and results in chemisorption; and these cases are treated in Section 4.

4. Chemisorption on CNT and Graphene

4.1. Chemisorption of gases on CNTs and graphene

As mentioned earlier, defects can be seen as sites with elevated reactivity that can affect many of the material's properties. From an adsorption point of view, this can also mean that a physisorptive processes over a defect-free graphitic surface can become chemisorptive, whenever an imperfection (see Sections 2.1.1 and 2.2.1) is found. In the following sections, we will mainly discuss the interaction of various gas molecules with a modified graphitic surface.

4.1.1. Gas chemisorption on CNTs

One of the most important researches is related to hydrogen storage capacity. In spite of the numerous publications on CNT as hydrogen storage material, there are contradictory reports on the quantity of hydrogen these carbon nanomaterials can uptake. This is mostly due to the fact that up to now, it is still unknown the exact nature of the sites on which hydrogen activation takes place before they are adsorbed on the carbon atoms of CNTs.[208] Lopez-Corral *et al.*[209] observed that H_2 adsorption occurred preferentially on C-defective sites. During hydrogen interaction with the C-defective nanotube, the H–H bond was broken after adsorption on the parallel vacancy (adsorption energy value of 2.52 eV), representing a chemisorptive phenomenon. Gayathri and Geetha also observed a considerable increase in the adsorption binding energy of H_2 (in the order of 50%) due to the presence of structural defects in SWCNTs.[210] When alkali–CNTs systems are used to adsorb some gases such as hydrogen, they form hydrides with a high degree of ionic bonding character. As a consequence, gas recovery is severely hindered, requiring an external energy supply to release the gas.[211,212]

The adsorption process of other gas molecules, such as oxygen and ozone, has also been studied in detail on nanotubes. The O_2 molecules dissociate exothermally and chemisorb at the dangling bonds of a vacancy. When an O_2 molecule approaches dangling bonds at a top site and/or bridge site of a vacancy, charges are transferred from carbon atoms to the oxygen molecule due to the larger electronegativity of oxygen atoms.[213] The resulting intramolecular Coulomb repulsion breaks the O–O bond exothermally

without an activation barrier. This interaction keeps the oxygen atoms apart, placing them at the opposite sides of the plane. Grujicic *et al.* observed that in both zigzag and armchair SWCNTs, molecular oxygen is physisorbed to defect-free portions of the nanotube walls, but chemisorbed to the topological defects such as SW.[214] Picozzi *et al.* investigated ozone adsorption on CNTs through first-principles calculations within the DFT.[50] They observed that the ozone adsorption process on ideal nanotubes is most likely due to physisorption, whereas when ozone adsorbs on SW defects, a strong chemisorption occurs, leading to relevant structural relaxations and to the formation of a C=O covalent bond. A similar observation was also made by Akdim *et al.*, where some orientations of the SW defects for both SWCNT chiralities resulted in lower formation energies, and stronger ozone adsorption.[215]

More complex molecules have also been targeted in several studies, given their importance in sensoring applications. Among the most investigated are NH_3 and NO_2. Chang *et al.*[216] studied the adsorption of NH_3 and NO_2 molecules on SWCNTs using DFT, and observed a small binding energy of NO_2 and NH_3 molecules to the SWCNT wall, indicating a physical and not a chemical adsorption. In sharp contrast with the case of perfect nanotube, the adsorption of NH_3 and NO_2 at the defect site of a SWCNT is generally chemical. DFT calculations were used by Tang and Cao to investigate the effect of a SW defect and a SV on the interaction of NO_X ($X = 1, 2, 3$) with a semiconducting SWCNT.[217] The adsorption of NO_X on the SWCNT with the monovacancy defect was more favorable energetically in comparison with the NO_X adsorption on the perfect CNT as well as the SW defect. Such stronger interactions of NO_X with the vacancy defect were ascribed to the presence of a dangling bond (carbene-like reactivity). The adsorption of NO_2 with the N end at the SW-defect site, which leads to the formation of C–N, is energetically more favorable than the O-down adsorption to form the C–O bond. However, the O-down adsorption of NO_2 at the SV is more favorable thermodynamically, compared to the adsorption of NO_2 with the N end. The adsorption affinity order of these nitrogen oxides over the SWCNT was found to be $NO_3 > NO_2 > NO$. As for NH_3 adsorption, Turabekova *et al.* observed that the preferred carbon atom site for chemisorption of NH_3 was located in the SW-defect region.[218]

4.1.2. Effect of dopants on gas chemisorption with CNTs

Cho and Park investigated hydrogen storage on Li-doped SWCNT using first-principles calculation based on DFT.[219] It was found that, through

Li-doping, two new adsorption sites for hydrogen molecules are created in addition to the inherent three adsorptive sites which are exterior, interior, and interstitial regions of pristine SWCNTs. The first site ("region 1") consisted on the nanotube sidewall whose electronic distribution status was influenced by the doped Li atoms. The second site ("region 2") existed on the positively charged Li atoms, which result from the transfer of electrons from the Li atoms to the SWCNTs. The adsorption coverage in region 1 at moderate temperature and pressures was similar to that of pristine SWCNTs, although its adsorption energy was slightly higher. As for the adsorption energy in region 2, it was approximately two times greater than that of pristine SWCNTs. In addition, at least three hydrogen molecules could be adsorbed on one charged Li atom in region 2. Zhang *et al.* examined the interaction between H_2 and Eu-doped SWCNT using first-principles DFT calculations.[220] The results indicated that each Eu atom could adsorb five H_2 molecules, thus providing an interesting system for hydrogen storage.

Boron-doped (8,0) SWCNTs were investigated using DFT calculations as sensor models to detect the presence of gaseous hydrogen cyanide (HCN), cyanogen chloride (CNCl), and formaldehyde (HCOH).[221,222] The replacement of a carbon by a boron atom made the system highly sensible, by enhancing the interaction between all the molecules and B-doped SWCNT (chemisorption), in contrast with the physisorption on the pristine SWCNTs.

Using first-principles calculations, Peng and Cho showed that boron and nitrogen-doped SWCNTs could detect CO and H_2O molecules.[223] The binding energies of CO and H_2O molecules with the B-doped CNTs indicated that these molecules underwent chemical adsorption, while physical adsorption occurred when CO or H_2O molecules adsorbed on the N-doped CNTs. Furthermore, the sensitivity of the devices could be controlled by adjusting the atomic doping level in the nanotube. Bai *et al.* studied the adsorption of NH_3 and NO_2 in B- or N-doped (10,0) SWCNTs using density functional computations.[224] NH_3 and NO_2 were only physisorbed in the (10,0) pristine SWCNTs with weak binding and little charge transfer. The N-doping did not change NH_3 adsorption in SWCNTs, but the B-doping yielded NH_3 chemisorption in SWCNTs feasible, with an adsorption energy of –0.70 eV and a charge transfer of 0.31 e. NO_2 was found to chemisorb on the B- or N-doped SWCNTs (adsorption energies of –1.05 eV and –0.59 eV, respectively). However, the very strong binding of NO_2 in B-doped SWCNTs makes desorption difficult, rendering its potential application in gas sensors impractical.

Wang *et al.* investigated the reactivities of the intrinsic and Al-doped (8,0) SWCNT with CO using DFT calculations,[225] and observed a dramatic

change on the electronic properties and geometric structures of the Al-doped SWCNTs after CO adsorption.

Mowbray *et al.* performed a computational screening of Transition Metal (TM)-doped (6,6) SWCNTs on the adsorption of various gases.[226] They demonstrated using *ab initio* calculations that a combined Cu- and Ni-doped metallic SWCNT device may work effectively as a multifunctional sensor for both CO and NH_3. The adsorption energies shown in Table 4 show that the earlier TMs tend to bind the adsorbates stronger than the late TMs. This could lead to the tuning of sensor sensitivity by simply varying the metal dopant.

Zhou *et al.* investigated the adsorption sensitivity of Pd-doped (5,5) SWCNTs to small gas molecules (SO_2, CH_3OH vapor, and CH_4) using DFT calculations.[227] The adsorption of SO_2 and CH_3OH on to the Pd-SWCNTs was attributed to a chemical adsorption and physical adsorption, respectively, while the interaction between CH_4 and Pd-SWCNT was an electrostatic one, and the formation of (Pd-SWCNT)–$(CH_4)^+$ complex indicated a charge transfer sensing mechanism.

Tabtimsai *et al.* studied the adsorption of NO_2, NH_3, H_2O, CO_2, and H_2 gases on the undoped and Zn-, Pd-, and Os-doped armchair (5,5) SWCNTs using DFT calculations.[228] The bond lengths between doped metal and neighbor carbon atoms, M–C, were in order: Zn–C (2.087 Å) > Pd–C (1.956 Å) > Os–C (1.911 Å). The adsorption abilities of the gases on the Zn-, Pd-, and Os-doped SWCNTs were remarkably increased as compared with the undoped SWCNT, and their adsorption abilities were: NO_2 > NH_3 > H_2O > CO_2 > H_2, as shown in Figure 21.

Table 4. Adsorption energies (E_{ads} in eV) for N_2, O_2, H_2O, CO, NH_3, and H_2S on a 3d transition metal-doped (6,6) SWCNTs.

	N_2	O_2	H_2O	CO	NH_3	H_2S
Ti	–0.61	–3.16	–1.09	–0.89	–1.39	–0.78
V	–0.76	–3.39	–1.08	–1.21	–1.46	–0.88
Cr	–0.57	–2.61	–0.97	–1.06	–1.35	–0.77
Mn	–0.70	–2.57	–0.89	–1.38	–1.32	–0.78
Fe	–0.77	–2.17	–0.84	–1.54	–1.31	–0.88
Co	–0.60	–1.88	–0.64	–1.23	–1.03	–0.58
Ni	–0.49	–2.00	–0.54	–1.16	–0.94	–0.69
Cu	–0.34	–1.02	–0.52	–0.97	–0.89	–0.63
Zn	–0.51	–0.90	–0.62	–1.07	–1.12	–0.67

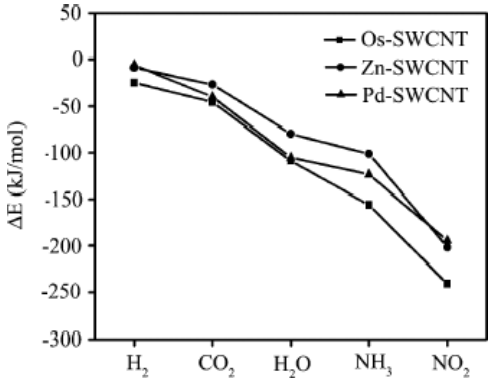

Figure 21. Adsorption energies (ΔE_{ads}) of the various gases adsorbed on Zn-, Pd-, and Os-doped (5,5) SWCNTs. Reprinted from Ref. 228 with permission. Copyright © 2011 Springer-Verlag.

Using the same (5,5) armchair SWCNT, Tabtimsai *et al.* investigated the Co-, Rh-, and Ir-doping effect on CO_2 and NO_2 adsorption using DFT calculations.[229] Co, Rh, and Ir atoms formed a pyramidal geometry with the SWCNTs side wall (Figure 22), with the doping atoms occupying the top of the pyramid. The adsorption abilities on the pristine and metal-doped SWCNTs were found to be in the order: Co-doped > Ir-doped > Rh-doped >> pristine SWCNTs for CO_2 and Ir-doped > Co-doped > Rh-doped >> pristine SWCNTs for NO_2.

Gas sensing (NO_2 and NH_3) properties of platinum derivatives on SWCNTs were studied by Pannopard *et al.*[230] DFT calculations showed that Pt (both deposited and doped) could enhance adsorption and charge transfer processes to a very large degree. For NO_2 adsorption (Figure 23, top), the Pt-doped SWCNT showed slightly smaller binding energies and gap changes than both the pristine SWCNT and Pt-deposited SWCNT, whereas for NH_3, (Figure 23, bottom), Pt-doped SWCNT showed the largest electron transfers to the SWCNT. A higher sensitivity of Pt-doped SWCNT for the detection of both NO_2 and NH_3 was attributed to larger energy gap changes and a larger charge transfer.

4.1.3. Gas chemisorption on graphene

Given the importance of a selected number of gases, such as N_2, O_2, CO, NH_3, NO_X, and the excellent properties exhibited by graphene, many of the studies previously performed for CNTs have been revisited for graphene,

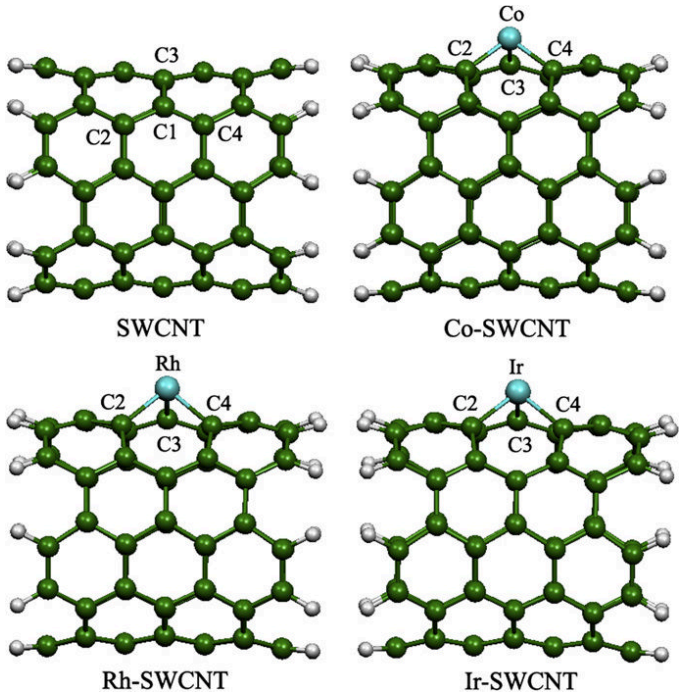

Figure 22. Optimized structures of pristine, Co-doped, Rh-doped, and Ir-doped armchair (5,5) SWCNTs. Reprinted from Ref. 229 with permission. Copyright © 2013 Elsevier B.V.

namely in what concerns the types of imperfections commonly found on the surface.

Zhang *et al.* studied the effects of SW defects on the interactions between NH_3, NO_2, and graphene, using DFT calculations.[231] They observed that both gases interacted rather weakly with pristine graphene. Introducing SW defect into the graphene structure had little effect on the NH_3 adsorption, but dramatically enhanced the adsorption of NO_2, causing significant deformation of the graphene sheet around the defective site (Figure 24). The distance between the N atom of NO_2 and SW-defect graphene sheet was 1.56 Å, whereas the sheet–molecule distance in pristine graphene was more than 2.80 Å, indicating the chemisorption of NO_2 on the defective graphene (E_{ads} = –1.10 eV), but physisorption on pristine graphene (E_{ads} = –0.40 eV).

Sanyal *et al.* studied the adsorption of various gases (O_2, CO, N_2, B_2, and H_2O) on graphene with DV defects with the help of *ab initio* DFT calculations.[232] They found that all molecules interacted strongly with the divacancy from the graphene layer. In addition, a metallic behavior of the graphene layer

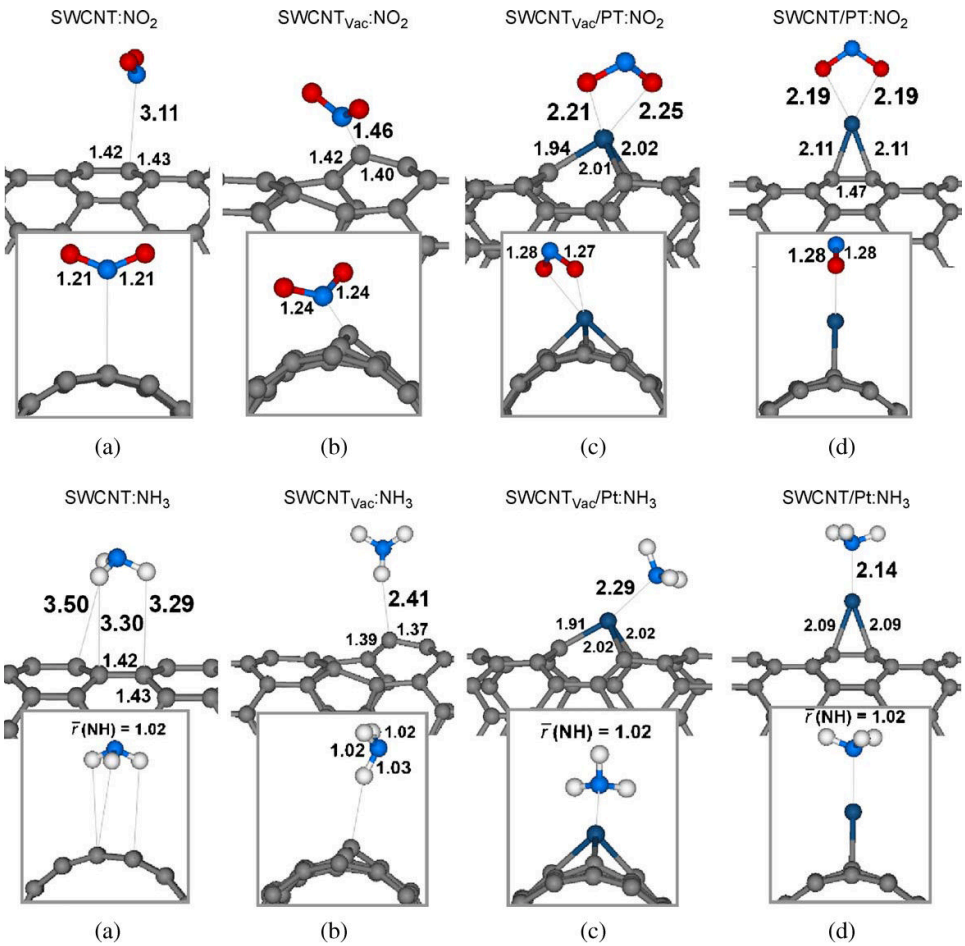

Figure 23. Front and side views of the most favorable binding geometries of NO_2 (top) and NH_3 (bottom) on (a) pristine SWCNT, (b) vacancy SWCNT, (c) Pt-doped SWCNT, and (d) Pt-deposited SWCNT. Reprinted from Ref. 230 with permission. Copyright © 2009 Elsevier Inc.

in the presence of CO and N_2 molecules was found, with a large density of states in the vicinity of the Fermi level, suggesting an increase in the conductivity. Furthermore, they showed that N_2 atoms could dissociate in the vicinity of the defects and occupy the place where the missing C atoms of the divacancy used to be. In that way, the defective graphene structure was healed geometrically, and at the same time doped with electron states.

Hydrogen sulfide (H_2S) is one of the major environmental pollutants having its sources in natural processes. It is a malodorous gas that can lead to death at concentrations higher than 250 ppm, and thus its detection is highly

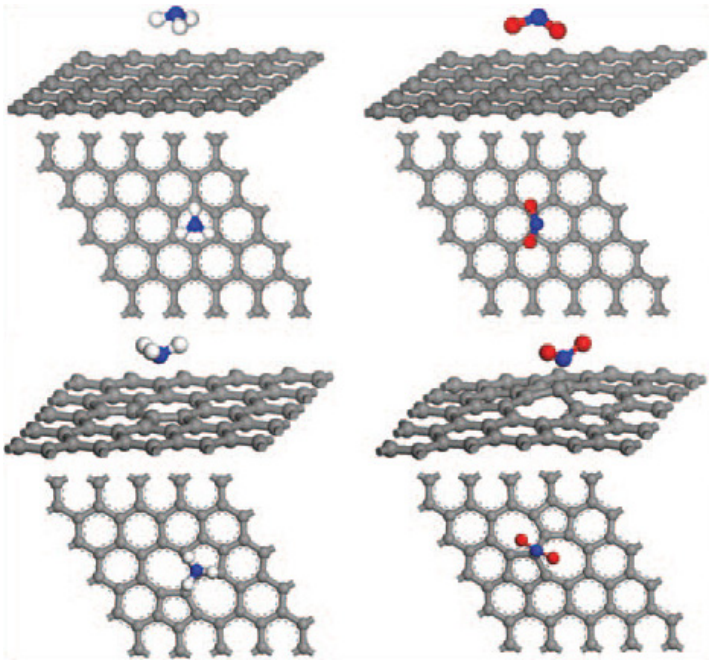

Figure 24. Schematic view of the favorable adsorption configurations of the NH_3 (left), NO_2 (right) molecules on pristine (top) and SW-defect (bottom) graphene. C, N, O, and H atoms are shown in gray, blue, red, and white, respectively. Reprinted from Ref. 231 with permission. Copyright © 2010 American Scientific Publishers.

sought. Zhang *et al.* studied the interaction between H_2S and graphene by DFT calculations and non-equilibrium Green's function formalism.[233] Based on the relatively small adsorption energy (–0.17 eV) and large graphene–molecule distance (2.58 Å), H_2S molecules were found to undergo weak physisorption on the pristine graphene. For the graphene with vacancy defects, the distance between H_2S and the defective graphene was found to decrease to 1.77 Å, and the adsorption energy was more than five times higher than that of the pristine graphene (–0.91 eV). The strong interaction was attributed to the presence of dangling bonds in the defective graphene caused by the missing carbon atom. Borisova *et al.* used DFT to study adsorption of H_2S molecules onto defective graphene as a function of vacancy concentration.[234] The calculations showed that a H_2S molecule interacts more strongly with the carbon atoms surrounding the vacancy than with the carbon atoms in a perfect arrangement. The most energetically favorable configuration was the one with the sulfur atom heading the center of the vacancy. Such a configuration facilitated the covalent binding of the sulfur atom with three carbon atoms

with unsaturated bonds. The chemisorption was followed by a release of the hydrogen atoms, which formed a H_2 molecule.

Analogously to the tips of nanotubes, carbon atoms present at the graphene edges also exhibit higher reactivities compared to those in the basal plane. Since the edges of graphene are very reactive, they may undergo oxidation and be terminated by oxygen atoms. When one molecule is attached to the oxygen atom of a C–O bond at the edge, the binding energies increase, indicating that graphene edges with terminating oxygen atoms play an important role in the adsorption of molecules.[235,236] Wood *et al.* used *ab initio* DFT calculations to explore the effect of chemical functionalization (presence of COOH, OH, NH_2, H_2PO_3, NO_2, and CH_3) on CO_2 and CH_4 adsorption within graphitic carbon edges.[236] They found that adsorption was a function not only of the chemical group but also of the gas geometry; polar groups (including COOH, NH_2, NO_2, and H_2PO_3) were found to be promising candidates for enhancing CO_2 and CH_4 capacity by strengthening adsorption and activating exposed edges and terraces to introduce additional binding sites.

As a direct result of the synthesis, purification and/or, surface modification, graphene sheets often present varying amounts of oxygenated functional groups, in addition to those already present at the edges. One of the most common methods to obtain single-layered graphene consists on the oxidation of graphite to graphite oxide, followed by the subsequent mechanical/chemical or thermal exfoliation of graphite oxide to GO sheets, and their eventual reduction back to graphene. This reduction step is often incomplete, and residual defects (oxygenated species that cannot be fully removed by chemical treatments) can be found throughout the graphitic surface. Although the exact structure of GO is still subject to intense debate, it is believed that for GO, the aromatic lattice of graphene is interrupted by epoxide, hydroxyl, carbonyl, and carboxylic groups.[237] The most accepted model is the one by Lerf and Klinowski,[238] where it is assumed that the heavily oxygenated graphite oxide contains hydroxyl and epoxide functional groups on the basal planes, in addition to carbonyl and carboxyl groups located at the edges.

In order to understand how GO sheets interact with nitrogen oxides, Tang and Cao studied the adsorption of NO_X ($X = 1, 2, 3$) and N_2O_4 on both graphene and GO (containing hydroxyl, epoxy, and carbonyl functional groups) using DFT calculations.[239] They found that the adsorption of nitrogen oxides on GO was generally stronger than that on pristine graphene. Furthermore, the GO provided various active defective sites, such as hydroxyl and carbonyl functional groups in addition to the carbon atoms near these

groups, which enhance the binding energies and charge transfers for the adsorption of nitrogen oxides on these materials, inducing the chemisorption of gas molecules. The adsorption interaction of NO_3 on both graphene and GO was found to be relatively stronger than other nitrogen oxides, followed by that of NO_2. In the case of GO with hydroxyl and epoxy groups, the interaction of nitrogen oxides with GO resulted in the formation of hydrogen bonds OH···O(N) between –OH and nitrogen oxides, as well as weak covalent bonds of C···N, depending on the adsorption configuration of NO_2 on GO. The formation of multiple hydrogen bonds OH···O between one NO_2 or NO_3 and GO was also assumed to be possible. For GO containing a vacancy defect decorated by the hydroxyl and carbonyl functional groups, NO_2 and NO_3 were found to be chemisorbed. The interactions of NO_2 and NO_3 with –OH were energetically more favorable than that at the carbon atom attached to –OH and with C=O. In the case of the adsorption on –OH, NO_2, and NO_3 abstracted the H atom to form nitrous acid- and nitric acid-like moieties, respectively. The adsorption of NO_2 and NO_3 at the carbon atom led to the newly formed weak covalent bonds C···N and C···O, respectively, as well as the hydrogen bond OH···O.

Although most studies mainly focus on the theoretical interaction between gases and graphitic surfaces, there are however some studies that address the experimental use of graphene-based materials in sensor applications. These are mainly related to the detection of hazardous gases such as NH_3 and NO_2, which can cause severe damage to human respiration systems. Detection of individual molecules of NH_3 and NO_2 using mechanically exfoliated graphene has been reported by Schedin *et al.*[240] Lu *et al.* studied the response of a thermally reduced graphene oxide (rGO) to low concentrations of NO_2 and NH_3 gases diluted in air at room temperature.[241,242] The sensing performance of the devices was attributed to the effective adsorption of NO_2 on the surface of reduced, *p*-type GO. Since NO_2 is a strong oxidizer with electron-withdrawing power, electron transfer from rGO to adsorbed NO_2 led to an enriched hole concentration and enhanced electrical conduction in the rGO sheet, being able to detect NO_2 down to 2 ppm. On the other hand, upon NH_3 exposure, the authors observed a decreased current passing through the device, possibly because adsorption of NH_3 (electron donator) lowered the hole concentration in GO, and thus rGO conductance. In another work, Ko *et al.* studied the NO_2 sensing capability of FLG (7–10 layers of graphene) obtained through the mechanical exfoliation of HOPG.[243] They showed that FLG possessed a fast response time, good reversibility, selectivity, and high sensitivity, as it can detect NO_2 molecules in the parts per million range. Yavari *et al.* showed that graphene films synthesized by CVD

enabled detection of trace amounts of NO_2 and NH_3 in air at room temperature and atmospheric pressure.[244] Detection limits of *ca.* 100 ppb for NO_2 and *ca.* 500 ppb for NH_3 were obtained. A hydrazine-reduced GO with different levels of reduction was also reported to detect NH_3 and NO_2 gases down to about 5 ppm in air.[245] A 3D network of graphene sheets (graphene foam) was also used to detect 20 ppm of NH_3 and NO_2 in air.[246] Finally, an epitaxially grown graphene was also found to lead to detection of 2.5 ppm of NO_2 in air.[247]

4.1.4. Effect of dopants on gas chemisorption with graphene

As we have seen in the previous section, the presence of defects can significantly increase the interaction between adsorbates and substrate when compared to a pristine graphitic surface. An alternative method that also results in higher adsorption energies is the introduction of chemical dopant species on the graphitic surface.[248] In fact, this area has been the subject of very intensive computational research and is the topic of our discussion in this section.

Zhang *et al.* studied the interaction between H_2S and doped graphene by DFT calculations and non-equilibrium Green's function formalism.[233] When one carbon atom is substituted by B or N atom in the super cell (assigned to B-graphene or N-graphene, respectively), it was found that the geometric structures of the doped graphene nanosheets had a planar configuration before and after adsorption of H_2S molecule, resulting in physisorption. In contrast, the geometry of graphene doped with Si (Si–graphene) deformed dramatically before and after adsorbing a H_2S molecule. The deviation of C–Si–C bond angles from the standard angle of sp^2 hybridization of 120° clearly indicates that the Si atom near the adsorption site has changed to a more sp^3-like hybridization. Compared to the distance of around 3.00 Å between the pristine graphene sheet and the S atom of physisorbed H_2S, the sheet–molecule distance between the Si–graphene and H_2S molecule is shortened to 2.53 Å. In addition, the E_{ads} of H_2S on Si–graphene is found to be –0.94 eV, which confirms that the Si–graphene is more favorable for H_2S adsorption than the pristine graphene. These results indicate that H_2S molecule is chemisorbed onto the Si–graphene. Further investigation of H_2S adsorption on the surface of graphene doped with Ca, Co, and Fe showed that H_2S molecule can bind to the surface with adsorption energies of –0.66, –1.80, and –1.92 eV, respectively. Because absorption energy of H_2S molecule is very high, it is worth noting that desorption of the H_2S could be quite difficult, thus hindering the use of these materials in sensor applications.

Zhang *et al.* reported first-principles simulation of the interactions between several small molecules (CO, NO, NO_2, and NH_3) and graphene sheets containing defects (single vacancies) and dopant species (B or N).[248] The calculation results suggest that the pristine graphene has weak interactions with all four gas molecules. The introduction of dopants and defects into the graphene significantly increases the molecule–graphene interaction. The minimum atom-to-atom distance between the CO and graphene is obtained when a vacancy was present (1.33 Å). This distance was close to the bond length of a C=C bond and was much shorter than that of any other types of graphene, which were 3.02 (pristine graphene), 2.97 (B-doped graphene), and 3.15 Å (N-doped graphene). The adsorption energy of CO over the defect reached −2.33 eV, which was more than one magnitude higher than that of the pristine and doped graphene. Similarly to CO, the presence of a defect on the graphene sheet also yielded the highest affinity to both NO (−3.04 eV adsorption energy and the NO–graphene distance of only 1.34 Å) and NO_2 (−3.04 eV adsorption energy and NO_2–graphene distance of only 1.42 Å), revealing the occurrence of a strong chemisorptive behavior. As for the adsorption of NH_3, this molecule showed a much stronger interaction with the B-doped graphene (−0.50 eV), which was attributed to the strong interaction between the electron-deficient B atom and the electron-donating N atom of NH_3. It was also found that the B-graphene underwent an obvious distortion upon NH_3 adsorption, indicating that the B-site is transformed from sp^2 to sp^3 hybridization. The B–N distance (1.66 Å) was very close to the B–N bond length in BH_3NH_3 (1.6576 Å), confirming the formation of a covalent bond between the NH_3 and the B-doped graphene.

Ao *et al.* investigated the enhancement of CO detection in Al-doped graphene using DFT calculations.[249] The results showed that CO molecules are only weakly adsorbed onto the intrinsic graphene with small binding energy value and a large distance (d = 3.767 Å) between the CO molecule and graphene, whereas CO molecules strongly interact with the Al-doped graphene, forming an Al–CO bond (d = 1.964 Å) that introduces a large amount of shallow acceptor states into the system. Physisorption of CO on pristine graphene did not alter the electron distribution for both CO molecule and graphene, implying the weak bonding characteristics. On the other hand, the chemisorption of CO on Al-doped graphene led to significant electron transfer from the graphene to CO molecule. The electrons not only accumulated on the O atom but also on the C atom of the molecule bond with the doped Al atom. The final position of Al atom in the chemisorbed CO–Al–graphene complex was thus a direct consequence of the maximized degree of sp^3 orbital hybridization with neighboring C atoms from both the graphene layer and

CO molecule. The effect of Al doping on graphene was also addressed by Sun *et al.*,[250] by studying the adsorption of HF by first-principles calculations. They found that Al-doped graphene had a higher adsorption energy (–7.164 eV) and shorter connecting distance to the HF molecule (2.235 Å) than pristine graphene (–0.071 eV and 3.661 Å). A charge accumulation between the HF molecule and the Al-doped graphene occurred, and the Al-doped graphene gained electrons from the H atom of the HF molecule. This charge transfer would form an ionic bond between the HF molecule and the Al-doped graphene, and the HF molecule acted as an electron donor of the system. Thus, the adsorption of HF molecules on Al-doped graphene can be considered chemisorption, while physisorption takes place on pristine graphene.

Dai and Yuan[251] studied the adsorption of multiple gas molecules (N_2, O_2, H_2, H_2O, CO, CO_2, NO, NO_2, NH_3, and SO_2) on P-doped graphene using DFT. When the P atom replaced a C atom in the graphene plane, the structure of the graphene underwent a significant rearrangement (due to the much larger size of the P atom with respect to C) and the P atom projects out of the graphene plane at a distance of 1.19 Å. Based on the calculated large distances from the graphene plane, H_2, H_2O, CO, CO_2, N_2, and NH_3 are considered to be physisorbed on P-doped graphene surface. On the other hand, O_2, NO, NO_2, and SO_2 molecules were found to strongly chemisorb onto the P-doped graphene, forming P–X (X = O, N, S) bonds with large adsorption energies (–1.0895, –0.5093, –1.8875, and –0.3216 eV, respectively).

In another work, Dai and Yuan[252] used DFT to study the adsorption of molecular oxygen on B-, N-, Al-, Si-, P-, Cr-, and Mn-doped graphene. The molecular oxygen was found to be chemisorbed on Cr-, Mn-, Al-, Si-, and P-doped graphene with large adsorption energies (E_{ads} in Table 5), and short bonds between the dopant atom and oxygen ($d_{X–O}$ in Table 5), indicating very stable adsorption of O_2. On the other hand, O_2 physisorbed over B- and N-doped graphene with small adsorption energies and longer distances to the graphene plane. B- and N- doped graphene retained a planar form, while other atoms project out of the graphene layer and induce a local curvature in graphene (Figure 25 and *h* in Table 5).

In an extension of their work, Dai *et al.*[253] studied the effect of doped graphene (boron, nitrogen, aluminum, and sulfur) to the adsorption of several other common gas molecules (NO, NO_2, NH_3, CO, CO_2, H_2O, SO_2, O_2, H_2, and N_2). First-principles calculations showed small adsorption energies and large molecule–graphene distances, pointing to no binding other than physisorption. For B-graphene, however, NO and NO_2 bind with a significant adsorption energy (E_a ~ 0.3 eV). For N-graphene, the largest

binding energies (E_a ~ 0.2 eV) are found with NO_2, SO_2, and O_2, but the corresponding dopant atom–molecule distances are rather large (d > 3 Å), suggesting that a true chemical bond was not formed. S-graphene could only bind the NO_2 molecule, with a rather large adsorption energy E_a= –0.83 eV, in a configuration that is similar to that of NO_2 on B-graphene. Finally, Al-graphene was the most reactive and found to bind all molecules except H_2, via the formation of strong Al–X(X = O, N, C) bonds of length $d_{Al–X}$ ~2 Å or less.

Table 5. Summary of atomic structures of the compounds, including the elevation of the dopant atoms above the graphene plane (h), the bond length between dopant (X) and O ($d_{X–O}$), and adsorption energy (E_{ads}).

Dopant	h (Å)	$d_{X–O}$ (Å)	E_{ads} (eV)
N	0.0000	3.3196	–0.1228
B	0.0000	3.5099	–0.0232
P	1.4591	1.6275	–1.0359
Si	1.4579	1.7109	–1.3132
Al	1.7584	1.8770	–1.5589
Mn	1.5555	1.8641	–2.0918
Cr	1.6487	1.7935	–2.6098

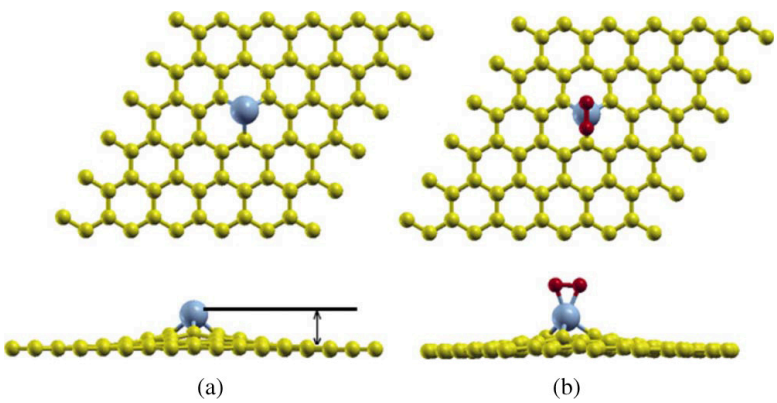

Figure 25. Most stable configuration of (a) Mn-doped graphene with an elevation h of 1.555 Å, and (b) O_2 on Mn-doped graphene. Reprinted from Ref. 252 with permission. Copyright © 2010 American Physical Society.

Li *et al.* investigated the catalytic activity of Fe-doped graphene by the first-principles method using the CO oxidation as a probe reaction.[254] The catalytic activity of Fe-graphene system was interpreted in light of an Eley–Rideal mechanism: due to the strong hybridization between 3d states of Fe and the 2p state of O_2, the latter could be efficiently activated by Fe; then CO could be inserted into the elongated O–O bond to form a carbonate-like intermediate state CO_3 with a moderate energy barrier (0.58 eV) via the Eley–Rideal mechanism. Finally, CO_3 reacted with another CO to produce two CO_2 molecules also with a rather modest energy barrier (0.57 eV).

The same reaction was also used by Lu *et al.* and Song *et al.* to assess the theoretical behavior of an Au-graphene[255] and Cu-graphene[256] catalyst, respectively. The high activity of Au- and Cu-doped graphene was attributed to the electronic resonance among electronic states of CO, O_2, and metal atoms, particularly, among the d states of the Au and Cu atoms and the antibonding $2\pi^*$ states of CO and O_2. Partially occupied d-orbital of Au is localized in the vicinity of the Fermi level due to the interactions between the Au atom and graphene.

Zhou *et al.* studied the adsorption of gas molecules (O_2, CO, NO_2, and NH_3) on transition metal embedded graphene[257] using a first-principles approach based on DFT. Their results showed that Ti and Au were the best in improving the chemical reactivity of graphene. Furthermore, when adsorbed on Ti or Au embedded graphene, the desorption barriers of these molecules were all quite high: close to 1 eV for NH_3 and well above 1.5 eV for other molecules, suggesting the high stability of these molecules on TM–graphene.

4.2. Chemisorption of liquids on CNTs and graphene

Most of the chemisorption studies hitherto carried out have been essentially on solids and gases and in the case of gases, the chemisorption of hydrogen on graphene is the most studied and has been dealt with in Section 4.1. Most of the chemisorption occurred on the defects/adatoms on the CNT or graphene substrate. Studies using DFT have shown that molecules such as tetracyanoethylene (TCNE) energetically prefer chemisorption on Si-doped graphene, whereas they favor physisorption on B- and N-doped graphenes. The interaction between TCNE molecules and graphene can be improved by doping, which induces a remarkable change in the electronic properties of graphene.[258] Among liquids, interesting observations have been reported for the adsorption of acetone on SWCNTs.[62] The adsorption of acetone on the SWCNT sample at different temperatures was followed using TPD studies. It was observed that

the activation energy for desorption of acetone was much larger than both the latent heat of vaporization of acetone from the liquid state (0.32 eV) and the activation energy of desorption of acetone multilayer from graphite. Following this observation, the adsorption of acetone on SWCNT was modeled using hybrid quantum mechanical and semiempirical calculations, which showed that acetone binds preferentially to defects present in the nanotubes and the binding energy was dependent on the diameter of the nanotubes. The calculated binding energies showed that acetone is strongly chemisorbed on CNTs and remained bound up to high temperatures unlike its behavior on graphite. Zheng *et al.* used molecular dynamics to simulate the effect of chemisorption of phenyl groups onto the walls of the CNTs on the interfacial bonding characteristics between the SWCNTs and the polymer CNT–polymer interface.[259] The simulations showed that functionalization of nanotubes at low densities of functionalized carbon atoms drastically increase their interfacial bonding and shear stress between the nanotubes and the polymer matrix.

Hydrogen chemisorption on graphene surfaces has been reported during the reaction of steam on carbon at high temperatures (900°C).[260] Chemisorption of water on carbon surfaces has been reported in the context of a study on the influence of water on the tribological properties of graphite.[261] Isotopically labeled water was adsorbed on graphite and was titrated by TPD coupled with mass spectrometry. The quantity of adsorbed water was studied in milled and unmilled graphite and concluded that the water adsorption was key to explain the friction behavior of graphite. The influence of water chemisorption on the electronic properties of the (8,0) CNT and the kinetic behavior of water chemisorption have been studied by DFT. The results show that the dissociative adsorption of the water molecule on the (8,0) CNT can decrease the energy gap. However, the chemisorption of water on the (8,0) CNT is found to be very difficult, and the smallest energy barrier of the chemisorption is 2.89 eV with the H and OH dissociated from water bonding at the opposite sites of carbon hexagon. However, the external electric field in the transverse direction or the substitution atom N on the CNT surface can obviously lower the energy barrier for water chemisorption.[52] Chemisorption of ILs covalently bonded to the nanotube or graphene surface has been described.[138] The covalent modification of CNTs by ILs was carried out in two ways: ILs were either directly grafted to the CNT surface[262] or generated on the CNT after the imidazole component is grafted.[263] Using similar approaches, Yang *et al.* reported a facile method to obtain polydisperse chemically converted graphene sheets that are covalently functionalized with amine-terminated IL.[264] The resulting graphene sheets, without any assistance from polymeric or surfactant stabilizers, can be stably dispersed

in water, dimethylformamide (DMF), and dimethyl sulfoxide (DMSO). The results from Atomic Force Microscopy (AFM), XPS, Fourier Transform Infrared spectroscopy (FTIR), XRD, Thermal Gravimetric Analysis (TGA), and TEM clearly indicate that the IL-NH_2 units were coupled to the surface of the graphene nanosheets.

The chemisorption of radionucleotide ions from solution onto CNTs is very important from the point of view of the safe disposal of radioactive waste. Functionalized MWCNTs and SWCNTs have been found to have a good uptake of radionucleotides. The experimental results and mechanistic aspects of these adsorption processes have been discussed in detail in a review article.[150] Compared to other adsorbates, the irreversible adsorption of radionuclides on MWCNTs is ideally suited for the use of CNTs as adsorbents for the long-term disposal of radionuclides. Strong surface complexation and/or chemisorption are considered to be the main adsorption mechanisms for radionuclides such as ^{243}Am(III) and $^{152+154}$Eu(III) on MWCNTs. Radionuclides can enter the inner channel of MWCNTs with time and form strong complexes in the central channel of MWCNTs and are not desorbed easily. The uptake of radionucleotides by CNTs is summarized in Table 6.

4.3. Chemisorption of solids on CNTs and graphene

4.3.1. *Alkali metals*

The alkali metal/CNT systems are promising materials for nanoelectronics, as increased conductivity was observed. They can be used for intercalated

Table 6. The maximum adsorption capacities (Q) of several crucial radionuclides on CNTs and other adsorbents. Adapted from Ref. 150 with permission.

Adsorbates	Adsorbents	Q	Conditions
U(VI)	Pristine CNTs	5.0 (mmol $g^{-}1$)	pH 4.0, T room temp.
	Na-magadite	5.5 (mmol $g^{-}1$)	pH 2.0, T 298 K
	Chitosan resins–amine	1.9 (mmol g^{-1})	pH 3.9, T 303 K
Eu(III)	MWCNTs	7.3 (μmol g^{-1})	pH 4.3, T 298 K
	ZSM-5 zeolite	15.9 (μmol g^{-1})	pH 3.6, T 298 K
	TiO_2	9.9 (μmol g^{-1})	pH 4.5, T 293 K
Th(IV)	Oxidized MWCNTs	65.8 (μmol g^{-1})	pH 1.9, T 303 K
	Diatomite	81.5 (μmol g^{-1})	pH 2.6, T 303 K
	SiO_2	2.6 (μmol g^{-1})	pH 3.5, T 293 K

or electrochemically doped materials, for the design of novel materials, for lithium batteries,[265] and for hydrogen storage.[266] For that latter application, the capacity of hydrogen storage of Li/CNT varies from 2.5[267] to 20%[266] by mass. It is of great importance to know the adsorption properties of alkali metals, graphene and CNTs to control the performance of such systems.

Rytkönen *et al.* studied the adsorption of alkali-metal atoms such as Li, Na, K, Rb, Cs, dimers, and (2 × 2) monolayers on graphene, using DFT, pseudopotentials, and a periodic substrate.[268] All alkaline atoms prefer to bind on the H6-site, Li lying closest to 1.84 Å and Cs farthest 3.75 Å from the surface. The adsorption energies range between 0.55 and 1.21 eV. The ordering of binding energies is Li > Cs ≥ Rb ≥ K > Na. Lithium has a moderate diffusion barrier of 0.21 eV, whereas the larger alkali metals are relatively mobile with diffusion barriers of 0.02–0.06 eV. Taking into account these calculations, lithium is the only alkali metal able to be chemisorbed on the graphene surface. The other alkali atoms are mobile on the surface with weak binding energies. Similar observation was also made by Nakada and Ishii.[269] These authors studied the adsorption and migration energies of several adatoms, from hydrogen to bismuth, on graphene. They found that lithium (binding energy 1.36 eV with a distance to the graphene layer of 1.62 Å and migration energy of 0.3 eV) is likely to be chemisorbed on the graphene surface. The calculations of Liu *et al.*[270] also point in this direction. The interaction of lithium with graphene and the effect of the Li–Li interaction on the binding of Li to graphene has been calculated using the local density approximation to the DFT.[271] Lithium binds to a H6-site at 1.64 Å from the graphene with a binding energy of 1.598 eV. The introduction of more Li atoms on the graphene sheet decreases the binding energy to 0.934 eV without changing the location and the distance between Li and graphene. There is substantial charge transfer from both lithium and carbon atoms (including those that do not surround the lithium) to a region between the Li and graphene at the minimum energy configuration. The calculations show that the Li–Li interaction is repulsive due to the charge transfer that takes place between Li and graphene, leaving a positively charged cation at the original location of the Li atom. The charge transfer remains significant even at long distances. Concerning the adsorption of Li on CNT, it has been also observed that the increase of Li/C ratio decreases the binding energy between the lithium atom and the nanotube and increases the Li–CNT distance.[272] This can be explained by the decrease of the ionicity of the Li–CNT bond, that is the effective charges of lithium ions decrease in the order: LiC_{64} (0.57e), LiC_8(0.39e), and LiC_4(0.27e). Senami *et al.*[273] investigated the adsorption of

lithium atoms on the surface of a (12,0) CNT by using *ab initio* quantum chemical calculations to clarify the interaction between lithium atoms and between a lithium atom and the CNT. The authors show that after the lithium attachment, charge is transferred from the Li atom to the CNT and the bond between the Li atom and the CNT has ionic property. The amount of charge transfer depends on the curvature of the CNT, being larger for the endohedral than the exohedral grafting. This explains that the *exo*-adsorption is weaker (1.70 eV) than the *endo* one (1.87 eV). The authors also observed that the repulsive force between lithium atoms strongly destabilize the system.

The binding of a series of alkali-metal ions (Li^+, Na^+, and K^+) to graphene and CNTs has also been studied by first-principles calculations.[274] The alkali-metal ions are at distances around 1.9, 2.3, and 2.7 Å, respectively, from the surface of the carbon nanostructures and bind on the H6-site. Li^+ shows the stronger binding energy (2.9 to 3.3 eV), followed by Na^+ with 3.0 to 2.2 eV and K^+ ion with a binding energy range of 1.3–2.2 eV. These values indicate that alkali-metal ions interact with the carbon nanostructures by chemisorption. Regarding the effect of the curvature, all the metal ions considered exhibit stronger binding to graphene compared to CNTs. Further, the binding energy increases as the diameter increases (curvature decreases) in the case of armchair CNTs, while such clear trends did not emerge in the case of zigzag CNTs. Concerning the effect of the chirality, Figure 26 shows that the monocationic alkali-metal ions are more stable for the armchair than for the zigzag CNTs.

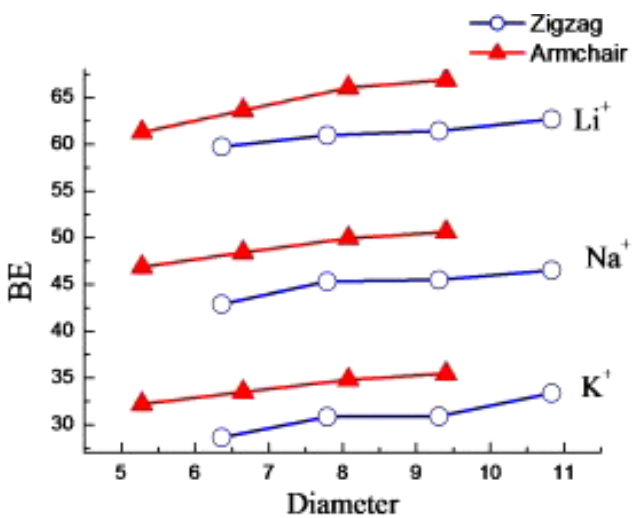

Figure 26. Basic Set Superposition Error (BSSE) corrected B3LYP-D/631G*//ONIOM (M062X/631G*: PM3) binding energy (kcal mol^{-1}) of metal ions with armchair and zigzag CNTs.[274]

4.3.2. Alkaline-earth metals

Alkaline-earth metals have attracted the attention as elements capable to form stable and uniform atomic coatings on carbon nanostructures, unlike transition metals, which tend to aggregate and form clusters.[275–280]

Liu *et al.* studied by first-principles DFT the adsorption behavior of alkaline-earth metals (Mg, Ca, and Sr) on capped SWCNTs ((5,5) and (9,0)) to shed light on (i) the difference between adsorption on pentagon and hexagon of capped CNTs,[281] and (ii) the effect of vacancy defects.[282] Ca and Sr are chemisorbed on the capped SWCNTs, Mg with low adsorption energies is considered as physisorbed. The authors show that there are significantly different adsorption behaviors between the different sites, being the hexagonal the preferred one. The authors also show that vacancy defects have a great impact on adsorption. Charge transfers are enhanced significantly in D-CNTs (defect CNTs), especially for Mg. The binding energies of Mg, Ca, and Sr increase from 12 meV, 0.96 eV, and 0.97 eV for (5,5) CNTs to 2.37 eV, 3.99 eV, 3.81 eV for D-CNTs, respectively. The presence of a defect site enhanced the binding of all alkaline-earth metals, the average increase of 2 eV on the binding energies make that Mg is chemisorbed when defects are introduced on the CNT.

Umadevi *et al.* studied the adsorption of alkaline-earth metal ions (Be^{2+}, Mg^{2+}, Ca^{2+}) on CNTs and graphene by first-principles calculations.[274] The dicationic species bind to H6-sites at distances around 1.3 Å, 1.9 Å, and 2.2 Å, respectively. Be^{2+} shows the highest binding energy (14–17 eV), followed by Mg^{2+} (10–13 eV) and finally Ca^{2+} (6–8 eV). Regarding the effect of the chirality, the dicationic alkaline-earth metal ions bind stronger to the zigzag than to the armchair CNTs, except for Ca^{2+}, which shows similar binding energies on both CNTs. Thus, the alkaline-earth metal ions show an opposite behavior when compared to alkaline-metal ions. In the case of dicationic metal ion complexes, the charge transfer is higher compared to that of the monocationic metal ion complexes explaining why the dicationic alkaline-earth metals show higher binding energies than the monocationic alkali-metal ions. The binding energy is also affected by the CNTs curvature, for larger diameter, the dicationic species are bound stronger. The energy binding is similar for CNTs (14, 0) and graphene.

4.3.3. d-metals

The adsorption of transition metal on CNT and graphene is one of the most studied due to the variety of possible applications of such systems. These

composites are promising materials for hydrogen storage or gas sensors,[283–287] the fabrication of metallic nanowires and nanomagnets when decorated with magnetic metal atoms,[288–290] and for catalysis.[4]

Single metal atoms

In this section, we will discuss first the chemisorption of single transition metal atoms onto graphene surface, followed by the adsorption onto CNT surface. The transition metal deposition on graphene and CNT has been studied by theoretical calculations. Usually, authors consider mainly three binding sites (Figure 4): on top of a carbon atom (T-site), on top of the center of a hexagon (H6-site), or the bridge position (B-site).

In general, transition metal adatoms are mainly chemisorbed on the graphene surfaces, showing high preference to adsorb with a η^6 hollow geometry. B- and T-sites are most stable for transition metals with filled or near-filled d-shell, such as Pd and Pt. Usually, the binding energies are found to be higher when increasing the electrons on the d-orbital until it is half-filled.

Hu *et al.*[291] studied the adsorption of 15 different transition metal adatoms, mainly 3d, on graphene using first-principles DFT with the generalized gradient approximation. For metals such as Sc, Ti, V, Fe, Co, and Ni, the authors found that H6-sites are the most stable, while Cu, Pd, and Pt, which have a filled or near-filled d-shell prefer B- and T-sites. They also found that the distortion of graphene layer is quite significant when the adatom occupies B- and T-sites. This distortion is mainly due to the formation of the covalent bond. Au, Ag, Zn, and half-filled transition metal atoms showed small adsorption energies. The intensity of the adsorption energy and the nature of the adsorption site can indicate the nature of the chemical bond. Therefore, Co, Ni, Pt, and Pd are considered as chemisorbed while Au, Ag, and Cu are physisorbed. Similar results were observed by Tang *et al.*[292] The authors investigated the adsorption energies, stable configurations, electronic structures, and magnetic properties of the graphene with Pt, Ag, and Au, using first-principles DFT. They found that B-site is the most stable adsorption for the Pt adatom, while Au prefers the T-site. The Ag adatom can be stabilized almost equally at the B- or the T-site.

Nakada and Ishii[269] studied the adsorption and migration energies of almost all periodic table atoms, from hydrogen to bismuth, including transition metals, on graphene. They used a first-principles band calculation technique based on DFT (Table 7).

The authors show that the H6-sites are the most stable sites for transition metal atoms, except for Cu, Pd, and Pt which prefer B-sites, and Ag and Au

Table 7. The most stable site when an adatom is adsorbed on graphene together with bond energy (top position, eV); distance between the adatom and graphene (middle position, Å); and migration energy for the most stable site (bottom position, eV). In bold cases, the most stable elements on graphene are defined by a bond distance of 2 Å and migration energy >0.5 eV. Reproduced from Ref. 3 with permission. Copyright © 2012 The Royal Society of Chemistry.

1	2	3	4	5	6	7	8	9	10	11	12	13	14	15	16	17	18
H																	**He**
1.96						**T**											
1.49						**B**											
0.60						**H**											
Li	**Be**											**B**	**C**	**N**	**O**	**F**	Ne
1.36	0.12											1.77	3.43	4.56	4.79	2.90	
1.62	2.93											2.04	1.65	1.62	1.59	1.87	
0.3	0.02											0.12	0.25	1.00	1.02	0.45	
Na	**Mg**											**Al**	**Si**	**P**	**S**	**Cl**	**Ar**
0.72	0.03											1.62	1.86	2.20	2.34	1.27	
2.22	3.21											2.04	2.03	2.09	2.08	2.56	
0.13	0.02											0.05	0.05	0.45	0.46	0.02	
K	**Ca**	**Sc**	**Ti**	**V**	**Cr**	**Mn**	**Fe**	**Co**	**Ni**	**Cu**	**Zn**	**Ga**	**Ge**	**As**	**Se**	**Br**	**Kr**
0.81	0.52	2.08	3.27	3.88	3.99	3.82	3.83	3.64	3.08	0.97	0.13	1.52	1.61	1.65	1.65	0.98	
2.58	2.14	1.76	1.56	1.47	1.42	1.38	1.38	1.42	1.47	2.03	3.02	2.11	2.16	2.22	2.25	2.78	
0.12	0.07	0.34	0.61	1.05	1.45	1.26	0.97	0.77	0.40	0.03	0.02	0.03	0.07	0.2	0.23	0.00	
Rb	**Sr**	**Y**	**Zr**	**Nb**	**Mo**	**Tc**	**Ru**	**Rh**	**Pd**	**Ag**	**Cd**	**In**	**Sn**	**Sb**	**Te**	**I**	Xe
0.75	0.33	1.98	3.42	4.68	3.71	5.22	4.43	3.32	1.90	0.35	0.10	1.29	1.34	1.19	1.08	0.75	
2.74	2.37	2.00	1.74	1.66	1.59	1.57	1.62	1.71	2.08	2.42	3.18	2.35	2.42	2.46	2.49	3.26	
0.09	0.04	0.12	0.39	0.83	1.47	1.40	0.96	0.39	0.06	0.01	0.01	0.02	0.03	0.03	0.09	0.00	
Cs	**Ba**	**La**	**Hf**	**Ta**	**W**	**Re**	**Os**	Ir	Pt	Au	Hg	Tl	Pb	Bi			
0.85	0.67	2.45	3.12	3.90	4.52	4.51	4.08	3.53	2.88	0.77	0.20	1.26	1.30	1.07			
2.54	2.49	2.07	1.85	1.65	1.60	1.58	1.61	1.70	2.12	2.41	3.13	2.48	2.53	2.57			
0.10	0.05	0.18	0.23	0.60	1.17	1.23	0.75	0.15	0.19	0.03	0.01	0.00	0.01	0.00			

the T-sites. The bond energy shows an increasing tendency with an increasing number of d-electrons until the d-orbital is half-filled. For filled or near-filled d shells, the binding energy tends to decrease. Considering the bond distances (between the adatoms and the graphene layer) smaller than 2 Å and the migration energies above 0.5 eV, Ti, V, Cr, Mn, Fe, and Co are chemisorbed for the 3d transition metals; Nb, Mo, Tc, and Ru for 4d transition metals; and Ta, W, Re, and Os for 5d transition metals.

Liu *et al.*[270] compared the adsorption of several metal adatoms on graphene by *ab initio* calculations. Most of the metal adatoms favor the H6-site, while Cu and Au adatoms prefer the T-site and Cr, Pd, Pt, and Ag adatoms take the B-site. All d-metal studied are chemisorbed with the exception of Ag, Cr, and Mn (see Figure 27 for binding energies). The diffusion barriers are very small for Cr, Mn, Cu, Ag, and Au adatoms on graphene. This study also points out that metal with near-filled or filled d-orbital show a weak interaction with graphene. Most of the transition metal adatoms are chemisorbed on CNT surface, as observed for graphene, and yield the strongest binding on the η^6-H6-site. Durgun *et al.*[293,294] studied the adsorption of 27 different atoms on (8,0) zigzag SWCNT and four atoms on a (6,6) armchair SWCNT.

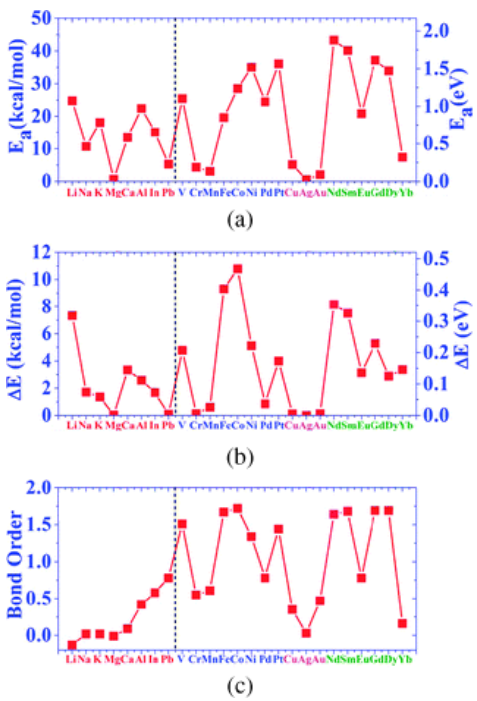

Figure 27. (a) Adsorption energy (E_a); (b) diffusion barrier (ΔE); (c) bond order of adatom–graphene systems.[270]

The authors calculated the atomic structure, binding geometry, binding energy, and resulting electronic structure of an individual-atom-adsorbed SWCNT using the first-principles pseudopotential plane wave method within the generalized gradient approximation (GGA). The binding energies were calculated as follows:

$$E_b^{u(p)} = E_T^{u(p)}[\text{SWCNT}] + E_T^{u(p)}[\text{A}] - E_T^{u(p)}[\text{A} + \text{SWCNT}],$$

where $E_T^{u(p)}[\text{SWCNT}]$ corresponds to the fully optimized structure of the CNT, $E_T^{u(p)}[\text{A}]$ to the free atom A, and $E_T^{u(p)}[\text{A} + \text{SWCNT}]$ to the atom adsorbed on a SWCNT. The authors considered four sites, the hollow site, the top site, and two bridge sites: the A-site axial to the C–C bond and the Z-site, site above the zigzag.

The results indicate that the properties of SWCNTs can be modified by the adsorbed metallic atoms. Most of the adatoms studied yield the strongest binding at the H6-site. Ni, Pd, Pt, Cu, Ag, and Au, however, seem to prefer the bridge site. The analyses of the binding energies showed that the transition metals with a few d electrons form strong bonds with the CNT, Sc, Co, Ti, Nb, and Ta with binding energies ranging from 2.4 to 1.8 eV (Table 8). Metals with near-filled or filled d-orbital showed relatively weak binding, such as Cu, Ag, Au, and Zn with binding energies ranging from 0.8 to 0.05 eV.

A systematic DFT study of the 3d transition metal interactions with planar graphene and curved (8,0) SWCNT graphitic surfaces has been reported.[295] The authors show that the adsorption of the adatoms is rather similar for graphene and CNT. Both graphene and (8,0) SWCNT surfaces presented η^6 hollow adsorption sites (η^6-H6-site) with metals that mainly bound covalently, and ionicity degrees that varied as expected with the metal electronegativity (charge transfer from the metal to the surface). The calculations show that 3d transition metal atoms were chemisorbed onto graphene in H6-site, with the exception of Cr, Mn, and Cu. These atoms were physisorbed and presented no energetically favored adsorption sites. As observed in previous examples, the binding energy increased as one moved in either direction away from the Cr/Mn couple of the 3d series. The $sp^{2+\eta}$ hybridization of (8,0) SWCNT surface, interact strongly with the d-orbitals than observed for graphene. Therefore, the magnetic moments were one unit less than the magnetic moments in graphene for systems containing Sc, Ti, or V.

The curvature of the CNT affects the binding energies as well as the binding geometry. In general, the smaller the diameter of the CNT, the stronger is the binding (see Section 2.2 to see rehybridization of CNTs). Chen *et al.*[296] reported the interaction of Pt adatom on CNT with several radius. The authors observed a decrease of the binding energies for larger

Table 8. Calculated binding energies and average carbon–adatom bond distances, $\bar{d}_{C-A}$ of individual atoms adsorbed at H-, Z-, A-, and T-sites of the (8,0) SWCNT[a] as described in Figure 27.

Atom	H(eV)	A(eV)	Z(eV)	T(eV)	ΔE_T(eV)	$\bar{d}_{C-A}$ (Å)	$\mu(\mu_B)$
Na	1.3	1.1	1.1	1.1	—	2.3	—
Mg	0.08	0.07	0.05	0.07	—	3.8	—
Sc	2.1(1.9)	1.4	1.5	→H	0.15	2.3(2.2)	0.64(1)
Ti	2.9(2.2)	2.1	2.7	2.1	0.58	2.2(2.2)	2.21(4)
V	3.2(1.4)	2.2	→H	→H	1.20	2.1(2.2)	3.67(5)
Cr	3.7(0.4)	2.5	→H	→H	2.25	2.0(2.3)	5.17(6)
Mn	3.4(0.4)	2.5	→H	→H	2.42	2.1(2.4)	5.49(5)
Fe	3.0(0.8)	2.5	→H	1.6	1.14	2.1(2.3)	2.27(4)
Co	2.8(1.7)	2.5	→H	→H	0.41	2.1(2.0)	1.05(3)
Ni	2.2	2.4(1.7)	2.3	→A	0.02	1.9(1.9)	0.04(2)
Cu	0.5	0.8(0.7)	0.6	→A	0.03	2.1(2.1)	0.53(1)
Zn	0.05(0.04)	0.05	0.03	0.04	0	3.7(3.7)	0(0)
Nb	3.9(1.8)	2.7	→H	→H	0.40	2.2(2.2)	2.86(5)
Mo	4.6(0.4)	3.0	→H	→H	0.32	2.2(2.2)	4(6)
Pd	1.1	1.7(1.7)	1.5	1.5	0	2.1(2.1)	0(0)
Ag	0.1	0.3(0.2)	→A	→A	0.03	2.7(2.5)	0.6(1)
Ta	2.8(2.4)	2.4	2.5	→H	0.73	2.1(2.2)	3.01(3)
W	3.4(0.9)	2.5	2.6	3.3	0.59	2.1(2.1)	2.01(6)
Pt	→Z	2.7(2.4)	2.4	→A	0	2.1(2.1)	0(2)
Au	0.3	0.6(0.5)	0.4	0.6	0.04	2.2(2.2)	1.02(1)
Al	1.6	1.4	1.5	→H	—	2.3	—
C	→Z	3.7	4.2	→A	—	1.5	—
Si	2.5	2.2	2.5	2.2	—	2.1	—
Pb	1.3(0.8)	1.0	1.2	→H	0.01	2.6(2.6)	0(2)
H	—	—	—	2.8	—	1.1	—
O	—	—	5.1	—	—	1.5	—
S	→A	2.8	2.4	→Z	—	1.9	—

[a] Binding energies, E_b, listed in the second through fifth columns are obtained from spin-unpolarized total energies calculated for the fully relaxed atomic structure. The binding energy E_b and $\bar{d}_{C-A}$ values given in parentheses are obtained from spin-polarized total energies calculated for the fully relaxed structure at the adsorption site where E_b has a minimum value. ΔE_T is the difference between spin-unpolarized and spin-polarized total energies. μ is the calculated magnetic moment (μ_B per supercell) of the magnetic ground state of the (A + SWCNT) system. The calculated magnetic moments of free atoms are presented in parentheses. →H implies that the adatom at the given site is not stable, and eventually it moves to the H6-site.[294]

CNTs and also a change on the binding geometry. Similar observation were reported by Menon *et al.*[297] who studied the interaction of Ni on graphite, (5,5) and (10,10) CNTs. The interaction of the adatom is stronger on the CNT surface. The binding geometry is also affected, while the H6-site is the most stable for graphite, it becomes unstable for CNT, being the T-site the most stable.

The interaction of transition metal adatoms with CNTs may also depend on whether the adatoms are adsorbed on the inside or outside surface of the CNT. Gao and Zhao[298] used first-principles calculations to investigate the binding energies, geometric structures, and electronic properties of 4d TM atoms adsorbed outside/inside SWCNTs. The most energetically favorable site is the same for interior and exterior adsorptions. The 4d elements from Y to Ru prefer η^6-H6-site, the Rh atom prefer an off-center η^5-H6-site, and finally Pd a bridge site. The binding mode is related to the valence electron configurations of the adatoms: for metals with filled or near-filled d-orbital, the sp-d hybridization with carbon becomes more difficult and they prefer to be in contact with less carbon atoms. The theoretical binding energy for Ru adsorption on nanotube or graphene surface is around 3.2 eV, which does not depend sensitively on tube diameter and chirality. In general, the binding energy of Ru atom outside CNT is higher than that inside CNT. Such difference becomes smaller as tube diameter increases, for example, from 0.31 eV for (6,6) tube to 0.06 eV for (12,12) tube. Due to curvature effect, the distribution of π electrons inside and outside the nanotube wall is uneven, resulting in higher electron density on the external surface of the CNT. When a Ru atom is adsorbed outside a CNT, the enriched π electrons due to curvature effect enhance the hybridization between the π electrons from carbon and the *d* electrons from Ru, leading to higher binding energy for exohedral adsorption.

The defects on CNTs also play an important role on the adsorption of transition metals. In a work of Shi *et al.*,[299] first-principles methods were applied to study the interaction of SW defects in a SWCNT with eight different metal atoms (Fe, Ni, Co, Ti, Cu, Al, Mg, and Mo), frequently used as catalysts in the growth of CNTs. They found that among the eight metals studied, only Mo and Ti always exhibited a positive cohesive energy, which indicates that there was no bonding of these metal atoms to CNT. Cohesive energies for Fe, Co, and Ni were relatively low, evidencing a strong attractive interaction with CNTs. In fact, these metals are regularly used as catalysts for the catalytic growth of CNTs. Several works have evidenced that interaction of Ni atoms with intrinsic defects (vacancies and SW) in SWCNTs enhances the Ni binding energies.[51,300,301] It was found that the orientation of the SW defects is closely related to the nature of the Ni adsorption, rather than to

tube chirality. Hydrogen desorption experiments using MWCNTs revealed that the desorption profile related to the defects disappeared after the impregnation of Ni nanoparticles, experimentally showing that the Ni adsorption occurs favorably on the defective sites.[302–304]

In conclusion, the single transition metal atoms are generally chemisorbed on graphene and CNT surfaces, except for the filled or near-filled d-orbital metals. Metals such as Cu, Ag, or Au show low energy binding, which is between physisorption and chemisorption. The binding geometry is usually on the H6-site, but also depends on the valence electronic configuration of the metal atoms. Finally, the adsorption configuration and binding energy of transition metals is similar in graphene and CNT; however, when the CNT curvature increases (smaller radius), the interaction between the atom and the CNT increases. Similarly, the adsorption of the adatom outside of the CNT is stronger than inside of the CNT. The presence of defects also increases the binding of transition metals to the carbon support.

Clusters

CNTs and graphene interacting with metal nanoparticles are gaining considerable interest as sensing materials and catalysts, in the synthesis of metallic nanowires, as well as in nanoelectronics applications as field effect transistor (FET) devices. The metal–CNT interface may constitute the central part of these applications. Platinum and gold clusters are the most studied systems due to their applications in catalysis and are discussed in the following two subsections.

Platinum clusters

Okamoto used DFT calculations to examine the interface between graphene and an icosahedral Pt_{13} cluster.[305] The calculations showed that the Pt_{13} cluster prefers to adsorb in a top site with the face of the icosahedron in contact with the graphene, with an adsorption energy of 2.08 eV. These results indicate that the interface of the metal clusters and graphene are stabilized when the metal atoms are just above the carbon atoms, as can be seen in Figure 28.

First-principles calculations based on DFT have been applied to investigate the interactions between Pt_n ($n = 1–4$) clusters and a graphene sheet.[306] For one platinum adatom (Pt_1), the adsorption energy is –2.17 eV on a B-site. $Pt_{2–4}$ clusters also prefer to adsorb near B-sites. In the non-defected graphene, the interfacial interaction between Pt_n and graphene becomes weaker as increasing the number of Pt atoms in clusters; 2.17 eV/atom for

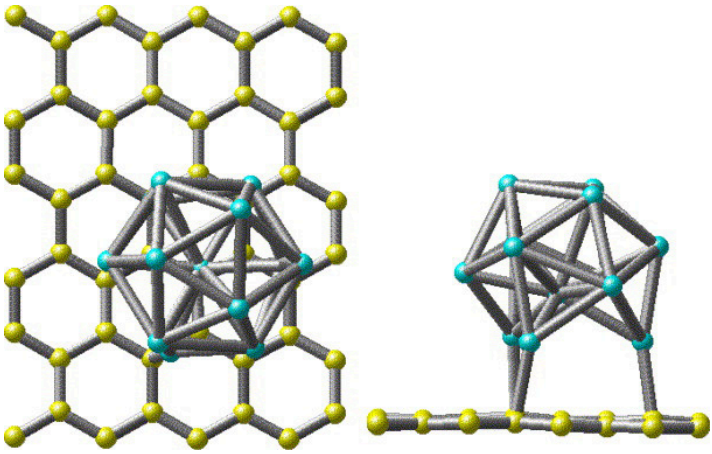

Figure 28. Optimized geometry of a Pt_{13} cluster on flat, defect-free graphene sheet: top view (left) and side view (right).[305]

Pt_1, 0.63 eV/atom for Pt_2, and 0.15 eV/atom for a triangular Pt_3. However, the tetrahedral Pt_4 cluster strongly interacts with the non-defective graphene sheet in comparison with the triangular Pt_3 cluster.

Similarly, Dai *et al.*[307] studied by first-principles total energy calculations the formation and structures of Pt clusters on graphene. The most stable adsorption site of a single Pt atom is the B-site. The stable atomic configuration of the Pt_2 is on the B-sites as well as for Pt_3, which prefers a linear configuration, the Pt atoms are located on the B-sites and E_{form} is 3.622 eV/atom. For Pt_4 clusters, tetrahedral configuration is the most stable among the three considered. The adsorption of a tetrahedral cluster is more stable over that of the quadrilateral and linear Pt_4. This is because a tetrahedral Pt_4 consists of four Pt triangles and the interatomic interaction is strong. With an increasing Pt coverage, the formation energy also increases and the absorbed Pt atoms have strong interatomic interactions and preferentially form clusters on graphene. With increasing numbers of adatoms, the adsorbed Pt can form dimers, linear atom chains, and 3D tetrahedral clusters. The 3D tetrahedral cluster is more stable than the planar clusters (dimer and linear chain) on graphene.

Okazaki-Maeda *et al.* studied the stable atomic configurations and the electronic structures of several Pt clusters, from 1 to 13 atoms, by first-principles calculations based on DFT.[308] The results for small clusters Pt_{1-5} show that the interfacial interaction energy determines the stability of the Pt/graphene system, resulting in the stabilization of the vertical adsorption of the planar cluster. However, for the bigger clusters $Pt_{>10}$, it is the cohesive energy

of the free Pt cluster, which determines the stability of the Pt/graphene system, resulting in the stabilization of the 3D cluster adsorption.

The defective sites on graphene sheets, the presence of five- and seven-membered rings, or the presence of doping atoms on graphene have an important role on the stabilization of the Pt nanoparticles. Their presence increased the adsorption energy of the Pt clusters. Okamoto calculated a significant increase of the adsorption energy between a graphene vacancy and an icosahedral Pt_{13} cluster.[305] The adsorption energy of the Pt_{13} cluster on a defect-free graphene was calculated to be 2.08 eV, while on a defective graphene sheet, it was 4.71 eV. The presence of five- or seven-membered ring on the graphene also raised the adsorption energy to 3.38 and 3.30 eV, respectively.

Fampiou and Ramasubramaniam performed a systematic study of the adsorption energetics, structural features, and electronic structure of platinum nanoclusters $Pt_{1–4}$ and Pt_{13} supported on both defective and defect-free graphene (Figure 29) using a combination of DFT and bond-order potential calculations.[309]

The Pt clusters bind strongly to the defective graphene. The stronger bonds are the unreconstructed divacancy, followed by the 5–8-5 defect (see Table 9 for adsorption energies).

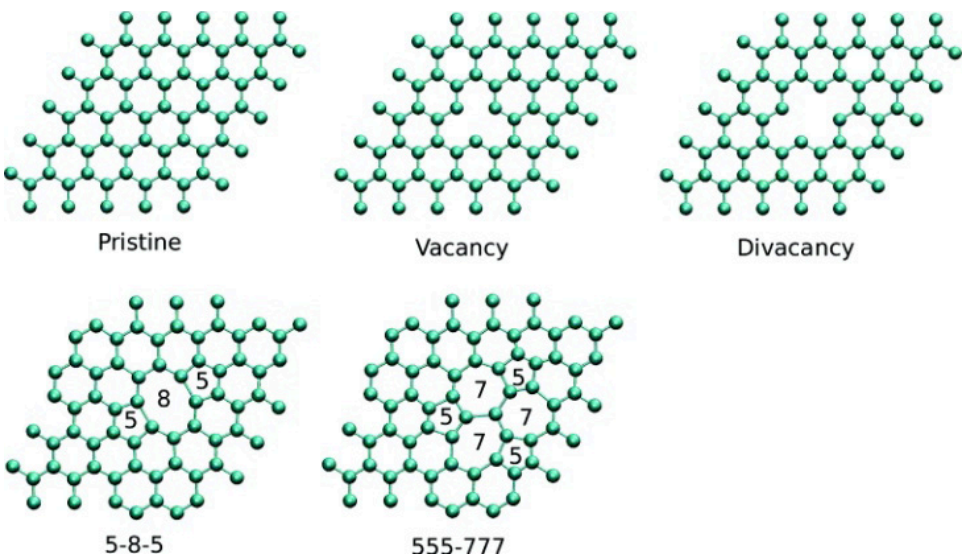

Figure 29. Defect-free and defective graphene substrates employed in the study. Pentagons, heptagons, and octagons associated with divacancy reconstructions are indicated.[309]

Table 9. Optimal adsorption energies for Pt adatom, Pt dimer, Pt trimer, Pt tetramers, and Pt_{13} clusters on pristine graphene, SV, unreconstructed divacancy, 5–8-5 reconstructed divacancy, and 555-777 reconstructed divacancy for both structural relaxation of high-symmetry clusters and annealed and relaxed clusters. Empirical Potential (EP) results are in parentheses. Adapted from Ref. 309.

Substrate	Pt adatom E_{ads} (eV)	Pt dimer E_{ads} (eV)	Pt trimer E_{ads} (eV)	Pt tetramer E_{ads} (eV)	Pt_{13} cluster E_{ads} (eV)
Pristine	–1.57 (–1.99)	–0.78 (–1.94)	–1.35 (–2.54)	–1.13 (–1.63)	–0.25 (–3.11)
Vacancy	–7.45 (–6.68)	–7.26 (–6.93)	–7.61 (–6.52)	–7.27 (–5.51)	–4.67 (–5.86)
Divacancy	–6.97 (–8.60)	–6.40 (–8.66)	–6.33 (–7.95)	–7.06 (–9.26)	–6.59 (–9.58)
5-8-5	–6.12 (–6.94)	–4.14 (–7.34)	–5.54 (–7.50)	–6.01 (–7.4)	–6.28 (–7.33)
555-777	–2.38 (–2.27)	–2.43 (–2.21)	–5.15 (–2.05)	–5.33 (–3.35)	–2.07 (–4.66)

In general, the clusters lose their high symmetry when they bind to the graphene. For Pt_{13} clusters, there is no resemblance to their high-symmetry icosahedral or cuboctahedral configurations. Instead, these are low symmetry, open shapes that are more strongly adsorbed (by several electron volts in some cases) and are thermodynamically more stable than the structures obtained from relaxation alone (Figure 30). The formation of strong bonds with the carbon substrate also increases the Pt–Pt bond length in a cluster. Finally, the electronic structure studies reveal a clear tendency for charge transfer from Pt clusters to the graphene substrate directly related to the strength of binding to the defect.

The effect of the presence of doping atoms on graphene on the adsorption of Pt clusters on the carbon surface was studied by Dai *et al.*[310] The authors studied the adsorption of Pt clusters on graphene and doped graphene (nitrogen-, boron-, and silicon-doped) using DFT. All doping atoms enhance the interaction between Pt and graphene. The adsorption energy of Pt clusters on Si-doped graphene is much higher than those on the N- and B-doped graphene. For instance, the adsorption energy on pristine and on Si-doped graphene for a Pt_2 cluster is 2.42 eV and 4.54 eV, respectively; and for a Pt_4 cluster 4.26 eV and 4.63 eV, respectively.

The adsorption of Pt clusters on CNT has also been intensively studied. Adsorption geometries and binding affinities of metal nanoparticles onto CNTs have been investigated through DFT calculations.[311] Clusters of 13 metal atoms were used as models for metal nanoparticles. Platinum particles strongly chemisorbs onto the CNT surface. For monolayer or multilayers of metal atoms on CNTs, most of the metal binding arises from metal–metal interaction rather than metal–graphene interaction.[183] This is due to high

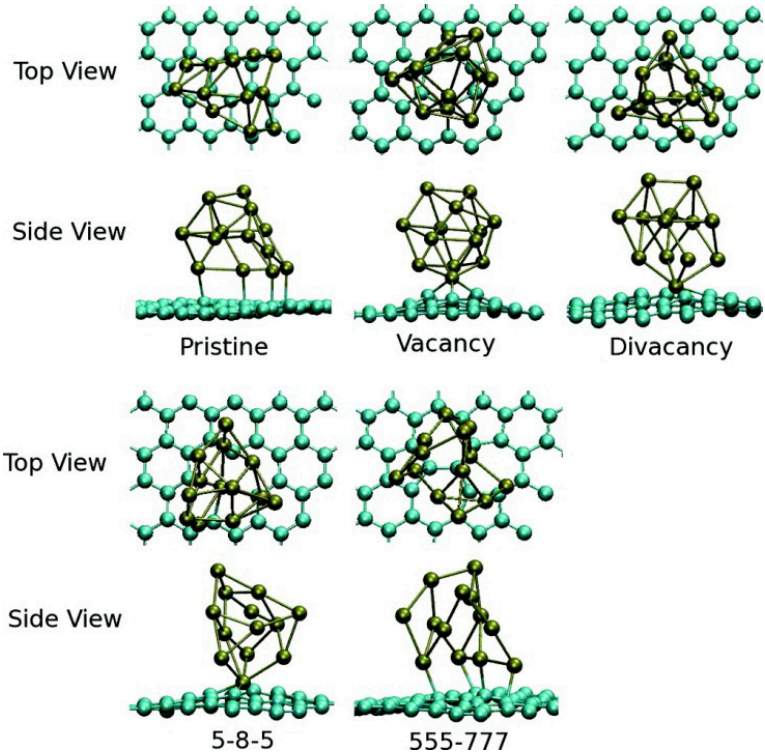

Figure 30. Selected low-energy configurations obtained by DFT structural relaxation of EP-based molecular dynamics annealing of Pt_{13} clusters on graphene. Cyan and gold spheres represent C and Pt atoms, respectively.[309]

cohesive energies of the metals in the bulk crystalline state. If only the metal–graphene part of the interaction is considered, the binding for Pt falls rapidly with layer thickness indicating perhaps a possible instability of the Pt films beyond a certain thickness. A critical cluster size of a few tens of metal atoms has been determined, below which the metal should wet a CNT surface uniformly, and above which non-uniform clustering is likely. Using a simple model, the author has shown that the critical cluster size for Pt is ~23, which is smaller than that for Pd (~30), implying a higher propensity of Pt to form a non-uniform coating, unless it is deposited in the form of ultrafine nanoparticles.

A first-principles electronic structure calculation was performed to explore stability and electronic structure of Pt_{13} cluster adsorbed on CNTs.[312] The stability of the Pt_{13} cluster on CNT (*ca.* 4.0 eV) is enhanced significantly compared with that on graphene. The increase of adsorption energy of Pt_{13} cluster on CNTs can be explained in terms of geometric factors. Due to the

curvature-induced pyramidalization and misalignment of π-orbitals of carbon atoms in SWCNTs, carbon atoms on the outside wall of the SWCNT have more sp^3 character than those on a flat graphene sheet. In addition, the nature of Pt–C bonding is hybridization between d-states of Pt atoms and p-states of adjacent C atoms. As a result, Pt atoms can strongly interact with carbon atoms in the case of CNTs, leading to an increase in the adsorption energy. CNTs with high curvature promotes the overlap between p and d wave functions, thus the adsorption energy of a single Pt atom on SWCNTs increases linearly with the curvature.[313] In the case of Pt_{13} cluster, three Pt atoms prefer to adsorb on bridge A sites resulting in a deformation of Pt cluster. High curvature makes Pt–C bonding stronger and the larger deformation results in smaller binding energy of the Pt cluster. Hence, it is possible to predict an optimal curvature of SWCNT for the adsorption of Pt_{13} cluster on SWCNTs. For a (10,0) semiconducting SWCNTs, the highest adsorption energy (4.1 eV) is at around 0.06 ($Å^{-1}$) curvature, which corresponds to a semiconducting SWCNT with 16.66 Å diameter. It was also reported that charge redistribution among Pt atoms takes place. Electronic structure of carbon-supported Pt cluster exhibits metallic characteristics, similar to a Pt metal surface.

In conclusion, Pt clusters chemisorb on graphene and CNTs surfaces. As observed for single adatoms, the presence of defects or doping atoms such as nitrogen, boron, or silicon have an important role on the stabilization of the Pt nanoparticles, increasing the binding energies. Also the curvature increases the bonding energies making the Pt_{13} cluster on CNT more stable than on graphene. Finally, Pt does not form stable metallic films, it prefers to form clusters due to the strong interatomic interactions of the absorbed Pt atoms.

Gold clusters

Density functional calculations were performed to study the interfaces of graphene with an icosahedral cluster of Au_{13}.[305] The gold cluster binds weaker than a Pt_{13} cluster on the graphene surface (E_{ads} = 0.90 eV for gold and E_{ads} = 2.08 eV for platinum). The results revealed that the introduction of a carbon vacancy or the presence of defects (five- and seven-membered rings) into the graphene increased the adsorption energy of the cluster onto the graphene surface. Similar adsorption energy was found for a cluster of Au_{10} on graphene.[314]

The adsorption of $Au_{1–4}$ clusters on graphene, as well as their mobility and clustering from pre-adsorbed fragments have been studied by DFT.[315] The cluster adsorption energies on graphene of all studied clusters range from –0.1 to –0.59 eV, and substantially exceed their diffusion barriers, which are

4–36 meV, only. All clusters diffuse along the C–C bonds, since none of them binds to the hollow sites in the centers of the carbon hexagons. The analysis of the densities of states shows which states contribute to the strong intracluster bonds, predominantly the 5d states, and which to the chemical bond between gold and carbon, *i.e.*, mostly s–d_{z2} cluster states hybridizing with p_z states of carbon. The formation of the strong Au–Au bonds is the driving force behind the tendency to form bigger clusters from smaller pre-adsorbed fragments.

The adsorption of Au_n (n = 1–5) on perfect and defective graphene has been studied by DFT calculations.[316] All the clusters are bonded to graphene through an anchor atom as observed by Martin *et al.* [315] and the geometries are similar to the corresponding free-standing clusters. Charge transfer between clusters and graphene shows strong size dependency, and the amount is larger in the presence of the SV on the graphene than on a pristine sheet.

The interaction of graphene with other transition metal clusters with interesting applications in catalysis has also been investigated in theoretical studies. Clusters of Co,[317] Ru,[318] and Fe[316,319] show strong interactions with graphene, which increase with the presence of vacancy defects. In the case of Ru_{13} clusters, the presence of B doping atoms further increases the binding energy between the graphene and the cluster.

In general, the strong interatomic interactions between d-metal atoms prevent the formation of atomic coating, thus forming metal clusters. The d-metal clusters strongly interact with graphene or CNTs. The presence of defects or doping atoms increases the binding energies as observed for single adatoms.

4.3.4. Adsorption of other metals, metalloids, and non-metals

The adsorption of other metals, metalloids, and non-metals (groups III to VI) on graphene and CNTs has been much less studied than the adsorption of alkali, alkaline-earth, and d-metals. In the systematic study of Nakada *et al.* about the adsorption of several adatoms on graphene by DFT calculations (see Table 7), the authors show that atoms of groups III to VI strongly bond to graphene.[269] Carbon shows the highest bond energy (3.43 eV) followed by sulfur (2.34 eV) and phosphorus (2.20 eV). The rest of the elements show bond energies in between 1.07 and 1.86 eV. Group III elements prefer to bond on the H6-site, except for boron which prefers the bridge sites. Group IV to VI prefers to bind on the bridge site. The adsorption of Al, In, and Pb on graphene has been studied by Liu *et al.* who show that Al and In

chemisorb on the surface on the hollow site.[270] However, Pb shows weaker bond energy (0.3 eV) and is physisorbed, in opposition to that observed before.

The adsorption of Al, C, Si, Pb, and S on SWCNTs has been investigated using the first-principles pseudopotential plane wave method within DFT.[294] Carbon and silicon form rather strong bonds with the SWCNTs. The calculated binding energies are high (*i.e.*, E_b = 4.2 and 2.5 eV, respectively for carbon and silicon). The bridge site is energetically favorable for both C and Si as observed for graphene. Sulfur also strongly bonds on the B-site (2.8 eV) of SWCNTs. Al and Pb prefer to bond on the H6-site with weaker binding energy (1.3 and 1.6 eV, respectively).

The selected adsorption behavior of sulfur atoms on SWCNTs was studied by DFT in terms of adsorption energy and charge transfer.[68] It is found that the adsorption on the tips is energetically preferred in perfect SWCNTs. The adsorption energy and charge transfer on five-membered ring with one dangling bond defects are significantly large with respect to perfect sites on SWCNTs, suggesting selective adsorption of sulfur on these defects. Importantly, adsorbed sulfur atoms can effectively stabilize these defects through the formation of S–C bond, which is not found for perfect SWCNTs. Shi *et al.* studied the adsorption of 10 different atoms (H, B, C, N, O, F, Si, P, Li, and Na) over SW defects in SWCNTs.[320] They observed that only the adsorption capacity of B, N, F, and Si among the 10 foreign atoms studied would benefit from this defect introduction (the presence of a heptagon reduced the binding energy by about 0.5 eV). Other atoms have a positive or near-zero cohesive energy, which implied a weak bonding to the CNTs.

4.3.5. Polymers

Chemisorption of polymers on the surfaces of graphene and CNTs has been extensively studied in the context of the important application in polymer–carbon composites. The non-covalent approach to the attachment of polymers on the surface of nanotubes and graphene has been discussed in Section 3.3.4. The interfacial characteristics of the polymer–carbon interphase directly influence the efficiency of nanotube reinforcements in improving mechanical, thermal, and electrical properties of the polymer nanocomposite. In a detailed review, Rahmat *et al.* have described the various techniques of interaction measurements, including experimental and modeling studies. It was concluded that an optimum CNT–polymer interaction is a key factor toward reaching the full potential of CNTs in nanocomposites.[321] Xue has studied the interactions of graphene and modified graphene[322,323] and CNT,

including the effect of CNT chirality and modified CNTs,[259,324] with PMMA and polyethylene (PE), by molecular mechanics and molecular dynamics simulations. The influence of chemical functionalization on the interfacial bonding characteristics of SWCNTs-reinforced polymer composites was investigated using molecular mechanics and molecular dynamics simulations. The simulations show that functionalization of nanotubes at low densities of functionalized carbon atoms drastically increases their interfacial bonding and shear stress between the nanotubes and the polymer matrix, where chemisorption to as little as 5.0% of the nanotube carbon atoms increases the shear stress by about 1000%. This indicates that increasing the load transfer between SWCNTs and a polymer matrix in a composite via chemisorption may be an effective way and chemical attachment of nanotubes during processing may be in part responsible for the enhanced stress transfer observed in some systems of the nanotube–polymer composites. Furthermore, this suggests the possibility to use functionalized nanotubes to effectively reinforce other kinds of polymer-based materials as well.[259]

To study the influence of the chemical functionalization on the interfacial bonding, the authors used a pullout simulation (Figure 31). The pullout simulations were performed to characterize the interfacial shear stress of the composites. They were carried out on graphene and modified graphene (graphene was modified with –COOH, NH_2, –OH, –F, phenyl, $–CH_3$, C_6H_{13},

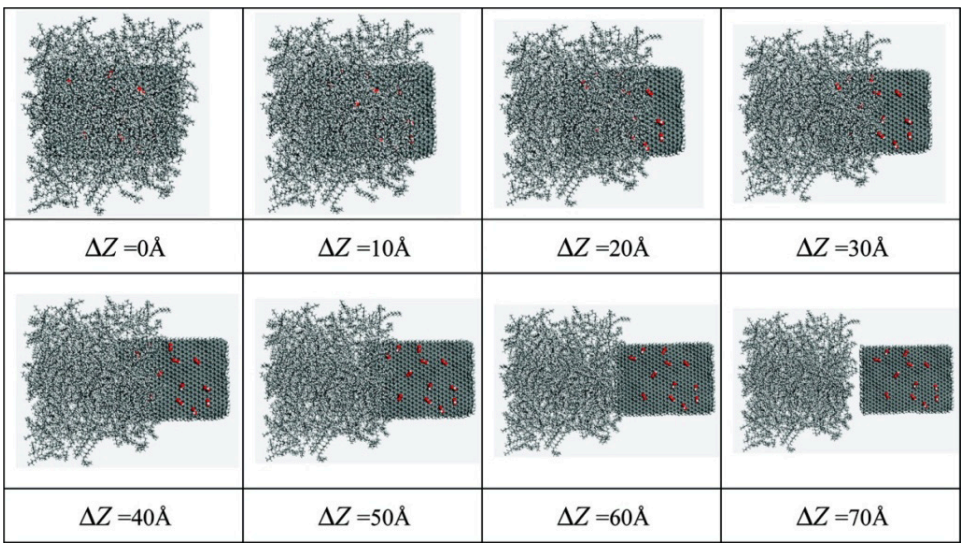

Figure 31. Snapshots from the molecular dynamics simulation of the pullout of the graphene with –COOH groups randomly chemisorbed to 2.5% of the carbon atoms.[322]

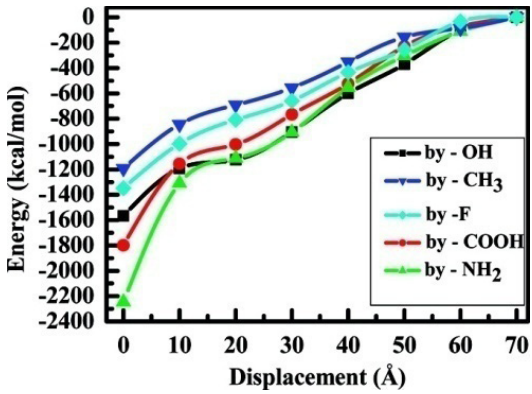

Figure 32. Interaction energy plots during the pullout of the graphene with different groups randomly chemisorbed to 2.5% of the carbon atoms from the PE matrix.[322]

and $-C_2H_4(C_2H_5)_2$ groups) embedded on PMMA and PE (Figure 32). The potential energy, the interaction energy, and the interfacial bonding energy were obtained in this way. When the degree of functionalization increases, both the interaction energy and interfacial bonding energy between the simulated graphene and the polymer increase to about four times the value for pristine graphene. As the interfacial bonding increased, an increase on the shear stress was also noticed. The shear stress of the graphene–polymer interface with weak non-bonded interactions can be increased by about 400% with the introduction of a relatively low density (10%) of chemical attachment.

In general, all chemical groups studied enhanced the interfacial bonding energy. The effect of the groups on the interfacial bonding energies between graphene and polymer are as follows: $-NH_2 > -COOH > -OH > -F > -CH_3 \approx$ phenyl $\approx C_6H_{13} \approx -C_2H_4(C_2H_5)_2$ (Figure 33).

In the case of CNTs, the authors also observed that the introduction of phenyl groups on the CNTs increased the interface bonding energy and the shear stress. They also noticed an effect of the chirality on the interfacial bonding characteristics between the SWCNTs and the PMMA matrix. Substantial adhesion exists between the nanotube and PMMA when the nanotube has a higher chiral index or larger chiral angle. For SWCNTs with similar molecular weights, diameters, and lengths, the armchair nanotube may be the best nanotube type for reinforcement.

In conclusion, the bonding energy and shear stress between the graphene or CNT and polymer increase with the increase of the concentration of functionalized groups. Therefore, the attachment of some suitable chemical

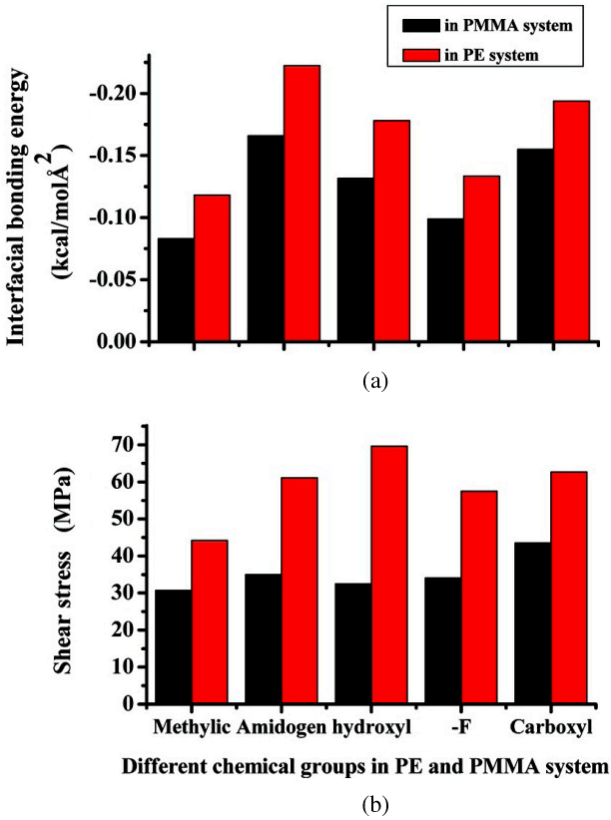

Figure 33. Influence of the graphene with different groups randomly chemisorbed to 2.5% of the carbon atoms on the interfacial bonding characteristics for the graphene–PE and graphene–PMMA systems.[322]

groups with a reasonable concentration to the graphene or CNT surface may be an effective way to significantly improve the load transfer between the graphene or CNTs and polymers to produce nanocomposites.

These modeling studies, as well as experimental studies that will be treated below, show that covalent interaction is an effective method to improve nanocomposite properties such as the Young's modulus, the tensile strength, or the shear stress. Usually, the functionalization of CNTs requires a premodification to introduce chemical groups on the surface, for example, via oxidation, ozone-mediated process, etc. During the functionalization process, some sp^2 carbons are converted to sp^3 carbons. Spectroscopic techniques, Raman and FTIR, allow understanding the interfacial bonding between the nanotubes or graphene and the polymer matrix. Raman spectroscopy allows distinguishing functionalization, thanks

to the increase in the D to G band intensity ratios and in the intensity of the D' band. FTIR allows observing the presence of functional groups on the carbon surface.

The functionalization of SWCNTs by H_2SO_4/HNO_3 and subsequent fluorination lead to the improvement in the dispersion of purified SWCNTs in an epoxy composite.[325] The functionalized nanotubes were highly dispersed and well integrated in the epoxy composites and the mechanical properties were enhanced. The Raman and FTIR spectroscopy were used to confirm the functionalization. The IR spectrum of the epoxy sample containing the functionalized nanotubes after heating for 2 h at 433 K shows an intense band at 1730 cm^{-1}, characteristic of the carbonyl (C = O) stretch of the ester derivatives (Figure 34). The epoxy group at 915 cm^{-1} has disappeared, indicating the occurrence of the esterification reaction between the carboxylic acid and epoxy.

Functionalized (f-MWCNT) and unfunctionalized (u-MWCNT) CNTS were incorporated to a PMMA matrix.[326] The IR and the Raman spectra show that functionalized CNTs are bonded to the thermoplastic polymer matrix which improves effectively the mechanical transfer.

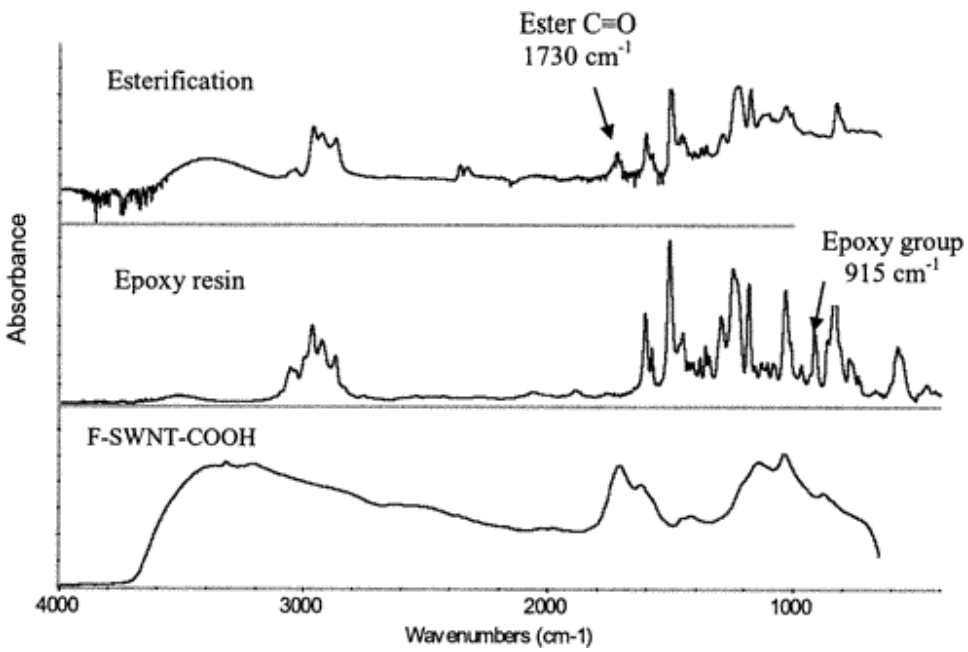

Figure 34. Attenuated Total Reflectance-Infrared (ATR-IR) spectra of the functionalized nanotubes (bottom), epoxy resin (middle), and product of the esterification reaction (top).[325]

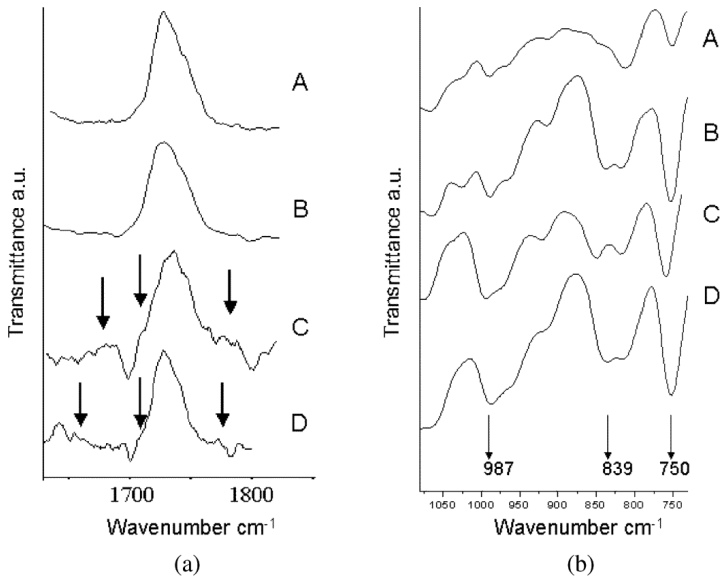

Figure 35. (a) IR spectra: (A) PMMA, (B) 1 wt.% u-MWCNT composite, (C) 1 wt.% MWCNT composite, and (d) 1.5 wt.% f-MWCNT composite. (b) Raman spectra: (A) PMMA, (B) 1 wt.% u-MWCNT composite, (C) 1 wt.% f-MWCNT composite, and (D) 1.5 wt.% f-MWCNT composite.[326]

The IR spectra of the composites (Figure 35a) shows a clear increase in the peaks at 987 and 750 cm^{-1} for f-MWCNT composite with respect to PMMA; the first band corresponds to νC–C of the main chain in PMMA and the second corresponds to a combination νC–C and ρCH_2. The increase in these bands is due to the addition of C atoms of f-MWCNT in the PMMA chain. The u-MWCNT composites show an increase in these bands too; however, the increase in the band at 987 cm^{-1} is smaller in sample B than that shown in samples C and D, showing that chemical groups in f-MWCNT have stronger interaction with the polymer. The Raman spectra (Figure 35b) of the ν C=O vibration covers the range from 1680 to 1820 cm^{-1}. Three new peaks are present for f-MWCNT composites which indicate the interaction of the functionalized CNT with the polymer matrix. In addition, these bands are not present in the PMMA and the u-MWCNT spectra and corroborate the interaction between f-MWCNT and PMMA groups.

CNTs and graphene are chemisorbed on the polymer matrix by covalent functionalization. In general, the introduction of CNTs and graphene enhances the mechanical properties of this kind of composites. Modeling together with experimental studies shed some light on the interaction

properties between the polymer matrix and the CNT or graphene. Raman and IR spectroscopies as well as XRD and TEM are important techniques to understand the bonding interaction of such materials.

5. Reactivity on CNTs and Graphene

Filamentous carbons have been produced for long, the first reports dating back to more than a century ago, where they were produced from hydrocarbons in metallic crucibles that were unintentionally acting as catalyst.[327] Today, catalysis constitutes an important aspect of CNT and graphene synthesis, and scientists from the catalysis community have been involved with the mechanisms of filamentous carbon formation for decades. Indeed, fibrous carbon (CNTs or carbon nanofibers (CNFs)) was considered as an unwanted by-product of reactions involving conversion of carbon-containing gases and all efforts were focused on how to prevent their formation, which was identified as one of the reasons of catalyst deactivation and reactor degradation for process involving carbon monoxide or hydrocarbon decomposition.[328] Additionally, researches on vapor-grown carbon fibers have allowed fixing the basis of CNT and CNF catalytic growth mechanisms.[329] Compared to catalysis for CNTs, the use of CNTs for catalysis, as catalyst support or directly as catalyst, is a relatively new topic of investigation, since the first report date back to 1993.[330] As far as graphene is concerned, the interest of the catalysis community is even more recent.[3] Attention has also been paid to the preparation of metal particles deposited on CNTs or graphene,[178,331,332] and specific activities/selectivity of CNT, fullerene, or graphene-supported catalysts were reported.[3,333,334] CNTs and graphene, and more particularly FLG offer a range of attractive properties (Table 10) and could constitute a new family of highly efficient catalysts or catalyst support. As far as CNTs are concerned, they are already produced on the semi-industrial scale and the current barriers to mass-market use of these materials include the availability of high-quality materials at low prices and in commercial quantities. Additionally, the key issue concerning standardization and toxicity of these materials should be carefully addressed. Currently, the main area of interest in this domain are (i) the understanding and characterization of nanocarbons surface chemistry; (ii) the involvement of CNT or FLG catalysts/supported catalysts in liquid or gas-phase reactions; (iii) oxidation and environmental catalysis; (iv) electrocatalysis for fuel cells; (v) the production of specific materials for gas sensors, and (vi) energy storage and conversion.[9,335,336]

Table 10. Characteristics of CNTs, CNFs, G, and FLG.

	SWCNTs	MWCNTs	CNFs	G/FLG
Diameter/thickness (nm)[a]	0.5–2 (1–1.5)	5–200 (10–40)	10–500 (50–100)	1 atom–3.5
Length/Surface	Few μm up to 20 cm	Few to hundreds μm	Few to hundreds μm	Few to hundreds μm^2
d_{002} (Å)	—	3.39–3.48	3.36–3.44	3.35–3.41
Apparent density (g/cm^3)	0.5–1 (film)	0.02–0.4[b]	0.3–1.4	0.03–1
S_{BET} (m^2/g)	400–900	150–450	10–250	70–2630
Porosity (cm^3/g)	Micro V_{micro}: 0.15–0.3	Meso V_{micro}: 0. 5–2	Meso V_{micro}: 0.2–2	Micro/meso V_{pore}: 0.1–0.5
Young modulus (TPa)	1.05–1.3	0.5–1.2	0.3–0.7	0.2–1
Tensile strength (GPa)	45 to 150	3–30 to 150[c]	3–12	5–130
Electrical resistivity (Ω.cm)	6.10^{-4}	$0.6–2.10^{-4}$	1.5–3	$10^{-3}–10^{-6}$
Electrical conductivity (S/cm)	550	80–1000	300	70–1000
Thermal conductivity[d] **(W/K.m)**	1000–6000[e]	300–3000	800–2000	600–6000

[a]Typical values in parentheses. [b]Defect-free MWCNTs. [c]Axial thermal conductivity at room temperature. [d]For a single rope of SWCNTs. [e]The lower value is for a powder and the upper one for short MWCNTs.

5.1. Surface chemistry of nanostructured carbon materials

The surface chemistry of nanocarbon materials is governed by basal and edge carbon atoms, as well as by the presence of defects (*i.e.*, structural carbon vacancies, non-aromatic rings). These imperfections and defects along the edges of graphene layers are the most active sites owing to high densities of unpaired electrons. On them, heteroatoms, such as oxygen, hydrogen, nitrogen, and sulfur can be chemisorbed leading to stable surface compounds, resulting in a complex surface chemistry, if compared to oxides such as silica or alumina. Although a direct analogy to the functional groups classified in organic chemistry exists, the chemical complexity of the carbon surface and the fact that the heteroatoms are often located into confined space cause that one cannot expect the full prediction of the behavior of those groups based on well-known organic chemistry reaction mechanisms. The concentration and distribution of the surface groups present on the carbon depend on the carbon type and the pretreatment applied. Although adsorption onto carbons is mainly of dispersive interaction type, surface chemistry plays an important role when specific interactions are considered. The surface chemistry of carbons determines their moisture content, catalytic properties, acid–base character, and adsorptive properties. It is related to the presence of heteroatoms other than carbon within the carbon matrix, and to the presence of carbene and carbyne structures[30] at the edges of the graphene layer in sp^2-hybridized carbon materials. The most common heteroatoms are oxygen, nitrogen, and hydrogen. They are bound to the edges of the graphite-like layers and form organic functional groups such as carboxylic acids, lactones, phenols, carbonyls, aldehydes, ethers, amines, or nitro compounds. These functional groups can be acidic, basic, or neutral in character. The acidic behavior is often associated with surface complexes or oxygen functionalities such as carboxyls, lactones, and phenols. On the other hand, functionalities like amines, pyrones, chromenes, ethers, and carbonyls are responsible for basic properties of the carbon surfaces. Basic properties associated with Lewis sites located at the π electron-rich regions within the basal planes of graphitic microcrystals, away from the edges, have also been proposed. We will concentrate our analysis to oxygen- and nitrogen-containing surface groups, since they are the most common and relevant for catalysis. It is however worth mentioning that a rich carbon functionalization chemistry exists for CNT and graphene.[337–339] Figures 36 and 37 represent the different types of oxygen- and nitrogen-containing functionalities generally observed on CNT and graphene.

Carbon surface oxidation is the most popular way of carbon surface modifications. It can be done either from a gaseous (oxygen, ozone, air, or

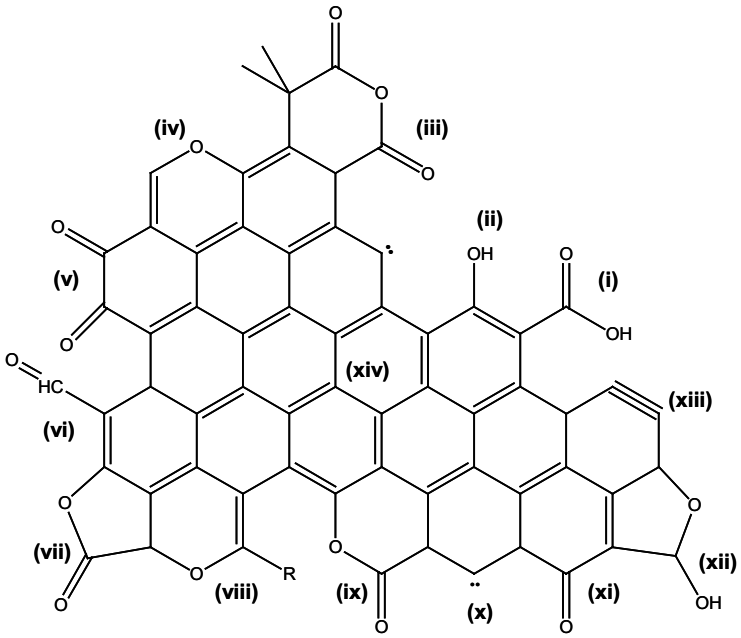

Figure 36. Oxygen-containing species, and specific sites generally present on CNT and graphene surface: (i) carboxylic acid, (ii) phenol, (iii) carboxylic anhydride, (iv) ether, (v) quinone, (vi) aldehyde, (vii) lactone, (viii) chromene, (ix) pyrone, (x) carbene-like species, (xi) carbonyl, (xii) lactol, (xiii) carbyne-like species, (xiv) π electron density on carbon basal plane.

nitric oxides) or liquid phase (nitric acid, hydrogen peroxide, potassium permanganate, sulfuric acid, sodium peroxydisulfide).[340] Air oxidation produced various oxygen-containing groups with the predominant population of weakly acidic groups such as phenols. The oxidation from the liquid phase is much more complex and results in more severe changes in carbon surface chemistry.[55] Higher is the temperature and stronger is the oxidant, more oxidized the carbon surface is. In some cases, strong oxidation, as that with nitric acid at its boiling point, can totally destroy the carbon structure. It is generally accepted that oxidation with strong oxidants such as nitric acid leads to the carbons with the predominant population of surface carboxylic groups, whereas treatment with hydrogen peroxide increases mainly the population of phenols. Nitric acid oxidation can also result in incorporation of few nitrogen as nitro groups likely attached the carbons at the edges of graphene planes.[341]

The oxygen-containing functionalities are considered as acidic or basic. The acidic surface groups (*i.e.*, carboxylic acid, lactone, and phenol groups) are formed when the carbon surface is exposed to oxygen via

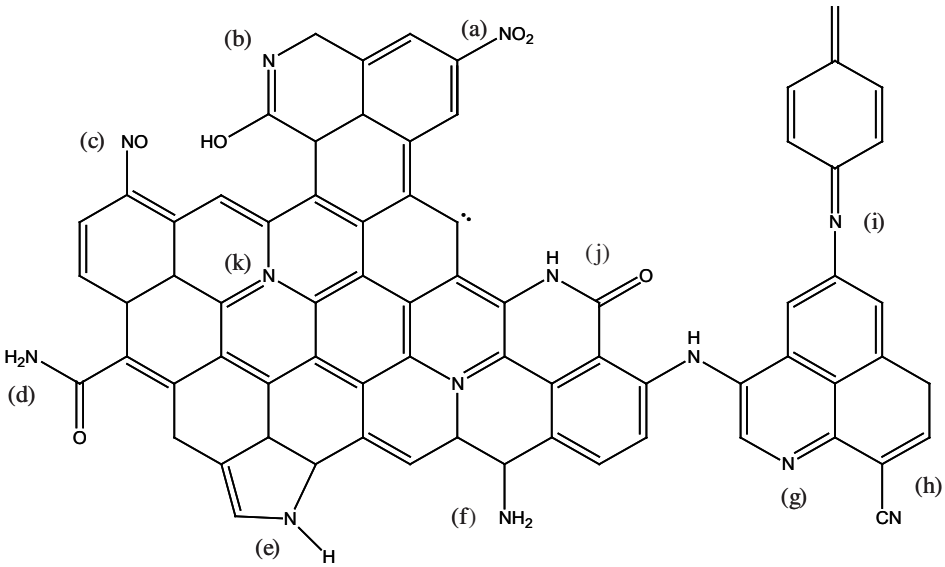

Figure 37. Nitrogen-containing species, and specific sites generally present on carbon surface: (a) nitroso group, (b) α-pyridone, (c) nitro group (abbreviated as N-X), (d) amide, (e) pyrrole-type nitrogen (abbreviated as N-5), (f) amine, (g) pyridine-like group (abbreviated as N-6), (h) nitrile, (i) imine, (j) lactam, (k) quaternary amine (abbreviated as N-Q).

reactions with oxidizing agents from solutions or gas phase, either at room or high temperatures. On the other hand, the basic groups are formed when an oxidized surface is reduced by heating at inert atmosphere at high temperatures. The decomposition of acidic groups results in active sites at the edges of the graphene layers, which upon cooling in inert atmosphere and re-exposure to air, attract oxygen and may form basic functional groups such as chromene or pyrone.[342] Although there is a general consensus about the type of surface functionalities, which determines the acidic character of a carbon material, the nature of carbon basic surfaces remains controversial and open for investigations. Generally speaking, oxygen-containing functionalities (*i.e.*, chromene, pyrone, quinones) and non-heteroatomic Lewis base sites, characterized by regions of π electron density on the carbon basal planes govern carbon basicity.[343]

As far as GO is concerned, its precise chemical structure has been the subject of considerable debate over the years, and even to this day no unambiguous model exists. There are many reasons for this, but the primary contributors are the complexity of the material (including sample-to-sample variability) due to its amorphous, berthollide character (*i.e.*, non-stoichiometric atomic composition) and the lack of precise analytical techniques for characterizing such

materials (or mixtures of materials). Despite these obstacles, considerable effort has been directed toward understanding the structure of GO, much of it with great success.[237] Cross polarization/magic angle spinning (CP/MAS) experiments displayed three broad resonances at 60, 70, and 130 ppm in the ^{13}C NMR spectrum of GO. Short-contact-time spectra display only signals at $\delta = 60$ and 70 ppm. Using model to show that all carbons in GO are quaternary, the peak at 60 ppm was assigned to tertiary alcohols, the peak at 70 ppm to epoxy (1, 2-ether) groups, and the peak at 130 ppm to a mixture of alkenes. Two weaker peaks at 168 and 193 ppm are sometimes observed, assigned to carboxyl (–COOH) and ketone groups (RR′C=O) at the edges of the platelets, respectively (Figure 38).[344] The reduction of GO to produce rGO partly restores the structure and properties of graphene.[345]

As in the case of oxygen, introduction of nitrogen to the carbon material can be performed both from liquid or gas phases using nitrogen-containing precursors. Ammonia is usually used as a gaseous precursor of nitrogen at temperatures between 673 and 1273 K. Usually the content of nitrogen in carbon materials is small, unless it is a constituent of the carbon precursor. So

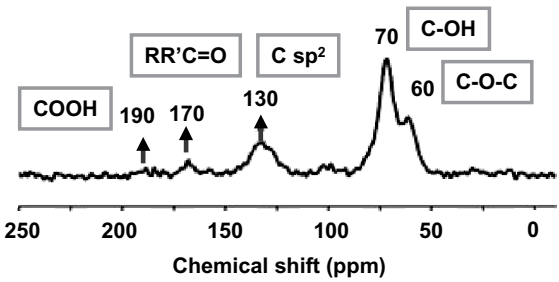

(a)

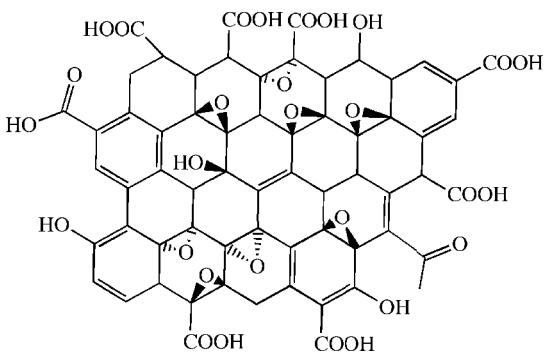

(b)

Figure 38. (a) Typical ^{13}C MAS-SSNMR spectra of ^{13}C-labelled GO and (b) idealized structure proposed for GO.

far, it has been demonstrated that the presence of nitrogen can be the key parameter for the performance of carbon nanomaterials as catalysts supports and for the catalytic activity.[34,346,347]

The type of nitrogen functionalities present on the carbon surface is the function of the treatment applied. This includes the type of nitrogen-containing precursor, the chemical activity of the carbon surface and, the most important one, temperature of heat treatment. The latter determines the type of chemistry owing to the fact that some nitrogen-containing species are unstable at high temperatures. According to the studies performed, lactams and imides structures are mainly formed by amination, and amide upon ammoxidation; the former are transformed to pyrrole and pyridine by heat treatments.[348] Like for oxygen, nitrogen-containing functionalities determine the acidic or basic character of carbons and thus its surface chemical reactivity or catalytic activity. Treatments of carbonaceous surfaces with nitrogen-containing reagents at low temperatures (less than 800 K) lead to the formation of lactams, imides, and amines, slightly acidic in their nature. On the other hand, treatments at high temperatures result in an increase in the N quaternary (N atoms incorporated in the graphitic layer in substitution of C atoms), pyridinic, and pyrrole-type structures. They are responsible for an increase in the surface polarity of the carbon, and basicity since both pyridine- and pyrrole-type structures are considered as basic.

Very marked effects of carbon surface chemistry have been reported on the adsorption of various species such as aromatics, dyes, heavy metals, pharmaceuticals, polar species such as alcohols, acids, or aldehydes and even small molecule gases.[349] Specific interactions include hydrogen bonding, acid/base, complexation, etc. These specific interactions are very important in catalysis. When carbon is used as support, the surface chemistry governs the catalyst dispersion, its loading, as well as the catalytic activity, or selectivity. The presence of, often confined, surface functional groups can influence surface diffusion, desorption, or provide suitable environment for gradient concentration that can affect both catalyst activity and selectivity. The surface functional groups determine the self-organization, the chemical stability, and the reactivity in adsorptive and catalytic processes.

5.2. Catalysis

Since some years, there is an increasing interest in the use of carbon nanomaterials in catalysis.[333,350–352] CNTs and CNFs constitute a new family of support offering a good compromise between the advantages of activated carbon and high surface area graphite. The main difference between CNTs and CNFs

involves the configuration of the underlying planes that are created by the alignment of the carbon atoms. CNTs display an axial alignment of concentric cylindrical planes that are mainly composed of hexagonal substructures, and can be subclassified into SWCNTs and MWCNTs by considering the number of axially aligned cylindrical tubes. CNFs are typically classified according to their graphene-sheet orientation, which is characterized by the angle Θ between the fiber axis and the graphene sheets. CNF is used as a general term. For a better clarity of discussion, the carbon nanostructures that are built from graphene sheets with different orientations are defined based on the angle between the graphene sheet and the fiber axis; for example, fishbone ($0 < \Theta < 90°$), ribbon or tube ($\Theta = 0°$), and platelet nanostructures ($\Theta = 90°$). These three typical types of carbon nanostructures are differentiated by the different ratios of edge planes to base planes at their edges.

The main advantages offered by CNT or CNF supports are (i) the high purity of the material can avoid self-poisoning; (ii) the mesoporous nature of these supports can be of interest for liquid-phase reactions, thus improving the mass transfer; (iii) the high thermal conductivity that permits to limit hot spots that can damage the catalyst; (iv) their well-defined and tunable structure; (v) their rich surface chemistry that offers numerous perspectives for adsorption and dispersion of the active phase; and (vi) the specific metal support interactions, due to high electrical conductivity of the support and to the tunable orientation of the graphene layers, that exists and that can directly affect catalytic activity and selectivity. The possibility to perform catalysis in a confined space is also of great interest.[26,27,353]

From a theoretical viewpoint, graphene provides the ultimate 2D model of a catalytic support. The reason is related to its high theoretical surface area (*ca.* 2630 $m^2 \cdot g^{-1}$), high conductivity, unique graphitized basal plane structure, and chemical tolerance. FLG, although having a lower surface area, presents the advantage of a potentially low manufacturing cost. Additionally, the scaled up and unswerving fabrication of graphene derivatives, such as GO and rGO, offers a wide range of possibilities to synthesize graphene-based functional materials that can be used either as supports for immobilizing active species or as metal-free catalysts.[3,354]

5.2.1. CNTs, CNFs, and FLG as metal-free catalyst

The use of metal-free carbons instead of metal-supported catalysts in synthetic chemistry has largely progressed over the last decade. This results mainly from diminishing supplies of metals used in common industrial processes, and the discovery and development of novel carbon forms

Table 11. Reactions catalyzed by carbon catalysts, and the type of surface chemistry required or the nature of the active sites.

Reactions	Surface chemistry/Active sites
Gas phase	
Oxidative dehydrogenation	Quinones
Dehydration of alcohols	Carboxylic acids
Dehydrogenation of alcohols	Lewis acids and basic sites
NO_x reduction (SCR with NH_3)	Acidic surface oxides (carboxylic and lactone) + basic sites (carbonyls or N5, N6)
NO oxidation	Basic sites, vacancies
SO_2 oxidation	Basic sites, pyridinic-N6
H_2S oxidation	Basic sites
Dehydrohalogenation	Pyridinic nitrogen sites
Liquid phase	
Hydrogen peroxide reactions	Basic sites
Catalytic ozonation	Basic sites
Catalytic wet air oxidation	Basic sites

as fullerenes, nanotubes, nanofibers, graphene, among others. Metal-free carbon-based catalysts are one of the most active research directions in nanomaterials and catalysis.[355] The advantages that nanocarbon catalysts have over metal catalysts include high efficiency, environmental compatibility, low energy consumption, and corrosion resistance. Nanocarbons can efficiently catalyze alkane conversion, chemical synthesis, energy catalysis, and other heterogeneous catalytic processes (Table 11).[356] The performance of a catalyst is influenced by the nature, concentration, and accessibility of the active sites that are capable of chemisorbing the reactants and form surface intermediates. It has been readily observed that functionalized carbons (containing oxygen, nitrogen, or other surface groups) are more efficient materials for catalysis than unfunctionalized ones. While functional group-rich materials, such as GO, exhibit high reactivity under mild conditions (their structure is not fully understood rendering mechanistic elucidation challenging), unfunctionalized graphene surfaces may not have a sufficient number of reactive sites to be a viable catalyst for many reactions. In the absence of defects, the basal planes are not very reactive, with the only active sites being present at the edges of the graphene layers as unsaturated carbon atoms. Nevertheless, pristine graphene can still find catalytic applications that make use of its

delocalized π-electron system, such as complexation reactions. On the other hand, cracking and dehydrogenation of hydrocarbons have been reported using unfunctionalized carbon nanomaterials like nanotubes and fullerenes, which could be advantageously replaced by graphene in the future.

Graphitic forms of carbon have an intriguing potential for catalysis. Early studies focused on simple redox processes, but the field has progressed to demonstrate that carbons enable reactions that are more sophisticated. These include complex functional group transformations and carbon–carbon or carbon–heteroatom bond formations. For example, C_{60} or rGO has been reported to catalyze the hydrogenation of nitrobenzene to aniline at room temperature under UV irradiation.[357,358] CNTs, CNFs, and graphene-based materials have been used as catalysts for many reactions; however, the most prominent example of heterogeneous catalysis by oxidized carbon materials is the selective oxidative dehydrogenation of hydrocarbons (ODH), and particularly of ethylbenzene (EB) to produce styrene.

The styrene monomer is extensively used in the manufacture of various important polymers or copolymers, so that industrial non-oxidative dehydrogenation of ethylbenzene (DE, Eq. 1) to styrene is one of the 10 most important industrial processes. This is a high energy-costing process, currently carried out in vapor phase at 873–973 K on potassium-promoted iron oxide catalysts.[359] Due to the thermodynamic equilibrium, the maximum conversion of EB is limited below 70%.

$$\text{(DE)}\quad C_6H_5C_2H_5 + H_2O \leftrightarrow C_6H_5C_2H_3 + H_2,\quad DH^0_{298} = +\,117.5\ \text{kJ mol}^{-1}\quad \text{(Eq. 1)}$$

$$\text{(ODE)}\quad C_6H_5C_2H_5 + \tfrac{1}{2}\,O_2 \rightarrow C_6H_5C_2H_3 + H_2O,\quad DH^0_{298} = -124.3\ \text{kJ mol}^{-1}\quad \text{(Eq. 2)}$$

The oxidative dehydrogenation of ethylbenzene (ODE), an exothermic reaction (Eq. 2), is an alternative route to the production of styrene that presents as main advantage the fact that conversions are not limited by equilibrium and can be carried out at lower temperatures (623–723 K). During the last decades, a group of catalysts was reported, such as alumina and various metal oxides and phosphates that showed an activity and selectivity in the ODE to styrene comparable to the iron catalyst. Evidence was gradually accumulated that the active sites were not located on the initial catalyst surface, but on a carbonaceous over layer. Thus, a large variety of carbon or graphite materials, including carbon nanomaterials have been studied in the literature for ODE.

During the first studies, the results were rationalized mainly in terms of textural properties of the carbon catalysts, *i.e.*, their surface area and pore sizes.

Then, comparing the activity of various carbon materials, Grunewald and Drago proposed that in addition to the large surface area of carbon materials, other factors might play a role, such as the surface structure and adsorption capacity.[360] In a subsequent paper, the same team studied various carbon materials differing in their texture. No direct relationship could be found between the activity and the surface area of the carbon materials, and it was observed that the most active catalysts were those with more mesopores and higher external surface area.[361] The importance of the texture of the carbon material was then addressed in various papers.[362–365] These reports show that materials consisting mainly of mesopores and macropores show better performances in the ODE, the smaller micropores being quickly blocked by carbon deposits. The most relevant conclusions of these works are reported in Ref. 365: (i) no direct proportionality between surface area and activity in the ODE reaction was observed; (ii) the pores of very small dimensions were quickly blocked due to coke deposition during the process; (iii) narrowing the pore sizes of the original activated carbons by coke deposition led to lower catalytic activity in the ODE reaction; and (iv) the textural effects were found to be important up to an average pore width of 1.2 nm; for larger pores sizes, the surface chemistry controls the catalyst performance. Systematic studies on the role of surface chemistry in the ODE were reported by Pereira *et al.*[366–368] The main results reported support the view that carbonyl/quinone groups on the surface are the active sites for this reaction, in agreement with earlier proposals.[369,370] These studies, based on the comparison of carbon materials with similar textural properties but different amounts of various oxygenated groups, have permitted to establish a linear correlation between the amount of surface carbonyl/quinone groups and the catalytic activity for ODE. This correlation was not a straight line through the origin, as active sites are generated on the carbon surface by oxygen present in the reacting mixture.[366] The experimental results were well described by a kinetic model based on a redox mechanism of the Mars–van-Krevelen type, where the quinone surface groups are reduced to hydroquinone by adsorbed EB, and reoxidized back to quinone by oxygen, as shown in Figure 39. Investigations by quasi *in situ* XPS confirm that the carbonyl/quinone and hydroxyl groups are involved in this reaction.[371] Recent works on the use of nanocarbons in ODE basically confirm the proposed mechanism based on a redox cycle involving the quinone surface groups.[372–374] This mechanism involves several steps: (i) EB adsorption at the graphene step edges, (ii) EB reaction with the oxygenated species also located at the graphite step edges leading to the dehydrogenation of EB to styrene, (iii) the simultaneous transformation of the dehydrogenating oxygen species to hydroxyl groups, which remain at the graphene edges, (iv) the styrene desorption from

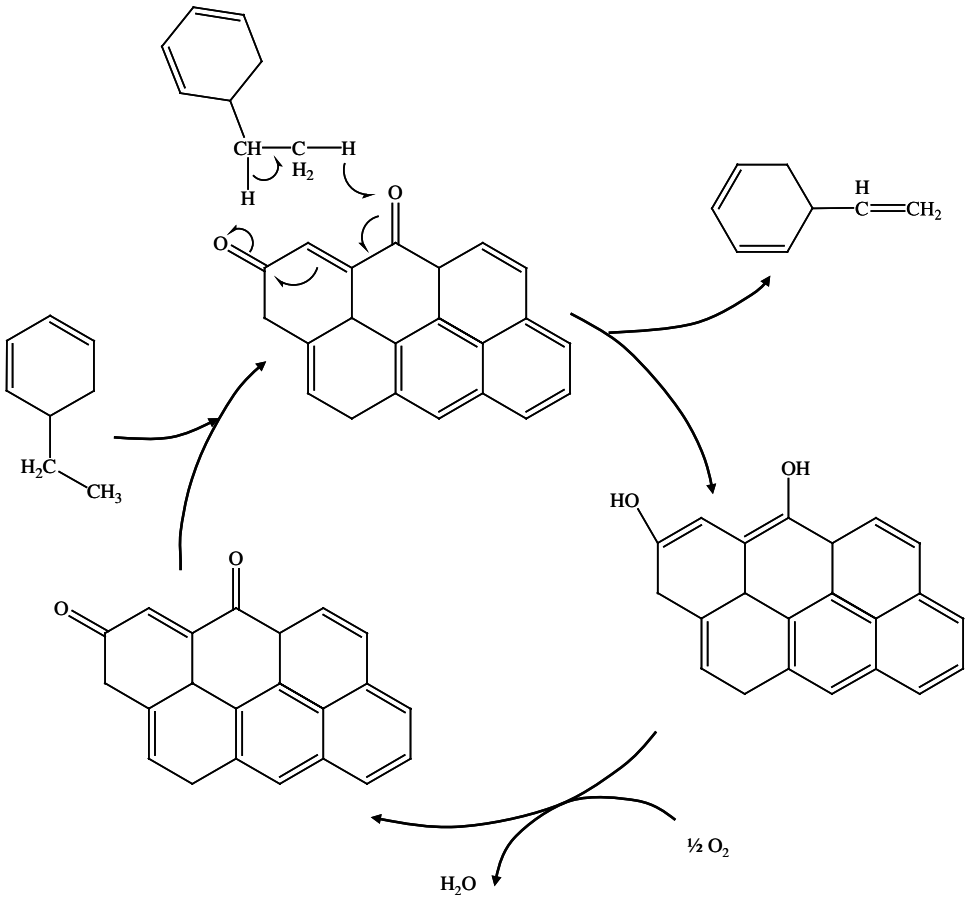

Figure 39. Proposed mechanism for ODE of EB on carbon materials.

the carbon surface, (v) gas-phase oxygen activation on the basal planes of the graphene layers, (vi) oxygen diffusion to the prismatic planes with the hydroxyl groups, (vii) reformation of the basic, chinoidic oxygen functionalities from the activated oxygen and the hydroxyl groups, and (viii) water desorption (Figure 39).

Due to their high active surface area, activated carbons were mainly studied as promising catalysts for the ODE. In spite of apparently promising results, the long-term stability of the catalyst is poor, since the ODE occurs in the presence of oxygen at relatively high temperatures, which affects the physicochemical properties of activated carbon. In addition, coke is always formed on the catalysts. Thus, a commercialization of the activated carbon catalysts for ODE to styrene is not possible. Accordingly, carbon catalysts, if to be used in industrial applications, should be further improved to achieve

high catalytic activity and selectivity, and stability during long time of operation. The remarkable properties of CNTs and CNFs, and particularly their high surface area and thermal stability have attracted the interest from the catalysis community.[355,371–373,375–380] It was reported that sp^2-bound carbon is required for the selective styrene formation, since sp^3-bound carbon led to the production of benzene instead of styrene. It has been shown that the microstructure of sp^2-bound carbon materials is of great importance in order to obtain high and stable efficiencies. CNFs have shown the highest styrene yields at the highest EB conversions as compared to CB and graphite. The comparative study of CNFs and CNTs of different structure has shown that more perfect CNTs, produced by the arc-discharge technique, are the most active catalysts in terms of reaction rates. The onion-like carbon was found to be the most efficient catalyst for the oxidative dehydrogenation reaction on a mass-referenced basis. CNTs and onions have shown a high and stable efficiency in the ODE reaction. The radius of curvature of the basic structural element of CNTs and onions and also their high aspect ratio seems to provide a high density of functional surface groups under reaction conditions. The perfectness of these carbon nanostructures provides also enough stability toward oxidation and is essential for gas-phase oxygen activation. Nevertheless, the good performances that some of these carbon nanomaterials claim to offer must be put into perspective. Indeed, most of the results have been obtained at temperatures in the range 793–823 K, whereas AC give high styrene yields at 623 K, a temperature at which CNTs show no significant activity. The main advantage of CNTs over AC is their higher stability toward oxidation. It is noteworthy that the effort in oxidative dehydrogenation reaction was mostly put on the conversion of EB, and fewer works have been done on the conversion of alkanes. One possible reason is that the intermediate product obtained in the ODH of EB is much more stable than those gotten in the ODH of alkanes, while the radical is stabilized by the delocalized π bonds. DFT calculations have shown that the barriers of the first step of the ODH of light hydrocarbons (methane, ethane, and propane) over zigzag-edge carbon clusters are higher (59–104 kJ mol^{-1}) than those for EB (18–58 kJ mol^{-1}), and the barrier of the second H abstraction is generally rate limiting (82–106 kJ mol^{-1}).[381] The catalytic performance of various nanocarbon catalysts for alkane ODE is shown in Table 12.

The catalytic activity of CNTs was evaluated for the ODH of propane to propene. It was found that a significant catalytic performance could be also achieved at high temperature, associated with the gasification of catalysts. However, phosphoric oxide addition could remarkably decrease the reaction temperature with respect to the high catalytic performance. For the oxidative

Table 12. Catalytic performance of nanocarbon catalysts in the oxidative dehydrogenation of light alkanes.

Catalysts	Reactants	Products	T (K)	Conv. (%)	Selec. (%)	Yield. (%)	Ref.
CNT, graphene	Butane	Ethene, propene, butene	676–873	—	—	—	382
CNT	Propane	Propene	773	42	40	17	383
CNT	Propane	Propene	673	6	25	1.5	384
Po_x- and Mo_x-doped CNT	Propane	Propene	625–775	40	40	15	385
P-doped CNT	Butane	Butene	723	20	60	12	386, 387

dehydrogenation of butane to butene on CNTs, it was confirmed that the catalytic behavior should be attributed to the quinone groups as active sites. The adsorption of butane and following cleavage of C–H bonding is rate-determining step for the dehydrogenation. The phosphoric addition could efficiently inhibit the total oxidation, consequently improving the catalytic selectivity.

Large surface area, functionalized carbon materials such as GO may find application in the activation of small molecules, such as O_2, for oxidation catalysis.[5] Exploiting the reactivity intrinsic to graphite oxide (GO tends to be highly acidic and strongly oxidizing), Bielawski *et al.* have identified this material as a powerful catalyst to be used in the generation of aldehydes or ketones from various alcohols, alkenes, and alkynes.[388] The authors demonstrated the efficient oxidation of benzyl alcohol to benzaldehyde (conversion >98%) in the presence of GO as catalyst. Further oxidation to benzoic acid was observed in only few amounts and only at elevated temperatures. Interestingly, this and other oxidation reactions of alcohols were performed under ambient conditions and did not proceed under a nitrogen atmosphere, suggesting that oxygen could be functioning as the terminal oxidant. In the same study, they also demonstrated that the scope of GO catalysis extends beyond simple oxidation reactions of alcohols. The successful oxidation of *cis*-stilbene to benzyl and hydration of various alkynes indicate that the scope of the reactivity of GO may be quite broad. The ability of GO to function as a carbocatalyst was further confirmed in another work by Bielawski *et al.*[389] where they produced chalcones in a single reaction vessel (>60% isolated yields). GO was found to function as an auto-tandem oxidation-hydration-aldol coupling catalyst, as various alkynes were hydrated *in situ* to their corresponding methyl ketones or alcohols were oxidized *in situ* to their corresponding aldehydes. The condensation of the methyl ketones with the

aldehydes was believed to proceed via a Claisen–Schmidt-type process, where the GO acted as an acid catalyst. When an alkyne was substituted for the methyl ketone, however, the condensation was likely preceded by hydration of the alkyne. Similarly, when an alcohol was substituted for the aldehyde, the condensation was preceded by oxidation of the alcohol. In yet another work by the same authors, GO was found to be an effective oxidant for use in a broad range of reactions, including the oxidation of olefins to their respective diones, methylbenzenes to their respective aldehydes, diarylmethanes to their respective ketones, and dehydrogenation of various hydrocarbons.[390] In this case, GO was found to be capable of oxidizing *cis*-stilbene to benzyl, optimizing the yield with regard to GO loading and reaction temperature. The authors then explored the ability of GO to oxidize more challenging substrates, including hydrocarbons possessing sp^3-hybridized C–H bonds. Various substrates with benzylic methylene groups were successfully converted to their corresponding ketone and unsaturated products. Since no reactivity was observed when hydrazine-reduced GO or natural flake graphite were used, as an explanation for the results obtained with GO, the authors suggested that the presence of the surface-bound oxygen-containing functionalities played an important role in the observed reactivity and product formation. The majority of the reactions discussed in this section was performed under relatively mild conditions and produced the desired product (aldehyde, acid, or ketone) in high yields, without the need for additional oxidants or metals as co-catalysts. However, reactivity results should be carefully evaluated, as to exclude the possibility of metal-mediated catalysis, due to potential contaminations (even in trace levels). Several advantages can be pointed out in these reactions using GO: use of a simple and inexpensive catalyst, metal-free reactivity, and facile recovery of the GO from the reaction media by simple filtration. It is worth noting that first encouraging results have also been obtained by using nitrogen-doped CNTs for oxidation reactions.[391]

5.2.2. Hydrogenation

One of the most investigated catalytic reactions is hydrogenation, both in the liquid and gas phases, and three types of reactions have been particularly studied: alkenes hydrogenation, chemoselective hydrogenation, and CO hydrogenation (Fischer–Tropsch synthesis). Several studies report that for liquid-phase hydrogenation, the use of CNTs or CNFs supports possessing large mesoporosity gave better catalytic activities than microporous activated carbon for which mass transfer limitations are operating.

One of the first reported applications of CNTs in heterogeneous catalysis was their use as supports for 3–7 nm Ru nanoparticles in the hydrogenation of cinnamaldehyde (CAL).[392] CAL contains both a C=C and a C=O bond in an α,β-unsaturated arrangement (Figure 40). Depending on which bonds is activated, hydrocinnamaldehyde (HCAL), cinnamyl alcohol (COL), or phenyl propanol (HCOL) can be obtained via the hydrogenation reaction. The possible reaction pathways are shown in Figure 40. In fact, the selective hydrogenation of the carbonyl group of the α,β-unsaturated aldehyde yielding the unsaturated alcohol remains a challenging task. This is of particular interest because of the importance of such alcohols in the fine chemicals industry.[393]

Pt, Pd, Rh, Ru metal nanoparticles, and Pt–Co, Pt–Ru bimetallic nanoparticles supported on CNTs show a high catalytic activity in this reaction. Pd and Rh are highly selective for HCAL, but not active for COL formation. For example, when using a 1 wt.% Rh/CNT for the production of HCAL, a selectivity of 100% was obtained.

The catalytic activity of Rh/CNT was three times higher than that of a 1 wt.% Rh/C, despite the fact that the latter has a surface area of 700 $m^2\ g^{-1}$, three times higher than that observed with CNTs as support (180 $m^2\ g^{-1}$).[394] Tessonnier *et al.* reported the interesting confinement effect of Pd nanoparticle catalysts deposited on the inner walls of CNTs for the selective hydrogenation of CAL to HCAL,[395] explained by the unusual interaction between Pd nanoparticles and the inner walls of the CNTs coupled with the relative lack of oxygenated surface groups on them.

In a study on the selective hydrogenation of CAL to COL using monometallic (Pt, Ru) and bimetallic (Pt–Ru) catalysts supported on various

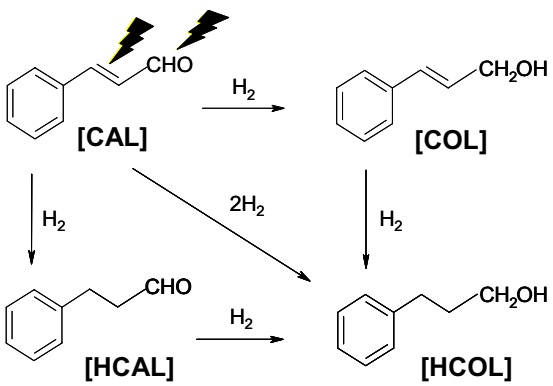

Figure 40. Reaction pathways for the hydrogenation of CAL.

carbon support (MWCNTs, SWCNTs, CNFs, AC), Vu *et al.* found that nanocarbon-supported catalysts present higher CAL conversions than those obtained with activated carbon as support, but poor selectivity toward COL (< 32%).[396] After a heat treatment under nitrogen at 973 K, Pt/CNT and especially PtRu/CNT catalysts exhibit an increase in the conversion rate and the selectivity toward COL (> 66%). Heat treatment did not influence the conversion and led to a decrease in selectivity toward COL on AC-supported catalysts. Such activity change is related to the influence of carbon surface chemistry on the adsorption of different aromatic compounds.[397,398] On heat-treated CNT samples, a π–π interaction between the CAL π electron ring and the basic π-sites of the CNT surface may increase the CAL adsorption capacity. By removal of the electronegative oxygen atoms from the carbon surface, an electron transfer from the CNT to the metal is enhanced leading to the increase in HCAL selectivity. The electron transfer from the nanotube support to metal particles has already been reported.[399] For bimetallic PtRu/CNT catalysts, a particle size and a structural effect have also been evidenced that permits to increase the selectivity, and Wide-Angle X-ray Scattering (WAXS) and Extended X-ray Absorption Fine Structure (EXAFS) point the formation of alloyed PtRu nanoparticles.[400]

Interestingly, in the case of Ru/CNF-supported catalysts, it was found that the oxygen groups had a significant effect on the reaction selectivity in selective hydrogenation reactions.[401] The selectivity for COL decreased from 58 to 8%, owing to an enhanced rate of HCAL production with decreasing number of surface oxygen groups (which was effected by increasing the treatment temperature). The hydrogenation of C=C bonds was significantly enhanced on CNFs with fewer oxygen groups. De Jong *et al.* also studied the influence of oxygen groups on the CNFs on their performance in the liquid-phase hydrogenation of CAL on CNF-supported Pt catalysts.[402] A linear decrease in hydrogenation activity with an increase in the number of acidic groups on the CNF supports was observed. The nature of the effect of oxygen groups on the properties of the Pt nanoparticles and, hence, the catalytic performance has also been investigated. XPS experiments that were performed at 308 K showed no clear evidence of a change in the electronic structure of the Pt particles, as induced by the presence of oxygen-containing groups on/inside the CNFs.[402] Therefore, it was suggested that hydrogenation was assisted by the adsorption of CAL onto the carbon support after removal of the oxygen-containing surface groups.

Bimetallic PtRu nanoparticles have been selectively confined inside or deposited outside CNTs, and a remarkable influence of nanoparticles location on catalyst performances has been evidenced.[403] The confined nanoparticles

display significantly higher selectivity and catalytic activity for CAL-selective hydrogenation into COL.

CNT-supported catalysts have also been tested for other hydrogenation reactions. For the hydrogenation of methyl-9-octadecenoate and 2-methyl-2-pentenal, Karousis *et al.*[404] reported higher activity of CNT-supported Pd with respect to an AC-supported catalyst. The Turnover Frequency (TOF) of hydrogenation of *trans*-stilbene to 1, 2-diphenylethane over Pt/CNT catalysts was reported to be six times higher than that over Pt/AC catalysts. The performances of metal catalysts supported on CNTs can be fully or partly interpreted by the structural and chemical characteristics of CNTs compared to other carbons and by the resulting metal–support interactions. It was concluded that for liquid-phase hydrogenation reactions, the use of mesoporous nanostructured carbon supports prevents significant mass transfer limitations thus improving the catalyst activity.

Syngas conversion (Fischer–Tropsch synthesis, FT synthesis) is one of the most important reactions to convert coal or biomass to fuel.[406] The reaction scheme is as follows:

$$nCO + (2n+1)H_2 \rightleftharpoons C_nH_{2n+2} + nH_2O$$
$$nCO + (2n)H_2 \rightleftharpoons C_nH_{2n} + nH_2O$$
$$nCO + (2n)H_2 \rightleftharpoons C_nH_{2n+1}OH + (n-1)H_2O$$

FT synthesis has already been industrialized in the 1930s.[407] The product distribution (alkane, alkene, alcohol) is usually too broad and unselective, extended from C_1 to C_{80} chains. Various supported catalysts such as Fe, Co, Ru on different supports have been tested for this reaction.[408,409] Developing FT catalyst with a controllable selectivity toward the hydrocarbons produced remains a challenge. Wang *et al.* have systematically investigated the role of supports in this reaction using Ru nanoparticles of the same size.[410] As it is shown in Table 13, the Ru/CNT catalyst provides a lower conversion rate than that of Ru/Al_2O_3, but higher than all the catalysts on other supports, also higher than that Ru/AC and Ru/graphite. Moreover, Ru/CNT exhibits the highest selectivity to diesel fuel (C_{10}–C_{20}). Their study revealed that the surface chemistry of CNTs determines the product selectivity.[410] Indeed, the pretreatment of CNTs with concentrated HNO_3 is necessary to obtain high C_{10}–C_{20} selectivity. The acid groups (–COOH) on the CNT generated by liquid-phase HNO_3 treatment do enhance the hydrocracking of heavier hydrocarbons, thus affording higher diesel fuel selectivity. This is an important advantage when using CNTs as support since the surface of CNTs is tunable by pretreatment.

Table 13. Effect of the supports used for Ru catalysts on FT synthesis.

Catalyst	CO conv./%	Selectivity/C-mol%				
		CH_4	C_2–C_4	C_5–C_9	C_{10}–C_{20}	C_{21}^+
Ru/SiO_2	**32**	**6.8**	**10**	**20**	**39**	**24**
Ru/Al_2O_3	40	3.1	6.8	17	36	37
Ru/H-β	24	13	21	52	14	0
Ru/AC	11	20	20	22	26	12
Ru/graphite	20	2.9	12	25	55	5.8
Ru/CNT	34	8.3	9.1	21	60	1.9

Tavasoli *et al.*[411,412] compared the performance of Co/CNTs with that of Co/γ-Al_2O_3 and found that CNT as support could reduce the metal–support interactions and enhance the Co reducibility. High Co dispersion or small Co particle size is achieved by using CNTs. It seems that the use of CNTs can facilitate both the reducibility and the dispersion of Co species. The small size of Co particles over the CNTs leads to a shift of product to lighter hydrocarbons. An increase in Co loading on CNTs could increase the size of Co particles and thus enhance the C_5+ selectivity. Other aspects such as confinement effect[413–415] were accounted for the different performance of CNTs as support in this reaction.

Reaction conditions: Ru, 3 wt%; $W = 0.5$ g; $H_2/CO = 1$; $P = 2.0$ MPa; $F = 20$ mL min^{-1}; $T = 533$ K; $t = 10$ h Ru/CNT exhibits a high selectivity to C_{10}–C_{20} (diesel fuel, 60%).

5.2.3. Oxidation and environmental catalysis

Metal-catalyzed alcohol oxidation in the liquid phase using oxygen as oxidant represents a well-known interesting catalytic process, but its industrial exploitation is limited by the strong deactivation of the catalysts.[416] Ru, Pt, Pd, and Au have been used as monometallic catalysts. The main requirement for a high selectivity and long durability has not been achieved yet.

Liquid-phase oxidation of benzyl alcohol to benzaldehyde has been investigated to reveal the differences between CNTs and AC as support for metal particles.[417] Catalytic tests have shown that Pd/CNT behaves differently from Pd/AC. Indeed, Pd/CNT exhibits a lower activity, but a higher selectivity toward benzaldehyde than Pd/AC. The Pd/AC catalyst provides a slightly higher selectivity toward toluene. The catalytic performance is also strongly dependent on the solvent used. A maximum of selectivity (92%) was

obtained on Pd/CNT for a 50% volume of cyclohexane; the corresponding value on Pd/AC is 74%. Modification of CNTs with ammonia before catalyst preparation can enhance significantly the activity and increase the TOF of the same reaction.[418] In liquid-phase reactions, the leaching of the active catalytic species remains an important issue for their application. In the above benzyl alcohol oxidation reaction, Pd on both AC and CNTs dissolves into the solution (from this the question arises whether the reaction is homogeneously or heterogeneously catalyzed). However, Pd leaching can be limited when CNTs are used as support: Pd/CNT exhibits a slightly more stable cycling (50% activity loss after seven runs) than Pd/AC (70% activity loss after 7 runs), even if a structural change in the catalysts is observed at the end of the reaction. A consistent improvement in the long-term use of such catalysts has been observed by modifying the monometallic Pd with gold. On recycling, Pd–Au bimetallic catalyst shows a reduced Pd leaching and exhibits stable catalytic performances over eight runs. Under similar conditions, Au–Pd on AC is less stable.[417]

Catalytic ozone dissociation and hydroxyl radical generation reactions are important for advanced oxidation processes in the wastewater treatment field and were used as probe reaction to investigate by DFT the synergetic effect of CNTs on a CuO/CNTs catalyst.[419] The 2p orbital's of C and the 4d of the Cu electronically interact rather than the C and O, which contributes to electronic deformation of the CuO/CNTs composite. CNTs not only act as a support and stabilizer but also play a direct role in regulating the electronic structure of a CuO/CNT hybrid. Furthermore, an electron is transferred from the CNTs to CuO during each CuO/CNTs-catalytic reaction accelerated by ozone decomposition and hydroxyl radical generation. Electronic charge transfer between CuO and CNTs as well as charge transfer between ozone and a CuO/CNTs composite are non-linear relationships, which verify a synergy effect for such host–guest catalyst systems. The same authors also studied the Pt/graphene system.[420] When Pt particles were supported on graphene, an electronic interaction occurred between Pt atoms and the graphene, leading to electron transfer from graphene to Pt atoms. Further electron transfer can be observed during further catalytic reactions on the surface of Pt/graphene composite, including the ozone decomposition reaction, superoxide radical generation reaction, and hydroxyl radical generation reaction. These results demonstrate that graphene not only acts as a support and stabilizer, but also plays a direct role in regulating the electronic structure of the Pt nanoparticle during reactions

In recent years, semiconductor-mediated photocatalysis has attracted worldwide attention for its potential in environmental and energy-related

applications. In a photocatalytic reaction, photogenerated electron–hole pairs are formed on the catalyst surface (*e.g.*, TiO_2). As opposed to an energy generation device, where the charge carriers are collected by an electrode, in a photocatalytic reaction, they are directly scavenged by different species present in solution. However, the photogenerated electrons and holes in the excited states are very unstable and can easily recombine, dissipating the input energy as heat, which results in low process efficiency. Therefore, the suppression of recombination of charge carriers is the key for the enhancement of photocatalytic activity of semiconductor photocatalysts.

As shown in Figure 41, when TiO_2 is irradiated with an UV light of wavelength corresponding to its band gap energy (3.2 eV), the electrons from the valence band can be excited to the conduction band. These photogenerated electron–hole pairs can either recombine or take part in redox reactions. The rate of recombination is fast (few nanoseconds); the majority of photogenerated electron–hole pairs recombine with dissipation of heat. Some electron–hole pairs can migrate to the surface, where they react with adsorbed electron acceptors and donors.[421,422] The migration and surface reactions are slow processes occurring from tens of nanoseconds to milliseconds.

The current efforts in photocatalysis are focused on (i) increasing the energy efficiency and (ii) improving the activity of the catalysts. The first effort is to engineer the band-gap of photoactive materials to harvest the sunlight with the highest efficiency. Besides the conventional doping and adding co-sorbents, carbon–semiconductor hybrid materials became a new class of photocatalysts, which recently has attracted a lot of attention. Composites that combine carbon and semiconductor photocatalysts could potentially offer desirable efficiency for separating electron–hole pairs.

Owing to its superior electron mobility and high SSA, graphene is considered a high performance support for photocatalysis.[423] Lightcap *et al.* demonstrated the viability of using a graphene as an electron transfer medium.[424] They showed that graphene was able to store and transport

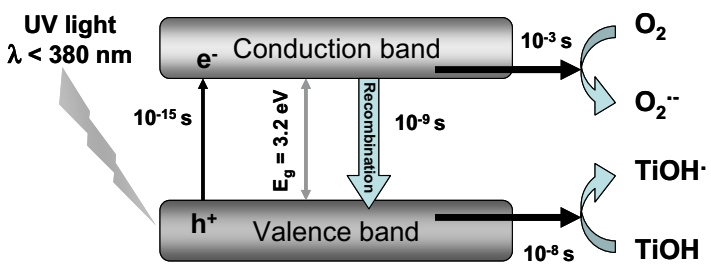

Figure 41. Illustration of the basic steps in photochemical mechanisms.

electrons through a stepwise electron transfer process: electrons were photogenerated in TiO_2 and then transferred to GO; then, part of these electrons were involved in the reduction of GO, whereas the remaining were stored in the rGO sheets; finally, upon introduction of silver nitrate, the stored electrons were used to reduce Ag^+ to Ag^0. Hence, graphene could be regarded as an effective tool to be used in the prevention of electron–hole recombination by accepting and transporting photoelectrons.[423] The incorporation of graphene into graphene-based semiconductor composites can improve them with unique properties of graphene and possibly induce new properties, such as high dye adsorption capacity, extended light absorption range, and enhanced charge separation and transportation properties, which enhance the overall photocatalytic performance.[423]

SWCNTs with certain chirality are semiconducting but with a very narrow band-gap that may be not suitable for band-gap engineering. However, a study reports that a shift of ~100 mV in the apparent Fermi level of the SWCNT-TiO_2 system with respect to the unsupported TiO_2 system indicates the Fermi level equilibration between the two systems.[425] The main purpose to use CNTs in photocatalysis (or photoelectrocatalysis) is to improve the efficiency of the catalysts rather than the band-gap engineering.[426,427] This can be achieved either by improving the transport pathway of photoinduced electrons thus reducing the probability for recombination of electrons and holes, or by stabilizing the active particles through enhanced anchoring. Kongkanand *et al.* showed that TiO_2 nanoparticles dispersed on SWCNT films improve photoinduced charge separation and transport of carriers to the collecting electrode surface.[425] There is also report that the presence of MWCNTs can efficiently inhibit the agglomeration of the TiO_2 nanoparticles and the formation of brookite TiO_2, so that CNT-supported TiO_2 composite catalyst possesses more photocatalytically active sites than pure titania.[428]

The use of CNTs in photocatalysis is mainly as support for photocatalytically active materials to form composite catalyst. The mostly tested reactions are the photodegradation of organic molecules, mainly dye molecules, using CNT-TiO_2 composites as catalysts. It is reported[429,430] that anchoring of TiO_2 onto CNTs apparently induces a synergistic effect on phenol removal, which can result in the complete disappearance of phenol in 4 h, whereas the complete removal of phenol (> 95%) is observed in 6 h for TiO_2 under UV light. In the case of visible light irradiation, this synergistic effect is more remarkable in that the complete removal of phenol is accomplished in 5 h and more than a double phenol removal rate is observed. Neat TiO_2 can only reach 41% of removal within the same reaction time, and the complete elimination of phenol is not attained after 10 h.[429,430] The enhanced

photodegradation of phenol under visible light irradiation was also observed by other groups.[431] This phenomenon is also explained by a kind of band-gap engineering between TiO_2 and CNTs, but it is more likely due to the loss of crystallinity of the TiO_2 nanoparticles, as evidenced by the red-shift of the composite catalyst in UV-Vis spectra compared to Degussa TiO_2 P25 samples.

5.2.4. Fuel cell catalysis

Fuel cells, based on the fuel oxidation reaction and ORR, are electrochemical energy devices that convert the chemical energy stored in the fuel, typically hydrogen in proton exchange membrane fuel cells (PEMFC) or methanol in direct methanol fuel cells (DMFC), and in the oxidizer directly into electricity. There are some essential differences between electrocatalysis and conventional catalysis. Electrocatalysis involves proton, oxygen, and electron transfer processes at gas/solid, liquid/solid, and gas/liquid/solid interfaces. The requirements for a good catalyst support are optimized transport properties and maximized extension of the various interfaces. Due to this complexity, it is reasonable to check whether graphene-based or CNT supports could perform better than the standard supports (CB) in electrocatalysis.

Graphene and graphene-based materials have been considered as one of the most promising alternatives as electrode materials in energy-related devices. The reason is related to the high surface area, high conductivity, unique graphitized basal plane structure, chemical tolerance, and a potential low manufacturing cost. The advantages of graphene-based composites, including nitrogen-doped graphene, have been demonstrated in the oxidation of methanol, ethanol, formic acid, in the reduction of oxygen, and in hydrogen fuel cells.[3,9,34,432–434]

The heterogeneous electron transfer (HET) is the fundamental process of electrochemical reaction. This term refers to electron transfer out of or into the graphene sheets from the surrounding environment. Given the enormous industrial importance of graphite-based electrodes, the question of where HET occurs is of paramount importance. There have been numerous approaches to establish HET from graphene sheets, usually using HOPG.[435] HOPG has a multilayer graphene structure with minimum defects. It has been shown that while the edge-plane of a graphene sheet exhibits a HET rate constant (k_e) on the order of 0.01 cm s^{-1}, the basal plane is effectively electrochemically inert, with k_b lower than 10^{-9} cm s^{-1}. Indeed, a graphene sheet can contain defects in the basal plane. In such a case, the defects are usually considered to be edge-plane sites, since they possess fast HET

kinetics. To exclude the defective sites on the basal plane of graphene sheets, an electrochemically inert material (MoO_2) was electrodeposited on the defects to prevent them from participating in the redox chemistry. The resulting defect-free graphene sheets exhibited a k_b limiting to zero.[436,437] Recently, it was demonstrated that the electrochemical response of graphene sheets is independent of the number of layers from a single graphene sheet to multilayer stacked graphene platelets.[437] Important consideration for practical and electrochemical applications of graphene is enormous surface area which in principle leads to the benefit of passivation of more resistant electrodes, in comparison with other carbon-based electrodes. This leads to longer stability of electrochemical performance.

Even though it is well known that the type of supporting material is regarded as one of the most important factors in the deactivation of PEMFCs, CB, which has poor corrosion resistance, is still widely used in the industry as well as in research. Electrochemical carbon corrosion causes the structural breakdown of carbon supports, which results in the separation of Pt particles from the supports and the agglomeration of Pt particles due to the weakened adhesion between metals and supports. Eventually, these result in the loss of active and expensive Pt surface area and a reduction in cell performance. Development of state-of-the-art electrocatalysts with inexpensive and commercially available materials to facilitate sluggish cathodic ORR is a key issue in the development of fuel cells and other electrochemical energy devices. The ORR occurs on the cathode side of a hydrogen fuel cell. Oxygen functions as an electron sink, stripping electrons from hydrogen fuel at the anode and creating the electrical pull that keeps the current running through electrical devices powered by the cell. Although great progress has been achieved in this area of research and development, there are still some challenges in both their ORR activity and stability. The emergence of graphene provides an excellent alternative to electrode materials and great efforts have been made to utilize G-based nanomaterials as promising electrode materials for ORR due to the high electrical conductivity, large SSA, profuse interlayer structure, and abounding functional groups involved. It should be noted that rational design of these G-based nanomaterials with well-defined morphology also plays an important role in their electrochemical performance for ORR. Considerable attempts were achieved to construct a variety of heteroatom-doped G nanomaterials or G-based nanocomposites, aiming at fully using their excellent properties in their application in ORR. Two representative examples are given below.

Sun *et al.* have prepared G-Co/CoO nanoparticles by self-assembly of Co nanoparticles onto the surface of graphene.[438] The Co nanoparticles tend to

form a layer (*ca*. 1 nm) of natural CoO once they are exposed to ambient environment. This CoO layer prevents Co from deep oxidation unless the Co/CoO nanoparticles (1 nm shell) are heated at an elevated temperature (70 °C). With this controlled oxidation, they obtained a series of G-Co/CoO nanoparticles with tunable Co size and CoO thickness. Compared to G- and C-Co/CoO nanoparticles, the G-Co/CoO nanoparticles show much enhanced catalytic activity for the ORR in O_2-saturated KOH (0.1 m) solution, and their activity depends on the CoO thickness; the G-Co/CoO nanoparticles with a 1 nm CoO shell show the maximum activity. This work demonstrates the importance of Co/CoO dimension and G as a support in tuning electrocatalysis for efficient ORR. The optimized G-Co/CoO nanoparticles have a comparative activity and better stability than the commercial C-Pt nanoparticles and may serve as a promising alternative to C-Pt catalysts for the ORR in alkaline solutions. N-graphene was demonstrated to act as a metal-free electrode with a much better electrocatalytic activity, long-term operation stability, and tolerance to crossover effect than platinum for oxygen reduction via a four-electron pathway in alkaline fuel cells.[439] The steady-state catalytic current at the N-graphene electrode was found to be *ca*. three times higher than that at the Pt/C electrode over a large potential range. The long-term stability, tolerance to crossover, and poison effect are also better than Pt/C for oxygen reduction in alkaline electrolyte. It is notable that the N-doped graphene film possesses remarkable electrocatalytic properties for ORR similar to that of nitrogen-containing vertically aligned CNTs.[440] Furthermore, this work clearly indicates that the important role of N-doping to ORR demonstrated with nitrogen-doped CNTs and N-graphene can be applied to other carbon materials for the development of various other metal-free efficient ORR catalysts for fuel cell applications, even new catalytic materials for applications beyond fuel cells.[441] The electrocatalytical mechanism of nitrogen-doped graphene in acidic environment was studied by using DFT.[442] The simulations demonstrate that the ORR on N-doped graphene is a direct four-electron pathway, which is consistent with the experimental observations. The simulation results on the electron transformation process show that the ORR is a four-electron pathway on the N-graphene but pure graphene does not have such catalytic activities. When H is introduced into the system, the sequential reactions can occur, including the formation of O–C chemical bond between oxygen and graphene, O–O bond break, and creation of water molecules. For each reaction step, the system energy decreases accordingly, indicating that the four-electron transformation reaction takes place spontaneously. The catalytic active sites on the N-graphene depend on spin density distribution and atomic charge distribution. The substituting

nitrogen atom introduces no-pair electrons to the graphene and changes the atomic charge distribution on it. Generally, the carbon atoms that possess highest spin density are the electrocatalytic active catalytic sites. If the negative value of spin density is small, the carbon atoms with large positive atomic charge density may act as the active sites.

As investigated, graphene, which shows strong corrosion resistance and provides strong adhesion with metal nanoparticles, is one of the best candidates for use as a commercial catalyst in PEMFCs. Moreover, using proper surface modification, it can also be used as a metal-free fuel cell catalyst, which may have a major impact on the future vehicle industry owing to its dramatic cost savings.

Up to now, the most studied application of CNTs in electrocatalysis is their use in fuel cell as support of active phase.[443–447] The most used electrocatalyst for fuel cells, both for anode and cathode, is Pt (or Pt alloy) nanoparticles supported on high surface area supports. Currently, CB, which is commonly available and cheap, is the mostly used support. However, despite its high surface area, the CB-based electrocatalyst support present two main problems: (i) it induces significant mass transfer limitations due to its dense structure, leading to a very low Pt utilization,[448] and (ii) CB is known to undergo electrochemical oxidation, forming surface oxides such as –OH, –COOH, and –C=O, which further react to give CO_2 at the cathode of the fuel cell.[449] As carbon corrodes, Pt nanoparticles will detach from the CB and aggregate into larger particles resulting in the loss of Pt surface area and in the subsequent lowering of the performance of fuel cells.[450,451] Wang *et al.* investigated the durability of CNTs and CB Vulcan XC-72 as Pt supports for PEMFC.[452] They found that CNTs are electrochemically more stable than Vulcan XC-72 with less surface oxide formation and 30% lower corrosion current under the investigated condition. As a result of high corrosion resistance, CNTs show lower loss of Pt surface area and ORR activity when used as support. Compared to commercial Pt/CB catalysts, Pt/SWCNT-based hydrogen fuel cells show improved performance at higher anodic pressures.[453] P. Kamat found that the activation enthalpies for O_2 reduction on Pt/SWCNT and Pt/CB exhibits similar values, thus confirming that the rate-determining step involved in the ORR is the same. Pt/SWCNT film on a rotating disk electrode, compared to a commercial Pt/ CB catalyst, shows a lower onset potential and a higher electron transfer rate constant for oxygen reduction. Such a good performance is attributed to the high porosity of SWCNT, which facilitates the diffusion of the reactant and thus the interaction with the Pt surface. Improved stability of the SWCNT support is also

confirmed by the minimal change in the oxygen reduction current during repeated cycling over a period of 36 h.[303]

The nature of the support contributes to the changes in the performance of electrocatalysts. B.Q. Xu *et al.* conduct a comprehensive study on the question whether SWCNTs or MWCNTs should be used as catalyst support for methanol oxidation.[454] They used MWCNTs (inner diameter 3–10 nm, outer diameter 6–20 nm, ratio of length to diameter 100–1000, 175 $m^2\ g^{-1}$) and SWCNTs (diameters of 1.25 ± 0.2 nm and lengths between 1 and 10 μm, 129 $m^2\ g^{-1}$) to prepare SWCNT/Nafion and MWCNT/Nafion composite film electrodes. Lower onset and peak potentials in CO stripping voltammograms on Pt-SWCNT/Nafion catalyst reveal a higher tolerance to CO poisoning on Pt. In methanol electrooxidation reaction, Pt-SWCNT/Nafion catalyst exhibits a significantly higher current density, lower onset potentials, and lower charge transfer resistances.[454] Further investigations have confirmed that Pt supported on SWCNTs exhibits higher performance than Pt/MWCNT and Pt/XC-72.[455]

Pt-based electrocatalysts display the significant activity and necessary stability in the harsh environment of the PEMFCs. However, the hydrogen-rich feeding gas in PEMFCs, produced by reforming or partial oxidation of hydrocarbons, usually contains CO as well; for DMFCs, the partial oxidation of methanol can also result in the presence of CO. The existence of CO will create troubles for the Pt catalyst-based full cell systems, as CO can adsorb strongly on the Pt surface and block the active sites from adsorbing fuels (H_2 or methanol), deteriorating the performance of the electrode. One possible solution for this CO poisoning problem involves the use of CO-tolerant electrocatalysts formed by alloying Pt with a second transition metal (*e.g.*, Ru, Mo). Among all the binary alloys, the PtRu/CNT has shown the most promising performance for both the hydrogen oxidation reaction in the presence of CO and the oxidation of methanol. This is because Ru can form oxygenated species at a lower potential than Pt and promote the oxidation of CO to CO_2.[456] The potential of CNFs as a catalyst support for the DMFC has also been investigated by the electrochemical oxidation of methanol at various temperatures.[457] The PtRu/CNF catalyst exhibited twice as high a power density as the PtRu catalyst supported on Vulcan XC-72 carbon. The microscopic analysis of the PtRu/CNF catalysts revealed that the bimetallic electrocatalysts were well dispersed on the CNF supports, and the particle size of the electrocatalysts was *ca.* 5 nm. The results of this work indicate that the performance of the carbon support materials is largely influenced by their electrical properties, morphology, and crystallographic structures. Recently, carbide–CNTs composites have been prepared as supports for fuel cells.[458,459]

The nanostructured WCx/CNTs do show electrocatalytic activity for ORR. The deposition of Pt nanoparticles on WCx/CNTs results in a higher electrocatalytic activity for the ORR and better immunity to methanol than Pt/CNT catalysts. The unique electrocatalytic properties of the novel Pt-WCx/CNT electrocatalyst are attributed to a synergistic effect between Pt, WCx, and CNTs. Similar synergistic effect is also found for Pt, Mo_2C, and CNTs.[459]

The electrocatalytic activity of N-CNTs toward ORR in alkaline conditions was evaluated using rotating ring disk electrode voltammetry, which showed a positive correlation between nitrogen content and ORR activities. By combining the results of ORR activity and material characterization, it is concluded that an increase in the nitrogen content of N-CNTs can effectively improve the ORR activities.[460] Dai *et al.* have shown that vertically aligned nitrogen-containing CNTs can act as a metal-free electrode with a much better electrocatalytic activity, long-term operation stability, and tolerance to crossover effect than platinum for oxygen reduction in alkaline fuel cells.[440] In air-saturated 0.1 M potassium hydroxide, they observed a steady-state output potential of 80 mV and a current density of 4.1 mA cm^{-2} at –0.22 V, compared with –85 mV and 1.1 mA cm^{-2} at –0.20 V for a Pt/CB electrode. The incorporation of electron-accepting nitrogen atoms in the conjugated nanotube carbon plane appears to impart a relatively high positive charge density on adjacent carbon atoms. This effect, coupled with aligning the CNTs, provides a four-electron pathway for the ORR on vertically aligned nitrogen-containing CNTs with a superb performance. A first-principles study was conducted to investigate the effect of several types of Pt- and N-doped CNTs, with varying doping concentrations, on the ORR at the air cathode in lithium-air batteries and fuel cells.[461] The computational results reveal that Pt-doped CNTs exhibit a greater O–O bond elongation, permitting an easier cleaving of O–O conjugations, than that of Pt-adsorbed CNTs. In addition, the search for a Pt substitute is conducted and this chapter intends to study the feasibility of N-doped CNTs. The results show that the catalytic activity of Pt-doped CNTs is higher than that of N-doped CNTs as revealed from the cleaved bond length of O–O. However, N-doped CNTs outperform both pristine and Pt-doped CNTs on the specific thermal capacity which can yield a higher structural stability in the ORR operation. The simulation results show that the energy gaps are shorter with higher concentrations of Pt or N doping. After comparing the slope tendencies between the Pt- and N-doped cases, N-doped CNTs exhibit a more dramatic decline than that of the Pt-doped CNTs. That will theoretically result in an easier catalytic activity for the ORR process.

The use of mixtures of CNTs (including N-doped CNTs) and graphene has also been reported, most of the time leading to improve electrocatalytic activity, but also durability.[462–467] In particular, the ORR charge transfer resistance of a Pt-graphene/MWCNT composite cathode was much smaller than that of the Pt-graphene cathode, and the maximum power density of the Pt-graphene/MWCNT composite cathode was four times higher than that of the Pt-graphene cathode.

Pt/CNTs and PtRu/CNTs[456] exhibit higher electrocatalytic activity than the CB-supported counterparts; the doping of nitrogen also has a beneficial role to play with respect to catalytic activity; CNTs have also been adopted to explore Pt-free catalysts, *e.g.*, TM/N/CNTs. Recently, a number of investigations have been carried out to incorporate CNTs into the components of fuel cells to improve the performance and lower the cost. CNTs have high strength and toughness to weight characteristics, which stimulate researchers to employ them as reinforcing fillers to improve the mechanical strength of PEM; their high surface area and thermal conductivity make them useful as electrocatalyst supports; they can also be applied in gas diffusion layers and current collectors because of their high electrical conductivity; their layered graphene tubular structure enables them to be a potential candidate for hydrogen storage. When blended with Nafion to make PEM, CNTs can improve the mechanical strength of the membrane; if functionalized with sulfonic acid group, they can improve the proton conductivity as well. New CNT-based modeling structures show high hydrogen storage ability, which almost meets the requirement set by the US DOE. Even though CNTs have been proved to be valuable in improving the PEFC performance, few challenges still need to be overcome before the widespread use of CNTs in PEFCs. One challenge arises from the inhomogeneous nature of as-grown CNTs. Regardless of the growth methods, the obtained CNTs are always with scattering helicity, number of layers, diameter, length, and topological defects. This, in turn, will affect their electrical properties, chemical stability, and interactions with other species, leading to the difficulty in predicting and manipulating their performance in PEFCs. CNT purity is another concern. Depending on the growth method and growing conditions, as-grown CNTs are usually accompanied with impurities, such as amorphous carbon, graphite particles, and metal particles. The knowledge on how these impurities can affect the PEFC performance is still not fully established.

5.3. Gas sensors

Gas sensors have attracted intensive research interest due to the demand of sensitive, fast response, and stable sensors for industry, environmental

monitoring, biomedicine, and so forth. The development of nanotechnology has created huge potential to build highly sensitive, low cost, portable sensors with low-power consumption. The extremely high surface-to-volume ratio and hollow structure of nanomaterials is ideal for the adsorption of gas molecules. Particularly, the advent CNTs and graphene has fueled the inventions of gas sensors that exploit their unique properties.[6,65,468–470] Upon exposure to certain gases, the changes in CNTs and graphene properties can be detected by various methods. Therefore, CNTs and graphene-based gas sensors and their mechanisms have been widely studied.

The structures used to design gas sensors are based on chemoresistors and FETs with 1D nanostructures. The basic construction blocks to design chemical sensors based on CNTs and graphene can be divided into two different configurations: two-terminal CNT/graphene devices or three-terminal transistor-like structures. In the case of two-terminal devices, these can be modeled by an electrical resistor or an electrical capacitor (see Figure 42). In the case of three-terminals, they are modeled by a bipolar junction transistor or a metal-oxide semiconductor FET, the latter being the most common.

An excellent gas sensor is obtained when an appropriate control of the chemical and physical variables associated with the detection is presented. Therefore, the use of 1D nanostructures improves the sensitivity, selectivity, stability, and response time. CNTs and graphene-based materials are promising candidates for designing gas sensors due to their excellent chemical and superficial properties derived of their chemical composition and high-aspect ratio between its length and diameter, respectively. Thanks to these nanocarbons, levels as low as parts per trillion or parts per billion can be detected in comparison with their predecessors based on microsystems, which could detect only parts per million. The fundamental reason limiting the resolution of such sensors is fluctuations due to thermal motion of charges and defects, which lead to intrinsic noise exceeding the sought-after signal from individual molecules, usually by many orders of magnitude. It has even been shown that micrometer-size sensors made from graphene are capable of detecting

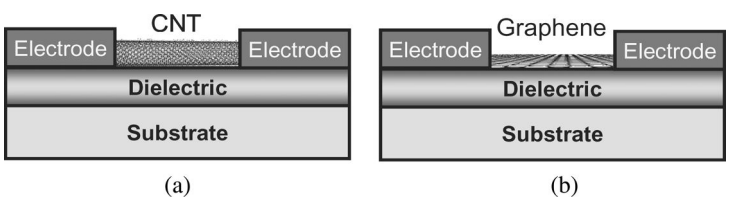

Figure 42. Cross section of resistive gas sensors and biosensors: (a) sensors based on CNTs and (b) sensors based on graphene.

individual events when a gas molecule attaches to or detaches from graphene's surface.[240] The adsorbed molecules change the local carrier concentration in graphene one by one electron, which leads to step-like changes in resistance. The achieved sensitivity is due to the fact that graphene is an exceptionally low-noise material electronically, which makes it a promising candidate not only for chemical detectors but also for other applications where local probes sensitive to external charge, magnetic field, or mechanical strain are required.

Due to its conductance changing as a function of extent of surface adsorption, large specific surface area, and low Johnson noise, recent experimental and theoretical works have demonstrated that graphene, and in particular monolayer graphene, is a promising candidate to detect a variety of molecules, such as gases to biomolecules.[471] Charge transfer between the adsorbed molecules and graphene is proposed to be responsible for the chemical response. As molecules adsorb to the surface of graphene, the location of adsorption experiences a charge transfer with graphene as a donor or acceptor, thus changing the Fermi level, carrier density, and electrical resistance of graphene.

CNTs-based sensors have demonstrated huge potential and found their application in various areas. Gas sensors based on both SWCNTs and MWCNTs have been developed. The nanotubes can be integrated with different sensor architectures by direct-growing, drop-deposition, printing, or DEP method. It has been proved both theoretically and experimentally that, the electrical resistance, thermoelectric power, and local density of states of SWCNTs can be reversibly changed by exposure to certain vapors. This can be attributed to the charge transfer between the molecules and the nanotubes, or the change of the charge carriers' lifetime in CNTs. Therefore, gas sensing FET or resistors that measure the resistance change of CNTs as the transducer is the most commonly used sensor structures. However, this limits the range of the gases that CNT sensors can detect, especially for the sensing of inert agents. Compared with the resistance sensors, CNTs-enhanced ionization chambers allow the detection of gas molecules with low adsorption energy, hence a wide range of vapors. With CNTs integrated, the breakdown voltage can be lowered significantly. Other promising methods to improve the sensing characteristics include the functionalization of CNTs and nanocomposites of CNTs with various polymers, which can broaden the sensing range or enhance the sensitivity. CNTs can also be integrated into resonators sensors.

CNTs have shown themselves as viable candidates for the development of low temperature and ambient pressure sensors.[6] For example, CNTs decorated with NP or polymeric species have shown the ability to detect gases

such as NO_2,[472,473] NH_3,[474,475] H_2,[476,477] CO,[478–480] NO,[481,482] CO_2,[483] and O_2.[484,485] While not as matured, the field of graphene-based sensors is growing,[486] and their electrical response to various chemical species is qualitatively similar to CNTs.[434] Several examples have been reported for the detection of both NO_2[242,245,487] and NH_3[244,488,489] with graphene-based devices. The detection limits range between the parts per billion and parts per million levels. This sensitivity is comparable to CNT-based sensors. Sensitivity to SO_2,[490] CO_2,[118] O_2,[491] CO,[240] and H_2O[240,492] has also been reported, but some discrepancy does exist for the response to H_2O. For example, Novoselov *et al.*[240] and Johnson *et al.*[492] reported that H_2O exposure decreased the resistance of graphene devices (increased device current), while Ruoff *et al.*[493] found that H_2O exposure actually increased device resistance. This difference in response to an identical analyte may be a consequence of the device fabrication. Detection of organic vapors like nonanol, octanoic acid, and trimethylamine has also been reported.[492] Snow *et al.*[494] have used graphene-based sensors for the detection of acetone, HCN, chloroethyl ethyl sulfide (a model for sulfur mustard gas), dimethyl methylphosphonate (a model for sarin), and dinitrotoluene. Their studies revealed that graphene-based devices showed equivalent or better sensitivity than CNT-based sensors to these particular analytes. The discrepancy in reported sensitivities (single molecule to ppm levels) toward gaseous and vapor analytes may be attributed to the preparation of the devices themselves. Specifically, Johnson *et al.*[492] concluded that the intrinsic sensitivity of graphene-based electrical sensors to particular analytes was rather low, and that contamination from the device fabrication, such as photoresists or solvent molecules, actually increased the device sensitivity toward a particular analyte. In fact, they found rather small analyte response once precautionary measures were taken to completely remove the contaminants. This observation is not entirely surprising due to the well-known phenomenon of increased analyte sensitivity with polymer or NP-decorated CNTs.[495] Using the approach of intentionally decorating graphene to boost analyte sensitivity, Kaniyoor *et al.*[496] found a twofold increase in H_2 sensitivity with Pt/G, as compared to Pt/MWCNTs. However, because no extra precautions were made to fully remove any contamination, this might be another example of residual photoresist or other residues artificially increasing the device response.

5.4. Bioreactivity and degradability of CNTs and graphene

A number of molecules of interest to biologists have been efficiently adsorbed on CNTs and graphene mainly using hydrogen bonds or van der Waal's

forces. Nanotubes coated with biomolecules on their surface have been studied extensively due to promising applications in drug release and as sensors used in medicine. Adsorption of biomolecules on to the nanotubes surface has been used as a selective probe to investigate electrochemical reactions, intermolecular interactions, and electrostatic interactions inside living cells depending on the functional nature of the coating. While it is too early to predict the widespread application of these sensors in everyday medicine, rapid progresses are being made in this field.[497] Due to their small diameters and high aspect ratio with lengths exceeding microns, nanotubes can be inserted into a living cell in a controlled but non-invasive manner. The development of biological interfaces for such novel carbon-based biomaterials may lead to new applications in various medical fields.[498]

Functionalization of the nanotubes has been an essential prerequisite to ensure the stable adsorption of biomolecules onto the nanotubes or graphene surface. Covalent functional groups introduced by acid treatment of CNTs have been used to anchor amino acids to the nanotubes.[499] However, it has been found that acid-functionalized nanotubes aggregated in the presence of salts that are commonly found in biological media and hence additional stabilization is achieved by attaching polymers such as PEG or reacting the side walls using a 1,3-dipolar cycloaddition reaction on CNTs.[500] More often, functionalization of CNTs can be carried out by coating CNTs with amphiphilic surfactant molecules or polymers. This method is preferred since it offers a wide choice of surface functions and retains the nanotubes structure intact. Large biomolecules such as proteins[501] and DNA[502] have been used to functionalize SWCNTs and have found application in bioimaging (Figure 43). Katoch *et al.* have investigated the binding of the dodecamer peptide, GAMHLPWHMGTL to graphene and graphite.[503] The peptide was incubated with both unexfoliated and mechanically exfoliated HOPG and the binding was investigated using atomic force microscopy, Raman spectroscopy, IR spectroscopy, and molecular dynamics simulations. Optical spectroscopy revealed that the peptide formed secondary structures both in powder form and in an aqueous medium. The dominant structure in the powder form is an α-helix, which undergoes a transition to a distorted helical structure in aqueous solution. The peptide formed a complex reticular structure upon adsorption on graphene and graphite, having a helical conformation different from α-helix due to its interaction with the surface (Figure 43).

Fluorescent SWCNTs thus functionalized have found applications as biomarkers or in imaging since SWCNT Near Infrared (NIR) fluorescence does not photobleach under high excitation powers and due to the high stokes

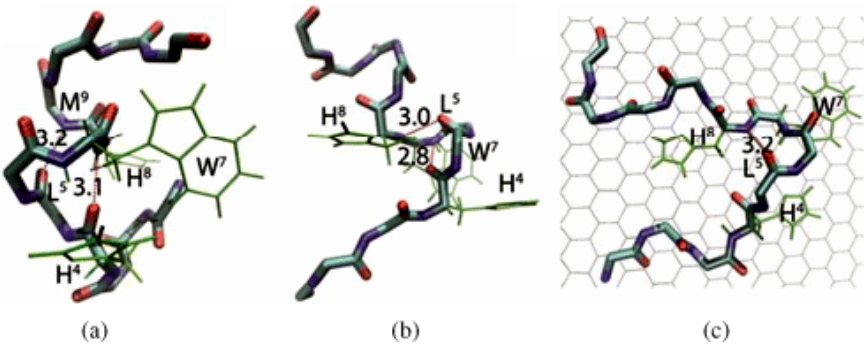

Figure 43. Molecular dynamics-based structure of GAM peptide (a) in vacuum, (b) in water, and (c) on a 5 nm × 5 nm graphene sheet. For clarity, only part of the graphene sheet is displayed. Reproduced from Ref. 503 with permission.

shifts obtained, permits the use of a wide range of excitation energies.[504] For graphene too, non-covalent functionalization with biomolecules such as chitosan (to cite one of the many examples) is the usual technique employed to improve biocompatibility.[505] The interaction of a variety of different biomolecules with the graphene surface and their impact on the biocompatibility of graphene-based materials have been described by Sanchez *et al.* in a review article.[506]

5.4.1. Biosensors

The electronic properties of nanotubes coupled with the specific recognition properties of the immobilized biosystems would indeed make for an ideal miniaturized sensor. One of the most studied applications of biofunctionalized nanotubes in medicine is the detection and analysis of dissolved glucose for the quick determination of glucose levels in diabetic patients. Glucose detection is usually carried out amperometrically using the enzyme glucose oxidase (G_{ox}) that catalyzes the oxidation of glucose to hydrogen peroxide.[507,508] Another application is in the detection of bacteria; a tyrosinase biosensor based on Fe_3O_4 magnetic nanoparticles (MNPs) coated on CNT nanocomposite has been reported that has been applied to detect the concentration of coliforms with a flow injection assay system. Negatively charged MNPs were adsorbed onto the surface of CNTs which were wrapped with cationic polyelectrolyte poly(dimethyldiallylammonium chloride). The Fe_3O_4 MNPs-coated CNTs nanocomposite was modified on the surface of a glassy carbon electrode. The biosensor was tested for the detection of coliforms represented by *E. coli*. The principle of the sensor was based on the detection

of phenol produced during the enzymatic reaction of *E. coli* in water. This sensor has a detection limit for bacteria of 10 cfu mL^{-1} and could find application in water quality analysis.[509] In comparison with nanotubes, graphene has found an even larger variety of sensor applications. The ease of film formation directly by CVD or from GO suspensions has made sample preparations easier for graphene when compared to CNTs. Graphene has the added advantage of being devoid of metallic impurities that makes its application in electrochemical and electronic sensing more viable when compared to nanotubes. In this context, graphene for direct electrochemistry of enzyme, its electrocatalytic activity toward small biomolecules (hydrogen peroxide, NADH, dopamine, etc.), and graphene-based enzyme biosensors have been reviewed in great detail.[8,20]

5.4.2. Drug delivery

The use of CNTs for drug delivery was investigated after the initial report that functionalized CNTs were able to enter cells without obvious toxicity.[497] Unlike various small drug molecules which are able to diffuse into cells, biomacromolecules cannot cross cell membranes. Intracellular delivery is thus required in order to use these molecules for therapeutic applications. Proteins can be either conjugated or non-covalently adsorbed onto nanotubes for intracellular delivery.[510] In addition to the introduction of nanotubes across cell walls *in vitro*, *in vivo* studies have been carried out for the use of nanotubes for drug delivery. Special attention has been focused on the targeted delivery of anti-cancer drugs to areas containing tumors. Passive targeting, relying on the enhanced permeability and retention effect of cancerous tumors, or active targeting guided by tumor targeting ligands, have been employed for various nanoparticle-based drug delivery systems. It was demonstrated that SWCNTs functionalized with PEG were effective in tumor targeting when conjugated with an arginine–glycine–aspartic acid peptide. It was concluded that surface functionalization of SWCNTs is also important for tumor targeting *in vivo*. Thus several drugs used in chemotherapy have been tested for their efficiency in targeting tumor cells using CNTs.[511] In the last few years, a number of publications have appeared on the use of graphene for drug delivery. Yang *et al.* used nanographene sheets (NGS) surface coated with PEG in tumor-bearing mice by *in vivo* fluorescence imaging. Highly efficient tumor passive targeting of NGS has been observed in several different tumor models without utilizing any targeting ligands, such as antibodies.[512] The authors reported that PEGylated NGS was an excellent *in vivo* tumor

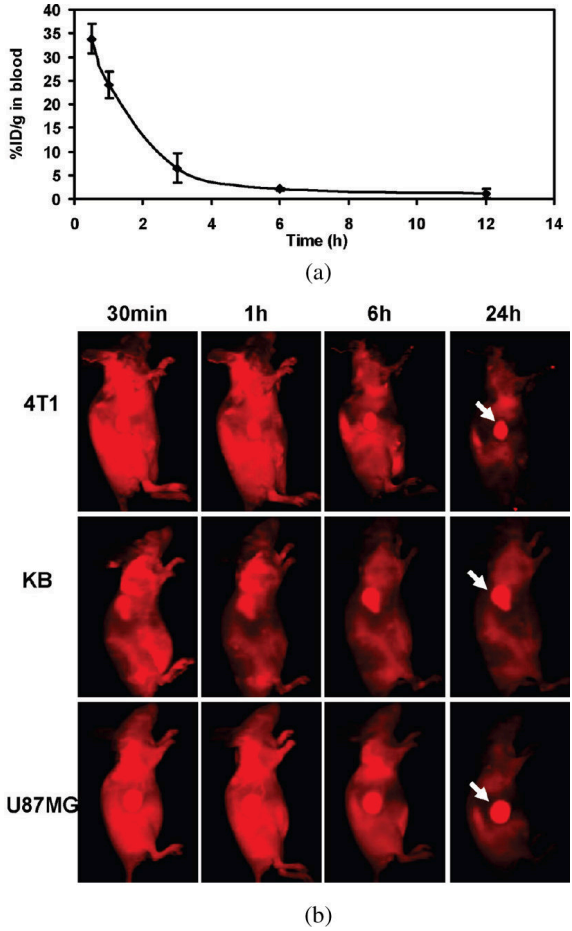

Figure 44. *In vivo* behaviors of NGS-PEG-Cy7. (a) The blood circulation curve of NGS-PEG-Cy7 determined by measuring Cy7 fluorescence in the blood at different time points post injection. The unit was a percentage of injected dose per gram tissue (% ID/g). Error bars were based on triplicated samples. (b) Spectrally unmixed *in vivo* fluorescence images of 4T1 tumor-bearing Balb/c mice, KB, and U87MG tumor-bearing nude mice at different time points post injection of NGS-PEG-Cy7. Mouse autofluorescence was removed by spectral unmixing in the above images. High tumor uptake of NGS-PEG-Cy7 was observed for all of the three tumor models. Hairs on Balb/c mice were removed before fluorescence imaging. From Ref. 512.

near-IR photothermal therapy agent without exhibiting noticeable toxicity to the treated mice (Figure 44). NGS functionalized with PEG was also used for attaching hydrophobic water-insoluble anticancer drugs (SN 38) and they

found that the resultant NGO–PEG–SN38 conjugate showed high water solubility with no loss of activity.[513]

5.4.3. Biodegradability and toxicity

While CNTs are being produced industrially in many different parts of the world, very little is known about their biodegradability. It is therefore difficult to estimate their lifetime in the environment and under what conditions can they be degraded, ideally by microorganisms. In a first study of its kind, Allen *et al.* showed that SWCNTs can be catalytically biodegraded over several weeks by the plant-derived enzyme, horseradish peroxidase (HRP) by incubating nanotubes with natural HRP and low concentrations of H_2O_2 at 277 K over 12 weeks under static conditions wherein a degradation of the nanotubes structure was observed.[514] More recent work showed that hypochlorite and reactive radical intermediates of the human neutrophil enzyme myeloperoxidase also catalyze the biodegradation of SWCNTs. Using molecular modeling, it was suggested that the interactions between the amine groups in the enzyme and the carboxylic groups in functionalized nanotubes play an important role in the catalytic reaction.[515] On the contrary, pristine, non-functionalized SWCNTs were resistant (no morphological changes observed) when exposed to the same biological oxidative conditions.[516] Based on these results, it is hypothesized that functionalized CNTs may be more readily eliminated from organs and tissues and may pose less toxicological risks compared to intact nanotubes.[517] Analogous to nanotubes, it has been observed that for graphene too, coating it with degradable amyloid fibrils can render the composite biodegradable.[518]

Toxicity of CNTs and graphene

It is known today that due to their high surface area, aspect ratio, and presence of metals arising from residual amounts of catalyst, CNTs have a potential to be toxic and are associated with pulmonary pathological mechanisms of inhaled particles and fibers.[519] The increase in SSA causes the enhancement of ionic dissolution and serious toxicity for soluble materials. It has been hypothesized that repeated exposure to SWCNTs and MWCNTs can increase the probability of lung disease.[520] Epidemiological studies have shown that inhaled toxic matter can also cause cardiovascular problems, including oxidative stress or migration of inhaled nanoparticles into the vasculature directly affecting the endothelial cells. Recent studies have demonstrated the effects of wall number (single or multiple), synthesis method, composition, exposure

formulation, and metal impurities of CNTs. Length-dependent effects of CNTs on cell growth and reactive oxygen species production have been reported.[521] Graphene is the youngest in the family of carbon nanomaterials. Its isolation, description, and mass fabrication have followed that of CNTs. Graphene's development and its adoption by many industries will increase unintended or intentional human exposure, creating the need to determine its safety profile. In a comprehensive review, Bussy *et al.*[522] compared the lessons learned from the development of CNTs with what is known about graphene. Despite both being carbon based, CNTs and graphene are two very distinct nanomaterials. The key physicochemical characteristics (structure, surface, colloidal properties) for graphene and CNTs (Table 14) at three different physiological levels have been considered: cellular, tissue, and whole body. The authors summarized the evidence for health effects of both materials at all three levels. Overall, graphene and its derivatives are characterized by a lower aspect ratio, larger surface area, and better dispersibility in most solvents compared to CNTs. Dimensions, surface chemistry, and impurities are equally important for graphene and CNTs in determining both mechanistic (aggregation, cellular processes, biodistribution, and degradation kinetics) and toxicological outcomes.

Colloidal dispersions of individual graphene sheets (or GO and other derivatives) can easily be engineered without metallic impurities, with high stability

Table 14. Physicochemical characteristics relevant to safety considerations of CNTs and graphene. Adapted from Ref. 522.

Physicochemical characteristics	Graphene	CNTs	Difference
Shape	Planar – mono or few-layers; tunable structure/shape (sheet, ribbon, triangle, hexagon) 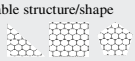	Cylindrical -SWCNT - MWCNT 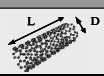	Completely different
Dimension (typical)	Thickness: 0.34 – 100 nm 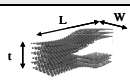 Lateral size: 0.1 – 10 µm	SWCNT: L: 10 nm to cm D: 0.4 – MWCNTs: L: 10 nm to µm D: 2 –200 nm	Similar
Surface - area - charge - coating	- Up to 2675 m^2/g; decrease in FLG - Varies with functionalization or coating - Varies with chemical nature (polymer, lipid), type, density & conformation	-SWCNT (>1000 m^2/g); MWCNT (50 – 500 m^2/g) - varies with functionalization or coating - varies with chemical nature (polymer, lipid), type, density & conformation	- Quite different -Similar - Similar
Elasticity/Stiffness	Young modulus of 1100 GPa; able of bending and rippling; stiffness increases in FLG	-SWCNT from 1 to 5 TPa; able of bending - MWCNT from 0.2 to 0.95 TPa	Similar
Colloidal stability - aqueous dispersibility - aggregation	Dispersibility: GO in H_2O Aggregation: stacking	Dispersibility Oxidized CNT in H_2O Aggregation: bundling and tangling	Very different
Durability	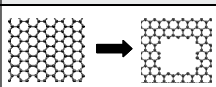 Enzyme degradation by defects in plan	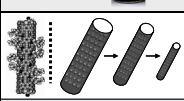 Enzyme degradation by unzipping and decrease of L & D	Different
Impurities	Varies with manufacturing process: mainly graphite and chemical residues from processing	Varies with manufacture process: metal catalysts (Fe, Co, Ni, Cu, Zn); carbon nanoparticles; amorphous carbon	Very different

and less aggregation. Very importantly, graphene nanostructures are not fiber-shaped. These features theoretically offer significant advantages in terms of safety over inhomogeneous dispersions of fiber-shaped CNTs. However, studies that directly compare graphene with CNTs are rare, making comparative considerations of their overall safety and risk assessment challenging. Typical rules for the development of graphene and its derivatives to enhance their overall safety and minimize the risks for adverse reactions in humans from exposure are (i) to use small, individual graphene sheets that macrophages in the body can efficiently internalize and remove from the site of deposition; (ii) to use hydrophilic, stable, colloidal dispersions of graphene sheets to minimize aggregation *in vivo*; and (iii) to use excretable graphene material or chemically modified graphene that can be degraded effectively. Such rules can only act as guidelines at the early stage in the development of graphene-based technologies, yet they offer a set of design principles for the fabrication and safe use of graphene material that will come in contact with the human body. In a broader context, the safety risks associated with graphene materials will be entirely dependent on the specific types of graphene materials and how they are investigated or applied. Therefore, generalizations about the toxicity of "graphene" as a whole will be inaccurate, possibly misleading, and should be avoided.

References

1. Serp, P. Carbon Nanotubes and Nanofibers in Catalysis. In *Carbon Materials for Catalysis*; Serp, P., Figueiredo, J. L., Eds.; John Wiley & Sons, Inc., Hoboken, N. J. USA, **2008**, pp. 309–372.
2. Su, D. S. Carbon Nanotubes and Related Carbonaceous Structures. In *Nanomaterials in Catalysis*; Serp, P., Philippot, K., Eds.; Wiley-VCH Verlag GmbH, Weinheim, Germany, **2013**, pp. 331–374.
3. Machado, B. F.; Serp, P. *Catal. Sci. Technol.* **2012**, *2*(1), 54–75.
4. Bacsa, R. R.; Serp, P. Decorated (Coated) Carbon Nanotubes: (X/CNTs). In *Carbon Meta-Nanotubes*; Monthioux, M., Ed.; John Wiley & Sons, Ltd., Chichester, UK, **2011**, pp. 163–221.
5. Su, C.; Loh, K. P. *Acc. Chem. Res.* **2012**, doi: 10.1021/ar300118v.
6. Wang, Y.; Yeow, J. T. W. *J. Sensors* **2009**, *2009*, 493904.
7. Zhang, T.; Mubeen, S.; Myung, N. V.; Deshusses, M. A. *Nanotechnology* **2008**, *19*(33), 332001.
8. Shao, Y.; Wang, J.; Wu, H.; Liu, J.; Aksay, I. A.; Lin, Y. *Electroanalysis* **2010**, *22*(10), 1027–1036.
9. Choi, H.-J.; Jung, S.-M.; Seo, J.-M.; Chang, D. W.; Dai, L.; Baek, J.-B. *Nano Energy* **2012**, *1*(4), 534–551.

10. Tozzini, V.; Pellegrini, V. *Phys. Chem. Chem. Phys.* **2013**, *15*(1), 80–89.
11. Ströbel, R.; Garche, J.; Moseley, P. T.; Jörissen, L.; Wolf, G. *J. Power Sources* **2006**, *159*(2), 781–801.
12. Ong, Y. T.; Ahmad, A. L.; Zein, S. H. S.; Tan, S. H. *Braz. J. Chem. Eng.* **2010**, *27*, 227–242.
13. Kemp, K. C.; Seema, H.; Saleh, M.; Le, N. H.; Mahesh, K.; Chandra, V.; Kim, K. S. *Nanoscale* **2013**, *5*(8), 3149–3171.
14. Terranova, M. L.; Orlanducci, S.; Rossi, M. *Carbon Nanomaterials for Gas Adsorption*; Pan Stanford Publishing, Singapore, **2012**.
15. Upadhyayula, V. K. K.; Deng, S.; Mitchell, M. C.; Smith, G. B. *Sci. Total Environ.* **2009**, *408*(1), 1–13.
16. Leenaerts, O.; Partoens, B.; Peeters, F. M. *Microelectron. J.* **2009**, *40*(4–5), 860–862.
17. Pan, B.; Xing, B. *Environ. Sci. Technol.* **2008**, *42*(24), 9005–9013.
18. Soares, J. S.; Jorio, A. *J. Nanotechnol.* **2012**, *2012*, 512738.
19. Balasubramanian, K.; Burghard, M. *Anal. Bioanal. Chem.* **2006**, *385*(3), 452–468.
20. Kuila, T.; Bose, S.; Khanra, P.; Mishra, A. K.; Kim, N. H.; Lee, J. H. *Biosens. Bioelectron.* **2011**, *26*(12), 4637–4648.
21. Paul, W.; Sharma, C. P. *Trends Biomater. Artif. Organs.* **2011**, *25*(3), 91–94.
22. Shim, M.; Shi Kam, N. W.; Chen, R. J.; Li, Y.; Dai, H. *Nano Lett.* **2002**, *2*(4), 285–288.
23. Carrero-Sánchez, J. C.; Elías, A. L.; Mancilla, R.; Arrellín, G.; Terrones, H.; Laclette, J. P.; Terrones, M. *Nano Lett.* **2006**, *6*(8), 1609–1616.
24. Foldvari, M.; Bagonluri, M. *Nanomed. Nanotechnol. Biol. Med.* **2008**, *4*(3), 183–200.
25. Shen, H.; Zhang, L.; Liu, M.; Zhang, Z. *Theranostics* **2012**, *2*(3), 283–294.
26. Serp, P.; Castillejos, E. *Chem Cat Chem* **2010**, *2*(1), 41–47.
27. Pan, X.; Bao, X. *Acc. Chem. Res.* **2011**, *44*(8), 553–562.
28. Choi, J. W.; Alexandrova, M.; Park, H. G. Carbon Nanotube Nanofluidics. In *Carbon Nanotubes Applications on Electron Devices*; Marulanda, J. M., Ed.; InTech, Rijeka, Croatia, **2011**, 405–454.
29. Bacsa, R. R.; Laurent, C.; Peigney, A.; Bacsa, W. S.; Vaugien, T.; Rousset, A. *Chem. Phys. Lett.* **2000**, *323*(5–6), 566–571.
30. Radovic, L. R.; Bockrath, B. *J. Am. Chem. Soc.* **2005**, *127*(16), 5917–5927.
31. Acik, M.; Chabal, Y. J. *Jpn. J. Appl. Phys.* **2011**, *50*(7), 070101.
32. Banhart, F.; Kotakoski, J.; Krasheninnikov, A. V. *ACS Nano* **2010**, *5*(1), 26–41.
33. Ayala, P.; Arenal, R.; Rümmeli, M.; Rubio, A.; Pichler, T. *Carbon* **2010**, *48*(3), 575–586.

34. Wang, H.; Maiyalagan, T.; Wang, X. *ACS Catal.* **2012**, *2*(5), 781–794.
35. Mak, K. F.; Shan, J.; Heinz, T. F. *Phys. Rev. Lett.* **2010**, *104*(17), 176404.
36. Craciun, M. F.; Russo, S.; Yamamoto, M.; Tarucha, S. *Nano Today* **2011**, *6*(1), 42–60.
37. Lui, C. H.; Li, Z.; Chen, Z.; Klimov, P. V.; Brus, L. E.; Heinz, T. F. *Nano Lett.* **2010**, *11*(1), 164–169.
38. Radovic, L. R. *J. Am. Chem. Soc.* **2009**, *131*(47), 17166–17175.
39. Ataca, C.; Akturk, E.; Sahin, H.; Ciraci, S. *J. Appl. Phys.* **2011**, *109*(1), 013704.
40. Robertson, A. W.; Bachmatiuk, A.; Wu, Y. A.; Schäffel, F.; Rellinghaus, B.; Büchner, B.; Rümmeli, M. H.; Warner, J. H. *ACS Nano* **2011**, *5*(8), 6610–6618.
41. Kleiner, A.; Eggert, S. *Phys. Rev. B* **2001**, *64*(11), 113402.
42. Ouyang, Y.; Peng, J.-C.; Wang, H.; Peng, Z.-H. *Chinese Phys. B* **2008**, *17*(8), 3123–3127.
43. Charlier, J.-C. *Acc. Chem. Res.* **2002**, *35*(12), 1063–1069.
44. Robinson, J. A.; Snow, E. S.; Bădescu, Ş. C.; Reinecke, T. L.; Perkins, F. K. *Nano Lett.* **2006**, *6*(8), 1747–1751.
45. Mawhinney, D. B.; Naumenko, V.; Kuznetsova, A.; Yates, J. T., Liu, Jr. J.; Smalley, R. E. *Chem. Phys. Lett.* **2000**, *324*(1–3), 213–216.
46. Hamon, M. A.; Hu, H.; Bhowmik, P.; Niyogi, S.; Zhao, B.; Itkis, M. E.; Haddon, R. C. *Chem. Phys. Lett.* **2001**, *347*(1–3), 8–12.
47. Monthioux, M.; Smith, B. W.; Burteaux, B.; Claye, A.; Fischer, J. E.; Luzzi, D. E. *Carbon*, **2001**, *39*(8), 1251–1272.
48. Stone, A. J.; Wales, D. J. *Chem. Phys. Lett.* **1986**, *128*(5–6), 501–503.
49. Bettinger, H. F. *J. Phys. Chem. B* **2005**, *109*(15), 6922–6924.
50. Picozzi, S.; Santucci, S.; Lozzi, L.; Valentini, L.; Delley, B. *J. Chem. Phys.* **2004**, *120*(15), 7147–7152.
51. Yang, S. H.; Shin, W. H.; Kang, J. K. *J. Chem. Phys.* **2006**, *125*(8), 084705.
52. Rivera, J. L.; Rico, J. L.; Starr, F. W. *J. Phys. Chem. C* **2007**, *111*(51), 18899–18905.
53. Shtogun, Y. V.; Woods, L. M. *Carbon* **2009**, *47*(14), 3252–3262.
54. Rossato, J.; Baierle, R. J.; Fazzio, A.; Mota, R. *Nano Lett.* **2004**, *5*(1), 197–200.
55. Gerber, I.; Oubenali, M.; Bacsa, R.; Durand, J.; Gonçalves, A.; Pereira, M. F. R.; Jolibois, F.; Perrin, L.; Poteau, R.; Serp, P. *Chem. Eur. J.* **2011**, *17*(41), 11467–11477.
56. Berber, S.; Oshiyama, A. *Physica B* **2006**, *376–377*, 272–275.
57. Yuan, J.; Liew, K. M. *Carbon* **2009**, *47*(6), 1526–1533.
58. Orellana, W.; Fuentealba, P. *Surf. Sci.* **2006**, *600*(18), 4305–4309.
59. Nevidomskyy, A. H.; Csányi, G.; Payne, M. C. *Phys. Rev. Lett.* **2003**, *91*(10), 105502.

60. Puri, B. R. *Chemistry and Physics of Carbon*; Walker, P. L., Ed.;. Marcel Dekker: New York, **1970**, p. 191.
61. Ding, D.; Wang, J.; Cao, Z.; Dai, J. *Carbon*, **2003**, *41*(3), pp. 579–582.
62. Chakrapani, N.; Zhang, Y. M.; Nayak, S. K.; Moore, J. A.; Carroll, D. L.; Choi, Y. Y.; Ajayan, P. M. *J. Phys. Chem. B* **2003**, *107*(35), 9308–9311.
63. Hilding, J. M.; Grulke, E. A. *J. Phys. Chem. B* **2004**, *108*(36), 13688–13695.
64. Proykova, A. Molecular Dynamics Simulation of Gas Adsorption and Absorption in Nanotubes. In *Carbon Nanotubes*; Popov, V.; Lambin, P., Eds.; Springer: Netherlands, **2006**, 187–207.
65. Liu, Y.; Dong, X.; Chen, P. *Chem. Soc. Rev.* **2012**, *41*(6), 2283–2307.
66. Zollo, G.; Gala, F. *J. Nanomater.* **2012**, *2012*, 152489.
67. Chen, C.-W.; Lee, M.-H.; Clark, S. J. *Diamond Relat. Mater.* **2004**, *13*(4–8), 1306–1313.
68. Lu, X.; Sun, C.; Li, F.; Cheng, H.-M. *Chem. Phys. Lett.* **2008**, *454*(4–6), 305–309.
69. Ji, L.; Zhang, Z. X.; Peng, L. M.; Xue, Z. Q.; Wu, J. L. *J. Phys. D: Appl. Phys.* **2003**, *36*(23), 3034.
70. Lee, E.-C.; Kim, Y. S.; Jin, Y. G.; Chang, K. J. *Phys. Rev. B* **2002**, *66*(7), 073415.
71. Alonso, J. A.; Arellano, J. S.; Molina, L. M.; Rubio, A.; Lopez, M. J. *IEEE Trans. Nanotechnol.* **2004**, *3*(2), 304–310.
72. Barone, V.; Heyd, J.; Scuseria, G. E. *J. Chem. Phys.* **2004**, *120*(15), 7169–7173.
73. Ganji, M. D.; Asghary, M.; Najafi, A. A. *Commun. Theor. Phys.* **2010**, *53*(5), 987.
74. Firlej, L.; Kuchta, B. *Colloids Surf. A* **2004**, *241*(1–3), 149–154.
75. Chen, D.-L.; Al-Saidi, W.; Johnson, K. Noble gas adsorption on carbon nanotubes: insight from a van der Waals density functional study. In *APS March Meeting 2011*. Dallas, Texas, 2011.
76. Jalili, S.; Majidi, R. *Physica E* **2007**, *39*(1), 166–170.
77. Simonyan, V. V.; Johnson, J. K.; Kuznetsova, A.; Yates, J. J. T. *J. Chem. Phys.* **2001**, *114*(9), 4180–4185.
78. Jijun, Z.; Alper, B.; Jie, H.; Jian Ping, L. *Nanotechnology* **2002**, *13*(2), 195.
79. Britz, D. A.; Khlobystov, A. N. *Chem. Soc. Rev.* **2006**, *35*(7), 637–659.
80. Yang, Q.-H.; Hou, P.-X.; Bai, S.; Wang, M.-Z.; Cheng, H.-M. *Chem. Phys. Lett.* **2001**, *345*(1–2), 18–24.
81. Masenelli-Varlot, K.; McRae, E.; Dupont-Pavlovsky, N. *Appl. Surf. Sci.* **2002**, *196*(1–4), 209–215.
82. Ashrafi, F.; Ghasemi, A. S.; Babanejad, S. A.; Rahimof, M. *Res. J. Appl. Sci., Eng. Technol.* **2010**, *2*(6), 547–551.
83. Furmaniak, S.; Terzyk, A. P.; Gauden, P. A.; Rychlicki, G. *J. Colloid Interf. Sci.* **2006**, *295*(2), 310–317.

84. Furmaniak, S.; Terzyk, A. P.; Gauden, P. A.; Harris, P. J. F.; Wiśniewski, M.; Kowalczyk, P. *Adsorption* **2010**, *16*(4–5), 197–213.
85. Sun, C. H.; Li, F.; Cheng, H. M.; Lu, G. Q. *Appl. Phys. Lett.* **2005**, *87*(24), 243109.
86. Chiang, Y.-C.; Lee, C.-Y. *J. Mater. Sci.* **2009**, *44*(11), 2780–2791.
87. Yoshiki, K.; Koichi, H. *Surf. Interface Anal.* **2008**, *40*(13), 1669–1672.
88. Muris, M.; Dupont-Pavlovsky, N.; Bienfait, M.; Zeppenfeld, P. *Surf. Sci.* **2001**, *492*(1–2), 67–74.
89. Hallock, R. B.; Kahng Y. H. *J. Low Temp. Phys.* **2004**, *134*(1–2), 21–30.
90. Jie, Z.; Yao, W.; Wenjun, L.; Fei, W.; Yangxin, Y. *Nanotechnology* **2007**, *18*(9), 095707.
91. Heroux, L.; Krungleviciute, V.; Calbi, M. M.; Migone, A. D. *J. Phys. Chem. B* **2006**, *110*(25), 12597–12602.
92. Fujiwara, A.; Ishii, K.; Suematsu, H.; Kataura, H.; Maniwa, Y.; Suzuki, S.; Achiba, Y. *Chem. Phys. Lett.* **2001**, *336*(3–4), 205–211.
93. Yang, C.-M.; Kanoh, H.; Kaneko, K.; Yudasaka, M.; Iijima, S. *J. Phys. Chem. B* **2002**, *106*(35), 8994–8999.
94. Iwata, S.; Sato, Y.; Nakai, K.; Ogura, S.; Okano, T.; Namura, M.; Kasuya, A.; Tohji, K.; Fukutani, K. *J. Phys. Chem. C* **2007**, *111*(41), 14937–14941.
95. Yoo, D.-H.; Rue, G.-H.; Chan, M. H. W.; Hwang, Y.-H.; Kim, H.-K. *J. Phys. Chem. B* **2003**, *107*(7), 1540–1542.
96. Matranga, C.; Bockrath, B. *J. Phys. Chem. B* **2005**, *109*(11), 4853–4864.
97. Ellison, M. D.; Crotty, M. J.; Koh, D.; Spray, R. L.; Tate, K. E. *J. Phys. Chem. B* **2004**, *108*(23), 7938–7943.
98. Albesa, A. G.; Fertitta, E. A.; Vicente, J. L. *Langmuir* **2009**, *26*(2), 786–795.
99. Bienfait, M.; Zeppenfeld, P.; Dupont-Pavlovsky, N.; Muris, M.; Johnson, M. R.; Wilson, T.; DePies, M.; Vilches, O. E. *Phys. Rev. B* **2004**, *70*(3), 035410.
100. Yim, W.-L.; Byl, O.; Yates, J. J. T.; Johnson, J. K. *J. Chem. Phys.* **2004**, *120*(11), 5377–5386.
101. Rawat, D. S.; Heroux, L.; Krungleviciute, V.; Migone, A. D. *Langmuir* **2005**, *22*(1), 234–238.
102. Ulbricht, H.; Moos, G.; Hertel, T. *Phys. Rev. B* **2002**, *66*(7), 075404.
103. Ulbricht, H.; Kriebel, J.; Moos, G.; Hertel, T. *Chem. Phys. Lett.* **2002**, *363*(3–4), 252–260.
104. Hilding, J.; Grulke, E. A.; Sinnott, S. B.; Qian, D.; Andrews, R.; Jagtoyen, M. *Langmuir* **2001**, *17*(24), 7540–7544.
105. Patchkovskii, S.; Tse, J. S.; Yurchenko, S. N.; Zhechkov, L.; Heine, T.; Seifert, G. *Proc. Natl. Acad. Sci. U. S. A.* **2005**, *102*(30), 10439–10444.
106. Tozzini, V.; Pellegrini, V. *J. Phys. Chem. C* **2011**, *115*(51), 25523–25528.

107. Miura, Y.; Kasai, H.; Dino, W.; Nakanishi, H.; Sugimoto, T. *J. Appl. Phys.* **2003**, *93*(6), 3395–3400.
108. Casolo, S.; Lovvik, O. M.; Martinazzo, R.; Tantardini, G. F. *J. Chem. Phys.* **2009**, *130*(5), 054704.
109. Stojkovic, D.; Zhang, P.; Lammert, P. E.; Crespi, V. H. *Phys. Rev. B* **2003**, *68*(19), 195406.
110. Sofo, J. O.; Chaudhari, A. S.; Barber, G. D. *Phys. Rev. B* **2007**, *75*(15), 153401.
111. Montoya, A.; Mondragón, F.; Truong, T. N. *Carbon* **2003**, *41*(1), 29–39.
112. Cabrera-Sanfelix, P. *J. Phys. Chem. A* **2008**, *113*(2), 493–498.
113. Liu, Y.; Wilcox, J. *Environ. Sci. Technol.* **2010**, *45*(2), 809–814.
114. Leenaerts, O.; Partoens, B.; Peeters, F. M. *Phys. Rev. B* **2008**, *77*(12), 125416.
115. Daykova, E.; Pisov, S.; Proykova, A. First-Principles and Molecular Dynamics Simulations of Methane Adsorption on Graphene. In *Carbon Nanotubes*; Popov, V., Lambin, P., Eds.; Springer: Netherlands, **2006**, pp. 209–210.
116. Sheng, L.; Ono, Y.; Taketsugu, T. *J. Phys. Chem. C* **2010**, *114*(8), 3544–3548.
117. Kayhan, E.; Prasad, R. M.; Gurlo, A.; Yilmazoglu, O.; Engstler, J.; Ionescu, E.; Yoon, S.; Weidenkaff, A.; Schneider, J. J. *Chem. Eur. J.* **2012**, *18*(47), 14996–15003.
118. Yoon, H. J.; Jun, D. H.; Yang, J. H.; Zhou Z.; Yang, S. S.; Cheng, M. M.-C. *Sens. Actuators B* **2011**, *157*(1), 310–313.
119. Rao, G. P.; Lu, C.; Su, F. *Sep. Purif. Technol.* **2007**, *58*(1), 224–231.
120. Rouquerol, J.; Rouquerol, F.; Sing, K. S. W. *Adsorption by Powders and Porous Solids*; Elsevier Science, London, UK, **1998**.
121. Kanellopoulos, N. *Nanoporous Materials: Advanced Techniques for Characterization, Modeling, and Processing*; Taylor & Francis, Boca Raton, Florida, USA, **2011**.
122. Dąbrowski, A. *Adv. Colloid Interface Sci.* **2001**, *93*(1–3), 135–224.
123. Yang, K.; Zhu, L.; Xing, B. *Environ. Sci. Technol.* **2006**, *40*(6), 1855–1861.
124. Johnson, I.; Denoyel, R.; Rouquerol, J.; Everett, D. H. *Colloids Surf.* **1990**, *49*(0), 133–148.
125. Moreno-Castilla, C. *Carbon* **2004**, *42*(1), 83–94.
126. Striolo, A.; Chialvo, A. A.; Gubbins, K. E.; Cummings, P. T. *J. Chem. Phys.* **2005**, *122*(23), 234712.
127. Marti, J.; Gordillo, M. C. *J. Chem. Phys.* **2001**, *114*(23), 10486–10492.
128. Maniwa, Y.; Kataura, H.; Abe, M.; Suzuki, S.; Achiba, Y.; Kira, H.; Matsuda, K. *J. Phys. Soc. Jpn.* **2002**, *71*, 2863.
129. Novoselov, K. S.; Geim, A. K.; Morozov, S. V.; Jiang, D.; Zhang, Y.; Dubonos, S. V.; Grigorieva, I. V.; Firsov, A. A. *Science* **2004**, *306*(5696), 666–669.
130. Gordillo, M. C.; Martí, J. *J. Phys.: Condens. Matter* **2010**, *22*(28), 284111.

131. Kolesnikov, A. I.; Zanotti, J.-M.; Loong, C.-K.; Thiyagarajan, P.; Moravsky, A. P.; Loutfy, R. O.; Burnham, C. J. *Phys. Rev. Lett.* **2004**, *93*(3), 035503.
132. Yavari, F.; Kritzinger, C.; Gaire, C.; Song, L.; Gulapalli, H.; Borca-Tasciuc, T.; Ajayan, P. M.; Koratkar, N. *Small* **2010**, *6*(22), 2535–2538.
133. Berashevich, J.; Chakraborty, T. *Phys. Rev. B* **2009**, *80*(3), 033404.
134. Rafiee, J.; Rafiee, M. A.; Yu, Z.-Z.; Koratkar, N. *Adv. Mater.* **2010**, *22*(19), 2151–2154.
135. Politano, A.; Marino, A. R.; Formoso, V.; Chiarello, G. *AIP Adv.* **2011**, *1*(4), 042130.
136. Kimmel, G. A.; Matthiesen, J.; Baer, M.; Mundy, C. J.; Petrik, N. G.; Smith, R. S.; Dohnálek, Z.; Kay, B. D. *J. Am. Chem. Soc.* **2009**, *131*(35), 12838–12844.
137. Cabrera-Sanfelix, P.; Darling, G. R. *J. Phys. Chem. C* **2007**, *111*(49), 18258–18263.
138. Tunckol, M.; Durand, J.; Serp, P. *Carbon* **2012**, *50*(12), 4303–4334.
139. Wu, B.; Hu, D.; Kuang, Y.; Liu, B.; Zhang, X.; Chen, J. *Angew. Chem. Int. Ed.* **2009**, *48*(26), 4751–4754.
140. Liu, Y.; Yu, L.; Zhang, S.; Yuan, J.; Shi, L.; Zheng, L. *Colloids Surf. A* **2010**, *359*(1–3), 66–70.
141. Dong, B.; Su, Y.; Liu, Y.; Yuan, J.; Xu, J.; Zheng, L. *J. Colloid Interf. Sci.* **2011**, *356*(1), 190–195.
142. Zhao, L.; Li, Y.; Liu, Z.; Shimizu, H. *Chem. Mater.* **2010**, *22*(21), 5949–5956.
143. Frolov, A. I.; Kirchner, K.; Kirchner, T.; Fedorov, M. V. *Faraday Discuss.* **2012**, *154*(0), 235–247.
144. Ghatee, M. H.; Moosavi F. *J. Phys. Chem. C* **2011**, *115*(13), 5626–5636.
145. Hernandez, Y.; Nicolosi, V.; Lotya, M.; Blighe, F. M.; Sun, Z.; De, S., Holland, M. T. B.; Byrne, M.; Gun'Ko, Y. K.; Boland, J. J.; Niraj, P.; Duesberg, G.; Krishnamurthy, S.; Goodhue, R.; Hutchison, J.; Scardaci, V.; Ferrari, A. C.; Coleman, J. N. *Nat. Nanotechnol.* **2008**, *3*(9), 563–568.
146. Wang, X.; Fulvio, P. F.; Baker, G. A.; Veith, G. M.; Unocic, R. R.; Mahurin, S. M.; Chi, M.; Dai, S. *Chem. Commun.* **2010**, *46*(25), 4487–4489.
147. Lee, J.; Aida, T. *Chem. Commun.* **2011**, *47*(24), 6757–6762.
148. Zhou, X.; Wu, T.; Ding, K.; Hu, B.; Hou, M.; Han, B. *Chem. Commun.* **2010**, *46*(3), 386–388.
149. Tung, T. T.; Kim, T. Y.; Shim, J. P.; Yang, W. S.; Kim, H.; Suh, K. S. *Org. Electron.* **2011**, *12*(12), 2215–2224.
150. Ren, X.; Chen, C.; Nagatsu, M.; Wang, X. *Chem. Eng. J.* **2011**, *170*(2–3), 395–410.
151. Carrillo-Carrion, C.; Lucena, R.; Cardenas, S.; Valcarcel, M. *Analyst* **2007**, *132*(6), 551–559.
152. Wang, X.; Lu, J.; Xing, B. *Environ. Sci. Technol.* **2008**, *42*(9), 3207–3212.

153. Yudasaka, M.; Fan, J.; Miyawaki, J.; Iijima, S. *J. Phys. Chem. B* **2005**, *109*(18), 8909–8913.
154. Agnihotri, S.; Rood, M. J.; Rostam-Abadi, M. *Carbon* **2005**, *43*(11), 2379–2388.
155. Lee, J.-W.; Kang, H.-C.; Shim, W.-G.; Kim, C.; Moon, H. *J. Chem. Eng. Data* **2006**, *51*(3), 963–967.
156. Sander, M.; Lu, Y.; Pignatello, J. J. *J. Environ. Qual.* **2005**, *34*(3), 1063–1072.
157. Mezgebe, M.; Jiang, L.-H.; Shen, Q.; Du, C.; Yu, H.-R. *Colloids Surf. A* **2012**, *415*(0), 86–90.
158. Lu, C.; Su, F. *Sep. Purif. Technol.* **2007,** *58*(1), 113–121.
159. Zhang, S.; Shao, T.; Bekaroglu, S. S. K.; Karanfil, T. *Water Res.* **2010**, *44*(6), 2067–2074.
160. Davis, J. J.; Green, M. L. H.; Allen, H.; Hill, O.; Leung, Y. C.; Sadler, P. J.; Sloan, J.; Xavier, A. V.; Chi Tsang, S. *Inorg. Chim. Acta* **1998**, *272*(1–2), 261–266.
161. Richard, C.; Balavoine, F.; Schultz, P.; Ebbesen, T. W.; Mioskowski, C. *Science* **2003**, *300*(5620), 775–778.
162. Karajanagi, S. S.; Vertegel, A. A.; Kane, R. S.; Dordick, J. S. *Langmuir* **2004**, *20*(26), 11594–11599.
163. Gotovac, S.; Honda, H.; Hattori, Y.; Takahashi, K.; Kanoh, H.; Kaneko, K. *Nano Lett.* **2007**, *7*(3), 583–587.
164. Ji, L.; Chen, W.; Duan, L.; Zhu, D. *Environ. Sci. Technol.* **2009**, *43*(7), 2322–2327.
165. Junkermeier, C. E.; Solenov, D.; Reinecke, T. L. *J. Phys. Chem. C* **2013**, *117*(6), 2793–2798.
166. Ferre-Vilaplana, A. *J. Phys. Chem. C* **2008**, *112*(10), 3998–4004.
167. Wu, T.; Cai, X.; Tan, S.; Li, H.; Liu, J.; Yang, W. *Chem. Eng. J.* **2011**, *173*(1), 144–149.
168. Xu, J.; Wang, L.; Zhu, Y. *Langmuir* **2012**, *28*(22), 8418–8425.
169. Ganesan, P.; Kamaraj, R.; Vasudevan, S. *J. Taiwan Inst. Chem. Eng.* (0), doi: 10.1016/j.jtice.2013.1001.1029.
170. Wang, L.; Yang, R. T.; Sun, C.-L. *AIChE J.* **2013**, *59*(1), 29–32.
171. Norzilah, A. H.; Fakhru'l-Razi, A.; Choong, T. S. Y.; Chuah, A. L. *J. Nanomater.* **2011**, *2011*, 495676.
172. Hsu, S.-C.; Lu, C. *J. Air Waste Manage. Assoc.* **2009**, *59*(8), 990–997.
173. Liao, Q.; Sun, J.; Gao, L. *Colloids Surf. A* **2008**, *312*(2–3), 160–165.
174. Li, Y.; Du, Q.; Liu, T.; Peng, X.; Wang, J.; Sun, J.; Wang, Y.; Wu, S.; Wang, Z.; Xia, Y.; Xia, L. *Chem. Eng. Res. Des.* **2013**, *91*(2), 361–368.
175. Duclaux, L. *Carbon* **2002**, *40*(10), 1751–1764.
176. Panchakarla, L. S.; Subrahmanyam, K. S.; Saha, S. K.; Govindaraj, A.; Krishnamurthy, H. R.; Waghmare, U. V.; Rao, C. N. R. *Adv. Mater.* **2009**, *21*(46), 4726–4730.

177. Zhang, L.; Yu, J.; Yang, M.; Xie, Q.; Peng, H.; Liu, Z. *Nat. Commun.* **2013**, *4*, 1443.
178. Wildgoose, G. G.; Banks, C. E.; Compton, R. G. *Small* **2006**, *2*(2), 182–193.
179. Nakada, K.; Ishii, A. DFT Calculation for Adatom Adsorption on Graphene. In *Graphene Simulation*; Gong, J. R., Ed.; InTech, Rijeka, Croatia, **2011**.
180. Fullam, S.; Cottell, D.; Rensmo, H.; Fitzmaurice, D. *Adv. Mater.* **2000**, *12*(19), 1430–1432.
181. Han, L.; Wu, W.; Kirk, F. L.; Luo, J.; Maye, M. M.; Kariuki, N. N.; Lin, Y.; Wang, C.; Zhong, C.-J. *Langmuir* **2004**, *20*(14), 6019–6025.
182. Liu, X.; Wang, C.-Z.; Hupalo, M.; Lin, H.-Q.; Ho, K.-M.; Tringides, M. *Crystals* **2013**, *3*(1), 79–111.
183. Maiti, A.; Ricca, A. *Chem. Phys. Lett.* **2004**, *395*(1–3), 7–11.
184. Sasaki, Y.; Kitaura, R.; Yamamoto, Y.; Arai, S.; Suzuki, S.; Miyata, Y.; Shinohara, H. *Appl. Phys. Express* **2012**, *5*(6), 065103.
185. He, D.; Cheng, K.; Li, H.; Peng, T.; Xu, F.; Mu, S.; Pan, M. *Langmuir* **2012**, *28*(8), 3979–3986.
186. Claussen, J. C.; Kumar, A.; Jaroch, D. B.; Khawaja, M. H.; Hibbard, A. B.; Porterfield, D. M.; Fisher, T. S. *Adv. Funct. Mater.* **2012**, *22*(16), 3399–3405.
187. Williams, G.; Seger, B.; Kamat, P. V. *ACS Nano* **2008**, *2*(7), 1487–1491.
188. Nethravathi, C.; Rajamathi, J. T.; Ravishankar, N.; Shivakumara, C.; Rajamathi, M. *Langmuir* **2008**, *24*(15), 8240–8244.
189. Paek, S.-M.; Yoo, E.; Honma, I. *Nano Lett.* **2008**, *9*(1), 72–75.
190. Guo, S.; Sun, S. *J. Am. Chem. Soc.* **2012**, *134*(5), 2492–2495.
191. Jiang, K.; Eitan, A.; Schadler, L. S.; Ajayan, P. M.; Siegel, R. W.; Grobert, N.; Mayne, M.; Reyes-Reyes, M.; Terrones, H.; Terrones, M. *Nano Lett.* **2003**, *3*(3), 275–277.
192. Zhang, L.-S.; Liang, X.-Q.; Song, W.-G.; Wu, Z.-Y. *Phys. Chem. Chem. Phys.* **2010**, *12*(38), 12055–12059.
193. Groves, M. N.; Chan, A. S. W.; Malardier-Jugroot, C.; Jugroot, M. *Chem. Phys. Lett.* **2009**, *481*(4–6), 214–219.
194. Ma, P.-C.; Siddiqui, N. A.; Marom, G.; Kim, J.-K. *Composites Part A* **2010**, *41*(10), 1345–1367.
195. Srebnik, S. *J. Polym. Sci. Part B: Polym. Phys.* **2008**, *46*(24), 2711–2718.
196. Qin, S.; Qin, D.; Ford, W. T.; Herrera, J. E.; Resasco, D. E.; Bachilo, S. M.; Weisman, R. B. *Macromolecules* **2004**, *37*(11), 3965–3967.
197. Yang, M.; Koutsos, V.; Zaiser, M. *J. Phys. Chem. B* **2005**, *109*(20), 10009–10014.
198. O'Connell, M. J.; Boul, P.; Ericson, L. M.; Huffman, C.; Wang, Y.; Haroz, E.; Kuper, C.; Tour, J.; Ausman, K. D.; Smalley, R. E. *Chem. Phys. Lett.* **2001**, *342*(3–4), 265–271.

199. Steuerman, D. W.; Star, A.; Narizzano, R.; Choi, H.; Ries, R. S.; Nicolini, C.; Stoddart, J. F.; Heath, J. R. *J. Phys. Chem. B* **2002**, *106*(12), 3124–3130.
200. Lee, S.; Park, J.; Koo, C.; Lim, B.; Kim, S. *Macromol. Res.* **2008**, *16*(3), 261–266.
201. Star, A.; Stoddart, J. F. *Macromolecules* **2002**, *35*(19), 7516–7520.
202. Khan, U.; May, P.; O'Neill, A.; Coleman, J. N. *Carbon* **2010**, *48*(14), 4035–4041.
203. Wang, H.; Xia, B. Y.; Yan, Y.; Li, N.; Wang, J.-Y.; Wang, X. *J. Phys. Chem. B* **2013**, *117*(18), 5606–5613.
204. Terrones, M.; Martín, O.; González, M.; Pozuelo, J.; Serrano, B.; Cabanelas, J. C.; Vega-Díaz, S. M.; Baselga, J. *Adv. Mater.* **2011**, *23*(44), 5302–5310.
205. Lv, C.; Xue, Q.; Xia, D.; Ma, M.; Xie, J.; Chen, H. *J. Phys. Chem. C* **2010**, *114*(14), 6588–6594.
206. Freeman, D. D.; Choi, K.; Yu, C. *PLoS ONE* **2012**, *7*(11), e47822.
207. Shim, M.; Javey, A.; Shi Kam, N. W.; Dai, H. *J. Am. Chem. Soc.* **2001**, *123*(46), 11512–11513.
208. Sankaran, M.; Viswanathan, B. *Carbon* **2006**, *44*(13), 2816–2821.
209. López-Corral, I.; de Celis, J.; Juan, A.; Irigoyen, B. *Int. J. Hydrogen Energy* **2012**, *37*(13), 10156–10164.
210. Gayathri, V.; Geetha, R. *Adsorption* **2007**, *13*(1), 53–59.
211. Grochala, W.; Edwards, P. P. *Chem. Rev.* **2004**, *104*(3), 1283–1316.
212. Zimmermann, U.; Malinowski, N.; Näher, U.; Frank, S.; Martin, T. P. *Phys. Rev. Lett.* **1994**, *72*(22), 3542–3545.
213. Lee, S. M.; Lee, Y. H.; Hwang, Y. G.; Hahn, J. R.; Kang, H. *Phys. Rev. Lett.* **1999**, *82*(1), 217–220.
214. Grujicic, M.; Cao, G.; Singh, R. *Appl. Surf. Sci.* **2003**, *211*(1–4), 166–183.
215. Akdim, B.; Kar, T.; Duan, X.; Pachter, R. *Chem. Phys. Lett.* **2007**, *445*(4–6), 281–287.
216. Chang, H.; Lee, J. D.; Lee, S. M.; Lee, Y. H. *Appl. Phys. Lett.* **2001**, *79*(23), 3863–3865.
217. Tang, S.; Cao, Z. *J. Chem. Phys.* **2009**, *131*(11), 114706.
218. Turabekova, M. A.; Dinadayalane, T. C.; Leszczynska, D.; Leszczynski, J. *J. Phys. Chem. C* **2012**, *116*(10), 6012–6021.
219. Cho, J. H.; Park, C. R. *Catal. Today* **2007**, *120*(3–4), 407–412.
220. Zhang, Z. W.; Li, J. C.; Jiang, Q. *J. Phys. Chem. C* **2010**, *114*(17), 7733–7737.
221. Zhang, Y.; Zhang, D.; Liu, C. *J. Phys. Chem. B* **2006**, *110*(10), 4671–4674.
222. Wang, R.; Zhang, D.; Zhang, Y.; Liu, C. *J. Phys. Chem. B* **2006**, *110*(37), 18267–18271.
223. Peng, S.; Cho, K. *Nano Lett.* **2003**, *3*(4), 513–517.
224. Bai, L.; Zhou, Z. *Carbon* **2007**, *45*(10), 2105–2110.

225. Wang, R.; Zhang, D.; Sun, W.; Han, Z.; Liu, C. *J. Mol. Struct. THEOCHEM* **2007**, *806*(1–3), 93–97.
226. Mowbray, D. J.; García-Lastra, J. M.; Arocena, I. L.; Rubio, Á.; Thygesen, K. S.; Jacobsen, K. W. Computational Design of Chemical Nanosensors: Transition Metal Doped Single-Walled Carbon Nanotubes. In *Chemical Sensors: Simulation and Modeling*; Korotcenkov, G., Ed.; Momentum Press, New York, NY, USA, **2012**.
227. Zhou, X.; Tian, W. Q.; Wang, X.-L. *Sens. Actuators B* **2010**, *151*(1), 56–64.
228. Tabtimsai, C.; Keawwangchai, S.; Wanno, B.; Ruangpornvisuti, V. *J. Mol. Model.* **2012**, *18*(1), 351–358.
229. Tabtimsai, C.; Wanno, B.; Ruangpornvisuti, V. *Mater. Chem. Phys.* **2013**, *138*(2–3), 709–715.
230. Pannopard, P.; Khongpracha, P.; Probst, M.; Limtrakul, J. *J. Mol. Graphics Modell.* **2009**, *28*(1), 62–69.
231. Zhang, Y.-H.; Zhou, K.-G.; Xie, K.-F.; Gou, X.-C.; Zeng, J.; Zhang, H.-L.; Peng, Y. *J. Nanosci. Nanotechnol.* **2010**, *10*(11), 7347–7350.
232. Sanyal, B.; Eriksson, O.; Jansson, U.; Grennberg, H. *Phys. Rev. B* **2009**, *79*(11), 113409.
233. Zhang, Y.-H.; Han, L.-F.; Xiao, Y.-H.; Jia, D.-Z.; Guo, Z.-H.; Li, F. *Comput. Mater. Sci.* **2013**, *69*, 222–228.
234. Borisova, D.; Antonov, V.; Proykova, A. *Int. J. Quantum Chem.* **2013**, *113*(6), 786–791.
235. Lin, X.; Ni, J.; Fang, C. *J. Appl. Phys.* **2013**, *113*(3), 034306.
236. Wood, B. C.; Bhide, S. Y.; Dutta, D.; Kandagal, V. S.; Pathak, A. D.; Punnathanam, S. N.; Ayappa, K. G.; Narasimhan, S. *J. Chem. Phys.* **2012**, *137*(5), 054702.
237. Dreyer, D. R.; Park, S.; Bielawski, C. W.; Ruoff, R. S. *Chem. Soc. Rev.* **2010**, *39*(1), 228–240.
238. Lerf, A.; He, H.; Forster, M.; Klinowski, J. *J. Phys. Chem. B* **1998**, *102*(23), 4477–4482.
239. Tang, S.; Cao, Z. *J. Chem. Phys.* **2011**, *134*(4), 044710.
240. Schedin, F.; Geim, A. K.; Morozov, S. V.; Hill, E. W.; Blake, P.; Katsnelson, M. I.; Novoselov, K. S. *Nat. Mater.* **2007**, *6*, 652–655.
241. Lu, G.; Ocola, L. E.; Chen, J. *Appl. Phys. Lett.* **2009**, *94*(8), 083111.
242. Ganhua, L.; Leonidas, E. O.; Junhong, C. *Nanotechnology* **2009**, *20*(44), 445502.
243. Ko, G.; Kim, H. Y.; Ahn, J.; Park, Y. M.; Lee, K. Y.; Kim, J. *Curr. Appl. Phys.* **2010**, *10*(4), 1002–1004.
244. Yavari, F.; Castillo, E.; Gullapalli, H.; Ajayan, P. M.; Koratkar, N. *Appl. Phys. Lett.* **2012**, *100*(20), 203120.

245. Fowler, J. D.; Allen, M. J; Tung, V. C.; Yang, Y.; Kaner, R. B.; Weiller, B. H. *ACS Nano.* **2009**, *3*(2), 301–306.
246. Yavari, F.; Chen, Z.; Thomas, A. V.; Ren, W.; Cheng, H.-M.; Koratkar, N. *Sci. Rep.* **2011**, *1*, 166.
247. Pearce, R.; Iakimov, T.; Andersson, M.; Hultman, L.; Spetz, A. L.; Yakimova, R. *Sens. Actuators B* **2011**, *155*(2), 451–455.
248. Yong-Hui, Z.; Ya-Bin, C.; Kai-Ge, Z.; Cai-Hong, L.; Jing, Z.; Hao-Li, Z.; Yong, P. *Nanotechnology.* **2009**, *20*(18), 185504.
249. Ao, Z. M.; Yang, J.; Li, S.; Jiang, Q. *Chem. Phys. Lett.* **2008**, *461*(4–6), 276–279.
250. Sun, Y.; Chen, L.; Zhang, F.; Li, D.; Pan, H.; Ye, J. *Solid State Commun.* **2010**, *150*(39–40), 1906–1910.
251. Jiayu, D.; Jianmin Y. *J. Phys.: Condens. Matter* **2010**, *22*(22), 225501.
252. Dai, J.; Yuan, J. *Phys. Rev. B* **2010**, *81*(16), 165414.
253. Dai, J.; Yuan, J.; Giannozzi, P. *Appl. Phys. Lett.* **2009**, *95*(23), 232105.
254. Li, Y.; Zhou, Z.; Yu, G.; Chen, W.; Chen, Z. *J. Phys. Chem. C* **2010**, *114*(14), 6250–6254.
255. Lu, Y.-H.; Zhou, M.; Zhang, C.; Feng, Y.-P. *J. Phys. Chem. C* **2009**, *113*(47), 20156–20160.
256. Song, E. H.; Wen, Z.; Jiang, Q. *J. Phys. Chem. C* **2011**, *115*(9), 3678–3683.
257. Miao, Z.; Yun-Hao, L.; Yong-Qing, C.; Chun, Z.; Yuan-Ping, F. *Nanotechnology* **2011**, *22*(38), 385502.
258. Yong, Y.; Song, B.; Liu, K.; He, P. *J. Appl. Phys.* **2012**, *111*(8), 083713.
259. Zheng, Q.; Xue, Q.; Yan, K.; Gao, X.; Li, Q.; Hao, L. *Polymer* **2008**, *49*(3), 800–808.
260. Yang, R. T.; Yang, K. L. *Carbon* **1985**, *23*(5), 537–547.
261. Rietsch, J.-C.; Brender, P.; Dentzer J.; Gadiou, R.; Vidal, L.; Vix-Guterl, C. *Carbon* **2013**, *55*(0), 90–97.
262. Guo, S.; Dong, S.; Wang, E. *Adv. Mater.* **2010**, *22*(11), 1269–1272.
263. Park, M. J.; Lee, J. K.; Lee, B. S.; Lee, Y.-W.; Choi, I. S.; Lee, S.-g. *Chem. Mater.* **2006**, *18*(6), 1546–1551.
264. Yang, H.; Shan, C.; Li, F.; Han, D.; Zhang, Q.; Niu, L. *Chem. Commun.* **2009**, *0*(26), 3880–3882.
265. Kaskhedikar, N. A.; Maier, J. *Adv. Mater.* **2009**, *21*(25–26), 2664–2680.
266. Chen, P.; Wu, X.; Lin, J.; Tan, K. L. *Science* **1999**, *285*(5424), 91–93.
267. Yang, R. T. *Carbon* **2000**, *38*(4), 623–626.
268. Rytkönen, K.; Akola, J.; Manninen, M. *Phys. Rev. B* **2007**, *75*(7), 075401.
269. Nakada, K.; Ishii, A. *Solid State Commun.* **2011**, *151*(1), 13–16.
270. Liu, X.; Wang, C. Z.; Hupalo, M.; Lu, W. C.; Tringides, M. C.; Yao, Y. X.; Ho, K. M. *Phys. Chem. Chem. Phys.* **2012**, *14*(25), 9157–9166.

271. Khantha, M.; Cordero, N. A.; Molina, L. M.; Alonso, J. A.; Girifalco, L. A. *Phys. Rev. B* **2004**, *70*(12), 125422.
272. Rangel, E.; Ramirez-de-Arellano, J. M.; Magana, L. F. *Phys. Status Solidi B* **2011**, *248*(6), 1420–1424.
273. Senami, M.; Ikeda, Y.; Fukushima, A.; Tachibana, A. *AIP Adv.* **2011**, *1*(4), 042106.
274. Umadevi, D.; Sastry, G. N. *Chem. Phys. Lett.* **2012**, *549*(0), 39–43.
275. Lee, H.; Ihm, J.; Cohen, M. L.; Louie, S. G. *Phys. Rev. B* **2009**, *80*(11), 115412.
276. Yoon, M.; Yang, S.; Hicke, C.; Wang, E.; Geohegan, D.; Zhang, Z. *Phys. Rev. Lett.* **2008**, *100*(20), 206806.
277. Yang, X.; Zhang, R. Q.; Ni, J. *Phys. Rev. B* **2009**, *79*(7), 075431.
278. Ataca, C.; Akturk, E.; Ciraci, S. *Phys. Rev. B* **2009**, *79*(4), 041406.
279. Nguyen, M. C.; Cha, M.-H.; Bae, J.; Kim, Y.; Kim, M.; Ihm, J. *Chem Phys Chem* **2011**, *12*(4), 777–780.
280. Cazorla, C.; Shevlin, S. A.; Guo, Z. X. *Phys. Rev. B* **2010**, *82*(15), 155454.
281. Liu, W.; Xu, S.; Li, C.; Yuan, G. *Diamond Relat. Mater.* **2012**, *29*, 59–62.
282. Liu, W.; Xu, S.; Yuan, G.; Xu, Y. *Physica B* **2013**, *408*(0), 46–50.
283. Mubeen, S.; Zhang, T.; Yoo, B.; Deshusses, M. A.; Myung, N. V. *J. Phys. Chem. C* **2007**, *111*(17), 6321–6327.
284. Mota, R.; Fagan, S. B.; Fazzio, A. *Surf. Sci.* **2007**, *601*(18), 4102–4104.
285. Brieno-Enriquez, K. M.; Ledesma-Garcia, J.; Perez-Bueno, J. J.; Godinez, L. A.; Terrones, H.; Angeles-Chavez, C. *Mater. Chem. Phys.* **2009**, *115*(2–3), 521–525.
286. Suttisawat, Y.; Rangsunvigit, P.; Kitiyanan, B.; Williams, M.; Ndungu, P.; Lototskyy, M. V.; Nechaev, A.; Linkov, V.; Kulprathipanja, S. *Int. J. Hydrogen Energy* **2009**, *34*(16), 6669–6675.
287. Park, S.-J.; Lee, S.-Y. *Int. J. Hydrogen Energy* **2010**, *35*(23), 13048–13054.
288. Wu, H.-Q.; Yuan, P.-S.; Xu, H.-Y.; Xu, D.-M.; Geng, B.-Y.; Wei, X.-W. *J. Mater. Sci.* **2006**, *41*(20), 6889–6894.
289. Liu, Q.; Ren, W.; Chen, Z.-G.; Liu, B.; Yu, B.; Li, F.; Cong, H.; Cheng, H.-M. *Carbon* **2008**, *46*(11), 1417–1423.
290. Tamburri, E.; Toschi, F.; Guglielmotti, V.; Scatena, E.; Orlanducci, S.; Terranova, M. L. *J. Nanopart. Res.* **2009**, *11*(6), 1311–1319.
291. Hu, L.; Hu, X.; Wu, X.; Du, C.; Dai, Y.; Deng, J. *Physica B* **2010**, *405*(16), 3337–3341.
292. Tang, Y.; Yang, Z.; Dai, X. *J. Magn. Magn. Mater.* **2011**, *323*(20), 2441–2447.
293. Durgun, E.; Dag, S.; Bagci, V. M. K.; Gulseren, O.; Yildirim, T.; Ciraci, S. *Phys. Rev. B* **2003**, *67*(20), 201401.

294. Durgun, E.; Dag, S.; Ciraci, S.; Gulseren, O. *J. Phys. Chem. B* **2004**, *108*(2), 575–582.
295. Valencia, H.; Gil, A.; Frapper, G. *J. Phys. Chem. C* **2010**, *114*(33), 14141–14153.
296. Chen, G.; Kawazoe, Y. *Phys. Rev. B* **2006**, *73*(12), 125410.
297. Menon, M.; Andriotis, A. N.; Froudakis, G. E. *Chem. Phys. Lett.* **2000**, *320*(5–6), 425–434.
298. Gao, H. L.; Zhao, J. J. *J. Chem. Phys.* **2010**, *132*(23), 234704.
299. Meng, F. Y.; Zhou, L. G.; Shi, S.-Q.; Yang, R. *Carbon* **2003**, *41*(10), 2023–2025.
300. Fan, Y.; Goldsmith, B. R.; Collins, P. G. *Nat. Mater.* **2005**, *4*(12), 906–911.
301. Yang, S. H.; Shin, W. H.; Lee, J. W.; Kim, S. Y.; Woo, S. I.; Kang, J. K. *J. Phys. Chem. B* **2006**, *110*(28), 13941–13946.
302. Kim, H.-S.; Lee, H.; Han, K.-S.; Kim, J.-H.; Song, M.-S.; Park, M.-S.; Lee, J.-Y.; Kang, J.-K. *J. Phys. Chem. B* **2005**, *109*(18), 8983–8986.
303. Kongkanand, A.; Kuwabata, S.; Girishkumar, G.; Kamat, P. *Langmuir* **2006**, *22*(5), 2392–2396.
304. Axet, M. R.; Amoroso, F.; Bottari, G.; D'Amora, A.; Zangrando, E.; Faraone, F.; Drommi, D.; Saporita, M.; Carfagna, C.; Natanti, P.; Seraglia, R.; Milani, B. *Organometallics* **2009**, *28*(Copyright (C) 2011 American Chemical Society (ACS). All Rights Reserved.), 4464–4474.
305. Okamoto, Y. *Chem. Phys. Lett.* **2006**, *420*(4–6), 382–386.
306. Okazaki-Maeda, K.; Yamakawa, S.; Morikawa, Y.; Akita, T.; Tanaka, S.; Hyodo, S.; Kohyama, M. *J. Phys. Conf. Ser.* **2008**, *100*(7), 072044.
307. Xian-Qi, D.; Ya-Nan, T.; Jian-Hua, Z.; Ya-Wei, D. *J. Phys.: Condens. Matter* **2010**, *22*(31), 316005.
308. Okazaki-Maeda, K.; Morikawa, Y.; Tanaka, S.; Kohyama, M. *Surf. Sci.* **2010**, *604*(2), 144–154.
309. Fampiou, I.; Ramasubramaniam, A. *J. Phys. Chem. C* **2012**, *116*(11), 6543–6555.
310. Dai, X.-Q.; Tang, Y.-N.; Dai, Y.-W.; Li, Y.-H.; Zhao, J.-H.; Zhao, B.; Yang, Z.-X. *Phys. Rev. B* **2011**, *20*(5), 056801.
311. Park, N.; Sung, D.; Lim, S.; Moon, S.; Hong, S. *Appl. Phys. Lett.* **2009**, *94*(7), 073105.
312. Cuong, N. T.; Fujiwara, A.; Mitani, T.; Chi, D. H. *Comput. Mater. Sci.* **2008**, *44*(1), 163–166.
313. Chi, D. H.; Cuong, N. T.; Tuan, N. A.; Kim, Y.-T.; Bao, H. T.; Mitani, T.; Ozaki, T.; Nagao, H. *Chem. Phys. Lett.* **2006**, *432*(1–3), 213–217.
314. Okazaki-Maeda, K.; Akita, T.; Tanaka, S.; Kohyama, M. *Mater. Trans.* **2008**, *49*(11), 2441–2444.
315. Martin, A.; Biplab, S.; Olle, E.; Natalia, V. S. *J. Phys.: Condens. Matter* **2011**, *23*(20), 205301.

316. Srivastava, M. K.; Wang, Y.; Kemper, A. F.; Cheng, H.-P. *Phys. Rev. B* **2012**, *85*(16), 165444.
317. Liu, L.; Su, Y.; Gao, J.; Zhao, J. *Physica E* **2012**, *46*(0), 6–11.
318. Liu, X.; Yao, K. X.; Meng C. G.; Han, Y. *Dalton Trans.* **2012**, *41*(4), 1289–1296.
319. Lim, D.-H.; Negreira, A. S.; Wilcox, J. *J. Phys. Chem. C* **2011**, *115*(18), 8961–8970.
320. Zhou, L. G.; Shi, S. Q. *Carbon* **2003**, *41*(3), 613–615.
321. Rahmat, M.; Hubert, P. *Compos. Sci. Technol.* **2011**, *72*(1), 72–84.
322. Lv, C.; Xue, Q.; Xia, D.; Ma, M.; Xie, J.; Chen, H. *J. Phys. Chem. C* **2010**, *114*(14), 6588–6594.
323. Lv, C.; Xue, Q.; Xia, D.; Ma, M. *Appl. Surf. Sci.* **2012**, *258*(6), 2077–2082.
324. Zheng, Q.; Xue, Q.; Yan, K.; Gao, X.; Li, Q.; Hao, L. *J. Appl. Phys.* **2008**, *103*(4), 044302.
325. Zhu, J.; Kim, J.; Peng, H.; Margrave, J. L.; Khabashesku, V. N.; Barrera, E. V. *Nano Letters* **2003**, *3*(8), 1107–1113.
326. Velasco-Santos, C.; Martínez-Hernández, A. L.; Fisher, F. T.; Ruoff, R.; Castaño, V. M. *Chem. Mater.* **2003**, *15*(23), 4470–4475.
327. Hughes, T. V.; Chambers, C. R. *U.S. patent 405, 480.* **1889**.
328. Bartholomew, C. H. *Catal. Rev.* **1982**, *24*(1), 67–112.
329. *Carbon Filaments and Nanotubes: Common Origins, Differing Applications?* Biró, L. P.; Bernardo, C. A.; Tibbetts, G. G.; Lambin, P., Eds. In NATO Science Series E: Applied Sciences, Vol. 372, **2001**.
330. Moy, D.; Hoch, R. *WO 93/24214 to Hyperion Catalysis International INC.* **1993**.
331. Ponce, A. A.; Sims, C. M.; Liu, Z.; Gaskell, K. J.; Lai, L. C.; Chiou, W. A.; Eichhorn, B. W. *J. Mater. Sci.* **2013**, *48*(6), 2670–2680.
332. Georgakilas, V.; Gournis, D.; Tzitzios, V.; Pasquato, L.; Guldi, D. M.; Prato, M. *J. Mater. Chem.* **2007**, *17*(26), 2679–2694.
333. De Jong, K. P.; Geus, J. W. *Catal. Rev.* **2000**, *42*(4), 481–510.
334. Goldshleger, N. F. *Fullerene Sci. Technol.* **2001**, *9*(3), 255–280.
335. Candelaria, S. L.; Shao, Y.; Zhou, W.; Li, X.; Xiao, J.; Zhang, J.-G.; Wang, Y.; Liu, J.; Li, J.; Cao, G. *Nano Energy* **2012**, *1*(2), 195–220.
336. Wu, Z.-S.; Zhou, G.; Yin, L.-C.; Ren, W.; Li, F.; Cheng, H.-M. *Nano Energy* **2012**, *1*(1), 107–131.
337. Hirsch, A.; Vostrowski, O. Functionalization of Carbon Nanotubes. In *Functional Molecular Nanostructures*; Schlüter, A. D., Ed.; Springer: Berlin Heidelberg, **2005**, pp. 193–237.
338. Tasis, D.; Tagmatarchis, N.; Bianco, A.; Prato, M. *Chem. Rev.* **2006**, *106*(3), 1105–1136.

339. Georgakilas, V.; Otyepka, M.; Bourlinos, A. B.; Chandra, V.; Kim, N.; Kemp, K. C.; Hobza, P.; Zboril, R.; Kim, K. S. *Chem. Rev.* **2012**, *112*(11), 6156–6214.
340. Stein, A.; Wang, Z.; Fierke, M. A. *Adv. Mater.* **2009**, *21*(3), 265–293.
341. Salame, I. I.; Bandosz, T. J. *J. Colloid Interf. Sci.* **2001**, *240*, 252–258.
342. Menendez, J. A.; Phillips, J.; Xia, B.; Radovic, L. R. *Langmuir* **1996**, *12*, 4404–4410.
343. Fuente, E.; Menendez, J. A.; Suarez, D.; Montes-Moran, M. A. *Langmuir* **2003**, *19*(8), 3505–3511.
344. Park, S.; Hu, Y.; Hwang, J. O.; Lee, E.-S.; Casabianca, L. B.; Cai, W.; Potts, J. R.; Ha, H.-W.; Chen, S.; Oh, J.; Kim, S. O.; Kim, Y.-H.; Ishii, Y.; Ruoff, R. S. *Nat. Commun.* **2012**, *3*, 638.
345. Pei, S.; Cheng, H.-M. *Carbon* **2012**, *50*(9), 3210–3228.
346. Stohr, A.; Boehm, H. P.; Schlogl, R. *Carbon* **1991**, *29*, 707–720.
347. Mabena, L. F.; Ray, S. S.; Mhlanga, S. D.; Coville, N. J. *Appl. Nanosci.* **2011**, *1*, 67–77.
348. Boehm, P. Catalytic Properties of Nitrogen-Containing Carbons. In *Carbon Materials for Catalysis*; Figueiredo, P. S. a. J. L., Ed.; J. Wiley & Sons: Hoboken (NJ), **2009**, pp. 219–265.
349. Bandosz, T. Surface Chemistry of Carbon Materials. In *Carbon Materials for Catalysis*; Figueiredo, P. S. a. J. L., Ed.; J. Wiley & Sons: Hoboken (NJ), **2009**, pp. 45–92.
350. Zhu, J.; Holmen A.; Chen, D. *Chem Cat Chem* **2013**, *5*(2), 378–401.
351. Serp, P.; Corrias, M.; Kalck, P. *Appl. Catal. A* **2003**, *253*(2), 337–358.
352. Bitter, J. H. *J. Mater. Chem.* **2010**, *20*(35), 7312–7321.
353. Pan, X.; Bao, X. *Chem. Commun.* **2008**, (47), 6271–6281.
354. Garg, B.; Ling, Y.-C. *Green Mater.* **2013**, *1*(1), 47–61.
355. Yu, D.; Nagelli, E.; Du, F.; Dai, L. *J. Phys. Chem. Lett.* **2010**, *1*(14), 2165–2173.
356. Sun, X.; Wang, R.; Su, D. *Chin. J. Catal.* **2013**, *34*(3), 508–523.
357. Li, B.; Xu, Z. *J. Am. Chem. Soc.* **2009**, (131), 16380–16382.
358. Gao, Y.; Ma, D.; Wang, C.; Guan, J.; Bao, X. *Chem. Commun.* **2011**, *47*(8), 2432–2434.
359. Kochleofl, K., in *Handbook of Heterogeneous Catalysis*; Ertl, G., Knözinger, H., Schüth, F., Weit Kamp, J. Eds.; Wiley-VCH: Weinheim, **1997**, pp. 2151–2159.
360. Grunewald, G. C.; Drago, R. S. *J. Mol. Catal.* **1990**, *58*, 227–233.
361. Drago, R. S.; Jurczyk, K. *Appl. Catal. A.* **1994**, *112*, 117–124.
362. Guerrero-Ruiz, A.; Rodríguez-Ramos, I. *Carbon* **1994**, *32*, 23–29.
363. Kane, M. S.; Kao, L. C.; Mariwala, R. K.; Hilscher, D. F.; Foley, H. C. *Ind. Eng. Chem. Res.* **1996**, *35*(10), 3319–3331.

364. Pereira, M. F. R.; Órfão, J. J. M.; Figueiredo, J. L. *Carbon* **2002**, *40*, 2393–2401.
365. Pereira, M. F. R.; Órfão, J. J. M.; Figueiredo, J. L. *Colloids Surf. A* **2004**, *241*, 165–171.
366. Pereira, M. F. R.; Órfão, J. J. M.; Figueiredo, J. L. *Appl. Catal. A* **1999**, *184*, 153–160.
367. Pereira, M. F. R.; Órfão, J. J. M.; Figueiredo, J. L. *Appl. Catal. A* **2000**, *196*, 43–54.
368. Pereira, M. F. R.; Órfão, J. J. M.; Figueiredo, J. L. *Appl. Catal. A* **2001**, *218*, 307–318.
369. Iwasawa, Y.; Nobe, H.; Ogasawara, S. *J. Catal.* **1973**, *31*, 444–449.
370. Schraut, A.; Emig, G.; Hofmann, H. *J. Catal.* **1988**, *112*, 221–228.
371. Maciá-Agulló, J. A.; Cazorla-Amorós, D.; Linares-Solano, A.; Wild, U.; Su, D. S.; Schlögl, R. *Catal. Today* **2005**, *102–103*, 248–253.
372. Delgado, J. J.; Su, D. S.; Rebmann, G.; Keller, N.; Gajovic, A.; Schlogl, R. *J. Catal.* **2006**, *244*, 126–129.
373. Delgado, J. J.; Vieira, R.; Rebmann, G.; Su, D. S.; Keller, N.; Ledoux, M. J.; Schlögl, R. *Carbon* **2006**, *44*, 809–812.
374. Zhao, T. J.; Sun, W. Z.; Gu, X. Y.; Ronning, M.; Chen, D.; Dai, Y. C.; Yuan, W. K.; Holmen, A. *Appl. Catal. A* **2007**, *323*, 135–146.
375. Su, D. S.; Delgado, J. J.; Liu, X.; Wang, D.; Schlögl, R.; Wang, L.; Zhang, Z.; Shan, Z.; Xiao, F. S. *Chem. Asian J.* **2009**, *4*, 1108–1113.
376. Maksimova, N.; Mestl, G.; Schlögl, R. *Stud. Surf. Sci. Catal.* **2001**, *133*, 383–389.
377. Mestl, G.; Maksimova, N. I.; Keller, N.; Roddatis, V. V.; Schlögl, R. *Angew. Chem. Int. Ed.* **2001**, *40*(11), 2066–2068.
378. Delgado, J. J.; Chen, X.; Tessonnier, J. P.; Schuster, M. E.; Del Rio, E.; Schlögl, R.; Su, D. S. *Catal. Today* **2010**, *150*, 49–54.
379. Su, D.; Maksimova, N. I.; Mestl, G.; Kuznetsov, V. L.; Keller, V.; Schlögl, R.; Keller, N. *Carbon* **2007**, *45*, 2145–2151.
380. Pereira, M. F. R.; Figueiredo, J. L.; Órfão, J. J. M.; Serp, P.; Kalck, P.; Kihn, Y. *Carbon* **2004**, *42*(14), 2807–2813.
381. Khavryuchenko, O. V.; Frank, B.; Trunschke, A.; Hermann, K.; Schlögl, R. *J. Phys. Chem. C* **2013**, *117*(12), 6225–6234.
382. Jang, D.; Jang, H.; Kim, G.; Kim, G.-J. *Res. Chem. Intermed.* **2011**, *37*(9), 1145–1156.
383. Sui, Z. J.; Zhou, J. H.; Dai, Y. C.; Yuan, W. K. *Catal. Today* **2005**, *106*, 90–94.
384. Rinaldi, A.; Zhang, J.; Frank, B.; Su, D. S.; Hamid, S. B. A.; Schlögl, R. *Chem Sus Chem* **2010**, *3*(2), 254–260.
385. Bai, Z.; Li, P.; Liu, L.; Xiong, G. *Chem Cat Chem* **2012**, *4*(2), 260–264.

386. Zhang, J.; Liu, X.; Blume, R.; Zhang, A.; Schlögl, R.; Su, D. *Science* **2008**, *322*, 73–77.
387. Liu, X.; Frank, B.; Zhang, W.; Cotter, T. P.; Schlögl, R.; Su, D. S. *Angew. Chem. Int. Ed.* **2011**, *50*(14), 3318–3322.
388. Dreyer, D. R.; Jia, H.-P.; Bielawski, C. W. *Angew. Chem. Int. Ed.* **2010**, *49*(38), 6813–6816.
389. Jia, H.-P.; Dreyer, D. R.; Bielawski, C. W. *Adv. Synth. Catal.* **2011**, *353*, 528–532.
390. Jia, H.-P.; Dreyer, D. R.; Bielawski, C. W. *Tetrahedron* **2011**, *67*(24), 4431–4434.
391. Chizari, K.; Deneuve, A.; Ersen, O.; Florea, I.; Liu, Y.; Edouard, D.; Janowska, I.; Begin, D.; Pham-Huu, C. *Chem Sus Chem* **2012**, *5*(1), 102–108.
392. Planeix, J. M.; Coustel, N.; Coq, B.; Brotons, V.; Kumbhar, P. S.; Dutartre, R.; Geneste, P.; Bernier, P.; Ajayan, P. M. *J. Am. Chem. Soc.* **1994**, *116*(17), 7935–7936.
393. Gallezot, P.; Richard, D. *Catal. Rev. - Sci. Eng.* **1998**, *40*(1–2), 81–126.
394. Giordano, R.; Serp, P.; Kalck, P.; Kihn, Y.; Schreiber, J.; Marhic, C.; Duvail, J.-L. *Eur. J. Inorg. Chem.* **2003**, *4*, 610–617.
395. Tessonnier, J.-P.; Pesant, L.; Ehret, G.; Ledoux, M. J.; Pham-Huu, C. *Appl. Catal. A* **2005**, *288*(1–2), 203–210.
396. Vu, H.; Gonçalves, F.; Philippe, R.; Lamouroux, E.; Corrias, M.; Kihn, Y.; Plee, D.; Kalck, P.; Serp, P. *J. Catal.* **2006**, *240*(1), 18–22.
397. Garcia, T.; Murillo, R.; Cazorla-Amorós, D.; Mastral A. M.; Linares-Solano A. *Carbon* **2004**, *42*(8–9), 1683–1689.
398. Nevskaia, D. M.; Castillejos-Lopez, E.; Guerrero-Ruiz, A.; Muñoz, V. *Carbon*, **2004**, *42*(3), 653–665.
399. Choi, H. C.; Shim, M.; Bangsaruntip, S.; Dai, H. *J. Am. Chem. Soc.* **2002**, *124*(31), 9058–9059.
400. Teddy, J.; Falqui, A.; Corrias, A.; Carta, D.; Lecante P.; Gerber, I.; Serp, P. *J. Catal.* **2011**, *278*(1), 59–70.
401. Toebes, M. L.; Prinsloo, F. F.; Bitter, J. H.; Dillen A. J. v.; Jong, K. P. d. *J. Catal.* **2003**, *214*, 78–87.
402. Toebes, M. L.; Zhang, Y. H.; Hajek, J.; Nijhuis, T. A.; Bitter, J. H.; Dillen, A. J. v.; Murzin, D. Y.; Koningsberger, D. C.; Jong, K. P. d. *J. Catal.* **2004**, *226*, 215–225.
403. Castillejos, E.; Debouttière, P.-J.; Roiban, L.; Solhy, A.; Martinez, V.; Kihn, Y.; Ersen, O.; Philippot, K.; Chaudret, B.; Serp, P. *Angew. Chem. Int. Ed.* **2009**, *48*(14), 2529–2533.
404. Karousis, N.; Tsotsou, G.-E.; Evangelista, F.; Rudolf, P.; Ragoussis, N.; Tagmatarchis, N. *J. Phys. Chem. C* **2008**, *112*(35), 13463–13469.

405. Liu, G. J.; Larson, E. D.; Williams, R. H.; Kreutz, T. G.; Guo, X. B. *Energy Fuels* **2011**, *25*, 415–437.
406. Huber, G. W.; Iborra, S.; Corma, A. *Chem. Rev.* **2006**, *106*(9), 4044–4098.
407. Leckel, D. *Energy Fuels* **2009**, *23*, 2342–2358.
408. vanNiekerk, M. J.; Fletcher J. C. Q.; Oconnor, C. T. *Appl. Catal. A* **1996**, *138*(1), 135–145.
409. Iglesia, E. *Appl. Catal. A* **1997**, *161*(1–2), 59–78.
410. Kang, J. C.; Zhang, S. L.; Zhang, Q. H.; Wang, Y. *Angew. Chem. Int. Ed.* **2009**, *48*(14), 2565–2568.
411. Tavasoli, A.; Sadagiani, K.; Khorashe, F.; Seifkordi, A. A.; Rohaniab, A. A.; Nakhaeipour, A. *Fuel Process. Technol.* **2008**, *89*(5), 491–498.
412. Tavasoli, A.; Abbaslou, R. M. M.; Trepanier, M.; Dalai, A. K. *Appl. Catal. A* **2008**, *345*(2), 134–142.
413. Chen, W.; Fan, Z. L.; Pan, X. L.; Bao, X. H. *J. Am. Chem. Soc.* **2008**, *130*(29), 9414–9419.
414. Abbaslou, R. M. M.; Tavassoli, A.; Soltan, J.; Dalai, A. K. *Appl. Catal. A* **2009**, *367*(1–2), 47–52.
415. Pan, X. L.; Fan, Z. L.; Chen, W.; Ding, Y. J.; Luo, H. Y.; Bao, X. H. *Nat. Mater.* **2007**, *6*(7), 507–511.
416. Mallat, T.; Baiker, A. *Chem. Rev.* **2004**, *104*(6), 3037–3058.
417. Villa, A.; Wang, D.; Dimitratos, N.; Su, D. S.; Trevisan, V.; Prati, L. *Catal. Today* **2010**, *150*(1–2), 8–15.
418. Villa, A.; Wang, D.; Spontoni, P.; Arrigo, R.; Su, D.; Prati, L. *Catal. Today* **2010**, *157*(1–4), 89–93.
419. Qin, W.; Wei, L.; Dong, C.; Xiao, X.; Zheng, Z.; Yang, Y. *Chem. Phys. Lett.* **2013**, doi: 10.1016/j.cplett.2013.1004.1004.
420. Qin, W.; Li, X. *J. Phys. Chem. C* **2010**, *114*(44), 19009–19015.
421. Hoffmann, M. R.; Martin, S. T.; Choi, W. Y.; Bahnemann, D. W. *Chem. Rev.* **1995**, *95*(1), 69–96.
422. Krishna, V.; Pumprueg, S.; Lee, S. H.; Zhao, J.; Sigmund, W.; Koopman, B.; Moudgil, B. M. *Process. Saf. Environ. Protect.* **2005**, *83*(B4), 393–397.
423. Xiang, Q.; Yu, J.; Jaroniec, M. *Chem. Soc. Rev.* **2012**, *41*(2), 782–796.
424. Lightcap, I. V.; Kosel, T. H.; Kamat, P. V. *Nano Lett.* **2010**, *10*(2), 577–583.
425. Kongkanand, A.; Dominguez, R. M.; Kamat, P. V. *Nano Lett.* **2007**, *7*(3), 676–680.
426. Woan, K.; Pyrgiotakis, G.; Sigmund, W. *Adv. Mater.* **2009**, *21*(21), 2233–2239.
427. Lam, S.-m.; Sin, J.-c.; Abdullah, A. Z.; Mohamed, A. R. Fullerenes, Nanotubes, Carbon Nanostruct. **2013**, DOI: 10.1080/1536383X 2012.690458.

428. Wang, Q.; Yang, D.; Chen, D. M.; Wang, Y. B.; Jiang, Z. Y. *J. Nanopart. Res.* **2007**, *9*(6), 1087–1096.
429. Wang, W. D.; Serp, P.; Kalck, P.; Silva, C. G.; Faria, J. L. *Mater. Res. Bull.* **2008**, *43*(4), 958–967.
430. Wang, W. D.; Serp, P.; Kalck, P.; Faria, J. L. *Appl. Catal. B* **2005**, *56*(4), 305–312.
431. An, G. M.; Ma, W. H.; Sun, Z. Y.; Liu, Z. M.; Han, B. X.; Miao, S. D.; Miao, Z. J.; Ding K. L. *Carbon* **2007**, *45*(9), 1795–1801.
432. Zhu, C.; Dong, S. *Nanoscale*, **2013**, *5*(5), 1753–1767.
433. Hur, S. H.; Park, J.-N. *J. Chem. Eng.* **2013**, *8*(2), 218–233.
434. Kauffman, D. R.; Star, A. *Analyst* **2010**, *135*(11), 2790–2797.
435. Pumera, M. *Chem. Soc. Rev.* **2010**, *39*(11), 4146–4157.
436. Davies, T. J.; Hyde, M. E.; Compton, R. G. *Angew. Chem.* **2005**, *117*(32), 5251–5256.
437. Goh, M. S.; Pumera, M. *Chem. Asian J.* **2010**, *5*(11), 2355–2357.
438. Guo, S.; Zhang, S.; Wu L.; Sun, S. *Angew. Chem. Int. Ed.* **2012**, *51*(47), 11770–11773.
439. Qu, L.; Liu, Y.; Baek, J.-B.; Dai, L. *ACS Nano* **2010**, *4*(3), 1321–1326.
440. Gong, K.; Du, F.; Xia, Z.; Durstock, M.; Dai, L. *Science* **2009**, *323*(5915), 760–764.
441. Chen, H.; Sun, F.; Wang, J.; Li, W.; Qiao, W.; Ling, L.; Long, D. *J. Phys. Chem. C* **2013**, *117*(16), 8318–8328.
442. Zhang, L.; Xia Z. *J. Phys. Chem. C* **2011**, *115*(22), 11170–11176.
443. Li, W. Z.; Liang, C. H.; Qiu, J. S.; Zhou, W. J.; Han, H. M.; Wei, Z. B.; Sun, G. Q.; Xin, Q. *Carbon* **2002**, *40*(5), 791–794.
444. Li, W. Z.; Liang, C. H.; Zhou, W. J.; Qiu, J. S.; Zhou, Z. H.; Sun, G. Q.; Xin, Q. *J. Phys. Chem. B* **2003**, *107*(26), 6292–6299.
445. Li, W. Z.; Liang, C. H.; Zhou, W. J.; Qiu, J. S.; Li, H. Q.; S. G. Q.; Xin, Q. *Carbon* **2004**, *42*(2), 436–439.
446. Liu, J.; Lai, L.; Sahoo, N. G.; Zhou, W.; Shen, Z.; Chan, S. H. *Aust. J. Chem.* **2012**, *65*(9), 1213–1222.
447. Zhang, W.; Ravi, S.; Silva, P. *Rev. Adv. Mater. Sci.* **2011**, *29*, 1–14.
448. Ralph, T. R.; Hogarth, M. P. *Platinum Met. Rev.* **2002**, *46*(1), 3–14.
449. Kangasniemi, K. H.; Condit, D. A.; Jarvi, T. D. *J. Electrochem. Soc.* **2004**, *151*(4), E125–E132.
450. Liu, J. G.; Zhou, Z. H.; Zhao, X. X.; Xin, Q.; Sun, G. Q.; Yi, B. L. *Phys. Chem. Chem. Phys.* **2004**, *6*(1), 134–137.
451. Shao, Y. Y.; Yin, G. P.; Gao, Y. Z. *J. Power Sources* **2007**, *171*(2), 558–566.
452. Wang, X.; Li, W. Z.; Chen, Z. W.; Waje, M.; Yan, Y. S. *J. Power Sources* **2006**, *158*(1), 154–159.

453. Girishkumar, G.; Rettker, M.; Underhile, R.; Binz, D.; Vinodgopal, K.; McGinn, P.; Kamat, P. *Langmuir*, **2005**, *21*(18), 8487–8494.
454. Wu, G.; Xu, B. Q. *J. Power Sources* **2007**, *174*(1), 148–158.
455. Chen, Y.; Zhang, G. J.; Ma, J. A.; Zhou, Y. M.; Tang, Y. W.; Lu, T. H. *Int. J. Hydrogen Energy* **2010**, *35*(19), 10109–10117.
456. Carmo, M.; Paganin, V. A.; Rosolen, J. M.; Gonzalez, E. R. *J. Power Sources* **2005**, *142*(1–2), 169–176.
457. Kim, C.; Kim, Y. J.; Kim, Y. A.; Yanagisawa, T.; Park, K. C.; Endo, M.; Dresselhaus, M. S. *J. Appl. Phys.* **2004**, *96*(10), 5903–5905.
458. Liang, C. H.; Ding, L.; Li, C. A.; Pang, M.; Su, D. S.; Li, W. Z.; Wang, Y. M. *Energy Environ. Sci.* **2010**, *3*(8), 1121–1127.
459. Pang, M.; Li, C.; Ding, L.; Zhang, J.; Su, D. S.; Li, W. Z.; Liang, C. H. *Ind. Eng. Chem. Res.* **2010**, *49*(9), 4169–4174.
460. Chen, Z.; Higgins, D.; Chen, Z. *Carbon* **2010**, *48*(11), 3057–3065.
461. San, C. H.; Hong, C. W. *J. Electrochem. Soc.* **2012**, *159*(5), K116–K121.
462. Jhan, J.-Y.; Huang, Y.-W.; Hsu, C.-H.; Teng, H.; Kuo, D.; Kuo, P.-L. *Energy* **2013**, *53*(0), 282–287.
463. Yun, Y. S.; Kim, D.; Tak, Y.; Jin, H.-J. *Synth. Met.* **2011**, *161*(21–22), 2460–2465.
464. Wu, G.; More, K. L.; Xu, P.; Wang, H.-L.; Ferrandon, M.; Kropf, A. J.; Myers, D. J.; Ma, S.; Johnston, C. M.; Zelenay, P. *Chem. Commun.* **2013**, *49*(32), 3291–3293.
465. Jyothirmayee Aravind, S. S.; Imran Jafri, R.; Rajalakshmi, N.; Ramaprabhu, S. *J. Mater. Chem.* **2011**, *21*(45), 18199–18204.
466. Jha, N.; Jafri, R. I.; Rajalakshmi, N.; Ramaprabhu, S. *Int. J. Hydrogen Energy* **2011**, *36*(12), 7284–7290.
467. Lv, R.; Cui, T.; Jun, M.-S.; Zhang, Q.; Cao, A.; Su, D. S.; Zhang, Z.; Yoon, S.-H.; Miyawaki, J.; Mochida, I.; Kang, F. *Adv. Funct. Mater.* **2011**, *21*(5), 999–1006.
468. Wujcik, E. K.; Monty, C. N. *Wiley Interdiscip. Rev. Nanomed. Nanobiotechnol.* **2013**, *5*(3), 233–249.
469. Mahar, B.; Laslau, C.; Yip, R.; Yu, S. *IEEE Sens. J.* **2007**, *7*(2), 266–284.
470. Yavari, F.; Koratkar, N. *J. Phys. Chem. Lett.* **2012**, *3*(13), 1746–1753.
471. Brownson, D. A. C.; Banks, C. E. *Analyst* **2010**, *135*(11), 2768–2778.
472. Kong, J.; Franklin, N. R.; Zhou, C.; Chapline, M. G.; Peng, S.; Cho, K.; Dai, H. *Science* **2000**, *287*(5453), 622–625.
473. Kauffman, D. R.; Star, A. *J. Phys. Chem. C* **2008**, *112*(12), 4430–4434.
474. Bekyarova, E.; Kalinina, I.; Itkis, M. E.; Beer, L.; Cabrera, N.; Haddon, R. C. *J. Am. Chem. Soc.* **2007**, *129*(35), 10700–10706.

475. Qi, P.; Vermesh, O.; Grecu, M.; Javey, A.; Wang, Q.; Dai, H.; Peng, S.; Cho, K. J. *Nano Lett.* **2003**, *3*(3), 347–351.
476. Jennifer, S.-O.; Hung-Ta, W.; Byoung, S. K.; Zhuangchun, W.; Fan, R.; Andrew, G. R.; Stephen, J. P. *Nanotechnology* **2005**, *16*(10), 2218.
477. Kong, J.; Chapline, M. G.; Dai, H. *Adv. Mater.* **2001**, *13*(18), 1384–1386.
478. Star, A.; Joshi, V.; Skarupo, S.; Thomas, D.; Gabriel, J.-C. P. *J. Phys. Chem. B* **2006**, *110*(42), 21014–21020.
479. Kauffman, D. R.; Sorescu, D. C.; Schofield, D. P.; Allen, B. L.; Jordan, K. D.; Star, A.. *Nano Lett.* **2010**, *10*(3), 958–963.
480. Bittencourt, C.; Felten, A.; Espinosa, E. H.; Ionescu, R.; Llobet, E.; Correig, X.; Pireaux, J. J. *Sens. Actuators B* **2006**, *115*(1), 33–41.
481. Kauffman, D. R.; Star, A. *Nano Lett.* **2007**, *7*(7), 1863–1868.
482. Oleksandr, K.; Brett, L. A.; Alexander, S. *Nanotechnology* **2007**, *18*(37), 375502.
483. Star, A.; Han, T. R.; Joshi, V.; Gabriel, J. C. P.; Grüner, G. *Adv. Mater.* **2004**, *16*(22), 2049–2052.
484. Kauffman, D. R.; Shade, C. M.; Uh, H.; Petoud, S.; Star, A. *Nat. Chem.* **2009**, *1*(6), 500–506.
485. Collins, P. G.; Bradley, K.; Ishigami, M.; Zettl, A. *Science* **2000**, *287*(5459), 1801–1804.
486. Ratinac, K. R.; Yang, W.; Ringer, S. P.; Braet, F. *Environ. Sci. Technol.* **2010**, *44*(4), 1167–1176.
487. Hwang, E. H.; Adam, S.; Das Sarma, S. *Phys. Rev. B* **2007**, *76*(19), 195421.
488. Hugo, E. R.; Prasoon, J.; Awnish, K. G.; Humberto, R. G.; Milton, W. C.; Srinivas, A. T.; Peter, C. E. *Nanotechnology* **2009**, *20*(24), 245501.
489. Lu, G.; Yu, K.; Ocola, L. E.; Chen, J. *Chem. Commun.* **2011**, *47*(27), 7761–7763.
490. Ren, Y.; Zhu, C.; Cai, W.; Li, H.; Ji, H.; Kholmanov, I.; Wu, Y.; Piner, R. D.; Ruoff, R. S. *Appl. Phys. Lett.* **2012**, *100*(16), 163114.
491. Chen, C. W.; Hung, S. C.; Yang, M. D.; Yeh, C. W.; Wu, C. H.; Chi, G. C.; Ren, F.; Pearton, S. J. *Appl. Phys. Lett.* **2011**, *99*(24), 243502.
492. Dan, Y.; Lu, Y.; Kybert, N. J.; Luo, Z.; Johnson, A. T. C. *Nano Lett.* **2009**, *9*(4), 1472–1475.
493. Jung, I.; Dikin, D.; Park, S.; Cai, W.; Mielke, S. L.; Ruoff, R. S. *J. Phys. Chem. C* **2008**, *112*(51), 20264–20268.
494. Robinson, J. T.; Perkins, F. K.; Snow, E. S.; Wei, Z.; Sheehan, P. E. *Nano Lett.* **2008**, *8*(10), 3137–3140.
495. Kauffman, D. R.; Star, A. *Angew. Chem. Int. Ed.* **2008**, *47*(35), 6550–6570.
496. Kaniyoor, A.; Imran Jafri, R.; Arockiadoss, T.; Ramaprabhu, S. *Nanoscale* **2009**, *1*(3), 382–386.
497. Liu, Z.; Tabakman, S.; Welsher, K.; Dai, H. *Nano Res.* **2009**, *2*(2), 85–120.

498. Saito, N.; Usui, Y.; Aoki, K.; Narita, N.; Shimizu, M.; Hara, K.; Ogiwara, N.; Nakamura, K.; Ishigaki, N.; Kato, H.; Taruta, S.; Endo, M. *Chem. Soc. Rev.* **2009**, *38*(7), 1897–1903.
499. Zeng, L.; Alemany, L. B.; Edwards, C. L.; Barron, A. R. *Nano Res.* **2008**, *1*(1), 72–88.
500. Tagmatarchis, N.; Prato, M. *J. Mater. Chem.* **2004**, *14*(4), 437–439.
501. Wu, P.; Chen, X.; Hu, N.; Tam, U. C.; Blixt, O.; Zettl, A.; Bertozzi, C. R. *Angew. Chem. Int. Ed.* **2008**, *47*(27), 5022–5025.
502. Zheng, M.; Jagota, A.; Semke, E. D.; Diner, B. A.; McLean, R. S.; Lustig, S. R.; Richardson, R. E.; Tassi, N. G. *Nat. Mater.* **2003**, *2*(5), 338–342.
503. Katoch, J.; Kim, S. N.; Kuang, Z.; Farmer, B. L.; Naik, R. R.; Tatulian, S. A.; Ishigami, M. *Nano Lett.* **2012**, *12*(5), 2342–2346.
504. Jeng, E. S.; Moll, A. E.; Roy, A. C.; Gastala, J. B.; Strano, M. S. *Nano Lett.* **2006**, *6*(3), 371–375.
505. Fan, H.; Wang, L.; Zhao, K.; Li, N.; Shi, Z.; Ge, Z.; Jin, Z. *Biomacromol.* **2010**, *11*(9), 2345–2351.
506. Sanchez, V. C.; Jachak, A.; Hurt, R. H.; Kane, A. B. *Chem. Res. Toxicol.* **2011**, *25*(1), 15–34.
507. Ye, J.-S.; Wen, Y.; De Zhang, W.; Ming, Gan L.; Xu, G. Q.; Sheu, F.-S. *Electrochem. Commun.* **2004**, *6*(1), 66–70.
508. Kwon, S.-Y.; Kwen, H.-D.; Choi, S.-H. *J. Sensors* **2012**, *2012*, 784167.
509. Cheng, Y.; Liu, Y.; Huang, J.; Li, K.; Xian, Y.; Zhang, W.; Jin, L. *Electrochim. Acta* **2009**, *54*(9), 2588–2594.
510. Shi, N. W. Kam; Jessop, T. C.; Wender, P. A.; Dai, H. *J. Am. Chem. Soc.* **2004**, *126*(22), 6850–6851.
511. Liu, Z.; Fan, A. C.; Rakhra, K.; Sherlock, S.; Goodwin, A.; Chen, X.; Yang, Q.; Felsher, D. W.; Dai, H. *Angew. Chem. Int. Ed.* **2009**, *48*(41), 7668–7672.
512. Yang, K.; Zhang, S.; Zhang, G.; Sun, X.; Lee, S.-T.; Liu, Z. *Nano Lett.* **2010**, *10*(9), 3318–3323.
513. Liu, Z.; Robinson, J. T.; Sun, X.; Dai, H. *J. Am. Chem. Soc.* **2008**, *130*(33), 10876–10877.
514. Allen, B. L.; Kichambare, P. D.; Gou, P.; Vlasova, I. I.; Kapralov, A. A.; Konduru, N.; Kagan, V. E.; Star, A. *Nano Lett.* **2008**, *8*(11), 3899–3903.
515. Kagan, V. E.; Konduru, N. V.; Feng, W.; Allen, B. L.; Conroy, J.; Volkov, Y.; Vlasova, I. I.; Belikova, N. A.; Yanamala, N.; Kapralov, A.; Tyurina, Y. Y.; Shi, J.; Kisin, E. R.; Murray, A. R.; Franks, J.; Stolz, D.; Gou, P.; Klein-Seetharaman, J.; Fadeel, B.; Star, A.; Shvedova, A. A. *Nat. Nanotechnol.* **2010**, *5*(5), 354–359.
516. Allen, B. L.; Kotchey, G. P.; Chen, Y.; Yanamala, N. V. K.; Klein-Seetharaman, J.; Kagan, V. E.; Star, A. *J. Am. Chem. Soc.* **2009**, *131*(47), 17194–17205.

517. Bianco, A.; Kostarelos, K.; Prato, M. *Chem. Commun.* **2011**, *47*(37), 10182–10188.
518. Li, C.; Adamcik, J.; Mezzenga, R. *Nat. Nanotechnol.* **2012**, *7*(7), 421–427.
519. Kostarelos, K. *Nat. Biotechnol.* **2008**, *26*(7), 774–776.
520. Jong, W. H. D.; Borm, P. J. A. *Int. J. Nanomedicine* **2008**, *3*(2), 133–149.
521. Patel, H. J.; Kwon, S. *J. Expos. Sci. Environ. Epidemiol.* **2013**, *23*(1), 101–108.
522. Bussy, C.; Ali-Boucetta, H.; Kostarelos, K. *Acc. Chem. Res.* **2012**, *46*(3), 692–701.

This page intentionally left blank

Chapter 3

Chemical Manipulation of Graphene in Dispersions

*Jesús Iván Tapia and Mildred Quintana**

Instituto de Física, Universidad Autónoma de San Luis Potosí
77290 SLP, México

1. Introduction 186

2. Liquid-Phase Exfoliated Graphene 187
   2.1. Ultrasonication of graphite 187
      2.1.1. Graphene dispersions in organic solvents 188
      2.1.2. Graphene dispersions in surfactant solutions 190
   2.2. Non-ultrasonication techniques 190
      2.2.1. Intercalation compounds 190
      2.2.2. Ionics compounds 191
      2.2.3. Ball-milling production 193
      2.2.4. Supercritical fluids 194
      2.2.5. Unzipping of carbon nanotubes 194
3. Other Nanostructures from Liquid-Phase Exfoliated Graphene 195
   3.1. Deformation, folding, and stabilization 196
   3.2. Ultrasonication of graphite 196
      3.2.1. Tiopronin as antioxidant molecule 196
      3.2.2. Transformation of few-layer graphene into MWNTs 197
4. Covalent Functionalization of Graphene in Dispersions 199
   4.1. Free radical addition 201
   4.2. Dienophiles addition 201
5. Graphene Composites 204
   5.1. Graphene/polymer composites 206
   5.2. Synthesis of graphene/polymer composites 207
   5.3. Graphene/inorganic material composites 208

* Corresponding author. E-mail: mildred@ifisica.uaslp.mx

5.4. Synthesis of graphene–inorganic nanocomposites 209
5.5. Miscellaneous applications of graphene 210
6. Conclusions 212
Acknowledgments 212
References 212

1. Introduction

Thanks to its 2D nature, graphene has a host of unique electronic properties not seen in thicker carbon films or other carbon nanostructures. This includes conduction electrons that travel near to the speed of light and have zero mass.[1] Besides, graphene is the thinnest known material and the strongest ever measured, it shows record thermal conductivity and stiffness, it is impermeable to gases and it has the right proportion between brittleness and ductility.[2] As a consequence, graphene has rapidly emerged as a rising star in the field of material science. However, in order to improve and extend the applications of graphene, a methodology for a mass-scale production is still necessary.

Several methods have been established for graphene preparation, such as micromechanical cleavage,[3] chemical vapor deposition,[4] graphitization of silicon carbide,[5] anodic bonding,[6] unzipping of carbon nanotubes (CNTs),[7] organic synthesis,[8] reduction of graphene oxide (GO),[9] polymer-coated graphene,[10] liquid-phase exfoliation of graphite,[11] electrochemical exfoliation of graphite,[12] graphite intercalation,[13,14] and ball-milling processing of graphite,[15] most of them remaining as demonstration techniques, mainly for basic research, and for providing proof of concept devices. Instead, the recent progress in making stable graphene dispersions[9–15] allows the production of graphene sheets on a more preparative scale and permits the manipulation of the graphene layers by chemical reactions. Then, chemically manipulated graphene samples can be incorporated more easily into new functional materials. The applications of graphene include composites,[16] supercapacitors,[17] batteries,[18] fuel cells,[19] inks,[20] flexible touch screen displays,[21] intelligent coatings,[22] sensors,[23] photonics, and optoelectronic devices.[24]

Dispersions of GO can be produced in large scale.[25] However, this material consists of graphene-like sheets, chemically functionalized with moieties such as carboxyl, hydroxyl, and epoxides, which stabilize the graphene sheets in polar solvents such as water. This functionalization disrupts the electronic structure of graphene. Indeed, GO is an insulator rather than a semimetal and then is conceptually different from graphene.[26] Although the functional groups can be removed by reduction, so far this leaves a significant number

of defects, which continue to disrupt the electronic properties. For this reason, in the present work, GO will not be covered.

Herein, we describe (i) the recent progress in the production of stable dispersions of graphene; (ii) the advances on the chemical functionalization of graphene in this dispersion; (iii) the formation of other carbon nanostructures from liquid-phase graphene; and finally (iv) the integration of graphene layers in composite materials.

The micromechanical cleavage was the first methodology used for the isolation of graphene. This methodology provides a monolayer with excellent structural and electronic qualities.[1–3] However, this procedure is still evaluated as a model technique for basic research. The laborious and time-consuming process of cleavage layer by layer is considered a major hurdle for scaling up to large-scale production.[27] At its place, the use of ultrasound has been expended to automate the cleavage process for graphitic particles in various solvents.

2. Liquid-Phase Exfoliated Graphene

2.1. Ultrasonication of graphite

During the last decades, ultrasound has found important applications in a wide range of materials and chemical syntheses.[28] Both the physical and chemical effects of ultrasound arise from acoustic cavitation that includes the formation, growth, and collapse of bubbles in liquids irradiated with high-intensity ultrasound. During bubble collapse, localized hot spots with ~5000 K and pressures of hundreds of bars are formed within liquids irradiated. These hot spots generate highly reactive species involving radicals from sonolysis of solvent vapor.[29] Recently, some works have shown that by adequately choosing the solvent, the combined mechanochemical effects of high-intensity ultrasound can, in a single step, readily induce exfoliation of graphite to produce graphene.[30] This is a simple, direct, and one-step method to produce graphene by dispersing the as-received graphite in organic solvents, mixed solvent, and surfactant solutions.

Even more, continuous ultrasound can also induce dramatic morphology changes in exfoliated graphite, rolling the nanoribbons in carbon nanoscrolls (CNS).[31] The energy produced by ultrasound irradiation allows the synthesis of various carbon NP at room temperature and atmospheric pressure.[32] During graphene transformation, the precise control over chemical reactions is a key factor for the successful synthesis of other carbon nanoparticles (NPs). In this direction, it is generally accepted, that during the ultrasonication of

polar solvents, high pressures and high temperatures generated by the implosion of cavitation bubbles cause violent collisions between particles at very high speed. These extreme conditions in air-saturated sonicated solutions allow solvent dissociation until the formation of peroxyl radicals.[33] The radical reactions are usually destructive being ultrasonic treatments very effective in breaking C–C bonds.[34] In fact, prolonged sonication treatments result in graphene layers with a higher number of defects and reduction of the sheet size.[35] These defects mostly consist in oxidized carbon atoms at graphene edges in the form of epoxy, carbonyl, and carboxyl groups.

2.1.1. Graphene dispersions in organic solvents

According to Hernandez *et al.*,[11] the exfoliation of graphite in organic solvents can occur only if the net energetic cost is very small. In chemistry, this energy balance is expressed as the enthalpy of mixing per volume unit. The enthalpy of mixing is dependent on the balance of graphene and solvent surface energies.

In order to obtain high yields of exfoliated graphene from graphite, the surface energy of the solvent should match the surface energy of graphite. Based on thermodynamic considerations, authors suggested, and then experimentally demonstrated, that exfoliation and dispersion of pristine graphite to yield graphene is favored for solvents whose surface energy matches or it is very close to that of graphite (~70–80 mJ m^{-2}).[36] In this direction, amide solvents have been recognized among the most successful solvents to disperse other carbon nanostructures as fullerene and CNTs.[37] In fact, the two solvents more frequently used to disperse carbon nanostructures are *N,N*-dimethylformamide (DMF) and *N*-methyl-1–2-pyrrolidone (NMP). By ultrasonication of graphite in these solvents, graphene dispersion was firstly obtained in concentration up to 0.01 mg mL^{-1} with yields of 1% of monolayer.[11] Later, the concentration of graphene in dispersions was increased up to 1.2 mg mL^{-1} with yields of up to 4% monolayer by increasing the sonication for longer times up to 460 h. However, it was observed that longer sonication treatment introduces higher concentration of defects on the graphene sheets. Following this strategy, Tour and coworkers later described isolation of graphene monolayers ultrasonicating graphite dispersed in ortho-dichlorobenzene.[38] Bourlinos *et al.* achieved dispersions of graphene in a variety of organic solvents, including perfluorinated aromatic molecules, pyridine, and chloroacetate. The resulting dispersions showed noticeable high yields achieved by using a combination of extended bath sonication and careful centrifugation.[39] The dispersible material includes mainly monolayer and few-layer graphene (FG), as well as

ultrathin-layered graphitic sheets, which have relatively few amounts of defects. This means that the extended aromatic system of the graphene monolayer is not disrupted and then the electrical conductivity of graphene is almost unaffected. Thus, ultrasonication of graphite in an organic solvent, which makes its atomic planes chemically loosened and intercalated, is a simple process that leads to stable dispersions of submicrometer graphene crystallites and allows mass production for industry applications. However, solvents owning high boiling point prevents its complete evaporation after thermal and annealing processes, resulting in the detriment of the physical properties of the final film or material.[11] To address this problem, Coleman and coworkers, later demonstrated that reasonably stable dispersions of graphene in volatile solvents such as acetone, chloroform, and isopropanol can be prepared in concentrations as high as 0.5 mg mL^{-1}. The dispersions consist of sheets of ~1 μm length and thickness of less than 10 layers. Dispersions in volatile solvents facilitate, for example, the deposition of graphene into substrates (Figure 1).[40]

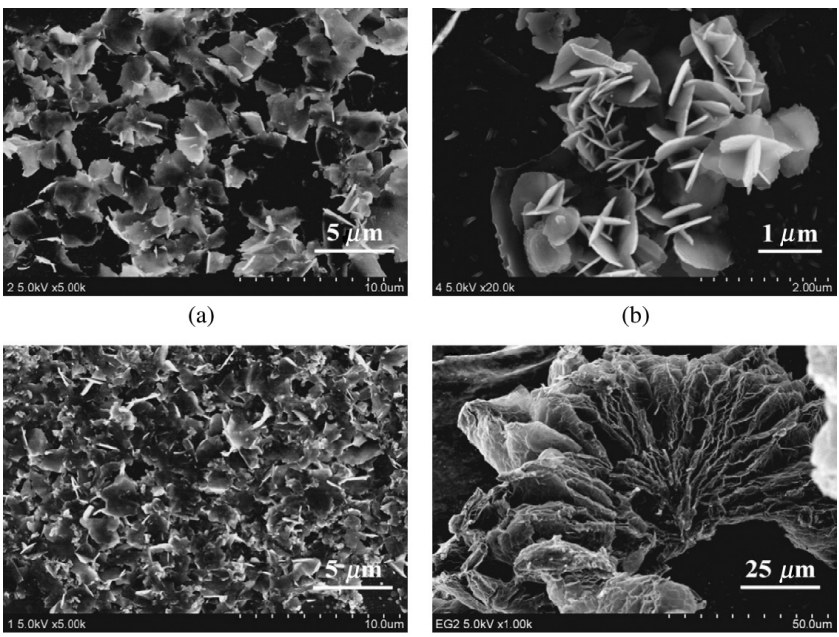

Figure 1. FESEM images of graphene nanosheets from graphene/DMF/H_2O (9:1, v:v) after 6.5 h sonication at various powers: (a) 80 W, (b) 120 W, (c) 80 W, after preservation for two months, and (d) expanded graphite as a comparison. These samples were obtained by depositing graphene/DMF/H_2O solutions onto glass substrates and drying under vacuum at 40 °C. Reproduced from Ref. 26 with permission. Copyright © 2013 Elsevier.

2.1.2. Graphene dispersions in surfactant solutions

Coleman and coworkers have successfully obtained water-soluble graphene by the aqueous-phase exfoliation of graphite in the presence of the surfactant sodium cholate, at concentrations up to 0.3 mg mL^{-1}. In this method, authors used low-power sonication for long times up to 400 h, followed by centrifugation to yield stable dispersions. Transmission electron microscopy (TEM) analysis shows the flakes consist of 1–10 stacked monolayers with up to 20% of monolayer. This material presents the advantage that dispersions can be easily cast into high-quality, free-standing films.[41] Later, the same group stabilized graphene by a range of 12 ionic and non-ionic surfactants. In all cases, the degree of exfoliation, as characterized by flake length and thickness, was similar. The dispersed flakes were typically 750 nm long and, on average, four layers thick (Figure 2). However, the dispersed concentration varied from solvent to solvent. For the ionic surfactants, the concentration scaled with the square of the zeta potential of the surfactant-coated flakes. This suggests that the concentration is proportional to the magnitude of the electrostatic potential barrier, which stabilizes surfactant-coated flakes against aggregation. For the non-ionic surfactants, the dispersed graphene concentration scaled linearly with the magnitude of the steric potential barrier stabilizing the flakes.[42]

2.2. Non-ultrasonication techniques

2.2.1. Intercalation compounds

Valles *et al.* showed that alkali metal graphite intercalation compounds (GICs) can readily and spontaneously exfoliate in NMP, yielding stable solutions of negatively charged graphene sheets and ribbons. These sheets can be deposited on a variety of substrates, thus enabling a large-scale route to graphene deposits and composites. Authors showed that mild dissolution of graphite only requires the addition of electrons (reduction) to the graphene layers for its exfoliation. Synthesizing GICs, such as the ternary potassium salt, it is necessary to accomplish this procedure.[43] Exposure of the potassium GIC to NMP readily and spontaneously exfoliates the intercalated graphite and yields air-sensitive solutions of reduced graphene sheets, affording a virtually unlimited amount of one-atom thick layers.

A different approach was proposed for the production of single- and double-layer clean large area graphene from re-exfoliation of expandable graphene. This procedure involves the use of saturated acid mixture of H_2SO_4 and HNO_3 to form the GIC (Figure 3). The mixture is then heated until 800–900 °C where the sample is rapidly expanded. Graphene sheets are later easily dispersed in DMF.[44]

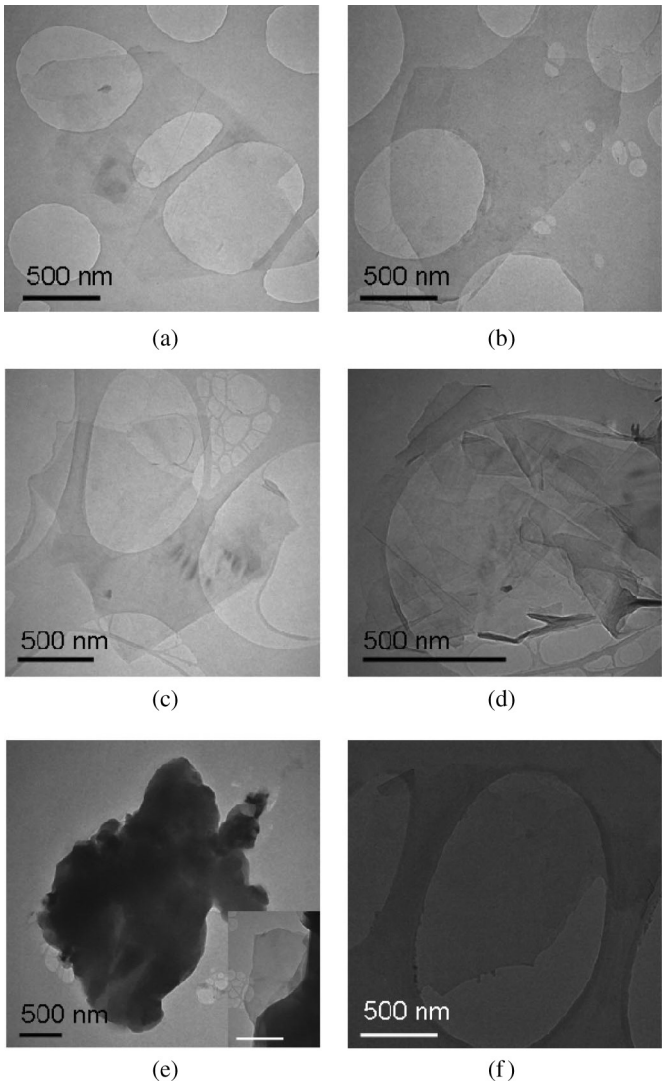

Figure 2. Selected TEM images of flakes prepared by surfactant processing. (a) A monolayer (*albeit* with a small piece of square debris close to its left-hand edge). (b) A bilayer. (c) A trilayer. (d) A disordered multilayer. (e) A very large flake. Inset: A close-up of an edge of a very large flake showing a small multilayer graphene flake protruding. (f) A monolayer from a sample prepared by sediment recycling. Reproduced from Ref. 41 with permission. Copyright © 2009 ACS.

2.2.2. Ionics compounds

Ionic liquids (ILs) have been proposed as "green" alternatives to conventional solvents because of their unique properties such as negligible vapor pressure, thermal stabilities, wide electrochemical potential window, low

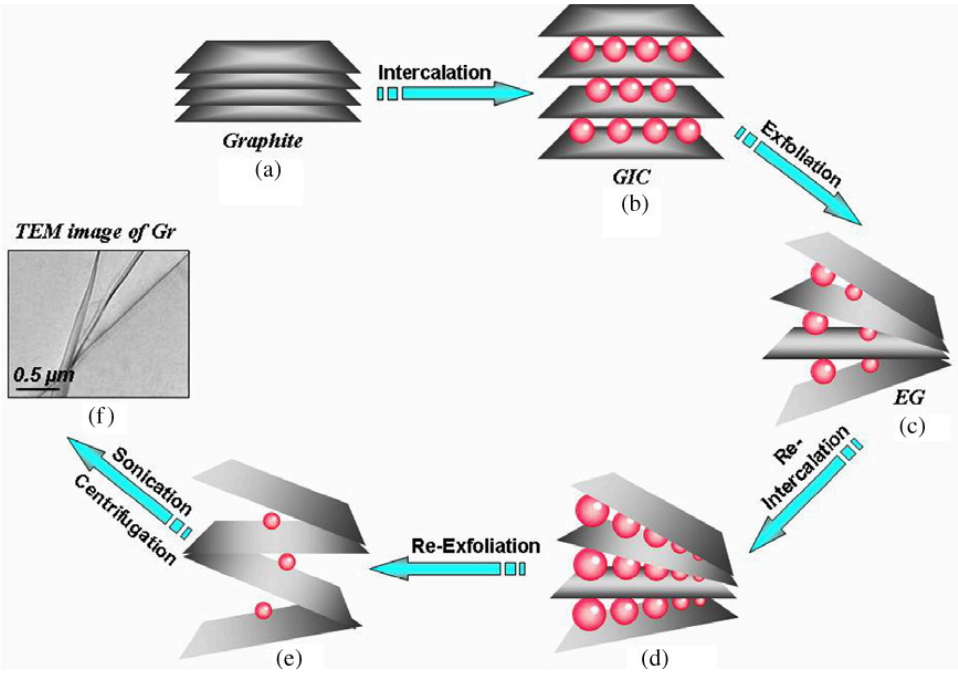

Figure 3. The steps involved in the synthesis of graphene sheets. (a) Natural graphite, (b) formation of GIC on acid treatment, (c) formation of expanded graphene on thermal exfoliation, (d) re-intercalation of expanded graphene, (e) re-exfoliation of expanded graphene, and (f) formation of single- and double-layer graphene sheets after ultrasonication and centrifugation. Reproduced from Ref. 44 with permission. Copyright © 2011 Elsevier.

viscosity, good ion conductivity, and recyclability. The high dielectric constant of ILs provides shielding for the stacking interactions caused by van der Waals interaction and helps to disperse graphene from graphite effectively.[45]

In this direction, Lu *et al.* demonstrated a facile means to generate fluorescent carbon nanoribbons, nanoparticles, and graphene from graphite electrode using IL-assisted electrochemical exfoliation. Through a time-dependence study of products exfoliated from the graphite anode, they found the reconstruction of the exfoliation mechanism based on the interplay of anodic oxidation and anion intercalation. They investigated the role of water in the exfoliation mechanism and discovered that controlling the ratio of water to ILs in the electrolyte can generate a diverse range of nanostructured carbon materials. They found that by tuning the water content and type of counterions in the ILs, the fluorescence, as well as the distribution of the nanomaterial, could be tuned. This method of nanomaterial preparation is highly versatile and industrially scalable.[46]

In particular, graphene prepared as colloidal suspensions is especially prone to further chemical processing (*e.g.*, functionalization with molecules, nanoparticles, etc.), which is advantageous for the synthesis of hybrid structures and composite materials with a view to, *e.g.*, energy or biomedical applications.

2.2.3. Ball-milling production

As an alternative method, large quantities of inexpensive materials such as graphite and melamine can be used for massive and fast production of FG with low concentration of defects. The methodology uses mechanochemical activation by ball milling to exfoliate graphite through interactions with melamine (2,4,6-triamine-1,3,5-triazine) in solid conditions.[15] The milling treatments can be modulated in order to achieve graphene flakes with desired sizes. Once graphite is exfoliated by the milling treatment, the resulting solid mixtures can be dispersed in water or DMF to produce relatively concentrated dispersions. The as-prepared dispersions are stable at room temperature within weeks and they can be washed by filtration to remove melamine. Graphene samples can be dispersed in virtually any solvent, opening the way to chemical functionalization (Figure 4).

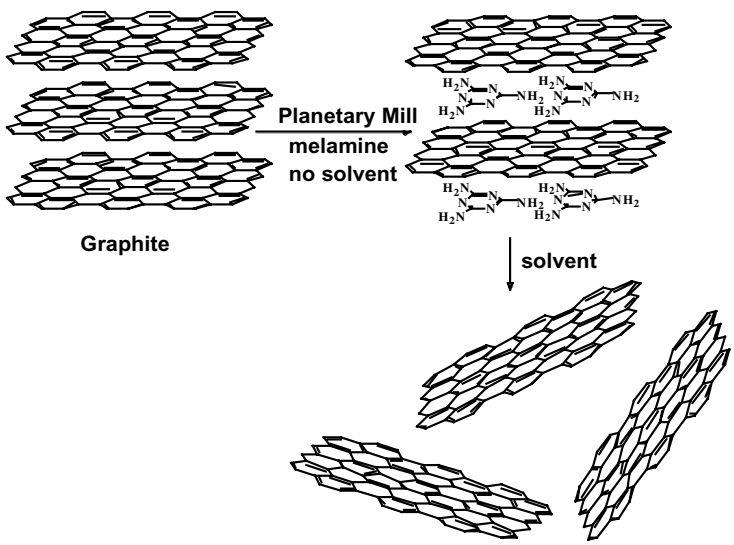

Figure 4. Schematic illustration for the exfoliation of graphite through ball-milling approach. Reproduced from Ref. 15 with permission. Copyright © 2011 RCS.

2.2.4. Supercritical fluids

Rangappa and coworkers have synthesized graphene by supercritical solvent exfoliation of natural graphite. This process is possible from the time when fluids reach or exceed their critical point, they show various unique properties, such as outstanding wetting of surfaces, low interfacial tension, low viscosity, and high diffusion coefficients. Then a rapid, one-pot supercritical fluid exfoliation process for high-yield production of graphene sheets can be performed in which about 90–95% of the exfoliated sheets are less than 8 layers with approximately 6–10 of monolayers. This procedure is simple and involves direct conversion of graphite crystals to high-quality graphene under supercritical fluids such as ethanol, NMP, and DMF. This is a non-covalent, solution-phase method to produce defect-free, unoxidized graphene with good conduction and electron-carrier capacity.[47] By using expandable graphite (EG) as starting material and following the same strategy, Liu *et al.* prepared FG in supercritical DMF in less than 15 min. The yield of the process is about 7 wt.% in optimum conditions (Figure 5).[48]

2.2.5. Unzipping of carbon nanotubes

Pristine graphene nanoribbons have also been produced by chemical unzipping of CNTs. This method describes a simple solution-based oxidative

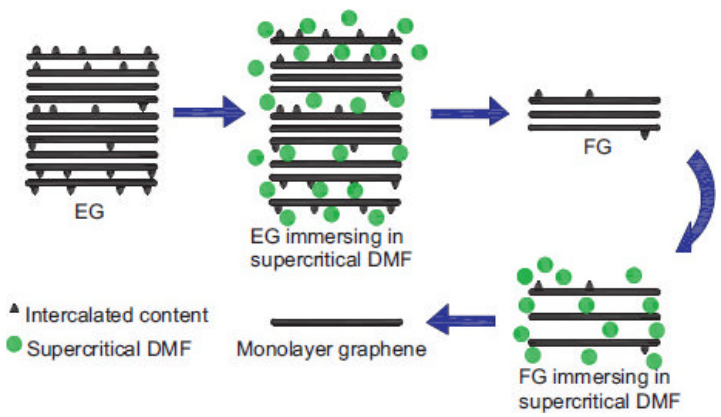

Figure 5. The schematic representation for fabricating FG and single-layer graphene by exfoliation of EG in supercritical DMF. It includes two steps: (i) producing FG by supercritical DMF from EG and (ii) producing monolayer graphene by supercritical DMF from FG. Reproduced from Ref. 48 with permission. Copyright © 2012 Elsevier.

process for producing a nearly 100% yield of nanoribbon structures by lengthwise cutting and unraveling of multiwalled carbon nanotube (MWNT) sidewalls. Ribbon structures with high water solubility are obtained. Subsequent chemical reduction of the nanoribbons from MWNTs results in restoration of electrical conductivity.[49]

3. Other Nanostructures from Liquid-Phase Exfoliated Graphene

The chemical and physical properties of the different carbon nanostructures are mainly associated with their structural configuration. Fullerenes, tubes (CNT), scrolls (CNS), fibers (CNF), cones (CNC), onions (CNO), diamonds (CND), and graphene exhibit distinctive chemical and physical properties derived from the coordination, size, and shape of the specific carbon NP. For example, while CNS presents a very similar behavior to CNT in their axial deformation sensitivity, they exhibit a radial response upon charge injection up to one order of magnitude larger, making CNS efficient nanoactuators.[50] Thus, the mastery over the size and shape of carbon NP synthesis enables manipulation of its properties and enhances its utility for a given application.

During the last decades, a successful synthesis of carbon NP in a wide diversity of shapes and sizes has been achieved by stochastic chemical reactions mediated by physically controlled environments.[51] The production of carbon NP has been reached even if the current understanding of their synthesis is far from been able to provide atomistic details for the evolution pathways that a carbon precursor may take to form well-defined NP. Consequently, the deterministic large-scale synthesis, implicating precise control of the coordination, size, shape, crystallinity, location, orientation, and yield of carbon NP, remains as a critical issue. In order to advance this limitation, different approaches have been taken. For example, the synthesis of CNT, CNC, or CNF can be selectively obtained by adjusting the catalyst seed in plasma-enhanced chemical vapor deposition (PECVD) growth[52] and the making of only one type of CNT is possible by using purified single chirality CNT as seeds for subsequent metal catalyst-free growth in vapor phase epitaxy.[53] As a completely different approach, the isolation of graphene layers by micromechanical cleavage and later by solution-phase exfoliation of graphite has opened new alternatives in the search for the controlled synthesis of other carbon NP. In this direction, graphene has been defined as the mother of all graphitic forms since it can be wrapped up into 0D buckyballs, rolled into 1D nanotube, or stacked into 3D graphite.[2]

3.1. Deformation, folding, and stabilization

Graphene layers present strong interlayer van der Waals interactions that can lead to self-assemble into larger structures.[54] In order to reproducibly prepare other carbon nanostructures, the potential barriers associated with graphene deformation need to be overcome, at the same time, the folding processes must be guided and the final structures need to be well stabilized.[55] For example, in the synthesis of fullerenes, a plausible mechanism involves the dissociation of graphene structures to very small clusters, which subsequently coalesce to form fullerene cages.[56] Recently, the direct visualization in real time, of a process of fullerene formation from a graphene sheet was accomplished by aberration-corrected TEM.[57] In this experiment, the graphene changes its shape under the influence of the electron beam, forming the fullerene molecule absorbed on the graphene substrate and finally the fullerene rolls back and forth on the graphene surface, because the energy of the van der Waals interaction of a fullerene with the substrate is significantly reduced compared to a graphene layer.[58] Other examples in the literature include the implementation of molecular dynamics simulations to investigate the rolled of a graphene sheet into CNS describing its formation and stability.[59] It was also demonstrated that water nanodroplets and CNT[60] activate and guide the folding of a graphene nanoribbon into several sizes and shapes. These simulations describe the bending, folding, sliding, and rolling of the graphene sheet in vacuum and in the presence of solvent, leading to stable graphene rings, helices, and knots. In the same direction, the roll-up of nanomembranes was theoretically investigated introducing wrinkles to control the preferential rolling direction.[61] Experimentally, it was verified that individual graphene sheet presents high elasticity[62] enough to fold into CNS. Indeed, CNS have been prepared by chemical methods[31] or assisted by alcohols.[63] Following this direction, CNTs are often visualized as rolled-up graphene sheets. By using first-principles and classical molecular dynamics simulations, a method was demonstrated to synthesize CNTs by realizing the ideally visualized process of rolling up a graphene ribbon. This process is possible due to the physical principle of bending of thin films driven by induced stress produced during surface gas adsorption.[64]

3.2. Ultrasonication of graphite

3.2.1. Tiopronin as antioxidant molecule

We have recently demonstrated that the damage created in graphene sheets during exfoliation of graphite by ultrasonication in DMF is considerably

reduced under the addition of *N*-2-mercapto-propionyl glycine (tiopronin).[65] Tiopronin is an antioxidant molecule that inhibits reactions promoted by oxygen, peroxides, and radicals.[66] The sonication of graphite in the presence of tiopronin allows the production of larger graphene sheets and the formation of CNFs. The growth of CNFs has been reported as result of the condensation of organic pieces of polyaromatics[67] or by the radical polymerization of conjugated carbon polymers.[68] Then, the appearance of these nanofibers during the sonication of graphene in the presence of tiopronin was an indicative of the occurrence of organic reactions. These reactions take place close to the edges cutting graphene into small pieces that later aggregate forming the fibers as being insoluble in DMF. This mechanism was supported by the localization of the chemically active sites by using Au nanorods as contrast markers.[69] Tiopronin and its fragments, including amine, amide, thiol, and carboxylic moieties, are stabilizers for gold nanoparticles (Au NPs).[70] By using TEM, Au nanorods were mostly found placed on the nanofibers as consequence of the chemical functionalization of the small graphene fragments by acoustic cavitation. This protocol generates dispersions with a higher yield of larger graphene sheets containing fewer concentration of defects than those obtained by common sonication treatments (Figure 6).

3.2.2. Transformation of few-layer graphene into MWNTs

In a similar methodology, we used ferrocene aldehyde (Fc-CHO) to template the formation of MWNT during the sonication of graphene dispersions in DMF.[71] A long-held dream has been to try to grow CNTs by directed rolling

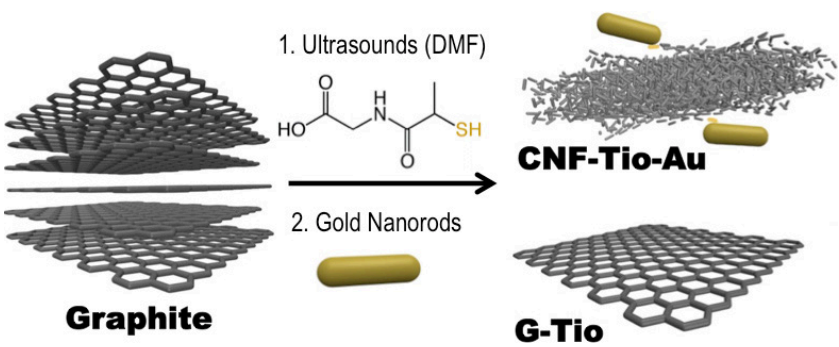

Figure 6. Under ultrasonication treatment, the production of high-quality graphene layers by exfoliation of graphite was achieved via addition of tiopronin as an antioxidant. Reproduced from Ref. 65 with permission. Copyright © 2012 RCS.

and sealing process (Figure 7). Recently, we demonstrated the feasibility of this approach reporting the direct formation of MWNTs by ultrasonication of graphite in DMF upon addition of Fc-CHO. Fc-CHO was used since it is a reducing agent that can inhibit reactions promoted by oxygen, peroxides, and radicals. At the same time, ferrocene derivatives are also used in the synthesis of CNTs as catalysts and carbon source (Figure 7).[72]

We have suggested a mechanism of action for the formation of the MWNTs (Figure 8):

1. Ultrasonication exfoliates graphite, breaks the graphitic basal structure, and produces small graphene fragments.
2. Fc-CHO reduces the concentration of radical reactive species that slice graphene into small moieties.

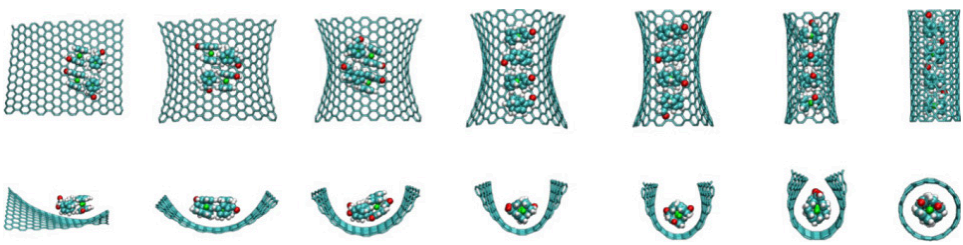

Figure 7. Slow motion rolls up. Fc-CHO molecules templates the rolling of the graphene sheet. Reproduced from Ref. 73 with permission. Copyright © 2013 Wiley.

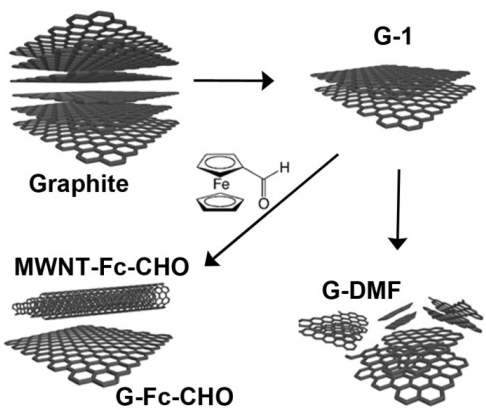

Figure 8. Ultrasound-assisted synthesis of MWNTs from graphene. Reproduced from Ref. 71 with permission. Copyright © 2012 ACS.

3. Fc-CHO localizes itself at the edges of graphene, templates the rolling up of a sheet to form a nanoscroll, where it remains trapped.
4. Fc-CHO finally accepts and donates unpaired electrons to the graphene edges and converts the less stable scroll into a MWNT.

This new methodology truly matches the notion that CNTs are rolled-up graphene layers. The proposed mechanism is general and will lead to controlled production of carbon nanostructures by simple ultrasonication treatments.[73]

4. Covalent Functionalization of Graphene in Dispersions

The unique and superior properties of graphene make it the nanomaterial of choice for a broad range of applications, including transistors, integrated circuits, displays, sensors, and nanocomposite materials. Despite its high potentials, major challenges still remain. These include poor solubility, intrinsic zero band gap energy, low reactivity, and the availability of well-defined pristine graphene in large quantity, which have hampered the rapid development of graphene-based functional devices. Many of these challenges can be potentially addressed through chemical functionalization of the material.[74]

The functionalization of pristine graphene sheets with organic functional groups has been developed for several purposes. The main one is probably, the dispersibility of graphene in common organic solvents or water. This is usually achieved after the attachment of certain organic groups.[75] The dispersion of graphene sheets in organic solvents or water is a crucial move toward the formation of nanocomposite materials, including graphene. In addition, organic functional groups such as chromophores or other functional moieties offer new properties that could be combined with the properties of graphene such as conductivity. In most cases, when organic molecules are covalently attached on the graphene surface, its extended aromatic character is perturbed, enabling the control of its electronic properties. The development of a band gap through chemical doping is a powerful method for the use of graphene in nanoelectronic devices.[76]

Graphene is defined as a pristine two-dimensional sp^2-hybridized carbon sheet. The coexistence of sp^3 carbons in the lattice is inherently classified as defects, where these defects can be on the basal edges or inside defects in the plane. The ratio between carbon atoms with sp^2 and sp^3 hybridization in the graphitic lattice is an indication of the degree of oxidation or a covalent functionalization reaction. This ratio is estimated using Raman spectroscopy as the I_D/I_G ratio, where I_D and I_G are the intensities of the peaks at ~1350 and

1580 cm^{-1}, which correspond to the number of sp^3 and sp^2 carbon atoms, respectively. In principle, graphene can be functionalized at the two surface faces and at the edges. Evidence indicates that functional moieties attack both graphene faces, altering the energetics, allowing chemical bonds that would be unstable if only one surface was exposed.[77,78] Even though graphene has been considered as an inert material toward chemical attack, some groups have observed a considerable reactivity of the graphene layer.[79,80] In some instances, this process might result in unpaired electrons, which would be created at sites adjacent to the point of covalent bonding, enhancing the reactivity there, and leading to a chain reaction from the initial point of attack.[81] Under this perspective, the graphene edges are considered more reactive than the surface faces. It is expected that zigzag edges will display higher reactivity as compared to the armchair ones. However, it is technically challenging to control the edge structure, so that, in practice, graphene contains a combination of the two basic types of edge configuration, which makes it difficult to control the functionalization process.[82] Defects are considered additional reactive sites, which usually facilitate graphene functionalization in both surface faces and edges. All the current methods for graphene production yield layers with defects, including structural imperfections and chemical impurities randomly distributed.[83] Thus, chemical reactions are expected to occur at both faces and edges (Figure 9). Based on previous

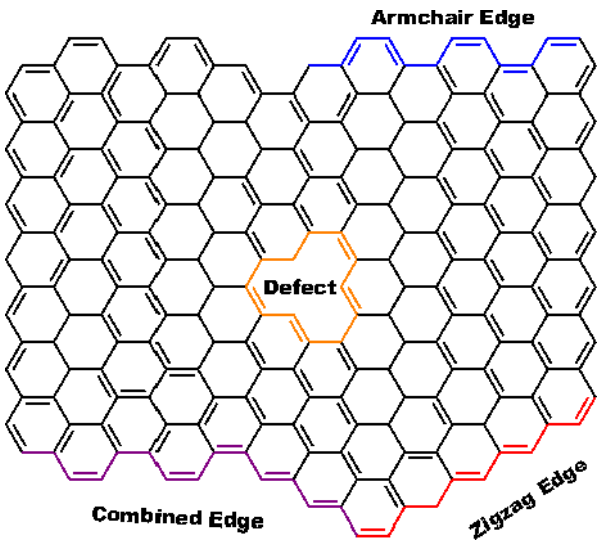

Figure 9. Schematic representation of reactive sites in graphene sheets: surface faces, edges, and defects. Reproduced from Ref. 84 with permission. Copyright © 2013 ACS.

works and theoretical experience with fullerene and CNTs, the most attractive organic species for the reaction with sp^2 carbons of graphene are organic free radicals and dienophiles.[84] Usually, both reactions produce intermediate reactive components that are produced under certain conditions in the presence of graphene.

4.1. Free radical addition

Upon heating of a diazonium salt, a highly reactive free radical is produced, which attacks the sp^2 carbon atoms of graphene forming a covalent bond. This reaction has been used by Tour and coworkers to decorate graphene with nitrophenyls.[85] The graphene sheets in this work were produced through the chemical unzipping of CNTs. A measurement of the conductivity of a graphene sheet through a simple device during chemical functionalization with diazonium salts results in a remarkable decrease in conductivity due to disruption of the aromatic system by transformation of carbon atoms from sp^2 to sp^3 hybridization. The conductivity of the graphene sheets was shown to decrease in a controlled manner; showing that conductivity can be controlled by reaction time. An alternative free radical addition method includes the reaction of benzoyl peroxide with graphene sheets by a photochemical reaction. The reaction introduces spatially localized defects into the basal plane of graphene.[86]

4.2. Dienophiles addition

Apart from free radicals, dienophiles also react with sp^2 carbons of graphene. For example, azomethine ylide reacts through a 1,3 dipolar cycloaddition being one of the most common dienophiles that have been successfully applied in the functionalization of carbon nanostructures: fullerenes, nanotubes, onions, and nanohorns.[87] The reaction affords a variety of organic derivatives, which display interesting applications in several areas; these include polymer composites, biotechnology, nanoelectronic devices, drug delivery, and solar cells. In this direction, after the successful production of graphene sheets directly from graphite dispersed in organic solvents, Georgakilas and coworkers showed that the graphene sheets could be substituted with pyrrolidine rings via a 1,3 dipolar cycloaddition of azomethine ylide.[88] The organically modified graphene sheets are easily dispersible in polar organic solvents and water. Later, we utilized 1,3-dipolar cycloaddition to graphene sheets by employing precursors of paraformaldehyde and a specifically designed NH_2-terminated α-amino acid. The protonated terminal amino groups were shown to selectively bind gold nanorods (Figure 10).[89,90]

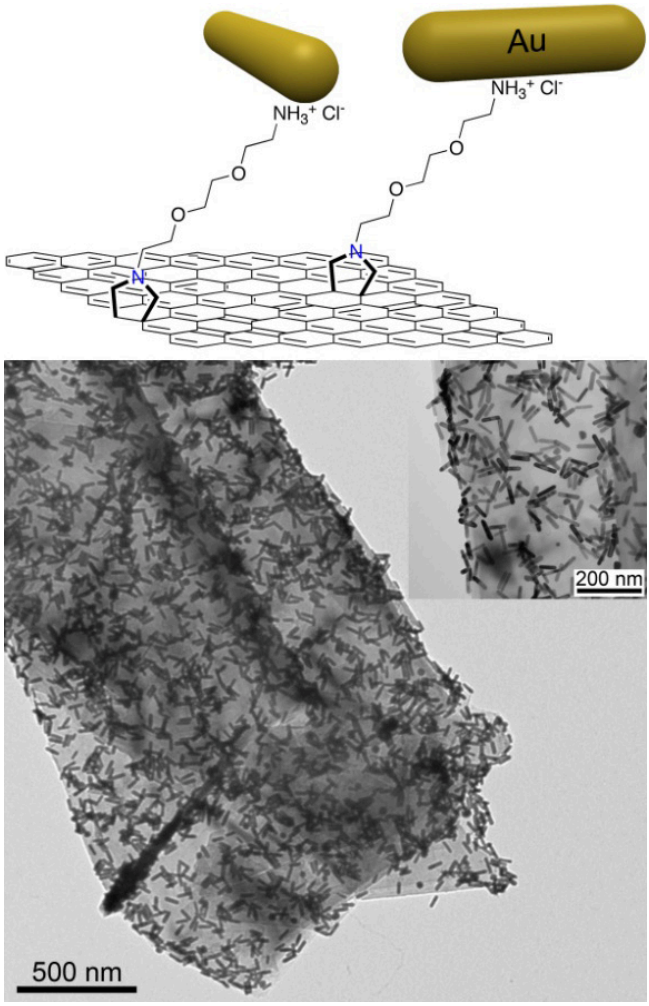

Figure 10. Graphene functionalization by 1,3-dipolar cycloaddition in DMF dispersions. Reproduced from Ref. 90 with permission. Copyright © 2010 Wiley.

Later, we functionalized exfoliated graphene in DMF using dendrons in two different reactions: 1,3-dipolar cycloaddition and amide-bond condensation reaction on the pre-existing carboxylic groups. The free amino groups at the tips of the dendrons act as ligands in the complexation of Au NPs, which are introduced as contrast markers for the identification of the reactive sites.[70] With this, we demonstrated that graphene sheets could be selectively functionalized on the borders in the entire lattice (Figure 11).

Phenyl and alkyl azides react with the C–C bonds of graphene by the formation of the reactive intermediate nitrene. The reaction of organic azides

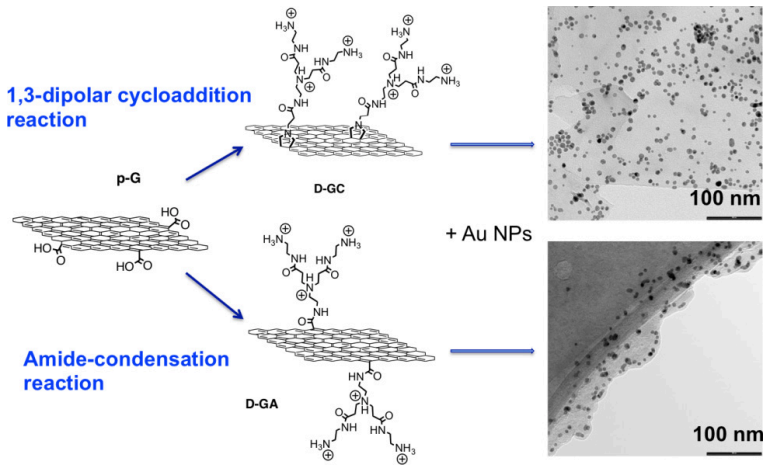

Figure 11. Selective functionalization of bulk graphene or graphene edges. Reproduced from Ref. 69 with permission. Copyright © 2011 RCS.

with graphene has been used successfully by several research groups affording a variety of organic graphene derivatives. Liu and coworkers attached various para-substituted perfluorophenylazide (PFPA) functionalities to the graphene by thermal and photochemical activation via a three-membered aziridine ring. These modifications result in varying solubility–dispersibility and surface energy of the modified graphene.[91]

Nitrene addition has also been used in the functionalization of graphene sheets with phenylalanine. The graphene sheets were reacted with Boc-protected azidophenylalanine in *o*-DCB. The product was determined to have 1 phenylalanine substituent per 13 carbons.[92] He and Gao developed a facile and versatile method for the introduction of various functional groups and polymeric chains onto graphene sheets via nitrene cycloaddition. This strategy allows various kinds of functional moieties and polymers to be covalently bonded to graphene, resulting in functional graphene sheets and 2D macromolecular brushes, respectively. The functionalized graphene sheets show enhanced chemical and thermal stabilities compared with GO and can be further modified by different chemical reactions, including amidation, surface-initiated polymerization, and reduction of metal ions. The resulting functionalized graphene sheets are electrically conductive and display excellent dispersibility and processability in solvents.[93]

In addition, the solvent must also be able to undergo sonochemical reactions during the sonication to produce radical functionalization of the graphene sheet. A convenient sonochemical method was described for the

preparation of polystyrene-functionalized graphene starting from graphite flakes and a reactive monomer, styrene. Ultrasonic irradiation of graphite in styrene results in the mechanochemical exfoliation of graphite flakes to single-layer and FG sheets combined with functionalization of the graphene with polystyrene chains.[94]

5. Graphene Composites

Long-range π-conjugation in graphene yields remarkable and unique properties, such as high values of its Young's modulus (~1.0 TPa), large theoretical specific surface area (2630 $m^2\ g^{-1}$), excellent thermal conductivity (~5000 W $m^{-1}\ K^{-1}$), high mobility of charge carriers (200,000 $cm^2\ V^{-1}\ s^{-1}$), and optical transmittance (~97.7%). These excellent properties support graphene as ideal building blocks in nanocomposites. In general, nanocomposites are multiphase materials, in which one phase (dispersed phase) in the nanosize regime is dispersed in a second phase (matrix/continuous phase), resulting in a combination of the individual properties of the component materials (Figure 12).[16b]

The main motivating factor for probing the research of the graphene-based nanocomposites is the desire to combine the favorable properties of

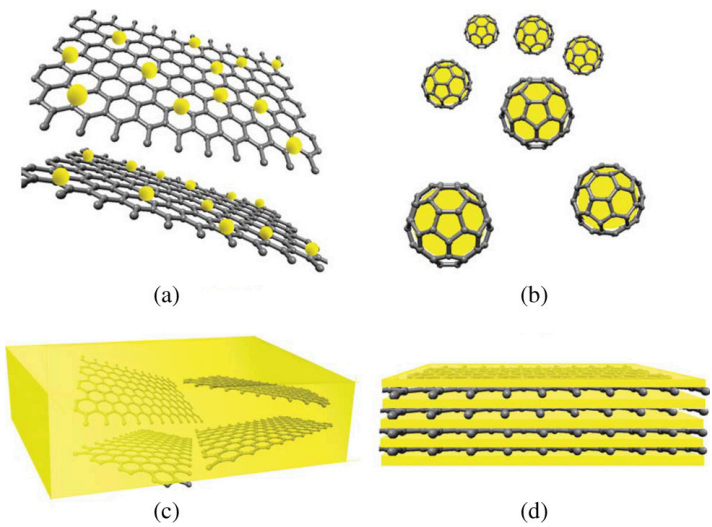

Figure 12. Schematic illustration of architectures of graphene-based nanocomposites: (a) graphene-supported nanocomposites; (b) graphene-encapsulated nanocomposites; (c) graphene-incorporated nanocomposites; and (d) graphene-based multilayered nanocomposites. Reproduced from Ref. 16b with permission. Copyright © 2012 RSC.

graphene with other constituent nanomaterials (the second components). The benefits of graphene in constructing inorganic nanocomposites include the following[16b]:

1. *Planar structure.* It is usually difficult to achieve a good decoration of nanomaterials on the CNTs, when the size of them is in the same range as or larger than the diameters of the CNT. Whereas, graphene has a unique basal plane structure, which make it possible for graphene to load microspheres with diameter size even bigger than several hundred nanometers. Furthermore, the 2D structure makes it possible for graphene-based nanocomposites to be synthesized by new synthesis methods which could not be used in CNT-based nanocomposites synthesis, such as the thermal decomposition of graphene precursor-intercalated inorganic materials.
2. *High surface area.* Compared with CNTs, graphene, with higher surface area, improves interfacial contact with the other components. The large surface of graphene could prevent the aggregation of secondary components, so that some unique properties in the nanoscale could be preserved. On the other hand, most of the extraordinary properties of graphene nanosheets are only associated with individual sheets. However, the high surface area makes graphene to form irreversible agglomerates. While the second components could act as spacers between graphene nanosheets to minimize the agglomeration.
3. *Electrical and optical properties.* Most of the research on graphene focuses on the electrical properties. As a zero band gap semiconductor, graphene displays a remarkably high electron mobility under ambient conditions, with reported values up to 15,000 $cm^2\ V^{-1}\ s^{-1}$. Moreover, the observed mobilities are nearly independent of temperature, suggesting that an ultrahigh mobility could be realized in graphene at room temperature. By minimizing impurity scattering, mobilities of graphene in excess of 200,000 $cm^2\ V^{-1}\ s^{-1}$ were achieved. This is of importance as nanocomposites with graphene as the electron carrier may perform better in applications that involve charge transfer processes, such as sensors, supercapacitors, and electrocatalysis. Moreover, considering the high optical transparency, graphene-based nanocomposites could be fabricated into transparent conductive films, which show promise for application in solar cells, advanced electronics, etc.
4. *Mechanical properties.* It was reported that defect-free monolayer graphene has a Young's modulus of 1.0 TPa and fracture strength of 130 GPa. Despite some structural distortion, the measured elastic modulus of

freely suspended graphene monolayers is still as high as 0.25 TPa. The advantages of graphene in mechanical properties make it facile to fabricate and process graphene-based nanocomposites into devices with various applications. Furthermore, it was also reported that the mechanical stability of graphene nanosheets could be improved by dispersing inorganic nanomaterials on them.

5. *Thermal properties.* In a non-contact measurement using the confocal micro-Raman spectroscopy, a thermal conductivity value of about 5000 W m^{-1} K^{-1} was obtained for a suspended single-layer graphene. The high thermal conductivity makes graphene-based nanocomposites with excellent thermal stability, which could be important in some electronic devices or catalytic reactions with heat release, such as fuel cells and lithium-ion batteries (LIBs).
6. *Low cost and simple procedure of production.* As we have mentioned in this contribution, graphene can readily form stable colloids dispersion in various solvents, which make it possible to process graphene-based nanocomposites directly using solution processing techniques, while the chemical functionalization in advance is necessary for CNT, due to their poor dispersion. In addition, the solution processing methods start with graphite as the raw material, resulting in the production cost of graphene-based materials in large quantities much lower than that of CNT.

The synthesis of first ever graphene-based composites graphene/polystyrene was reported in 2006, by Ruoff and coworkers. Their main observation was low percolation threshold, which they had computed to be 0.1 vol.% of graphene for the composite. This work attracted considerable attention which led to the further development of different composites with graphene.[16a]

We can classify graphene composites under two major groups: (i) graphene/polymer composites and (ii) graphene/inorganic material composites.[16a]

5.1. Graphene/polymer composites

In graphene/polymer nanocomposites, graphene can dramatically improve properties such as electrical conductivity, thermal conductivity, and mechanical strength. Moreover, these improvements are often observed experimentally at low loadings of graphene, owing to their large interfacial area and high aspect ratio.

The most simple and straightforward method to fabricate polymer composites is solution mixing. To achieve good dispersion, the compatibility of the polymer and filler (graphene in this case) in the required solvent is

important. GO is easily dispersed in water, due to its oxygen functionality, but graphene has very low solubility, hence graphene is being regularly sonicated in water in an ultrasonic bath, to achieve good dispersion before mixing it with different aqueous solutions of polymers, *e.g.*, poly-methyl methacrylate (PMMA), poly-aniline (PANI), poly-urethene, and poly-vinyl alcohol (PVA).

5.2. Synthesis of graphene/polymer composites

The mechanism for the interaction in polymer/graphene nanocomposites depends on the polarity, molecular weight, hydrophobicity, reactive groups, etc., present in the polymer, graphene/graphite, and solvent. There are three main strategies for incorporating the polymer at the core of the host-layered materials.[95]

***In situ* intercalative polymerization:** In the *in situ* interactive polymerization method, graphene or modified graphene is first swollen within the liquid monomer. A suitable initiator is then diffused and polymerization is initiated either by heat or radiation. A variety of polymer nanocomposites have been prepared using this method.

Solution intercalation: Solution intercalation is based on a solvent system in which the polymer or prepolymer is solubilized and graphene or modified graphene layers are allowed to swell. Graphene or modified graphene can be dispersed easily in a suitable solvent, such as water, acetone, chloroform, tetrahydrofuran (THF), DMF, or toluene, owing to the weak forces that stack the layers together. The polymer then adsorbs onto the delaminated sheets and when the solvent is evaporated, the sheets reassemble, sandwiching the polymer to form the nanocomposites. This strategy can be employed to synthesize epoxy-based nanocomposites but solvent removal is a critical issue. The driving force for polymer intercalation from solution is the entropy gained by desorption of the solvent molecules, which compensates for the decrease in conformational entropy of the intercalated polymer chains. Therefore, a relatively large number of solvent molecules need to be desorbed from the filler to accommodate the incoming polymer chains. The main advantage of this method is that it allows the synthesis of intercalated nanocomposites based on polymers with low or even no polarity.

Melt intercalation: In the melt intercalation technique, no solvent is required and graphite, graphene, or modified graphene is mixed with the

polymer matrix in the molten state. A thermoplastic polymer is mixed mechanically at elevated temperatures using conventional methods, such as extrusion and injection molding. The polymer chains are then intercalated or exfoliated to form nanocomposites. This is a popular method for preparing thermoplastic nanocomposites. Polymers, which are unsuitable for adsorption or *in situ* polymerization, can be processed using this technique.

5.3. Graphene/inorganic material composites

Based on the different kinds of inorganic components, graphene–inorganic nanocomposites could be further classified into graphene–metal nanocomposites, graphene–carbon nanocomposites, graphene–metal compound nanocomposites, and graphene–non-metal nanocomposites. In graphene–metal nanocomposites reported in literature, the majority of the second components are noble metals, such as Au, Ag, Pt, and Pd. Graphene can not only reduce the consumption of noble metal, but also establish significant electronic interaction with them. In addition, other metal nanomaterials such as Cu, Sn, Co, bimetals, and alloys were also used for fabricating inorganic composites of graphene. The combination of graphene with other carbon building blocks (CNT, fullerene, carbon black (CB), carbon sphere, and CNFs) offers fascinating prospects for the design of new carbon materials, especially the composites of graphene with CNT. Both graphene and CNT show remarkable electrical, thermal, mechanical, and structural properties. The assembly of them into nanocomposites produces carbon materials with large specific surfaces, high electrical conductivities, and unique mechanical properties.[16b]

The synthesis of graphene–metal compound nanocomposites has been reported. The metal compounds include oxides, hydroxides, sulfides, selenides, nitride, inorganic salt, clay, etc. Among these metal compounds, semiconductor and magnetic nanomaterials were intensively studied. It has been demonstrated that there exists charge-transfer as well as electronic and magnetic interactions between graphene and the attached semiconducting oxide or magnetic nanomaterials. Graphene as an electron transport channel could bring enhanced properties and improved performance of metal compound nanomaterials in various applications.[16b]

Non-metallic materials, such as S, Si, SiO_2, Si_3N_4, SiOC, CN, and C_3N_4, have also been reported for preparing their corresponding nanocomposites with graphene. Some of the graphene–non-metal nanocomposites were synthesized to develop metal-free catalysts to substitute metal catalysts.[16b]

5.4. Synthesis of graphene–inorganic nanocomposites

Nowadays, a number of strategies have been put forward for the fabrication of graphene–inorganic nanocomposites. Nonetheless, they fall into two basic classes. One main approach involves the formation of nanocrystallites in the presence of pristine or functionalized graphene nanosheets, and then the nanocrystallites directly grow into nanomaterials such as NPs, nanowires, nanorods, and nanofilms on the surface of the graphene nanosheets, which belong to *in situ* techniques; while the second key approach involves the prior synthesis of nanomaterials in the desired dimensions and morphology, then modified and subsequently connected to the surface of functionalized graphene nanosheets, which is named as *ex situ* techniques.[16b]

***In situ* growth on a graphene surface:** Among the two approaches, *in situ* growth is more widely used in the synthesis of graphene–inorganic nanocomposites. The main advantage of this route is that the protecting surfactant or extra linker molecules could be avoided, which may imply a tedious experimental procedure, and also influence the functions of the nanocomposites. Another advantage of the *in situ* approach is that a variety of chemical and physical synthesis techniques could be used, including solution deposition methods, direct decomposition of precursors, hydrothermal/solvothermal techniques, gas-phase deposition, sol–gel processing, template method, and so on.

***Ex situ* approach: assembly on graphene surface:** In the *ex situ* approach, inorganic components were synthesized in advance and then attached to the surface of graphene via linking agents that utilize covalent or non-covalent interactions (van der Waals interactions, hydrogen bonding, π–π stacking, or electrostatic interactions). In this approach, either the inorganic components or graphene (or both) require modification with functional groups. The type of functionalization and thus, the strength of interaction determine the loading of the inorganic nanomaterials on the graphene surface. This self-assembly-based method is excellent at overcoming any incompatibilities between nanomaterials syntheses and the formation of nanocomposites. Compared to *in situ* growth, the better distribution, size, and feeding amount control of the second components on graphene could be obtained by the self-assembled methods. Using this methodology, we have produced a functionalized graphene with a tailored distribution of polycationic, quaternized, ammonium pendants which provides an sp^2 carbon nanoplatform to anchor a totally inorganic tetraruthenate catalyst, mimicking the oxygen evolving center of natural PSII in photosynthetic systems (Figure 13).[96] The resulting hybrid

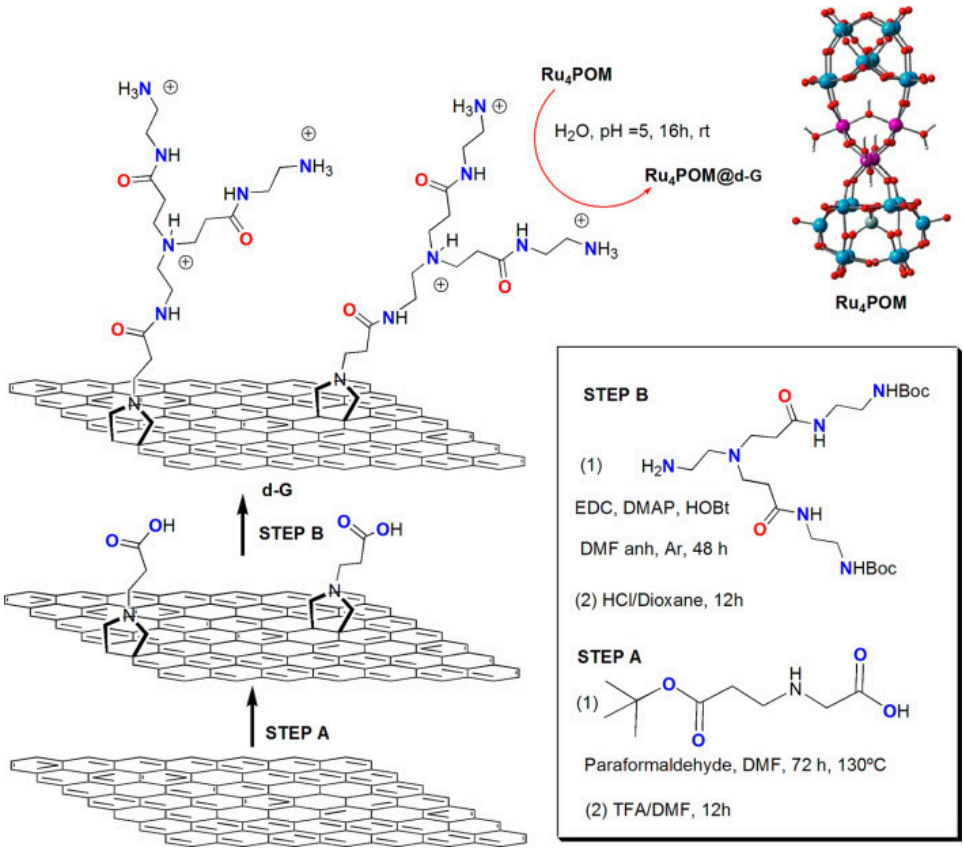

Figure 13. Synthesis of graphene nanoplatform supporting Ru_4POM. Reproduced from Ref. 96 with permission. Copyright © 2013 ACS.

material displays oxygen evolution at overpotential as low as 300 mV at neutral pH with negligible loss of performance after 4 h testing. This multilayer electroactive asset enhances the turnover frequency by one order of magnitude with respect to the isolated catalyst, and provides a definite upgrade of the CNT material, with a similar surface functionalization.

5.5. Miscellaneous applications of graphene

Owing to its unique properties, graphene has been attracted more attention for application in various areas such as field-effect transistors, sensors, and electromechanical resonators. Recently, graphene and graphene-based materials have been selected as electrode materials of energy-related devices, and quite promising results have been obtained.[97]

Graphene is considered to be one of the strongest materials ever measured and can produce improvements in the mechanical properties of polymer matrices at very small loadings. The most impressive are increases in tensile strength and elastic modulus. The large aspect ratio and high electrical conductivity of graphene make it promising conductive fillers in polymers to improve the electrical properties. Various polymers, including PMMA, PVA, PVC, PP, PE, PA12, and PS, have been used as matrices to prepare electrically conductive graphene/polymer composites. A theoretical study by Xie *et al.* predicted that graphene is more effective for conductivity improvement than competing nanofillers such as CNTs because of their large specific surface area. With high conductivity and mechanical properties, graphene/polymer composites have possible uses as antistatic coatings.[98]

In view of the high thermal conductivity, high thermal stability, and the flat surface of graphene, which can minimize the geometric contribution to the thermal interface resistance, it is expected that a small amount of graphene can significantly improve the thermal properties of polymer matrices. Based on the theoretical and experimental results, the thermal conductivity of polymer matrices can be significantly improved with a small graphene loading, and the thermal conductivity improvement of graphene-based composites is more efficient than that of CNT-based composites. The outstanding thermal properties of graphene-based composites can be attributed to a favorable combination of the high aspect ratio, two-dimensional geometry, and stiffness of graphene, and the low interfacial thermal resistance between graphene and the polymer matrix.[97]

In addition to mechanical, electrical, and thermal properties, many other functional properties of graphene/polymer composites, such as bioactivity, microwave absorption, and gas permeability, were also reported.

Low permeability: Gas and water barriers are also an important application of graphene/polymer composites. It was reported that graphene low permeability could be used for the development of graphene/polymer composites since they present good gas barrier properties. This is very important for their use as physical barriers for gases such as O_2, N_2, and He in packaging materials.[99]

Antibacterial toxicity: Recently, it has been reported that graphene-based materials also exhibited strong antibacterial toxicity, for example Santos and coworkers developed the fabrication of a nanocomposite containing poly(*N*-vinylcarbazole) (PVK) and graphene (G) in solutions and thin films. The antimicrobial properties of the electrodeposited PVK–G films and solution-based PVK–G were investigated against *Escherichia coli* (*E. coli*) and *Bacillus subtilis*

(*B. subtilis*). Microbial growth after exposure to the nanocomposite, metabolic assay, and live–dead assay of the bacterial solutions exposed to PVK–G presented fewer viable and active bacteria than those exposed to pure PVK or pure graphene solutions.[100]

6. Conclusions

Here, we have described the recent strategies in the preparation of stable dispersions of graphene that allow its organic functionalization, as well as the integration of graphene layers with other materials as metals, polymers, or surfaces. The wide-ranging advantage of these methodologies is that they result in stable dispersions of graphene, producing dispersible materials that comprise mainly FG and/or monolayer graphene with few concentration of defects. Additionally, the resulting graphene sheets are stabilized by the interactions with the solvent and are suitable materials for performing organic reactions. The control over the organic reactions performed on graphene layers is expected to increment the number of its applications. Graphene can be efficiently incorporated with other materials by the attachment of the appropriated moieties allowing the design of advance materials and devices. Then, chemical manipulation of graphene is expected to drive this material to the next generation of advanced nanomaterials.

Acknowledgments

Thanks are given to CONACYT through the project CB-166914 and PROMEP/103.5/12/3953. JIT thanks CONACYT for the scholarship number 346987.

References

1. Novoselov, K. S.; Geim, A. K.; Morozov, S. V.; Jiang, D.; Katsnelson, M. I.; Grigorieva, V.; Dubonos, S. V.; Firsov, A. A. *Nature* **2005**, *408*, 197–200.
2. Geim, A. K. *Science* **2009**, *324*, 1530–1534.
3. Novoselov, K. S.; Geim, A. K.; Morozov, S. V.; Jiang, Y.; Zhang, Y.; Dubonos, S. V.; Grigorieva, I. V.; Firsov, A. A. *Science* **2004**, *306*, 666–669.
4. Reina, A.; Jia, X.; Ho, J.; Nezich, D.; Son, H.; Bulovic, V.; Dresselhaus, M. S.; Kong, J. *Nano Lett.* **2009**, *9*, 30–35.
5. Emtsev, K. V.; Bostwick, A.; Horn, K.; Jobst, J.; Kellogg, G. L.; Lay, L.; McChesney, J. L.; Ohta, T.; Reshanov, S. A.; Röhrl, J.; Rotenberg, E.; Schmid, A. K.; Waldmann, D.; Weber, H. B.; Seyller, T. *Nat. Mater.* **2009**, *8*, 203–207.

6. Balan, A.; Kumar, R.; Boukhicha, M.; Beyssac, O.; Bouillard, J. C.; Taverna, D.; Sacks, W.; Marangolo, M.; Lacaze, E.; Gohler, R.; Escoffier, W.; Poumiroi, J. M.; Shukla, A. *J. Phys. D: Appl. Phys.* **2010**, *43*, 374013.
7. Kosynkin, D. V.; Higginbotham, A. L.; Sinitskii, A.; Lomeda, J. R.; Dimiev, A.; Price, K.; Tour, J. M. *Nature* **2009**, *458*, 872–876.
8. Yang, X.; Dou, X.; Rouhanipour, A.; Zhi, L.; Räder, H. J.; Müller, K. *J. Am. Chem. Soc.* **2008**, *130*, 4216–4217.
9. Zhu, Y.; Murali, S.; Stoller, M. D.; Ganesh, K. J.; Cai, W.; Ferreira, P. J.; Pirkle, A.; Wallace, R. M.; Cychosz, K. A.; Thommes, M.; Su, D.; Stach, E. A.; Ruoff, R. S. *Science* **2011**, *332*, 1537–1541.
10. Li, X.; Wang, X.; Zhang, L.; Dai, H. *Science* **2008**, *319*, 1229–1232.
11. Hernandez, Y.; Nicolsi, V.; Loyta, M.; Blighe, F. M.; Sun, Z.; De, S.; McGovern, I. T.; Holland, B.; Byrne, M.; Gun´Ko, Y. K.; Boland, J. J.; Niraj, P.; Duesberg, G.; Krishnamurty, S.; Goodhue, R.; Hutchinson, J.; Scardaci, V.; Ferrari, A. C.; Coleman, J. N. *Nat. Nanotechnol.* **2008**, *3*, 563–568.
12. Lu, J.; Yang, J.; Wang, J.; Lim, A.; Wang, S.; Loh, K. P. *ACS Nano* **2009**, *3*, 2376–2375.
13. Valles, C.; Drummond, C.; Saadaoui, H.; Furtado, C. A.; He, M.; Roubeau, O.; Ortolani, L.; Monthioux, M.; Pénicaud, A. *J. Am. Chem. Soc.* **2008**, *130*, 15802–15804.
14. Englert, J. M.; Dotzer, C.; Yang, G.; Schmid, M.; Papp, C.; Gottfried, J. M.; Steinrück, H.-P.; Spiecker, E.; Hauke, F.; Hirsch, A. *Nature Chem.* **2011**, *3*, 279–286.
15. León, V.; Quintana, M.; Herrero, M. A.; Fierro, J. L. G.; de la Hoz, A.; Prato, M.; Vázquez, E. *Chem. Commun.* **2011**, *47*, 10936–10938.
16. (a) Stankovich, S.; Dikin, D. A.; Dommett, H. B.; Kohlhaas, K. M.; Zimney, E. J.; Stach, E. A.; Piner, R. D.; Nguyen, S. T.; Ruoff, R. S. *Nature* **2006**, *442*, 282–286. (b) Bai, S.; Shen, X. *RCS Advances* **2012**, *2*, 64–98.
17. Wu, Q.; Xu, Y.; Yao, Z.; Liu, A.; Shi, G. *ACS Nano* **2010**, *4*, 1963–1970.
18. Yoo, E.; Kim, J.; Hosono, E.; Zhou, H.; Kudo, T.; Honma, I. *Nano Lett.* **2008**, *8*, 2277–2282.
19. Qu, L.; Liu, Y.; Baek, J. B.; Dai, L. *ACS Nano* **2010**, *4*, 1321–1326.
20. Lucechinger, N. A.; Athanassious, E. K.; Stark, W. J. *Nanotech.* **2008**, *19*, 445201.
21. Wang, S.; Ang, P. K.; Wang, Z.; Tang, A. L. L.; Thong, J. T. L.; Loh, K. P. *Nano Lett.* **2010**, *10*, 92–98.
22. Lee, V.; Whittaker, L.; Jaye, C.; Baroudi, K. M.; Fischer, D. A.; Banerjee, S. *Chem. Mater.* **2009**, *21*, 3905–3916.
23. Mohanty, N.; Berry, V. *Nano Lett.* **2008**, *8*, 4469–4476.
24. Bonaccorso, F.; Sun, Z.; Hassan, T.; Ferrari, C. *Nat. Photonics* **2010**, *4*, 611–622.

25. Stankovicha, S.; Dikina, D. A.; Pinera, R. D.; Kohlhaasa, K. A.; Kleinhammesc, A.; Jiac, Y.; Wuc, Y.; Nguyenb, S. T.; Ruoff, R. S. *Carbon* **2007**, *45*, 1558–1565.
26. Gomez, C.; Weitz, R. T.; Bittner, A. M.; Scolari, M.; Mews, A.; Burghard, M.; Kern, K. *Nano Lett.* **2007**, *7*, 3499–3503.
27. Zhu, L.; Zhao, X.; Li, Y.; Yu, X.; Li, C.; Zhang, Q. *Mat. Chem. Phys.* **2013**, *137*, 984–990.
28. Suslick, K. S.; Hyeon, T.; Fanf, M. *Chem. Mater.* **1996**, *8*, 2172–2179.
29. Xu, H.; Suslick, K. S. *J. Am. Chem. Soc.* **2011**, *133*, 9148–9151.
30. Coleman, J. N. *Acc. Chem. Rev.* **2012**, *46*, 14–22.
31. Viculis, L. M.; Mack, J. J.; Kaner, R. B. *Science* **2003**, *299*, 1361.
32. Bang, J. H.; Suslick, K. S. *Adv. Mater.* **2010**, *22*, 1039–1059.
33. Misik, V.; Riesz, P. *Free Radical Biol. Med.* **1996**, *20*, 129–138.
34. Guittonneau, F.; Abdelouas, A.; Grambow, B.; Huclier, S. *Ultrason. Sonochem.* **2010**, *17*, 391–398.
35. Khan, U.; O´Neil, A.; Loyta, M.; De, S.; Coleman J. N. *Small* **2010**, *6*, 864–871.
36. Paredes, J. I.; Villar-Rodil, S.; Solís-Fernández, P.; Fernández-Merino, M. J.; Guardia, L.; Martínez-Alonso, A.; Tascón, J. M. D. *J. Alloy Compd.* **2012**, *536S*, S450–S455.
37. (a) Giordani, S.; Bergin, S. D.; Nicolosi, V.; Lebedkin, S.; Kappes, M. M.; Blau, W. J.; Coleman, J. N. J. *J. Phys. Chem. B* **2006**, *110*, 15708–15718. (b) Furtado, C. A.; Kim, U. J.; Gutierrez, H. R.; Pan, L.; Dickey, E. C.; Eklud, P. C. *J. Am. Chem. Soc.* **2004**, *126*, 6095–6105. (c) Landi, B. J.; Ruf, H. J.; Worman, J. J.; Raffaelle, R. P. *J. Phys. Chem. B* **2004**, *108*, 17098–17095.
38. Hamilton, C. E.; Lomeda, J. R.; Sun, Z.; Tour, J. M.; Barron, A. R. *Nano Lett.* **2009**, *9*, 3460.
39. Bourlinos, A. B.; Georgakilas, V.; Zboril, R.; Steriotis, T. A.; Stubos, A. K. *Small* **2009**, *5*, 1841.
40. O´Neil, A.; Khan, U.; Nirmalraj, P. N.; Boland, J.; Coleman, J. N. *J. Phys. Chem. C* **2011**, *115*, 5422–5428.
41. Loyta, M.; King, P. J.; Khan, U.; De, S.; Coleman, J. N. *ACS Nano* **2010**, *4*, 3155–3162.
42. Smith, R. J.; Loyta, M.; Coleman, J. N. *New J. Phys.* **2010**, *12*, 125008.
43. Valles, C.; Drummond, C.; Saadaoui, H.; Furtado, C. A.; He, M.; Roubeau, O.; Ortolani, L.; Monthioux, M.; Penicaud, A. *J. Am. Chem. Soc.* **2008**, *130*, 15802–15804.
44. Dhakate, S. R.; Chauhan, N.; Sharma, S.; Tawale, J.; Singh, S.; Sahare, P. D.; Mathur, R. B. *Carbon* **2011**, *49*, 1946–1954.
45. Hardacre, C.; Holbrey, J. D.; Nieuwenhuyzen, M.; Youngs, T. G. A. *Acc. Chem. Res.* **2007**, *40*, 1146–1155.

46. Lu, J.; Yang, J.; Wang, J.; Lim, A.; Wang, S.; Loh, K. P. *ACS Nano* **2009**, *3*, 2367–2375.
47. Rangappa, D.; Koji, S.; Wang, M.; Gautam, U. K.; Golberg, D.; Itoh, H.; Ichihara, M.; Honma, I. *Chem. Eur. J.* **2010**, *16*, 6488–6494.
48. Liu, C.; Hu, G.; Gao, H.; *J. Supercrit. Fluids* **2012**, *63*, 99–104.
49. Kosynkin, D. V.; Higginbotham, A. L.; Sinitskii, A.; Lomeda, J. R.; Dimiev, A.; Price, K. B.; Tour, J. M. *Nature* **2009**, *458*, 872–876.
50. Rurali, R.; Coluci, V. R.; Galvao, D. S. *Phys. Rev. B* **2006**, 085414.
51. Moriarty, P. *Rep. Prog. Phys.* **2001**, *64*, 297–381.
52. Merkulov, V. I.; Guillorn, M. A.; Lowndes, D. H.; Simpson, M. L. *Appl. Phys. Letts.* **2001**, *79*, 1178–1180.
53. Liu, J.; Wang, C.; Tu, X.; Liu, B.; Chen, L.; Zheng, M.; Zhou, C. *Nat. Comm.* **2012**, *3*, 1199.
54. Zhu, L.; Zhao, X.; Li, Y.; Yu, X.; Li, C.; Zhang, Q. *Mater. Chem. Phys.* **2013**, *137*, 984–990.
55. Patra, N.; Wang, B.; Král. P. *Nano Lett.* **2009**, *9*, 3766–3771.
56. (a) Smalley, R. E. *Acc. Chem. Res.* **1992**, *25*, 98–105. (b) Goroff, N. S. *Acc. Chem. Res.* **1996**, *29*, 77–83. (c) Kroto, H. W.; McKay, K. *Nature* **1988**, *331*, 328–331.
57. Ulbricht, H.; Moos, G.; Hertel, T. *Phys. Rev. Lett.* **2003**, *90*, 095501.
58. Chuvilin, A.; Kaiser, U.; Bichoutskaia, E.; Besley, N. A.; Khlobystov, A. N. *Nature Chem.* **2010**, 450–453.
59. Braga, S. F.; Coluci, V. R.; Legoas, S. B.; Giro, R.; Galvao, D. S.; Baughman, R. H. *Nano Lett.* **2004**, *4*, 881–884.
60. Patra, N.; Song, Y.; Král, P. *ACS Nano* **2011**, 1798–1804.
61. Cendula, P.; Kiravittaya, S.; Mönch, I.; Schumann, J.; Schmidt, O. G. *Nano Lett.* **2011**, *11*, 236–240.
62. Lee, C.; Wei, X.; Kysar, J. W.; Hone, J. *Science* **2008**, *321*, 385–388.
63. Sidorov, A.; Mud, D.; Sumanasekera, G.; Ouseph, P. J.; Jayanthi, C. S.; Wu, S.-Y. *Nanotechnology* **2009**, *20*, 055611.
64. Yu, D.; Liu, F. *Nano Lett.* **2007**, *7*, 3046–3050.
65. Quintana, M.; Grzelczak, M.; Spyrou, K.; Kooi, B.; Bals, S.; Van Tendeloo, G.; Rudolf, P.; Prato, M. *Chem. Comm.* **2012**, *48*, 12159–12161.
66. Rice-Evans, C. A.; Diplock, A. T. *Free Radical Biol. Med.* **1993**, *15*, 77–96.
67. Wang, S.; Tang, L. A.; Bao, Q.; Lin, M.; Deng, S.; Goh, B. M.; Loh, K. P. *J. Am. Chem. Soc.* **2009**, *131*, 16832–16837.
68. Feng, X.; Liang, Y.; Zhi, L.; Thomas, A.; Wu, D.; Lieberwirth, I.; Kolb, U.; Mullen, K. *Adv. Funct. Mater.* **2009**, *19*, 2125–2129.
69. Quintana, M.; Montellano, A.; del Rio-Castillo, A. E.; Van Tendeloo, G.; Bittencourt, C.; Prato, M. *Chem. Comm.* **2011**, *47*, 9330–9332.

70. Dahl, J. A.; Maddux, B. L. S.; Hutchison, J. E. *Chem. Rev.* **2007**, *107*, 2228–2269.
71. Quintana, M.; Grzelczak, M.; Spyrou, K.; Calvaresi, M.; Bals, S.; Kooi, B.; Van Tendeloo, G.; Rudolf, P.; Zerbeto, F.; Prato, M. *J. Am. Chem. Soc.* **2012**, *134*, 13310–13315.
72. Cao, A.; Dickerel, P. L.; Sawyer, W. G.; Ghasemi-Nejhad, M. N.; Ajayan, P. M. *Science* **2005**, *310*, 1307–1310.
73. Calvaresi, M.; Quintana, M.; Rudolf, P.; Zerbetto, F.; Prato, M. *Chem. Phys. Chem.* **2013**, doi: 101002/cphc.201300337.
74. Park, J.; Yan, M. *Acc. Chem. Res.* **2013**, *46*, 181–189.
75. Niyogi, S.; Bekyarova, E.; Itkis, M. E.; Zhang, H.; Shepperd, K.; Hicks, J.; Sprinkle, M.; Berger, C.; Ning Lau, C.; de Heer, W. A.; Conrad, E. H.; Haddon, R. C. *Nano Lett.* **2010**, *10*, 4061.
76. Vasilios, G.; Michal, O.; Athanasios, B.; Vimlesh, C.; Namdong, K.; Christian, K.; Pavel, H.; Radek, Z.; Kwang, S. K. *Chem. Rev.* **2012**, *112*, 6156–6214.
77. Elias, D. C.; Nair, R. R.; Mohiuddin, T. M. G.; Morozov, S. V.; Blake, P.; Halsall, M. P.; Ferrari, A. C.; Boukhvalov, D. W.; Katsnelson, M. I.; Geim, A. K.; Novoselov, K. S. *Science* **2009**, *323*, 610–613.
78. Sofo, J. O.; Chaudhari, A. S.; Barber, G. D. *Phys. Rev. B* **2007**, *75*, 153401.
79. Sharma, R.; Baik, J. H.; Perera, J. C.; Strano, M. S. *Nano Lett.* **2010**, *10*, 398–405.
80. Quintana, M.; Spyro, K.; Grzelczak, M.; Browne, W. R.; Rudolf, P.; Prato, M. *ACS Nano.* **2010**, *4*, 3527–3533.
81. Loh, K. P.; Bao, Q.; Ang, P. K.; Yang, J. *J. Mater. Chem.* **2010**, *2*, 2277–2289.
82. Yan, L.; Zheng, Y. B.; Zhao, F.; Li, S.; Gao, X.; Xu, B.; Weiss, P. S.; Zhao, Y. *Chem. Soc. Rev.* **2012**, *41*, 97–114.
83. Banhart, F.; Kotakoski, J.; Krasheninnikov, A. V. *ACS Nano* **2010**, *5*, 26–41.
84. Quintana, R.; Vazquez, E.; Prato, M. *Acc. Chem. Res.* **2013**, *46*, 138–148.
85. Kosynkin, D. V.; Higginbotham, A. L.; Sinitskii, A.; Lomeda, J. R.; Dimiev, A.; Price, B. K.; Tour, J. M. *Nature* **2009**, *458*, 872.
86. Liu, H.; Ryu, S.; Chen, Z.; Steigerwald, L.; Nuckolls, C.; Brus, L. E. *J. Am. Chem. Soc.* **2009**, *131*, 17099–17101.
87. Georgakilas, V.; Bourlinos, A. B.; Gournis, D.; Tsoufis, T.; Trapalis, C.; Alonso, A. M.; Prato, M. J. *Am. Chem. Soc.* **2008**, *130*, 8733.
88. Georgakilas, V.; Bourlinos, A. B.; Zboril, R.; Steriotis, T. A.; Dallas, P.; Stubos, A. K.; Trapalis, C. *Chem. Commun.* **2010**, *26*, 1766–1768.
89. Quintana, M.; Spyrou, K.; Grzelczak, M.; Brown, W. R.; Rudolf, P.; Prato, M. *ACS Nano* **2010**, *4*, 3527–3533.
90. Quintana, M.; Grzelczak, M.; Prato, M. *Phys. Status Solidi B* **2010**, *247*, 2645–2648.
91. Liu, L. H.; Lerner, M. M.; Yan, M. *Nano Lett.* **2010**, *10*, 3754.
92. Strom, T. A.; Dillon, E. P.; Hamilton, C. E.; Barron, A. R. *Chem. Commun.* **2010**, *46*, 4097.

93. He, H.; Gao, C. *Chem. Mater.* **2010**, *22*, 5054.
94. Xu, H.; Suslick, K. S. *J. Am. Chem. Soc.* **2011**, *133*, 9148–9151.
95. Kuilla, T.; Bhadrab, S.; Yaoa, D.; Kimc, N. H.; Bosed, S.; Leea, J. H. *Prog. Poly. Sci.* **2010**, *35*, 1350–1375.
96. Quintana, M.; Montellano-López, M.; Rapino, S.; Toma, F. M.; Iurlo, M.; Carraro, M.; Sartore, A.; Maccato, C.; Ke, X.; Bittencourt, C.; Da Ros, T.; Van Tendeloo, G.; Marcaccio, M.; Paolucci, M.; Prato, M.; Bonchio, M. *ACS Nano* **2013**, *7*, 811–817.
97. Liang, M.; Luo, B.; Zhi, L.; Liang, M.; Luo, B.; Zhi, L. *Int. J. Energy Res.* **2009**, *33*, 1161–1170.
98. Xie, S. H.; Liu, Y. Y.; Li, J. Y. *Appl. Phys. Lett.* **2008**, *92*, 243121–243121-3. Du, J.; Cheng, H.-M. *Macromol. Chem. Phys.* **2012**, *213*, 1060–1077.
99. Koening, P. S.; Wang, L.; Pellegrino, J.; Bunch, S. *Nature Nanotech.* **2012**, *7*, 728–732.
100. Santos, C. M.; Tria, M. C. R.; Vergara, R. A. M. V.; Ahmed, F.; Advincula, R. C.; Rodriges, D. F. *Chem. Comm.* **2011**, *47*, 8892–8894.

This page intentionally left blank

Chapter 4

On Thermodynamic Characteristics of the Thermal Desorption of Hydrogen from Hydrogenated Graphene Layers

*Yury S. Nechaev**

Bardin Institute for Ferrous Metallurgy
Kurdjumov Institute of Metals Science and Physics
Vtoraya Baumanskaya St., 9/23
Moscow 105005, Russia

T. Nejat Veziroglu

International Association for Hydrogen Energy
5794 SW 40 St. # 303
Miami, FL 33155, USA

1. Introduction 220

2. Analysis and Comparison of Data 223
   2.1. Consideration of data on theoretical graphanes (CH) 223
   2.2. Consideration of data on hydrogen thermal desorption from theoretical and experimental graphanes 226
   2.3. Consideration of a thermodynamic probability of existence of hydrogenated graphenes–graphanes possessing of a very high binding energy 228
   2.4. Consideration of data on hydrogen desorption in the hydrogenated mono- and bilayer epitaxial graphene samples 230
3. Analysis and Comparison of Data 235
   3.1. Analysis of the Raman spectroscopy data on thermal desorption of hydrogen from hydrogenated graphene flakes 235
   3.2. Analysis of the STM and STS data on reversible hydrogenation of epitaxial graphene and graphite surfaces 237

* Corresponding author. E-mail: Yuri1939@inbox.ru

3.3. Analysis of the HREELS/LEED data on thermal desorption of hydrogen from hydrogenated graphene on SiC substrate 239
3.4. Analysis of the Raman spectroscopy data on thermal desorption of hydrogen from hydrogenated graphene layers on SiO_2 substrate 242
3.5. Analysis of TDS and STM data on HOPG treated by deuterium 244
3.6. Analysis of PES and ARPES data on dehydrogenation of graphene/SiC samples 245
3.7. Analysis of TDS and STM data on HOPG treated by hydrogen 246
4. A Possibility of Intercalation of Solid H_2 into Hydrogenated Graphite Nanofibers, Relevance to the Hydrogen On-Board Storage Problem 250
5. Conclusions 253
Acknowledgments 254
References 255

1. Introduction

As has been noted in a number of articles between 2007–2013, the hydrogenation of graphene, a single layer of carbon atoms arranged in a honeycomb lattice,[1,2] as a prototype of covalent chemical functionalization and an effective tool to open the band gap of graphene, is of fundamental importance.

It is relevant to the actual problem of the hydrogen on-board storage, and also to the actual related problem of the thermodynamic stability and thermodynamic characteristics of the following systems:

1. double-side hydrogenated graphene (theoretical graphane of composition CH[3,4] and experimental graphane[5]);
2. theoretical single-side hydrogenated graphene of composition CH (SSHG,[6–8]);
3. theoretical SSHG of composition C_2H (graphone,[9]);
4. experimental hydrogenated epitaxial graphene, bigraphene, and a few-layer graphene on SiO_2 or other substrates (Ref. 5 and others);
5. experimental and theoretical single-external-side hydrogenated single-walled carbon nanotubes of composition about C_2H and experimental hydrofullerene $C_{60}H_{36}$ (Refs. 10–13 and analytical review [14]);

6. experimental single-internal-side hydrogenated graphene nanoblisters possessing of a very high Young's modulus (with intercalated into them H_2 gas of a high pressure) formed on surface of highly oriented pyrolytic graphite (HOPG) or epitaxial graphene under the definite atomic hydrogen treatment (Refs. 15–21);
7. experimental hydrogenated graphite nanofibers (GNFs)[18–21] possessing of a very high Young's modulus with intercalated into them solid H_2 of a high density, that is relevant to the problem of the hydrogen on-board storage.

In this analytical review, results are presented of the thermodynamic analysis and comparison of some theoretical and experimental data (especially, from the most cited works[3,5] and from the near non-cited ones[18–21]).

As was noted in Ref. 8, the double-side hydrogenation of graphene is now well understood, at least from theoretical point of view. For example, Sofo *et al.*[3] predicted theoretically a new insulating material of CH composition called graphane (double-side hydrogenated graphene), in which each hydrogen atom adsorbs on top of a carbon atom from both sides (so that hydrogen atoms adsorbed in different carbon sublattices are on different sides of the monolayer plane). The formation of graphane was attributed to the efficient strain relaxation for the sp^3 hybridization, accompanying with a strong (diamond-like or other) distortion of the graphene network.[3,22] In contrast to graphene (zero-gap semiconductor), graphane is an insulator with an energy gap $E_g \approx 5.4$ eV.[4,23]

If only hydrogen atoms adsorbed on one side of graphene (in graphane) are retained, we obtain graphone of C_2H composition, which is a magnetic semiconductor with $E_g \approx 0.5$ eV and a Curie temperature $T_c \approx 300$–400 K.[24]

As was noted in Ref. 6, neither graphone nor graphane are suitable for real practical applications, since the former has a low value of E_g and undergoes rapid disordering because of hydrogen migration to neighboring vacant sites even at a low temperature[9] and the latter cannot be prepared on a solid substrate.

SSHG of CH composition[7,25] is an alternative: in contrast to graphane, hydrogen atoms are adsorbed only on one side; in contrast to graphone, they are adsorbed on all carbon atoms rather than on every second carbon atom. The value of E_g in SSHG is sufficiently high (by 1.6 eV lower than in graphane[6,7]), and it can be prepared on a solid substrate in principle.[6] But, this quasi-two-dimensional carbon–hydrogen theoretical system is shown[6] to have a relatively low thermal stability, which makes it difficult to use SSHG in practice.

As was noted in Ref. 7, it may be inappropriate to call the covalently bonded SSHG system sp^3 hybridized, since the characteristic bond angle of 109.5° is not present anywhere, *i.e.*, there is no diamond-like strong distortion of the graphene network, rather than in graphane.[3] Generally in the case of a few hydrogen atoms interacting with graphene or even for graphane, the underlining carbon atoms are displaced from their locations (*i.e.*, there may be the diamond-like local distortion of the graphene network), showing the signature of sp^3 bonded system. However, in SSHG, all the carbon atoms remain in one plane, making it difficult to call it sp^3 hybridized; obviously, this is some specific sp^3-like hybridization. Such model is taken into account (in this analytical study) in a number of works.[10–21]

In a number of works considered in Ref. 25, it was shown that hydrogen chemisorption corrugates the graphene sheet (in fullerene, carbon nanotube,[26] graphite,[27] and graphene[28]), and transforms it from a semimetal into a semiconductor[3,5]; this can even induce magnetic moments.[29–31]

It is worth to repeat that the prediction[3] for the double-side hydrogenated graphene (a free-standing membrane) was partially (in terms of Ref. 8) confirmed by Elias *et al.*[5] They[5] demonstrated that graphene can react with atomic hydrogen, which transforms this highly conductive zero-overlap semimetal into an insulator of a high thermal stability, and the double-side hydrogenation of graphene is reversible. The authors[5] themselves expressed some doubts, relevant to the complete adequacy of the experimental graphane[5] to the theoretical one.[3] They[5] supposed, alternatively, that the produced by them experimental graphane (a free-standing membrane) may have "a more complex hydrogen bonding than the one suggested by theory",[3] and that the latter may be as the "until-now-theoretical material".

In the case of the epitaxial graphene (on substrate such as SiO_2[5] or others), hydrogenation occurs only on the top basal plane of graphene, and obviously, it is not accompanied with a strong (diamond-like or other) distortion of the graphene network, but only with some, it is rippling. The first experimental indication of such a specific single-side hydrogenation came from Elias *et al.*[5] The authors[5] mentioned a possible contradiction with the theoretical results of Sofo *et al.*,[3] which had downplayed the possibility of a single-side hydrogenation. They[5] supposed an important facilitating role of the material rippling (for hydrogenation of graphene on SiO_2) and believed that such a single-side hydrogenated epitaxial graphene can be a disordered material, similar to graphene oxide, rather than a new graphene-based crystal — the experimental graphane produced by them. In other words, the two different materials have been produced in work by Ref. 5.

On the other hand, it is expedient to note that changes in Raman spectra of graphene caused by hydrogenation were rather similar (with respect to locations of D, G, D′, 2D, and (D + D′) peaks) both for the epitaxial graphene on SiO_2 and for the free-standing graphene membrane (Figure 3 in Ref. 5).

As is supposed by many scientists (for instance, Refs. 5 and 8), such a single-side hydrogenation of epitaxial graphene occurs because the diffusion of hydrogen along the graphene–SiO_2 interface is negligible and perfect graphene is impermeable to any atom and molecule.[32] But these two aspects are of the kinetic character, and therefore they can not influence the thermodynamic predictions.[3,24,31]

Authors of Ref. 8 noted that their test calculations (relevant to Ref. 32 results) show that the barrier for the penetration of a hydrogen atom through the six-membered ring of graphene is larger than 2.0 eV. Thus, they[8] believe (H. G. Xiang and M.-H. Whangbo, private communication) "that it is almost impossible for a hydrogen atom to pass through the six-membered ring of graphene at room temperature".

In the present analytical review, a real possibility is considered of a situation when a hydrogen atom can pass through the graphene network at room temperature. This is the case when relevant defects exist in graphene, for instance, as grain boundaries and/or vacancies.[33–42] It is related to the further consideration (in this analytical study) of data[15–21] mentioned above.

Previous theoretical studies[24,31] suggest that single-side hydrogenation of ideal (perfect) graphene would be thermodynamically unstable. Thus (in terms of Ref. 8), it remains a puzzle why the single-side hydrogenation of epitaxial graphene is possible (and even reversible, according to Ref. 5 data), and why the hydrogenated species are stable at room temperatures.[5,43]

This puzzle situation is also considered in the present analytical review. And the main aim of this study is to show a real possibility (at least, from the thermodynamic point of view) for the existence of hydrogenated graphene-based nanostructures[18–21] possessing of a very high Young's modulus, and also to show a real possibility of intercalation in such nanostructures of solid molecular hydrogen under definite hydrogenation conditions, that is of relevance to the actual problem of the hydrogen storage in fuel-cell-powered vehicles.[18–21]

2. Analysis and Comparison of Data[3–5,25,18–21]

2.1. Consideration of data[3,25] on theoretical graphanes (CH)

In a work by Ref. 3, the stability of graphane (a fully saturated extended two-dimensional hydrocarbon derived from a single graphene sheet with formula CH) has been predicted on the basis of first-principle total-energy calculations.

All of the carbon atoms are in sp^3 hybridization forming a hexagonal network (a strongly diamond-like distorted graphene network) and the hydrogen atoms are bonded to carbon on both sides of the plane in an alternative manner. It has been found[3] that graphane can have two favorable conformations: (i) a chair-like (diamond-like) conformer and (ii) a boat-like (zigzag-like) one.

The diamond-like conformer (Figure 1 in Ref. 3 or Figure 4D in Ref. 5) is more stable, rather than the zigzag-like one. It was concluded[3] from results of calculations of the binding energy ($\Delta H_{\text{bind.(graphane[3])}}$) — the difference between the total energy of the isolated atoms and the total energy of the compounds (Table 1 in Ref. 3) and the standard energy of formation ($\Delta H^0{}_{\text{f298(graphane[3])}}$, Figure 2 in Ref. 3) of the compounds ($CH_{\text{(graphane[3])}}$) from crystalline graphite ($C_{\text{(graphite)}}$) and gaseous molecular hydrogen ($H_{2\text{(gas)}}$) at (as was noted in Ref. 3) standard pressure (usually, 0.1 MPa) and temperature (usually, 298 K) conditions.

For the diamond-like graphane, the former quantity is $\Delta H_{\text{bind.(graphane[3])}} = 6.56$ eV/atom (Table 1 in Ref. 3), and the latter one is $\Delta H_1 = \Delta H^0{}_{\text{f298(graphane[3])}} = -0.15$ eV/atom (Figure 2 in Ref. 3). The latter quantity corresponds to the following reaction:

$$C_{\text{(graphite)}} + \frac{1}{2} H_{2\text{(gas)}} \rightarrow CH_{\text{(graphane[3])}}, \quad (\Delta H_1), \tag{1}$$

where ΔH_1 is the standard energy (enthalpy) change for this reaction.

By using the theoretical[3] quantity $\Delta H^0{}_{\text{f298(graphane[3])}}$, one[18–21] can evaluate (in the framework of the thermodynamic method of cyclic processes, for instance, Ref. 44), a value of the energy of formation (ΔH_2) of graphane ($CH_{\text{(graphane[3])}}$) from graphene ($C_{\text{(graphene)}}$) and gaseous atomic hydrogen ($H_{\text{(gas)}}$). For this, it is necessary to include in the consideration the following three additional reactions:

$$C_{\text{(graphene)}} + H_{\text{(gas)}} \rightarrow CH_{\text{(graphane[3])}}, \quad (\Delta H_2), \tag{2}$$

$$C_{\text{(graphene)}} \rightarrow C_{\text{(graphite)}}, \quad (\Delta H_3), \tag{3}$$

$$H_{\text{(gas)}} \rightarrow \frac{1}{2} H_{2\text{(gas)}}, \quad (\Delta H_4), \tag{4}$$

where ΔH_2, ΔH_3, and ΔH_4 are the standard energy (enthalpy) changes.

Reaction (2) can be presented as a sum of Reactions (3), (4), and (1); hence (in the framework of the thermodynamic method of cyclic processes[44]):

$$\Delta H_2 = (\Delta H_3 + \Delta H_4 + \Delta H_1). \tag{5}$$

Substituting in Eq. (5), the known experimental values (Ref. 45 and/or other related Handbooks) of $\Delta H_4 = -2.26$ eV/atom and $\Delta H_3 \approx -0.05$ eV/atom,[25,45] and also the theoretical[3] value of $\Delta H_1 = -0.15$ eV/atom, one[18–21] can obtain a desired value of $\Delta H_2 = -2.5 \pm 0.1$ eV/atom. The quantity of $-\Delta H_2$ (according to Refs. 18–21) characterizes the break-down energy of C–H sp^3 bond in graphane,[3] of relevance to breaking away of one hydrogen atom from the material, which is $\Delta H_{(C–H)graphane[3]} = -\Delta H_2 = 2.5 \pm 0.1$ eV.

For evaluating of the above-mentioned value of ΔH_3, one can use, for instance, experimental data[45] on the graphite sublimation energy at 298 K ($\Delta H_{subl.(graphite)[45]} = 7.41 \pm 0.05$ eV/atom) and theoretical data[25] on the binding cohesive energy at about 0 K for graphene ($\Delta H_{cohes.(graphene)[25]} = 7.40$ eV/atom, Figure 1 in Ref. 25). Hence, neglecting the temperature dependence of these quantities (in the interval of 0–298 K), one[18–21] can obtain the value of $\Delta H_3 \approx -0.05$ eV/atom.

$\Delta H_{cohes.(graphene[25])}$ quantity characterizes the breakdown energy of 1.5 C–C sp^2 bond in graphene,[25] relevant to breaking away of one hydrogen atom from the material. Hence, one[18–21] can evaluate the breakdown energy of C–C sp^2 bonds in graphene, which is $\Delta H_{(C–C)graphene[25]} = 4.93$ eV. This theoretical[25] quantity coincides with the similar empirical quantities (obtained in Refs. 18–21 from $\Delta H_{subl.(graphite)[45]}$) for C–C sp^2 bonds in graphene and graphite, which are $\Delta H_{(C–C)graphene[18–21,45]} \approx \Delta H_{(C–C)graphite[18–21,45]} = 4.94 \pm 0.03$ eV. The similar empirical quantity for C–C sp^3 bonds in diamond (obtained in Refs. 18–21 from the diamond sublimation energy $\Delta H_{subl.(diamond)[45]}$) is $\Delta H_{(C–C)diamond[18–21,45]} = 3.69 \pm 0.02$ eV.

It is expedient to note that in Ref. 25, chemisorption of hydrogen on graphene was studied using atomistic simulations with the second generation of reactive empirical bond order Brenner interatomic potential. According to data,[25] the cohesive energy of graphane (CH) in the ground state is $\Delta H_{cohes.(graphane[25])} = 5.03$ eV/atom(C) (Figure 1 in Ref. 25). It results[25] in the hydrogen binding energy, which is $\Delta H_{(C–H)graphane[25]} = 1.50$ eV/atom(H) (Table 1 in Ref. 25).

The theoretical $\Delta H_{bind.(graphane[3])}$ quantity[3] characterizes the breakdown energy of one C–H sp^3 bond and 1.5 C–C sp^3 bonds (Figure 1 in Ref. 3 or Figure 4D in Ref. 5). Hence, by using the above-mentioned values of $\Delta H_{bind.(graphane[3])}$ and $\Delta H_{(C–H)graphane[3]}$, one[18–21] can evaluate the breakdown energy of C–C sp^3 bonds in the theoretical graphane,[3] which is $\Delta H_{(C–C)graphane[3]} = 2.7$ eV. And by using the above-noted theoretical[25] values of $\Delta H_{cohes.(graphane[25])}$ and $\Delta H_{(C–H)graphane[25]}$, one can evaluate (in the similar manner) the breakdown energy of C–C sp^3 bonds in the theoretical graphane,[25] which is $\Delta H_{(C–C)graphane[25]} = 2.35$ eV.

Comparing in such a way[18–21] values of $\Delta H_{(C–C)graphane[3]}$, $\Delta H_{(C–C)graphane[25]}$, $\Delta H_{(C–C)graphene[25]}$, $\Delta H_{(C–C)graphene[18–21,45]}$, $\Delta H_{(C–C)graphite[18–21,45]}$, and $\Delta H_{(C–C)diamond[18–21,45]}$ shows that the elastic and intrinsic strength properties (and particularly, a Young's modulus) of the theoretical[3,25] graphanes can be much less than those for perfect (*i.e.*, without defects) graphene,[1,25] perfect graphite,[45] or perfect diamond.[45]

2.2. Consideration of data on hydrogen thermal desorption from theoretical[3,4] and experimental[5] graphanes

In Ref. 4, the process of hydrogen thermal desorption (TDS) from graphane (in the sense of Ref. 3) had been studied using the method of molecular dynamics. The temperature dependence (for $T = 1300–3000$ K) of the time ($\tau_{0.01}$) of hydrogen desorption onset (*i.e.*, the time of the removal of ~1% ($-\Delta C$) of the initial hydrogen concentration $C_0 \approx 0.5$ (in atomic fractions), $-\Delta C/C_0 \approx 0.01$) from the $C_{54}H_{7(54\,+\,18)}$ cluster (with 18 hydrogen passivating atoms at the edges to saturate the dangling bonds of sp^3-hybridized carbon atoms) was calculated.[4] The corresponding activation energy ($E_a = 2.46 \pm 0.17$ eV) and the corresponding near-temperature-independent frequency factor ($A = (2.1 \pm 0.5) \times 10^{17}$ s^{-1}) were also calculated.[4]

The process of hydrogen desorption (at $T = 1300–3000$ K) was described[4] in terms of the following standard Arrhenius relationship:

$$1/\tau_{0.01[4]} = A \exp(-E_a/k_B T), \tag{6}$$

where k_B is the Boltzmann constant.

The authors[4] supposed that their results do not contradict the experimental data,[5] according to which (Figure 3A in Ref. 5) the near-complete desorption of hydrogen ($-\Delta C/C_0 \approx 0.9$) from a graphane membrane was achieved by annealing it in argon at $T = 723$ K for 24 h (*i.e.*, $\tau_{0.9(membr.[5])723\ K} = 8.64 \times 10^4$ s). By using Eq. (6), the authors[4] evaluated the quantity of $\tau_{0.01(graphane[4])}$ for $T = 300$ K (~1×10^{24} s) and for $T = 600$ K (~2×10^3 s); but they noted that the above two values of $\tau_{0.01(graphane[4])}$ should be considered as rough estimates. In such a manner (Eq. 6), one can evaluate the quantity of $\tau_{0.01(graphane[4])723\ K} \approx 0.7$ s for $T = 723$ K, which is much less (by five orders) of $\tau_{0.9(membr.[5])723\ K}$.

In the framework of the formal kinetics approximation of the first-order rate reaction,[46] a characteristic quantity for the reaction of hydrogen desorption is $\tau_{0.63}$ — the time of the removal of ~63% ($-\Delta C$) of the initial hydrogen

concentration C_0 (*i.e.*, $-\Delta C/C_0 \approx 0.63$) from the hydrogenated graphene. Such a first-order rate reaction (desorption) can be described by the following equations[14,46]:

$$dC/dt = -KC, \tag{7}$$

$$(C/C_0) = \exp(-Kt) = \exp(-t/\tau_{0.63}), \tag{8}$$

$$K = (1/\tau_{0.63}) = K_0 \exp(-\Delta H_{\text{des.}}/k_B T), \tag{9}$$

where $K = (1/\tau_{0.63})$ is the reaction (desorption) rate constant; $\Delta H_{\text{des.}}$ is the reaction (desorption) activation energy; K_0 is the per-exponential (or frequency) factor of the reaction rate constant.

For the case of a non-diffusion-rate-limiting kinetics, the quantity of K_0 is the corresponding vibrational frequency ($K_0 = \nu$), and Eq. (9) is related to the Polanyi–Wigner one.[14]

By substituting in Eq. (8), the quantities of $t = \tau_{0.01(\text{graphane}[4])723\text{ K}}$ and $(C/C_0) = 0.99$, one can evaluate the desired quantity $\tau_{0.63(\text{graphane}[4])723\text{ K}} \approx 70$ s. Hence, using Eq. (9) results in the quantity of $A_{\text{an.}[4]} = 2 \times 10^{15}$ s^{-1}.

Analogically, one can evaluate the desired quantity $\tau_{0.63(\text{membr.}[5])723\text{ K}} \approx 3.8 \times 10^4$ s, which differs from $\tau_{0.63(\text{graphane}[4])723\text{ K}}$ by about three orders.

By substituting in Eq. (9), the quantity of $K = K_{(\text{membr.}[5])723\text{ K}} = 1/\tau_{0.63(\text{membr.}[5])723\text{ K}}$ and supposing that $\Delta H_{\text{des.}} = \Delta H_{\text{des.(membr.}[5])} \approx \Delta H_{\text{C–H(graphane}[3])} = -\Delta H_{2[3]}$, one can evaluate (in such an approximation) the quantity $K_{0(\text{membr.}[5])[3]} = -\nu_{(\text{membr.}[5])[3]} \approx 7 \times 10^{12}$ s^{-1} (for the experimental graphane membranes[5]).

The obtained quantity of $\nu_{(\text{membr.}[5])[3]}$ is less by one and half orders of the vibrational frequency $\nu_{\text{RD}[5]} = 2.5 \times 10^{14}$ s^{-1} corresponding to the D Raman peak (1342 cm^{-1}) for hydrogenated graphene membrane and epitaxial graphene on SiO_2 (Figure 3 in Ref. 5), the activation of which in the hydrogenated samples authors[5] attribute to breaking of the translation symmetry of C–C sp^2 bonds after formation of C–H sp^3 bonds. The obtained quantity of $\nu_{(\text{membr.}[5])[3]}$ is less by one order of the vibrational frequency $n_{\text{HREELS}[47]} = 8.7 \times 10^{13}$ s^{-1} corresponding to an additional high-resolution electron energy loss spectroscopy (HREELS) peak (Figure 3 in Ref. 47) arising from C–H sp^3 stretching appears at 369 meV after a partial hydrogenation of the epitaxial graphene. The authors[47] supposed that this peak can be assigned to the vertical C–H bonding, giving direct evidence for hydrogen attachment on the epitaxial graphene surface.

Taking into account $\nu_{\text{RD}[5]}$ and $\nu_{\text{HREELS}[47]}$ quantities, and substituting in Eq. (9) quantities of $K = K_{(\text{membr.}[5])723\text{ K}} = 1/\tau_{0.63(\text{membr.}[5])723\text{ K}}$ and

$K_0 \approx K_{0(\text{membr.}[5])[47]} \approx \nu_{\text{HREELS}[47]}$, one can evaluate $\Delta H_{\text{des.}(\text{membr.}[5])[47]} = \Delta H_{\text{C–H}(\text{membr.}[5])[47]} \approx 2.66$ eV. The obtained (in such approximation) value of $\Delta H_{\text{C–H}(\text{membr.}[5])[47]}$ coincides (within the errors) with the experimental[13] value of the breakdown energy of C–H sp^3-like bonds in hydrofullerene $C_{60}H_{36}$ ($\Delta H_{\text{C–H}(\text{C60H36}[13])} = 2.64 \pm 0.01$ eV).

The above analysis of the related data shows that the experimental[5] graphene membranes (hydrogenated up to the near-saturation) can be used for the following TDS characteristics, of relevance to Eq. (9), of the empirical character: $\Delta H_{\text{des.}(\text{membr.}[5])[13,47]} = \Delta H_{\text{C–H}(\text{membr.}[5])[13,47]} = 2.6 \pm 0.1$ eV, $K_{0(\text{membr.}[5])[13,47]} = \nu_{\text{C–H}(\text{membr.}[5])[13,47]} \approx 5 \times 10^{13}\ \text{s}^{-1}$. The above analysis also shows that it is the case of a non-diffusion-rate-limiting kinetics, when Eq. (9) corresponds to the Polanyi–Wigner one.[14] And certainly, these tentative results could be directly confirmed (and/or modified) by receiving and treatment (within Eqs. (8) and (9)) of experimental data on $\tau_{0.63[5]}$ at several annealing temperatures.

The above-noted fact that the empirical quantity $\tau_{0.63(\text{membr.}[5]723\ \text{K})}$ is much larger (by about three orders), rather than the theoretical one ($\tau_{0.63(\text{graphane}[4]723\ \text{K})}$), is consistent with the mentioned in Ref. 5 alternative possibility that the experimental graphane membrane[5] (a free-standing membrane) may have a more complex hydrogen bonding than the one suggested by theory.[3] It may be true and for the further theoretical development.[4]

2.3. Consideration of a thermodynamic probability of existence of hydrogenated graphenes–graphanes*[18–21] possessing of a very high binding energy

In connection with the above consideration, it seems expedient to consider a thermodynamic probability (possibility) of existence of hydrogenated graphene–graphane* ($CH_{\text{graphane}*[18–21]}$) possessing of the values of $\Delta H_{(\text{C–H})\text{graphane}*[18–21]} \approx 2.6$ eV[3–5,12,13,18–21] and $\Delta H_{(\text{C–C})\text{graphane}*[18–21]} \approx 4.9$ eV.[18–21] It corresponds to a very high binding (cohesive) energy ($\Delta H_{\text{bind.}(\text{graphane}*[18–21])} \approx 10$ eV/atom) in comparison with those (above considered) for theoretical graphanes.[3,4,25] For showing of such a thermodynamic probability, it is necessary to include in the consideration two more additional reactions[18,19]:

$$C_{(\text{gas})} \rightarrow C_{(\text{graphene})} \qquad (\Delta H_{10}) \qquad (10)$$

$$C_{(\text{gas})} + H_{(\text{gas})} \rightarrow CH_{(\text{graphane}*[18–21])} \qquad (\Delta H_{11}) \qquad (11)$$

where ΔH_{10} and ΔH_{11} are the standard energy (enthalpy) changes.

Reaction (11) can be presented as a sum of Reaction (2) applied for graphane* as (2*) and Reaction (10); hence (in the framework of the thermodynamic method of cyclic processes[44]):

$$\Delta H_{11} = (\Delta H_{2^*} + \Delta H_{10}). \quad (12)$$

Substituting in Eq. (12) the above-considered values of $\Delta H_{2^*} \approx \Delta H_2 \approx -\Delta H_{\text{C–H(membr.[5])[13,47]}} = -2.6 \pm 0.1$ eV/atom and $\Delta H_{10} \approx -\Delta H_{\text{cohes.(graphene)[25]}} \approx -\Delta H_{\text{cohes.(graphene)[18–21,45]}} \approx -\Delta H_{\text{subl.(graphite)[45]}} = -7.41 \pm 0.05$ eV/atom, one[18–21] can obtain a desired value of $\Delta H_{11} = -10.0 \pm 0.1$ eV/atom. The quantity of $-\Delta H_{11}$ corresponds to the binding (cohesive) energy of graphane* ($-\Delta H_{11} = \Delta H_{\text{bind.(graphane*[18–21])}} = \Delta H_{\text{cohes.(graphane*[18–21])}}$. According to Refs. 18–21, the quantity $-\Delta H_{11}$ characterizes the breakdown energy of one (C–H) sp^3-like bond and 1.5 (C–C) sp^3-like bonds, relevant to breaking away of one hydrogen atom and one neighboring carbon atom from the material*, *i.e.*,

$$\begin{aligned}\Delta H_{11} &= -\Delta H_{\text{bind.(graphane*[18–21])}} \\ &= -\Delta H_{\text{(C–H)graphane*[18–21]}} - 1.5\ \Delta H_{\text{(C–C)graphane*[18–21]}}. \quad (13)\end{aligned}$$

Hence, substituting in Eq. (13) the above-noted $\Delta H_{\text{(C–H)graphane*[18–21]}}$ value, one[18–21] can evaluate the desired quantity $\Delta H_{\text{(C–C)graphane*[18–21]}} \approx 4.9$ eV, which coincides (within the errors) with the analogical quantities for perfect graphene and perfect graphite.

The same value of $\Delta H_{\text{(C–C)}} \approx 4.9$ eV can be evaluated (in a similar manner[18–21]), for instance, for hydrogenated (up to composition C_2H) single-walled graphite nanotubes*[10–12] and hydrofullerene* $C_{60}H_{36}$[13]

Comparing of the obtained in such a way values of $\Delta H_{\text{(C–C)graphane*[18–21]}}$, $\Delta H_{\text{(C–C)nanotubes*[18–21]}}$, $\Delta H_{\text{(C–C)hydrofullerene*[18–21]}}$, $\Delta H_{\text{(C–C)graphene[25]}}$, $\Delta H_{\text{(C–C)graphene[18–21,45]}}$, and $\Delta H_{\text{(C–C)graphite[18–21,45]}}$ shows that the elastic and intrinsic strength properties (and particularly, a Young's modulus (E)) of graphane*-like nanostructures can be close to those for graphene.

In this connection, it is relevant to note that a unique experimental value from work[48] (mentioned in Ref. 5 as Ref. *S*3) of a Young's modulus of graphene is $E_{\text{graphene[48]}} = 1.0$ TPa.

As was noted in Ref. 5 (pp. 1-S–2-S), when a hydrogenated graphene membrane had no free boundaries (a rigidly fixed membrane), in the expanded regions of it, the lattice was stretched isotropically by nearly 10% (*i.e.* the elastic deformation degree $\varepsilon_{\text{fix.membr.[5]}} \approx 0.1$) with respect to pristine graphene (Figure S1B in Ref. 5). This amount of stretching ($\varepsilon \approx 0.1$) is close to the limit

of possible elastic deformations in graphene (Ref. *S*3 = Ref. 48), and, indeed, they[5] observed some of their membranes to rupture during hydrogenation. They[5] believed that the stretched regions are likely to remain non-hydrogenated. They[5] found that instead of exhibiting random stretching, hydrogenated graphene membranes normally split into domain-like regions of the size of the order of 1 μm, and that the annealing of such membranes led to complete recovery of the periodicy in both stretched and compressed domains.

By using the experimental value[5] of the degree of elastic deformation ($\varepsilon_{\text{fix.membr.[5]}} \approx 0.1$) of the hydrogenated fixed graphene membranes and the experimental value[48] of a Young's modulus of graphene ($E_{\text{graphene[48]}} = 1.0$ TPa), one can evaluate (within Hooke's law approximation) the stretching stress value ($\sigma_{\text{fix.membr.[5]}} \approx (\varepsilon_{\text{fix.membr.[5]}}\ E_{\text{graphene[48]}}) \approx 0.1$ TPa) in the expanded regions (domains or grains) of the material.[5]

This analytical result is consistent with the analytical results of the further consideration (in this study) of the related data from Refs. 15–21, of relevance to a possibility of existence of hydrogenated graphane*-like nanostructures possessing of a Young's modulus value close to the graphene one ($E_{\text{graphane*[18–21]}} \approx E_{\text{graphene[48]}} = 1.0$ TPa).

2.4. Consideration of data[5] on hydrogen desorption in the hydrogenated mono- and bilayer epitaxial graphene samples

In Ref. 5, both the graphene membrane samples (considered above) and the epitaxial graphene and bigraphene samples (on substrate SiO_2) were exposed to a cold hydrogen dc plasma (for 2 h to reach the saturation in the measured characteristics). A low-pressure (0.1 mbar) hydrogen/argon mixture (10% H_2) was used.

Raman spectra for hydrogenated and subsequently annealed graphene membranes (Figure 3B in Ref. 5) were rather similar to those for epitaxial graphene samples (Figure 3A in Ref. 5), but with some notable differences. If hydrogenated simultaneously (for 1 h) and before reaching the saturation (a partial hydrogenation), the D peak area for a membrane was by a factor of about two greater than the area for graphene on a substrate (Figure 3A, inset in Ref. 5), which indicates the formation of twice as many C–H sp^3 bonds in the membrane. As has been also noted in Ref. 5, this result agrees with the general expectation that atomic hydrogen attaches to both sides of membranes.

Moreover,[5] the D peak area became up about three times greater than the G peak area after prolonged exposures (for 2 h, a near-complete hydrogenation) of membranes to atomic hydrogen (Figure 3B in Ref. 5).

As is also seen from Figure 3 in Ref. 5, the integrated intensity area of the D peak in Figure 3B corresponding to the adsorbed hydrogen saturation concentration in the graphene membranes is larger by factor of about three of the area of the D peak in Figure 3A corresponding to the hydrogen concentration in the epitaxial graphene samples.

It may be related to some partial hydrogenation (for instance, localized in some defect nanoregions[33–42,49]) of the epitaxial graphene samples even after the prolonged (for 3 h) exposures, *i.e.*, after reaching of their near-saturation.

It is expedient to note that in Ref. 5, the absolute values of the adsorbed hydrogen concentration (C_0) were considered, neither for the hydrogenated graphene membranes, nor for the hydrogenated epitaxial graphene samples.

According to D. C. Elias, private communication, a near-complete desorption of hydrogen ($-\Delta C/C_0 \approx 0.95$) from a hydrogenated epitaxial graphene on a substrate SiO_2 (Figure 3B in Ref. 5) was achieved by annealing it in 90% Ar/10% H_2 mixture at $T = 573$ K for 2 h (*i.e.*, $\tau_{0.95(\text{epitax.}[5])573\ \text{K}} = 7.2 \times 10^3$ s). Hence, by using Eq. (8), one can evaluate the quantity of $\tau_{0.63(\text{epitax.}[5])573\ \text{K}} = 2.4 \times 10^3$ s, which is by about six orders less of the evaluated quantity of $\tau_{0.63(\text{membr.}[5])573\ \text{K}} = 1.5 \times 10^9$ s.

It can be taken into account that changes in Raman spectra of graphene[5] caused by hydrogenation were rather similar (with respect to locations of D, G, D′, 2D, and (D + D′) peaks) both for the epitaxial graphene on SiO_2 and for the free-standing graphene membrane (Figure 3 in Ref. 5). Hence, one can suppose that $K_{0(\text{epitax.}[5])} = \nu_{\text{C–H(epitax.}[5])} \approx K_{0(\text{membr.}[5])[13,47]} = \nu_{\text{C–H(membr.}[5])[13,47]} \approx 5 \times 10^{13}$ s^{-1}. Then, by substituting in Eq. (9) quantities of $K = K_{(\text{epitax.}[5])573\ \text{K}} = 1/\tau_{0.63(\text{epitax.}[5])573\ \text{K}}$ and $K_0 \approx K_{0(\text{membr.}[5])[13,47]}$, one can evaluate $\Delta H_{\text{des.(epitax.}[5])} = \Delta H_{\text{C–H(epitax.}[5])} \approx 2.0$ eV. Here, the case is supposed of a non-diffusion-rate-limiting kinetics, when Eq. (9) corresponds to the Polanyi–Wigner one.[14]

Certainly, these tentative thermodynamic characteristics of the hydrogenated epitaxial graphene on a substrate SiO_2[5] could be directly confirmed and/or modified by receiving and treatment (within Eqs. (8) and (9) of experimental data on $\tau_{0.63(\text{epitax.}[5])}$ at several annealing temperatures.

And it is easy to show that: (i) these analytical results are not consistent with the mass spectrometry data (Figure S5 in Ref. 5) on TDS of hydrogen from a specially prepared single-side graphane; (ii) they can not be described in the framework of the theoretical models and characteristics of thermal stability of SSHG[6] or graphone.[9]

According to the further considerations (in this study), it may be a hydrogen desorption case of a diffusion-rate-limiting kinetics, when $K_0 \neq \nu$, and Eq. (9) does not correspond to the Polanyi–Wigner one.[14]

By using the method[14] for treatment of TDS spectra, relevant to the mass spectrometry data (Figure S5 in Ref. 5) on TDS of hydrogen from a specially prepared single-side graphane (under heating from, obviously, the room temperature to 573 K for 6 min), one can obtain the following results: (i) the total integrated area of the TDS spectra corresponds to ~2×10^{-8} g of desorbed hydrogen; (ii) the TDS spectra can be approximated by three TDS peaks (#1, #2, and #3); (iii) TDS peak #1 (~30% of the total area, $T_{\max\#1} \approx 370$ K) can be characterized by the activation energy $E_{\text{TDS-peak \#1[5]}} = 0.6 \pm 0.3$ eV and by the per-exponential factor of the reaction rate constant $K_{0(\text{TDS-peak \#1[5]})} \approx 2 \times 10^7$ s^{-1}; 4); TDS peak #2 (~15% of the total area, $T_{\max\#2} \approx 445$ K) can be characterized by the activation energy $E_{\text{TDS-peak \#2[5]}} = 0.6 \pm 0.3$ eV and by the per-exponential factor of the reaction rate constant $K_{0(\text{TDS-peak \#2[5]})} \approx 1 \times 10^6$ s^{-1}; 5); TDS peak #3 (~55% of the total area, $T_{\max\#3} \approx 540$ K) can be characterized by the activation energy $E_{\text{TDS-peak \#3[5]}} = 0.23 \pm 0.05$ eV and by the per-exponential factor of the reaction rate constant $K_{0(\text{TDS-peak \#3[5]})} \approx 2.4$ s^{-1}.

These analytical results show that all the three above-noted TDS processes ($\#1_{\text{TDS[5]}}$, $\#2_{\text{TDS[5]}}$, and $\#3_{\text{TDS[5]}}$) may be related to a hydrogen desorption case of a diffusion-rate-limiting kinetics,[14] when in Eq. (9) the quantity of $K_0 \approx (D_{0\text{app.}}/L^2)$ and the quantity of $\Delta H_{\text{des.}} = Q_{\text{app.}}$, where $D_{0\text{app.}}$ is the per-exponent factor of the apparent diffusion coefficient ($D_{\text{app.}} = D_{0\text{app.}}\exp(-Q_{\text{app.}}/k_{\text{B}}T)$), L is the characteristic diffusional size (length), and $Q_{\text{app.}}$ is the apparent diffusion activation energy.

TDS process $\#3_{\text{TDS[5]}}$ may be related to TDS process (or peak) I in Refs. 14 and 18–21, for which the apparent diffusion activation energy is $Q_{\text{app.I}} \approx 0.2$ eV $\approx E_{\text{TDS-peak \#3[5]}}$ and $D_{0\text{app.I}} \approx 3 \times 10^{-3}$ cm^2/s. Hence, one can evaluate the quantity of $L_{\text{TDS-peak \#3[5]}} \approx (D_{0\text{app.I}} / K_{0(\text{TDS-peak \#3[5]})})^{1/2} \approx 3.5 \times 10^{-3}$ cm, which may be related to the linear size of the graphene specimens.

Thus, TDS process $\#3_{\text{TDS[5]}}$ may be related to chemisorption models "H" and/or "G" (Figure 1) corresponding to TDS process (or peak) I in Refs. 14 and 18–21.

TDS processes $\#1_{\text{TDS[5]}}$ and $\#2_{\text{TDS[5]}}$ may be related (in some extent) to chemisorption models "H" and/or "G" (Figure 1). Model "H" corresponds to TDS process (or peak) II in Refs. 14, 16, and 18–21, for which the apparent diffusion activation energy $Q_{\text{app.II}} \approx 1.2$ eV (that is comparatively close to $E_{\text{TDS-peak \#1,2[5]}}$, Table 1) and $D_{0\text{app.II}} \approx 2 \times 10^3$ cm^2/s.

Obviously, chemisorption models "H" and/or "G" (Figure 1) can be applied only for the defect nanoregions in the epitaxial graphene flakes[5] (for instance, vacancies, grain boundaries (domains), and/or triple junctions (nodes) of the grain-boundary network [33–42,49]), where the dangling carbon bonds can occur.

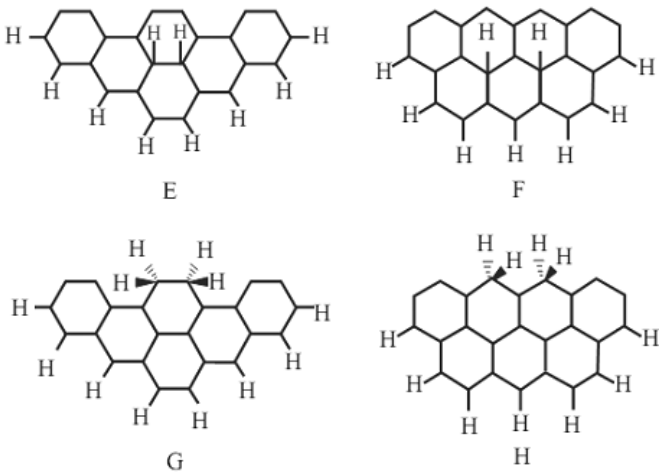

Figure 1. Schematics (used in Refs. 14, 16, and 18–21) of some theoretical models (*ab initio* molecular orbital calculations[50]) of chemisorption of atomic hydrogen on graphite on the basal and edge planes.

It is expedient to note that the above-considered (in Sections 2.1–2.3) chemisorption of atomic hydrogen on graphene membranes[3–5] may be related to model "F*",[14,16,18–21] which is of relevance to chemisorption of a single hydrogen atom on one of carbon atoms possessing of three not occupied (by hydrogen) nearest carbons (but not two hydrogen atoms on two carbons, as in model "F"). Model "F*" is characterized[14,16,18–21] by the quantity $\Delta H_{(C–H)"F*"[14,18–21]} \approx 2.5$ eV that coincides with the similar quantities for graphanes[3–5] (Table 1).

In a work by Ref. 5, the same hydrogenation procedures of the 2 h long exposure have been applied also to the third system — bilayer epitaxial graphene on SiO_2/Si wafer. Bilayer samples showed little change in their charge carrier mobility and a small D Raman peak, as compared to single-layer epitaxial graphene on SiO_2/Si wafer exposed to the same hydrogenation procedures (Figure S7 in Ref. 5). The authors[5] believed that higher rigidity of bilayers suppressed their rippling, thus reducing the probability of hydrogen adsorption.

The further consideration (in this study) of some other known experimental data on hydrogenation and thermal stability characteristics of monolayer, bilayer, and three-layer epitaxial graphene systems shows an important role of some defects in graphene networks,[33–42,49] relevant to the probability of hydrogen adsorption and the permeability of graphene networks for atomic hydrogen.

Table 1. Some analytical (an.) results of Section 2.

Quantity ⇒ Material ⇓	$\Delta H_{(C-H)}$ (eV)	$\Delta H_{(bind.)}$ (eV)	$\Delta H_{(C-C)}$ (eV)	$\Delta H_{(des.)}$ (eV)	$K_{0(des.)}$ (s^{-1})
Graphane[3]	$(2.5 \pm 0.1)_{an.}$	6.56	$(2.7)_{an.}$	$(2.5)_{an.}$	—
Graphane[25]	1.50	5.03	$(2.35)_{an.}$	$(1.5)_{an.}$	—
Graphane[4]	2.46 ± 0.17	—	—	2.46 ± 0.17	$(2.1 \pm 0.5) \times 10^{17}$
Graphane$[4]_{an.}$	2.46 ± 0.17	—	—	2.46 ± 0.17	2.0×10^{15}
Graphane membrane$[5]_{an.}$	2.5 ± 0.1 2.6 ± 0.1	—	—	2.5 ± 0.1 2.6 ± 0.1	7×10^{12} 5×10^{13}
Graphane epitaxial $[5]_{an.}$	1.84 1.94	—	—	1.84 1.94	7×10^{12} 5×10^{13}
Graphane epitaxial, TDS #1 $[5]_{an.}$	—	—	—	0.6 ± 0.3	2×10^{7}
Graphane epitaxial, TDS #2 $[5]_{an.}$	—	—	—	0.6 ± 0.3	1×10^{6}
Graphane epitaxial, TDS #3 $[5]_{an.}$	—	—	—	0.23 ± 0.05	2.4
Graphene[25]	—	7.40	$(4.93)_{an.}$	—	—
Graphane*[18–21]	2.6	9.95	4.9	2.6	—
Graphite[18–21,45]	—	7.41 ± 0.05	4.94 ± 0.03	—	—
Diamond[18–21,45]	—	7.38 ± 0.04	3.69 ± 0.02	—	—
Hydrofullerene $C_{60}H_{36}$[13]	2.64 ± 0.01	—	—	—	—
Hydrogenated SSCNs (C_2H)[12]	2.5 ± 0.2	—	—	—	—

Some analytical results of Section 2 are presented in Table 1.

3. Analysis and Comparison of Data[15,17,51–59]

3.1. Analysis of the Raman spectroscopy data[51] on thermal desorption of hydrogen from hydrogenated graphene flakes

In Ref. 51, the hydrogenation of single and bilayer graphene flakes by an argon–hydrogen plasma produced in a reactive ion etching (RIE) system was reported. It was analyzed into two cases: (i) one where the graphene flakes are electrically insulated from the chamber electrodes (by the SiO_2 substrate) and (ii) one where the flake is in electric contact with the source electrode (a graphene device). Electronic transport measurements in combination with Raman spectroscopy were used to link the electric mean free path to the optically extracted defect concentration, which is related to the defect distance ($L_{\text{def.}}$). It was shown that under the chosen plasma conditions, the process does not introduce considerable damage to the graphene sheet and that a rather partial hydrogenation ($C_H \leq 0.05\%$) occurs primarily due to the hydrogen ions from the plasma and not due to fragmentation of water adsorbates on the graphene surface by highly accelerated plasma electrons. To quantify the level of hydrogenation, the integrated intensity ratio (I_D/I_G) of Raman bands was used. The hydrogen coverage (C_H) determined from the defect distance ($L_{\text{def.}}$) does not exceed ~0.05%.

The heating of the hydrogenated single graphene flakes (on the SiO_2 substrate) in a nitrogen environment on a hot plate, with temperature ranging from 348 to 548 K, each time (Δt) for 1 min was performed.[51] As can be seen in Figure 2c in Ref. 51, heating results in a decrease of the integrated intensity ratio (I_D/I_G) of Raman bands. Within a formal kinetics approach,[14,46] the averaged kinetic data for samples of 20, 40, and 10 min exposure can be treated by using Eq. (7) transformed to a more suitable form (7′): $K \approx -((\Delta C/\Delta t)/C)$, where $\Delta t = 60$ s, ΔC and C are determined from Figure 2c in Ref. 51.

It results in finding five values of the reaction (desorption) rate constant (K) for five temperatures (T = 348, 398, 448, 498, and 548 K). Their temperature dependence is described by Eq. (9). Hence, the desired quantities are determined (Table 2): the reaction (desorption) activation energy $\Delta H_{(\text{des.})[51]} = 0.11 \pm 0.07$ eV, and the per-exponential factor of the reaction rate constant $K_{0(\text{des.})[51]} \approx 0.15\ \text{s}^{-1}$. Hence, the desorption time, for instance, at 553 K is $\tau_{0.63(\text{des.})[51]553\ \text{K}} \approx 70$ s (Table 2).

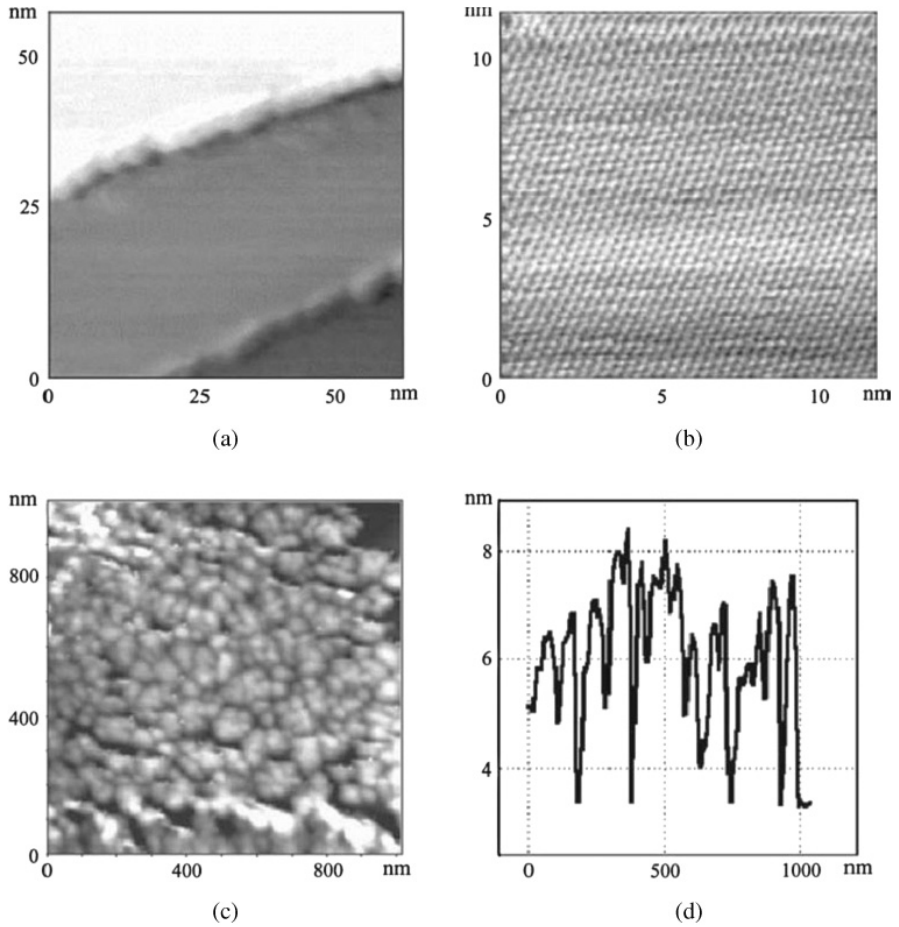

Figure 2. STM images of the untreated HOPG sample (under ambient conditions) taken from areas of (a) 60.8 × 60.8 nm and (b) 10.9 × 10.9 nm (high-resolution image of the square in image (a)). (c) AFM image (area of 1 × 1 nm) of the HOPG sample subjected to atomic hydrogen dose (D) of 1.8×10^{16} H^0/cm^2. (d) Surface height profile obtained from the AFM image reported in (c). The STM tunnel V_{bias} and current are 50–100 mV and 1–1.5 mA, respectively. From Ref. 15 with permission.

The obtained quantities of $\Delta H_{(des.)[51]}$ and $K_{0(des.)[51]}$ are close (within the errors) to those for TDS process # 3 (Table 1). These two desorption processes may be related to TDS process (or peak) I in Refs. 14 and 18–21, for which the apparent diffusion activation energy is $Q_{app.I} \approx 0.2$ eV $\approx E_{TDS\text{-}peak\ \#3[5]} \approx \Delta H_{(des.)[51]}$.

By taking into account the facts that the RIE exposure regime[51] is characterized of a form of $(I_D/I_G) \sim L_{def.}^{-2}$ (for $(I_D/I_G) < 2.5$), $L_{def.} \approx 11$–17 nm

Table 2. Some analytical results of Sections 3.1-3.3.

Quantity ⇒ Material ⇓	$\Delta H_{(\text{des.})}$ (eV)	$K_{0(\text{des.})}$ (s^{-1})	$\tau_{0.63(\text{des.})553\ \text{K}}$ (s)
Graphene flakes/SiO_2[51]	0.11 ± 0.07	0.15	70
Graphene/Ni[52]	—	—	130
HOPG[52]	—	—	130
(SiC-D/QFMLG-H)[55]	0.7 ± 0.2	9×10^2	—
(SiC-D/QFMLG)[55]	2.0 ± 0.6	1×10^6	—

(Figure 4 in Ref. 51) and $C_H \leq 5 \times 10^{-4}$, one can suppose that the hydrogen adsorption centers in the single graphene flakes (on the SiO_2 substrate) are related to some point nanodefects (for instance, vacancies and/or triple junctions (nodes) of the grain-boundary network[33–42,49]) of diameter $d_{\text{def.}} \approx$ const. In such a model, the quantity C_H can be satisfactory and described as

$$C_H \approx n_H\,(d_{\text{def.}})^2/(L_{\text{def.}})^2, \tag{14}$$

where $n_H \approx$ const. is a number of hydrogen atoms adsorbed by a center.

As was also found, after the Ar/H_2 plasma exposure, the (I_D/I_G) ratio for bilayer graphene device is larger than that for single graphene device (inset in Figure 4 in Ref. 51). As was noted[51], this observation is in contradiction to the Raman ratios after exposure of graphene to atomic hydrogen[5] (Section 2.4) and when other defects are introduced.

3.2. Analysis of the STM and STS data[52] on reversible hydrogenation of epitaxial graphene and graphite surfaces

In Ref. 52, the effect of hydrogenation on the topography and electronic properties of graphene (grown by chemical vapor deposition (CVD) on top of a nickel surface) and graphite (HOPG) surfaces were studied by scanning tunneling microscopy (STM) and spectroscopy (STS). The surfaces were chemically modified using 40 min Ar/H_2 plasma (of the power 3 W) treatment (Figure 1 in Ref. 52). It has been determined that the hydrogen chemisorption on the surface of graphite/graphene opens on average an energy bandgap of 0.4 eV around the Fermi level. Although the plasma treatment modifies the surface topography in an irreversible way (Figure 1 in Ref. 52), the change in the electronic properties can be reversed by moderate thermal annealing (10 min at 553 K) and the samples can be hydrogenated again to yield a similar, but slightly reduced, semiconducting behavior after the second hydrogenation.

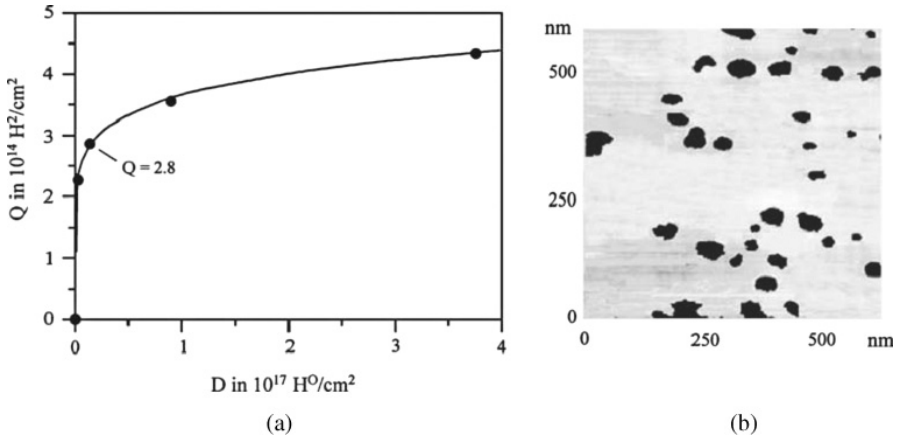

Figure 3. (a) Hydrogen storage efficiency of HOPG samples, desorbed molecular hydrogen (Q) versus dose (D) of atomic hydrogen exposure. (b) STM image for 600 × 600 nm area of the HOPG sample subjected to atomic hydrogen dose of 1.8×10^{16} H^0/cm^2, followed by hydrogen TDS. From Ref. 15 with permission.

These data[52] show that the time of desorption from both the epitaxial graphene/Ni samples and HOPG samples of about 99% of hydrogen under 553 K annealing is $\tau_{0.99(\text{des.})[52]553\ \text{K}} \approx 6 \times 10^2$ s. Hence, by using Eq. (8), one can evaluate the quantity $\tau_{0.63(\text{des.})[52]553\ \text{K}} \approx 130$ s (Table 2), which is close (within the errors) to the similar quantity $\tau_{0.63(\text{des.})[51]553\ \text{K}} \approx 70$ s (Table 2) for the epitaxial graphene flakes[51] considered in Section 3.1.

Figure 3 in Ref. 53 is related to graphene/Ni samples (Figure 1 in Ref. 52). As is noted in Ref. 53, Figure 3 shows a 9 × 9 nm^2 topographic image acquired in the constant current STM mode of the surface of graphene grown on nickel by CVD. Before plasma treatment, the CVD graphene exhibits a Moiré pattern superimposed to the honeycomb lattice of graphene (Figure 3a in Ref. 53). This is due to the lattice parameter mismatch between the graphene and the nickel surfaces and it is the characteristic of most epitaxial graphene samples.

On the other hand,[53] for the hydrogenated CVD graphene, the expected structural changes are twofold. First, the chemisorption of hydrogen atoms will change the sp^2 hybridization of carbon atoms to tetragonal sp^3 hybridization, modifying the surface geometry. Second, the impacts of heavy Ar ions, present in the plasma, could also modify the surface by inducing geometrical displacement of carbon atoms (rippling graphene surface) or creating vacancies and other defects (for instance, grain or domain boundaries[33–42,49]). Figure 3b in Ref. 53 shows the topography image of

the surface CVD graphene after the extended (40 min) plasma treatment. The nano-order-corrugation increases after the treatment and there are brighter nanoregions (of about 1 nm in height and several nanometers in diameter) in which the atomic resolution is lost or strongly distorted. It has been also found[53] that these bright nanoregions present a semiconducting behavior while the rest of the surface remains conducting (Figures 3c–d in Ref. 53).

It is reasonable to assume that most of the chemisorbed hydrogen is localized into these bright nanoregions, which have a blister-like form. Moreover, it is also reasonable to assume that the monolayer (single) graphene flakes on the Ni substrate are permeable to atomic hydrogen only in these defect nanoregions. This problem[8,32] has been formulated in Section 1.

A similar model may be valid and relevant for the HOPG samples (Figure 1 in Ref. 52. Figures 1 and 2 in Ref. 53 are related to graphene/SiO_2 samples.[53,54]

It has been found[53] that when graphene is deposited on a SiO_2 surface, the charged impurities present in the graphene/substrate interface produce strong inhomogeneities of the electronic properties of graphene. On the other hand, as has been shown,[53] how homogeneous graphene grown by CVD can be altered by chemical modification of its surface (by the chemisoption of hydrogen). It strongly depresses the local conductance at low bias indicating the opening of a bandgap in graphene.

The charge inhomogeneities (defects) of epitaxial hydrogenated graphene/SiO_2 samples do not show long-range ordering, and the mean spacing between them is $L_{\text{def.}} \approx 20$ nm (Figure 2 in Ref. 53). It is reasonable to assume[53] that the charge inhomogeneities (defects) are located at the interface between the SiO_2 layer (300 nm thick) and the graphene flake.

A similar quantity ($L_{\text{def.}} \approx 11$–$17$ nm (Figure 4 in Ref. 51)) for the hydrogen adsorption centers in the single graphene flakes on the SiO_2 substrate has been considered in Section 3.1.

3.3. Analysis of the HREELS/LEED data[55] on thermal desorption of hydrogen from hydrogenated graphene on SiC substrate

In Ref. 55, hydrogenation of deuterium-intercalated quasi-free-standing monolayer graphene on SiC(0001) was obtained and studied with low-energy electron diffraction (LEED) and HREELS. While the carbon honeycomb structure remains intact, it has been shown that a significant band gap

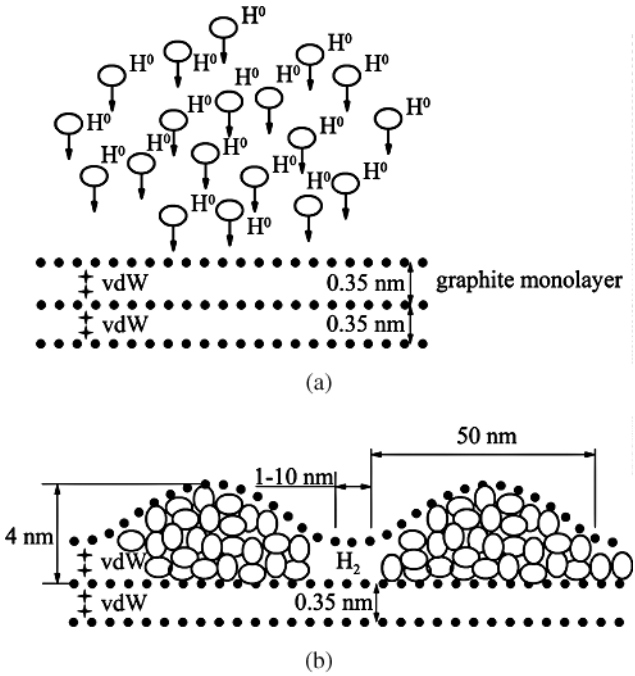

Figure 4. Model showing the hydrogen accumulation (intercalation) in HOPG, with the formation of blister-like nanostructures. (a) Preatomic hydrogen interaction step. (b) H_2, captured inside graphene blisters, after the interaction step. Sizes are not drawn exactly in scale. From Ref. 15 with permission.

opens in the hydrogenated material. Vibrational spectroscopy evidences for hydrogen chemisorption on the quasi-free-standing graphene was provided and its thermal stability was studied (Figure 3 in Ref. 55).

Deuterium intercalation, transforming the buffer layer in quasi-free-standing monolayer graphene (denoted as SiC-D/QFMLG), was performed with a D atom exposure of ~5×10^{17} cm^{-2} at a surface temperature of 950 K. Finally, hydrogenation up to saturation of quasi-free-standing monolayer graphene was performed at room temperature with a H atom exposure > 3×10^{15} cm^{-2}. The latter sample is denoted as SiC-D/QFMLG-H to stress the different isotopes used, first, to prepare quasi-free-standing monolayer graphene (the D-intercalation step), and second, to hydrogenate it.

According R. Bisson, private communication, the temperature indicated at each point in Figure 3 in Ref. 54 corresponds to successive temperature ramp (not linear) of 5 min, *i.e.*, the fifth point at 600 K on Figure 3 has been obtained after four previous HREELS/LEED measurements and three previous ramps of 5 min to lower temperatures.

Within a formal kinetics approach (for the first-order reactions),[14,46] one can treat the above-noted points at T_i = 543 K, 611 K, and 686 K, by using Eq. (8) transformed to a more suitable form (8′): $K_i \approx -(\ln(C/C_{0i})/t)$, where t = 300 s, and the corresponding quantities C_{0i} and C are determined from Figure 3 in Ref. 54.

This leads to values of the reaction (hydrogen desorption from SiC-D/QFMLG-H samples) rate constant (K_i) for three temperatures (T_i = 543, 611, and 686 K). Their temperature dependence is described by Eq. (9). Hence, the desired quantities are determined (Table 2): the reaction (hydrogen desorption) activation energy $\Delta H_{\text{des.(SiC-D/QFMLG-H)[55]}} = 0.7 \pm 0.2$ eV, and the per-exponential factor of the reaction rate constant $K_{0\text{des.(SiC-D/QFMLG-H)[55]}} \approx 9 \times 10^2\ \text{s}^{-1}$.

The obtained quantity $\Delta H_{\text{des.(SiC-D/QFMLG-H)[55]}}$ is close (within the errors) to the similar ones ($E_{\text{TDS-peak \#1[5]}}$ and $E_{\text{TDS-peak \#2[5]}}$) for TDS processes #1 and #2 (Section 2.4, Table 1). But the obtained quantity $K_{0\text{des.(SiC-D/QFMLG-H)[55]}}$ differs by several orders from the similar ones ($K_{0\text{des.(TDS-peak \#1[5])}}$ and $K_{0\text{des.(TDS-peak \#2[5])}}$) for TDS processes #1 and #2 (Section 2.4, Table 1). Nevertheless, these three desorption processes may be (in some extent) related to chemisorption models "H" and/or "G" (Figure 1). Model "H" corresponds to TDS process II in Refs. 14 and 18–21, for which the apparent diffusion activation energy is $Q_{\text{app.II}} \approx 1.2$ eV.

In the same way, one can treat the points (from Figure 3 in Ref. 54) at T_i = 1010, 1120, and 1200 K, those are related to the intercalated deuterium desorption from SiC-D/QFMLG samples. It results in finding the desired quantities (Table 2): the reaction (deuterium desorption) activation energy $\Delta H_{\text{des.(SiC-D/QFMLG)[55]}} = 2.0 \pm 0.6$ eV, and the per-exponential factor of the reaction rate constant $K_{0\text{des.(SiC-D/QFMLG)[55]}} \approx 1 \times 10^6\ \text{s}^{-1}$. It may be related[55] to hydrogen chemisorbed on the silicon atoms of the SiC substrate below the graphene plane. Formally, this desorption process (obviously, of a diffusion-limiting character) may be described similarly to TDS process (peak) III in Refs. 14 and 18–21, and (within such a model) the apparent diffusion activation energy may be close to the breakdown energy of the Si–H bonds. As was concluded in Ref. 55, the exact intercalation mechanism (hydrogen diffusion through the anchored graphene lattice, at defect or at boundary of the anchored graphene layer) remains an open question.

It is reasonable to assume that the quasi-free-standing monolayer graphene on the SiC-D substrate is permeable to atomic hydrogen (at room temperature) in some defect nanoregions (probably, in vacancies and/or triple junctions (nodes) of the grain-boundary network[33–42,49]).

It is expedient to note that the HREELS data[55] on bending and stretching vibrations C–H frequencies in SiC-D/QFMLG-H samples (153 meV (3.7×10^{13} s^{-1}) and 331 meV (8.0×10^{13} s^{-1}), respectively) are consistent with the considered in Section 2.2 related HREELS data[47] for the epitaxial graphene.

The obtained characteristics (Table 2) of the desorption processes[51,52,55] show that these processes may be of a diffusion-rate-controlling character.[14]

3.4. Analysis of the Raman spectroscopy data[56] on thermal desorption of hydrogen from hydrogenated graphene layers on SiO_2 substrate

In Ref. 56, graphene layers on SiO_2/Si substrate have been chemically decorated by radio frequency hydrogen plasma (the power of 5–15 W, the pressure of 1 Tor) treatment for 1 min. As has been shown, hydrogen coverage investigation by Raman spectroscopy and micro-X-ray photoelectron spectroscopy (PES) characterization demonstrates that the hydrogenation of single-layer graphene on SiO_2/Si substrate is much less feasible than that of bilayer and multilayer graphene; both the hydrogenation and dehydrogenation processes of the graphene layers are controlled by the corresponding energy barriers, which show significant dependence on the number of layers.

The results[56] on bilayer graphene/SiO_2/Si are in contradiction to the results[5] (Section 2.4) on a negligible hydrogenation of bilayer epitaxial graphene on SiO_2/Si wafer, when obviously other defects are produced.

Within a formal kinetics approach,[14,46] the kinetic data from Figure 6a in Ref. 56 for single-layer graphene samples (1LG-5W and 1LG-15W ones) can be treated. By using Eq. (7) transformed to a more suitable form (7′): $K \approx -((\Delta C/\Delta t)/C)$, where $\Delta t = 1800$ s, ΔC and C are determined from Figure 6a in Ref. 56.

It results in findings for 1LG-15W samples three values of the $I_{[56]}$ reaction rate constant $K_{I[56](1LG\text{-}15W)}$ for three temperatures ($T = 373$, 398, and 423 K), and three values of the $II_{[56]}$ reaction rate constant $K_{II[55](1LG\text{-}15W)}$ for three temperatures ($T = 523$, 573, and 623 K). Hence, by using Eq. (9), the desired quantities for 1LG-15W samples are determined (Table 3): the $I_{[56]}$ reaction activation energy $\Delta H_{des.I[56](1LG\text{-}15W)} = 0.6 \pm 0.2$ eV, the per-exponential factor of the $I_{[55]}$ reaction rate constant $K_{0des.I[56](1LG\text{-}15W)} \approx 2 \times 10^4$ s^{-1}, the $II_{[56]}$ reaction activation energy $\Delta H_{des.II[56](1LG\text{-}15W)} = 0.19 \pm 0.07$ eV, and the per-exponential factor of the $II_{[56]}$ reaction rate constant $K_{0des.II[56](1LG\text{-}15W)} \approx 3 \times 10^{-2}$ s^{-1}.

Table 3. Some analytical (an.) results of Sections 3.4–3.7 and 4.

Quantity ⇒ Samples ⇓	$\Delta H_{(\text{des.})\text{I}}$ **(eV)**	$K_{0(\text{des.})\text{I}}$ **(s^{-1})**	$\Delta H_{(\text{des.})\text{II}}$ **(eV)**	$K_{0(\text{des.})\text{II}}$ **(s^{-1})**
1LG-15W (graphene)[56]	0.6 ± 0.2	2×10^{4}	0.19 ± 0.07	3×10^{-2}
2LG-15W (bigraphene)[56]	—	—	0.9 ± 0.3	1×10^{3}
1LG-5W (graphene)[56]	0.15 ± 0.04	2×10^{-2}	0.31 ± 0.07	5×10^{-1}
2LG-5W (bigraphene)[56]	0.50 ± 0.15	2×10^{3}	0.40 ± 0.15	1
HOPG[57], TDS-peaks I, II	0.6 ± 0.2	1.5×10^{4}	1.0 ± 0.3	2×10^{6}
Graphene/SiC[17]	—	—	3.6	2×10^{14}
HOPG[59], TDS-peaks I, II	2.4[59]	—	4.1[59]	—
HOPG[59], TDS-peak I	$(2.4 \pm 0.5)_{\text{an.}}$	$(2 \times 10^{10})_{\text{an.}}$	—	—
GNF[61,62], TDS-peak I,II	$(2.4 \pm 0.5)_{\text{an.}}$	—	—	—

It also results in findings for 1LG-5W samples four values of the $\text{I}_{[56]}$ reaction rate constant $K_{\text{I}[56](1\text{LG-5W})}$ for four temperatures (T = 348, 373, 398, and 423 K), and two values of the $\text{II}_{[56]}$ reaction rate constant $K_{\text{II}[56](1\text{LG-5W})}$ for two temperatures (T = 523 and 573 K). Hence, by using Eq. (9), one can evaluate the desired quantities for 1LG-5W specimens (Table 3): the $\text{I}_{[56]}$ reaction activation energy $\Delta H_{\text{des.I}[56](1\text{LG-5W})} = 0.15 \pm 0.04$ eV, the per-exponential factor of the $\text{I}_{[56]}$ reaction rate constant $K_{0\text{des.I}[56](1\text{LG-5W})} \approx 2 \times 10^{-2}$ s^{-1}, the $\text{II}_{[56]}$ reaction activation energy $\Delta H_{\text{des.II}[56](1\text{LG-5W})} = 0.31 \pm 0.07$ eV, and the per-exponential factor of the $\text{II}_{[56]}$ reaction rate constant $K_{0\text{des.II}[56](1\text{LG-5W})} \approx 0.5$ s^{-1}.

A similar treatment of the kinetic data from Figure 6c in Ref. 56 for bilayer graphene 2LG-15W samples results in the findings of four values of the $\text{II}_{[56]}$ reaction rate constant $K_{\text{II}[56](2\text{LG-15W})}$ for four temperatures (T = 623, 673, 723, and 773 K). Hence, by using Eq. (9), the desired quantities are found (Table 3): the $\text{II}_{[56]}$ reaction activation energy $\Delta H_{\text{des.II}[56](2\text{LG-15W})} = 0.9 \pm 0.3$ eV, the per-exponential factor of the $\text{II}_{[56]}$ reaction rate constant $K_{0\text{des.II}[56](2\text{LG-15W})} \approx 1 \times 10^{3}$ s^{-1}.

A similar treatment of the kinetic data from Figure 6c in Ref. 56 for bilayer graphene 2LG-5W samples results in the findings of four values of the $\text{I}_{[56]}$ reaction rate constant $K_{\text{I}[56](2\text{LG-5W})}$ for four temperatures (T = 348, 373, 398, and 423 K), and three values of the $\text{II}_{[56]}$ reaction rate constant $K_{\text{II}[56](2\text{LG-5W})}$ for three temperatures (T = 573, 623, and 673 K). Their temperature dependence is described by Eq. (9). Hence, one can evaluate the desired quantities (Table 3): the $\text{I}_{[56]}$ reaction activation energy $\Delta H_{\text{des.I}[56](2\text{LG-5W})} = 0.50 \pm 0.15$ eV, the per-exponential factor of the $\text{I}_{[56]}$ reaction rate constant $K_{0\text{des.I}[56](2\text{LG-5W})} \approx 2 \times 10^{3}$ s^{-1}, the $\text{II}_{[56]}$ reaction activation energy

$\Delta H_{\text{des.II[56](2LG-5W)}} = 0.40 \pm 0.15$ eV, and the per-exponential factor of the $\text{II}_{[56]}$ reaction rate constant $K_{0\text{des.II[56](2LG-5W)}} \approx 1\ \text{s}^{-1}$.

The obtained characteristics (Table 3) of the desorption processes $\text{I}_{[56]}$ and $\text{II}_{[56]}$ show that these processes may be of a diffusion-rate-controlling character.[14]

3.5. Analysis of TDS and STM data[57] on HOPG treated by deuterium

In Ref. 57, results are presented of an STM study of graphite (HOPG) treated by atomic deuterium, which reveal the existence of two distinct hydrogen dimer states on graphite basal planes (Figures 1 and 2b, from Ref. 57). The density functional theory calculations allow[57] to identify the atomic structure of these states and to determine their recombination and desorption pathways. As has been supposed,[57] direct recombination is only possible from one of the two dimer states. As has been concluded,[57] this results in increased stability of one dimer species and explains the puzzling double peak structure observed in temperature programmed desorption (TPD or TDS) spectra for hydrogen on graphite (Figure 2a, from Ref. 57).

By using the method described in Ref. 14 of TPD (TDS) peak treatment (for the first-order reactions), relevant to TPD (TDS) peak $\text{I}_{[57]}$ (~65% of the total area, $T_{\text{max\#I[57]}} \approx 473$ K) in Figure 2a in Ref. 57, one can obtain values of the reaction $\text{I}_{[57]}$ rate constant ($K_{\text{I[57]}} = 1/\tau_{0.63\text{(des.)I[57]}}$) for several temperatures (for instance, $T = 458$, 482, and 496 K). Their temperature dependence can be described by Eq. (9). Hence, the desired quantities are defined (Table 3): the reaction (desorption) $\text{I}_{[57]}$ activation energy $\Delta H_{\text{(des.)I[57]}} = 0.6 \pm 0.2$ eV, and the per-exponential factor of the reaction $\text{I}_{[57]}$ rate constant $K_{0\text{(des.)I[57]}} \approx 1.5 \times 10^4\ \text{s}^{-1}$.

In a similar way, relevant to TPD (TDS) peak $\text{II}_{[57]}$ (~35% of the total area, $T_{\text{max\#II[57]}} \approx 588$ K) in Figure 2a in Ref. 57, one can obtain values of the reaction $\text{II}_{[57]}$ rate constant ($K_{\text{II[57]}} = 1/\tau_{0.63\text{(des.)II[57]}}$) for several temperatures (for instance, $T = 561$ and 607 K). Hence, the desired quantities are defined (Table 3): the reaction (desorption) $\text{II}_{[57]}$ activation energy $\Delta H_{\text{(des.)II[57]}} = 1.0 \pm 0.3$ eV, and the per-exponential factor of the reaction $\text{II}_{[57]}$ rate constant $K_{0\text{(des.)II[57]}} \approx 2 \times 10^6\ \text{s}^{-1}$.

The obtained characteristics (Table 3) of the desorption processes $\text{I}_{[57]}$ and $\text{II}_{[57]}$ show that these processes, very probably, are of a diffusion-rate-controlling character.[14] In a diffusion-rate-controlling case, these processes can not be described by using the Polanyi–Wigner equation (as it has been done in Ref. 57).

The observed in Ref. 57 "nanodimer states" or "nanoprotrusions" (Figures 1 and 2b in Ref. 57) may be related to defect nanoregions, very probably, as grain (domain) boundaries[49] and/or triple and other junctions (nodes) of the grain-boundary network in the HOPG samples. Some defect nanoregions at the grain-boundary network (hydrogen adsorption centers $\#I_{[57]}$, mainly, the "dimmer B" structures) can be related to TPD (TDS) peak $I_{[57]}$, the others (hydrogen adsorption centers $\#II_{[57]}$, mainly, the "dimmer A" structures) to TPD (TDS) peak $II_{[57]}$.

In Figures 1a and 2b in Ref. 57, one can imagine some grain-boundary network (with the grain size of about 2–5 nm) decorated (in some nanoregions at grain boundaries) by some bright nanoprotrusions.

Similar "nanoprotrusions" are observed and in graphene/SiC systems (Figures 1 and 2 in Ref. 58 and Figures 1 and 2 in Ref. 17).

In Figures 1a and 2b in Ref. 58, one can also imagine some grain-boundary network[33–42,49] (with the grain size of about 2–5 nm) decorated (in some nanoregions at grain boundaries) by some bright nanoprotrusions.

In Ref. 58, hydrogenation of single graphene on SiC substrate was studied by a beam of atomic deuterium 10^{12}–10^{13}/cm^2/s (corresponding to $P_D \approx 10^{-4}$ Pa) at 1600 K and the time of exposure to 5–90 s. It was observed that the formation of graphene blisters intercalated with hydrogen in them (Figures 1 and 2 in Ref. 58), similar to those observed on graphite[57] and graphene/SiO_2.[17]

Blisters[58] disappeared after keeping the samples in vacuum at 1073 K (~15 min). Hence, by using Eq. (8), one can evaluate the quantity of $\tau_{0.63(\text{des.})[58]1073\ \text{K}} \approx 5$ min, which coincides (within the errors) with the similar quantity of $\tau_{0.63(\text{des.})[59]1073\ \text{K}} \approx 7$ min evaluated for graphene/SiC samples[17] (Section 3.6, Table 3).

A near-complete such decoration of the grain-boundary network[33–42,49] can be imagined in Figure 1b in Ref. 17. And, as is seen in Figure 2 in Ref. 17, such decoration nanoregions (obviously, at the grain boundaries[33–42,49]) have a blister-like cross-section of height of about 1.7 nm and width of 10 nm order.

According to the thermodynamic analysis (presented in Section 3.7, Eq. (15)), such blister-like decoration nanoregions (at the grain boundaries[33–42,49]) may contain the intercalated gaseous molecular hydrogen at a high pressure.

3.6. Analysis of PES and ARPES data[17] on dehydrogenation of graphene/SiC samples

Atomic hydrogen exposures (at a pressure $P_H \approx 1 \times 10^{-4}$ Pa and temperature $T = 973$ K) on a monolayer graphene grown on the SiC(0001) surface are

shown[17] to result in hydrogen intercalation. It is shown[17] that the hydrogen intercalation induces a transformation of the monolayer graphene and the carbon buffer layer to bilayer graphene without a buffer layer. The STM, LEED, and core-level PES measurements reveal that hydrogen atoms can go underneath the graphene and the carbon buffer layer. This transforms the buffer layer into a second graphene layer.[17] Hydrogen exposure (15 min) results initially in the formation of bilayer graphene (blister-like) islands of height ~0.17 nm and a linear size of ~20–40 nm, covering about 40% of the sample (Figures 1b, 1e, 2a, and 2b in Ref. 17). With larger (additional 15 min) atomic hydrogen exposures, the islands grow in size and merge until the surface is fully covered with bilayer graphene (Figures 1c, 1f, 2c, and 2d in Ref. 17). A $(\sqrt{3} \times \sqrt{3})$ $R30°$ periodicity is observed on the bilayer areas (Figure 3 in Ref. 17). Angle-resolved photoelectron spectroscopy (ARPES) and energy-filtered X-ray photoelectron emission microscopy (XPEEM) investigations of the electron band structure confirm that after hydrogenation, the single π-band characteristic of monolayer graphene is replaced by two π-bands that represent bilayer graphene (Figure 6 in Ref. 17).

Annealing an intercalated sample, representing bilayer graphene, to a temperature of 1123 K, or higher, re-establishes the monolayer graphene with a buffer layer on SiC(0001).

The dehydrogenation was performed by subsequently annealing (for a few minutes duration) the hydrogenated samples at different temperatures, from 1023 to 1273 K. After each annealing step, the depletion of hydrogen was probed by PES and ARPES (Figures 4 and 5 in Ref. 17). From these data, one can determine, by using Eqs. (8) and (9), the tentative quantities: $\tau_{0.63(\text{des.})[17]}$ (at 1023 K and 1123 K), $\Delta H_{(\text{des.})[17]} \approx 3.6$ eV and $K_{0(\text{des.})[17]} \approx 2 \times 10^{14}$ s^{-1} (Table 3). These results can be interpreted within the model (noted in Ref. 17) of the interaction of hydrogen and silicon atoms at the graphene–SiC interface resulting in Si–C bonds at the intercalated islands. Obviously, the quantities of $K_{0(\text{des.})[17]}$ and $\Delta H_{(\text{des.})[17]}$ correspond to the Polanyi–Wigner equation,[14] of relevance for the Si–C bonds.[17]

3.7. Analysis of TDS and STM data[15,59] on HOPG treated by hydrogen

Atomic hydrogen accumulation in HOPG samples and etching their surface on hydrogen TDS have been studied in Ref. 15 using an STM and atomic force microscope (AFM). STM investigations[15] revealed that the surface morphology of untreated reference HOPG samples was found to be atomically

flat (Figure 2a), with a typical periodic structure of graphite (Figure 2b). Atomic hydrogen exposure (treatment) of the reference HOPG samples (30–125 min at atomic hydrogen pressure $P_H \approx 10^{-4}$ Pa and near-room temperature (~300 K)) to different atomic hydrogen doses (D) has drastically changed the initially flat HOPG surface into a rough surface, covered with nanoblisters of the average radius ~25 nm and the average height ~4 nm (Figures 2c and 2d).

TDS of hydrogen has been found on heating of the HOPG samples under mass spectrometer control. As is shown in Figure 3a, with the increase of the total hydrogen doses (D) to which HOPG samples have been exposed the desorbed hydrogen amounts (Q) increase and the percentage of D retained in samples (Q) approaches toward a saturation stage. After TDS, no nanoblisters were visible on the HOPG surface, the graphite surface was atomically flat, and covered with some etch-pits of nearly circular shapes, one or two layers thick (Figure 3b). This implies that after release of the captured hydrogen gas, the blisters become empty of hydrogen and the HOPG surface restores back a flat surface morphology under action of the corresponding forces.

According to Ref. 15, nanoblisters found on the HOPG surface after atomic hydrogen exposure are simply monolayer graphite (graphene) blisters, containing hydrogen gas in molecular form (Figure 4). As is suggested in Ref. 15 (Figure 4), atomic hydrogen intercalates between layers in the graphite net through holes in graphene hexagons (due to the small diameter of atomic hydrogen compared to the hole size) and is then converted to a H_2 gas form which is captured inside the graphene blisters (due to the relatively large kinetic diameter of hydrogen molecules).

But such interpretation[15] is in contradiction with the results noted in Section 1[8,32] "that it is almost impossible for a hydrogen atom to pass through the six-membered ring of graphene at room temperature".

It is reasonable to assume (as it has been done in the previous sections) that in HOPG[15] samples, atomic hydrogen passes into the graphite near-surface closed nanoregions (the graphene nanoblisters) through defects (probably, mainly, through triple junctions of the grain and/or subgrain boundary network) in the surface graphene layer. And it is expedient to note that in Figure 3b, one can imagine some grain-boundary network decorated by the etch-pits.

It has been found[15] that the average blister has radius ~25 nm and height ~4 nm. Approximating the nanoblister to be a semi-ellipse form results in blister area ($S_b \approx 2.0 \times 10^{-11}$ cm^2) and its volume ($V_b \approx 8.4 \times 10^{-19}$ cm^3).[15] The amount of retained hydrogen in this sample is $Q \approx 2.8 \times 10^{14}$ H_2/cm^2

and the number of hydrogen molecules captured inside the blister is $n \approx (Q\,S_b) \approx 5.5 \times 10^3$.[15] Hence, (within the ideal gas approximation, with accuracy of order of the magnitude) the internal pressure of molecular hydrogen in a single nanoblister at near-room temperature ($T \approx 300$ K) is $P_{H2} \approx \{k_B\,(Q\,S_b)\,T/V_b\} \approx 10^8$ Pa.

The hydrogen molecular gas density in the blisters in Ref. 15 (at $T \approx 300$ K and $P_{H2} \approx 1 \times 10^8$ Pa) can be estimated as $\rho \approx \{(Q\,M_{H2}\,S_b)/V_b\} \approx 0.045$ g/cm^3, where M_{H2} is the hydrogen molecule mass. It agrees with data[60] (considered in Refs. 18–21) on the hydrogen (protium) isotherm of 300 K.

These results[15] can be quantitatively described[18–21] (with accuracy of order of magnitude), within the thermodynamic approach,[44,46] by using the condition (equation) of the thermal-elastic equilibrium for the reaction of $(2H_{(gas)} \rightarrow H_{2(gas_in_blisters)})$, as follows[18]:

$$(P_{H2}/P^0{}_{H2}) \approx (P_H/P^0{}_H)^2 \exp\{[\Delta H_{dis} - T\Delta S_{dis} - P^*{}_{H2}\,\Delta V)]/k_B\,T\}, \quad (15)$$

where $P^*{}_{H2} \approx P_{H2} \approx 1 \times 10^8$ Pa is related to the blister "wall" backpressure (caused by $P^*{}_{H2}$), the so-called surface pressure;[44] $P_H \approx 1 \times 10^{-4}$ Pa is the atomic hydrogen pressure corresponding to the atomic flux[15]; $P^0{}_{H2} = P^0{}_H = 1$ Pa is the standard pressure[44,46]; $\Delta H_{dis} = 46.4$ eV is the experimental value[45] of the dissociation energy (enthalpy) of one molecule of gaseous hydrogen (at room temperatures); $\Delta S_{dis} = 11.8\ k_B$ is the dissociation entropy[45]; $\Delta V \approx (S_b\,r_b/n)$ is the apparent volume change; $r_b \approx 30$ nm is the radius of curvature of nanoblisters (at the nanoblister edge, Figure 4b); N_A is the Avogadro number; $T \approx 300$ K; the quantity of $(P^*{}_{H2}\Delta V)$ is related to the work of the nanoblister surface increase when intercalation of one molecule of H_2.

The value of the tensile stresses σ_b (caused by $P^*{}_{H2}$) in the graphene nanoblister "walls" of a thickness d_b and a radius of curvature r_b can be evaluated from another condition (equation) of the thermal-elastic equilibrium of the system in question, which is related to Eq. (15), as follows[18,44]:

$$\sigma_b \approx (P^*{}_{H2}\,r_b/2\,d_b) \approx (\varepsilon_b\,E_b), \quad (16)$$

where ε_b is a degree of elastic deformation of the graphene nanoblister walls, and E_b is a Young's modulus of the graphene nanoblister walls.

Substituting in the first part of Eq. (16) the quantities of $P^*{}_{H2} \approx 1 \times 10^8$ Pa, $r_b \approx 30$ nm, and $d_b \approx 0.15$ nm results in the value of $\sigma_{b[15]} \approx 1 \times 10^{10}$ Pa.

The degree of elastic deformation of the graphene nanoblister walls, apparently reaches $\varepsilon_{b[15]} \approx 0.1$ (Figure 4b). Hence, within a Hooke's law approximation (the second part of Eq. (16)), one can estimate (with accuracy of one–two orders of the magnitude) the value of a Young's modulus of the graphene nanoblister walls[15]: $E_{b[15]} \approx (\sigma_{b[15]}/\varepsilon_{b[15]}) \approx 0.1$ TPa. It is close (within the errors) to the experimental value[48] of a Young's modulus of graphene ($E_{graphene[48]} = 1.0$ TPa). The experimental value[5] of the degree of elastic deformation ($\varepsilon_{fix.membr.[5]} \approx 0.1$) of the hydrogenated fixed graphene membranes and the assumed stretching stress value ($\sigma_{fix.membr.[5]} \approx (\varepsilon_{fix.membr.[5]}\ E_{graphene[48]}) \approx 0.1$ TPa) in the expanded regions (domains or grains) of the material are considered in Section 2.3.

The experimental data[15,59] (Figure 2 in Ref. 59) on the TDS of hydrogen from graphene nanoblisters in pyrolytic graphite (Figures 2–4) can be approximated by three TDS peaks (# $I_{[59]}$ with $T_{max\#I[59]} \approx 1123$ K, # $II_{[59]}$ with $T_{max\#II[59]} \approx 1523$ K, and # $III_{[59]}$ with $T_{max\#III[59]} \approx 1273$ K). But their treatment, with using the above-mentioned (in previous sections) method,[14] is difficult due to some uncertainty, relevant to the zero level of the J_{des} quantity (in Figure 2 in Ref. 59). Nevertheless, TDS peak # $I_{[59]}$ can be characterized by the activation desorption energy $\Delta H_{(des.)\#I[59]} = 2.4 \pm 0.5$ eV and by the per-exponential factor of the reaction rate constant $K_{0(des.)\#I[59]} \approx 2 \times 10^{10}$ s^{-1} (Table 3).

Analysis[18–21] has shown that TDS peak $I_{[59]}$ is related to TDS peak (process) III in Refs. 14 and 18–21, for which the apparent diffusion activation energy $Q_{app.III} = (2.6 \pm 0.3)$ eV and $D_{0app.III} \approx 3 \times 10^{-3}$ cm^2/s.

Hence, one can obtain (with accuracy of one–two orders of the magnitude) a reasonable value of the diffusion characteristic size of $L_{TDS\text{-}peak\#I[59]} \approx (D_{0app.III}/K_{0(des.)\#I[59]})^{1/2} \approx 4$ nm, which is related to the separation distance between the graphene nanoblisters (Figure 4b) or (within the errors) to the separation distance between etch-pits (Figure 3b) in the HOPG specimens.[15,59]

Thus, TDS peak (process) $I_{[59]}$ is related to TDS peak (process) III in Refs. 14 and 18–21, which is related to model "F*"[14,18–21]] (Figure 1) considered in Section 2.4. Model "F*" is characterized[14,18–21] by the quantity $\Delta H_{(C–H)"F*"[14,18–21]} = (2.5 \pm 0.3)$ eV ($\approx Q_{app.III}$) that coincides with the similar quantities for graphanes (Table 1).

Finally, it is reasonable to assume that the inner surfaces ("walls") in the graphene nanoblisters in HOPG[15,59] are hydrogenated, and that the graphene "walls" situation is related to some hydrogenated graphenes (Table 1). Obviously, such hydrogenation of the inner graphene surfaces in the

nanoblisters[15,59] occurs under action of the gaseous molecular hydrogen of a high pressure (P^*_{H2}) intercalated into the stressed (expanded) hydrogenated graphene nanoblister "walls" possessing of a high Young's modulus.

As is considered in Section 4, a similar (in some extent) situation may occur in hydrogenated GNFs.

4. A Possibility[18–21] of Intercalation of Solid H_2 into Hydrogenated Graphite Nanofibers,[61,62] Relevance to the Hydrogen On-Board Storage Problem

Such a real possibility (considered in Refs. 18–21) is based on the following facts.

1. As is followed from data in Figures 5 and 6 (from Ref. 60), a solid molecular hydrogen (or deuterium) of density of $\rho_{H2} = 0.3–0.5$ g/cm^3(H_2) can exist at 300 K and the external pressure of $P = 30–50$ GPa.
2. As is followed from data in Figures 2–4 (from Ref. 15) and Eqs. (15) and (16) (from Ref. 18), the external surface pressure of $P = P^*_{H2} = 30–50$ GPa at $T \approx 300$ K may be provided (at the expense of the association energy of atomic hydrogen ($T\Delta S_{dis} - \Delta H_{dis}$)) into some closed hydrogenated (in gaseous atomic hydrogen with the corresponding pressure P_H) graphene nanostructures possessing of a high Young's modulus ($E_{graphene} \leq 1$ TPa).
3. As has been shown in Ref. 18, the treatment of the obtained in Refs. 61 and 62 data (Figure 7 from Ref. 61) on hydrogenation of GNFs results in the experimental value of the hydrogen density $\rho_{H2} = (0.5 \pm 0.2)$ g(H_2)/cm^3(H_2) (or $\rho_{(H2–C\ system)} \approx 0.2$ g(H_2)/cm^3(H_2–C system)) of the intercalated high-purity reversible hydrogen (~17 mass.% H_2) (Figure 8) corresponding, according to data from Figures 5 and 6, to the state of solid molecular hydrogen at the surface pressure of $P = P^*_{H2[61]} \approx 50$ GPa and $T \approx 300$ K.
4. Substituting in Eq. (16) the quantities of $P^*_{H2[61]} \approx 5 \times 10^{10}$ Pa, $\varepsilon_{b[61]} \approx 0.1$ (Figure 7), the largest possible value of $E_{b[61]} \approx 10^{12}$ Pa, the largest possible value of the tensile stresses ($\sigma_{b[61]} \approx 10^{11}$ Pa) in the edge graphene "walls" (of a thickness of $d_{b[61]}$ and a radius of curvature of $r_{b[61]}$) of the slit-like closed nanopores of the lens shape (Figure 7), one[18] can obtain the quantity of ($r_{b[61]}/d_{b[61]}$) ≈ 4. It is reasonable to assume $r_{b[61]} \approx 20$ nm (Figure 7); hence, a reasonable value follows of $d_{b[61]} \approx 5$ nm. A similar result can be obtained,[18] supposing the quantity of $E_{b[61]} \approx 10^{11}$ Pa (as it is for the hydrogenated graphene nanoblisters in HOPG,[15] Section 3.7).

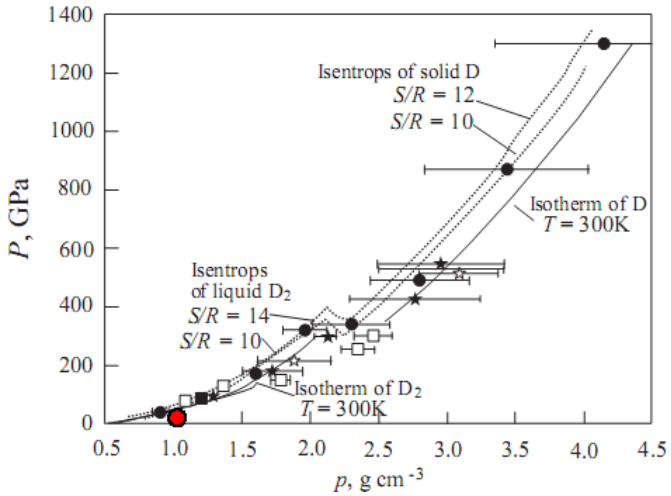

Figure 5. Isentropes (at entropies S/R = 10, 12, and 14, in units of the gas constant R) and isotherms (at T = 300 K) of molecular and atomic deuterium. The symbols show the experimental data, and curves fit calculated dependences. The density (ρ) of protium was increased by a factor of two (for the scale reasons). Thickened portion of the curve is an experimental isotherm of solid form of molecular hydrogen (H_2). The red additional symbol corresponds to a value of the twinned density $\rho \approx 1$ g/cm^3 of solid H_2 (at $T \approx 300$ K) and a near-megabar value of the external compression pressure $P \approx 50$ GPa.[18] From Ref. 60 with permission.

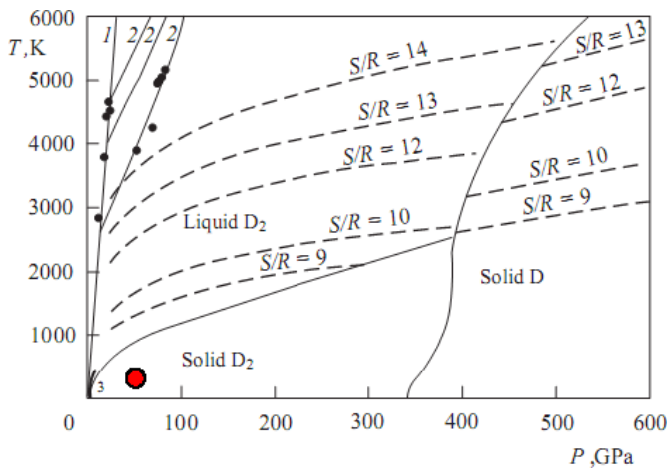

Figure 6. Phase diagram, adiabats, and isentropes of deuterium calculated with the equation of state: 1 and 2 are a single and a doubled adiabat, • is the experimental data, 3 is the melting curve, thickened portion of the curve is the experimental data. The red additional symbol corresponds to a value of temperature $T \approx 300$ K and a near-megabar value of the external compression pressure $P \approx 50$ GPa.[18] From Ref. 60 with permission.

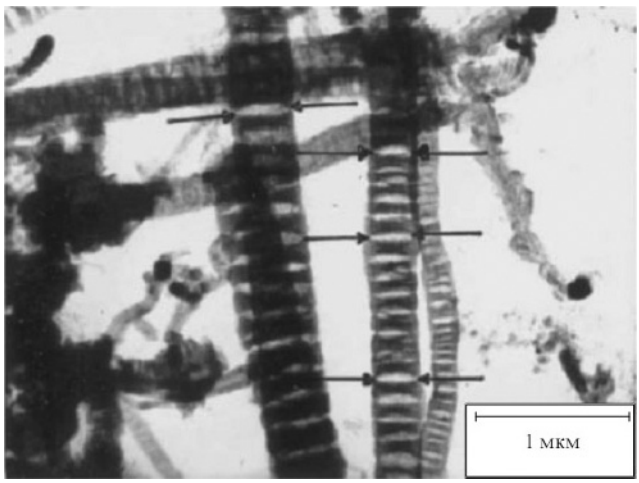

Figure 7. Micrographs[61] of hydrogenated GNFs after release from them (at ~300 K for ~10 min[61,62]) of intercalated (obviously, reversible) high-purity hydrogen (~17 mass.% — the gravimetrical reversible hydrogen capacity[61]). It occurs under a sharp decrease of the external (locking-like) pressure of H_2 (from ~10 MPa to ~1 MPa, at ~300 K[61,62]). The arrows in the picture indicate some of the slit-like closed nanopores of the lens shape (between hydrogenated graphite (graphene) nanoregions), where the intercalated reversible high-purity hydrogen was localized. Dehydrogenation of the hydrogenated graphite (graphene) nanoregions, relevant to the covalent bonded "non-reversible" hydrogen in them, occurs during TDS annealing at elevated temperatures. Two TDS peaks ($I_{[61,62]}$, $II_{[61,62]}$) were observed[61,62]; peak $I_{[61,62]}$ is related to TDS peak III in Refs. 14, 18–21, (Table 3). It allows us to realize a multicycle process[61] of charging–discharging of the same samples, of relevance to the intercalated reversible hydrogen, with the permanently hydrogenated graphite (graphene) nanoregions.

5. As has been noted in Refs. 18–21, a definite residual plastic deformation of the hydrogenated graphite (graphene) nanoregions is observed in Figure 7. Such plastic deformation of the nanoregins during hydrogenation of GNFs may be accompanied with some mass transfer resulting in such thickness ($d_{b[61]}$) of the walls.[61]
6. A very important role of the spillover effect,[63–69] relevant to hydrogenation of GNFs,[61,62] has been shown.[18–21]
7. Some relevant data presented in Figures 8 and 9 point to a breakthrough character of results,[18–21] of relevance for solving of the actual problem[70,71] of the hydrogen on-board storage in fuel-cell-powered vehicles.

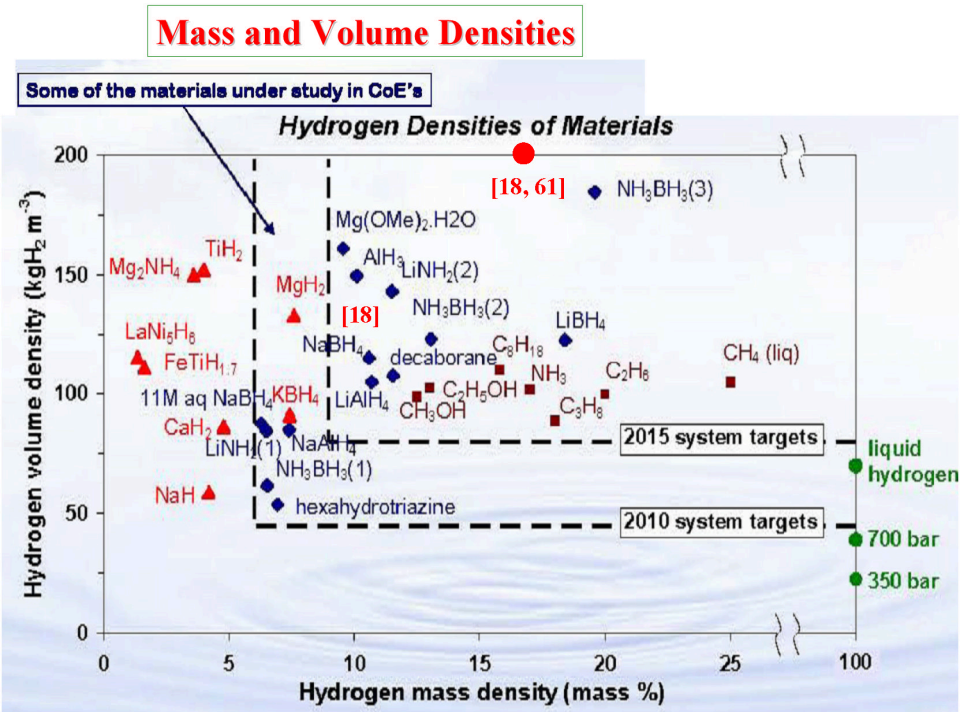

Figure 8. US DOE targets[70] is shown (in the face of known achievements), relevant to gravimetric and volumetric hydrogen on-board storage densities for 2010 (6.0 mass.% H_2, 45 kg(H_2)/m^3(system)) and for 2015 (9.0 mass.% H_2, 81 kg(H_2)/m^3 (systems)). The additional symbol is related to the solid hydrogen intercalated into the hydrogenated GNFs[18,61] (Figure 7). From Ref. 72 with permission.

5. Conclusions

1. Consideration of some the most cited works[3–9,17,25,51–59,62] and the nearly by non-cited ones[18–21,61] on the thermodynamic stability of a number of hydrogenated graphene layers systems (Tables 1–3) has shown the need for further related (mainly, experimental) studies for determination of a complete and compatible set of thermodynamic characteristics of such systems.
2. The alternative viewpoint[5] that experimental graphane (a free-standing membrane[5]) may have "a more complex hydrogen bonding than the one suggested by theory[3]", and that epitaxial graphene[5] may be a different material, rather than the theoretical graphane[3] (Table 1) has been confirmed.

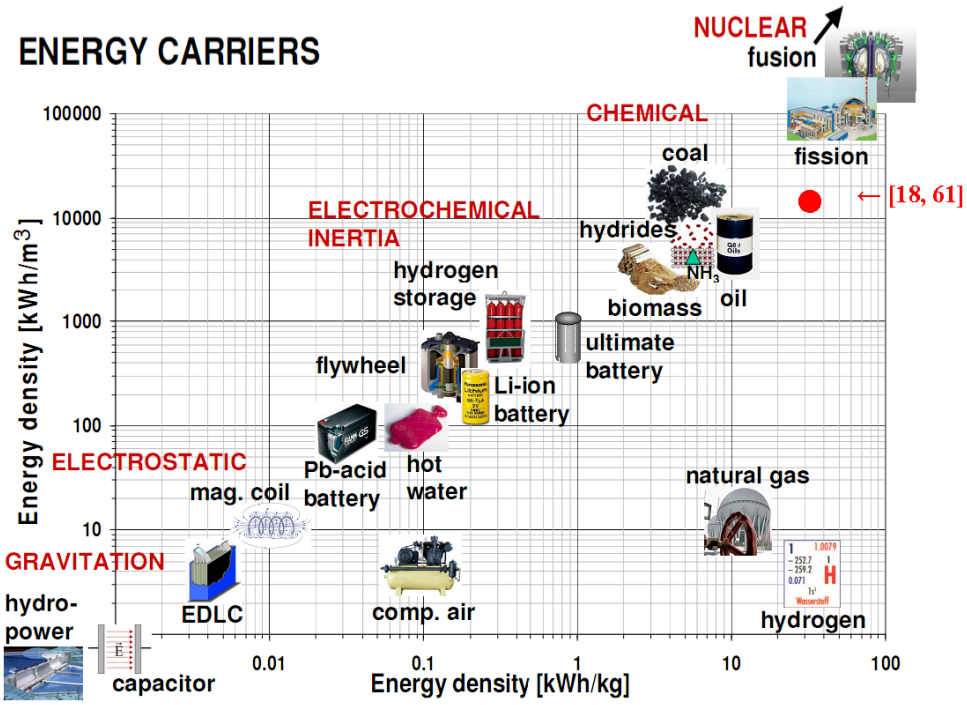

Figure 9. The known data on volumetric and gravimetric energy densities for different energy carriers is shown. The additional symbol is related to the solid hydrogen intercalated into the hydrogenated GNFs[18,61] (Figure 7). From Ref. 73 with permission.

3. A thermodynamic probability for the existence of hydrogenated graphenes–graphanes*[18–21] possessing of a very high binding (cohesive) energy, in comparison with theoretical graphane[3] (Table 1) has been shown.
4. A breakthrough character (Figures 8 and 9) of analytical results[18–21] on the solid hydrogen intercalated in hydrogenated graphite nanofibers (Figure 7), relevant for solving of the actual problem[71,73] of the hydrogen on-board storage in fuel-cell-powered vehicles has been shown.
5. A constructive open discussion on the considered thermodynamic aspects of the hydrogenated graphene layers systems seems expedient and relevant for promotion of the further developments.

Acknowledgments

The author is grateful to H. G. Xiang, M.-H. Whangbo, D. C. Elias, C. Casiraghi, A. Eckmann, N. Tombros, B. J. Van Wees, A. Castellanos-Gomez, R. Bisson, T. Yu, L. Hornekaer, and Z. Waqar for their helpful

discussions, valuable completion, and/or reading of the related parts of the present analytical results.

References

1. Geim, A. K.; Novoselov, K. S. *Nat. Mater.* **2007**, *6*, 183–191.
2. Palerno, V. *Chem. Commun.* **2013**, *49*, 2848–2857.
3. Sofo, J. O.; Chaudhari, A. S.; Barber G. D. *Phys. Rev. B* **2007**, *75*, 153401-1–153401-4.
4. Openov, L. A.; Podlivaev, A. I. *Tech. Phys. Lett.* **2010**, *36*, 31–33.
5. Elias, D. C.; Nair, R. R.; Mohiuddin, T. M. G.; Morozov, S. V.; Blake, P.; Halsall, M. P.; Ferrari, A. C.; Boukhvalov, D. W.; Katsnelson, M. I.; Geim, A. K.; Novoselov, K .S. *Science* **2009**, *323*, 610–626.
6. Openov, L. A.; Podlivaev, A. I. *Tech. Phys.* **2012**, *57*, 1603–1605.
7. Pujari, B. S.; Gusarov, S.; Brett, M.; Kovalenko, A. *Phys. Rev. B* **2011**, *84*, 041402-1–041402-6.
8. Xiang, H. J.; Kan, E. J.; Wei, S.-H.; Gong, X. G.; Whangbo, M.-H. *Phys. Rev. B* **2010**, *82*, 165425-1–165425-4.
9. Podlivaev, A. I.; Openov, L. A. *Semiconductors* **2011**, *45*, 958–961.
10. Nikitin, A.; Li, X.; Zhang, Z.; Ogasawara, H.; Dai, H.; Nilsson, A. *Nano Lett.*, **2008**, *8*, 162–167.
11. Nikitin, A.; Näslund, L.-A.; Zhang, Z.; Nilsson, A. *Surf. Sci.*, **2008**, *602*, 2575–2580.
12. Bauschlicher, Jr. C. W.; So, C. R. *Nano Lett.* **2002**, *2*, 337–341.
13. Pimenova, S. M.; Melkhanova, S. V.; Kolesov, V. P.; Lobach, A. S. *J. Phys. Chem. B* **2002**, *106*, 2127–2130.
14. Nechaev, Yu. S. *J. Nano Res.* **2010**, *12*, 1–44.
15. Waqar, Z. *J. Mater. Sci.* **2007**, *42*, 1169–1176.
16. Nechaev, Yu. S.; Alexeeva, O. K.; Oechsner, A. *J. Nanosci. Nanotechnol.* **2009**, *9*, 3949–3958.
17. Watcharinyanon, S.; Virojanadara, C.; Osiecki, J. R.; Zakharov, A. A.; Yakimova, R.; Uhrberg, R. I. G.; Johansson, L. I. *Surf. Sci.* **2011**, *605*, 1662–1668.
18. Nechaev, Yu. S. *Int. Sc. J. Fundam. Appl. Phys.* **2012**, *1*, 38–60 (in Russian).
19. Nechaev, Yu. S. *J. Nano Res.* **2011**, *15*, 75–93.
20. Nechaev, Yu. S. *Int. J. Hydrogen Energy* **2011**, *36*, 9023–9031.
21. Nechaev, Yu. S. *Open Fuel Cell J.* **2011**, *4*, 16–29.
22. Xiang, H.; Kan, E.; Wei, S.-H.; Whangbo, M.-H.; Yang J. *Nano Lett.* **2009**, *9*, 4025–4030.
23. Lebegue, S.; Klintenberg, M.; Eriksson, O.; Katsnelson, M. I. *Phys. Rev. B: Condens. Matter Mater. Phys.* **2009**, *79*, Article ID 245117.

24. Zhou, J.; Wang, Q.; Sun, Q.; Chen, X. S.; Kawazoe, Y.; Jena, P. *Nano Lett.* **2009**, *9*, 3867–3870.
25. Dzhurakhalov, A. A.; Peeters, F. M. *Carbon*, **2011**, *49*, 3258–3266.
26. Ruffieux, P.; Gröning, O.; Bielmann, M.; Mauron, P.; Schlapbach, L.; Gröning, P. *Phys. Rev. B* **2002**, *66*, 245416-1–245416-8.
27. Sha, X.; Jackson, B. *Surf. Sci.* **2002**, *496*, 318–330.
28. Sluiter, M. H. F.; Kawazoe, Y. *Phys. Rev. B* **2003**, *68*, 085410-1–085410-7.
29. Yazyev, O. V.; Helm, L. *Phys. Rev. B* **2007**, *75*, 125408-1–125408-5.
30. Lehtinen, P. O.; Foster, A. S.; Ma, Y.; Krasheninnikov, A. V.; Nieminen, R. M. *Phys. Rev. Lett.* **2004**, *93*, 187202-1–187202-4.
31. Boukhvalov, D. W.; Katsnelson, M. I.; Lichtenstein, A. I. *Phys. Rev. B* **2008**, *77*, 035427-1–035427-7.
32. Jiang, D.; Cooper, V. R.; Dai, S. *Nano Lett.* **2009**, *9*, 4019–4024.
33. Brito, W. H.; Kagimura, R.; Miwa, R. H. *Appl. Phys. Lett.* **2011**, *98*, Article ID 213107.
34. Tapasztó, L.; Nemes-Incze, P.; Dobrik, G.; Jae-Yoo, K.; Hwang, C.; Biró, L. P. *Appl. Phys. Lett.* **2012**, *100*, Article ID 053114.
35. Banhart, F.; Kotakoski, J.; Krasheninnikov, A. V. *ACS Nano* **2011**, *5*, 26–41.
36. Yazyev, O. V.; Louie, S. G. *Phys. Rev. B: Condens. Matter Mater. Phys.* **2010**, *81*, Article ID 195420.
37. Kim, K.; Lee, Z.; Regan, W.; Kisielowski, C.; Crommie, M. F.; Zettl, A. *ACS Nano* **2011**, *5*, 2142–2146.
38. Koepke, J. C.; Wood, J. D.; Estrada, D.; Ong, Z.-Y.; He, K. T.; Pop, E.; Lyding, J. W. *ACS Nano* **2013**, *7*, 75–86.
39. Zhang, J.; Zhao, J. *Carbon* **2013**, *55*, 151–159.
40. Yakobson, B. I.; Ding, F. *ACS Nano* **2011**, *5*, 1569–1574.
41. Cockayne, E.; Rutter, G. M.; Guisinger, N. P.; Crain, J. N.; First, P. N.; Stroscio, J. A. *Phys. Rev. B: Condens. Matter Mater. Phys.* **2011**, *83*, Article ID 195425.
42. Zhang, J.; Zhao, J.; Lu, J. *ACS Nano* **2012**, *6*, 2704–2711.
43. Sessi, P.; Guest, J. R.; Bode, M.; Guisinger, N. P. *Nano Lett.* **2009**, *9*, 4343–4347.
44. Bazarov, I. P. *Thermodynamics*, Vysshaya Shkola: Moscow, 1976.
45. Karapet'yants, M. K.; Karapet'yants, M. L. *Osnovnye Termodinamicheskie Konstanty Neorganicheskikh i Organicheskikh Veshchestv (Fundamental Thermodynamic Constants of Inorganic and Organic Substances)*, Khimiya: Moscow, 1968.
46. Zhukhovitskii, A. A.; Shvartsman, L. A. *Physical Chemistry*, Metallurgiya: Moscow, 1987.
47. Xie, L.; Wang, X.; Lu, J.; Ni, Z.; Luo, Z.; Mao, H.; Wang, R.; Wang, Y.; Huang, H.; Qi, D.; Liu, R.; Yu, T.; Shen, Z.; Wu, T.; Peng, H.; Özyilmaz, B.; Loh, K.; Wee, A. T. S.; Ariando; Chen, W. *Appl. Phys. Lett.* **2011**, *98*, Article ID 193113.

48. Lee, C.; Wei, X.; Kysar, J. W.; Hone, J. *Science* **2008**, *321*, 385–388.
49. Eckmann, A.; Felten, A.; Mishchenko, A.; Britnell, L.; Krupke, R.; Novoselov, K. S.; Casiraghi, C. *Nano Lett.* **2012**, *12*, 3925–3930.
50. Yang, F. H.; Yang, R. T. *Carbon* **2002**, *40*, 437–444.
51. Wojtaszek, M.; Tombros, N.; Garreta, A.; Van Loosdrecht, P. H. M.; Van Wees, B. J. *J. Appl. Phys.* **2011**, *110*, Article ID 063715.
52. Castellanos-Gomez, A.; Wojtaszek, M.; Arramel, A.; Tombros, N.; Van Wees, B. J. *Small* **2012**, *8*, 1607–1613.
53. Castellanos-Gomez, A.; Arramel, A.; Wojtaszek, M.; Smit, R. H. M.; Tombros, N.; Agraït, N.; Van Wees, B. J. Rubio-Bollinger, G. *Bol. Grupo Esp. Carbón* **2012**, *25*, 18–22.
54. Castellanos-Gomez, A.; Smit, R. H. M.; Agraït, N.; Rubio-Bollinger, G. *Carbon* **2012**, *50*, 932–938.
55. Bocquet, F. C.; Bisson, R.; Themlin, J.-M.; Layet, J.-M.; Angot, T. *Phys. Rev. B: Condens. Matter Mater. Phys.* **2012**, *85*, Article ID 201401.
56. Luo, Z.; Yu, T.; Kim, K.-J.; Ni, Z.; You, Y.; Lim, S.; Shen, Z.; Wang, S.; Lin, J. *ACS Nano* **2009**, *3*, 1781–1788.
57. Hornekaer, L.; Šljivančanin, Ž.; Xu, W.; Otero, R.; Rauls, E.; Stensgaard, I.; Lægsgaard, E.; Hammer, B.; Besenbacher, F. *Phys. Rev. Lett.* **2006**, *96*, Article ID 156104.
58. Balog, R.; Jørgensen, B.; Wells, J.; Lægsgaard, E.; Hofmann, P.; Besenbacher, F.; Hornekær, L. *J. Am. Chem. Soc.* **2009**, *131*, 8744–8745.
59. Waqar, Z.; Klusek, Z.; Denisov, E.; Kompaniets, T.; Makarenko, I.; Titkov, A.; Saleem, A. *Electrochem. Soc. Proc.* **2000**, *16*, 254–265.
60. Trunin, R. F.; Urlin, V. D.; Medvedev, A. B. *Phys. Usp.* **2010**, *53*, 605–622.
61. Gupta, B. K.; Tiwari, R. S.; Srivastava, O. N. *J. Alloys Compd.* **2004**, *381*, 301–308.
62. Park, C.; Anderson, P. E.; Chambers, A.; Tan, C. D.; Hidalgo, R.; Rodriguez, N. M. *J. Phys. Chem. B* **1999**, *103*, 10572–10581.
63. Lin, Y.; Ding, F.; Yakobson, B. I. *Phys. Rev. B: Condens. Matter Mater. Phys.* **2008**, *78*, Article ID 041402.
64. Singh, A. K.; Ribas, M. A.; Yakobson, B. I. *ACS Nano* **2009**, *3*, 1657–1662.
65. Wang, L.; Yang, R. T. *Energy Environ. Sci.* **2008**, *1*, 268–279.
66. Wang, L.; Yang, R. T. *Catal. Rev. — Sci. Eng.* **2010**, *52*, 411–461.
67. Gao, Y.; Zhao, N.; Li, J.; Liu, E.; He, C.; Shi, C. *Int. J. Hydrogen Energy* **2012**, *37*, 11835–11841.
68. Wang, L.; Yang, R. T. *Carbon* **2012**, *50*, 3134–3140.
69. Han, S. S.; Jung, H.; Jung, D. H.; Choi, S.-H.; Park, N. *Phys. Rev. B: Condens. Matter Mater. Phys.* **2012**, *85*, Article ID 155408.
70. Satyapal, S.; Petrovic, J.; Read, C.; Thomas, G.; Ordaz, G. *Catal. Today* **2007**, *120*, 246–257. Available at: www.eere.energy.gov/hydrogenandfuelcells.

71. *DOE targets for onboard hydrogen storage systems for light-duty vehicles*, **2012**. Available at: http://wwwl.eere.energy.gov/hydrogenandfuelcells/storage/pdfs/targets_onboard_hydro_storage.pdf.
72. Fruchart, D. Large scale development of metal hydrides for stationary and nomad hydrogen storage units. Which are potential partners to built innovative solutions for sustainable and clean energy systems? In *Materials of Int. Hydrogen Research Showcase 2011*, University of Birmingham, UK, April 13–15, **2011**. Available at: http://www.uk-shec.org.uk/uk-shec/showcase/ShowcasePresentations.html.
73. Zuettel, A. Hydrogen the future energy carrier. In: *Materials of Int. Hydrogen Research Showcase 2011*, University of Birmingham, UK, April 13–15, **2011**. Available at: http://www.uk-shec.org.uk/uk-shec/showcase/ShowcasePresentations.html.

Cumulative Index of Volumes 5 and 6

Adsorption on and reactivity of CNT and graphene, Vol. 5:40–42
  chemisorption on CNT and graphene
    gases, Vol. 5:83–97
    liquids, Vol. 5:97–99
    solids, Vol. 5:99–122
  effects of interactions with nanotubes on IR spectra of small molecules, Vol. 5:59
  nitrogen-containing species on carbon surface, Vol. 5:126
  oxygen-containing species, Vol. 5:125
  physisorption on CNTs and graphene, Vol. 5:54–55
    gases, Vol. 5:55–66
    liquids, Vol. 5:66–77
    solids, Vol. 5:77–83
  reactivity on CNTs and graphene, Vol. 5:122
    bioreactivity and degradability of CNTs and graphene, Vol. 5:153–160
    catalysis, Vol. 5:128–150
    gas sensors, Vol. 5:150–153
    main advantages offered by CNT or CNF supports, Vol. 5:129
    nanostructured carbon materials, surface chemistry of, Vol. 5:124–128
  structure and adsorption sites, Vol. 5:42
    graphene and few layer graphene (FLG), Vol. 5:42–49
AEPA (2-aminoethylphosphonic acid), Vol. 5:79
Amperometric glucose biosensors
  with detection of H_2O_2, Vol. 6:93–101
  with direct electron transfer, Vol. 6:88–93
APTES (3-aminopropyltriethoxysilane), Vol. 5:79
Atomic collapse on graphene, Vol. 5:14–16

Bilayer-graphene, Vol. 5:8
Biocompatibility of graphene, Vol. 6:197
Bioreactivity and degradability of CNTs and graphene, Vol. 5:153–160
  biodegradability and toxicity, Vol. 5:158
  biosensors, Vol. 5:155–156
  drug delivery, Vol. 5:156–158
Biosensor applications, graphene for, Vol. 6:83–87
  biosensors for glucose, Vol. 6:87–88
    amperometric glucose biosensors with detection of H_2O_2, Vol. 6:93–101

amperometric glucose biosensors with direct electron transfer, Vol. 6:88–93
mass-sensitive glucose biosensors, Vol. 6:101–102
nucleic acids, Vol. 6:103–112
proteins, Vol. 6:112–113
amino acids, Vol. 6:119–122
cancer biomarkers, Vol. 6:113–117
immunoglobulins, Vol. 6:122–124
thrombin, Vol. 6:117–119

Cancer biomarkers, Vol. 6:113–117
Carbon
elastic properties of several allotropes, Vol. 5:17
graphene as allotropes of. *See* Graphene
Carbon adatoms, Vol. 5:23–24
defects with, Vol. 5:24
Carbon nanofibers (CNFs), Vol. 5:122
characteristics of, Vol. 5:123
Carbon nanostructures, Vol. 5:4
Carbon nanotubes (CNT), Vol. 5:40
characteristics of, Vol. 5:123
physisorption and chemisorption
common features characterizing, Vol. 5:55
difference between, Vol. 5:54
presence of defects, Vol. 5:51–54
molecular orbitals (MO), Vol. 5:53
non-hexagonal rings, Vol. 5:52
rehybridization, Vol. 5:50
side view of nanotube structure, Vol. 5:52
structure
and adsorption sites of, Vol. 5:49–54
and its specific uses, Vol. 5:40–41
toxicity of, Vol. 5:158–160
Carbon vacancies, Vol. 5:21–23
defects in graphene, Vol. 5:21–23
double vacancies, Vol. 5:22
single vacancy, Vol. 5:21
Chemisorption on CNT and graphene
gases, Vol. 5:83–97
on CNTs, Vol. 5:83–84
effect of dopants on graphene, Vol. 5:93–97
effect of dopants on with CNTs, Vol. 5:84–87
on graphene, Vol. 5:87–93
liquids, Vol. 5:97–99
hydrogen chemisorption on, Vol. 5:98
solids, Vol. 5:99–122
adsorption of other metals, metalloids, and non-metals, Vol. 5:115–116
alkali metals, Vol. 5:99–101
alkaline-earth metals, Vol. 5:102
clusters, Vol. 5:109
d-metals, Vol. 5:102–103
gold clusters, Vol. 5:114–115
platinum clusters, Vol. 5:109–114
polymers, Vol. 5:116–122
single metal atoms, Vol. 5:103–109
CNT. *See* Carbon nanotubes (CNT)
CNT and graphene, adsorption on and reactivity of, Vol. 5:40–42
chemisorption on CNT and graphene
gases, Vol. 5:83–97
liquids, Vol. 5:97–99
solids, Vol. 5:99–122

effects of interactions with nanotubes on IR spectra of small molecules, Vol. 5:59
nitrogen-containing species on carbon surface, Vol. 5:126
oxygen-containing species, Vol. 5:125
physisorption on CNTs and graphene, Vol. 5:54–55
gases, Vol. 5:55–66
liquids, Vol. 5:66–77
solids, Vol. 5:77–83
reactivity on CNTs and graphene, Vol. 5:122
bioreactivity and degradability of CNTs and graphene, Vol. 5:153–160
catalysis, Vol. 5:128–150
gas sensors, Vol. 5:150–153
main advantages offered by CNT or CNF supports, Vol. 5:129
nanostructured carbon materials, surface chemistry of, Vol. 5:124–128
structure and adsorption sites, Vol. 5:42
graphene and FLG, Vol. 5:42–49
Covalent functionalization of graphene in dispersions, Vol. 5:199–201
dienophiles addition, Vol. 5:201–204
free radical addition, Vol. 5:201

Defects in graphene, Vol. 5:45
atomic scale properties of, Vol. 5:29
carbon adatoms, Vol. 5:23–24
with carbon adatoms, Vol. 5:24, 46
carbon vacancies, Vol. 5:21–23
double vacancies, Vol. 5:22
single vacancy, Vol. 5:21
compendium of formation and migration energies, Vol. 5:20
dislocation-like defects, Vol. 5:48–49
divacancy, Vol. 5:46
doping of graphene, Vol. 5:28
edge configuration and types of edge defects, Vol. 5:44–45
in edges of graphene layer, Vol. 5:49
effect of defects on properties of graphene, Vol. 5:27–30
extrinsic, Vol. 5:45
foreign adatoms, Vol. 5:47
grain boundaries, Vol. 5:26–27
grain boundary loops, Vol. 5:24–25
intrinsic, Vol. 5:22, Vol. 5:45
mechanical properties of, Vol. 5:30
monovacancy, Vol. 5:46
noncarbon adatoms and substitutional impurities, Vol. 5:25–26
one-dimensional defects, Vol. 5:48–49
point defects, Vol. 5:46–48
single and multiple vacancies, Vol. 5:46
Stone–Wales defects, Vol. 5:18, 21, 46
structural defects in, Vol. 5:19–21
ways of connecting graphene sheets, Vol. 5:48
Dendrimer composite, carbon nanotube and, Vol. 6:206–207
covalent functionalization, Vol. 6:207–211
non-covalent functionalization, Vol. 6:211–213

Dirac point, Vol. 5:15
DNA biosensor, graphene-based, Vol. 6:179–181
DNA–carbon nanotube composite, Vol. 6:197
  applications, Vol. 6:202–206
  influence of temperature on oligonucleotide adsorption, Vol. 6:200–201
  structure and properties, Vol. 6:198–200

Energy conversion, carbon nanomaterials for, Vol. 6:213
  blue energy, Vol. 6:218–220
  energy-efficient nanoelectrical devices, Vol. 6:222–227
  hydrogen storage, Vol. 6:213–218
  voltage generation through flow, Vol. 6:220–222
Energy storage applications
  graphene-based materials for, Vol. 6:2–4
  nanomaterials (graphene-based) for energy conversion and storage, Vol. 6:51–52
Enzymatic biosensor
  graphene-based electrochemical, Vol. 6:160–163
  graphene–carbon nanotube-based, Vol. 6:176–178
  inorganic nanoparticles-modified graphene-based, Vol. 6:171–174
  organic molecular-modified graphene-based, Vol. 6:163–166
  polymer-modified graphene-based, Vol. 6:166–171

Few-layer graphene (FLG), Vol. 5:42
  characteristics of, Vol. 5:123
  structure and adsorption sites, Vol. 5:42–49
FLG. *See* Few-layer graphene (FLG)
Fullerenes, Vol. 5:2, 4

Glucose, biosensors for, Vol. 6:87–88
Grain boundaries, Vol. 5:26–27, 30
  atomic structure in graphene, Vol. 5:28
Grain boundary loops (GBL), Vol. 5:24–25
  atomic configurations of, Vol. 5:25
Granular activated carbon (GAC), Vol. 5:74
Graphene
  adsorption on and reactivity of. *See* Carbon nanotubes and graphene, adsorption on and reactivity of
  adsorption sites of, Vol. 5:47
  AFM nanoindentation of monolayer graphene membrane, Vol. 5:18
  application of, Vol. 6:11–15
  characteristics of, Vol. 5:123
  characterization of, Vol. 6:6
    morphological characterization, Vol. 6:6–9
    structural characterization, Vol. 6:9–11
  defects in, Vol. 5:see defects in graphene
  dirac fermions, Vol. 5:10, 11
  in dispersions
    chemical manipulation of, Vol. 5:186–187
    covalent functionalization of, Vol. 5:199–204
    phonon dispersion at zero stress, Vol. 5:19
  edge shape, Vol. 5:43, 44
    configurations, Vol. 5:43
  elastic properties of, Vol. 5:16–19
    monolayer graphene, experiment vs theory, Vol. 5:18
  electronic properties of, Vol. 5:8
    atomic collapse on graphene, Vol. 5:14–16

band structure, Vol. 5:5–8
chirality and quantum hall effect, Vol. 5:10–11
few-layered graphene, Vol. 5:8–10
Klein tunneling in graphene, Vol. 5:11–14
energy dispersion, Vol. 5:6
intrinsic defects in, Vol. 5:22
isolation, Vol. 5:2. *See also Micromechanical cleavage*
magnetism in, Vol. 5:30
miscellaneous applications of, Vol. 5:210–212
physisorption and chemisorption
common features characterizing, Vol. 5:55
difference between, Vol. 5:54
quantum electrodynamics (QED), Vol. 5:10
quantum hall effect (QHE), Vol. 5:11
staking orders in, Vol. 5:8
effect of, Vol. 5:9
structural defects in, Vol. 5:19–21
atomic scale properties of, Vol. 5:29
carbon adatoms, Vol. 5:23–24
carbon vacancies, Vol. 5:21–23
compendium of formation and migration energies, Vol. 5:20
doping of graphene, Vol. 5:28
effect of defects on properties of graphene, Vol. 5:27–30
grain boundaries, Vol. 5:26–27
grain boundary loops, Vol. 5:24–25
mechanical properties of, Vol. 5:30
noncarbon adatoms and substitutional impurities, Vol. 5:25–26
Stone–Wales defects, Vol. 5:18, 21
structure, Vol. 5:2, 3
and adsorption sites, Vol. 5:42–49
electronic structure of, Vol. 5:6
and its specific uses, Vol. 5:40–41
lattice vectors of graphene unit cell, Vol. 5:5
synthesis of. *See* Synthesis of graphene
three adsorption sites of, Vol. 5:47
topology of defective, Vol. 5:48
toxicity of, Vol. 5:158–160
Graphene and carbon nanotube-based nanomaterial, Vol. 6:190–191
biocompatibility of graphene, Vol. 6:197
carbon nanomaterials for energy conversion, Vol. 6:213
blue energy, Vol. 6:218–220
energy-efficient nanoelectrical devices, Vol. 6:222–227
hydrogen storage, Vol. 6:213–218
voltage generation through flow, Vol. 6:220–222
carbon nanotube and dendrimer composite, Vol. 6:206–207
covalent functionalization, Vol. 6:207–211
non-covalent functionalization, Vol. 6:211–213
DNA–carbon nanotube composite, Vol. 6:197
applications, Vol. 6:202–206
influence of temperature on oligonucleotide adsorption, Vol. 6:200–201

structure and properties, Vol. 6:198–200
Graphene-based composites, Vol. 6:66
for lithium ion batteries, Vol. 6:68–73
for oxygen reduction reaction, Vol. 6:66–68
for supercapacitors, Vol. 6:74–75
Graphene-based electrochemical biosensor, Vol. 6:148–150
biomolecular-modified graphene-based enzymatic biosensor, Vol. 6:174–175
electrochemical properties of graphene, Vol. 6:158–160
functionalization of graphene, Vol. 6:155–158
graphene-based DNA biosensor, Vol. 6:179–181
graphene-based electrochemical enzymatic biosensor, Vol. 6:160–163
graphene–carbon nanotube-based enzymatic biosensor, Vol. 6:176–178
inorganic nanoparticles-modified graphene-based enzymatic biosensor, Vol. 6:171–174
N-doped graphene-based enzymatic biosensor, Vol. 6:178–179
organic molecular-modified graphene-based enzymatic biosensor, Vol. 6:163–166
polymer-modified graphene-based enzymatic biosensor, Vol. 6:166–171
synthesis and characterization of graphene, Vol. 6:150–155
Graphene-based materials for energy storage applications, Vol. 6:2–4
Graphene-based supercapacitor, Vol. 6:15
applications of, Vol. 6:40
emergency management, Vol. 6:41
public transport, Vol. 6:41
starter for fuel-efficient stop–start systems, Vol. 6:40–41
graphene/conducting polymer composite supercapacitor, Vol. 6:32–40
metal nanoparticle/oxide-decorated graphene supercapacitor, Vol. 6:25–31
reduced graphene oxide (rGO) supercapacitor, Vol. 6:16–21
surface-modified graphene supercapacitor, Vol. 6:21–25
Graphene composites, Vol. 5:204–206
graphene/inorganic material composites, Vol. 5:208
graphene/polymer composites, Vol. 5:206–207
synthesis of graphene–inorganic nanocomposites, Vol. 5:209–210
synthesis of graphene/polymer composites, Vol. 5:207–208
Graphene–nucleic acid composites, Vol. 6:192
adsorption of nucleic acids on graphene, Vol. 6:193–197
functionalization of graphene, Vol. 6:192–193
Graphenium, Vol. 5:3
Graphite, Vol. 5:2, 4

High-Angle Annular Dark-Field (HAADF) mode, Vol. 5:79
Highly ordered pyrolytic graphite (HOPG), Vol. 5:65
High-Resolution Transmission Electron Microscopy (HRTEM), Vol. 5:79

Janus graphene, Vol. 5:77
static water contact angle measurements in fabrication procedures of, Vol. 5:78

Klein paradox, Vol. 5:11, 12

Liquid-phase exfoliated graphene
non-ultrasonication techniques
ball-milling production, Vol. 5:193
intercalation compounds, Vol. 5:190
ionics compounds, Vol. 5:191–193
supercritical fluids, Vol. 5:194
unzipping of carbon nanotubes, Vol. 5:194–195
ultrasonication of graphite, Vol. 5:187–188
graphene dispersions in organic solvents, Vol. 5:188–189
graphene dispersions in surfactant solutions, Vol. 5:190
Liquid-phase synthesis of graphene, Vol. 6:52–53
from expanded graphite, Vol. 6:53–55
from graphite oxide, Vol. 6:56–57

Mass-sensitive glucose biosensors, Vol. 6:101–102
Mermin–Wagner theorem, Vol. 5:6–7
Micromechanical cleavage, Vol. 5:2, 3
Multiwalled CNTs (MWCNTs), Vol. 5:59, 60–62, 74–75

Nanomaterials (graphene-based) for energy conversion and storage, Vol. 6:51–52
Nanostructured carbon materials, surface chemistry of, Vol. 5:124–128
Nanostructures from liquid-phase exfoliated graphene, Vol. 5:195
deformation, folding, and stabilization, Vol. 5:196
ultrasonication of graphite
tiopronin as antioxidant molecule, Vol. 5:196–197
Vol. 5:transformation of few-layer graphene into MWNTs, Vol. 5:197–199
Nanotubes, Vol. 5:2, 4
Natural organic matter (NOM), Vol. 5:67, 74
N-doped graphene-based enzymatic biosensor, Vol. 6:178–179
Nitrogen-doped graphene, Vol. 6:57–59
applications of
lithium ion batteries, Vol. 6:64–65
oxygen reduction reaction of fuel cells, Vol. 6:61–63
synthesis of, Vol. 6:59–61
Nitrogen-doped graphene (N-graphene), Vol. 5:80–81
Noncarbon adatoms and substitutional impurities, Vol. 5:25–26

Physisorption on CNTs and graphene, Vol. 5:54–55
adsorption energies, Vol. 5:86–87
debundling of CNTs by physisorption of polymer, Vol. 5:82
gases, Vol. 5:55–66
chemical vapor deposition (CVD) synthesis, Vol. 5:65
on CNTs bundles, Vol. 5:59–62
effects of interactions with nanotubes on IR spectra of small molecules, Vol. 5:59
on graphene, Vol. 5:62–66

HOMO and LUMO orbitals, Vol. 5:65
on individual CNTs, Vol. 5:55–59
mechanism to fix and remove gaseous CO_2 molecules, Vol. 5:64
proposed microscopic mechanism for hydrogen storage, Vol. 5:63
liquids, Vol. 5:66–77
adsorption curves for SWCNTs and MWCNTs, Vol. 5:75
adsorption of water on CNTs and graphene, Vol. 5:68–71
on CNTs and graphene of ions and molecules from Vol. 5:solution, 73–77
of ionic liquids on graphene and CNTs, Vol. 5:71–73
liquid–solid surface interaction, Vol. 5:66
of liquids on doped CNTs and graphene, Vol. 5:77
non-covalent functionalization of PILs, Vol. 5:72
pi-pi interactions and hydrogen bonding between bisphenol A and graphene, Vol. 5:76
resistivities, Vol. 5:70
surface wetting phenomenon, Vol. 5:67
water adsorbed in SWCNTs, Vol. 5:69
"wettability" for solid phase, Vol. 5:66
molecular modeling of ideal stilbenoid dendrimer, Vol. 5:82
of noble gases, Vol. 5:57
solids, Vol. 5:77–83
metals and semiconductors, Vol. 5:77–79
of metals and semiconductors on doped CNTs or graphene, Vol. 5:80–81
polymer adsorption on doped graphene or CNTs, Vol. 5:82–83
of polymers, Vol. 5:81–82
Poly(methyl methacrylate) (PMMA)-mediated transfer approach, Vol. 5:77
Projector Augmented-Wave (PAW) method, Vol. 5:78

Relativistic charge carriers, Vol. 5:14

Single-walled CNTs (SWCNTs), Vol. 5:56, 57, 58, 60, 74–75, 97–98
front and side views of most favorable binding geometries, Vol. 5:89
optimized structures of pristine, Co-doped, Rh-doped, and Ir-doped, Vol. 5:88
Stone–Wales defects, Vol. 5:18, 21, 46
Supercapacitors
graphene-based, Vol. 6:15
applications of, Vol. 6:40–41
graphene/conducting polymer composite supercapacitor, Vol. 6:32–40
metal nanoparticle/oxide-decorated graphene supercapacitor, Vol. 6:25–31
rGO supercapacitor, Vol. 6:16–21
surface-modified graphene supercapacitor, Vol. 6:21–25
graphene-based composites for, Vol. 6:74–75
Surface wetting phenomenon, Vol. 5:67

Synthesis of graphene, Vol. 6:4–6
liquid-phase, Vol. 6:52–53
from expanded graphite, Vol. 6:53–55
from graphite oxide, Vol. 6:56–57

Thermodynamic characteristics of thermal desorption of hydrogen, Vol. 5:220–223
HREELS/LEED data on thermal desorption of hydrogen from hydrogenated graphene on SiC substrate, Vol. 5:239–242
hydrogen desorption in hydrogenated mono- and bilayer epitaxial graphene samples, Vol. 5:230–233
on hydrogen thermal desorption from theoretical and experimental graphanes, Vol. 5:226–228
intercalation of solid H_2 into hydrogenated graphite nanofibers, relevance to the hydrogen on-board storage problem, Vol. 5:250–253
PES and ARPES data on dehydrogenation of graphene/SiC samples, Vol. 5:245–246
Raman spectroscopy data on thermal desorption of hydrogen from hydrogenated graphene flakes, Vol. 5:235–237
Raman spectroscopy data on thermal desorption of hydrogen from hydrogenated graphene layers on SiO_2 substrate, Vol. 5:242–244
STM and STS data on reversible hydrogenation of epitaxial graphene and graphite surfaces, Vol. 5:237–239
TDS and STM data on HOPG treated by deuterium, Vol. 5:244–245
TDS and STM data on HOPG treated by hydrogen, Vol. 5:246–250
on theoretical graphanes (CH), Vol. 5:223
thermodynamic probability of existence of hydrogenated graphenes–graphanes possessing, Vol. 5:228–230
3D graphite crystal, Vol. 5:2
Trilayer graphene, lattice structure of, Vol. 5:43

"Wettability" for solid phase, Vol. 5:66

This page intentionally left blank

World Scientific Series on Carbon Nanoscience

Handbook of Carbon Nano Materials

Volume 6
Graphene — Energy and Sensor Applications

Editors

Francis D'Souza

Karl M. Kadish

World Scientific

Handbook of Carbon Nano Materials

Volume 6

Graphene — Energy and Sensor Applications

This page intentionally left blank

World Scientific Series on Carbon Nanoscience

Handbook of Carbon Nano Materials

Volume 6
Graphene — Energy and Sensor Applications

Editors

Francis D'Souza
University of North Texas, USA

Karl M. Kadish
University of Houston, USA

World Scientific

NEW JERSEY • LONDON • SINGAPORE • BEIJING • SHANGHAI • HONG KONG • TAIPEI • CHENNAI

Published by

World Scientific Publishing Co. Pte. Ltd.
5 Toh Tuck Link, Singapore 596224
USA office: 27 Warren Street, Suite 401-402, Hackensack, NJ 07601
UK office: 57 Shelton Street, Covent Garden, London WC2H 9HE

Library of Congress Control Number: 2012470297

British Library Cataloguing-in-Publication Data
A catalogue record for this book is available from the British Library.

HANDBOOK OF CARBON NANO MATERIALS
(In 2 Volumes)
Volume 6: Graphene — Energy and Sensor Applications

Copyright © 2014 by World Scientific Publishing Co. Pte. Ltd.

All rights reserved. This book, or parts thereof, may not be reproduced in any form or by any means, electronic or mechanical, including photocopying, recording or any information storage and retrieval system now known or to be invented, without written permission from the Publisher.

For photocopying of material in this volume, please pay a copying fee through the Copyright Clearance Center, Inc., 222 Rosewood Drive, Danvers, MA 01923, USA. In this case permission to photocopy is not required from the publisher.

ISBN 978-981-4566-69-8 (Set)
ISBN 978-981-4566-73-5 (Vol. 6)

Typeset by Stallion Press
Email: enquiries@stallionpress.com

Printed in Singapore.

Contents

Preface ix

List of Contributors xi

Chapter 1 Graphene-Based Materials for Energy Storage Applications 1

Tapas Kuila, Partha Khanra, Nam Hoon Kim and Joong Hee Lee

1. Introduction 2
2. Synthesis of Graphene 4
3. Characterization of Graphene 6
   - 3.1. Morphological characterization 6
   - 3.2. Structural characterization 9
4. Application of Graphene 11
5. Graphene-Based Supercapacitor 15
   - 5.1. rGO supercapacitor 16
   - 5.2. Surface-modified graphene supercapacitor 21
   - 5.3. Metal nanoparticle/oxide-decorated graphene supercapacitor 25
   - 5.4. Graphene/conducting polymer composite supercapacitor 32
   - 5.5. Applications of graphene-based supercapacitor 40
     - 5.5.1. Starter for fuel-efficient stop–start systems 40
     - 5.5.2. Public transport 41
     - 5.5.3. Emergency management 41
     - 5.5.4. Other applications 42
6. Conclusions 42

Acknowledgments 43

References 43

Chapter 2 Graphene-Based Nanomaterials for Energy Conversion and Storage 51
Chenzhen Zhang, Nasir Mahmood, Han Yin and Yanglong Hou

1. Introduction 51
2. Liquid-Phase Synthesis of Graphene 52
   2.1. Liquid-phase synthesis from expanded graphite 53
   2.2. Liquid-phase synthesis from graphite oxide 56
3. Nitrogen-Doped Graphene: Synthesis and Applications 57
   3.1. Synthesis of nitrogen-doped graphene 59
   3.2. Applications of nitrogen-doped graphene 61
      3.2.1. Oxygen reduction reaction of fuel cells 61
      3.2.2. Lithium ion batteries 64
4. Graphene-Based Composites: Synthesis and Applications 66
   4.1. Graphene-based composites for oxygen reduction reaction 66
   4.2. Graphene-based composites for lithium ion batteries 68
   4.3. Graphene-based composites for supercapacitors 74
5. Conclusions 75
References 75

Chapter 3 Graphene for Biosensor Applications 83
Alexander Zöpfl, Wendy Patterson and Thomas Hirsch

1. Introduction 83
2. Biosensors for Glucose 87
   2.1. Amperometric glucose biosensors with direct electron transfer 88
   2.2. Amperometric glucose biosensors with detection of H_2O_2 93
   2.3. Mass-sensitive glucose biosensors 101
3. Nucleic Acids 103
4. Proteins 112
   4.1. Cancer biomarkers 113
   4.2. Thrombin 117
   4.3. Amino acids 119
   4.4. Immunoglobulins 122
5. Other Biologically Relevant Analytes 124
6. Conclusions 131
References 133

Chapter 4 Graphene-Based Electrochemical Biosensor 147
Qian Zhang, Ling Zhang, Yang Liu and Jinghong Li

1. Introduction 148
2. Synthesis and Functionalization of Graphene 150
   2.1. Synthesis and characterization of graphene 150
   2.2. Functionalization of graphene 155
3. Electrochemical Properties of Graphene 158
4. Graphene-Based Electrochemical Enzymatic Biosensor 160
   4.1. The introduction of electrochemical enzymatic biosensor 160
   4.2. Organic molecular-modified graphene-based enzymatic biosensor 163
   4.3. Polymer-modified graphene-based enzymatic biosensor 166
   4.4. Inorganic nanoparticles-modified graphene-based enzymatic biosensor 171
   4.5. Biomolecular-modified graphene-based enzymatic biosensor 174
   4.6. Graphene–carbon nanotube-based enzymatic biosensor 176
   4.7. N-doped graphene-based enzymatic biosensor 178
5. Graphene-Based DNA Biosensor 179
6. Conclusions and Perspectives 181

Acknowledgments 182
References 182

Chapter 5 Graphene and Carbon Nanotube-Based Nanomaterial: Application in Biomedical and Energy Research 189
Hemant Kumar, Debabrata Pramanik, Santosh Mogurampelly, V. Vasumathi, Bidisha Nandy and Prabal K. Maiti

1. Introduction 190
2. Graphene–Nucleic Acid Composites 192
   2.1. Functionalization of graphene 192
   2.2. Adsorption of nucleic acids on graphene 193
   2.3. Biocompatibility of graphene 197
3. DNA–Carbon Nanotube Composite 197
   3.1. Structure and properties 198
   3.2. Influence of temperature on oligonucleotide adsorption 200
   3.3. Applications 202
      3.3.1. Solubilization and sorting of carbon nanotube 202
      3.3.2. DNA–CNT hybrid in sensing mechanism 202
      3.3.3. Supercapacitors 204
      3.3.4. Cellular delivery of DNA strands 204

4. Carbon Nanotube and Dendrimer Composite 206
4.1. Covalent functionalization 207
4.1.1. "Grafting to" approach 207
4.1.2. "Grafting from" approach 209
4.2. Non-covalent functionalization 211
5. Carbon Nanomaterials for Energy Conversion 213
5.1. Hydrogen storage 213
5.1.1. Historical development 216
5.1.2. Improving hydrogen storage by chemical functionalization 217
5.2. Blue energy 218
5.3. Voltage generation through flow 220
5.4. Energy-efficient nanoelectrical devices 222
5.4.1. Carbon nanotube-based FETs 223
5.4.2. Nanotubes and graphene as interconnectors 225
5.4.3. Flexible electronics: Thin film transistor 226
5.4.4. Photovoltaic devices 226
6. Conclusions and Outlook 227
Acknowledgments 229
References 229

Cumulative Index of Volumes 5 and 6 237

Preface

We are pleased to present the third two-volume set of *The Handbook of Carbon Nanomaterials*. What started out to be a one-time publication of a "*Handbook*" set to mark the 25th anniversary of the discovery of Fullerenes in 2011, now appears to be a successful publication series. This is primarily due to the multiple new discoveries which continue to be published on the basic properties and applications of fullerenes, carbon nanotubes and graphene materials.

The first published set of volumes in the *Handbook of Carbon Nanomaterials* comprised 23 chapters in two volumes which summarized research developments in the field of carbon nanomaterials as seen through the eyes of more than three dozen leading researchers from around the world. The topics covered four general areas. The first part of the book dealt with the chemistry of fullerenes and carbon nanotubes, including organic functionalization, reactivity, perfluoroalkylation, and fullerenes linked to photosensitizers. The second part covered the chemistry and physics of endohedral fullerenes. The third part of the book covered the molecular and supramolecular chemistry of fullerenes and carbon nanotubes while the fourth described topics related to photoinduced energy and electron transfer. Finally, applications of fullerenes, carbon nanotubes and graphenes as applied to organic molecular electronics, polymers composites, thermal conductive materials, photovoltaics and sensing were presented.

The second published set of volumes in the *Handbook of Carbon Nanomaterials* (Volumes 3 and 4) contained material from leading authors on medicinal and bio-related applications and on topics ranging from materials to fundamental applications. Specific topics covered in Volume 3 were fullerenes in biology and medicine, the current state of the art of toxicity studies of fullerenes and carbon nanotubes, methods of detection of carbon nanotubes in living cells, carbon nanotechnology in regenerative medicine, chemical and biochemical sensors based on carbon nanotubes, molecular recognition

approach for separating left- and right-handed structures of single wall carbon nanotubes and open cage fullerene. The specific topics covered in Volume 4 were functionalization of graphene, electrochemical conversion and storage of energy, nanocarbon based molecular architectures for light energy conversion, electrochemistry of fullerenes as applicable for functional devices, fullerenes as self-assembled morphological materials, semiconductor carbon nanotube optics, near-filed optics of nanotubes and energy transfer at the nanoscale level, understanding the role of metal catalysts in chiral selective growth of carbon nanotubes, and finally, computational studies on the stability of fullerenes and metallofullerenes.

The current two volume set (Volumes 5 and 6) is dedicated in large part to recent discoveries on graphene. There are nine chapters in this set; the first four chapters (Volume 5) summarize the basic science of graphene. Specific topics include fundamental properties of graphene, adsorption and reactivity of graphene, chemical manipulation of graphene in dispersions, and thermodynamic characterization of thermal desorption of hydrogen from hydrogenated graphene layers. The next five chapters (Volume 6) provide an up-to-date summary of energy and sensor applications of graphene. The topics covered in this volume include graphene materials for energy conversion and storage applications, graphene for biosensor and electrochemical biosensor applications, and finally, carbon nanomaterials in biomedical and energy research.

Like the previous four volumes, the current two-volume set of the Handbook has been written as a hands-on reference guide for scientists working in the fields of biology, medicine, chemistry, physics, materials science, solid-state physics and nanotechnology. The coverage of topics presented is both in-depth and comprehensive. When combined with the perspectives for future research given by the contributing authors, this series makes an invaluable reference source that should be considered essential reading for both students and advanced researchers in the field.

The editors would like to acknowledge the contributors for their timely submission of the state-of-the-art reviews. Last, but not least, the staff of World Scientific Publishing Co. is acknowledged for their immense help in bringing out this publication in a timely manner.

Francis D'Souza
Denton, TX, USA

Karl M. Kadish
Houston, TX, USA
August 7, 2013

List of Contributors

M. Rosa Axet
Laboratoire de Chimie de Coordination
UPR CNRS 8241
Composante ENSIACET
Université de Toulouse
UPS/INP/LCC
4 allée Emile Monso, BP 44362
31432 Toulouse Cedex 4, France
Chapter 2 (Vol. 5)

Revathi R. Bacsa
Laboratoire de Chimie de Coordination
UPR CNRS 8241
Composante ENSIACET
Université de Toulouse
UPS/INP/LCC
4 allée Emile Monso, BP 44362
31432 Toulouse Cedex 4, France
Chapter 2 (Vol. 5)

Thomas Hirsch
Institute of Analytical Chemistry, Chemo- and Biosensors
University of Regensburg
93053 Regensburg, Germany
thomas.hirsch@ur.de
Chapter 3 (Vol. 6)

Yanglong Hou
Department of Materials Science and Engineering
College of Engineering
Peking University
Beijing 100871, China
hou@pku.edu.cn
Chapter 2 (Vol. 6)

Partha Khanra
Advanced Wind Power System Research Center
Department of BIN Fusion Technology
Chonbuk National University
Jeonju, Jeonbuk 561-756, Korea
Chapter 1 (Vol. 6)

Nam Hoon Kim
Advanced Wind Power System Research Center
Department of BIN Fusion Technology
Chonbuk National University
Jeonju, Jeonbuk 561-756, Korea
Chapter 1 (Vol. 6)

Tapas Kuila
Surface Engineering and Tribology Division
CSIR-Central Mechanical Engineering Research Institute
Council of Scientific and Industrial Research (CSIR)
Mahatma Gandhi Avenue
Durgapur — 713209, India
Chapter 1 (Vol. 6)

Hemant Kumar
Centre for Condensed Matter Theory
Department of Physics
Indian Institute of Science
Bangalore 560012, India
Chapter 5 (Vol. 6)

Joong Hee Lee
Advanced Wind Power System Research Center
Department of BIN Fusion Technology
and Department of Polymer and Nano Science and Technology
Chonbuk National University
Jeonju, Jeonbuk 561-756, Korea
jhl@chonbuk.ac.kr
Chapter 1 (Vol. 6)

Jerzy Leszczynski
Interdisciplinary Center for Nanotoxicity
Department of Chemistry and Biochemistry
Jackson State University
Jackson, MS 39217, USA
jerzy@icnanotox.org
Chapter 1 (Vol. 5)

Jinghong Li
Department of Chemistry
Beijing Key Laboratory for Analytical Methods and Instrumentation
Tsinghua University
Beijing 100084, China
jhli@mail.tsinghua.edu.cn
Chapter 4 (Vol. 6)

Yang Liu
Department of Chemistry
Beijing Key Laboratory for Analytical Methods and Instrumentation
Tsinghua University
Beijing 100084, China
Chapter 4 (Vol. 6)

Bruno F. Machado
Laboratoire de Chimie de Coordination
UPR CNRS 8241
Composante ENSIACET
Université de Toulouse
UPS/INP/LCC
4 allée Emile Monso, BP 44362
31432 Toulouse Cedex 4, France
Chapter 2 (Vol. 5)

Nasir Mahmood
Department of Materials Science and Engineering
College of Engineering
Peking University
Beijing 100871, China
Chapter 2 (Vol. 6)

Prabal K. Maiti
Centre for Condensed Matter Theory
Department of Physics
Indian Institute of Science
Bangalore 560012, India
maiti@physics.iisc.ernet.in
Chapter 5 (Vol. 6)

Santosh Mogurampelly
Centre for Condensed Matter Theory
Department of Physics
Indian Institute of Science
Bangalore 560012, India
Present address: Department of Physics, University of Rome "La Sapienza", Ple A. Moro 2, 00185, Rome, Italy.
Chapter 5 (Vol. 6)

Bidisha Nandy
Centre for Condensed Matter Theory
Department of Physics
Indian Institute of Science
Bangalore 560012, India
Chapter 5 (Vol. 6)

Yury S. Nechaev
Bardin Institute for Ferrous Metallurgy
Kurdjumov Institute of Metals Science and Physics
Vtoraya Baumanskaya St., 9/23
Moscow 105005, Russia
Yuri1939@inbox.ru
Chapter 4 (Vol. 5)

Wendy Patterson
Institute of Analytical Chemistry, Chemo- and Biosensors
University of Regensburg
93053 Regensburg, Germany
Chapter 3 (Vol. 6)

Henry P. Pinto
Interdisciplinary Center for Nanotoxicity
Department of Chemistry and Biochemistry
Jackson State University
Jackson, MS 39217, USA
Chapter 1 (Vol. 5)

Debabrata Pramanik
Centre for Condensed Matter Theory
Department of Physics
Indian Institute of Science
Bangalore 560012, India
Chapter 5 (Vol. 6)

Mildred Quintana
Instituto de Física
Universidad Autónoma de San Luis Potosí
77290 SLP, México
mildred@ifisica.uaslp.mx
Chapter 3 (Vol. 5)

Philippe Serp
Laboratoire de Chimie de Coordination
UPR CNRS 8241
Composante ENSIACET
Université de Toulouse
UPS/INP/LCC

4 allée Emile Monso, BP 44362
31432 Toulouse Cedex 4, France
philippe.serp@ensiacet.fr
Chapter 2 (Vol. 5)

Jesús Iván Tapia
Instituto de Física
Universidad Autónoma de San Luis Potosí
77290 SLP, México
Chapter 3 (Vol. 5)

V. Vasumathi
REQUIMTE, Department of Chemistry
University of Porto
Rua do Campo Alegre 687
4168–007 Porto, Portugal
Chapter 5 (Vol. 6)

T. Nejat Veziroglu
International Association for Hydrogen Energy
5794 SW 40 St. # 303
Miami, FL 33155, USA
Chapter 4 (Vol. 5)

Han Yin
Department of Materials Science and Engineering
College of Engineering
Peking University
Beijing 100871, China
Chapter 2 (Vol. 6)

Chenzhen Zhang
Department of Materials Science and Engineering
College of Engineering
Peking University
Beijing 100871, China
Chapter 2 (Vol. 6)

Ling Zhang
College of Chemistry and Life Science
Shenyang Normal University
Shenyang 110034, China
Chapter 4 (Vol. 6)

Qian Zhang
College of Chemistry
Liaoning University
Shenyang 110036, China
Chapter 4 (Vol. 6)

Alexander Zöpfl
Institute of Analytical Chemistry, Chemo- and Biosensors
University of Regensburg
93053 Regensburg, Germany
Chapter 3 (Vol. 6)

Contents of Volumes 5 and 6

Volume 5 Graphene — Fundamental Properties

1. Fundamental Properties of Graphene
   Henry P. Pinto and Jerzy Leszczynski
2. Adsorption on and Reactivity of Carbon Nanotubes and Graphene
   M. Rosa Axet, Revathi R. Bacsa, Bruno F. Machado and Philippe Serp
3. Chemical Manipulation of Graphene in Dispersions
   Jesús Iván Tapia and Mildred Quintana
4. On Thermodynamic Characteristics of the Thermal Desorption of Hydrogen from Hydrogenated Graphene Layers
   Yury S. Nechaev and T. Nejat Veziroglu

Volume 6 Graphene — Energy and Sensor Applications

1. Graphene-Based Materials for Energy Storage Applications
   Tapas Kuila, Partha Khanra, Nam Hoon Kim and Joong Hee Lee
2. Graphene-Based Nanomaterials for Energy Conversion and Storage
   Chenzhen Zhang, Nasir Mahmood, Han Yin and Yanglong Hou
3. Graphene for Biosensor Applications
   Alexander Zöpfl, Wendy Patterson and Thomas Hirsch
4. Graphene-Based Electrochemical Biosensor
   Qian Zhang, Ling Zhang, Yang Liu and Jinghong Li
5. Graphene and Carbon Nanotube-Based Nanomaterial: Application in Biomedical and Energy Research
   Hemant Kumar, Debabrata Pramanik, Santosh Mogurampelly, V. Vasumathi, Bidisha Nandy and Prabal K. Maiti

This page intentionally left blank

Chapter 1

Graphene-Based Materials for Energy Storage Applications

Tapas Kuila, Partha Khanra†, Nam Hoon Kim† and Joong Hee Lee†,‡,§*

**Surface Engineering and Tribology Division*
CSIR-Central Mechanical Engineering Research Institute
Council of Scientific and Industrial Research (CSIR)
Mahatma Gandhi Avenue, Durgapur — 713209, India

†Advanced Wind Power System Research Center
Department of BIN Fusion Technology

‡Department of Polymer and Nano Science and Technology
Chonbuk National University, Jeonju, Jeonbuk 561–756, Korea

1. Introduction 2
2. Synthesis of Graphene 4
3. Characterization of Graphene 6
   3.1. Morphological characterization 6
   3.2. Structural characterization 9
4. Application of Graphene 11
5. Graphene-Based Supercapacitor 15
   5.1. rGO supercapacitor 16
   5.2. Surface-modified graphene supercapacitor 21
   5.3. Metal nanoparticle/oxide-decorated graphene supercapacitor 25
   5.4. Graphene/conducting polymer composite supercapacitor 32
   5.5. Applications of graphene-based supercapacitor 40
      5.5.1. Starter for fuel-efficient stop–start systems 40
      5.5.2. Public transport 41

§ Corresponding author. E-mail: jhl@chonbuk.ac.kr

5.5.3. Emergency management 41
5.5.4. Other applications 42
6. Conclusions 42
Acknowledgments 43
References 43

1. Introduction

The development of new materials for energy storage devices, such as batteries, capacitors, and supercapacitors, is growing rapidly in response to the demand for new power sources due to the continuous depletion of fossil fuels.[1–14] The most commonly used energy resources, such as oil, coal, and nuclear fuel, cannot be recovered after consumption. In order to preserve the limited energy supply, the development and storage of renewable energy have attracted significant attention. Ongoing research on energy storage materials has shown that supercapacitors can serve as portable energy sources and advanced energy storage solutions for applications in renewable energy, smart grids, biomass and urban lifestyle devices, and in the consumer care industries.[1–3,14] In comparison to conventional lead acid or alkaline batteries, supercapacitors have smaller size, more flexible packaging, lighter weight, longer life, higher power capability, wide thermal operating range, and more efficiency.[1] A supercapacitor can store electrical energy by forming a double layer of electrolyte ions on the surface of conductive electrodes. The specific capacitance that arises due to this ion adsorption is called electrical double-layer capacitance (EDLC). In addition to EDLC, supercapacitor may also store energy by battery-type oxidation–reduction reactions, which lead to pseudocapacitive behavior.[1–3,14,15] Supercapacitor can be used in memory backup devices, space equipment, electric vehicles, military weapons, and in various electronic equipment used in daily life.[16–18] It can be operated at very high charge and discharge rates, with lifetimes exceeding millions of cycles, in contrast to conventional capacitors or batteries. However, the energy stored in the supercapacitor is still lower than that of batteries, which limits its application. Generally, porous carbon materials such as activated carbon, mesoporous carbon, carbon aerogels, and carbon nanotubes (CNTs) have been used as electrode materials in supercapacitor devices.[19–23] It has been found that the energy density of supercapacitor devices using porous carbon materials is about 4–5 watt-hours per kg (Wh kg^{-1}). However, the energy density of lead acid batteries is in the range of 26–34 Wh kg^{-1}.[1] Therefore, much attention has been paid to the development of supercapacitor electrode materials with high power density, without sacrificing cycle life or power density.

Graphene, a monolayer of carbon atoms tightly packed into a two-dimensional (2D) honeycomb lattice, has attracted significant attention due to its unique electrical conductivity, large surface area, and electrochemical stability.[24–33] Because of its unique features, graphene has been used extensively as a material for supercapacitor electrodes. However, the volume production of graphene for the commercialization of graphene-based energy storage devices has not been reported. There are several methods for the laboratory-scale production of graphene, such as the micromechanical exfoliation of highly oriented pyrolytic graphite, epitaxial growth on electrically insulating surfaces, thermal expansion, chemical vapor deposition (CVD), and chemical oxidation — reduction method.[34–45] Among such techniques, the liquid-phase production of graphene from graphene oxide (GO) is the most promising. However, the graphene produced during the reduction of GO agglomerates together to form three-dimensional (3D) graphitic structure. Moreover, the chemical reduction of GO involves toxic reducing agents that are harmful to human health and the environment.[44,46] In order to overcome these problems, the surface modification of GO is carried out prior to reduction.[43,47] The presence of a surface modifier on graphene prevents agglomeration, and the monolayer structure of graphene is preserved.[47] Various naturally occurring reducing agents have been used for the reduction of GO, such as D-sugar, carrot, ascorbic acid, green tea solution, baker's yeast, protein, dextran, bacterial respiration, and glycine.[46] Electrochemical and thermal reduction are also very effective methods to obtain graphene sheets from GO.[46] It has been found that pristine graphene is hydrophobic in nature, and is thus unsuitable for application to electrochemical supercapacitors. The presence of remaining oxygen functionalities of GO after reduction or the hydrophilic groups of the modifier play an important role for the enhancement of specific capacitance.[46] The oxygen functionalities and other functional groups take part in the redox reaction and directly enhance the specific capacitance of the electrode materials by contributing pseudocapacitance.[15] The specific capacitance of graphene-based materials can be increased by enhancing the pseudocapacitance. Different transition metal oxides such as RuO_2, NiO, MnO_2, MoO_3, Co_3O_4, and SnO_2 are being studied as candidate materials for pseudocapacitor electrodes.[48–54] However, the metal oxides deliver low power density and poor rate capability due to poor electronic conductivity. In order to obtain high-performance supercapacitors, it is important to develop graphene/metal oxide composite materials with high specific capacitance and power density.[55–57] Similarly, conducting polymers show substantially high values of specific capacitance owing to their large pseudocapacitance.[57–60] Therefore, many attempts have been made to

prepare composite materials based on graphene and conducting polymers to achieve electrode materials with high capacitance and improved stability.

The recent strategies for the synthesis of single-layer graphene, its identifications by different characterization techniques, and possible applications have been highlighted. The application of graphene-based materials as energy storage materials for the fabrication of supercapacitor devices has been discussed in detail. Different kinds of graphene-based materials such as reduced graphene oxide (rGO), metal oxide or metal nanoparticle/rGO composites, conducting polymer/rGO composites, and graphene/CNT hybrid have been used extensively for the fabrication of supercapacitor electrode materials.[55–57,61–65] The morphological and structural configurations of the rGO and its composites with metal oxides or conducting polymers has been confirmed by X-ray diffraction (XRD), atomic force microscopy (AFM), transmission electron microscopy (TEM), field emission scanning electron microscopy (FESEM), Fourier transform infrared (FTIR) spectroscopy, Raman spectroscopy, X-ray photoelectron spectroscopy (XPS), etc.

2. Synthesis of Graphene

Important properties such as high electrical conductivity, excellent mechanical flexibility, good electrochemical stability, and large surface area are associated with monolayer graphene. Therefore, volume production of single-layer graphene has attracted significant interest. There are several methods for the preparation of single-layer graphene. Li *et al.* prepared large-area graphene films on the order of centimeters on copper substrates by CVD using methane gas as a carbon source.[66] Bae *et al.* prepared 30-inch monolayer graphene films for use in transparent electrodes by CVD on Cu substrate.[67] Graphene was also prepared from polymer by CVD.[38] A few layers of graphene have been grown on the surface of SiO_2/Si. Polystyrene, polyacrylonitrile, and polymethylmethacrylate (PMMA) have been used as carbon sources. This study shows that the growth of graphene occurs by the pyrolysis of polymer at 1000°C for 1 min under a 50-nm-thick Ni capping layer. Graphene has been synthesized by CVD from PMMA and polystyrene at temperatures as low as 400°C. When benzene was used as the hydrocarbon source, monolayer graphene flakes with excellent quality were achieved at a growth temperature as low as 300°C. Guermoune *et al.* prepared large-area and high-quality graphene by CVD using liquid alcohol as the precursor of graphene.[68] Alcohol vapor exposure times of 5 min and an average growth temperature of 850°C yielded continuous graphene monolayer films, as inferred from Raman spectroscopy. Graphene grown on copper (Cu) substrate by CVD can

be separated and transferred to an arbitrary substrate. At first, the graphene film deposited on the Cu substrate is finely coated with a thin layer of PMMA, followed by the dissolution of the Cu substrate using 0.1 M ammonium persulfate (APS) solution. The PMMA-coated graphene then floats on the surface of the solution. The PMMA/graphene film is then rinsed with distilled water several times to remove the etchant residue. After proper washing with distilled water, the film can be transferred onto a desired substrate under floating conditions. Bilayer graphene was directly grown on SiO_2 substrates by CVD with the decomposition of the carbon source on the top of a nickel catalyst at 1000 °C.[41] After cooling down to room temperature, the bilayer graphene was formed between the nickel layer and the SiO_2 substrates. Liu *et al.* synthesized graphene by the thermal decomposition of 6H-SiC (000–1) in a vacuum chamber.[69] The micromechanical exfoliation of graphite produces high-quality graphene and with very good electronic properties. However, this method is not suitable for the volume production of graphene. Sonochemical preparation is an alternate method for the production of defect-free large-area graphene. Hao *et al.* prepared functionalized graphene directly from graphite and 7,7,8,8-tetracyanoquinodimethane (TCNQ).[70] Similarly, the continuous sonication of graphite mixed with different surfactants (sodium dodecyl benzene sulfonate (SDBS) and sodium cholate) can also produce functionalized graphene. It has been found that more than 40% of the graphene has a thickness of less than 3.5 nm, and ~3% of it is monolayer graphene. An *et al.* separated a single layer of graphene by the "molecular wedging" of 1-pyrenecarboxylic acid into the interlayer spacing of graphite, followed by exfoliation under ultrasonic conditions.[71] Bose *et al.* achieved monolayer graphene by the sonication of graphite and 9-anthralene carboxylic acid (9-ACA) in aqueous ethanol. However, the yield for the monolayer graphene production in this technique is very low (~4–5%). One-step electrochemical exfoliation of graphite to graphene is very useful in this respect.[72] Liu *et al.* reported one-step electrochemical exfoliation in the presence of ionic liquid electrolyte.[73] Ionic liquid played the role of a surface modifier, and the graphene prepared by this route was dispersed in a range of organic solvents. Khanra *et al.* synthesized a single layer of graphene by the one-step electrochemical exfoliation of graphite using 9-ACA as a surface modifier and electrolyte.[33] Similarly, sodium polystyrene sulfonate (PSS) and SDBS can also be used for the electrochemical synthesis of graphene.

The most successful approach for the synthesis of graphene is the chemical oxidation of graphite to graphite oxide, followed by the conversion of graphite oxide to single-layer GO, and then the reduction of GO to graphene sheets.[15,43,44] The chemical oxidation of graphite can be performed by the

modified Hummer's method, Staudenmaier method, or by using Jone's reagent or peroxides. High-quality potassium permanganate and concentrated sulfuric acid are used in modified Hummer's method, while Staudenmaier's method involves potassium chlorate, sulfuric acid, and nitric acid. Chromic acid is known as Jone's reagent, and can be prepared *in situ* by the reaction of potassium dichromate and sulfuric acid. The oxidized product of graphite is sonicated to obtain GO, which can be reduced to obtain graphene sheet. However, the reduction of GO produces an agglomerated structure of graphene sheets resulting in the loss of the superior properties of graphene. Moreover, the use of toxic reducing chemicals should be minimized for the benefit of human health and the environment. In order to prevent the agglomeration of graphene, the surface modification of graphene is crucial to maintain the superior features. This can be done by covalent and non-covalent surface modification techniques.[47] In order to overcome the toxicity problem, several kinds of green reducing agents and techniques have been used.[46] However, discussion about the detailed procedures for the surface modification of graphene and green reducing agents is beyond the scope of the present study, which highlights the energy storage applications of graphene.

3. Characterization of Graphene

The synthesis and characterization of single-layer graphene from graphite or multilayer graphene have attracted great interest due to the extraordinary physicochemical properties that can be obtained. There are several techniques for the identification of graphene, which can be broadly divided into two categories: morphological characterization and structural characterization.

3.1. Morphological characterization

The morphological characterization of graphene can be performed using AFM, TEM, and FESEM. The thickness of single-layer graphene has been reported to be 0.34–1.2 nm, and the determination of these thicknesses is very important. AFM is the only tool available to examine the thickness of graphene. The presence of surface modifier on the surface of graphene can easily be seen in 3D images of graphene sheet, as reported by Bose *et al.* for PSS-modified graphene (Figure 1).[74] A higher thickness observed (2 nm) was attributed to the adsorption of the PSS on the graphene. In contrast, the average thickness of hydrazine-reduced GO is only 0.8 nm, which suggests the formation of single-layer graphene.

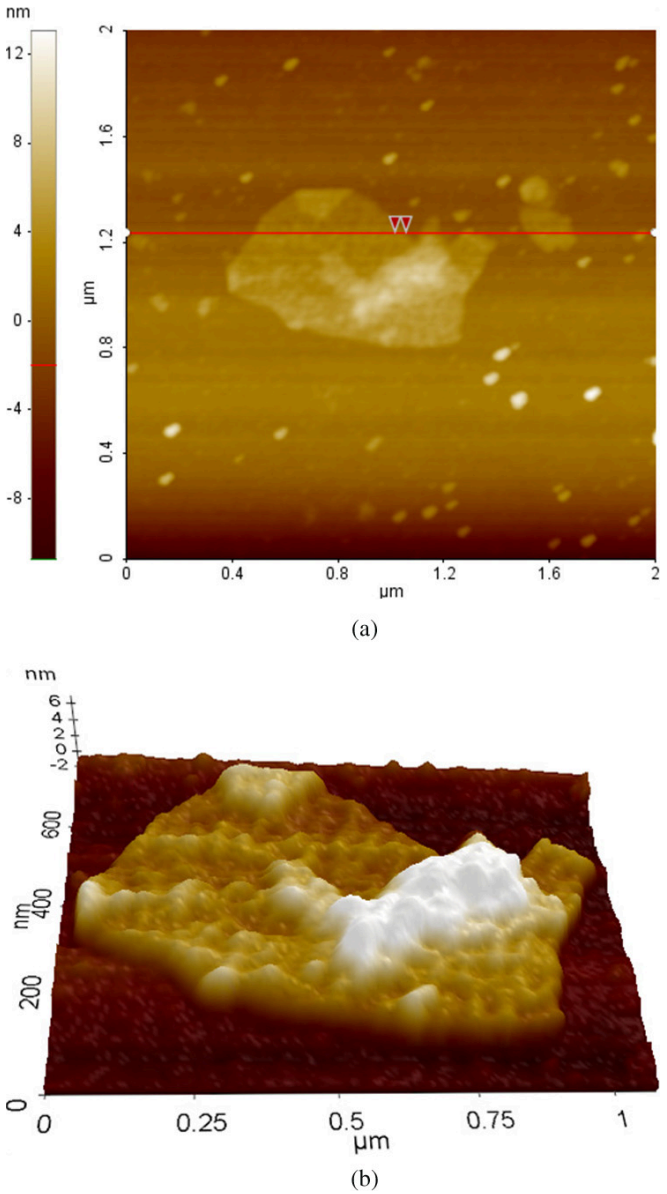

Figure 1. (a) Non-contact-mode AFM image of graphene nanosheets (GNS) on SiO_2 substrate from an aqueous dispersion and (b) 3D representation of AFM image showing the adsorption of polymer over GNS. Reproduced from Ref. 74 with permission.

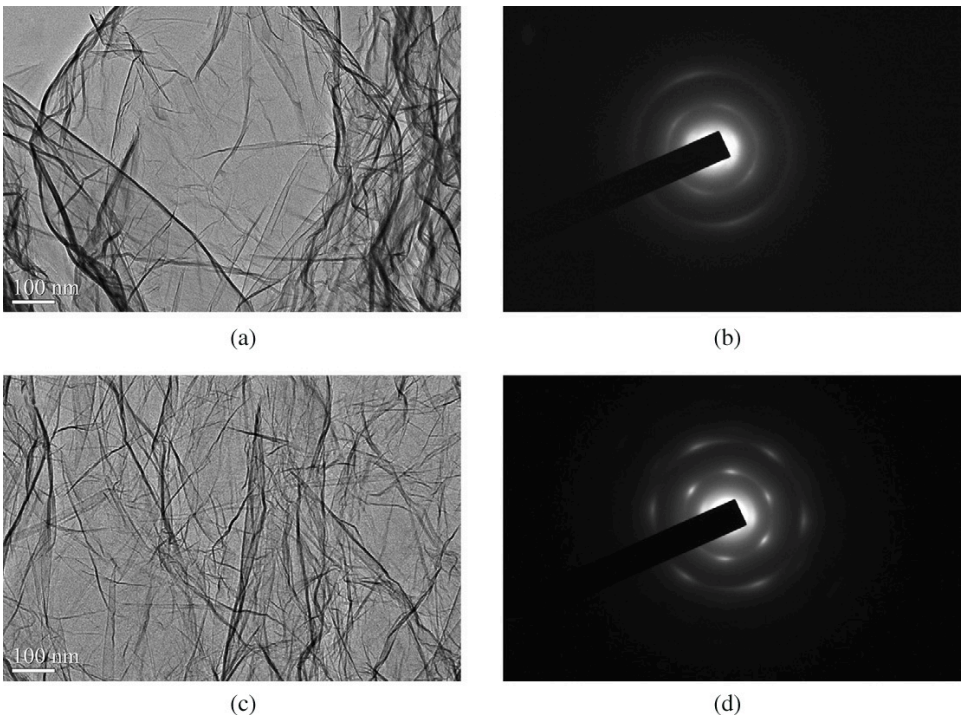

Figure 2. TEM images of FGS300 (a) and FGS300-700 (c); SAED images of FGS300 (b) and FGS300-700 (d). Reproduced from Ref. 75 with permission.

TEM and high-resolution TEM (HR-TEM) are very helpful for the identification of transparent graphene sheets with wrinkles, and the detection of number of layers. Typical waving and curving structures of graphene are shown in Figures 2a and 2c.[75] The corrugation and scrolling of graphene sheets arise due to the thermodynamic stability of the 2D membrane resulting from microscopic crumpling via bending or buckling. Jin *et al.* investigated the differences in microstructure between graphite and graphene. It was observed that the sheets of graphite are darker, thicker, and larger compared to graphene sheets, as shown in Figures 3a and 3b.[76] HR-TEM images provide useful information about the number of layers in graphene sheets. The edges of the suspended graphene films always tend to fold back, allowing for a cross-sectional view of the graphene sheets. The folding of one or two layers at the edges of the sheets appear as one or two dark lines, respectively. The appearance of few dark lines in the graphene sheets clearly suggests the formation of a few-layer graphene. Small-angle electron diffraction (SAED) pattern analysis suggests the formation of crystalline graphene sheets. A sixfold

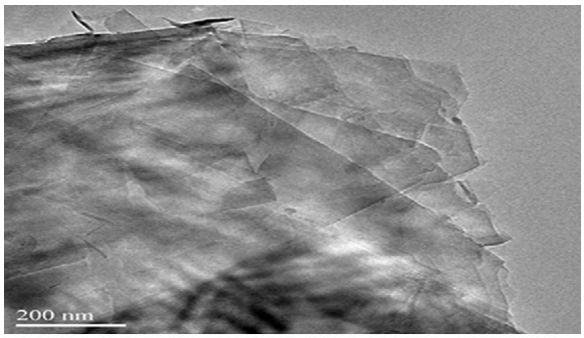

(a)

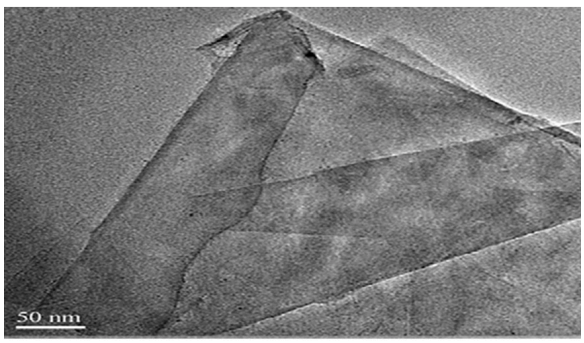

(b)

Figure 3. (a, b) HR-TEM images of graphite. Reproduced from Ref. 76 with permission.

hexagonal symmetry in the SAED pattern is formed for crystalline graphene, as shown in Figure 2b and 2d. The appearance of an unresolved spot in the SAED pattern may be an indication of the presence of organic molecules on the surface of graphene sheets. Mesoporous structure with pores can be examined by FESEM image analysis. Zhang and Shi have shown that the unique 3D morphology effectively prevents restacking of the graphene sheets, which provides great promise in the preparation of self-supported and binder-free graphene-based EDLC electrodes.[77]

3.2. Structural characterization

The structural characterization of graphene is very important to detect the presence of functional groups on its surfaces. The presence of hydrophilic functional groups directly takes part in the oxidation–reduction reaction during the electrochemical tests showing pseudocapacitance behavior. The

oxygen functional groups of graphene can be determined by FTIR and XPS.[43,44] Similarly, the defect contents in graphene also influence the specific capacitance behavior of graphene. The main oxygen functional groups present on the surface of graphene are hydroxyl (–OH), carboxyl (–COOH), epoxy, and alkoxy. Peaks corresponding to –OH stretching and bending vibration appear in the FTIR spectrum at ~3400 and 1400 cm^{-1}, respectively. The presence or absence of –COOH functionalities can be confirmed by the appearance or disappearance of a peak at ~1725 cm^{-1}.[43,44] The presence of epoxy and alkoxy functional groups in GO is made evident by the appearance of two peaks at 1231 and 1051 cm^{-1}. Similarly, the chemical functionalization of graphene can be confirmed by the appearance of new peaks that are not related to GO or graphene.

XPS is very helpful to analyze the chemical composition of graphene or graphene-based composites. The deconvoluted XPS of graphene in the C1s and O1s region confirm the presence of oxygen-containing functional groups. Different types of functional groups can be detected by the following C1s spectra: C–C/C=C (284.2 eV), C–O (286.1 eV), C=O (288.1 eV), and O–C=O (289.7 eV).[43,44] The presence of nitrogen in graphene is confirmed by N1s spectra at ~400 eV. Sulfur-containing functional groups are detected by S2p spectra in the region of 167–168 eV. XPS elemental analysis provide exact information about the chemical composition in graphene or graphene-based materials by the subtraction of the Shirley background followed by curve fitting of the substrate contribution. The C/O atomic ratios of GO have been reported to be 2.2, whereas for rGO, it may vary between 6 and 33.[44,46]

Raman scattering is highly sensitive to the electronic structure of graphene and graphene-based materials. It can provide useful information about the defect concentration and restoration of chemical composition in graphene. Bulk graphite shows the two most intense peaks, one at 1575 cm^{-1} (G peak) and another at ~2880 cm^{-1}, historically designated as the G′ peak, since it is the most significant peak and always appears in graphite samples.[78,79] The G band originates from the in-plane vibration of aromatic carbons and is attributed to the doubly degenerated (E_{2g}) phonon mode symmetry. In contrast, chemically derived graphene shows three peaks at 1352 (D), 1572 (G), and 2692 (2D) cm^{-1}. This is attributed to the creation of defects in graphene compared to raw graphite. Interestingly, the peak width of the G-band may increase by 2–3 cm^{-1} in graphene compared to raw graphite. However, the nature and number of bands for CVD-grown graphene may be similar to that of graphite. This is attributed to the very low defect content in CVD-grown graphene. The intensity ratios of the D band

to the G band (I_D/I_G) are very informative in determining surface defects of chemically functionalized graphene. I_D/I_G ratios greater than unity indicate the creation of sp^3 defects within the sp^2 network structure of graphene. For graphite and CVD-grown graphene, this ratio is much lower than unity. However, for chemically derived graphene, it may be ≥1. The most important band in Raman spectra is the 2D band, which is very useful for the determination of the number of layers in graphene. Monolayer graphene shows a single sharp 2D peak, and bilayer graphene shows a much broader and upshifted 2D band. The 2D band of graphite consists of two peaks. The G band intensity of monolayer graphene is lower than that of bi-, tri-, or multilayer graphene. The intensity of the G-band increases linearly with increasing number of layers, as shown in Figure 4.[80]

4. Application of Graphene

Graphene has attracted significant interest in the areas of polymer composites, drug delivery, biosensors, nanoelectronics, transistors, supercapacitors, Li-ion batteries, and H_2 storage. Graphene can convert an insulating polymer into an electrically conductive composite. The electrical conductivity of phenyl isocyanate-modified graphene-filled polystyrene composites was increased by a factor of 10^{12} compared to that of polystyrene composites filled with non-reduced GO. The chemically converted graphene/polystyrene composites prepared by solution blending followed by compression molding exhibited a percolation threshold of 0.19 vol.% and an electrical conductivity of 72.18 S m^{-1} at only ~2.45 vol.%.[81] The *in situ* polymerized and reduced polystyrene/graphene (2 wt.%) composites had an electrical conductivity of 2.9×10^{-2} S m^{-1}.[75] Bose *et al.* demonstrated that the electrical conductivity of polypyrrole (PPy)/rGO composites is much higher than that of PPy/GO composites.[82] However, the electrical conductivity of polyaniline/GO composites (σ = 231.2 S m^{-1}) was slightly lower than that of polyaniline/rGO (σ = 168.7 S m^{-1}), probably due to a decrease in the extent of doping of Polyaniline (PANi) and morphological changes of the composites during the reduction, reoxidation, and reprotonation processes.[83]

rGO acts as an "electron wire" between the active sites of biomolecules and glass carbon electrodes. The presence of defect sites in rGO increases its interactions with biomolecules to an extent comparable to that of CVD-grown graphene. Graphene-based biosensors and devices have been shown to exhibit good sensitivity and selectivity for the detection of glucose, cholesterol, hemoglobin, hydrogen peroxide, small biomolecules, DNA, heavy metal ions, and poisonous gaseous molecules.[84]

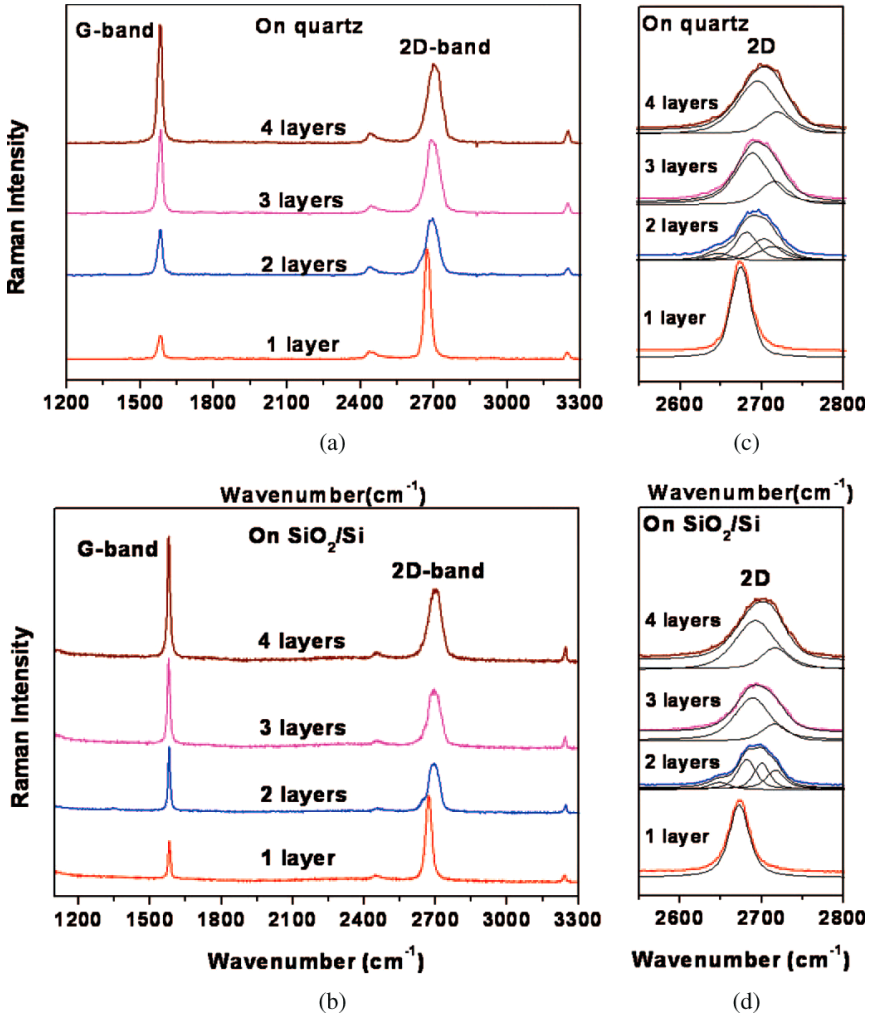

Figure 4. The Raman spectra of monolayer, bilayer, three-layer, and four-layer graphene on quartz (a) and SiO_2 (300 nm)/Si substrate (b). The enlarged 2D band regions with curve fit are also shown in panels (c) and (d). Reproduced from Ref. 80 with permission.

The aim of nanoelectronics is to process, transmit, and store information by taking advantage of the nanoproperties of materials, which are distinctly different from the macroscopic properties of materials. The absence of a band gap in graphene makes it an attractive material for use in semiconductor technology, field-effect transistor devices, transparent electrode materials, optoelectronic materials, and supercapacitor devices.[6,11–13,85–87] Flexible,

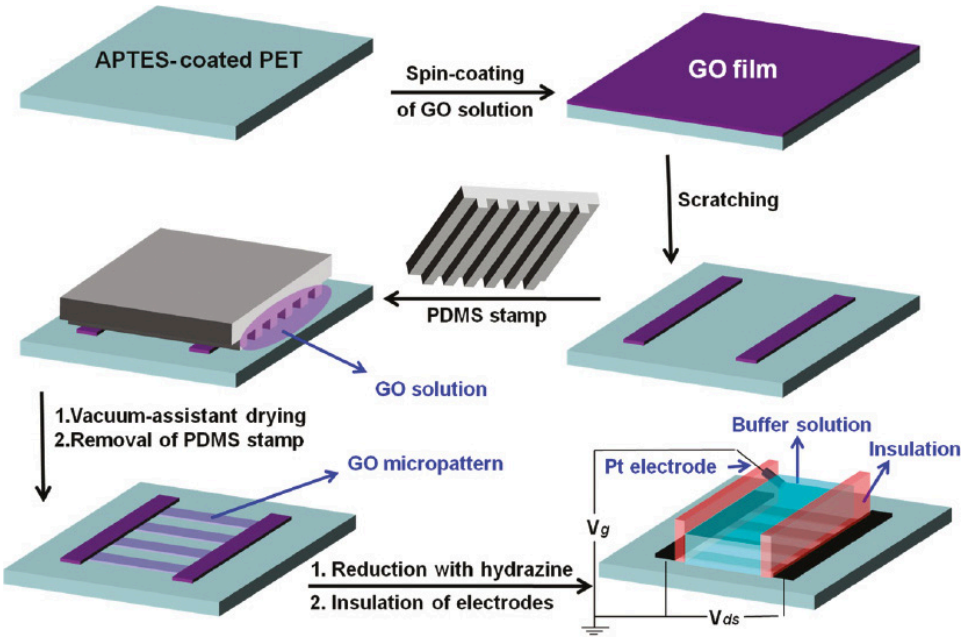

Figure 5. Schematic illustration for the fabrication of all-rGO TFT. Reproduced from Ref. 5 with permission.

transparent, and conductive electrodes can be prepared by depositing rGO on the polyethylene terephthalate (PET) substrates. The deposition of *p*-type and *n*-type materials on rGO film has been used to produce semiconducting graphene for flexible photovoltaic applications. Eda *et al.* demonstrated the controllable deposition of rGO thin films with thicknesses ranging from a single monolayer to several layers over large areas. The optoelectronic properties of the resulting films can change by several orders of magnitude, making these rGO films potentially useful for flexible and transparent semiconductors.[6] He *et al.* fabricated a thin-film transistor (TFT) made of rGO, as shown in Figure 5.[5] The fabricated electronic sensor was extremely flexible with high transparency, and showed good sensitivity for detecting proteins in a physiological buffer. Yan *et al.* demonstrated that solution-processable rGO thin films can be used as efficient anode materials for high-efficiency and high-stability organic solar cells (OSCs).[127] The lifetime of rGO-doped cells is much longer than that of poly(3,4-ethylenedioxythiophene)-poly-(styrenesulfonate) (PEDOT:PSS) electrodes. These results clearly demonstrate that chemically reduced GO is a promising interfacial material and a practical replacement for conventional PEDOT:PSS, and can thus advance

the realization of high-efficiency, high-stability, and low-cost OSCs by high-throughput roll-to-roll manufacturing.[13]

H_2 storage is of significant interest in fuel cell research, and in the application of hydrogen technologies to motor vehicles. The large surface area of graphene makes it a potentially ideal material for hydrogen storage. However, NIST Center scientists have reported that graphene does not store hydrogen well in its original form.[88] According to their research, if GO sheets are stacked on top of one another, then the resulting graphene framework can accumulate hydrogen in greater quantities.[88] It is well known that the reduction of GO can induce it to stack, resulting in the formation of a graphitic framework. The controlled reduction of GO with mild reducing agents can be used to obtain large-area graphene, which is suitable for hydrogen storage in fuel cells.[89] The Brunauer-Emmett-Teller (BET) surface area of glucose-reduced GO was reported to be 1205.8 $m^2\ g^{-1}$ by N_2 adsorption at 77 K, and its hydrogen storage capacity was 2.7 wt.% at a temperature of 298 K and an atmospheric pressure of 25 bar. This glucose-reduced GO is therefore a promising material for fuel cells, as it has outstanding H_2 storage properties.

Chemically derived graphene and its composites have been extensively used for the fabrication of anode materials in Li-ion batteries. Chen *et al.* showed that the Li-ion storage of graphene at high discharge rate approaches 480 mA h g^{-1} after 100 cycles at a current density of 500 mA g^{-1}, and 320 mA g^{-1} after 300 cycles at 2 A g^{-1}.[90] A 3D porous composite of silicon and graphene as an anode material has been prepared by magnesiothermic reduction and spray granulation.[91] The porous materials exhibit a reversible capacity of ~900 mA h g^{-1} with very little fading. It has been found that Si/graphene composites can be cycled at extremely high Li-ion extraction rates, such as 5 A g^{-1} and 10 A g^{-1}, for over 100 cycles. Qin *et al.* have shown that the modification of $LiMnPO_4$ nanoparticles with graphene gives rise to improved electrochemical performance compared with conventional pyrolytic carbon-coated nanoparticles. The $LiMnPO_4$/graphene composites reveal a high capacity of 149 mA h g^{-1} at 0.1 C, 90 mA h g^{-1} at 1 C, and 64 mA h g^{-1} at 5 C charge/discharge rates.[92] A series of graphene/metal oxide composite anode materials for Li-ion batteries have also been prepared.[93] Ultrasmall tin dioxide (SnO_2) nanoparticles dispersed in graphene have been reported. The pliable graphene sheets effectively ease the volume expansion of SnO_2 during charge/discharge, and thus, the SnO_2/graphene nanocomposites show much improved cycling stability.

Among all of these applications, the use of graphene as a supercapacitor electrode material has been studied extensively. Supercapacitors are unique

for their ability to combine the energy storage properties of batteries with the power discharge characteristics of capacitors. This is attributed to the large surface area of the activated carbon capacitors with a thin layer of electrolyte. The energy stored in a supercapacitor is proportional to the charged surface area and inversely proportional to the thickness of the dielectric. They are able to hold a very high charge, which can be released in a controlled manner. Supercapacitors have several advantages over batteries: (i) they can operate in a wide range of temperature from +70 °C to –40 °C, suggesting that supercapacitors can deliver efficient power to starting and ignition systems in cold weather without relying on batteries; (ii) supercapacitors are lightweight and smaller in size; (iii) they can handle millions of charge and discharge cycles; (iv) they can provide up to 10 times more power than batteries; (v) supercapacitors can be fully recharged in 1 or 2 min; and (vi) the potential for cost savings. The price of ultracapacitors has fallen by 99% in the past decade, compared to the decrease of only 30–40% in battery prices. Because of these benefits, graphene supercapacitors have attracted significant attention over other energy storage devices such as H_2 storage and Li-ion batteries. Thus, graphene-based energy storage electrode materials for supercapacitors will be discussed in detail.

5. Graphene-Based Supercapacitor

Graphene-based supercapacitors consist of two electrodes immersed in an electrolyte solution. They can store charge by EDLC, where the energy is stored by ion adsorption. The accumulation of charge is purely electrostatic, and there is no faradic reaction. The large surface area of graphene is helpful for the electrostatic charge storage. The charge is also stored by oxidation–reduction reaction on the surface of electrode. This kind of charge storage mechanism is known as pseudocapacitance. We briefly summarize the recent advances in the application of graphene and graphene-based composite materials in the field of supercapacitors. Specific capacitance can be calculated from cyclic voltammogram (CV) curves using the equation, $C = S/2\ mk\Delta V$, where C is the specific capacitance, S is the area surrounded by the CV curve, m is the mass cast onto the electrode, k is the scan rate, and ΔV is the potential range. The specific capacitance can also be calculated from charge–discharge cycles using the equation, $C = I\Delta t/m\Delta V$, where I is the applied current and Δt is discharge time (s). Similarly, the energy density and power density of a supercapacitor electrode can be determined according to $E = CV^2/2$ and $P = E/\Delta t$, respectively.

5.1. rGO supercapacitor

GO is an insulating material, and thus, its specific capacitance is very low due to its high equivalent series resistance (ESR). However, this does not mean that the specific capacitance of a good conductor is always better than that of poorly conducting materials. It has been found that the specific capacitance of GO increases significantly after its reduction by chemical, thermal, or electrochemical methods. However, the complete removal of oxygen functionalities without introducing any functional groups on the surface of graphene always tends to decrease the specific capacitance of rGO.

The specific capacitance of a supercapacitor based on chemically reduced graphene electrodes has been found to be 180–200 F g^{-1} in aqueous electrolyte. Fan *et al.* studied the effect of reduction time on the supercapacitor performance of graphene sheets.[94] The content of C and N in graphene sheets increased with an increase of reduction time. However, the specific surface areas and the specific capacitance decreased. This is attributed to the agglomeration of graphene sheets and loss of surface functional groups. It was found that the graphene sheets prepared with a reduction time of 30 min had the highest specific capacitance of 192 F g^{-1} in a 6 M KOH electrolyte. Liu *et al.* prepared graphene-based electrode materials by the reduction of GO dispersion using hydrazine monohydrate at 95 °C for 2 h.[95] 1-Ethyl-3-methylimidazolium tetrafluoroborate ($EMIMBF_4$) was used as an electrolyte for the electrochemical experiments. Coin-size capacitor cells were assembled in a glove box using $EMIMBF_4$ ionic liquid electrolyte. It has been shown that the efficiency of a supercapacitor device can be increased by using an organic electrolyte instead of an aqueous electrolyte. Generally, with aqueous electrolyte, the operating voltage is only 1.2 V for a symmetric supercapacitor. In order to obtain high energy density, it is essential to introduce pseudocapacitance with EDLC. The energy density for the designed supercapacitor was increased to 136 Wh kg^{-1} at 80 °C from the room temperature value (85.6 Wh kg^{-1}). Zhang *et al.* prepared highly conductive and porous activated rGO by KOH reduction of a colloidal GO dispersion.[96] The flexible graphene paper showed a very high specific surface area (2400 m^2 g^{-1}) and electrical conductivity (5880 S m^{-1}). A two-electrode configuration for electrochemical testing was designed, which exhibited a very high power density of about 500 kW kg^{-1}. The specific capacitance and energy density for activated graphene material were recorded as 120 F g^{-1} and 26 Wh kg^{-1}, respectively. Jin *et al.* prepared a stable aqueous dispersion of rGO by KOH reduction of a GO dispersion at 80 °C for 1 h.[97] The as-prepared material showed a maximum specific capacitance of (200 F g^{-1}) in 6.0 M aqueous

KOH electrolyte at a scan rate of 5 mV s^{-1}. Urea-reduced GO exhibited excellent specific capacitance behavior, as observed by Lei *et al.* Paper made from rGO showed a volumetric capacitance of 196 F cm^{-3}.[98] 93% of the specific capacitance was retained after 1200 charge–discharge cycles.

Graphene prepared by alkaline hydrothermal reduction of GO showed a specific capacitance of ~145 F g^{-1} in organic electrolyte (1 M lithium bis-(trifluoromethanesulfonyl)imide (LiTFSI) in acetonitrile) and 95 F g^{-1} in an ionic liquid electrolyte ethylmethylimidazolium bis-(trifluoromethanesulfonyl) imide (EMITFSI).[99] The energy density and power density of the graphene-modified electrode were recorded as 30 W h kg^{-1} and 12.5 kW kg^{-1} in organic electrolyte. In contrast, the energy density was increased to 43 W h kg^{-1}, while the electrochemical experiments were carried out in ionic liquid electrolyte. However, the power density was decreased to 11.5 kW kg^{-1} in ionic liquid electrolyte. Chen *et al.* and Lee *et al.* prepared nitrogen-doped graphene by the hydrothermal reduction of GO.[100,101] Amino acid was used as the nitrogen source for the surface modification of graphene during hydrothermal synthesis. The 3D architecture of N-doped graphene is shown in Figures 6b and 6c. The doping of nitrogen on the surface of graphene sheets was confirmed by N1s XPS analysis, as shown in Figure 6d. The C1s XPS of the hydrothermally reacted materials showed a considerable reduction of GO using amino acid. A charge–discharge cycle study showed ~95.2% retention of the specific capacitance after 4000 cycles. The material showed a very high power density of 205.0 kW kg^{-1} at an ultra-fast discharge rate of 185 A g^{-1}. Lee *et al.* prepared nitrogen-doped graphene sheets using a simple hydrothermal reaction with GO and hexamethylenetetramine (HMT).[101] The specific capacitance of the HMT-rGO was recorded as 161 F g^{-1} at a current density of 0.5 A g^{-1}. Figure 7 shows that the specific capacitance of HMT-rGO decreased with increasing scan rate. The CV curve showed that the specific capacitance originated from only the EDLC. The area surrounded by the CV curve increased with increasing scan rate, indicating a surface-confined electrochemical process. The retention in specific capacitance of the HMT-rGO was above 98%, confirming very good cyclic stability of the HMT-GO. The electrochemical performance of the rGO and HMT-rGO were compared by electrochemical impedance spectroscopy (EIS) analysis, as shown in Figure 8. It was seen that the HMT-rGO had good electrical conductivity compared to the rGO. The calculated charge-transfer resistance (R_{ct}) of HMT-rGO was found to be 6.78. In contrast, R_{ct} for rGO was determined to be 67.45, indicating a large *iR* drop and poor electrochemical performance. Li *et al.* reported the preparation of KOH-modified graphene sheets, and discussed their performance as a supercapacitor electrode.[102] The specific capacitance and energy density of

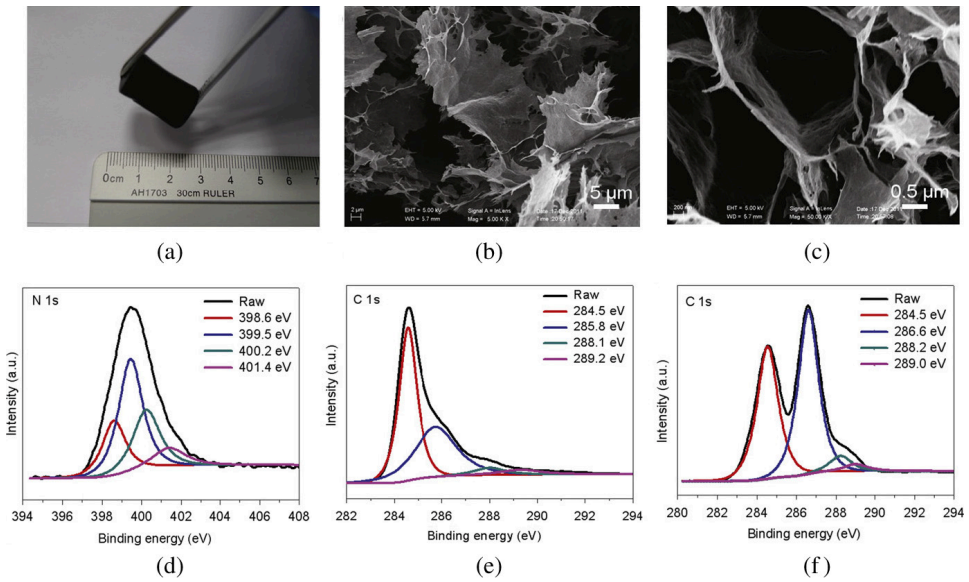

Figure 6. Photographs, SEM images, and XPS spectra of a typical nitrogen-doped graphene hydrogel (GN-GH). (a) Photographs of a typical GN-GH using GO and ethylenediamine (100 μL) as precursors after hydrothermal process at 180 °C for 12 h; (b) SEM image of the typical GN-GH microstructures; (c) magnified SEM image of the typical GN-GH microstructures; (d) the high-resolution XPS spectra of the N1s region for typical GN-GH; (e) the high-resolution XPS spectra of the C1s region for the typical GN-GH; (f) the high-resolution XPS spectra of the C1s region for the GN-GH. Reproduced from Ref. 100 with permission.

pristine graphene sheets were recorded as 101 F g^{-1} and 14.0 W h kg^{-1}, respectively. In contrast, the specific capacitance was improved by 35% after the KOH modification of graphene sheets, and the value was 136 F g^{-1} at a scan rate of 10 mV s^{-1}. However, the value was decreased to 123 F g^{-1} when the scan rate was increased to 20 mV s^{-1}. Jiang *et al.* prepared N_2-doped graphene by the concentrated ammonia-assisted hydrothermal reduction of GO.[103] XPS analysis showed that the doping level of N_2 was 7.2% at 180 °C for 12 h, and the oxygen content in GO (24.8%) was decreased to 8.5% after reduction. A high specific capacitance of 144.6 F g^{-1} at a current density of 0.2 A g^{-1} was achieved. Under identical conditions, the specific capacitance of pristine graphene was recorded as 116.7 F g^{-1}. The increased specific capacitance is attributed to the high level of N_2 doping on the graphene surface.

A high-performance supercapacitor electrode material was prepared via the flame-induced reduction of GO paper.[104] The resulting rGO paper had a high surface area of 275 m^2 g^{-1}, as evident from the N_2

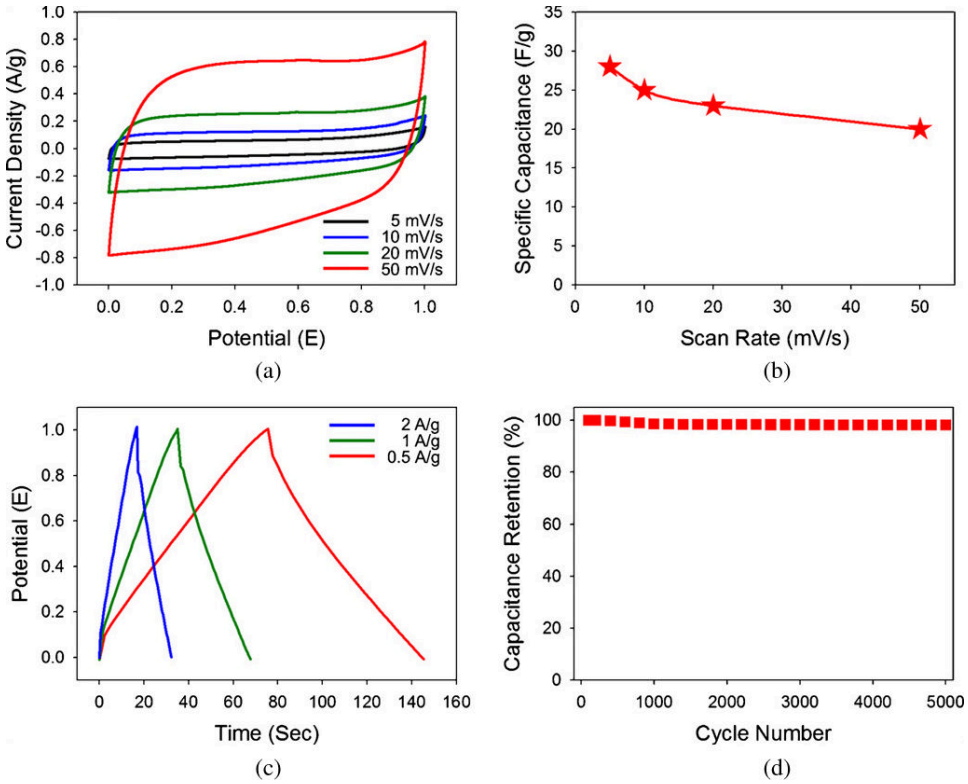

Figure 7. Two-electrode system with symmetric nitrogen-doped graphene sheets (NGS) hexamethylenetetramine (HMT)-40: (a) CV curves depending on scan rate, (b) galvanostatic charging–discharging curves at various current densities, (c) specific capacitance with different current densities, and (d) variation in the capacitance retention of NGS-HMT-40 for a 5000-cycle test. Reproduced from Ref. 101 with permission.

adsorption–desorption isotherm of GO and rGO samples shown in Figure 9. The high surface area of rGO compared with pristine GO is due to the better exfoliation after the flame-induced reduction due to the evolution of moisture and CO_2. XPS analysis showed the presence of a certain amount of oxygen functional groups, which help to improve the specific capacitance by the contribution of pseudocapacitance. The specific capacitance of the rGO electrode was determined as 160 F g^{-1} at a current density of 1 A g^{-1} in an aqueous KOH electrolyte. EIS analysis showed that the ESR for rGO was 0.93 and 2.63 Ω in KOH and Et_4NBF_4 electrolyte, respectively. Thus, it is seen that the intrinsic resistance of the rGO electrode was low and the flame treatment had a large contribution to the overall ESR. Zhu *et al.* reported a versatile method to obtain high-performance electrode materials by the

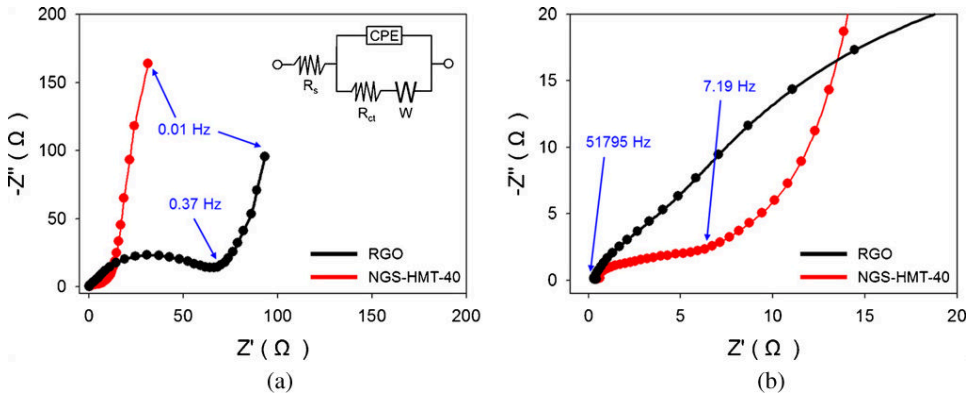

Figure 8. Nyquist plots of rGO and NGS-HMT-40. Reproduced with the permission from Ref. 101.

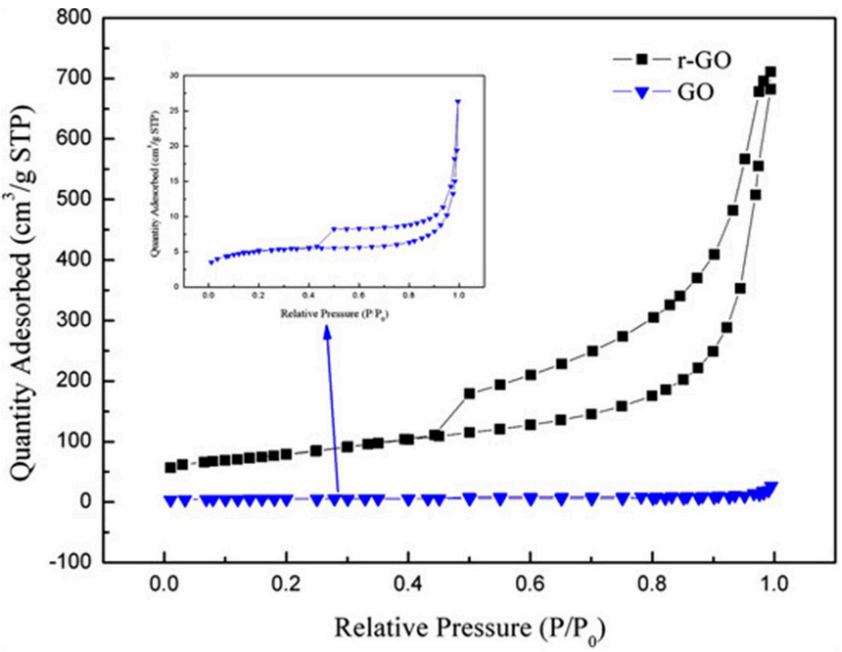

Figure 9. N_2 adsorption–desorption isotherms of GO and rGO paper samples. Reproduced from Ref. 104 with permission.

simultaneous exfoliation and reduction of graphite oxide.[105] They showed that the reduction occurs inside a commercial microwave oven within 1 min. The specific capacitance of the material in KOH electrolyte was found to be 191 F g^{-1}. Chen *et al.* prepared rGO-based supercapacitor by the reduction

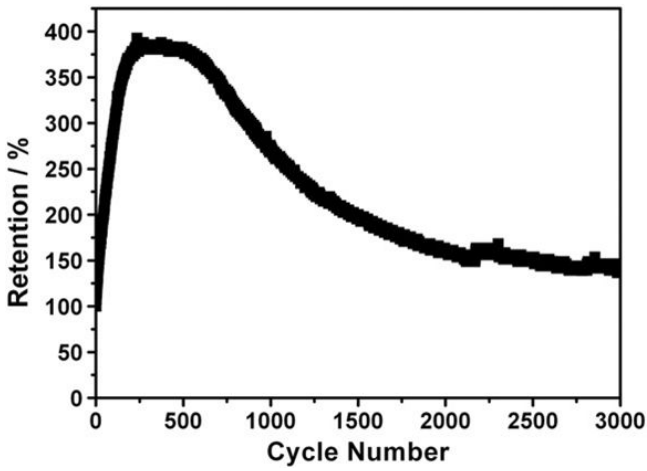

Figure 10. The life performance of rGO in $BMIPF_6$. Reproduced from Ref. 106 with permission.

of GO using HBr. Two-electrode systems were fabricated in ionic liquid electrolytes of 1-butyl-3-methylimidazolium hexafluorophosphate ($BMIPF_6$) and 1-butyl-3-methylimidazolium tetrafluoroborate ($BMIBF_4$).[106] It was seen that the electrochemical performance of the designed electrode was much better in $BMIPF_6$ electrolyte than in $BMIBF_4$. The life retention was 141% of the initial specific capacitance after 3000 charge–discharge cycles (Figure 10). The outstanding performance of the electrode largely depended on the wide electrochemical window (4 V) in $BMIBF_6$ electrolyte.

Le *et al.* demonstrated the thermal reduction of GO at 200°C in N_2 atmosphere.[107] The specific capacitance of rGO varied from 48 to 132 F g^{-1}, depending on the potential scan rate, which ranged from 0.5 to 0.01 V s^{-1}. 1 M H_2SO_4 was used as the electrolyte. Ye *et al.* showed that the partially exfoliated and rGO at low temperature about 200 °C and ambient pressure performed well as an energy storage electrode material.[108] A maximum specific capacitance of 315 F g^{-1} at a current density of 100 mA g^{-1} in 1 M KOH electrolyte was recorded.

5.2. Surface-modified graphene supercapacitor

Surface functional groups play an important role in determining the specific capacitance of graphene. The functional groups take part in faradic reaction and enhance the capacitance behavior by contributing pseudocapacitance. Kuila *et al.* prepared surface-modified graphene by the reduction of GO in

the presence of sulfonated poly-ether-ether-ketone (SPEEK).[15] The SPEEK-modified graphene (SPG) formed a stable dispersion in water and obeyed Beer's law at low concentration. The adsorption of SPEEK onto the surfaces of graphene was confirmed by FTIR, AFM, and TEM image analysis. The SPG-modified electrode showed a very high specific capacitance value of 476 F g^{-1} at a current density of 6.6 A g^{-1}. The very high specific capacitance value was due to the contribution by the faradic reaction of SPG during the electrochemical experiments. The $-SO_3H$ functionalities of SPG directly took part in the oxidation–reduction reaction, as shown in the CV graph in Figure 11.[15] The appearance of a sharp redox peak in the CV curve clearly suggests the pseudocapacitance of SPG. It was further supported by the non-linear charge–discharge slope at 0.5 V. Yu *et al.* prepared graphene functionalized by sodium 4-aminoazobenzene-4′-sulfonate (SAS) and its aryl diazonium salt (ADS), starting with GO.[109] The maximum dispersibilities of SAS- and ADS-functionalized graphene (SAS-G and ADS-G) in water were 1.4 and 2.9 mg mL^{-1}, respectively. The electrical conductivity of ADS-G (1120 S m^{-1}) was found to be higher than that of SAS-G (149 S m^{-1}). This is attributed to the better restoration of the π-electronic conjugated structure of the graphene in ADS-G compared to SAS-G. Electrochemical experiments showed that the specific capacitance of ADS-G (210 F g^{-1}) was superior to that of the SAS-G (170 F g^{-1}). The superior specific capacitance of ADS-G was attributed to the two-step reduction of GO and its good dispersibility in water. The presence of oxygen functional groups of ADS-G took part in the faradic reaction, and the pseudocapacitance was much higher compared to SAS-G. Bose *et al.* demonstrated the preparation of 9-ACA-modified graphene by the one-step sonochemical exfoliation of graphite.[72] 9-ACA was adsorbed on the surface of graphene by the non-covalent interaction of π-electrons. The graphene-based ultracapacitors exhibited a high specific capacitance of 148 F g^{-1}. However, the low production yield (2.3%) was not good for volume production of graphene. Khanra *et al.* presented a green route for the one-step electrochemical exfoliation of graphite to graphene with high production yield.[33] They used two graphite rods as a cathode and anode and passed electricity through them under certain conditions. 9-ACA dissolved in water at a pH ≥ 8 was used as both an electrolyte and a surface modifier for graphene. 9-ACA was adsorbed on the surface of *in situ* synthesized graphene by π–π interaction, which facilitated the formation of a stable dispersion in water. An electrochemical experiment showed a very high value of specific capacitance (577 F g^{-1}) with a retention of 83.4% after 1000 charge–discharge cycles. The coulombic efficiency was recorded as 102%, indicating suitability as an energy storage electrode material.

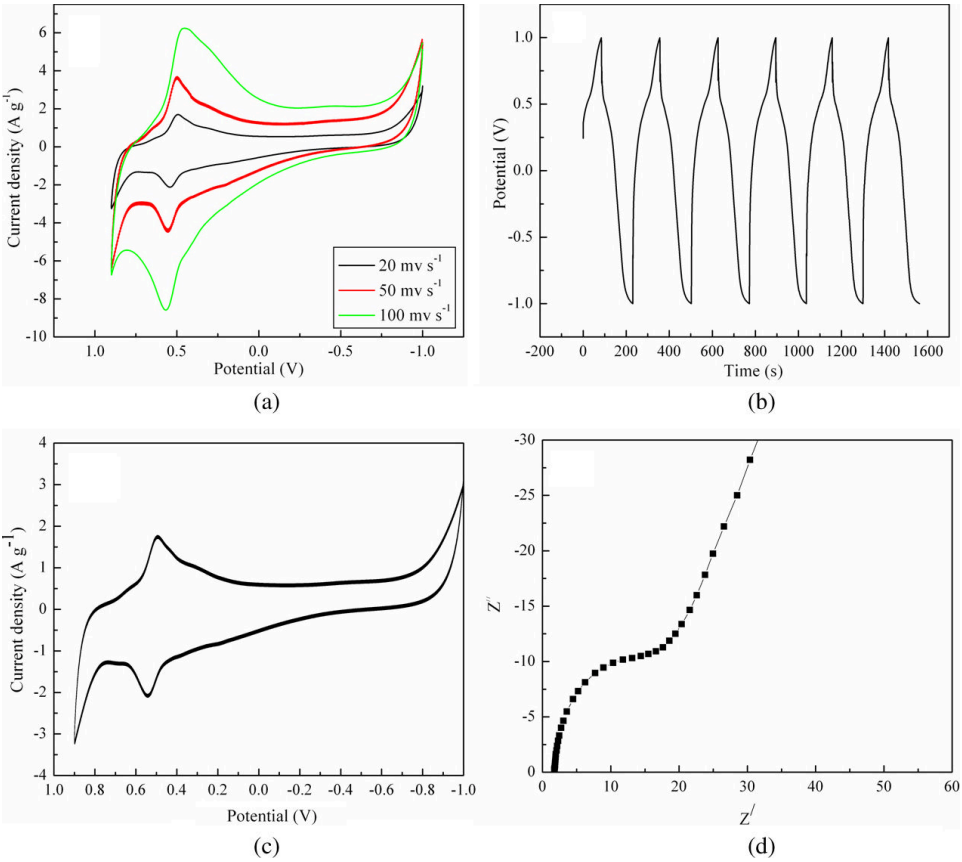

Figure 11. (a) CV of SPG at various scan rates; (b) charge/discharge behavior of SPG-based supercapacitors performed at a constant current density of 6.6 A g^{-1}; (c) CV curves of SPG recorded at a scan rate of 20 mV s^{-1} up to 10th cycle; (d) EIS curve of SPG sheets. Reproduced from Ref. 15 with permission.

Ai *et al.* showed an efficient approach for the preparation of graphene functionalized with benzoxazole and benzimidazole, and their application in high-performance supercapacitors.[110] The functionalized graphene exhibited good electrochemical performance, with a high specific capacitance (730 and 781 F g^{-1} for benzoxazole- and benzimidazole-grafted graphene (BO-G and BI-G), respectively, at a current density of 0.1 A g^{-1}). The very high specific capacitance originated from the contribution by the faradic reaction, as evidenced in Figure 12. The proposed electrochemical oxidation–reduction reaction is shown in Figure 13. The retention in specific capacitance was 85% after 2000 charge–discharge cycles, confirming the good cycling stability and

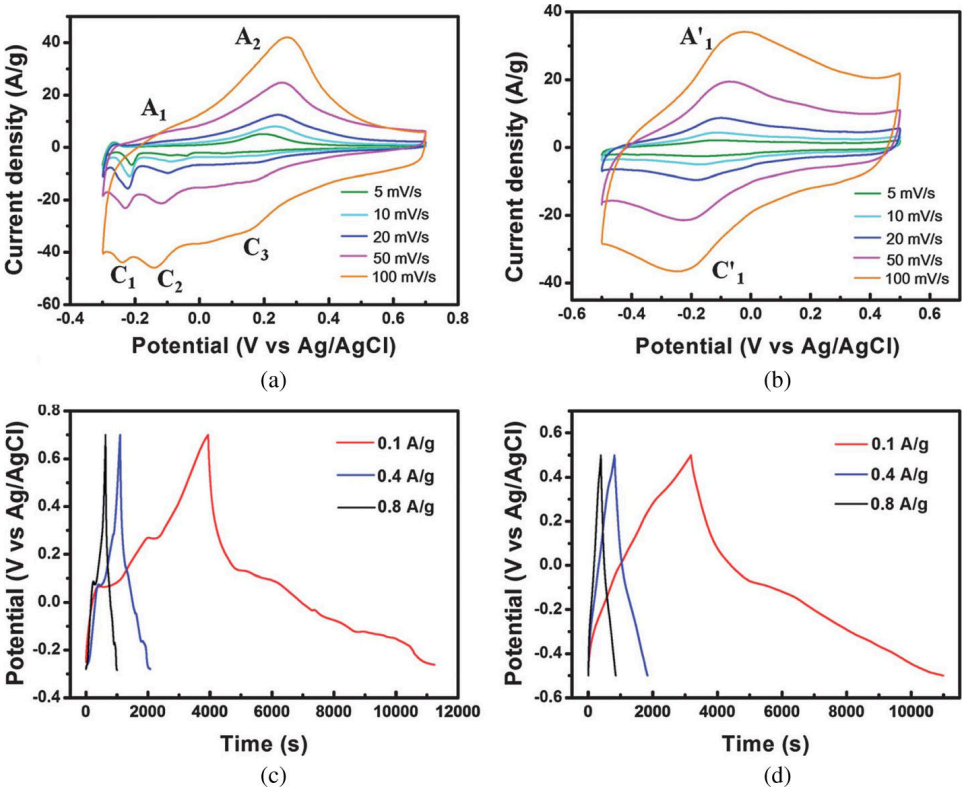

Figure 12. CVs for the BO-G (a) and BI-G (b) materials at different scan rates; charge–discharge curves of BO-G (c) and BI-G (d) at different galvanostatic current densities. Reproduced from Ref. 110 with permission.

the potential for energy storage applications. An *et al.* studied the supercapacitor performance of graphene functionalized with 1-pyrene carboxylic acid (PCA) acid.[71] They prepared a monolayer of functionalized graphene directly from graphite in a water–ethanol mixture, and PCA was used as an exfoliating agent. PCA-functionalized graphene exhibited an extremely high specific capacitance (~120 F g^{-1}), power density (~105 kW kg^{-1}), and energy density (~9.2 Wh kg^{-1}). Ghosh *et al.* prepared PCA-functionalized graphene for energy storage applications.[111] The specific capacitance of the functionalized graphene sheets was found to be ~200 F g^{-1} in aqueous KOH electrolyte. In contrast, the specific capacitance of non-functionalized graphene electrodes was recorded as ~30 F g^{-1}. The high specific capacitance was attributable to the hydrophilic nature of the functionalized graphene sheets, which resulted in good wetting with the aqueous KOH electrolyte. Kim *et al.*

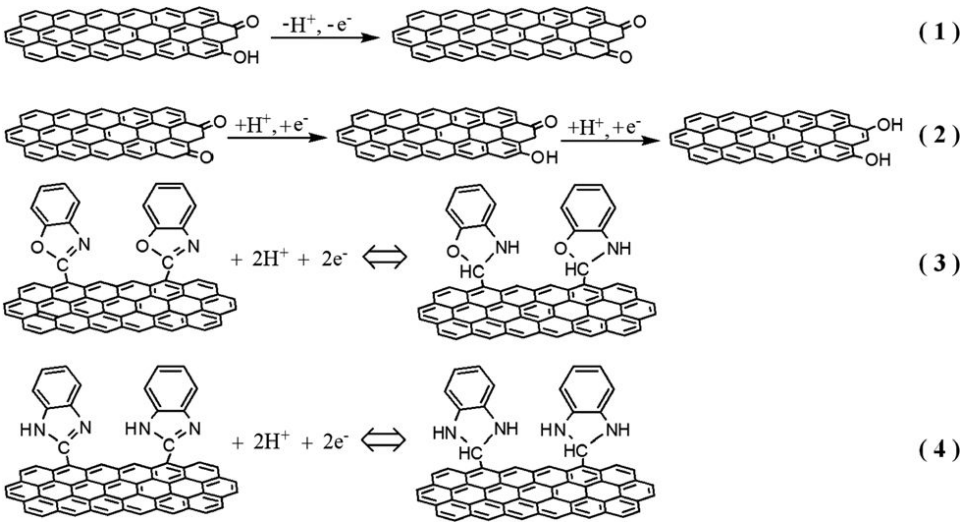

Figure 13. The proposed electrochemical reactions of redox-active functional groups on BO-G and BI-G. Reproduced from Ref. 110 with permission.

reported the functionalization of graphene using ionic liquids, and on its use as a high-performance supercapacitor electrode.[112] A supercapacitor was assembled with an ionic-liquid-modified graphene electrode and a 1-ethyl-3-methylimidazolium bis(trifluoromethylsulfonyl)amide-modified electrolyte, and showed a stable electrochemical response with an operating voltage of up to 3.5 V. The ESR of the designed device was estimated to be 3.7 Ω, and a maximum energy density of 6.5 $Wh\,kg^{-1}$ with a power density of 2.4 kW kg^{-1} was achieved.

5.3. Metal nanoparticle/oxide-decorated graphene supercapacitor

The energy storage capacity of an EDL capacitor is low compared to that of a battery. However, EDL capacitors have excellent cyclic stability and run for a long time without chemical change during the charge/discharge process. To improve the performance characteristics of a supercapacitor, such as the specific capacitance and the energy density, pseudocapacitance, *i.e.*, the Faradic redox reaction, is desirable. Although functionalized graphene has good pseudocapacitive behavior, insufficient pore size distribution can hinder the formation of a large number of double layers and the rapid transportation of ions. Thus, to improve the performance of a supercapacitor,

metal-oxide-decorated graphene composites have attracted significant interest. Pure metal-oxide-based supercapacitor electrode materials have been investigated, such as RuO_2, IrO_2, MnO_2, NiO, TiO_2, V_2O_5, Co_3O_4, SnO_2, ZnO, Fe_2O_3, and WO_3. However, most of the metal oxides are weak electrical conductors, and they generate high ohmic resistance, and reduce the rate capability.[113–132] In order to address these shortcomings, carbon materials such as CB (carbon black), CNT, and graphene have been hybridized with metal oxide. Low-dimensional metal-oxide-decorated graphene composites enable production with large surface area, as well as control of the porous structure, which enhances the area of the EDL (electrical double layer) easily by ion channels of electrolyte.

Among the metal oxides, RuO_2 is the best commercial metal oxide and has been studied most often as an electrode for supercapacitors. However, the use of this metal oxide has some limitations due to its toxicity, high production cost, and limited resources. In contrast, other metal oxides such as nickel oxide and hydroxide, cobalt oxide and hydroxide, and manganese oxide are readily available, environmentally friendly, and less expensive.[114] Needle-like MnO_2 nanocrystal/GO composite was prepared using $MnCl_2.4H_2O$ and $KMnO_4$ in isopropyl alcohol. Mn^{2+} ions generated via the dissolution of manganese chloride in isopropanol were bound favorably with negatively charged oxygen functional groups. Moreover, in the presence of Mn^{7+} ions from the $KMnO_4$, the speed of the redox reaction increased. The reaction mechanism is shown below:

$$4MnO_4^- + 3C + H_2O = 4MnO_2 + 2HCO_3^- + CO_3^{2-}$$

Similarly, GO/MnO_2 composites were prepared with different feeding ratios of manganese oxide, and the electrochemical performance was investigated. Figure 14 shows the TEM images of MnO_2-decorated graphene collected at different times. The symmetric and rectangular curves of the composite were responsible for the excellent supercapacitor performance in 1 M Na_2SO_4 electrolyte. The specific capacitance values of pure nano-MnO_2 and graphene/nano-MnO_2 were recorded as 197 and 211 F g^{-1}, respectively,[115] at a current density of 0.2 A g^{-1}. The oxygen functional groups help the formation of a double layer with electrolyte due to dipolar interaction with electrolyte, and could take part in the Faradic reaction. Li *et al.* reported a different level of oxidation on the surface of graphene composed with rod-shaped MnO_2. The composites exhibited the specific capacitance of 124 F g^{-1} in 1 M Na_2SO_4 at a scan rate of 200 mA g^{-1}, and the retention rate was 78.7% after 1000 charge–discharge cycles. The loss of stability may be attributed to

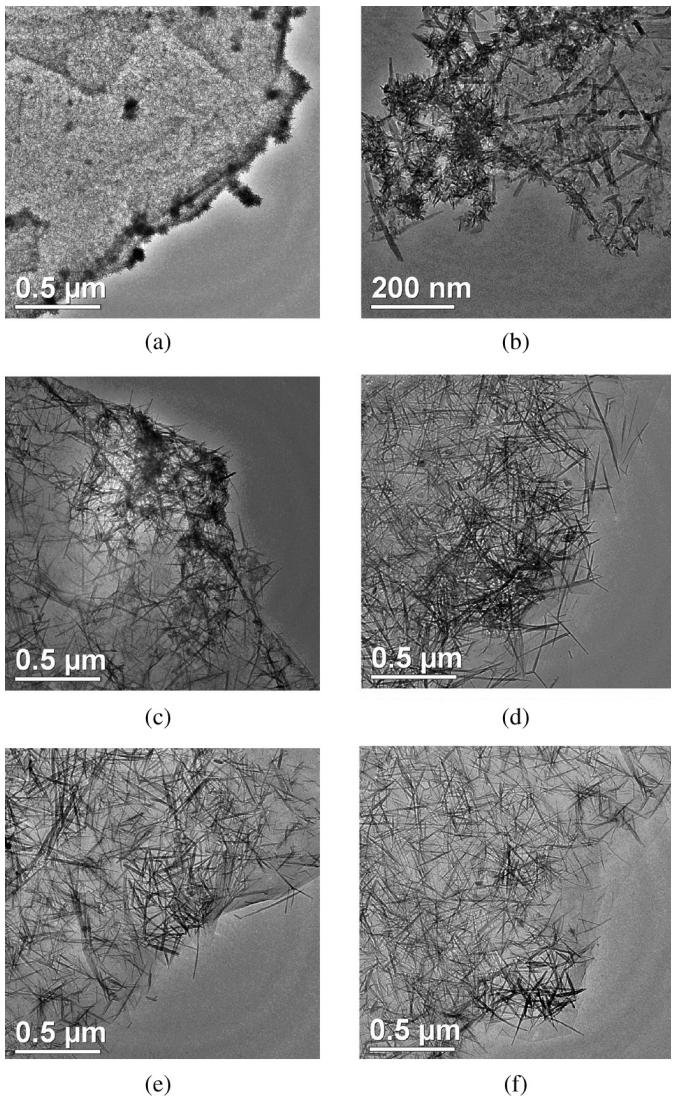

Figure 14. TEM images of MnO_2-decorated graphene samples collected at different time intervals: (a) 10 s, (b) 1 min, (c) 3 min, (d) 5 min, (e) 10 min, and (f) 30 min. Reproduced from Ref. 115 with permission.

the merits and demerits of oxygen-containing functional groups on the surface of graphene.[116] The highly conducting graphene surface is suitable for supercapacitor applications. In addition, the growth of manganese oxide via self-sacrificial reduction using $KMnO_4$ is limited by the initially formed oxide. Therefore, ethanol-mediated manganese oxide growth in a high-pH medium

was an excellent method for preparing graphene/MnO_2 composite. Chen *et al.* demonstrated that this method is excellent for the preparation of supercapacitor electrodes with a specific capacitance of 365 F g^{-1} with an MnO_2/rGO ratio of 99:1. However, with increasing graphene content, the capacitance value decreased, indicating the increase of EDL behavior due to the graphene layers.[117] Lei *et al.* developed a facile method to immobilize MnO_2 on the surface of carbonaceous materials. MnO_2 was directly grown on the surface of CNTs using $KMnO_4$. The resulting composite exhibited a specific capacitance of 193 F g^{-1} in 1 M Na_2SO_4 aqueous electrolyte at a current density of 0.2 A g^{-1}. Moreover, 70% of the specific capacitance was retained after 1300 cycles.[118] In order to achieve good specific capacitance, the use of porous electrode materials is desirable. The electrochemical performance of a hybrid-graphene/MnO_2-coated microfiber textile composite was studied for supercapacitor applications. The microfibers were coated with GO, and then MnO_2 electrodeposited onto the surface of GO. The measured specific capacitance value reached to 315 F g^{-1}, and ~95% of the capacitance was retained after 5000 charge/discharge cycles.[119] However, it is very difficult to control the distribution of MnO_2 particles on the surface of graphene. In order to achieve homogeneous distribution of the metal particles, a 3D network with conductive wrapping on the surface of graphene/MnO_2 composite was introduced. The 3D graphene composite system involved a graphene/MnO_2/CNT hybrid and a graphene/MnO_2/PEDOT:PSS hybrid. The measured specific capacitance value was as high as ~380 F g^{-1} with 95% retention of the specific capacitance after 3000 charge–discharge cycles.[120]

For the commercialization of supercapacitors, the energy density needs to be increased by improving the operating voltage. Non-aqueous electrolytes like ionic liquid were used to design high-performance supercapacitors.[121] Fan *et al.* demonstrated the use of graphene/MnO_2 as a positive electrode, and activated carbon nanofiber as a negative electrode in 1 M aqueous Na_2SO_4 electrolyte.[122] Birnessite-type MnO_2-coated graphene composite was synthesized using a mixture of graphene powder and $KMnO_4$ subjected to microwave irradiation. Flower-like MnO_2 structure was formed. The specific capacitance and energy density of the composites were recorded as 113 F g^{-1} and 51 Wh kg^{-1}, respectively. This kind of supercapacitor device also exhibited ~97% capacitance retention after 1000 charge–discharge cycles.[122] Similarly, Cao *et al.* developed an MnO_2/graphene composite for use as positive and negative electrodes. The operating voltage for this electrode was 2 V. The measured energy density and power density measured in 1 M Na_2SO_4 aqueous electrolyte[123] at a scan rate 5 mV s^{-1} were 25 Wh kg^{-1} and 100 kW kg^{-1}, respectively.

Recently, flexible energy storage devices have emerged as a key technological challenge for portable electronics, miniature biomedical devices, and paper-like personal electronics. The use of polymer gel-like electrolytes is a hopeful approach to commercialization, and could enable light weight, flexibility, high power density, fast charge/discharge, and safety for daily use. For portable and flexible electronics applications, aqueous and non-aqueous electrolyte is not suitable. Therefore, Gao *et al.* demonstrated graphene decorated with freestanding metal oxide (Mn_3O_4) as a positive electrode, using freestanding CNT/graphene composite as a negative electrode, and potassium polyacrylate/KCl as a polymer gel electrolyte. Manganese oxide was prepared by reacting $Mn(CH_3COO)_2.4H_2O$ with NaOH. The performance of the resulting composite depends on the manganese oxide loading with rGO. The measured specific capacitances were 321 and 252 F g^{-1} when the Mn_3O_4 content was varied from 50 to 25% at a current density of 0.5 A g^{-1}. The composite with 50% loading exhibited a remarkable rate capacity along with a specific capacitance of 243 F g^{-1} at a current density of 10 A g^{-1}. An operating voltage window at 1.8 V and a remarkable capacitance retention of 86% were achieved after 10,000 cycle.[124] Similarly, Lee *et al.* developed rod-shaped Mn_3O_4 on the surface of graphene using a hydrothermal method. A significant improvement in the cyclic stability (100%) was recorded after 10,000 charge/discharge cycles[125] at a current density of 5 A g^{-1}. For large-scale applications, such as constant power sources for hybrid electrical vehicles or fuel-cell-mediated electrical vehicles, a large amount of electroactive materials is required. Unfortunately, a large mass has always hindered the contact of the electrolyte with the chemically active surface area. Therefore, freestanding, lightweight, and high-conducting 3D graphene is an ideal supporting electrode material that can support the loading of large masses of active materials. Rather than 2D graphene, 3D graphene has become a major source of interest, because of its high specific surface area, stable structure, and good charge transfer path. Moreover, it is useful as a flexible electrode. He *et al.* developed an excellent symmetrical supercapacitor consisting of a 3D graphene/MnO_2 composite. Sandwich arrangements separated by a membrane and encapsulated PET membranes were arranged as a flexible electrode. The supercapacitor performance was tunable by the MnO_2 loading on the 3D structure. 3D graphene was prepared using the standard reported CVD method. Then, MnO_2 was synthesized by electrodeposition using an aqueous solution containing $Mn(NO_3)_2$ and $NaNO_3$. At 465 F g^{-1}, the specific capacitance value was higher than the other literature values, which was obtained with a mass loading of 0.1 mg cm^{-2} at a scan rate of 2 mV s^{-1}.[125]

Apart from manganese oxide, $Ni(OH)_2$-based graphene composite has been explored as an excellent supercapacitor material. Numerous efforts have been made to prepare $Ni(OH)_2$ and its composites due to its high theoretical specific capacitance value (2082 F g^{-1}).[126] Wang *et al.* synthesized $Ni(OH)_2$ on the surface of graphene and investigated the electrochemical performance. Hexagonal, single-crystalline $Ni(OH)_2$ was directly grown on the surface of lightly oxidized graphene, and exhibited high specific capacitances of ~1335 F g^{-1} and ~945 F g^{-1} at current densities of 2.8 and 45.7 A g^{-1}, respectively. The high specific capacitance with excellent rate capability indicated potential applicability for supercapacitors. The specific capacitance of presynthesized $Ni(OH)_2$ and graphene composite showed lower specific capacitance compared to *in situ*-grown $Ni(OH)_2$ on the surface of graphene. The outstanding performance of directly grown nanoplates on graphene sheets suggests that the electrochemical performance is dependent not only on the chemical composition of the graphene composite, but also on the morphology and bonding in the composites.[126] Yan *et al.* synthesized a composite of graphene decorated with hierarchical flower-like nickel hydroxide for supercapacitor applications. They designed a high-voltage asymmetric supercapacitor using $Ni(OH)_2$/graphene and porous graphene as the positive and negative electrodes, respectively. The measured specific capacitance in the high voltage region of 0–1.6 V was 218.4 F g^{-1}, and the energy density was 77.8 Wh kg^{-1}. This performance indicated that the growth of nanomaterials and the fabrication of the electrode played important roles in the positive synergistic effects.[127] Ge *et al.*[128] synthesized 3D flower-like nickel oxide and measured the specific capacitance as 346 F g^{-1} at a current density of 1.5 Ag^{-1}.

Along with manganese and nickel-based oxides, cobalt-oxide-based graphene composites have been studied, because of their highest theoretical specific capacitance value (3560 F g^{-1}) and good electrical conductivity.[129] Therefore, Co_3O_4/rGO was prepared using a two-step surfactant-assisted method to facilitate the assembly of Co_3O_4 scrolls with the reduced graphene. The resulting composite yielded good specific capacitance, and excellent cyclic stability and rate capability. In particular, the SDS surfactant formed lamellar micelles in the solution, and Co^{2+} cations were formed from the CoC_2O_4 precursor. Then, anisotropic growth by a rolling process occurred due to the electrostatic interaction between Co^{2+} cations and anion groups on the SDS. In the presence of GO, the scrolls became large, because of the ionic bonding between the oxygen functionalities of GO and Co^{2+} cations. The specific capacitance of the resultant composite at a scan rate of 5 mV s^{-1} was 159.8 F g^{-1} in 6 M KOH aqueous solution.[56] Another simple way to obtain Co_3O_4-decorated graphene is hydrothermal reduction using

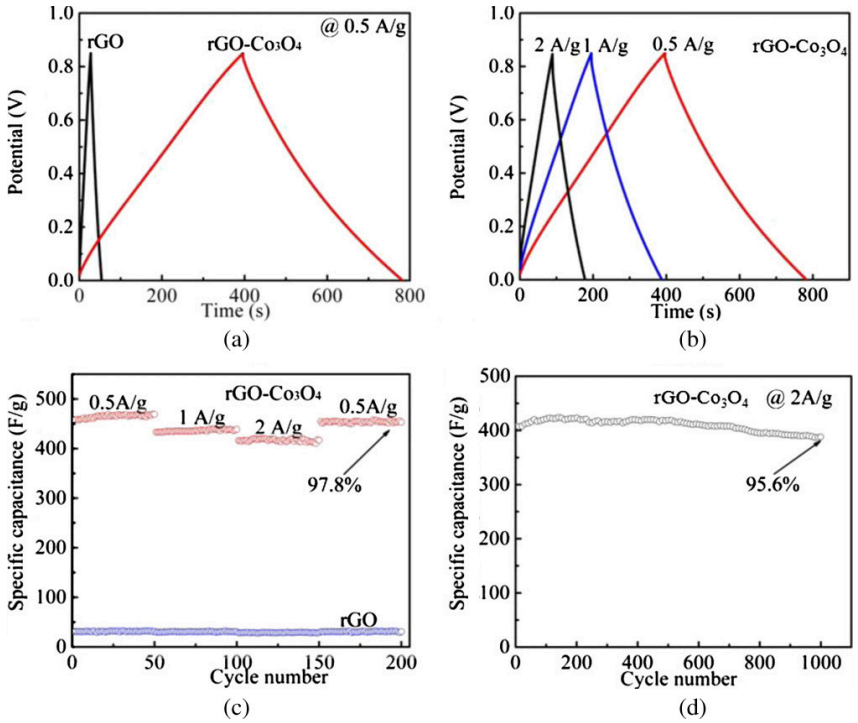

Figure 15. (a) Charge–discharge curves of the rGO and the rGO–Co_3O_4 composite electrodes at a current density of 0.5 A g^{-1}, (b) charge–discharge curves of the rGO–Co_3O_4 composite electrodes at different current densities (0.5, 1.0, and 2.0 A g^{-1}), (c) cycling stability of rGO–Co_3O_4 composite electrodes upon progressively varying the current density, and (d) long-term stability of the rGO–Co_3O_4 composite electrode upon charge/discharge at a current density of 2.0 A g^{-1}. Reproduced from Ref. 130 with permission.

$Co(CH_3COO)_2$ precursor and GO. The resulting composite performed well as a capacitor electrode, exhibiting a high specific capacitance of 472 F g^{-1} at a scan rate of 2 mV s^{-1} in 2 M KOH electrolyte. Figure 15 shows the electrochemical performance of the rGO–Co_3O_4 electrodes at different current densities.[130] Another significant process explored the preparation of electrode materials with the help of Co_3O_4 and 3D graphene. 3D graphene was first synthesized by CVD using nickel foam and nickel substrate. Then, the nickel foam was removed using HCl (3 M) solution at 80 °C, leaving freestanding 3D graphene foams. Nanowires of Co_3O_4 were decorated using a hydrothermal process. The 3D porous structure increased the specific surface area of graphene, and Co_3O_4 acted as a redox site, which helped to increase the

pseudocapacitance. Therefore, the specific capacitance value reached 1100 F g^{-1} at a high current density 10 A g^{-1}. In addition, due to the *in situ* growth of Co_3O_4 on the surface of graphene and the porous network, the rate capability was remarkably high compared to other composites.[131]

Another important metal oxide is Fe_2O_3, which has potential catalytic applications, as an anode for lithium batteries, and in magnetic devices and supercapacitors. Several efforts have reported its use as an electrode material for supercapacitors. However, depending on the morphology and chemical composition, the electrochemical performance in supercapacitor applications was very low. Karthikeyan *et al.* developed a symmetric cell assembled using pristine Fe_3O_4–graphene composites as electrode materials for supercapacitors. The cyclic stability was remarkably high compared to pristine Fe_3O_4. The specific capacitance and energy density were 72 F g^{-1} and 9 Wh kg^{-1}, respectively, with a high current density of 3.75 A g^{-1}. The symmetric cell exhibited remarkable cycle life with over 99.5% columbic efficiency and no change in the capacitance until 100,000 cycles. In addition, the R_{ct} value markedly decreased from 4.7 to 0.6 Ω after 100,000 cycles. The results indicate that magnetite nanoparticles over the surface of the graphene sheets disperse uniformly, and they facilitate electrolyte adsorption and improve the electrical conductivity. Moreover, the composites stabilize the electrode–electrolyte interface and consequently improve the rate capabilities substantially.[132]

5.4. Graphene/conducting polymer composite supercapacitor

Conducting polymers exhibit significantly high values of specific capacitance, but in terms of stability, they are not yet satisfactory. In contrast, carbon-based nanomaterials offer reasonable stability, and thus, composite materials based on graphene and conducting polymers should be considered to achieve high-performance supercapacitor electrodes. Bose *et al.* prepared PSS-modified graphene/PPy composite by *in situ* polymerization of pyrrole in an aqueous dispersion of graphene.[74] The specific capacitance value of the graphene/PPy composite was found to be 267 F g^{-1} at a scan rate of 100 mV s^{-1}. The composite retained almost 90% of the specific capacitance after 500 cycles, corroborating the improved electrochemical cyclic stability of the nanocomposite. Lai *et al.* prepared graphene/PPy composite for supercapacitor applications.[133] High specific capacitance was achieved using an N-doped graphene/PPy electrode with a value of ~393 F g^{-1}. PPy nanowires showed excellent specific capacitance behavior in the presence of graphene sheets.[134] The composite electrode exhibited a high specific capacitance of ~165 F g^{-1}

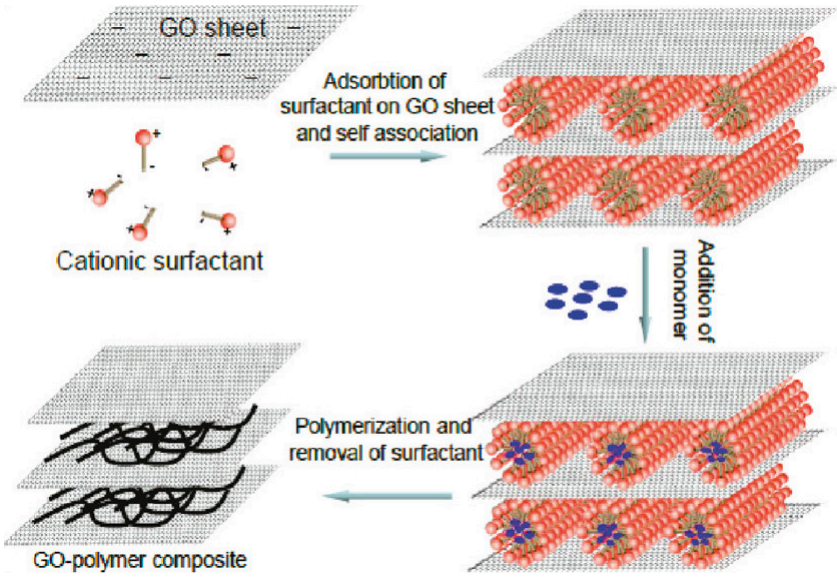

Figure 16. Schematic of the formation process of GOPPy composite. Reproduced from Ref. 135 with permission.

with a nearly ideal rectangular CV with increasing voltage scanning rates and high electrochemical cyclic stability. The retention of specific capacitance was more than 92% after 1000 charge–discharge cycles at a current density of 1 A g^{-1}. Zhang *et al.* demonstrated the preparation of a sandwich composite of layered GO and PPy, as shown in Figure 16.[135] The layered structure of the solid GO sample with stacked GO sheets can be seen in the FESEM image shown in Figure 17. The composite exhibited excellent electrocapacitive performance with a high specific capacitance over 500 F g^{-1}. It was found that the retention of the original capacitance was over 70% for the composite electrode GOPPy-F after 1000 cycles. In contrast, only 30% was retained for the pure PPy-F electrode, indicating a much better cycle ability of the composite material than the pure polymer electrode. Davies *et al.* demonstrated a pulsed electropolymerization technique to create a flexible, uniform graphene/PPy composite for supercapacitor electrodes.[136] Figure 18 shows the electrochemical performance of graphene sheets and their composite with PPy. It is evident from the CV curves that the pseudocapacitance due to PPy significantly enhanced the specific capacitance of the composites. The specific capacitance of graphene sheets was recorded as 63 F g^{-1}. In contrast, the specific capacitance of the graphene/PPy composite was found to be 237 F g^{-1} at a scan rate of 10 mV s^{-1}. The power density of graphene sheets and the

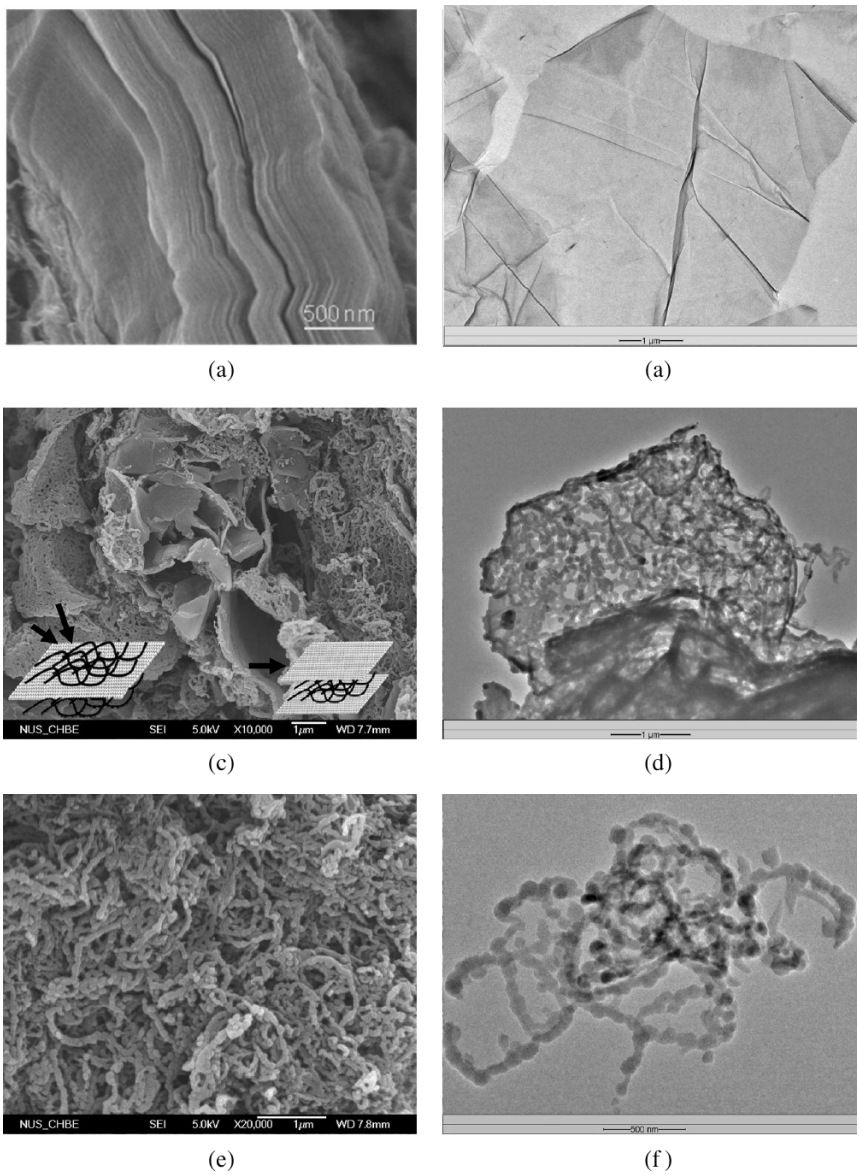

Figure 17. FESEM images of (a) GO, (c) GOPPy-F, and (e) PPy-F and TEM images of (b) GO, (d) GOPPy-F, and (f) PPy-F. Reproduced from Ref. 135 with permission.

composites were 315 and 1184 W kg^{-1}, respectively, at a scan rate of 10 mV s^{-1}. Chang *et al.* synthesized graphene/PPy composites by the electrooxidation of 0.1 M pyrrole in an aqueous solution containing appropriate amounts of GO.[137] GO was reduced to graphene during the electropolymerization of

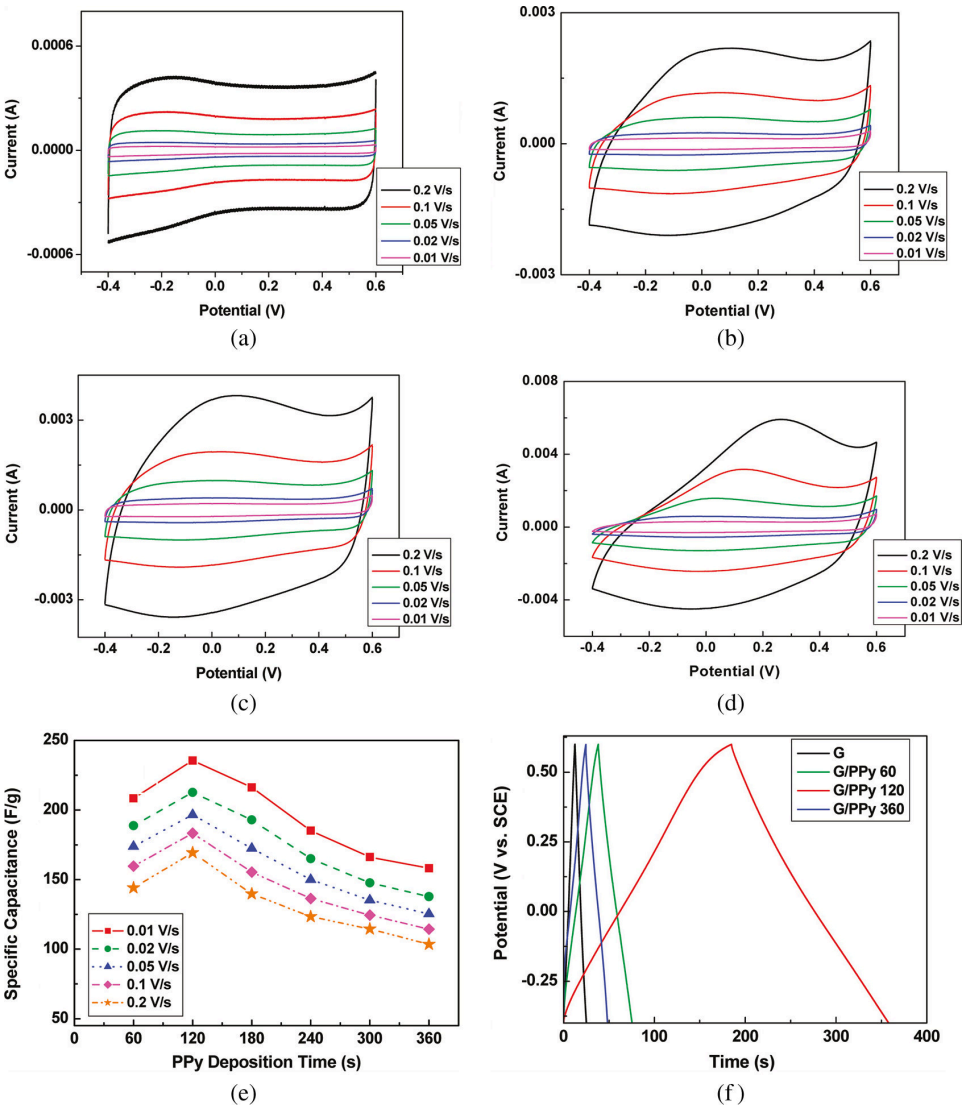

Figure 18. CV curves for the (a) G, (b) G/PPy 60, (c) G/PPy 120, and (d) G/PPy 360 electrodes in a KCl solution between –0.4 and 0.6 V versus SCE at scan rates of 0.01, 0.02, 0.05, 0.1, and 0.2 V s^{-1}. (e) Specific capacitance of all G/PPy electrodes by electrodeposition time, as determined by CV with different scan rates. (f) Galvanostatic charge–discharge curves for the G, G/PPy 60, G/PPy 120, and G/PPy 360 electrodes for comparison at a current density of 1 A g^{-1} between –0.4 and 0.6 V versus SCE in 1 M KCl. Reproduced from Ref. 136 with permission.

pyrrole. The specific capacitance (424 F g^{-1}) of the composites was estimated from galvanostatic discharge curves in 1 M H_2SO_4 at a current density of 1 A g^{-1}. Wang *et al.* found that the specific capacitance of the rGO/PPy composite was 224 F g^{-1} at a current density of 240 A g^{-1} within electrochemical windows of 0.8 V in 3 M KCl aqueous solution.[138] Ding *et al.* described the preparation of rGO/CNT/PPy ternary composites by the electropolymerization of pyrrole in the presence of functionalized graphene and oxidized CNTs.[139] The specific capacitance of the ternary composite film was 300 F g^{-1} at a current density of 1 A g^{-1}. After 1000 cycling tests, the capacitance decreased by only about 2%. The advantage of the preparation of graphene/PPy composite by one-step electrochemical method over *in situ* polymerization is procedural simplicity. In addition to the easy synthesis of the rGO/PPy composite, this protocol provides no polymeric binders, and conducting materials are needed while preparing supercapacitors.

Liu *et al.* synthesized high-quality GO/PANi composites by the *in situ* polymerization of aniline.[140] Due to the synergistic effects, the as-synthesized GO-PANi electrode material exhibited higher specific capacitance (200 F g^{-1}) at a current density of 1.0 A g^{-1}. Wang *et al.* showed that the specific capacitance of GO/PANi composites is largely dependent on the mesh size of the graphite materials.[141] It was proposed that the composites were combined through electrostatic interaction (doping process), hydrogen bonding, and π–π stacking interaction. The specific capacitance of the GO/PANi (GO: aniline = 1:200) composites were recorded as 746 F g^{-1} (using 12,500-mesh graphite as a starting material) at a current density of 2 A g^{-1}. In contrast, the specific capacitance was decreased to 627 F g^{-1} when using 500-mesh graphite as a starting material with the GO:aniline ratio fixed to 1:50. The improved specific capacitance is attributed to the synergistic effect between the two components. The effect of rGO on the electrochemical properties of the activated carbon cloth (ACC)/PANi composite was investigated.[142] The charge-transfer resistance of ACC/PANi was decreased with the addition of rGO due to the interactions between rGO, ACC, and PANi. The as-prepared composite with rGO showed improved rate performance and cyclability as a supercapacitor electrode.

Graphene/PANi nanofiber composites were prepared by the *in situ* polymerization of aniline monomer in the presence of GO dispersion in acidic medium.[58] The effect of the mass feed ratio of GO on the specific capacitance and electrical conductivity was investigated. With different concentrations of aniline monomer relative to the GO content (10, 50, and 80%), the obtained composites were designed as PAGO10, PAGO50, and PAGO80, respectively. Table 1 shows the electrical conductivity and specific

Table 1. List of the conductivities of all composites and the specific capacitances (f/g) of the composites at different current loadings based on the discharge branch in 2 M H_2SO_4.[58]

		Cycle 1			Cycle 5		
Samples	**Conductivity (S m^{-1})**	**0.1 A g^{-1}**	**0.5 A g^{-1}**	**1 A g^{-1}**	**0.1 A g^{-1}**	**0.5 A g^{-1}**	**1 A g^{-1}**
PANi-F	10.6	420	145	140	280	140	130
PAGO10	231.3	320	256	199	225	219	170
PAGO50	15.5	207	147	130	195	147	130
PAGO80	0.4	158	148	143	165	148	143
GO	0.2	0.8	—	—	0.8	—	—
PAG10	168.7	214	284	168	212	213	179
PAG50	22.8	180	175	135	155	154	128
PAG80	143.0	480	260	210	410	260	200
GR	277.2	20	—	—	20	—	—

capacitance of GO, PANi-F, and their composites before and after reduction. Gomez *et al.* prepared graphene/PANi composites by *in situ* polymerization of aniline monomer.[143] The resulting composite was dissolved in *N*-methyl-2-pyrrolidone (NMP). Nafion was used as a binder, and cast onto the graphite electrode. A specific capacitance of 300–500 F g^{-1} at a current density of 0.1 Ag^{-1} was observed with graphene/PANi composite materials. Xu *et al.* showed the preparation of hierarchical composites of PANi nanowire arrays on GO sheets for energy storage applications.[144] The morphologies of PANi nanowires were controlled by adjusting the ratios of aniline to GO, which was attributed to different nucleation processes. The nucleation and growth mechanism of PANi nanowires on GO sheets are shown in Figure 19. The composites showed a high specific capacitance of 555 F g^{-1} at a current density of 0.2 A g^{-1}, and kept 92% of its original capacitance after 2000 consecutive charge–discharge cycles. In contrast, the pure PANi kept only 72% of its initial capacitance. The better stability of PANi/GO composite came from the synergistic effect of GO and the PANi nanowire arrays. The specific capacitance of the graphene/PANi composites decreased to a small extent with the introduction of CNTs as a filler.[145] It was found that the specific capacitance of the graphene/CNT/PANi composite in 6 M KOH was 1046 F g^{-1}. The capacitance value for a graphene/PANi hybrid was recorded as 1035 F g^{-1}, and that of pure PANi was 115 F g^{-1}. It was also found that the cyclic stability of the graphene/CNT/PANi composite was significantly

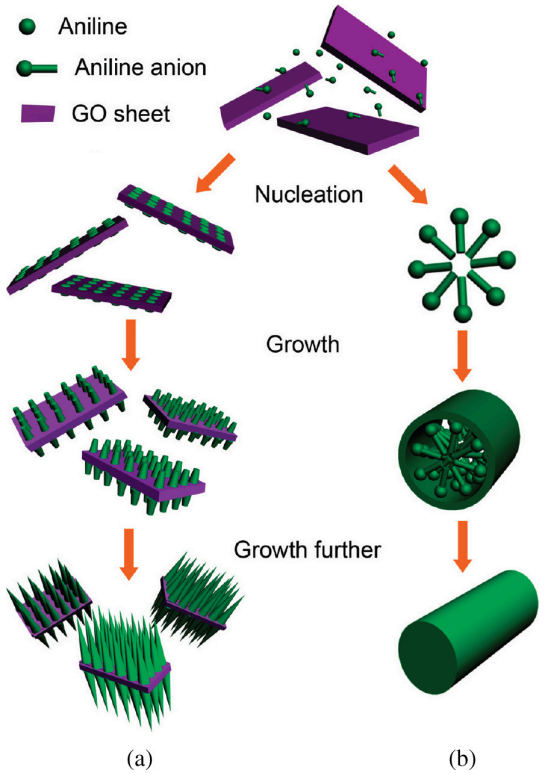

Figure 19. Schematic of nucleation and growth mechanism of PANi nanowires: (a) heterogeneous nucleation on GO nanosheets; (b) homogeneous nucleation in bulk solution. Reproduced from Ref. 144 with permission.

higher than that of graphene/PANi or CNT/PANi composites. PANi-grafted rGO (PANi-g-rGO) composite was prepared for supercapacitor applications by the *in situ* chemical oxidative grafting of aniline in the presence GO, as shown in Figure 20.[146] The electrical conductivity and specific capacitance of the composite materials were found to be 866 S m^{-1} and 250 F g^{-1}, indicating its utility as a supercapacitor electrode for green energy storage applications. Yan *et al.* reported a very high specific capacitance of 1046 F g^{-1} at a scan rate 1 mV s^{-1} for graphene/PANi composites prepared by *in situ* polymerization.[147] They achieved a very high energy and power density of 39 W h kg^{-1} and 70 kW kg^{-1} for the composites, respectively, suggesting their utility for energy supercapacitor applications. Wu *et al.* designed a supercapacitor device using graphene/PANi composite films, as shown in Figure 21.[17] The device showed a large electrochemical capacitance (210 F g^{-1})

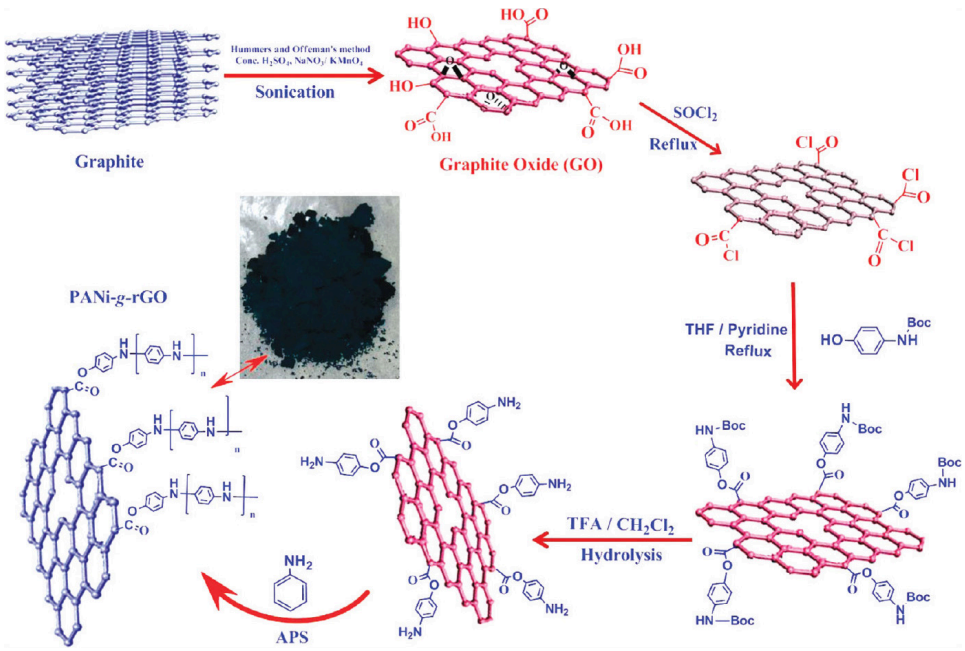

Figure 20. Schematic governing the preparation of PANi-g-rGO with a digital picture of the sample in the middle. Reproduced from Ref. 146 with permission.

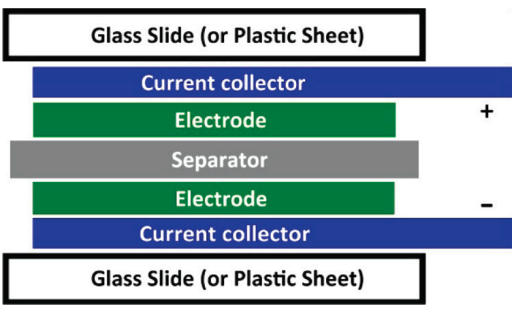

Figure 21. Schematic illustration of a supercapacitor cell. Reproduced from Ref. 17 with permission.

at a discharge rate of 0.3 A g^{-1}, and exhibited greatly improved electrochemical stability and rate performance.

Zhang *et al.* showed the one-step electropolymerization of aniline in the presence of GO dispersions.[148] Different amounts of GO were utilized to investigate the effect on the electrochemical performance of the composite

electrode. The highest specific capacitance of the GO/PANi composite was found to be 1136.4 F g^{-1} with a GO content of 10 mg L^{-1} at a scan rate of 1 mV s^{-1}. The GO/PANi composite exhibited good cyclic stability and more than 89% retention of its initial capacitance after 1000 cycles. Wang *et al.* reported the synthesis of graphene/PANi composite paper by *in situ* anodic electropolymerization.[149] Graphene paper was used as the working electrode, and the PANi was deposited homogeneously on its surfaces. The effect of the durations (60, 300, and 900 s) of electropolymerization on the electrochemical performance was investigated in detail. It was found that the composite material obtained with 900 s of polymerization showed the highest specific capacitance of 233 F g^{-1}, which is much larger than that of the pristine graphene paper (147 F g^{-1}). Hu *et al.* prepared a highly porous graphene/PANi composite electrode by *in situ* electrochemical polymerization on an Indium Tin Oxide (ITO) substrate in a reverse micelle electrolyte.[27] A very high specific capacitance of 878 F g^{-1} could be achieved at a current density of 1 A g^{-1}. Feng *et al.* synthesized graphene/PANi composite film on ITO substrate by the one-step electrochemical polymerization of aniline.[150] The supercapacitor showed a high specific capacitance of 640 F g^{-1} with a retention life of 90% after 1000 charge/discharge cycles.

5.5. Applications of graphene-based supercapacitor

Supercapacitors can be regarded as the next generation of energy storage devices. Based on the high power density of supercapacitors, there are several applications, such as the starter for fuel-efficient stop–start systems, public transport, emergency management, industry, solar energy storage, etc.

5.5.1. Starter for fuel-efficient stop–start systems

The high power capability of EDLC has applications where short-time power peaks are required. Supercapacitors can supply high current for a short duration of time required for the starting of heavy diesel engines. Moreover, supercapacitors can work in a wide temperature range, and in certain cases, its efficiency is improved at high temperature. The ideal condition for lead acid batteries is ambient temperature. In cold weather, a car's engine faces problems in terms of ignition and starting. This is attributed to the battery electrolyte becoming more viscous at temperatures below zero, and also to chemical processes slowing down in such conditions. In contrast, a supercapacitor stores electrical energy by an electrostatic charge storage mechanism,

and is not affected by wide variation of temperature. Thus, supercapacitors are useful for the cold starting of diesel engines for trucks and trains, and for providing emergency power to various subsystems.

5.5.2. Public transport

In the automotive industry, ultracapacitors are used for regenerative braking applications due to their ability to charge quickly. The heavy hybrid vehicle market is already well acquainted with the ultracapacitor market, and has attracted significant attention worldwide. The ultracapacitors are used to store and reuse the energy that comes from regenerative braking. The mean power of a small car is ~30 kW, and its peak power should be ~60 kW. Supercapacitors can supply power needed by an electrical vehicle to respond to the city road traffic conditions. However, to insure a certain amount of autonomy, it is essential to hybridize supercapacitors with batteries. The use of graphene-based supercapacitors in public transport may reduce the emission of CO_2 from the engine, and it could be the greenest and most economical way of powering inner-city buses. It has been proposed by a Chinese company and its US partner that buses can store energy by charging ultracapacitor banks at a bus stop. The buses can also capture energy from braking and store energy directly from solar panels.

5.5.3. Emergency management

The ability to fast charging and discharging makes ultracapacitors suitable for building "intelligent" power management systems, or smart grids. This kind of electrical grid system can provide flexibility to the suppliers and consumers of electricity. The supercapacitors accumulate excessive energy when the current supply exceeds demand. This energy is released to support periods of excessive demand. Uninterruptable power supplies (UPS) may find some economic interest in the use of electrochemical double-layer (ECDL) capacitors in the area of power quality systems and telecom backup stations.

Supercapacitors are frequently used in electrical blade pitch systems for wind turbines. The main role of supercapacitors in such systems is to constantly adjust the positions of the turbine blades to ensure safe rotor speed (which is known as pitch control). In addition, supercapacitors can provide backup power when the main system experiences power failure. The supercapacitors provide an independent source of power for shutting down the system and smoothing the flow of wind farm output to consumers.

5.5.4. Other applications

There are many diverse applications of supercapacitors in the industrial sector. Some examples include elevators, cranes, pallet trucks in the electric transportation domain, as well as loaders, shovel trucks, forklifts, robots, portable welding machines, radars, and torpedoes, and also memory supplies in phones or computers, and pulsed lasers. Supercapacitors can store solar energy directly from solar panels and can deliver the stored energy on demand.

6. Conclusions

Chemically derived graphene and related composite materials have attracted significant attention for the fabrication of supercapacitor devices. rGO, surface-modified graphene, metal oxide/graphene, metal-nanoparticle-decorated graphene, and conducting polymer/graphene composites have been synthesized for the development of highly efficient energy storage supercapacitor devices. The specific capacitance of rGO is largely dependent on the presence of remaining oxygen functional groups on the surface of graphene. The specific capacitance of graphene can be increased by the introduction of hydrophilic functional groups by proper surface modification of graphene. The wettability of the surface-modified graphene with the electrolyte is improved compared to rGO, and takes part in the faradic reaction. Thus, the specific capacitance is enhanced due to the pseudocapacitance. Similarly, metal oxide/graphene and metal-nanoparticle-decorated graphene take part in the faradic reaction, and thus, the specific capacitance, energy density, and power density are improved significantly compared with pure rGO. The use of metal oxide in supercapacitors is well established due to the faradic reaction, which results in high specific capacitance. The electrochemical stability and performance are enhanced significantly after their hybridization with graphene. Depending on the structure, morphology, and types of metal, the specific capacitance of the composites has been found to be 800–1200 F g^{-1}. Among the different types of metal oxide, MnO_2/graphene composites have been extensively studied, and show excellent electrochemical performance. The energy density and power density are in the range of 20–60 Wh kg^{-1} and 80–100 kW kg^{-1}, respectively. PPy and PANi have been used to prepare graphene-based composite materials for the development of high-performance supercapacitor devices. The specific capacitance of the PPy and PANi-based graphene composite depends on the morphology of the corresponding conducting polymer. It has been found that the specific capacitance

of nanostructured PANi or PPy perform well in comparison to that of the microstructured PPy or PANi-based graphene composites. The energy density of the graphene and related composite electrodes can be further increased by replacing aqueous electrolyte with the organic electrolyte. In some cases, the operating voltage is increased to 7 V from 1–2 V for aqueous electrolyte. However, the energy density of graphene-based supercapacitors is far below that of lead acid batteries. Thus, there is sufficient need to carry out further research on how to improve the energy density of supercapacitors for the complete replacement of existing batteries.

Acknowledgments

This study was supported by the Converging Research Center Program (2013K000404) through the Ministry of Science, ICT & Future Planning and the Basic Science Research Program through the National Research Foundation (NRF) funded by the Ministry of Education of Korea (NRF-2013R1A1A2011608). It was also supported by research funds of Chonbuk National University in 2013. Dr. Tapas Kuila is also thankful to DST Inspire Programme, New Delhi, India and Prof. Gautam Biswas, the Director of CSIR-CMERI, Durgapur, India.

References

1. Zhu, Y.; Murali, S.; Stoller, M. D.; Ganesh, K. J.; Cai, W.; Ferreira, P. J.; Pirkle, A.; Wallace, R. M.; Cychosz, K. A.; Thommes, M.; Su, D.; Stach, E. A.; Ruoff, R. S. *Science* **2011**, *332*, 1537.
2. Xu, B.; Yue, S.; Sui, Z.; Zhang, X.; Hou, S.; Cao, G.; Yang, Y. *Energy Environ. Sci.* **2011**, *4*, 2826.
3. Zhang, D.; Zhang, X.; Chen, Y.; Wang, C.; Ma, Y. *Electrochim. Acta* **2012**, *69*, 364.
4. Stine, R.; Robinson, J. T.; Sheehan, P. E.; Tamanaha, C. R. *Adv. Mater.* **2010**, *22*, 5297.
5. He, Q.; Wu, S.; Gao, S.; Cao, X.; Yin, Z.; Li, H.; Chen, P.; Zhang, H. *ACS Nano* **2011**, *5*, 5038.
6. Eda, G.; Fanchini, G.; Chhowalla, M. *Nat. Nanotechnol.* **2008**, *3*, 270.
7. Yuan, W.; Li, B.; Li, L. *Appl. Surf. Sci.* **2011**, *257*, 10183.
8. Rangel, E.; Ramírez-Arellano, J. M.; Carrillo, I.; Magana, L. F. *Int. J. Hydrogen Energ.* **2011**, *36*, 13657.
9. Du, A.; Zhu, Z.; Smith, S. C. *J. Am. Chem. Soc.* **2010**, *132*, 2876.
10. Cho, J. H.; Yang, S. J.; Lee, K.; Park, C. R. *Carbon* **2011**, *36*, 12286.

11. Ng, Y. H.; Iwase, A.; Bell, N. J.; Kudo, A.; Amal, R. *Catal. Today* **2011**, *164*, 353.
12. Wu, S.; Yin, Z.; He, Q.; Huang, X.; Zhou, X.; Zhang, H. *J. Phys. Chem. C* **2010**, *114*, 11816.
13. Yun, J. M.; Yeo, J. S.; Kim, J.; Jeong, H. G.; Kim, D. Y.; Noh, Y. J.; Kim, S. S.; Ku, B. C.; Na, S. I. *Adv. Mater.* **2011**, *23*, 4923.
14. Yoo, J. J.; Balakrishnan, K.; Huang, J.; Meunier, V.; Sumpter, B. G.; Srivastava, A.; Conway, M.; Reddy, A. L. M.; Yu, J.; Vajtai, R.; Ayayan, P. M. *Nano Lett.* **2011**, *11*, 1423.
15. Kuila, T.; Mishra, A. K.; Khanra, P.; Kim, N. H.; Uddin, Md. E.; Lee, J. H. *Langmuir* **2012**, *28*, 9825.
16. Yang, X.; Zhu, J.; Qiu, L.; Li, D. *Adv. Mater.* **2011**, *23*, 2833.
17. Wu, Q.; Xu, Y.; Yao, Z.; Liu, A.; Shi, G. *ACS Nano* **2010**, *4*, 1963.
18. Pandolfo, A. G.; Hollenkamp, A. F. *J. Power Sources* **2006**, *157*, 11.
19. Zhao, B.; Liu, P.; Jiang, Y.; Pan, D.; Tao, H.; Song, J.; Fang, T.; Xu, W. *J. Power Sources* **2012**, *198*, 423.
20. Kim, C. H.; Pyun, S. I.; Shin, H. C. *J. Electrochem. Soc.* **2002**, *149*, A93.
21. Probstle, H.; Schmitt, C.; Fricke, J. *J. Power Sources* **2002**, *105*, 189.
22. Li, Q. A.; Jiang, R. R.; Dou, Y. Q.; Wu, Z. X.; Huang, T.; Feng, D.; Yang, J. P.; Yu, A.S.; Zhao, D. Y. *Carbon* **2011**, *49*, 1248.
23. Frackowiak, E.; Beguin, F. *Carbon* **2002**, *40*, 1775.
24. Geim, A. K.; Novoselov, K. S. *Nat. Mater.* **2007**, *6*, 183.
25. Hernandez, Y.; Nicolosi, V.; Lotya, M.; Blighe, F. M.; Sun, Z.; De, S.; McGovern, I. T.; Holland, B.; Byrne, M.; Gun'ko, Y. K.; Boland, J. J.; Niraj, P.; Duesberg, G.; Krishnamurthy, S.; Goodhue, R.; Hutchison, J.; Scardaci, V.; Ferrari, A. C.; Coleman, J. N. *Nat. Nanotechnol.* **2008**, *3*, 563.
26. Kim, K. S.; Zhao, Y.; Jang, H.; Lee, S. Y.; Kim, J. M.; Kim, K. S.; Ahn, J. H.; Kim, P.; Choi, J. Y.; Hong, B. H. *Nature* **2009**, *457*, 706.
27. Hu, L.; Tu, J.; Jiao, S.; Hou, J.; Zhu, H.; Fray, D. *J. Phys. Chem. Chem. Phys.* **2012**, *14*, 15652.
28. Kuila, T.; Bhadra, S.; Yao, D.; Kim, N. H.; Bose, S.; Lee, J. H. *Prog. Polym. Sci.* **2010**, *35*, 1350.
29. Xia, F.; Farmer, D. B.; Lin, Y. M.; Avouris, P. *Nano Lett.* **2010**, *10*, 715.
30. Liu, Y.; Yu, D.; Zeng, C.; Miao, Z.; Dai, L. *Langmuir* **2010**, *26*, 6158.
31. Lim, C. X.; Hoh, H. Y.; Ang, P. K.; Loh, K. P. *Anal. Chem.* **2010**, *82*, 7387.
32. Yang, K.; Wan, J.; Zhang, S.; Zhang, Y.; Lee, S. T.; Liu, Z. *ACS Nano* **2011**, *5*, 516.
33. Khanra, P.; Kuila, T.; Bae, S. H.; Kim, N. H.; Lee, J. H. *J. Mater. Chem.* **2012**, *22*, 24403.
34. Novoselov, K. S. *Science* **2004**, *306*, 666.

35. Ferrari, A. C.; Meyer, J. C.; Scardaci, V.; Casiraghi, C.; Lazzeri, M.; Mauri, F.; Piscanec, S.; Jiang, D.; Novoselov, K. S.; Roth, S.; Geim, A. K. *Phys. Rev. Lett.* **2006**, *97*, 187401.
36. Mattevi, C.; Kim, H.; Chhowalla, M. *J. Mater. Chem.* **2011**, *21*, 3324.
37. Kim, K. S.; Zhao, Y.; Jang, H.; Lee, S. Y.; Kim, J. M.; Kim, K. S.; Ahn, J. H.; Kim, P.; Choi, J. Y.; Hong, B. H. *Nature* **2009**, *457*, 706.
38. Byun, S. J.; Lim, H.; Shin, G. Y.; Han, T. H.; Oh, S. H.; Ahn, J. H.; Choi, H. C.; Lee, T. W. *J. Phys. Chem. Lett.* **2011**, *2*, 493.
39. Kim, K. S.; Lee, H. J.; Lee, C.; Lee, S. K.; Jang, H.; Ahn, J. H.; Kim, J. H.; Lee, H. J. *ACS Nano* **2011**, *5*, 5107.
40. Sun, Z.; Yan, Z.; Yao, J.; Beitler, E.; Zhu, Y.; Tour, J. M. *Nature* **2010**, *468*, 549.
41. Peng, Z.; Yan, Z.; Sun, Z.; Tour, J. M. *ACS Nano* **2011**, *5*, 8241.
42. Yan, Z.; Peng, Z.; Sun, Z.; Yao, J.; Zhu, Y.; Ajayan, P. M.; Tour, J. M. *ACS Nano* **2011**, *5*, 8187.
43. Kuila, T.; Khanra, P.; Bose, S.; Kim, N. H.; Ku, B. C.; Moon, B.; Lee, J. H. *Nanotechnology* **2011**, *22*, 305710.
44. Kuila, T.; Bose, S.; Khanra, P.; Mishra, A. K.; Kim, N. H.; Lee, J. H. *Carbon* **2012**, *50*, 914.
45. Park, S.; Dikin, D. A.; Nguyen, S. T.; Ruoff, R. S. *J. Phys. Chem. C* **2009**, *113*, 15801.
46. Kuila, T.; Mishra, A. K.; Khanra, P.; Kim, N. H.; Lee, J. H. *Nanoscale* **2013**, *5*, 52.
47. Kuila, T.; Bose, S.; Mishra, A. K.; Khanra, P.; Kim, N. H.; Lee, J. H. *Prog. Mater. Sci.* **2012**, *57*, 1061.
48. Brezesinsk, T.; Wang, J.; Tolbert, S. H.; Dunn, B. *Nat. Mater.* **2010**, *9*, 146.
49. Xia, H.; Meng, Y. S.; Yuan, G.; Cui, C.; Lu, L. *Electrochem. Solid-State Lett.* **2012**, *15*, A60.
50. Liang, K.; Tang, X.; Hu, W. *J. Mater. Chem.* **2012**, *22*, 11062.
51. Lang, X.; Hirata, A.; Fujita, T.; Chen, M. *Nat. Nanotechnol.* **2011**, *6*, 232.
52. Xia, X. H.; Gu, C. D.; Zhao, X. B. *RSC Adv.* **2012**, *2*, 1835.
53. Tang, W.; Liu, L.; Tian, S.; Yue, Y.; Wu, Y.; Zhu, K. *Chem. Commun.* **2011**, *47*, 10058.
54. Li, R.; Ren, X.; Zhang, F.; Du, C.; Liu, L. *Chem. Commun.* **2012**, *48*, 5010.
55. Zhao, B.; Song, J.; Liu, P.; Xu, W.; Fang, T.; Jiao, Z.; Zhang, H.; Jiang, Y. *J. Mater. Chem.* **2011**, *21*, 18792.
56. Zhou, W.; Liu, J.; Chen, T.; Tan, K. S.; Jia, X.; Luo, Z.; Cong, C.; Yang, H.; Li, C. M.; Yu, T. *Phys. Chem. Chem. Phys.* **2011**, *13*, 14462.
57. Li, Z.; Mi, Y.; Liu, X.; Liu, S.; Yang, S.; Wang, J. *J. Mater. Chem.* **2011**, *21*, 14706.

58. Zhang, K.; Zhang, L. L.; Zhao, X. S.; Wu, J. *Chem. Mater.* **2010**, *22*, 1392.
59. Jurewicz, K.; Delpeux, S.; Bertagna, V.; Beguin, F.; Frackowiak, E. *Chem. Phys. Lett.* 2001, **347**, 36.
60. Laforgue, A.; Simon, P.; Sarrazin, C.; Fauvarque, J. F. *J. Power Sources* **1999**, *80*, 142.
61. Cheng, Q.; Tang, J.; Ma, J.; Zhang, H.; Shinya, N.; Qin, L. C. *Phys. Chem. Chem. Phys.* **2011**, *13*, 17615.
62. Huang, Z. D.; Zhang, B.; Oh, S. W.; Zheng, Q. B.; Lin, X. Y.; Youself, N.; Kim, J. K. *J. Mater. Chem.* **2012**, *22*, 3591.
63. Beidaghi, M.; Wang, C. *Adv. Funct. Mater.* **2012**, *22*, 4501.
64. Li, F.; Song, J.; Yang, H.; Gan, S.; Zhang, Q.; Han, D.; Ivaska, A.; Niu, L. *Nanotechnology* **2009**, *20*, 455602.
65. Wang, W.; Hao, Q.; Lei, W.; Xia, X.; Wang, X. *RSC Adv.* **2012**, *2*, 10268.
66. Li, X.; Cai, W.; An, J.; Kim, S.; Nah, J.; Yang, D.; Piner, R.; Velamakanni, A.; Jung, I.; Tutuc, E.; Banerjee, S. K.; Colombo, L.; Ruoff, R. S. *Science* **2009**, *324*, 1312.
67. Bae, S.; Kim, H.; Lee, Y.; Xu, X.; Park, J. S.; Zheng, Y.; Balakrishnan, J.; Lei, T.; Kim, H. R.; Song, Y. I.; Kim, Y. J.; Kim, K. S.; Ozyilmaz, B.; Ahn, J. H.; Lee, B. H.; Iijima, S. *Nat. Nanotechnol.* **2010**, *5*, 574.
68. Guermoune, A.; Chari, T.; Popescu, F.; Sabri, S. S.; Guillemette, J.; Skulason, H. S.; Szkopek, T.; Siaj, M. *Carbon* **2011**, *49*, 4204.
69. Liu, Z. L.; Kang, C. Y.; Fan, L. L.; Xu, P. S.; Zou, C. W. *J. Appl. Phys.* **2013**, *113*, 014311.
70. Hao, R.; Qian, W.; Zhang, L.; Hou, Y. *Chem. Commun.* **2008**, 6576.
71. An, X.; Simmons, T.; Shah, R.; Wolfe, C.; Lewis, K. M.; Washington, M.; Nayak, S. K.; Talapatra, S.; Kar, S. *Nano Lett.* **2010**, *10*, 4295.
72. Bose, S.; Kuila, T.; Mishra, A. K.; Kim, N. H.; Lee, J. H. *Nanotechnology* **2011**, *22*, 405603.
73. Liu, N.; Luo, F.; Wu, H.; Liu, Y.; Zhang, C.; Chen, J. *Adv. Funct. Mater.* **2008**, *18*, 1518.
74. Bose, S.; Kim, N. H.; Kuila, T.; Lau, K. T.; Lee, J. H. *Nanotechnology* **2011**, *22*, 295202.
75. Du, Q.; Zheng, M.; Zhang, L.; Wang, Y.; Chen, J.; Xue, L.; Dai, W.; Ji, G.; Cao, J. *Electrochim. Acta* **2010**, *55*, 3897.
76. Jin, Y.; Jia, M.; Zhang, M.; Wen, Q. *Appl. Surf. Sci.* **2013**, *264*, 787.
77. Zhang, L.; Shi, G. *J. Phys. Chem. C* **2011**, *115*, 17206.
78. Ferrari, A. *Solid State Commun.* **2007**, *143*, 47.
79. Ferrari, A. C.; Meyer, J. C.; Scardaci, C.; Lazzeeri, M.; Mauri, F.; Piscanec, S.; Jiang, D.; Novoselov, K. S.; Roth, S.; Geim, A. K. *Phys. Rev. Lett.* **2006**, *97*, 187401.

80. Wang, Y. Y.; Ni, Z. H.; Yu, T.; Shen, Z. X.; Wang, H. M.; Wu, Y. H.; Chen, W.; Wee, A. T. S. *J. Phys. Chem. C* **2008**, *112*, 10637.
81. Pham, V. H.; Cuong, T. V.; Dang, T. T.; Hur, S. H.; Kong, B. S.; Kim, E. J.; Shin, E. W.; Chung, J. S. *J. Mater. Chem.* **2011**, *21*, 11312.
82. Bose, S.; Kuila, T.; Uddin, Md. E.; Kim, N. H.; Lau, A. K. T.; Lee, J. H. *Polymer* **2010**, *51*, 5921.
83. Zhang, K.; Zhang, L. L.; Zhao, X. S.; Wu, J. *Chem. Mater.* **2010**, *22*, 1392–1401.
84. Kuila, T.; Bose, S.; Khanra, P.; Mishra, A. K.; Kim, N. H.; Lee, J. H. *Biosens. Bioelectron.* **2011**, *26*, 4637.
85. Joung, D.; Chunder, A.; Zhai, L.; Khondaker, S. I. *Nanotechnology* **2010**, *21*, 165202.
86. Lee, C. G.; Park, S.; Ruoff, R. S.; Dodabalapur, A. *Appl. Phys. Lett.* **2009**, *95*, 023304.
87. Chen, Y.; Zhang, X.; Zhang, D.; Yu, P.; Ma, Y. *Carbon* **2011**, *49*, 573.
88. http://www.sciencedaily.com/releases/2010/03/100317161952.htm
89. Yuan, W.; Li, B.; Li, L. *Appl. Surf. Sci.* **2011**, *257*, 10183.
90. Chen, X. C.; Wei, W.; Lv, W.; Su, F. Y.; He, Y. B.; Li, B.; Kang, F.; Yang, Q. H. *Chem. Commun.* **2012**, *48*, 5904.
91. Xin, X.; Zhou, X.; Wang, F.; Yao, X.; Xu, X.; Zhu, Y.; Liu, Z. *J. Mater. Chem.* **2012**, *22*, 7724.
92. Qin, Z.; Zhou, X.; Xia, Y.; Tang, C.; Liu, Z. *J. Mater. Chem.* **2012**, *22*, 21144.
93. Wang, X.; Zhou, X.; Yao, K.; Zhang, J.; Liu, Z. *Carbon* **2011**, *49*, 133.
94. Fan, L. Z.; Liu, J. L.; Ud-Din, R.; Yan, X.; Qu, X. *Carbon* **2012**, *50*, 3724.
95. Liu, C.; Yu, Z.; Neff, D.; Zhamu, A.; Jang, B. Z. *Nano Lett.* **2010**, *10*, 4863.
96. Zhang, L. L.; Zhao, X.; Stoller, M. D.; Zhu, Y.; Ji, H.; Murali, S.; Wu, Y.; Perales, S.; Clevenger, B.; Ruoff, R. S. *Nano Lett.* **2012**, *12*, 1806.
97. Jin, Y.; Jia, M.; Zhang, M.; Wen, Q. *Appl. Surf. Sci.* **2013**, *264*, 787.
98. Lei, Z.; Lu, L.; Zhao, X. S. *Energy Environ. Sci.* **2012**, *5*, 6391.
99. Perera, S. D.; Mariano, R. G.; Nijem, N.; Chabal, Y.; Ferraris, J. P.; Balkus, Jr., K. J. *J. Power Sources* **2012**, *215*, 1.
100. Chen, P.; Yang, J. J.; Li, S. S.; Xiao, T. Y.; Qian, Y. H.; Yu, S. H. *Nano Energy* **2013**, *2*, 249.
101. Lee, W. D.; Ko, J. M.; Kim, J. D. *Electrochim. Acta* **2012**, *85*, 459.
102. Li, Y.; Zijll, M. V.; Chiang, S.; Pan, N. *J. Power Sources* **2011**, *196*, 6003.
103. Jiang, B.; Tian, C.; Wang, L.; Sun, L.; Chen, C.; Nong, X.; Qiao, Y.; Fu, H. *Appl. Surf. Sci.* **2012**, *258*, 3438.
104. Sun, D.; Yan, X.; Lang, J.; Xue, Q. *J. Power Sources* **2013**, *222*, 52.
105. Zhu, Y.; Murali, S.; Stoller, M. D.; Velamakanni, A.; Piner, R. D.; Ruoff, R. S. *Carbon* **2010**, *48*, 2118.

106. Chen, Y.; Zhang, X.; Zhang, D.; Ma, Y. *Mater. Lett.* **2012**, *68*, 475.
107. Le, L. T.; Ervin, M. H.; Qiu, H.; Fuchs, B. E.; Lee, W. Y. *Electrochem. Commun.* **2011**, *13*, 355.
108. Ye, J.; Zhang, H.; Chen, Y.; Cheng, Z.; Hu, L.; Ran, Q. *J. Power Sources* **2012**, *212*, 105.
109. Yu, D. S.; Kuila, T.; Kim, N. H.; Khanra, P.; Lee, J. H. *Carbon* **2013**, *54*, 310.
110. Ai, W.; Zhou, W.; Du, Z.; Du, Y.; Zhang, H.; Jia, X.; Xie, L.; Yi, M.; Yu, T.; Huang, W. *J. Mater. Chem.* **2012**, *22*, 23439.
111. Ghosh, S.; An, X.; Shah, R.; Rawat, D.; Dave, B.; Kar, S.; Talapatra, S. *J. Phys. Chem. C* **2012**, *116*, 20688.
112. Kim, T. Y.; Lee, H. W.; Stoller, M.; Dreyer, D. R.; Bielawski, C. W.; Ruoff, R. S.; Suh, K. S. *ACS Nano* **2011**, *5*, 436.
113. Conway, B. E. *Electrochemical Supercapacitors: Scientific Fundamentals and Technological Applications*; Plenum Pub Corp, **1999**, p. 259.
114. B´elanger, D.; Brousse, T.; Long, J. W. *Electrochem. Soc. Interface.* **2008**, *17*, 49.
115. Chen, S.; Zhu, J.; Wu, X.; Han, Q; Wang, X. *ACS Nano* **2010**, *4*, 2822.
116. Li, Y.; Zhao, N.; Shi, C.; Liu, E.; He, C. *J. Phys. Chem. C* **2012**, *116*, 25226.
117. Chen, C. Y.; Fan, C. Y.; Lee, M. T.; Chang, J. K. *J. Mater. Chem.* **2012**, *22*, 7697.
118. Lei, Z.; Shi, F.; Lu, L. *ACS Appl. Mater. Interfaces* **2012**, *4*, 1058.
119. Yu, G.; Hu, L.; Vosgueritchian, M.; Wang, H.; Xie, X.; McDonough, J. R.; Cui, X.; Cui, Y.; Bao, Z. *Nano Lett.* **2011**, *11*, 2905.
120. Yu, G.; Hu, L.; Liu, N.; Wang, H.; Vosgueritchian, M.; Yang, Y.; Cui, Y.; Bao, Z. *Nano Lett.* **2011**, *11*, 4438.
121. Kim, B.; Chung, H.; Kim, W. *Nanotechnology* **2012**, *23*, 155401.
122. Fan, Z.; Yan, J.; Wei, T.; Zhi, L.; Ning, G.; Li, T.; Wei, F. *Adv. Funct. Mater.* **2011**, *21*, 2366.
123. Cao, J.; Wang, Y.; Zhou, Y.; Ouyang, J. H.; Jia, D.; Guo, J. *J. Electroanal. Chem.* **2013**, *689*, 201.
124. Gao, H.; Xiao, F.; Ching, C. H.; Duan, H. *ACS Appl. Mater. Interfaces* **2012**, *4*, 7020.
125. He, Y.; Chen, W.; Li, X.; Zhang, Z.; Fu, J.; Zhao, C.; Xie, E. *ACS Nano* **2013**, *7*, 174.
126. Wang, H.; Casalongue, H. S.; Liang, Y.; Dai, H. *J. Am. Chem. Soc.* **2010**, *132*, 7472.
127. Yan, J.; Fan, Z.; Sun, W.; Ning, G.; Wei, T.; Zhang, Q.; Zhang, R.; Zhi, L.; Wei, F. *Adv. Funct. Mater.* **2012**, *22*, 2632.
128. Ge, C.; Hou, Z.; He, B.; Zeng, F.; Cao, J.; Liu, Y.; Kuang, Y. *J. Sol-Gel Sci. Technol.* **2012**, *63*, 146.

129. Hamdani, M.; Singh, R. N.; Chartier, P. *Int. J. Electrochem. Sci.* **2010**, *5*, 556.
130. Xiang, C.; Li, M.; Zhi, M.; Manivannan, A.; Wu, N. *J. Power Sources* **2013**, *226*, 65.
131. Dong, X. C.; Xu, H.; Wang, X. W.; Huang, Y. X.; Chan-Park, M. B.; Zhang, H.; Wang, L. H.; Huang, W.; Chen, P. *ACS Nano* **2012**, *6*, 3206.
132. Karthikeyan, K.; Kalpana, D.; Amaresha S.; Lee, Y. S. *RSC Advances* **2012**, *2*, 12322.
133. Lai, L.; Wang, L.; Yang, H.; Sahoo, N. G.; Tam, Q. X.; Liu, J.; Poh, C. K.; Lim, S. H.; Shen, Z.; Lin, J. *Nano Energy* **2012**, *1*, 723.
134. Biswas, S.; Drzal, L. T. *Chem. Mater.* **2010**, *22*, 5667.
135. Zhang, L. L.; Zhao, S.; Tian, X. N.; Zhao, X. S. *Langmuir* **2012**, *22*, 17624.
136. Davies, A.; Audette, P.; Farrow, B.; Hassan, F.; Chen, Z.; Choi, J. Y.; Yu, A. *J. Phys. Chem. C* **2011**, *115*, 17612.
137. Chang, H. S.; Chang, C. K.; Tsai, Y. C.; Liao, C. S. *Carbon* **2012**, *50*, 2331.
138. Wang, J.; Xu, Y.; Zhu, J.; Ren, P. *J. Power Sources* **2012**, *208*, 138.
139. Ding, B.; Lu, X.; Yuan, C.; Yang, S.; Han, Y.; Zhang, X.; Che, Q. *Electrochim. Acta* **2012**, *62*, 132.
140. Liu, Y.; Deng, R.; Wang, Z.; Liu, H. *J. Mater. Chem.* **2012**, *22*, 13619.
141. Wang, H.; Hao, Q.; Yang, X.; Lu, L.; Wang, X. *ACS Appl. Mater. Interface* **2010**, *2*, 821.
142. Zhong, M.; Song, Y.; Li, Y.; Ma, C.; Zhai, X.; Shi, J.; Guo, Q.; Liu, L. *J. Power Sources* **2012**, *217*, 6.
143. Gomez, H.; Ram, M. K.; Alvi, F.; Villalba, P.; Stefanakos, E.; Kumar, A. *J. Power Sources* **2011**, *196*, 4108.
144. Xu, J.; Wang, K.; Zu, S. Z.; Han, B. H.; Wei, Z. *ACS Nano* **2010**, *4*, 5019.
145. Yan, J.; Wei, T.; Fan, Z.; Qian, W.; Zhang, M.; Shen, X.; Wei, F. *J. Power Sources* **2010**, *195*, 3041.
146. Kumar, N. A.; Choi, H. J.; Shin, Y. R.; Chang, D. W.; Dai, L.; Baek, J. B. *ACS Nano* **2012**, *6*, 1715.
147. Yan, J.; Wei, T.; Shao, B.; Fan, Z.; Qian, W.; Zhang, M.; Wei, F. *Carbon* **2010**, *48*, 487.
148. Zhang, Q.; Li, Y.; Feng, Y.; Feng, W. *Electrochim. Acta* **2013**, *90*, 95.
149. Wang, D. W.; Li, F.; Zhao, J.; Ren, W.; Chen, Z. G.; Tan, J.; Wu, Z. S.; Gentle, I.; Lu, G. Q.; Cheng, H. M. *ACS Nano* **2009**, *3*, 1745.
150. Feng, X. M.; Li, R. M.; Ma, Y. W.; Chen, R. F.; Shi, N. E.; Fan, Q. L.; Huang, W. *Adv. Funct. Mater.* **2011**, *21*, 2989.

This page intentionally left blank

Chapter 2

Graphene-Based Nanomaterials for Energy Conversion and Storage

*Chenzhen Zhang, Nasir Mahmood, Han Yin and Yanglong Hou**

Department of Materials Science and Engineering
College of Engineering, Peking University
Beijing 100871, China

1. Introduction 51
2. Liquid-Phase Synthesis of Graphene 52
   2.1. Liquid-phase synthesis from expanded graphite 53
   2.2. Liquid-phase synthesis from graphite oxide 56
3. Nitrogen-Doped Graphene: Synthesis and Applications 57
   3.1. Synthesis of nitrogen-doped graphene 59
   3.2. Applications of nitrogen-doped graphene 61
      3.2.1. Oxygen reduction reaction of fuel cells 61
      3.2.2. Lithium ion batteries 64
4. Graphene-Based Composites: Synthesis and Applications 66
   4.1. Graphene-based composites for oxygen reduction reaction 66
   4.2. Graphene-based composites for lithium ion batteries 68
   4.3. Graphene-based composites for supercapacitors 74
5. Conclusions 75
References 75

1. Introduction

Graphene, one-atom-thick layers of sp^2-bonded carbon packed in a hexagonal lattice,[1] is now renowned for its extraordinary electronic, mechanical, physical, and electrochemical properties and potential applications in the fields of nanodevices and nanocatalysis.[2,3] The commonly used methods for the

* Corresponding author. E-mail: hou@pku.edu.cn

synthesis of graphene include mechanical exfoliation, chemical vapor deposition (CVD), epitaxial growth, liquid-phase exfoliation, *etc.* As a simple, facile, and low-cost approach for mass production, liquid-phase synthesis has attracted tremendous interest not only for the preparation of single- and few-layer graphene but also for the modification and functionalization of graphene materials.[4] On the other hand, both theoretical and experimental studies have suggested that the intentional incorporation of heteroatoms into graphene structure could significantly modulate its electronic and chemical properties.[5,6] In this context, several kinds of doped graphene materials have been synthesized and investigated, including nitrogen-doped,[7] boron-doped,[8] and sulfur-doped graphene.[9] Recently, a lot of research is focusing on the graphene and graphene-based composites designed for renewable energy,[10] which mainly involves the cathodic oxygen reduction reaction (ORR) of a fuel cell, rechargeable lithium ion batteries (LIBs), field-effect transistors (FET), and supercapacitors. The results exhibit huge potential of graphene in such fields of energy conversion and storage.[11–14]

Herein, recent advancement in the fabrication of graphene, especially nitrogen-doped graphene, via liquid-phase approach will be presented. Then, the latest progress of graphene-based nanomaterials applied for the cathodic ORR, LIBs, and supercapacitors will be introduced and discussed. Graphene materials evolved so fast in terms of synthetic strategies as well as applications. Here is a summary that will be helpful for further development.

2. Liquid-Phase Synthesis of Graphene

Liquid-phase synthesis is a common way to produce graphene in a variety of solvents. This approach avoids some harsh reaction conditions (*e.g.*, high temperature) and is a facile and large-scale method. In general, significant numbers of lattice defects into graphene structure are of great influence on the conductivity and crystallinity of graphene. In this context, liquid-phase synthesis of graphene from expanded graphite (EG)[15,16] and graphite[17–19] could effectively reduce defects and obtain high-quality graphene. On the other hand, graphite oxide (GO) is regarded as another widely used starting material for the liquid-phase synthesis of graphene, which can be easily prepared by the Hummers method.[20] Although some oxygen-containing groups (*e.g.*, hydroxyl and/or carboxyl groups) will remain in the graphene fabricated from GO,[21] they give graphene a significant advantage not only for better dispersion in some solvents[22,23] but also for its further functionalization (*e.g.*, as a substrate of graphene-based composites[24]). Although sonication is one of the necessary steps in liquid-phase process for graphene

from EG, graphite, and GO, some sonication-free liquid-phase methods, including supercritical CO_2 technique,[25] ionic-liquid-assisted electrochemical approach,[26] and spontaneous exfoliation,[27] are also employed to produce graphene. Over the past decade, a lot of research about liquid-phase synthesis of graphene has been reported, especially using EG and GO as precursors. These experimental results will be summarized in the following sections.

2.1. Liquid-phase synthesis from expanded graphite

For a better liquid-phase synthetic process, graphite is usually pretreated with heat treatment[28] or microwave irradiation[29] to expand. High-quality aqueous dispersed graphene can be synthesized via using 7,7,8,8-tetracyanoquinodimethane (TCNQ) anion as a stabilizer and EG as a starting material.[30] The loose EG was obtained after a rapidly heating process and then mixed with TCNQ by grinding with the aid of dimethyl sulfoxide (DMSO), which could effectively dissolve TCNQ and make it diffuse into the interlayers of EG and stack on graphite layers via π–π interaction. The resultant mixture was dispersed in KOH solution to reduce TCNQ to TCNQ anion.[31] With the aid of sonication, TCNQ anion-absorbed graphene was peeled off from EG and stably dispersed in water (Figure 1). Transmission electron microscopy (TEM) images suggest that continuous sonication could divide graphene into small pieces, including large amount of isolated graphene with various dimensions as well as small quantity of graphene nanoribbon (GNR). The typical selected area electron diffraction (SAED) of graphene clearly shows a distinct hexagonal lattice[32] (Figure 2). The thickness of exfoliated graphene was measured to be *ca*. two to three layers. The perfect crystallinity and low defect degree confirmed by Raman spectroscopy[30] exhibited the high quality of as-synthesized graphene. Furthermore, the modified graphene could also be stably dispersed in some polar solvents, such as *N*,*N*-dimethylformamide (DMF) and DMSO, but not soluble in ethanol. This approach using TCNQ as a stabilizer provides an effective way to obtain high-quality graphene well dispersed in polar solvents.

In addition, 4-bromophenyl-modified EG was synthesized through an *in-situ* diazonium formation procedure using 4-bromoaniline as precursor.[33] The following sonication process in DMF led to the successful exfoliation of functionalized EG and produced thin graphene (less than five layers) with higher solubility in DMF than the pristine graphene. In another study, easily soluble EG was synthesized using fluorinated graphite intercalation compound (GIS) in a single insertion and thermal expansion process, and its interlayer distance was up to 17% larger than that of the normal EG.[34]

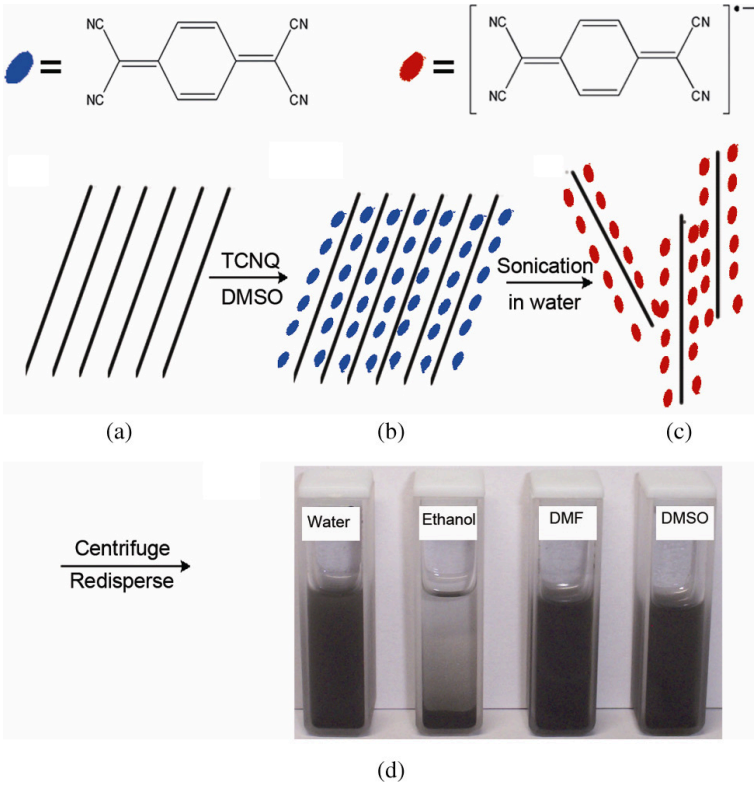

Figure 1. Scheme of the preparation of TCNQ anion-stabilized graphene: (a) pretreated EG; (b) TCNQ insertion into the interlayer of EG; (c) TCNQ anion-stabilized graphene; (d) photograph of TCNQ anion-stabilized graphene dispersed in different solvents (water, ethanol, DMF, and DMSO). Reproduced from Ref. 30 with permission. Copyright © 2008 The Royal Society of Chemistry.

Solvothermal approach is another common liquid-phase method to fabricate graphene from EG. For example, large-flake graphene membranes were exfoliated from graphite using a solvothermal method in oleyl amine. With a high concentration of 0.15 mg mL^{-1}, the graphene oleyl amine dispersion predominantly consisted of single-layer graphene and could be stabilized against re-aggregation. Besides, the electrical characteristic of the exfoliated graphene suggested its high quality.[35] In another example, monolayer and bilayer graphene were produced via a solvothermal-assisted exfoliation process with the aid of a highly polar organic solvent, acetonitrile.[36] EG was used as the starting material prepared from commercial expandable graphite. The solvothermal process could introduce acetonitrile molecules into the interlayer of EG. After sonication, monolayer and bilayer graphene could be

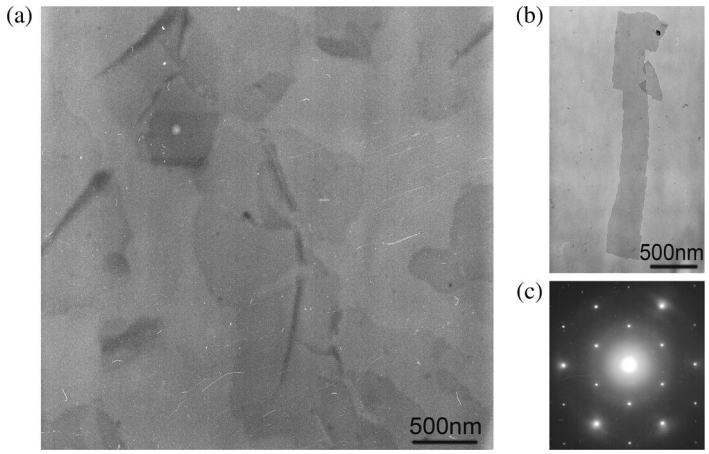

Figure 2. TEM images of (a) several isolated graphene and (b) GNR; (c) the SAED pattern of graphene. Reproduced from Ref. 30 with permission. Copyright © 2008 The Royal Society of Chemistry.

peeled off from EG and stably dispersed in acetonitrile (Figure 3). Raman spectroscopy is one of the most direct and non-destructive techniques to characterize the quality of graphene.[37] The G band (*ca.* 1600 cm^{-1}) is commonly observed for all graphitic structures due to the first-order scattering of E_{2g} mode, whereas the D band (*ca.* 1350 cm^{-1}) is associated with a series of structural defects. Moreover, the 2D band (*ca.* 2700 cm^{-1}) can be used to distinguish graphene with different layers.[38] Raman spectrum of graphite showed that it consisted of more than 10 layers. For graphene obtained after centrifugation at 600 and 2000 rpm, the 2D bands of Raman spectra were in good agreement with those for bilayer and monolayer graphene,[39] respectively (Figure 4). The reason to choose acetonitrile, compared to *N*-methyl-2-pyrrolidone (NMP), DMF, DMSO, *etc.*, was that it had low boiling point which led to a reaction environment with high pressure and thus favored the insertion of acetonitrile molecules into the EG interlayer. Interestingly, no N 1s peak was observed in the X-ray photoelectron spectroscopy (XPS) of as-synthesized graphene,[36] suggesting no nitrogen doping or acetonitrile adsorption occurred during the solvothermal synthesis. The distinct advantage of this method was that no stabilizer or modifier was involved, and the defect-free nature and the intrinsic properties of graphene are well maintained. Furthermore, the solvothermal process resulted in a significantly improved yield of monolayer and bilayer graphene compared to the previous studies, and thus opened up an effective route for the preparation of high-yield graphene with high quality.

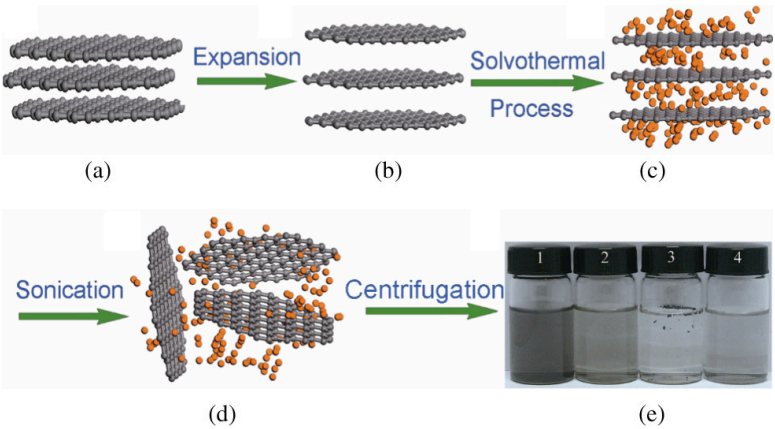

Figure 3. Scheme of the preparation of graphene via solvothermal process in acetonitrile: (a) pristine expandable graphite; (b) EG; (c) acetonitrile molecules insertion into the interlayer of EG; (d) exfoliated graphene dispersed in acetonitrile; (e) photograph of four samples obtained under different conditions. Reproduced from Ref. 36 with permission. Copyright © 2009 Springer.

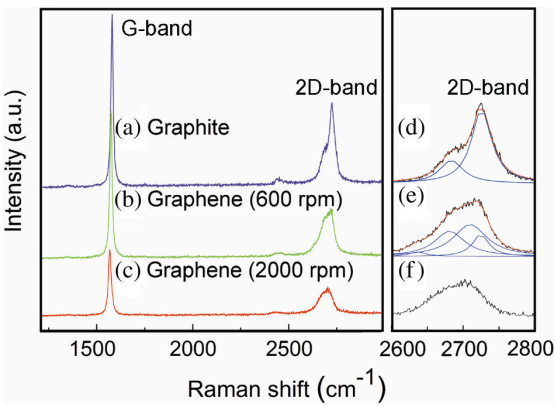

Figure 4. Raman spectra of (a, d) thick graphite, (b, e) bilayer graphene, and (c, f) monolayer graphene, respectively. Reproduced from Ref. 39 with permission. Copyright © 2006 American Physical Society.

2.2. Liquid-phase synthesis from graphite oxide

GO, one of the main precursors for the synthesis of graphene, is usually prepared by the Hummers method mainly using graphite, concentrated sulfuric acid, sodium nitrate, potassium permanganate, and hydrogen peroxide as reagents.[40] After oxidation, a lot of oxygen-containing groups, such as

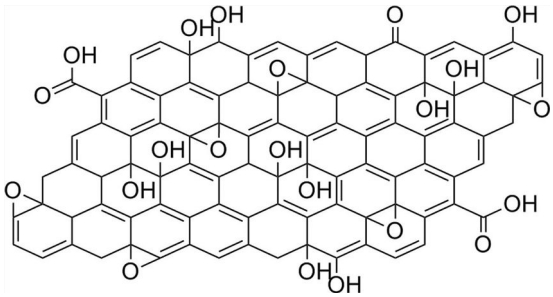

Figure 5. The structural model of GO.

hydroxyl, carboxyl, and epoxy groups, are introduced into the graphite structure (Figure 5).

To achieve reduced graphite oxide (rGO), hydrazine (N_2H_4) and sodium borohydride ($NaBH_4$) are two most commonly used reducing agents. By using N_2H_4 for the reduction of GO at 100 °C, the C/O atomic ratio in rGO (10.3) could be significantly improved compared to that in GO (2.7), indicating that most oxygen-containing groups have been removed.[41] In the case of $NaBH_4$, the C/O atomic ratio in rGO was 8.6, and the corresponding conductivity was 45 S m^{-1},[42] lower than that of the sample reduced by N_2H_4 (~200 S m^{-1}). Furthermore, rGO can also be reduced by the addition of hydroquinone for 20 h.[43] However, the toxicity and harmfulness of above chemicals should be considered. As a result, an environmentally friendly and facile approach based on the Fe reduction of GO was developed (Figure 6). Interestingly, the as-synthesized graphene with residual Fe showed a high adsorption capacity for methylene blue at room temperature, and can be easily separated from the solution by an external magnetic field.[44]

On the other hand, solvothermal process offers a green chemistry route to producing rGO from GO, and the C 1s XPS spectrum of GO shows a significant decrease of oxygen-related peak at 286–289 eV after solvothermal reduction.[45] The number of defects and the oxygen content in graphene could be further decreased via liquid-phase reaction in DMF using N_2H_4 as reducing agent.[46] Similarly, solvothermal process of GO in NMP also resulted in de-oxygenation and reduction, yielding a stable rGO dispersion.[47]

3. Nitrogen-Doped Graphene: Synthesis and Applications

Doped graphene materials have attracted more and more attention because of their enhanced performance used in many practical applications. For example, sulfur-doped graphene was synthesized via directly annealing GO and

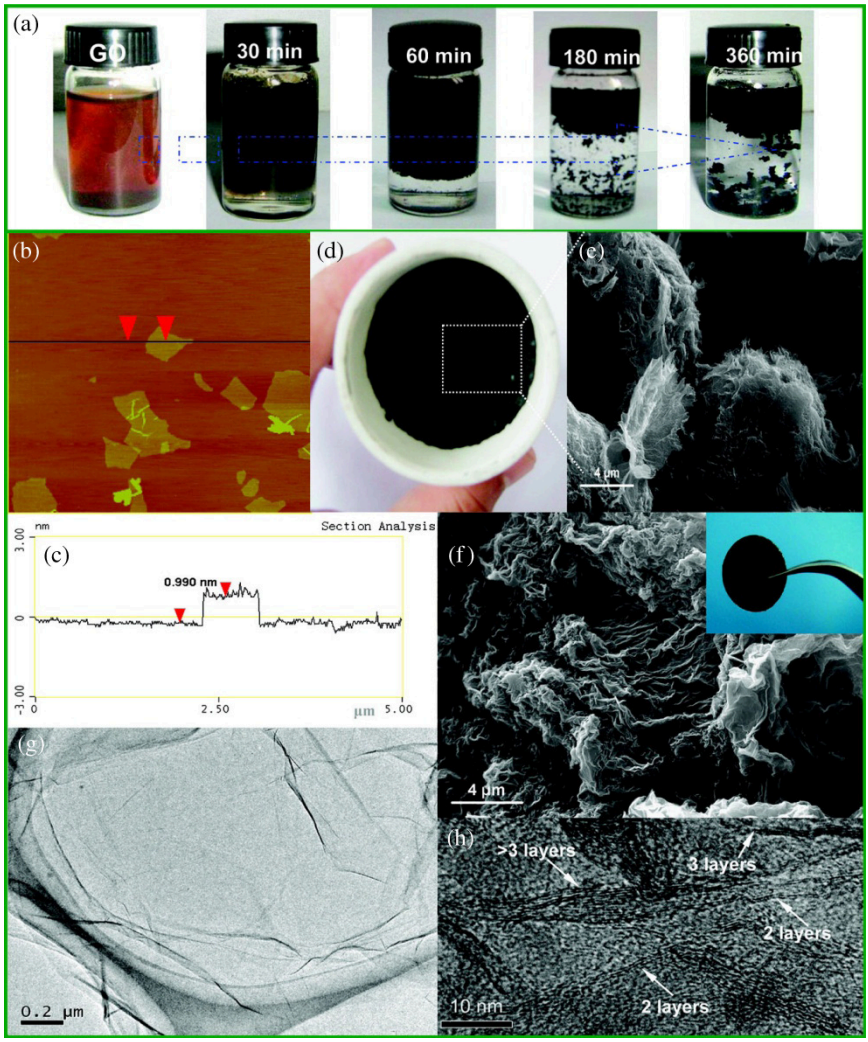

Figure 6. (a) Photograph of GO dispersion before and after Fe reduction with different reduction times. (b) AFM image of GO dispersed on mica and (c) the corresponding height profile. (d) Photograph and (e) SEM image of rGO for 30 min without acid treatment. (f) SEM and (g, h) TEM images of rGO for 360 min at different magnifications. Reproduced from Ref. 44 with permission. Copyright © 2011 American Chemical Society.

benzyl disulfide in argon. The resultant material acted as a metal-free ORR catalyst, exhibiting a greater electrochemical activity than the commercial Pt/C (20% Pt loaded on carbon black).[48] In another example, phosphorus-doped graphene was prepared by CVD method using triphenylphosphine

(TPP) as a phosphorus source, based on which phosphorus-doped double-layered graphene FET was developed and it showed high stability in air.[49] For boron-doped graphene, it could be produced through a CVD approach using boron powder and ethanol as boron and carbon precursors, respectively. Due to its high conductivity, transparency, and p-type semiconductor characteristic, the resultant boron-doped graphene was used as an active electrode in photovoltaic devices.[50] Among all the doped graphene materials, nitrogen-doped graphene has been most extensively investigated. The preparation of nitrogen-doped graphene and its applications in the fields of ORR and LIBs will be summarized in the following sections.

3.1. Synthesis of nitrogen-doped graphene

Nitrogen-doped graphene has been synthesized by a variety of methods, including CVD,[51–53] thermal annealing,[54–59] plasma treatment,[60,61] arc discharge,[62,63] and liquid-phase reaction.[64,65] In the early time, nitrogen-doped GNR was fabricated by an electrothermal reaction with ammonia.[66] Afterward, some chemical doping and reduction methods (for example, thermal annealing of GO[67]) as well as CVD technique[68] were proposed to obtain nitrogen-doped graphene. However, all these three processes need high reaction temperature in gas atmosphere, and such conditions might hinder the large-scale production and commercialization of nitrogen-doped graphene. To address this challenge, liquid-phase synthetic strategy is developed. A two-step liquid-phase process was used to synthesize nitrogen-doped graphene.[69] First, graphene was prepared by a solvothermal-assisted exfoliation process in acetonitrile using EG as the starting material.[36] After repeated centrifugation at 500 and 1500 rpm, few-layer graphene was collected and then dispersed in acetonitrile for further supercritical reaction (Figure 7). Raman spectra suggested that the resultant nitrogen-doped graphene still kept high crystal structure without significant defects. Besides, the nitrogen content in nitrogen-doped graphene could be tuned by increasing the supercritical reaction time from 2 to 24 h, which reached up to 4.56 at.%.[69]

To simplify the synthetic process of nitrogen-doped graphene in liquid phase, solvothermal reduction of GO colloidal dispersion in the presence of N_2H_4 and NH_3 H_2O at pH of 10 was carried out. The nitrogen content of as-synthesized nitrogen-doped graphene was 4–5 wt.%, while the oxygen content was more than 8 wt.%.[70] Similarly, using dicyandiamide instead of N_2H_4 could also produce nitrogen-doped graphene via solvothermal reaction. However, the problem of this approach was the high

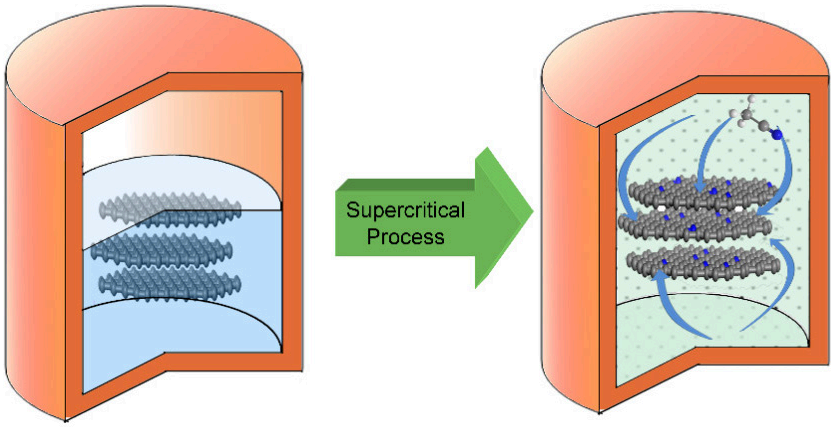

Figure 7. Scheme of the preparation of nitrogen-doped graphene via supercritical reaction in acetonitrile: (a) few-layer graphene obtained by solvothermal exfoliation and centrifugation, and mixed with acetonitrile in corundum lined autoclave; (b) nitrogen-doped graphene formed after supercritical reaction at 310 °C. Reproduced from Ref. 69 with permission. Copyright © 2011 American Chemical Society.

oxygen content (20.85 at.%), which would decrease the conduction of nitrogen-doped graphene and impede its electrochemical application.[71] A better way for the liquid-phase synthesis of nitrogen-doped graphene with low oxygen content is highly desired.

Very recently, a facile, one-step solvothermal method was developed to synthesize nitrogen-doped graphene from GO only in the presence of ammonia solution.[72] The elemental composition and nitrogen bonding modes of nitrogen-doped graphene was investigated by XPS measurement. The C 1s XPS spectra showed a considerable degree of oxidation in GO, corresponding to the carbon atoms in different functional groups: C–C (284.8 eV), C–O (286.8 eV), C=O (287.8 eV), and COOH (289.0 eV).[73] After solvothermal reduction and doping, the peak intensity of oxygen-containing groups became much weaker in nitrogen-doped graphene, and an additional component appeared at 285.8 eV, attributed to the formation of C–N bonds.[74] Interestingly, the nitrogen content was measured to be 10.6 at.% by XPS, higher than that in the nitrogen-doped graphene prepared at high temperatures,[75,76] while the oxygen content was 4.9 at.%, much lower than other nitrogen-doped graphene synthesized in liquid phase.[77–80] Furthermore, the various nitrogen states were analyzed by N 1s XPS spectra. Five typical nitrogen states, including pyridinic N (*ca.* 398.3 eV), pyrrolic N (*ca.* 400.1 eV),

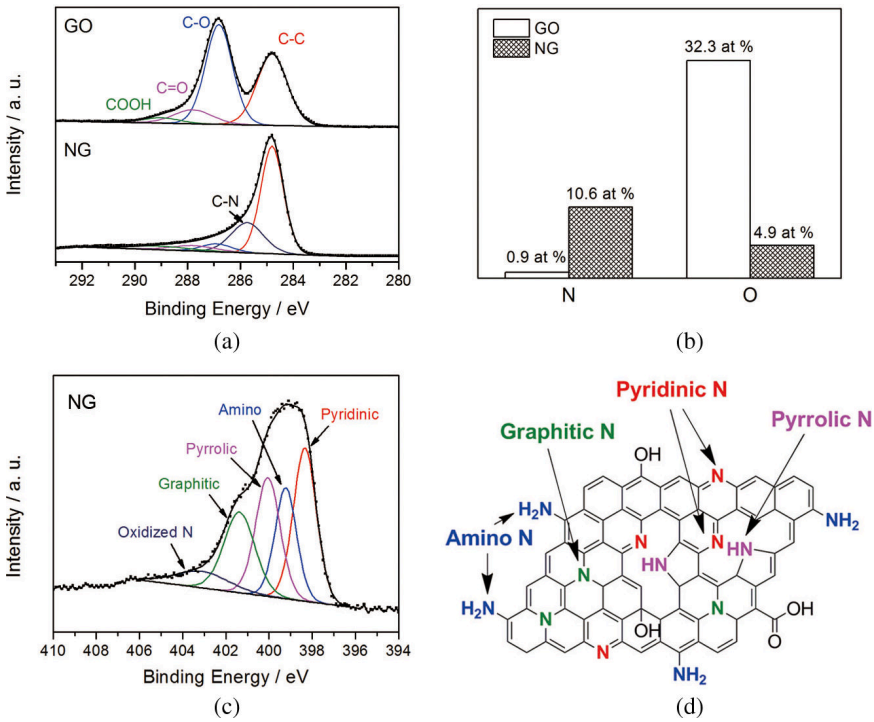

Figure 8. XPS spectra of nitrogen-doped graphene: (a) C 1s XPS spectra of GO and nitrogen-doped graphene; (b) percentages of nitrogen and oxygen in GO and nitrogen-doped graphene; (c) N 1s XPS spectrum of nitrogen-doped graphene; (d) scheme of nitrogen-doped graphene. Reproduced from Ref. 72 with permission. Copyright © Copyright 2012 Elsevier Ltd.

graphitic N (*ca.* 401.4 eV), oxidized N (402–404 eV),[81] and amino N (*ca.* 399.2 eV),[82,83] were found in the nitrogen-doped graphene structure (Figure 8). So we can see this approach offers a very simple way to produce high-yield nitrogen-doped graphene with high nitrogen content and low oxygen content.

3.2. Applications of nitrogen-doped graphene

3.2.1. Oxygen reduction reaction of fuel cells

A fuel cell is an electrochemical device that converts chemical energy directly into electrical energy with high efficiency and low emission of pollutants.[84] Platinum (Pt) has long been regarded as the best catalyst for both oxidation reaction on the anode and reduction reaction on the cathode.[85] For cathodic ORR, however, the commercialization of Pt catalyst is hindered by its limited

reserve, high cost, as well as susceptibility to the crossover effect, CO deactivation, and time-dependent drift.[86] Aiming at reducing the use of the precious Pt and hence the cost of a fuel cell, non-precious metal (*e.g.*, metal chalcogenides[87,88] and metal-N_4 compounds[89,90]) and metal-free[91,92] electrocatalysts for ORR have been largely investigated. After the development of vertically aligned nitrogen-doped carbon nanotube (CNT) array as an efficient metal-free ORR catalyst,[93] more and more studies about nitrogen-doped carbon materials, particularly nitrogen-doped graphene, have been reported.

The ORR mechanism on nitrogen-doped graphene has been theoretically studied. In general, O_2 could be reduced by the following two pathways: one is a direct four-electron transfer pathway, where O_2 is reduced to water or OH^- in an acidic or alkaline environment[94]; the other is a two-electron transfer pathway, where O_2 is partly reduced to H_2O_2 or OOH^- in an acidic or alkaline environment.[95] In experimental aspect, the ORR performance associated with nitrogen-doped graphene was largely investigated. The oxygen reduction process could be confirmed from cyclic voltammetry (CV) curve, where a well-defined cathodic peak appeared in the presence of O_2, but featureless voltammetric current observed within the same potential range under N_2.[96] The catalytic activity can be determined by linear sweep voltammetry (LSV) measurement.[97] For the nitrogen-doped graphene prepared via liquid-phase approach in the presence of ammonia solution,[72] its LSV curve showed a significantly enhanced ORR performance of both the onset potential and current density compared to the chemically converted graphene (CCG), close to the commercial Pt/C. Similar to the case of nitrogen-doped CNTs, the enhanced catalytic performance of nitrogen-doped graphene compared to the undoped graphene is due to the electron-accepting ability of nitrogen atoms that creates a net positive charge on adjacent carbon atoms in the graphene structure to readily attract electrons from the anode; besides, the nitrogen-induced charge delocalization changes the chemisorption mode of O_2 from the usual end-on adsorption to a side-on adsorption, which effectively weakens the O–O bond and thus facilitates the ORR process.[93]

The kinetic parameters including electron transfer number (n) were analyzed on the basis of Koutecky–Levich (K-L) equations[98]:

$$\frac{1}{J} = \frac{1}{J_K} = \frac{1}{B\omega^{1/2}} \qquad \text{(Eq. 1)}$$

$$B = 0.2nFC_0(D_0)^{2/3}(\upsilon)^{-1/6} \qquad \text{(Eq. 2)}$$

in which J is the measured current density, J_K is the kinetic-limiting current density, ω is the electrode rotating rate, n is the electron transfer number, F is the Faraday constant (F = 96,485 C mol^{-1}), C_0 is the bulk concentration of O_2 ($C_0 = 1.2 \times 10^{-6}$ mol cm^{-3}), D_0 is the diffusion coefficient of O_2 in 0.1 M KOH ($D_0 = 1.9 \times 10^{-5}$ cm^2 s^{-1}), and υ is the kinetic viscosity (υ = 0.01 cm^2 s^{-1}). The constant 0.2 is adopted when the rotation rate is expressed in revolutions per minute. According to Eqs. (1) and (2), the electron transfer number can be calculated from the slope of K-L plot measured by rotating disk electrode (RDE) voltammetry (Figure 9).

For practical application in fuel cells, the crossover effect should be considered because the fuel molecule (*e.g.*, methanol) may pass through the membrane from anode to cathode and poison the cathode catalyst.[99] In this context, the possible methanol crossover effect of nitrogen-doped graphene has been tested and the result showed its excellent resistance to the methanol effect.[100] Furthermore, durability of catalysts is another important consideration in fuel-cell technology.[101] In general, the commercial Pt/C suffers a big current loss of ~40% after 20,000 s current–time (*i–t*) test.[102] In contrast, nitrogen-doped graphene exhibits much less performance attenuation of *ca.* 15%.[72]

On the other hand, although the role of various nitrogen states (such as pyridinic N, pyrrolic N, graphitic N, amino N, *etc.*) on electrocatalytic properties has been studied, it remains complicated.[103] Generally, the improved catalytic activity toward ORR can be attributed to the pyridinic N or graphitic N[38,91,101]; but some uncertain factors (*e.g.*, the graphitic degree[101]) might interfere with the results. Interestingly, using a deamination approach and comparing the ORR performance of graphene with and without amino group, it is proved that the amino N, with its considerable stability, makes a great contribution to the excellent electrocatalytic performance in ORR.[72] Furthermore, the roles of pyridinic, pyrrolic, and graphitic nitrogen states in ORR were studied using a simple annealing method at various temperature to obtain nitrogen-doped graphene with different nitrogen states and contents.[72] By analyzing the relationship between the content of each nitrogen state and ORR properties (including onset potential, electron transfer number, and current density), it can be concluded that the graphitic N and amino N decide the onset potential and electron transfer number, while the graphitic and pyridinic nitrogen states are the key factors to enhance the current density in ORR process (Figure 10).

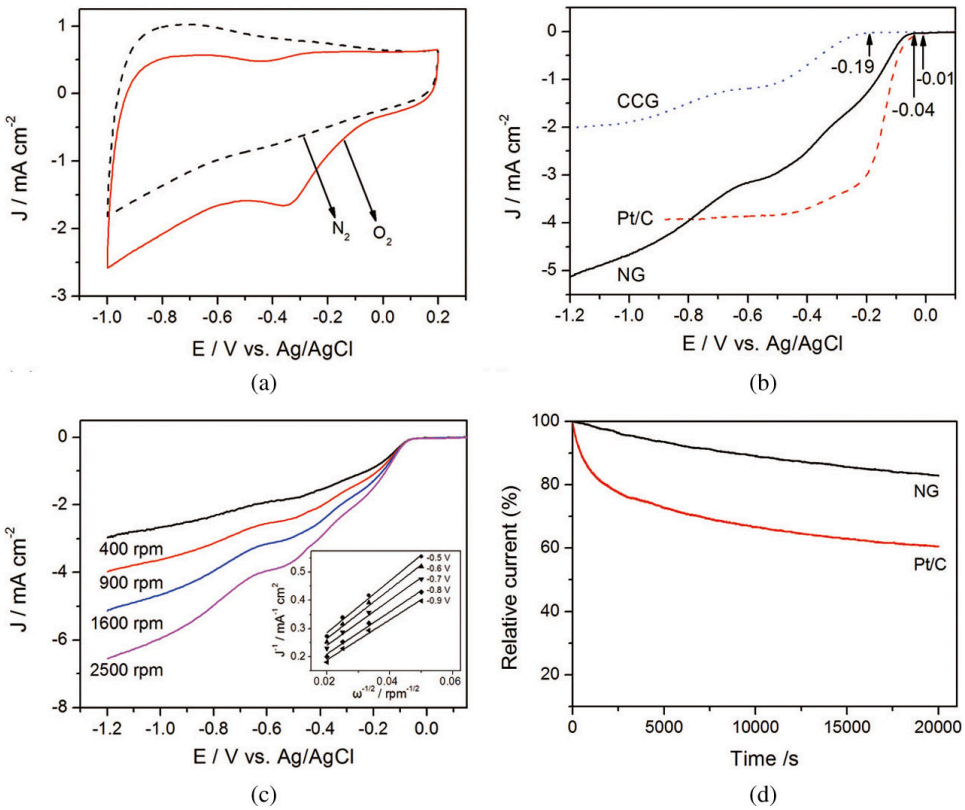

Figure 9. (a) CV curves of nitrogen-doped graphene in a N_2– and O_2-saturated 0.1 M KOH solution at a scanning rate of 100 mV s^{-1}; (b) LSV curves of CCG, Pt/C, and nitrogen-doped graphene in an O_2-saturated 0.1 M KOH solution at a scanning rate of 10 mV s^{-1} and a rotation speed of 1600 rpm; (c) RDE curves of nitrogen-doped graphene in an O_2-saturated 0.1 M KOH solution with various rotation speeds at a scanning rate of 10 mV s^{-1}. Inset shows the K-L plots of J^{-1} versus $\omega^{-1/2}$ at different electrode potentials derived from RDE measurements; (d) current–time response of nitrogen-doped graphene and Pt/C at –0.28 V in an O_2-saturated 0.1 M KOH at a rotation speed of 1600 rpm. Reproduced from Ref. 72 with permission. Copyright © 2012 Elsevier Ltd.

3.2.2. Lithium ion batteries

In recent years, nitrogen-doped graphene has been used as an anode material for LIBs[104] due to its fascinating properties, such as high electrical electronic properties and excellent mechanical flexibility. Compared to the undoped graphene, nitrogen-doped graphene prepared via CVD approach

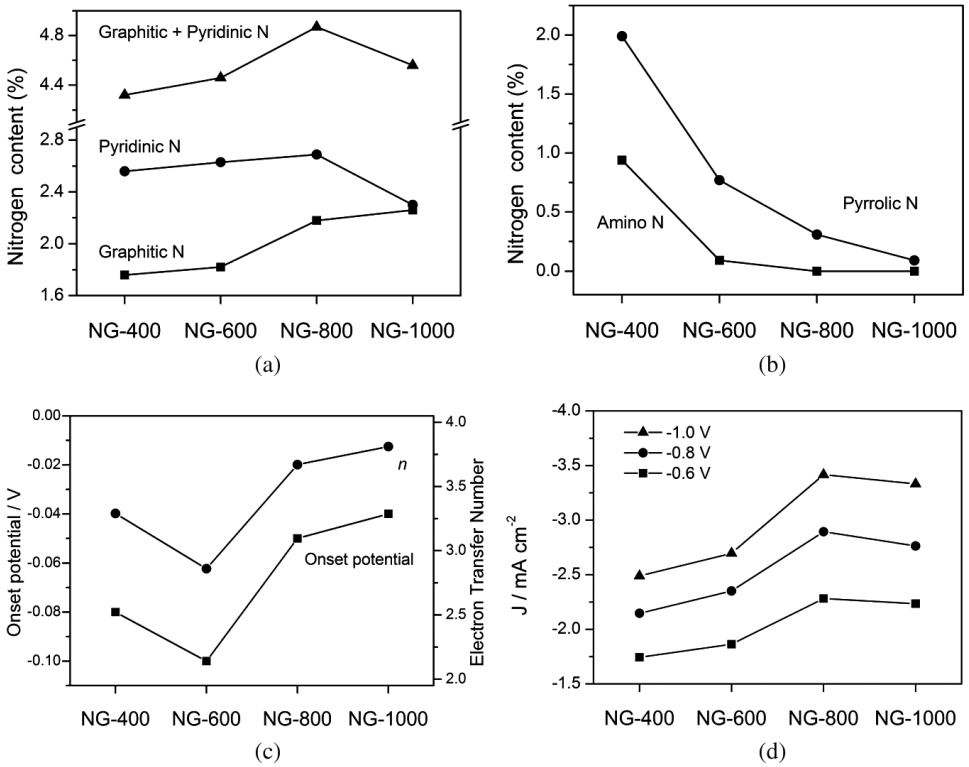

Figure 10. The content of (a) pyridinic N, graphitic N, (b) pyrrolic N and amino N in nitrogen-doped graphene; the change of (c) onset potential, electron transfer number, and (d) current density at different potentials in nitrogen-doped graphene. Reproduced from Ref. 72 with permission. Copyright © 2012 Elsevier Ltd.

showed almost double reversible discharge capacity because of the large number of surface defects introduced from nitrogen doping (Figure 11).[105] In another study, nitrogen-doped graphene was synthesized by heat treatment under an ammonia atmosphere, and possessed a reversible capacity of *ca.* 900 mAh g^{-1} at a current density of 42 mA g^{-1} and a capacity of *ca.* 250 mAh g^{-1} at a high current density of 2.1 A g^{-1}.[106] The excellent performance of nitrogen-doped graphene might be attributed to the introduction of nitrogen atoms, the enhanced conductivity, and the increased electrode/electrolyte wettability. Furthermore, research has revealed that both pyridinic and graphitic nitrogen states play an effective role in lithium insertion and extraction.[107]

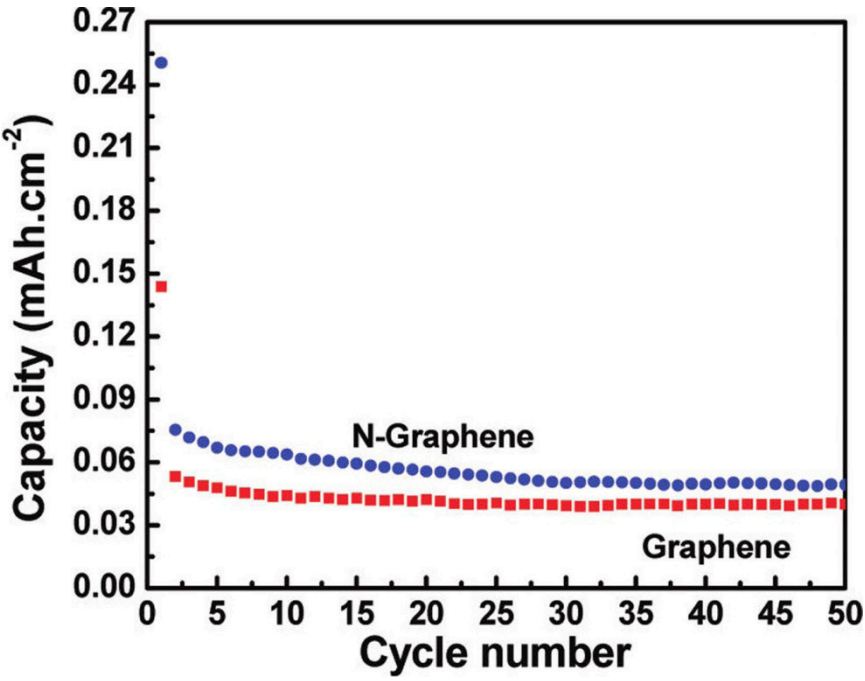

Figure 11. Electrochemical performance of nitrogen-doped graphene and undoped graphene. Reproduced from Ref. 105 with permission. Copyright © 2010 American Chemical Society.

4. Graphene-Based Composites: Synthesis and Applications

In the 21st century, more and more renewable energy materials as well as their devices, such as fuel cells,[108] LIBs,[109] supercapacitors,[110] and solar cells,[111] have been developed due to the resource shortage and environmental pollution. Owing to its unique two-dimensional structure and outstanding properties, graphene is a promising material for applications in the above energy-related systems.[112–115] Examples mainly include the use of graphene-based composites as cathodic ORR catalysts in fuel cells,[116] high-performance electrodes in LIBs[117] and supercapacitors,[118] and counter electrodes in solar cells,[119] which will be systematically summarized in the following sections.

4.1. Graphene-based composites for oxygen reduction reaction

A number of efforts have been devoted to seeking an alternative material with high ORR activity and low price for replacing platinum (Pt) in fuel cells.

Among them, graphene-based composites exhibited excellent electrochemical performance toward ORR.

Graphene materials can be used as catalyst supports instead of carbon black[120] and CNTs[121] to produce graphene/Pt composites. Pt nanoparticles supported on the functionalized graphene sheets have showed excellent stability after 5000 cycles, and much higher electrochemical surface area and ORR activity than that of commercial Pt/C (20% Pt loaded on carbon black). The enhanced performance could be ascribed to the smaller particle size and less aggregation of Pt nanoparticles on graphene.[122] Besides, Pt nanoparticles supported on the graphene nanoplatelets exhibited greatly improved durability of two to three times than that of Pt/CNT and the commercial Pt/C.[123] Interestingly, the morphology, structure, and dispersing state of Pt nanoparticles could affect the electrocatalytic performance, and the three-dimensional multilayer graphene/Pt nanoparticles composite constructed by layer-by-layer self-assembly showed prominent ORR activity.[124]

In the case of non-precious metal catalysts, materials based on metal chalcogenides and metal nitride compounds have received a great deal of research interest. Co_3O_4 nanocrystals and reduced graphene oxide composite synthesized by a two-step liquid-phase method could be used as a high-performance bifunctional catalyst for both ORR and oxygen evolution reaction (OER). Interestingly, the individual Co_3O_4 and reduced graphene oxide have little ORR catalytic activity; however, the Co_3O_4/graphene composite has shown an unexpected high electrocatalytic performance, which could be further enhanced by the nitrogen doping of graphene. The result indicated that the synergistic coupling between Co_3O_4 and graphene was very important to the high ORR activity of the composite.[125] In another study, $Co_{1-x}S$ nanoparticles were prepared on the reduced graphene oxide via a low-temperature liquid-phase reaction and a following high-temperature annealing process. Due to the desirable morphology, size, and phase of $Co_{1-x}S$ nanoparticles controlled by the reduced graphene oxide substrate, as well as the strong electrochemical coupling between reduced graphene oxide and $Co_{1-x}S$ nanoparticles, the resultant composite showed an unprecedented high catalytic performance among all cobalt chalcogenides-based ORR catalysts.[126]

Metallophthalocyanine (MPc), a kind of metal-N_4 compounds, is another promising candidate, which might turn out to be an efficient ORR electrocatalyst owing to its high catalytic activity; however, the instability of MPc seriously impedes its practical application in fuel cells.[127] To overcome this problem, several carbon materials have been introduced as substrates to the MPc system.[128,129] In the study of carbon-supported iron(II) phthalocyanine (FePc) and cobalt(II) phthalocyanine (CoPc) composites, the results of both

electrochemical measurement and theoretical calculation showed that FePc/carbon had a superior catalytic activity to CoPc/carbon, but was much less stable than CoPc/carbon.[130] In this case, nitrogen-doped graphene, prepared by a simple solvothermal process, could be used as a support to fabricate FePc/nitrogen-doped graphene composite.[131] The TEM image of the as-synthesized composite showed that FePc with a typical columnar morphology[132] supported on the surface of nitrogen-doped graphene. The slight shifts of well-defined peaks in both Fourier transform infrared (FTIR) and Raman spectra indicated a possible π–π interaction between two components.[133,134] XPS result further suggested the elemental composition of the FePc/nitrogen-doped graphene composite, with 2.04 at.% of iron, 2.08 at.% of oxygen, and 12.85 at.% of nitrogen (Figure 12).

The FePc/nitrogen-doped graphene composite exhibited significantly enhanced ORR onset potential and current density compared to the pure FePc and nitrogen-doped graphene, the performance of which was even superior to that of commercial Pt/C.[131] Moreover, since durability is one of the major concerns in current fuel-cell technology, and is a big challenge for MPc electrocatalyst, the stability of FePc and FePc/GX composites (GX=nitrogen-doped graphene, graphene oxide, and reduced graphene oxide) was investigated.[131] Pure FePc showed the largest current loss in a 6000 s *i–t* test, of which the current density was much lower than that of Pt/C after 1000 s. Obviously, with the aid of graphene-related substrates, FePc/graphene oxide and FePc/reduced graphene oxide composites suggested a much improved stability, close to that of commercial Pt/C. Interestingly, FePc/nitrogen-doped graphene composite exhibited the best catalytic activity and stability among all the materials (even superior to Pt/C), probably because nitrogen-doped graphene could optimize the electrical property of graphene and thus had a better catalytic performance than FePc/undoped graphene composite (Figure 13).

4.2. Graphene-based composites for lithium ion batteries

LIB is widely used as a convenient power source for various portable electronic devices due to its high energy density, high voltage, long cycling life, and good environment compatibility.[135] A LIB consists of an anode (negative electrode), a cathode (positive electrode), an electrolyte, and a separator,[136] and its performance strongly depends on the structures and properties of both electrodes. Graphite is a commercialized anode material for LIBs owing to its high Coulombic efficiency; however, the theoretical capacity of graphite

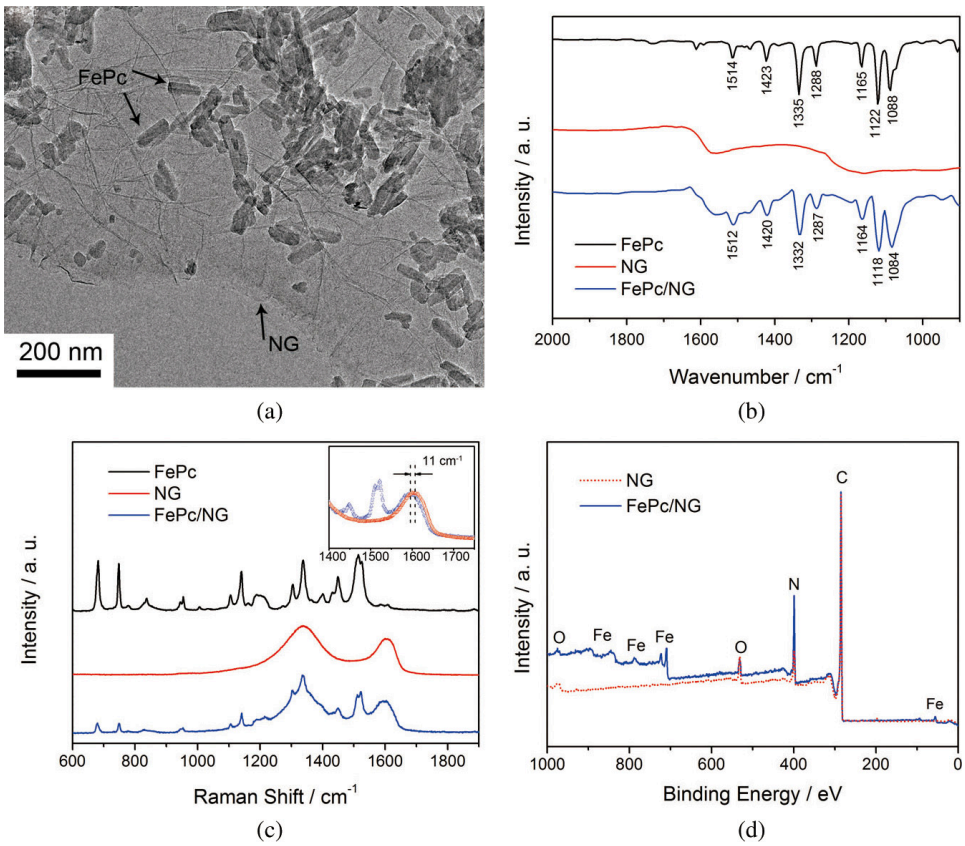

Figure 12. (a) TEM image of FePc/nitrogen-doped graphene composite; (b) FTIR and (c) Raman spectra of FePc, nitrogen-doped graphene, and FePc/nitrogen-doped graphene composite; (d) XPS survey spectra of nitrogen-doped graphene and FePc/nitrogen-doped graphene composite. Reproduced from Ref. 131 with permission. Copyright © 2012 The Royal Society of Chemistry.

is low (372 mAh g^{-1}), and hence an alternative anode material is highly required.[137]

Compared to graphite, graphene possesses a much higher specific capacity which has been confirmed by the experimental results.[138,139] On the other hand, many metals and their chalcogenides are also promising anode materials for LIBs as they have huge theoretical capacities.[140,141] So far, research has shown that combining metal chalcogenides with graphene to form composites can improve the electrochemical performance of both components in LIBs.[142,143] For example, SnO_2 has a high theoretical

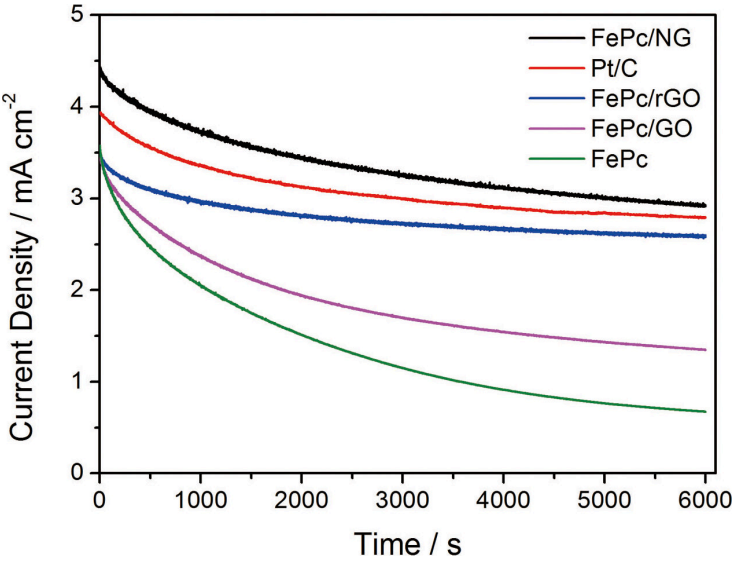

Figure 13. The *i–t* curves of each ORR catalyst at –0.25 V in an O_2-saturated 0.1 M KOH at a rotation speed of 1600 rpm. Reproduced from Ref. 131 with permission. Copyright © 2012 The Royal Society of Chemistry.

capacity of 782 mAh g^{-1}, and thus can be a good substitute for the graphite anode; however, the major problems of SnO_2 are the volume expansion and particle agglomeration, which lead to the rapid capacity fading of SnO_2.[144] To overcome these issues, graphene was reassembled in the presence of SnO_2 nanoparticles, and the SnO_2/graphene composite suggested that both graphene and SnO_2 nanoparticles played an important role as anode materials to get a synergetic effect. The reason for the improved performance can be attributed to that the surrounding graphene limits the volume expansion of SnO_2 and that the pores between SnO_2 and graphene provide buffered spaces during the charge and discharge process (Figure 14).[145] In another example, Co_3S_4, a kind of cobalt sulfide,[146,147] was employed as an anode material for LIBs, and its performance could be further enhanced by the introduction of graphene.[148] In a typical synthesis, graphene was firstly produced via a solvothermal approach using GO as the starting material in the presence of NaOH solution. The Co_3S_4/graphene composite was then fabricated via a liquid-phase reaction by mixing $Co(CO)_{0.35}Cl_{0.20}(OH)_{1.10}$ (as cobalt source, prepared from $CoCl_2$ $6H_2O$ and urea), graphene, and thioacetamide (as sulfur source) in a Teflon-lined autoclave (Figure 14). The resultant Co_3S_4/graphene composite showed a high LIB performance because of the porous structure of Co_3S_4 and the conductive and elastic graphene matrix, which

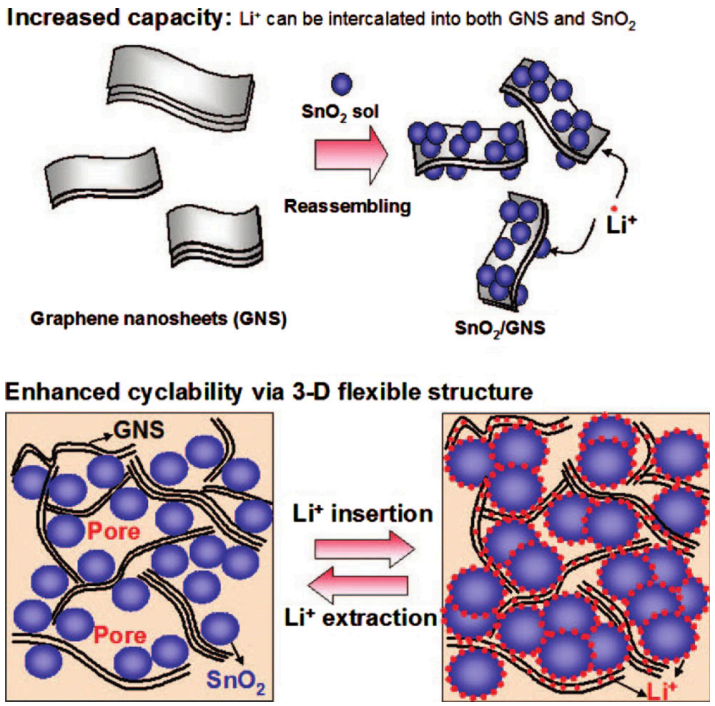

Figure 14. Scheme of the preparation and the structure of SnO_2/graphene composite. Reproduced from Ref. 145 with permission. Copyright © 2009 American Chemical Society.

enable both Li^+ and e^- to migrate and occupy all active sites of the composites and protect it from structural changes during lithium insertion and extraction.[148]

Another interesting work is about Ni_3S_4/nitrogen-doped graphene composite. It is well-known that nickel sulfides, such as NiS, NiS_2, $Ni_{3+x}S_2$, Ni_3S_2, Ni_3S_{4+x}, Ni_3S_4, Ni_6S_5, Ni_7S_6, and Ni_9S_8, have potential application in the field of LIBs due to their high theoretical capacities and low cost.[149–151] Among them, Ni_3S_4, with its high theoretical capacity (704.5 mAh g^{-1}), safety, and cost effectiveness, is a promising candidate for anode material in LIBs. However, the challenge associated with the synthesis of Ni_3S_4 lies in obtaining its pure phase, because Ni_3S_4 would be easily crystallized with impurities of NiS and/or NiS_2 by traditional solid-state methods at high temperature.[152,153] To solve this issue, a facile solvothermal approach was developed for the phase-controlled synthesis of Ni_3S_4 nanoparticles grown on the nitrogen-doped graphene. Nitrogen-doped graphene was prepared by treating GO in the presence of ammonia solution and NaOH. NaOH

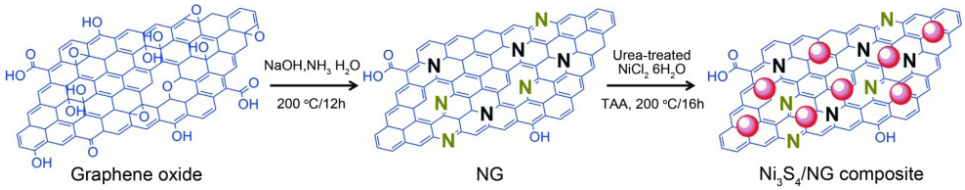

Figure 15. Scheme of the preparation of Ni_3S_4/nitrogen-doped graphene composite. Reproduced from Ref. 154 with permission. Copyright © 2013 Wiley.

is used to enlarge the size of graphene for the maximum loading of nanoparticles. Afterward, $NiCl_2$ $6H_2O$ was reacted with urea to produce $Ni_2(CO_3)(OH)_2$ as nickel precursor, while thioacetamide was used as sulfur source. (Figure 15).[154]

For a better electrochemical coupling between Ni_3S_4 and nitrogen-doped graphene, which is beneficial to the LIB performance, annealing treatment was further employed. When the annealing temperature reached higher than 250 °C, X-ray diffraction (XRD) characterization indicated the formation of a new phase of nickel sulfide, $NiS_{1.03}$. Nitrogen-doped graphene was used in this study because it had much better charge and discharge performance compared to undoped graphene. The elemental composition of the composite was investigated by XPS. The N 1s spectra of all composites could be resolved into two components, indicative of the presence of two nitrogen states (pyridinic N and graphitic N). The largest amount of pyridinic N in the Ni_3S_4/nitrogen-doped graphene-250 °C composite may hopefully endow it the best LIB performance among all composites because such nitrogen state have proved to be very effective during the charge and discharge process of LIBs[155] (Figure 16).

The electrochemical performance of Ni_3S_4/nitrogen-doped graphene-250 °C composite was firstly evaluated by the charge and discharge curves. Obviously, the charge and discharge capacities of the 2nd and 50th cycles are almost the same, indicating an extraordinary capacity retention and cyclic behavior of the composite. The cyclic behavior and Coulombic efficiency of Ni_3S_4/nitrogen-doped graphene-250 °C composite was then measured, and the results showed that the composite possessed excellent rate capability and very high charge and discharge capacities, with nearly 100% of Coulombic efficiency. As expected, the discharge capacity of pure Ni_3S_4 degraded fast in the initial cycles, probably due to the volume expansion of Ni_3S_4, some side reactions, and the formation of polysulfide anions that would pass through the separator membrane toward cathode and cause low conductivity. By addition

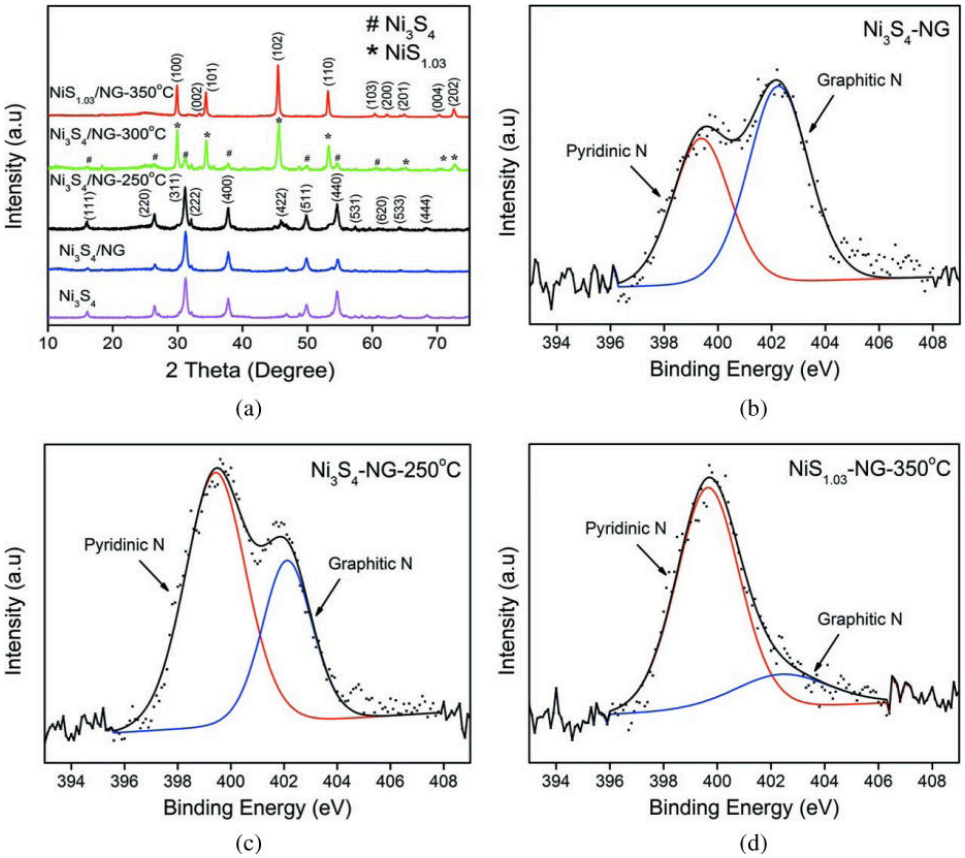

Figure 16. (a) XRD patterns of Ni_3S_4 and nickel sulfides/nitrogen-doped graphene composites; XPS N 1s spectra of (b) Ni_3S_4/nitrogen-doped graphene, (c) Ni_3S_4/nitrogen-doped graphene-250 °C, and (d) $NiS_{1.03}$/nitrogen-doped graphene-350 °C composites. Reproduced from Ref. 154 with permission. Copyright © 2013 Wiley.

of nitrogen-doped graphene, the cyclic behavior of Ni_3S_4/nitrogen-doped graphene composite was significantly improved because nitrogen-doped graphene could effectively save the structural changes in composite and also absorb the polysulfide anions due to the elastically strong and porous nature.[154] After annealing treatment, the performance of Ni_3S_4/nitrogen-doped graphene composite was further enhanced, and the Ni_3S_4/nitrogen-doped graphene-250 °C composite showed the highest discharge capacity. Surprisingly, when the current rate reached up to 4 C (C is taken to be 704.5 mAh g^{-1}), the Ni_3S_4/nitrogen-doped graphene-250 °C composite still showed a very stable performance, suggesting its great potential in LIBs to replace commercial graphite anode (Figure 17).

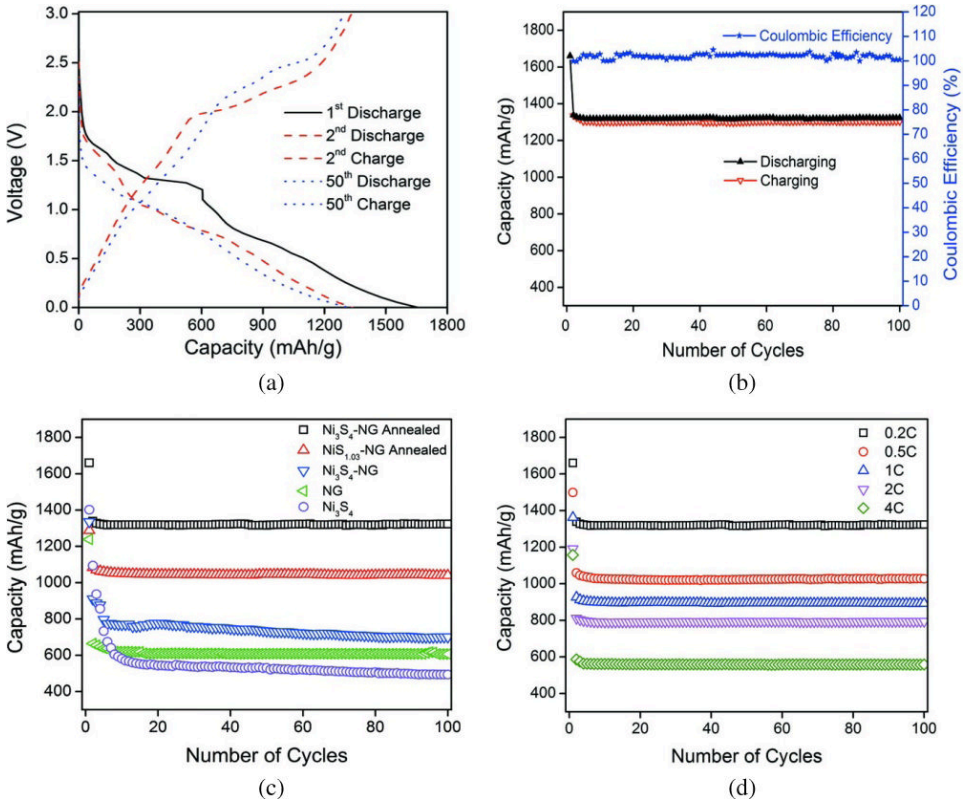

Figure 17. (a) Charge and discharge curves of Ni_3S_4/nitrogen-doped graphene-250 °C composite at 0.2 C in the voltage range of 3–0 V; (b) cyclic behavior and Coulombic efficiency of Ni_3S_4/nitrogen-doped graphene-250 °C composite at 0.2 C in the voltage range of 3–0 V; (c) comparison of discharge capacities of Ni_3S_4, nitrogen-doped graphene, and nickel sulfides/nitrogen-doped graphene composites at 0.2 C in the voltage range of 3–0 V; (d) comparison of discharge capacities of Ni_3S_4/nitrogen-doped graphene-250 °C composite at various current rates in the voltage range of 3–0 V. Reproduced from Ref. 154 with permission. Copyright © 2013 Wiley.

4.3. Graphene-based composites for supercapacitors

Apart from being used in the fields of fuel cells and LIBs, graphene-based composites can be also used for supercapacitors.[156,157] Supercapacitors are electrochemical devices for storing and releasing energy rapidly and reversibly,[158] which can be classified by different storage mechanisms into two groups: (i) electrical double-layer capacitors (EDLCs) and (ii) pseudocapacitors.[159] The storage mechanism of EDLC is non-faradic, while that of

pseudocapacitor is based on faradic and its electrode material for redox reaction includes electrically conducting polymers and metal oxides.[160] For example, MnO_2 is a promising material for pseudocapacitors owing to its high specific capacitance, cost effectiveness, and environmental friendliness,[161] but it suffered from poor electrical conductivity and low accessible surface.[162] With the aid of graphene, the nanostructured graphene/MnO_2 was prepared through the self-limiting deposition of MnO_2 particles on graphene surface under microwave irradiation. The composite displayed a high specific capacitance which was almost three times than that of pure graphene and MnO_2.[163] In another example, single-crystalline $Ni(OH)_2$ hexagonal nanoplates was *in situ* grown on the surface of lightly oxidized, electrically conducting graphene, and the composite showed significantly enhanced specific capacitance compared to $Ni(OH)_2$ grown on highly oxidized GO and $Ni(OH)_2$ physically mixed with graphene.[164]

5. Conclusions

The research about graphene and graphene-based nanomaterials started in 2004. As shown in Section 2, liquid-phase reaction is one of the most effective methods for the preparation of graphene materials because of its facile condition, inexpensive cost, and potential for large-scale production. In Section 3, synthesis and applications of nitrogen-doped graphene have been intensively discussed. The intentional incorporation of heteroatoms into graphene structure can effectively modify its electronic and chemical properties, and hence nitrogen-doped graphene exhibited promising potential in various fields, such as ORR of fuel cells and rechargeable LIBs. Finally, Section 4 shows the preparation of graphene-based composites and their practical uses in ORR, LIBs, and supercapacitors. The development of graphene-based nanomaterials is still at its initial stage, and this novel two-dimensional material may give our life more and more surprises in the next 10 years.

References

1. Novoselov, K. S.; Geim, A. K.; Morozov, S. V.; Jiang, D.; Zhang, Y.; Dubonos, S. V.; Grigorieva, I. V.; Firsov, A. A. *Science* **2004**, *306*, 666.
2. Wu, J. S.; Pisula, W.; Müllen, K. *Chem. Rev.* **2007**, *107*, 718.
3. Allen, M. J.; Tung, V. C.; Kaner, R. B. *Chem. Rev.* **2010**, *110*, 132.
4. Cui, X.; Zhang, C.; Hao, R.; Hou, Y. *Nanoscale* **2011**, *3*, 2118.
5. Lherbier, A.; Blase, X.; Niquet, Y.-M.; Triozon, F.; Roche, S. *Phys. Rev. Lett.* **2008**, *101*, 036808.

6. Wang, H.; Maiyalagan, T.; Wang, X. *ACS Catal.* **2012**, *2*, 781.
7. Parvez, K.; Yang, S.; Hernandez, Y.; Winter, A.; Turchanin, A.; Feng, X.; Müllen, K. *ACS Nano* **2012**, *6*, 9541.
8. Panchakarla, L. S.; Subrahmanyam, K. S.; Saha, S. K.; Govindaraj, A.; Krishnamurthy, H. R.; Waghmare, U. V.; Rao, C. N. R. *Adv. Mater.* **2009**, *21*, 4726.
9. Liang, J.; Jiao, Y.; Jaroniec, M.; Qiao, S. Z. *Angew. Chem. Int. Ed.* **2012**, *51*, 11496.
10. Sun, Y.; Wu, Q.; Shi, G. *Energy Environ. Sci.* **2011**, *4*, 1113.
11. Yan, X.-Y.; Tong, X.-L.; Zhang, Y.-F.; Han, X.-D.; Wang, Y.-Y.; Jin, G.-Q.; Qin, Y.; Guo, X.-Y. *Chem. Commun.* **2012**, *48*, 1892.
12. Zhou, X.; Wang, F.; Zhu, Y.; Liu, Z. *J. Mater. Chem.* **2011**, *21*, 3353.
13. Marconcini, P.; Cresti, A.; Triozon, F.; Fiori, G.; Biel, B.; Niquet, Y.-M.; Macucci, M.; Roche, S. *ACS Nano* **2012**, *6*, 7942.
14. Du, X. A.; Guo, P.; Song, H. H.; Chen, X. H. *Electrochim. Acta* **2010**, *55*, 4812.
15. Li, X.; Wang, X.; Zhang, L.; Lee, S.; Dai, H. *Science* **2008**, *319*, 1229.
16. Li, X.; Zhang, G.; Bai, X.; Sun, X.; Wang, X.; Wang, E.; Dai, H. *Nat. Nanotechnol.* **2008**, *3*, 538.
17. Hernandez, Y.; Nicolosi, V.; Lotya, M.; Blighe, F. M.; Sun, Z.; De, S.; McGovern, I. T.; Holland, B.; Byrne, M.; Gun'ko, Y. K.; Boland, J. J.; Niraj, P.; Duesberg, G.; Krishnamurthy, S.; Goodhue, R.; Hutchison, J.; Scardaci, V.; Ferrari, A. C.; Coleman, J. N. *Nat. Nanotechnol.* **2008**, *3*, 563.
18. Lotya, M.; Hernandez, Y.; King, P. J.; Smith, R. J.; Nicolosi, V.; Karlsson, L. S.; Blighe, F. M.; De, S.; Wang, Z. M.; McGovern, I. T.; Duesberg, G. S.; Coleman, J. N. *J. Am. Chem. Soc.* **2009**, *131*, 3611.
19. Lotya, M.; King, P. J.; Khan, U.; De, S.; Coleman, J. N. *ACS Nano* **2010**, *4*, 3155.
20. Hummers, W. S.; Offeman, R. E. *J. Am. Chem. Soc.* **1958**, *80*, 1339.
21. Gao, W.; Alemany, L. B.; Ci, L.; Ajayan, P. M. *Nat. Chem.* **2009**, *1*, 403.
22. Tung, V. C.; Allen, M. J.; Yang, Y.; Kaner, R. B. *Nat. Nanotechnol.* **2009**, *4*, 25.
23. Park, S.; An, J. H.; Piner, R. D.; Jung, I.; Yang, D. X.; Velamakanni, A.; Nguyen, S. T.; Ruoff, R. S. *Chem. Mater.* **2008**, *20*, 6592.
24. Williams, G.; Seger, B.; Kamat, P. V. *ACS Nano* **2008**, *2*, 1487.
25. Pu, N.-W.; Wang, C.-A.; Sung, Y.; Liu, Y.-M.; Ger, M.-D. *Mater. Lett.* **2009**, *63*, 1987.
26. Liu, N.; Luo, F.; Wu, H. X.; Liu, Y. H.; Zhang, C.; Chen, J. *Adv. Funct. Mater.* **2008**, *18*, 1518.

27. Behabtu, N.; Lomeda, J. R.; Green, M. J.; Higginbotham, A. L.; Sinitskii, A.; Kosynkin, D. V.; Tsentalovich, D.; Parra-Vasquez, A. N. G.; Schmidt, J.; Kesselman, E.; Cohen, Y.; Talmon, Y.; Tour, J. M.; Pasquali, M. *Nat. Nanotechnol.* **2010**, *5*, 406.
28. Jiang, B.; Tian, C.; Wang, L.; Xu, Y.; Wang, R.; Qiao, Y.; Ma, Y.; Fu, H. *Chem. Commun.* **2010**, *46*, 4920.
29. Janowska, I.; Chizari, K.; Ersen, O.; Zafeiratos, S.; Soubane, D.; Costa, V.; Speisser, V.; Boeglin, C.; Houllé, M.; Bégin, D.; Plee, D.; Ledoux, M.-J.; Pham-Huu, C. *Nano Res.* **2010**, *3*, 126.
30. Hao, R.; Qian, W.; Zhang, L.; Hou, Y. *Chem. Commun.* **2008**, 6576.
31. Umemoto, K.; Okamura, N. *Bull. Chem. Soc. Jpn.* **1986**, *59*, 3047.
32. Meyer, J. C.; Geim, A. K.; Katsnelson, M. I.; Novoselov, K. S.; Booth, T. J.; Roth, S. *Nature* **2007**, *446*, 60.
33. Sun, Z.; Kohama, S.-i.; Zhang, Z.; Lomeda, J. R.; Tour, J. M. *Nano Res.* **2010**, *3*, 117.
34. Lee, J. H.; Shin, D. W.; Makotchenko, V. G.; Nazarov, A. S.; Fedorov, V. E.; Kim, Y. H.; Choi, J.-Y.; Kim, J. M.; Yoo, J.-B. *Adv. Mater.* **2009**, *21*, 4383.
35. Zheng, J.; Di, C.-a.; Liu, Y.; Liu, H.; Guo, Y.; Du, C.; Wu, T.; Yu, G.; Zhu, D. *Chem. Commun.* **2010**, *46*, 5728.
36. Qian, W.; Hao, R.; Hou, Y.; Tian, Y.; Shen, C.; Gao, H.; Liang, X. *Nano Res.* **2009**, *2*, 706.
37. Das, A.; Pisana, S.; Chakraborty, B.; Piscanec, S.; Saha, S. K.; Waghmare, U. V.; Novoselov, K. S.; Krishnamurthy, H. R.; Geim, A. K.; Ferrari, A. C.; Sood, A. K. *Nat. Nanotechnol.* **2008**, *3*, 210.
38. Sheng, Z.-H.; Shao, L.; Chen, J.-J.; Bao, W.-J.; Wang, F.-B.; Xia, X.-H. *ACS Nano* **2011**, *5*, 4350.
39. Ferrari, A. C.; Meyer, J. C.; Scardaci, V.; Casiraghi, C.; Lazzeri, M.; Mauri, F.; Piscanec, S.; Jiang, D.; Novoselov, K. S.; Roth, S.; Geim, A. K. *Phys. Rev. Lett.* **2006**, *97*, 187401.
40. Cote, L. J.; Kim, F.; Huang, J. *J. Am. Chem. Soc.* **2009**, *131*, 1043.
41. Stankovich, S.; Dikin, D. A.; Piner, R. D.; Kohlhaas, K. A.; Kleinhammes, A.; Jia, Y.; Wu, Y.; Nguyen, S. T.; Ruoff, R. S. *Carbon* **2007**, *45*, 1558.
42. Shin, H.-J.; Kim, K. K.; Benayad, A.; Yoon, S.-M.; Park, H. K.; Jung, I.-S.; Jin, M. H.; Jeong, H.-K.; Kim, J. M.; Choi, J.-Y.; Lee, Y. H. *Adv. Funct. Mater.* **2009**, *19*, 1987.
43. Wang, G. X.; Yang, J.; Park, J.; Gou, X. L.; Wang, B.; Liu, H.; Yao, J. *J. Phys. Chem. C* **2008**, *112*, 8192.
44. Fan, Z.-J.; Kai, W.; Yan, J.; Wei, T.; Zhi, L.-J.; Feng, J.; Ren, Y.-m.; Song, L.-P.; Wei, F. *ACS Nano* **2011**, *5*, 191.

45. Zhou, Y.; Bao, Q.; Tang, L. A. L.; Zhong, Y.; Loh, K. P. *Chem. Mater.* **2009**, *21*, 2950.
46. Wang, H.; Robinson, J. T.; Li, X.; Dai, H. *J. Am. Chem. Soc.* **2009**, *131*, 9910.
47. Dubin, S.; Gilje, S.; Wang, K.; Tung, V. C.; Cha, K.; Hall, A. S.; Farrar, J.; Varshneya, R.; Yang, Y.; Kaner, R. B. *ACS Nano* **2010**, *4*, 3845.
48. Yang, Z.; Yao, Z.; Li, G.; Fang, G.; Nie, H.; Liu, Z.; Zhou, X.; Chen, X.; Huang, S. *ACS Nano* **2012**, *6*, 205.
49. Some, S.; Kim, J.; Lee, K.; Kulkarni, A.; Yoon, Y.; Lee, S.; Kim, T.; Lee, H. *Adv. Mater.* **2012**, *24*, 5481.
50. Li, X.; Fan, L.; Li, Z.; Wang, K.; Zhong, M.; Wei, J.; Wu, D.; Zhu, H. *Adv. Energy Mater.* **2012**, *2*, 425.
51. Luo, Z.; Lim, S.; Tian, Z.; Shang, J.; Lai, L.; MacDonald, B.; Fu, C.; Shen, Z.; Yu, T.; Lin, J. *J. Mater. Chem.* **2011**, *21*, 8038.
52. Jin, Z.; Yao, J.; Kittrell, C.; Tour, J. M. *ACS Nano* **2011**, *5*, 4112.
53. Zhang, L.; Zhao, X.; Ji, H.; Stoller, M.; Lai, L.; Murali, S.; McDonnell, S.; Cleveger, B.; Wallace, R. M.; Ruoff, R. *Energy Environ. Sci.* **2012**, *5*, 9618.
54. Zhang, L. S.; Liang, X. Q.; Song, W. G.; Wu, Z. Y. *Phys. Chem. Chem. Phys.* **2010**, *12*, 12055.
55. Guo, B.; Liu, Q.; Chen, E.; Zhu, H.; Fang, L.; Gong, J. R. *Nano Lett.* **2010**, *10*, 4975.
56. Geng, D.; Yang, S.; Zhang, Y.; Yang, J.; Liu, J.; Li, R.; Sham, T.-K.; Sun, X.; Ye, S.; Knights, S. *Appl. Surf. Sci.* **2011**, *257*, 9193.
57. Geng, D.; Chen, Y.; Chen, Y.; Li, Y.; Li, R.; Sun, X.; Ye, S.; Knights, S. *Energy Environ. Sci.* **2011**, *4*, 760.
58. Yoo, E.; Nakamura, J.; Zhou, H. *Energy Environ. Sci.* **2012**, *5*, 6928.
59. Lin, Z.; Waller, G.; Liu, Y.; Liu, M.; Wong, C.-P. *Adv. Energy Mater.* **2012**, *2*, 884.
60. Shao, Y.; Zhang, S.; Engelhard, M. H.; Li, G.; Shao, G.; Wang, Y.; Liu, J.; Aksay, I. A.; Lin, Y. *J. Mater. Chem.* **2010**, *20*, 7491.
61. Jeong, H. M.; Lee, J. W.; Shin, W. H.; Choi, Y. J.; Shin, H. J.; Kang, J. K.; Choi, J. W. *Nano Lett.* **2011**, *11*, 2472.
62. Ghosh, A.; Late, D. J.; Panchakarla, L. S.; Govindaraj, A.; Rao, C. N. R. *J. Exp. Nanosci.* **2009**, *4*, 313.
63. Li, N.; Wang, Z.; Zhao, K.; Shi, Z.; Gu, Z.; Xu, S. *Carbon* **2010**, *48*, 255.
64. Deng, D. H.; Pan, X. L.; Yu, L. A.; Cui, Y.; Jiang, Y. P.; Qi, J.; Li, W. X.; Fu, Q. A.; Ma, X. C.; Xue, Q. K.; Sun, G. Q.; Bao, X. H. *Chem. Mater.* **2011**, *23*, 1188.
65. Wang, D.-W.; Gentle, I. R.; Lu, G. Q. *Electrochem. Commun.* **2010**, *12*, 1423.
66. Wang, X.; Li, X.; Zhang, L.; Yoon, Y.; Weber, P. K.; Wang, H.; Guo, J.; Dai, H. *Science* **2009**, *324*, 768.

67. Li, X.; Wang, H.; Robinson, J. T.; Sanchez, H.; Diankov, G.; Dai, H. *J. Am. Chem. Soc.* **2009**, *131*, 15939.
68. Zhang, C.; Fu, L.; Liu, N.; Liu, M.; Wang, Y.; Liu, Z. *Adv. Mater.* **2011**, *23*, 1020.
69. Qian, W.; Cui, X.; Hao, R.; Hou, Y.; Zhang, Z. *ACS Appl. Mater. Interfaces* **2011**, *3*, 2259.
70. Long, D.; Li, W.; Ling, L.; Miyawaki, J.; Mochida, I.; Yoon, S.-H. *Langmuir* **2010**, *26*, 16096.
71. Zhang, Y.; Fugane, K.; Mori, T.; Niu, L.; Ye, J. *J. Mater. Chem.* **2012**, *22*, 6575.
72. Zhang, C.; Hao, R.; Liao, H.; Hou, Y. *Nano Energy* **2013**, *2*, 88.
73. Lee, K. R.; Lee, K. U.; Lee, J. W.; Ahn, B. T.; Woo, S. I. *Electrochem. Commun.* **2010**, *12*, 1052.
74. Pylypenko, S.; Queen, A.; Olson, T. S.; Dameron, A.; O'Neill, K.; Neyerlin, K. C.; Pivovar, B.; Dinh, H. N.; Ginley, D. S.; Gennett, T.; O'Hayre, R. *J. Phys. Chem. C* **2011**, *115*, 13667.
75. Lin, Z.; Song, M.-k.; Ding, Y.; Liu, Y.; Liu, M.; Wong, C.-p. *Phys. Chem. Chem. Phys.* **2012**, *14*, 3381.
76. Yang, S.-Y.; Chang, K.-H.; Huang, Y.-L.; Lee, Y.-F.; Tien, H.-W.; Li, S.-M.; Lee, Y.-H.; Liu, C.-H.; Ma, C.-C. M.; Hu, C.-C. *Electrochem. Commun.* **2012**, *14*, 39.
77. Hwang, J. O.; Park, J. S.; Choi, D. S.; Kim, J. Y.; Lee, S. H.; Lee, K. E.; Kim, Y.-H.; Song, M. H.; Yoo, S.; Kim, S. O. *ACS Nano* **2012**, *6*, 159.
78. Hasan, S. A.; Tsekoura, E. K.; Sternhagen, V.; Strømme, M. *J. Phys. Chem. C* **2012**, *116*, 6530.
79. Jiang, B.; Tian, C.; Wang, L.; Sun, L.; Chen, C.; Nong, X.; Qiao, Y.; Fu, H. *Appl. Surf. Sci.* **2012**, *258*, 3438.
80. Wu, P.; Qian, Y.; Du, P.; Zhang, H.; Cai, C. *J. Mater. Chem.* **2012**, *22*, 6402.
81. Pels, J. R.; Kapteijn, F.; Moulijn, J. A.; Zhu, Q.; Thomas, K. M. *Carbon* **1995**, *33*, 1641.
82. Lin, Y.-C.; Lin, C.-Y.; Chiu, P.-W. *Appl. Phys. Lett.* **2010**, *96*, 133110.
83. Kelemen, S. R.; Afeworki, M.; Gorbaty, M. L.; Kwiatek, P. J.; Solum, M. S.; Hu, J. Z.; Pugmire, R. J. *Energy Fuels* **2002**, *16*, 1507.
84. Steele, B. C. H.; Heinzel, A. *Nature* **2001**, *414*, 345.
85. Yu, Y.; Hu, Y.; Liu, X.; Deng, W.; Wang, X. *Electrochim. Acta* **2009**, *54*, 3092.
86. Wang, S.; Yu, D.; Dai, L.; Chang, D. W.; Baek, J.-B. *ACS Nano* **2011**, *5*, 6202.
87. Liang, Y.; Wang, H.; Zhou, J.; Li, Y.; Wang, J.; Regier, T.; Dai, H. *J. Am. Chem. Soc.* **2012**, *134*, 3517.
88. Wu, J.; Zhang, D.; Wang, Y.; Wan, Y.; Hou, B. *J. Power Sources* **2012**, *198*, 122.
89. Liu, R.; Malotki, C.; Arnold, L.; Koshino, N.; Higashimura, H.; Baumgarten, M.; Müllen, K. *J. Am. Chem. Soc.* **2011**, *133*, 10372.

90. Jahan, M.; Bao, Q.; Loh, K. P. *J. Am. Chem. Soc.* **2012**, *134*, 6707.
91. Yang, S.; Feng, X.; Wang, X.; Müllen, K. *Angew. Chem. Int. Ed.* **2011**, *50*, 5339.
92. Choi, H.-J.; Jung, S.-M.; Seo, J.-M.; Chang, D. W.; Dai, L.; Baek, J.-B. *Nano Energy* **2012**, *1*, 534.
93. Gong, K.; Du, F.; Xia, Z.; Durstock, M.; Dai, L. *Science* **2009**, *323*, 760.
94. Zhang, L.; Niu, J.; Dai, L.; Xia, Z. *Langmuir* **2012**, *28*, 7542.
95. Kurak, K. A.; Anderson, A. B. *J. Phys. Chem. C* **2009**, *113*, 6730.
96. Wang, S.; Zhang, L.; Xia, Z.; Roy, A.; Chang, D. W.; Baek, J.-B.; Dai, L. *Angew. Chem. Int. Ed.* **2012**, *51*, 4209.
97. Wang, S.; Iyyamperumal, E.; Roy, A.; Xue, Y.; Yu, D.; Dai, L. *Angew. Chem. Int. Ed.* **2011**, *50*, 11756.
98. Yu, D.; Zhang, Q.; Dai, L. *J. Am. Chem. Soc.* **2010**, *132*, 15127.
99. Lee, J.-S.; Park, G. S.; Kim, S. T.; Liu, M.; Cho, J. *Angew. Chem. Int. Ed.* **2012**, *52*, 1026.
100. Qu, L.; Liu, Y.; Baek, J.-B.; Dai, L. *ACS Nano* **2010**, *4*, 1321.
101. Liu, R.; Wu, D.; Feng, X.; Müllen, K. *Angew. Chem. Int. Ed.* **2010**, *49*, 2565.
102. Sun, Y.; Li, C.; Shi, G. *J. Mater. Chem.* **2012**, *22*, 12810.
103. Lai, L.; Potts, J. R.; Zhan, D.; Wang, L.; Poh, C. K.; Tang, C.; Gong, H.; Shen, Z.; Lin, J.; Ruoff, R. S. *Energy Environ. Sci.* **2012**, *5*, 7936.
104. Wu, Z.-S.; Ren, W.; Xu, L.; Li, F.; Cheng, H.-M. *ACS Nano* **2011**, *5*, 5463.
105. Reddy, A. L. M.; Srivastava, A.; Gowda, S. R.; Gullapalli, H.; Dubey, M.; Ajayan, P. M. *ACS Nano* **2010**, *4*, 6337.
106. Wang, H.; Zhang, C.; Liu, Z.; Wang, L.; Han, P.; Xu, H.; Zhang, K.; Dong, S.; Yao, J.; Cui, G. *J. Mater. Chem.* **2011**, *21*, 5430.
107. Cho, Y. J.; Kim, H. S.; Im, H.; Myung, Y.; Jung, G. B.; Lee, C. W.; Park, J.; Park, M.-H.; Cho, J.; Kang, H. S. *J. Phys. Chem. C* **2011**, *115*, 9451.
108. Zhang, M.; Dai, L. *Nano Energy* **2012**, *1*, 514.
109. Ye, J.; Liu, W.; Cai, J.; Chen, S.; Zhao, X.; Zhou, H.; Qi, L. *J. Am. Chem. Soc.* **2010**, *133*, 933.
110. Miller, J. R.; Outlaw, R. A.; Holloway, B. C. *Science* **2010**, *329*, 1637.
111. Wang, X.; Zhi, L.; Müllen, K. *Nano Lett.* **2007**, *8*, 323.
112. Xie, X.; Yu, G.; Liu, N.; Bao, Z.; Criddle, C. S.; Cui, Y. *Energy Environ. Sci.* **2012**, *5*, 6862.
113. Evanoff, K.; Magasinski, A.; Yang, J.; Yushin, G. *Adv. Energy Mater.* **2011**, *1*, 495.
114. Wu, Z.-S.; Winter, A.; Chen, L.; Sun, Y.; Turchanin, A.; Feng, X.; Müllen, K. *Adv. Mater.* **2012**, *24*, 5130.
115. Xue, Y.; Liu, J.; Chen, H.; Wang, R.; Li, D.; Qu, J.; Dai, L. *Angew. Chem. Int. Ed.* **2012**, *51*, 12124.

116. Xin, Y.; Liu, J.-g.; Jie, X.; Liu, W.; Liu, F.; Yin, Y.; Gu, J.; Zou, Z. *Electrochim. Acta* **2012**, *60*, 354.
117. Qiu, Y.; Yan, K.; Yang, S.; Jin, L.; Deng, H.; Li, W. *ACS Nano* **2010**, *4*, 6515.
118. He, Y.; Chen, W.; Li, X.; Zhang, Z.; Fu, J.; Zhao, C.; Xie, E. *ACS Nano* **2013**, *1*, 174.
119. Xu, Y.; Bai, H.; Lu, G.; Li, C.; Shi, G. *J. Am. Chem. Soc.* **2008**, *130*, 5856.
120. Antolini, E. *Appl. Catal. B* **2009**, *88*, 1.
121. Kongkanand, A.; Kuwabata, S.; Girishkumar, G.; Kamat, P. *Langmuir* **2006**, *22*, 2392.
122. Kou, R.; Shao, Y.; Wang, D.; Engelhard, M. H.; Kwak, J. H.; Wang, J.; Viswanathan, V. V.; Wang, C.; Lin, Y.; Wang, Y.; Aksay, I. A.; Liu, J. *Electrochem. Commun.* **2009**, *11*, 954.
123. Shao, Y.; Zhang, S.; Wang, C.; Nie, Z.; Liu, J.; Wang, Y.; Lin, Y. *J. Power Sources* **2010**, *195*, 4600.
124. Zhu, C.; Guo, S.; Zhai, Y.; Dong, S. *Langmuir* **2010**, *26*, 7614.
125. Liang, Y.; Li, Y.; Wang, H.; Zhou, J.; Wang, J.; Regier, T.; Dai, H. *Nat. Mater.* **2011**, *10*, 780.
126. Wang, H.; Liang, Y.; Li, Y.; Dai, H. *Angew. Chem. Int. Ed.* **2011**, *50*, 10969.
127. Li, W.; Yu, A.; Higgins, D. C.; Llanos, B. G.; Chen, Z. *J. Am. Chem. Soc.* **2010**, *132*, 17056.
128. Baranton, S.; Coutanceau, C.; Roux, C.; Hahn, F.; Léger, J.-M. *J. Electroanal. Chem.* **2005**, *577*, 223.
129. Dong, G.; Huang, M.; Guan, L. *Phys. Chem. Chem. Phys.* **2012**, *14*, 2557.
130. Chen, R.; Li, H.; Chu, D.; Wang, G. *J. Phys. Chem. C* **2009**, *113*, 20689.
131. Zhang, C.; Hao, R.; Yin, H.; Liu, F.; Hou, Y. *Nanoscale* **2012**, *4*, 7326.
132. Elemans, J. A. A. W.; van Hameren, R.; Nolte, R. J. M.; Rowan, A. E. *Adv. Mater.* **2006**, *18*, 1251.
133. Wang, S.; Goh, B. M.; Manga, K. K.; Bao, Q.; Yang, P.; Loh, K. P. *ACS Nano* **2010**, *4*, 6180.
134. Mensing, J. P.; Kerdcharoen, T.; Sriprachuabwong, C.; Wisitsoraat, A.; Phokharatkul, D.; Lomas, T.; Tuantranont, A. *J. Mater. Chem.* **2012**, *22*, 17094.
135. Liu, C.; Li, F.; Ma, L.-P.; Cheng, H.-M. *Adv. Mater.* **2010**, *22*, E28.
136. Arico, A. S.; Bruce, P.; Scrosati, B.; Tarascon, J.-M.; van Schalkwijk, W. *Nat. Mater.* **2005**, *4*, 366.
137. Liang, M.; Zhi, L. *J. Mater. Chem.* **2009**, *19*, 5871.
138. Yoo, E.; Kim, J.; Hosono, E.; Zhou, H.-s.; Kudo, T.; Honma, I. *Nano Lett.* **2008**, *8*, 2277.
139. Pan, D.; Wang, S.; Zhao, B.; Wu, M.; Zhang, H.; Wang, Y.; Jiao, Z. *Chem. Mater.* **2009**, *21*, 3136.

140. Zhang, W.-M.; Wu, X.-L.; Hu, J.-S.; Guo, Y.-G.; Wan, L.-J. *Adv. Funct. Mater.* **2008**, *18*, 3941.
141. Cao, F.-F.; Deng, J.-W.; Xin, S.; Ji, H.-X.; Schmidt, O. G.; Wan, L.-J.; Guo, Y.-G. *Adv. Mater.* **2011**, *23*, 4415.
142. Luo, B.; Wang, B.; Li, X.; Jia, Y.; Liang, M.; Zhi, L. *Adv. Mater.* **2012**, *24*, 3538.
143. Zhuo, L.; Wu, Y.; Wang, L.; Yu, Y.; Zhang, X.; Zhao, F. *RSC Adv.* **2012**, *2*, 5084.
144. Wang, Y.; Lee, J. Y.; Zeng, H. C. *Chem. Mater.* **2005**, *17*, 3899.
145. Paek, S.-M.; Yoo, E.; Honma, I. *Nano Lett.* **2008**, *9*, 72.
146. Wang, J.; Ng, S. H.; Wang, G. X.; Chen, J.; Zhao, L.; Chen, Y.; Liu, H. K. *J. Power Sources* **2006**, *159*, 287.
147. Wang, Q.; Jiao, L.; Han, Y.; Du, H.; Peng, W.; Huan, Q.; Song, D.; Si, Y.; Wang, Y.; Yuan, H. *J. Phys. Chem. C* **2011**, *115*, 8300.
148. Mahmood, N.; Zhang, C.; Jiang, J.; Liu, F.; Hou, Y. *Chem. Eur. J.* **2013**, *19*, 5183.
149. Wang, J.-Z.; Chou, S.-L.; Chew, S.-Y.; Sun, J.-Z.; Forsyth, M.; MacFarlane, D. R.; Liu, H.-K. *Solid State Ionics* **2008**, *179*, 2379.
150. Idris, N. H.; Rahman, M. M.; Chou, S.-L.; Wang, J.-Z.; Wexler, D.; Liu, H.-K. *Electrochim. Acta* **2011**, *58*, 456.
151. Aso, K.; Kitaura, H.; Hayashi, A.; Tatsumisago, M. *J. Mater. Chem.* **2011**, *21*, 2987.
152. Manthiram, A.; Jeong, Y. U. *J. Solid State Chem.* **1999**, *147*, 679.
153. An, C.; Zhang, Z.; Chen, X.; Liu, Y. *Mater. Lett.* **2006**, *60*, 3631.
154. Mahmood, N.; Zhang, C.; Hou, Y. *Small* **2013**, *9*, 1321.
155. Li, Y. F.; Zhou, Z.; Wang, L. B. *J. Chem. Phys.* **2008**, *129*, 104703.
156. Wang, D.-W.; Li, F.; Zhao, J.; Ren, W.; Chen, Z.-G.; Tan, J.; Wu, Z.-S.; Gentle, I.; Lu, G. Q.; Cheng, H.-M. *ACS Nano* **2009**, *3*, 1745.
157. Chen, S.; Zhu, J.; Wang, X. *J. Phys. Chem. C* **2010**, *114*, 11829.
158. Kötz, R.; Carlen, M. *Electrochim. Acta* **2000**, *45*, 2483.
159. Conway, B. E.; Birss, V.; Wojtowicz, J. *J. Power Sources* **1997**, *66*, 1.
160. Stoller, M. D.; Park, S. J.; Zhu, Y. W.; An, J. H.; Ruoff, R. S. *Nano Lett.* **2008**, *8*, 3498.
161. Chen, S.; Zhu, J.; Wu, X.; Han, Q.; Wang, X. *ACS Nano* **2010**, *4*, 2822.
162. Fischer, A. E.; Pettigrew, K. A.; Rolison, D. R.; Stroud, R. M.; Long, J. W. *Nano Lett.* **2007**, *7*, 281.
163. Yan, J.; Fan, Z.; Wei, T.; Qian, W.; Zhang, M.; Wei, F. *Carbon* **2010**, *48*, 3825.
164. Wang, H.; Casalongue, H. S.; Liang, Y.; Dai, H. *J. Am. Chem. Soc.* **2010**, *132*, 7472.

Chapter 3

Graphene for Biosensor Applications

*Alexander Zöpfl, Wendy Patterson and Thomas Hirsch**

Institute of Analytical Chemistry, Chemo- and Biosensors
University of Regensburg - 93053 Regensburg, Germany

1. Introduction 83
2. Biosensors for Glucose 87
   2.1. Amperometric glucose biosensors with direct electron transfer 88
   2.2. Amperometric glucose biosensors with detection of H_2O_2 93
   2.3. Mass-sensitive glucose biosensors 101
3. Nucleic Acids 103
4. Proteins 112
   4.1. Cancer biomarkers 113
   4.2. Thrombin 117
   4.3. Amino acids 119
   4.4. Immunoglobulins 122
5. Other Biologically Relevant Analytes 124
6. Conclusions 131
References 133

1. Introduction

Graphene has become a rising star within the family of carbon nanomaterials in recent years. This is reinforced by the European Commission's choice of graphene as a future emerging technology. Research in Europe involving graphene will be funded in one of the first so-called flagship initiatives with 1000 million euros over the next 10 years.[1] The scientific and technological roadmap of the graphene flagship describes graphene as a platform with many beneficial properties. It is a one-atom-thick material with extraordinary strength, but also high flexibility, also having unique electrical and optical

* Corresponding author. E-mail: thomas.hirsch@ur.de

properties. The first applications which can be transferred from academic research to industrial products are proposed for 2015. Transistors are predicted to lead the commercial success of the graphene story, followed by spin valves, flexible displays, radio frequency (RF) tags, ultra-light batteries, solar cells, ultrafast lasers, composite materials, and prostheses. Sensors and biosensors based on graphene are expected to be available on the market by 2017. For the preliminary phase, a ramp-up of 30 months with a total budget of 75 million euros is planned, where about 3–5% will be spent on the development of sensor technologies. Not only in Europe, but also in Asia (mainly Singapore) and in the United States, graphene is proclaimed as an important future key technology. Therefore, the question arises: Will graphene be smart enough to replace some of the materials currently used in biosensor technology?

Without a doubt, graphene is viewed as extremely attractive in many areas of research due to its extraordinary physical properties. As a simple description, one can envision graphene as a single layer of graphite consisting of exactly one layer of a polycyclic aromatic hydrocarbon network, with all carbon atoms hexagonally arranged in a planar condensed ring system of quasi-infinite size.[2] It has a metallic character and consists solely of carbon and hydrogen. A typical sample of 1 g graphene has a surface area of 2630 m^2.[3] It has a Young's modulus of approximately 1100 GPa, which indicates superior mechanical strength.[4] Its high thermal conductivity of 5000 $Wm^{-1}K^{-1}$ and high electrical conductivity of 1738 S m^{-1} are further outstanding properties of graphene. Many more exciting properties have been discovered since 2004 when Andre Geim and Konstantin Novoselov described a simple method for producing and characterizing individual graphene flakes.[5] The prospect of having all of these remarkable properties unified in one material is highly attractive. A combination of transparency, elasticity, and conductivity will immediately bring applications in flexible sensor arrays with electrical addressing and/or optical readout to mind.

The simple synthesis of graphene as described by Andre Geim and Konstantin Novoselov was performed by the so-called Scotch-tape method: A piece of adhesive tape is placed onto a piece of highly ordered pyrolytic graphite and is then removed. The graphite layers which stick to the tape will be cleaved by repeating this procedure again and again. Graphite flakes are transferred from one piece of tape to another and in each step, there is a chance that this layered material gets disrupted. In the last step, the transfer of the graphene to a substrate, the adhesive tape is placed onto and removed from a silicon wafer having a suitable oxide layer. The remaining graphene can be identified simply by interference contrast with an optical microscope. This

method allows single-, bi-, and multilayer graphene to be distinguished and gives access to the study of the physical properties of this unique carbon nanomaterial. For practical application, this synthesis is too laborious and inconvenient, therefore, nearly a dozen methods have been developed so far which allow the preparation of graphene of various dimensions, shapes, and quality.[6] The methods most commonly used are chemical vapor deposition (CVD),[7] epitaxial growth on silicon carbide,[8] or chemical exfoliation.[9] All of these methods are advantageous in some ways, and they are able to produce large quantities of graphene; however, the resulting products do not consist of well-defined, ordered molecules. Oftentimes, even within the same production technique, an ill-defined material (only somewhat resembling that of the ideal graphene at all) will result, and often with slightly different properties from batch to batch. The perfect graphene is characterized by a quasi-infinite size. This cannot be achieved by any preparation method. Graphene is comprised of only a surface, having no bulk phase, but there is always a border. At these edges, the carbon atoms are chemically bound to hydrogen, hydroxyl, carboxyl, and other impurities, influencing the characteristics of the materials. So, as for every nanomaterial, the properties depend strongly on the dimensions of the material. The smaller a perfect single flake, the higher the ratio of the surface to the border length, and the less the material can be claimed as perfect graphene. Furthermore, the structure itself can contain chemical functionalities or impurities, introduced by the synthesis or the transfer of this material. For chemically derived reduced graphene oxide (rGO), for example, elemental analysis showed that about 5% oxygen remains in this material. This has a tremendous influence on the behavior and the properties of rGO, which are no longer the same as found for graphene prepared by the Scotch-tape method. Additionally, many of the graphene materials synthesized have not been adequately classified and so the term "*graphene*" is often used for materials that differ significantly in chemical structure, shape, size, number of layers, and, therefore, in their properties. This problem was previously addressed,[10] but remains unresolved. It is therefore critical to first classify graphene materials before associating the materials with (biosensor) applications. Often this is neglected, and the term graphene is used without giving an exact characterization of the material. An urgent need for all carbon nanomaterials from graphene to graphite (Figure 1) is to come to a consensus to describe this manifold of materials. Furthermore, a standard characterization method is required whereby any researcher can immediately evaluate the quality of the material, in terms of the number of layers, chemical doping, crystallite size, or presence of impurities. All this information can be obtained from Raman spectroscopy studies.[11] Therefore, it should be a mandatory first

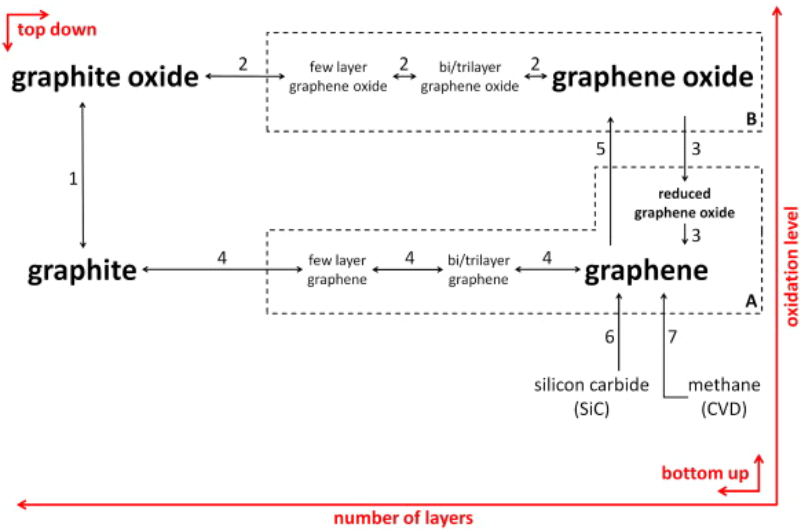

Figure 1. Classification of graphene-related materials. Preparation strategies: (1) Oxidation of graphite to graphite oxide. (2) Stepwise exfoliation of graphite oxide to give graphene oxide (GO) in aqueous colloidal suspensions by sonication and stirring. (3) Reduction of GO by chemical reactions, thermal annealing, flash reduction, enzymatic reduction, or electrodeposition. (4) Mechanical exfoliation of graphite to give graphene (scotch-tape method). (5) Oxidation of graphene sheets to GO. (6) Thermal decomposition of a SiC wafer. (7) Growth of graphene films by CVD. Group A includes graphene materials primarily used for their electronic properties, group B for their optical properties.[2] Reprinted from Ref. 12 with permission. Copyright © 2012 Elsevier.

step for all works regarding graphene synthesis to present a Raman spectrum instead of defining the material by one of the countless numbers acronyms found in literature, such as CRGO, GO, RGO, GR, G, GNS, EG, GNP, CCG, GE, GP, ERGO, GF, EGO, GS, GN, TRGO, CMG, FG, ERGNO, CRGNO, and many more. These acronyms allow for a high risk of confusion (*e.g.*, GO may denote graphite oxide or graphene oxide).

For modern biosensor applications, chemically exfoliated graphene is the most frequently used type. This material differs significantly from pristine graphene due to many defects in its chemical structure and small flake sizes having high polydispersity, yet still has plenty of interesting properties. In addition to the simple production method, GO can be dispersed in aqueous solutions and easily be modified with biomolecules via standard immobilization techniques. If the flakes are small, the material shows weak fluorescence which can be excited over nearly the entire visible range. After a reduction

step, the previously highly distorted aromatic system will be recovered, and the resulting material has been shown to exhibit good electrical conductance, as well as promising quenching abilities. The reduced chemically derived graphene (rGO) is also dispersible in water, but does not form stable solutions. It has a high tendency to aggregate due to excellent π-stacking properties. Nevertheless, chemically derived graphene as well as GO can be processed in solution and therefore transferred to any sensor surface by dip coating, drop casting, or spin coating. As the material in solution is very inhomogeneous, this is also the case for a sensor layer produced from such a solution. Furthermore, the desired one-atom-thick layer will not result, but rather, most likely, few-layered graphene will be deposited.

During the last decade, there have been numerous studies on biosensors employing graphene materials. In the following, we summarize the latest approaches reported on most relevant analytes such as glucose, nucleic acids, proteins, H_2O_2, lipids, pesticides, ions, and even whole cells and viruses.

2. Biosensors for Glucose

Sensors for glucose have been now studied for more than 50 years since Clark and Lyons first proposed the initial concept of enzyme-modified electrodes in 1962.[13] One reason is that diabetes continues to be an increasing worldwide public health problem. Sensors with good precision and accuracy are already commercially available. Such sensors consume only 100 μL of whole blood for the measurement, and results are displayed within a very short time. However, there are still many tasks and challenges for further research in glucose biosensors, for example, the electrical contact between the redox center of the enzyme and the electrode surface could be greatly improved.[14] Here, the electrical conductivity of graphene could be utilized. Another demanding need in the fabrication of enzymatic electrochemical sensors is the immobilization of the biomolecule onto the electrode. In principle, one can entrap the enzyme in a thin polymer film or covalently attach it to the electrode surface. For this first strategy, enzyme leaching can become an issue and long-term stability will be critical to monitor. The second approach is often accompanied by changes in the conformation of the biomolecule and therefore, limitations in the enzyme activity are observed. Furthermore, good electrical communication between the active site of the enzyme and the electrode is mandatory for achieving high sensitivity. The ultimate compromise between the choice of materials and immobilization strategies which results in the best biosensor for glucose detection has yet to be established. Thus, research in the field of glucose biosensors which can achieve high sensitivity,

long-term stability, and excellent selectivity is still a hot topic. Carbon nanomaterials, and especially graphene, have become more prevalent in this research within the last years due to its good electrical transport properties, high surface to volume ratio, as well as numerous possibilities to attach biomolecules.

In amperometric glucose sensing, there are mainly two prominent detection strategies: First, those that measure the direct electron transfer from the enzyme to the electrode during oxidation of glucose. Second, those techniques which catalyze the oxidation of the hydrogen peroxide produced by the enzyme in the presence of glucose. Both strategies are purported to be enhanced by including graphene materials in the sensor design.

2.1. Amperometric glucose biosensors with direct electron transfer

In the case of monitoring the direct electron transfer from the enzyme glucose oxidase (GOx) to the electrode, electrodes where the enzyme is entrapped in conducting polymers have been commonly used. However, by replacing the polymer with graphene, a mediator is no longer required. Direct electron transfer has been observed thus far on electrochemically reduced graphene oxide (ER-GO) on polylysine,[15] mixtures of 3-aminopropyltriethoxysilane (APTES) and graphene,[16] a hybrid material of multi-walled carbon nanotube (MWCNT) and ER-GO,[17] mesoporous materials in combination with ER-GO,[18] ionic liquid (IL)-modified GO,[19–21] bimetallic Au/Pd nanoparticle-decorated ER-GO,[22] and on CdS quantum dot-modified graphene.[23]

The simplest way to construct an amperometric glucose sensor containing graphene is to immobilize a thin film containing both GOx and the carbon nanomaterial onto an electrode.[24–26] GO produced by chemical oxidation of graphite has been used in all three studies. The sensor preparations differ by the fact that in the first case, a simultaneous deposition of graphene and enzyme was implemented, while in the second example, GOx was physisorped in a separate step after graphene deposition on the electrode. The sensor characteristics are nearly identical as can be seen from Table 1. As one example, Unnikrishnan *et al.*[24] dispersed GO together with GOx in 0.1 M phosphate buffer of pH 7. After sonication for 30 min, the solution was drop-casted onto a glassy carbon (GC) electrode. In a further step, the GO was electrochemically reduced by continuous potential cycling between –1.5 and 0 V vs Ag/AgCl for 15 cycles. The authors propose that during the sonication, a covalent linkage of the amino groups of the enzyme to the oxygen-containing moieties at the edge planes of the GO occur. However, evidence

Table 1. Comparison of graphene-based amperometric biosensors with direct electron transfer.

Electrode modification				GOx immobilization	E vs Ag/AgCl mV	Linear range mM	LOD μM	Sensitivity $\mu AmM^{-1}cm^{-2}$	K_m[(a)] mM	No interference by	Ref.
Electrode	Graphene	Composite	Membrane								
GC	ER-GO	MWCNT	Nafion	Polymer entrapment	350	0.01–6.5	4.7	—	—	—	17
GC	GO	Ferrocene	Chitosan	Ionic interaction	300	0.02–7.78	7.6	10	2.1	UA, AA	27
GC	rGO	ZnO	Nafion	Polymer entrapment	–430	0.02–6.24	—	—	—	—	29
GC	GO	—	Chitosan	Polymer entrapment	–437	0.08–12	20	38	—	—	26
GC	rGO	—	—	Sonication with GO	–440	0.1–27	—	1.9	—	DA, UA, AA	24
GC	rGO	—	—	Physisorption	–425	0.1–10	10	110	—	—	25
GC	rGO	Au	—	Chemical immobilization	–200	0.1–10	35	—	4.73	—	30
GC	ER-GO	ZrO_2	Chitosan, Nafion	Physisorption	–400	0.2–1.6	46	7.6	28.01	—	18
GC	ER-GO	PolyLysin	—	Polymer entrapment	–375	0.25–5	—	—	—	UA, AA	15
GC	rGO	Porphyrin	—	Physisorption	–365	0.5–10	200	17.3	—	—	28
GC	ER-GO	AuPd	Nafion	Physisorption	–105	0.5–3.5	6.9	267	10.5	AA, UA	22
GC	rGO	IL	—	Ionic interation	–412	0.8–20	267	—	—	—	20
GC	Graphene	APTES	Nafion	Chemical immobilization	–450	1.40–27.9	—	—	—	UA, AA, DA[(b)]	16

(*Continued*)

Table 1. (*Continued*)

Electrode modification				GOx immobilization	E vs Ag/AgCl mV	Linear range mM	LOD μM	Sensitivity μAmM^{-1}cm^{-2}	K_m[(a)] mM	No interference by	Ref.
Electrode	Graphene	Composite	Membrane								
Au	rGO	IL	—	Physisorption	–300	2–20	376	—	—	AA, UA	21
GC	rGO	IL	—	Ionic interation	–480	2–16	—	—	—	UA, AA	19
GC	GO	CdS	Nafion	Polymer entrapment	–327	2–16	700	1.76	1.6	UA, AA, AAP	23

[a] Michaelis–Menten constant (K_m).

[b] Also not interfered by AAP, billirubin, creatinine, ephedrine, ibuprofen, salicilate, tolbutamide, tetracycline, tolazamide.

for covalent binding was not provided. From the cyclic voltammogram of such an electrode, a redox peak at –447 mV vs Ag/AgCl can be ascribed to the reduction of the FAD to $FADH_2$, a co-factor of the GOx. A wide linear range for detecting glucose from 0.1 to 27 mM was found, with no interference from ascorbic acid (AA), uric acid (UA), or dopamine (DA) was observed. The sensor was also successfully used to measure glucose in diluted blood serum. For improvement of the selectivity as well as the stability, an additional layer of Nafion[16] or chitosan[26,27] was employed (Figure 2).

Mesoporous materials such as ZrO_2 have been used as a support material for amperometric glucose sensors.[18] The high surface area, large pore volume, narrow pore size distribution, as well as the tunable pore size, together with a modest conductivity, make this material an attractive host for enzyme immobilization. The sensor was fabricated by electrochemical reduction of GO on a GC electrode followed by electrodeposition of a thin chitosan film. This polymer layer provides positively charged amino groups which helps to attach the mesoporous ZrO_2 on top by drop casting. Following the deposition of the ZrO_2 layer, GOx was loaded onto the electrode. Direct electron transfer could be observed when glucose was added.

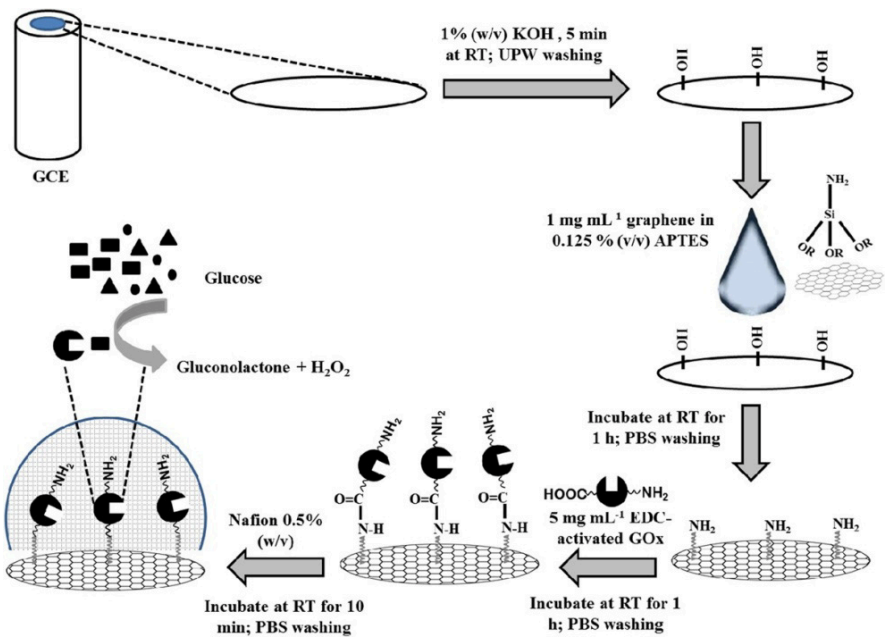

Figure 2. Scheme of the fabrication of the electrochemical glucose biosensor with APTES-modified graphene for enzyme immobilization. Reprinted from Ref. 16 with permission. Copyright © 2012 Elsevier.

A high Michaelis–Menten constant of 28.01 mM indicated limitations in mass transport which results in a slow response time in the minutes regime. The sensor was operated at 400 mV vs Ag/AgCl in phosphate buffer of pH 7.4. The detection limit for glucose was reported as 46 μM with a linear range from 0.2 to 1.6 mM. There was no study of interference and no real sample analysis presented. Nevertheless, the high sensitivity of 7.6 μA mM^{-1} cm^{-2} is remarkable. A comparison to the same sensor scheme without an ER-GO-layer resulted only in poor redox peaks, therefore one can conclude that the carbon nanomaterial is essential in providing the enhanced direct electron transfer. The simple electrostatic adsorption of the enzyme suffers from long-term stability. Therefore, rGO was modified with ILs possessing positively charged groups.[19] The better adhesion of the biomolecule to the carbon nanomaterial was proposed to be due to the ionic interaction. In case of 1-(3-aminopropyl)-3-methylimidazolium bromide, the sensor covers a linear range from 2 to 16 mM.[19] For the same sensor design with 1-vinyl-3-butylimidazolium bromide as the IL, a linear range from 0.8 to 20 mM was obtained[20] and with 1-butyl-3-methylimidazolium hexafluorophosphate, the linear range was reported between 2 and 20 mM.[21] Such modifications using ILs are not outstanding in their performance when compared with other sensors, which use direct electrochemistry for transduction.

Direct electron transfer in amperometric enzyme sensors, with and without the use of graphene, is limited due to the same reasons. The redox center is buried inside the structure of the protein which hinders the transfer of the electrons to the electrode. Therefore, electron transfer mediators have been widely used. Qiu *et al.*[27] describe such a system which uses graphene. Their sensor is fabricated by dropping ferrocene branched chitosan, GO, and GOx onto a GC electrode, as can be seen in Figure 3. Two effects are observed: First the immobilization of the enzyme is improved due to the electrostatic interaction of the naturally negatively charged enzyme in a positively charged polysaccharide. The native structure of the protein was not destroyed and no leaching was observed. Second, by the use of the redox mediator ferrocene, the sensitivity could be enhanced to 10 $\mu AmM^{-1}cm^{-2}$. A Michaelis–Menten constant of 2.1 mM was calculated. The capability of this biosensor was demonstrated in measuring plasma glucose level. The response displayed a linear glucose concentration range from 0.02 to 6.78 mM with a limit of detection (LOD) of 7.6 μM. By comparison of the resulting current densities, this sensor shows 2.7 times higher signal when GO is used. The working potential of the electrode is lowered to 300 mV vs Ag/AgCl, which increases the selectivity. No interference of AA or UA was found. This sensor has the best figures of merit for direct electron transfer to date.

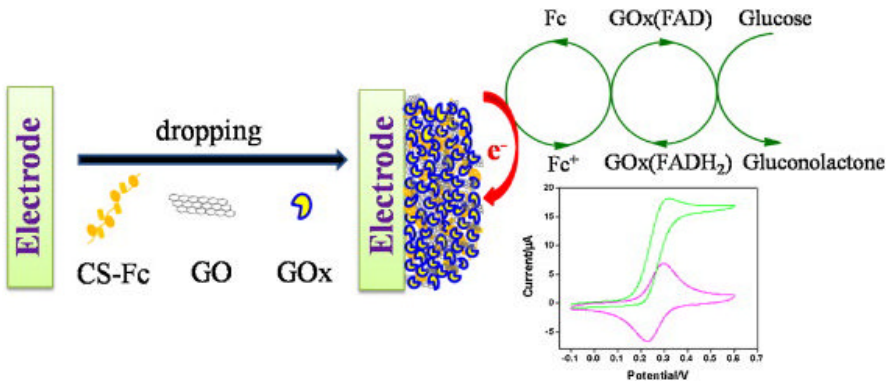

Figure 3. Sensor design of a GC electrode modified by ferrocene modified Chitosan (CS-Fc), GO, and GOx. The sensor exhibits excellent sensitivity and a low working potential of 300 mV vs Ag/AgC. Reprinted from Ref. 27 with permission. Copyright © 2011 Elsevier.

A novel platform for the *in situ* chemical immobilization of GOx was developed by Yang *et al.*[22] Citric acid, which was applied to the gold nanoparticles (AuNPs), was used as a capping and reducing agent. The carboxy groups of the citric acid, along with the amino groups of the GOx, form a peptide bond when immobilization takes place. The sulfur groups of the Au NP were used to anchor the system to rGO. After drop casting, the composite material onto a GC electrode, glucose could be detected within the range of 0.1 to 10 mM, with an LOD of 35 μM. An enhancement was found when ER-GO decorated with bimetallic nanoparticles of 1:1 Au:Pd was used. Extreme high sensitivity of 267 μA mM^{-1} cm^{-2} was reported. The enzyme was simply physically adsorbed on top of the composite material and covered by a thin film of Nafion.[22] A detection limit of 6.9 μM with linearity up to 3.5 mM was found. Other strategies, *e.g.*, the adsorption of iron(III) meso-tetrakis (*N*-methylpyridinium-4-yl) porphyrin onto graphene by π-stacking[28] do not result in better sensitivities or a larger linear range. All sensors which rely on direct electron transfer which use graphene are compared in Table 1.

2.2. Amperometric glucose biosensors with detection of H_2O_2

The glucose level often is indirectly monitored using amperometric biosensors by measuring the current in the oxidation of H_2O_2 produced during the enzymatic reaction of GOx with glucose. In the case of a GC electrode coated by a thin polymer film of chitosan incorporating rGO and GOx, the oxidation

occurs at 780 mV vs Ag/AgCl.[31] To enhance the kinetics and to minimize high overpotentials, metal and metal oxide nanoparticles are often introduced. Low working potentials are desired to diminish the risk of interference by other electroactive substances such as ascorbate, ureate, AAP, etc., which are often present in complex matrices. The introduction of additional nanomaterials for catalytic purposes is favorable for large surface area materials such as graphene. Furthermore, a support with high electrical conductance is needed to attach the nanoparticles without agglomeration. For this reason, graphene materials are of great interest, as they promote fast electron transfer kinetics and allow simple preparation strategies with respect to decoration by metal nanoparticles.

Composite materials consisting of palladium nanoparticles attached to graphene are very popular in the design of amperometric glucose sensors.[32,33] Synthesis can be performed in one step by simultaneous reduction of $PdCl_2$ and GO in an 85% hydrazine solution.[32] The resulting nanoparticles are attached to the carbon nanomaterial. With this method, agglomeration of the rGO is prevented. The electrode is modified by drop casting the nanohybrid material. For such electrodes, an increase in the LOD to 1.0 μM for the oxidation of hydrogen peroxide at 500 mV vs Ag/AgCl was found. For an identical sensor but without Pd nanoparticles, the detection limit was reported at 2.3 μM. To fabricate an amperometric glucose sensor, further immobilization of the enzyme is needed. This was perfomed by a well-known chemical coupling procedure via glutaraldehyde, which results in a peptide bond between GOx and rGO. Additional blocking is accomplished in the same way by the use of bovine serum albumin (BSA). An alternative strategy is the functionalization of GO with chitosan and reduction of GO with hydrazine in a solution containing $PdCl_2$.[33] A homogeneous distribution of Pd nanoparticles within the rGO-chitosan is found. This composite material was drop cast onto a GC electrode. In a last step, the GOx was chemically coupled to the electrode via glutaraldehyde chemistry. Such a sensor shows best glucose detection properties at a working potential of 700 mV vs SCE with linearity in current response in the concentration range from 1 to 10 mM. The LOD was reported to be 0.2 μM for glucose. It was found that AA as well as UA interfered with the detection of glucose at such a high electrode potential. Therefore, a suggestion was made to operate this sensor at –50 mV. Although this change in working potential increased the selectivity, the sensitivity of the system decreased by 93%.

A similar sensor concept was adopted by Shi *et al.*[34] Instead of palladium/platinum-black, a Pt nanomaterial was used along with GO. GO was drop cast on a Pt/Ir microelectrode, and Pt-black was electrochemically

deposited. However, detailed characterization of the resulting graphene material was not presented. It is not clear if the oxygen content of the carbon nanomaterial was changed during the process of the Pt-black formation at a voltage of 10 V for 1 min. Afterwards, GOx and BSA were attached to the surface by a coupling reaction via glutaraldehyde. The linear range for the detection of glucose from 1×10^{-3} to 2 mM was found, with a sensitivity of 78 μA mM^{-1} cm^{-2}. Therefore, platinum seems to further enhance the electron transfer during the oxidation of hydrogen peroxide as compared to palladium. Claussen *et al.*[35] also used Pt nanoparticles to catalyze the oxidation of hydrogen peroxide. In contrast to other reports, they do not use a GC or a metal electrode; they used graphene on a SiO_2 wafer as the electrode material. The graphene was produced by CVD and consists, on average, of 12 layers. It was functionalized by an oxygen plasma treatment and Pt nanoparticles were electrodeposited on the edges. The GOx was encased in a conductive polymer, poly(3,4-ethylenedioxythiophene) (PEDOT). This glucose sensor exhibits a broad linear range from 0.01 to 50 mM, with a detection limit of 0.3 μM. The advantage of this complicated technology to produce such a sensor is to have the ability to create a sensor array by structuring the graphene by plasma treatment.

When platinum is used as a metal coordination polymer (which allows an effective adsorption of GOx), the LOD for glucose decreases to 5 nM.[36] GO, modified with poly(*N*-vinyl-2-pyrrolidone) (PVP) and reduced by hydrazine was suspended together with *p*-phenylenediamine and H_2PtCl_4 before being drop cast onto the electrode. The electrode potential was adjusted to –300 mV vs SCE and the sensing behavior was not influenced by common interfering substances such as DA, AA, or UA. Another approach describes graphene decorated with platinum–gold alloy nanoparticles, synthesized by simultaneous reduction of Pt- and Au–salts in the presence of GO.[37] As expected, such an electrode is capable of detection of glucose. An LOD of 1 μM is reported. The drawback of this study is the high working potential of 700 mV vs Ag/AgCl, which limits the selectivity of this system.

In addition to Pt[35,38] and Pd,[32,33] Au[39,40] and Ag[41] have also been used as a component of the composite materials which use graphene for the design of enzymatic glucose sensors. A composite material consisting of rGO decorated with Ag nanoparticles was achieved in a one-pot synthesis by simultaneous reduction of $AgNO_3$ and GO by tannic acid.[41] It was demonstrated that this material can be used for glucose detection in the range of 2 to 10 mM. From these experiments, it is concluded that such materials are not comparable to the composite materials made from platinum and graphene. As can be seen from Table 2, gold is also inferior to platinum.

Table 2. Comparison of amperometric biosensors monitoring the oxidation of hydrogen peroxide.

Electrode modification											
Electrode	Graphene	Composite	Membrane	GOx immobilization	E vs Ag/AgCl mV	Linear range mM	LOD μM	Sensitivity $\mu AmM^{-1}cm^{-2}$	K_m mM	No interference by	Ref.
GC	GO	MOF/Pt		Physisorption	–255	0.00005–1	0.005	—	—	AA, DA, UA, Trp, Suc, AAP	36
CG	tGO	Pt	Chitosan	Polymer entrapment	400	0.001–5	0.6	—	—	—	38
Pt/Ir	GO	Pt-black		Chemical immobilization	500	0.001–2	1	78	—	UA, AA, AAP	34
GC	rGO	Pd-NP	Chitosan	Chemical immobilization	745	0.001–1	0.2	31	1.2	AA, UA	33
GC	rGO-SO_3H	Au	Nafion	Polymer entrapment	400	0.015–4.8	5	—	4.4	—	39
GC	rGO	Ppy		Vortexing	200	0.002–0.04	3	—	—	—	47
SPE	ER-GO	IL	BSA	Chemical immobilization	–200	0.005–10	1	22	—	AA, UA, DA	46
Graphene	CVD-G	Pt		Polymer entrapment	500	0.01–50	0.3	—	—	AA, UA, AAP	35
GC	rGO	IL	Nafion	Ionic interaction	–200	0.01–0.5	3.3	—	0.33	AA, DA, UA, Trp, Suc, AAP	45
GC	rGO	Pd-NP	BSA	Chemical immobilization	500	0.03–0.1	34	—	0.06	UA, AA, AAP	32
CG	N-doped G	—		Physisorption	–150	0.1–1.1	10	—	—	UA, AA	48

(*Continued*)

Table 2. (*Continued*)

Electrode modification												
Electrode	Graphene	Composite	Membrane	GOx immobilization	E vs Ag/AgCl mV	Linear range mM	LOD μM	Sensitivity $\mu AmM^{-1}cm^{-2}$	K_m mM	No interference by	Ref.
GC	rGO	Au	Chitosan	Polymer entrapment	–200	2–10	180	—	—	—	40
GC	rGO	Ag	Chitosan	Physisorption	–500	2–10	100	—	—	—	41
GC	rGO		Chitosan	Polymer entrapment	–790	2–22	20	—	—	—	31

Composite materials in electroanalytical sensors are most often prepared by simple drop casting of a relatively complex sensor cocktail. There has been little work done in the optimization and characterization of the resulting layer. By this simple technique in sensor fabrication, it is very easy to fabricate hybrid materials consisting of different nanomaterials. Gu *et al.*[42] describe a system consisting of a composite layer of rGO with gold nanoparticles (G-AuNP), together with quantum dots (CdSe-CdS), AuNPs and GOx within a Nafion membrane, drop cast onto a gold electrode (GE). The electrocatalytic oxidation scheme is depicted in Figure 4. This sensor exhibits a low working potential of –200 mV vs Ag/AgCl, which could increase the selectivity. One drawback of such systems may be the elaborate synthesis of the nanomaterials required to produce high quality materials in a reproducible manner. Also such approaches often lack thorough explanations as to why exactly that particular combination of materials works best.

Other nanomaterials that have demonstrated their ability to sense glucose which have been used in combination with graphene (albeit, reported without detailed analytical figures of merit) are ZnO,[43] Pt-Au,[37] and AuNPs.[37] In the case of ZnO, the hybrid material was encased with graphene, together with the enzyme, in a Nafion film. One purported advantage is that this sensor layer has excellent antibacterial properties. In another work, rGO modified with ZnO was used on a GC electrode for detecting glucose via direct electrochemistry.[29] GOx was attached by the electrostatic interaction between the enzyme and the graphene–hybrid material. The linear range of the sensor was reported from 0.02 to 6.24 mM, which in contrast to many other systems is quite narrow. A great enhancement in the sensor properties is reported when using fast Fourier transformation continuous cyclic voltammetry as a detection method in a flow injection system.[44] The sensor was fabricated by the drop casting of a dispersion of graphene and ZnO nanoparticles onto a GC electrode, which was finally covered by a thin film of Nafion. When integrating the signal from

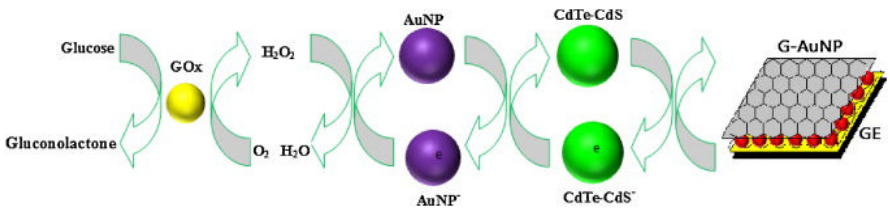

Figure 4. Electrocatalytic oxidation of glucose in a GOx/AuNP/CdTe-Cd-S/G-AuNP/GE sensor scheme. Reprinted from Ref. 42 with permission. Copyright © 2011 Elsevier.

–200 to 600 mV, an LOD of 0.02 μM was found for glucose and a linear range up to 20 mM was obtained.

A layer-by-layer fabrication approach using IL-modified reduced graphene oxide (IL-rGO) and sulfonated rGO (S-rGO) results in a hybrid material with a top layer of IL-rGO. As has been described by Gu *et al.*,[45] the IL-rGO layer provides a positive surface charge for the electrostatic attraction of GOx and a thin film of Nafion on a GC electrode.[45] The best sensor response was obtained using an assembly of five alternating layers. The LOD was estimated to be 3.3 μM for glucose. This sensor, operated at a low potential of –200 mV vs Ag/AgCl, was applied to a microdialysis probe which was successfully implanted into the striatum of a rat. A glucose concentration of 0.38 mM was monitored online. After an injection of insulin into the striatum of the rat, a decrease in the glucose level could be observed for about 25 min.

In contrast, by covalent attachment of GOx via glutaraldehyde coupling, a sensor based on ERGO modified with an IL exhibits a greater linear range (0.005 to 10 mM) with an LOD of 1 μM.[46] This illustrates the fact that it is not always clear which kind of immobilization works best. Although these sensors were both operated under the same conditions and exhibit the same selectivity, the chemically immobilized enzyme sensor[46] exhibits a sensitivity that is three times higher than the sensor where the enzyme was immobilized by ionic interaction.[45]

Alwarappan *et al.*[47] report a unique strategy for enhanced glucose biosensing. Here, they develop a GC electrode which is electrochemically modified by polypyrrole that acts as a host material for the immobilization of GOx, which is chemically functionalized by graphene. Unfortunately, the covalent modification of the enzyme with the graphene was not described in a convincing way. There is no real characterization of the formation of a specific bond between graphene and GOx. The protocol involves simply mixing rGO with the enzyme in phosphate buffer and vortexing for 50 s. Further purification of this mixture from unreacted enzyme as well as excess graphene was also not described. Also the immobilization protocol of the graphene–enzyme conjugate to the polypyrrole is completely absent. Therefore, one can only say that graphene and GOx was applied to a polypyrrole-modified electrode. Nevertheless, this system is reported to detect glucose with linearity in the range of 2 to 40 μM with an LOD of 3 μM.

Most studies of biosensors used for the detection of glucose use chemically derived graphene[17–27,29–34,36,38,40,41,45–48] with various strategies for the reduction of the GO. Electrochemical reduction has the advantage of convenience; electrode deposition can be performed simultaneously with the reduction step. In contrast, dispersed GO allows easy modification of the carbon

nanomaterial with molecules, nanoparticles, or biomolecules. To recover the high conductivity, the functionalized GO is reduced afterwards. Many studies lack proper characterization of the carbon nanomaterial and the final composite material. Therefore, it is often not clear which parameter contributes most to the enhanced sensor characteristics. To date, there has been little work on the investigation of the influence of the doping of the graphene itself. Wang *et al.*[48] present a study where they use nitrogen doped graphene in electrochemical biosensing. Nitrogen doping could be a potential strategy to regulate the electronic properties in carbon nanomaterials. By treating a chemically derived graphene with nitrogen plasma, it was possible to control the content of nitrogen atoms of the graphene from 0.11 to 1.35%. This was achieved by mixing rGO with chitosan and drop casting this mixture onto a GC electrode. The electrodes were then exposed to a nitrogen plasma for a specified time. Finally, GOx was physisorbed onto the modified electrodes. A comparison of undoped with N-doped graphene shows that there is an enhancement in the resulting peak current, as shown in Figure 5. This sensor could be used either to monitor the direct electron transfer from GOx or to measure the oxidation of hydrogen peroxide. The later technique was performed at 150 mV vs Ag/AgCl to achieve an LOD of 10 μM and a linear range of 0.1 to 1.1 mM for glucose. UA as well as AA showed no significant interference.

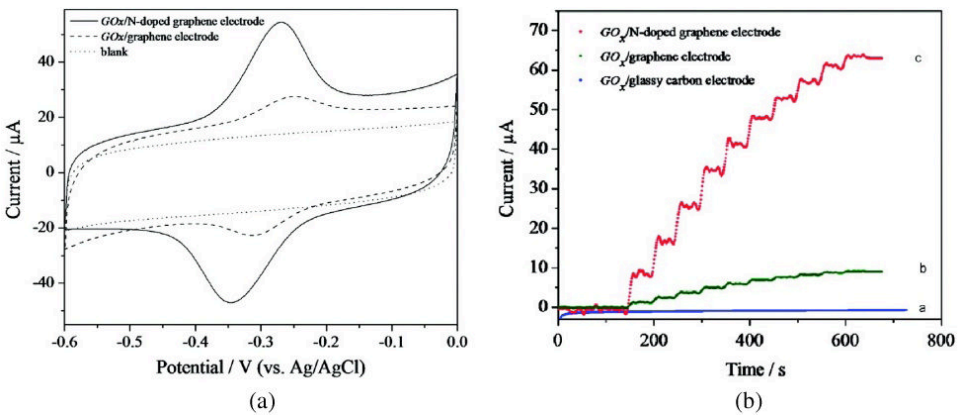

Figure 5. (a) Cyclic voltammograms of GOx immobilized on N-doped graphene electrode (solid line) and graphene electrode (dashed line) in N_2-saturated 0.1 M PBS solution (pH 7.0). The dotted line is for the background. Scan rate = 0.05 V·s^{-1}. (b). Current/time curves for GOx immobilized on GCE (blue), graphene electrode (green), and N-doped graphene electrode (red) at 0.15 V in 0.1 M PBS (pH 7.0) with successive addition of 0.1 mM glucose are also shown. Adapted from Ref. 48 with permission. Copyright © 2010 American Chemical Society.

In summary, much research has been made into the use of graphene in enzymatic electrochemical glucose sensing. Regarding hybrid materials, direct electrochemistry involving metallic nanoparticles for the oxidation of hydrogen peroxide was well studied. However, one can conclude that similar trends were found for the monitoring of glucose sensors with and without the use of graphene. It is interesting to note that in most published works, the outstanding properties of graphene are discussed to be beneficial for the biosensor design. Alwarappan *et al.*[49] systematically investigated the influence of the graphene material itself on the immobilization of GOx and the resulting electrochemical sensor properties. It is reported that there is almost no difference in the amount of immobilized enzyme as well as in the resulting current density for single-layer graphene (SLG), few-layer graphene (FLG), and multilayer graphene (MLG). This is surprising due to the fact that it is well known that SLG is a semimetallic conductor, whereas MLG acts as a metallic conductor.[50] Therefore, one can conclude that for glucose biosensing applications, it is less important which kind of graphene material is used. The greater challenge is to find a proper way to immobilize the enzyme or to design a hybrid material which can really improve the sensing properties in terms of better selectivity and higher sensitivity. To date, hybrid materials with platinum nanoparticles perform best in terms of sensitivity and the indirect detection of glucose by oxidation of hydrogen peroxide is superior to the direct electrochemical detection.

2.3. Mass-sensitive glucose biosensors

Biosensors for glucose which do not use electrochemical transduction are rarely reported. One example is the detection of glucose with a quartz crystal microbalance (QCM) by covering a gold-coated quartz crystal with a layer of graphene and dextran, functionalized by Concanavalin A.[51] The sensing principle is a displacement-based assay mode similar to the competitive-type immunoassay format. Concanavalin A is a lectin protein, which exhibits four saccharide binding sites with a high affinity to glucose. Graphene was used here as an affinity support for the immobilization of the dextran–protein complex (see Figure 6). It is necessary to use a displacement-based assay because of the small signal changes for such small molecules such as glucose, having a molar mass of 180 $g \cdot mol^{-1}$. The affinity of dextran to Concanavalin A (26.5 kDa) is lower than that of glucose, and therefore, signal amplification can be obtained by releasing the protein from the surface when glucose is present. The figures of merit of such a glucose sensor are a linear range from 0.01 to 7.5 mM and an LOD of

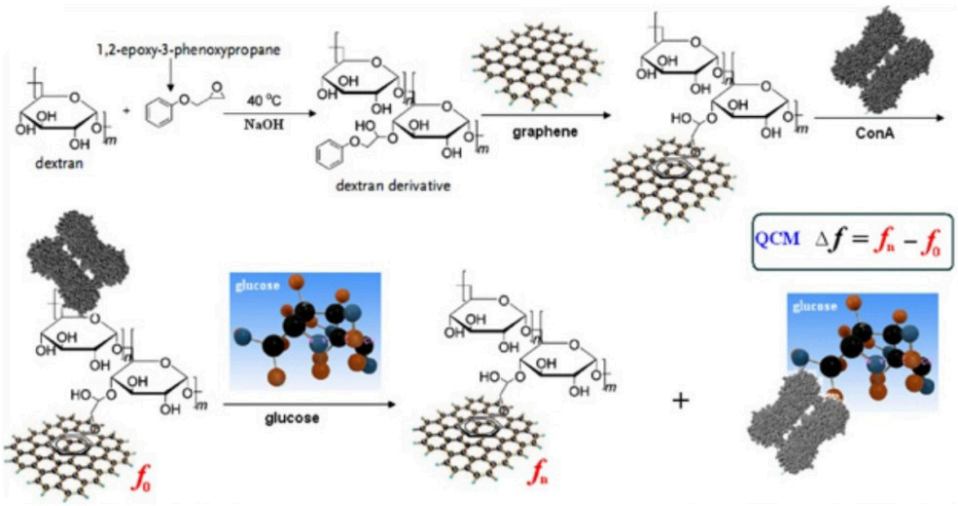

Figure 6. Fabrication process and measurement principle of the displacement-based QCM glucose sensor. Reprinted from Ref. 51 with permission. Copyright © 2011 Elsevier.

5 μM. Graphene, the thinnest nanostructure to date, is touted to be favorable for its high sensitivity, providing an ultrathin layer for the immobilization of receptors, with excellent long-term stability.

An electrochemiluminescence (ECL) biosensor for glucose is reported by Chen *et al.*[52] The enzyme was encapsulated in a thin film consisting of Nafion and graphene drop cast onto a GC electrode. The graphene used here was prepared chemically from graphite by oxidation according to Hummers method[53] followed by a reduction step with hydrazine. The resulting material was suspended together with Nafion and GOx and applied via drop casting onto a GC electrode. The electrode was placed in phosphate buffered solution of pH 7.4, supplied with a constant level of 30 μmol·L^{-1} luminol. When glucose was added to the solution, the enzyme produced hydrogen peroxide, which enhances the ECL of luminol. The sensor has a linear response for glucose from 2.0×10^{-3} to 0.1 mM with an LOD of 1 μM. In contrast to the same system without graphene, better electrochemical and ECL properties were found. Potential interfering substances, such as AA, UA, sucrose, lactose, and maltose have only negligible influence on the detection of glucose. It was also demonstrated that this sensor could be successfully used to detect glucose in human serum samples.

3. Nucleic Acids

Detection, monitoring, and analysis of DNA play an important role in human health aiding in the diagnosis of diseases and genetic mutations, fast detection of biological warfare agents, and in the development of improved pharmaceuticals. Thus, the development of DNA detection methods with increased sensitivity and accuracy is highly desirable and is anticipated to play an ever increasing role in the future of medicine.

A typical DNA biosensor system consists of a transducer surface with an immobilized single-stranded DNA (ssDNA) probe. Upon binding with the complementary single-stranded nucleic acid sequence, hybridization occurs and the pair is detected. The hybridization event is most typically measured optically, electrochemically, or by mass-sensitive detection. Historically, the greatest strides in DNA detection using biosensors have been made with the implementation of new or enhanced sensor materials. Such enhancers, or additives, have been critical to the advancement of this field. Various carbon nanostructures (such as carbon nanotubes) have been widely implemented in DNA biosensors. Among them, graphene has recently received particularly strong attention. This section will focus on the developments of graphene-based biosensors which employ a variety of detection schemes, sensor additives, and types of graphene for the detection of oligonucleotides.

Graphene-based DNA biosensors show great promise when applied to diagnosis of genetic diseases and environmental monitoring. The interaction between DNA molecules and graphitic materials has been studied theoretically and experimentally.[54–57] It is understood that the binding between graphene and nucleotides is dominated by the non-electrostatic π-stacking interaction,[55,56,58–60] which explains how probe DNA is immobilized on graphene. Primarily, fluorescence and electrochemical methods are used as the sensor detection method, with other optical and electrical methods becoming more prevalent. It has been well-demonstrated that the hybridization of complementary strands can be monitored with graphene-based sensors.

DNA hybridization can be detected using optical techniques such as fluorescence, chemiluminescence, surface plasmon resonance, or interferometry. Fluorescence quenching is the most common and least complicated detection method used for DNA sensors employing graphene.[61–84] A single strand of nucleic acids has a natural affinity to the aromatic system of graphene via π-stacking of its nucleobases. In this system, fluorescently labeled ssDNA adsorbs onto the surface of the graphene. The interaction between the dye molecule and the graphene brings them in close proximity, allowing energy

transfer to occur, effectively quenching the fluorescence of the fluorophore. Upon hybridization of the ssDNA with its complementary strand, the DNA desorbs from the graphene, and the fluorescence of the system is restored, as depicted in Figure 7. In such a way, so called "turn-on"/"turn-off" sensors can be constructed. Advances in the field of fluorescence DNA–graphene sensors include the implementation of multicolor monitoring for improved specificity.[85] Although fluorescence detection methods have proven to be highly sensitive, these sensors often suffer from low yield due to limited labeling efficiency, contamination issues, and require complex purification steps.

As an alternative, electrochemical sensing is often employed as a label-free, low cost, selective, and sensitive method, which detects the hybridization event and typically requires only a very small volume of material. An additional benefit of using GO in electrochemical sensing methods is that the GO can be electrochemically reduced, resulting in a more environmentally friendly and consistent rGO material. Among all types of electrochemical DNA sensors, those based on the direct oxidation of DNA are the simplest.[86,87] In such a system, the current signals of all four free DNA bases (guanine, adenine, thymine, and cytosine), as well as those of ssDNA and double-stranded DNA (dsDNA) can be separated when chemically reduced GO (CR-GO) is used as a mediator.[88–90] In contrast, graphite, CVD-produced graphene, and GC are significantly less sensitive and thus rGO is the material of choice for most graphene-based DNA biosensors.[91–97] The very low LOD reached by using rGO as a component of a DNA biosensor for electrochemical detection methods is attributed to the high electron transfer kinetics of the system. Most attribute this to the high density of edge plane-like defect sites and oxygen-containing functional groups in rGO, which provide active sites beneficial for accelerating electron transfer between the electrode and species in solution. DNA biosensors based on electrochemical detection techniques also offer the flexibility of various labels such as

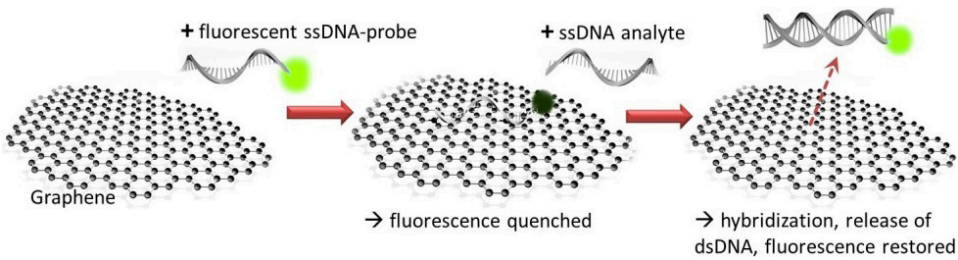

Figure 7. Mechanism of DNA detection via fluorescence quenching of molecular beacons.

enzyme and metal complexes and various organic compounds. Methylene blue is a common label used in DNA biosensors for electrochemical detection. A further significant advantage of such a system is that label-free systems can also be constructed when desired. Examples of such a system are detection based on a change in capacitance or detection of the oxidation of guanine (the most redox-active nitrogenous base in DNA).

Less widely implemented is the detection of DNA by direct electrical methods.[98] The complementary DNA interacts with graphene and an n-doping (electronic doping) effect, based on the graphene–nucleotide interaction, is observed and measurable. Another upcoming technique which has been applied to DNA biosensors is field effect transistors (FETs).[99,100]

The immobilization strategy of the probe DNA plays a key role in determining the final sensitivity of the sensor.[101] In that regard, graphene materials have emerged to efficiently immobilize DNA. With few exceptions,[102–105] rGO or GO is used for graphene-based DNA biosensors. However, as previously discussed, due to the lack of characterization of the graphene, which is very often not included in most works involving graphene-based biosensors, it is difficult to properly categorize and compare sensor systems. Most of the recent studies of DNA–graphene-based sensors specifically involve chemically processed, multilayer rGO. This material contains a high density of reactive edges providing functional groups and adsorption sites.

For better realization, recent literature concerning graphene-based DNA biosensors is sorted in Table 3 according to sensitivity. Here, the specific type of graphene that was used is listed for comparison. It is well understood that graphenes prepared by various methods contain various oxygen-containing groups and defects.[106] Thus, it is expected that different graphenes will exhibit different electrochemical behaviors after functionalization with ssDNA. A revealing study by Bonanni *et al.*[107] investigated the utility of four different chemically modified graphenes for functionalization by ssDNA. They explored several chemically modified graphenes, including graphite oxide, GO, chemically reduced GO, and ER-GO. All graphenes were covalently functionalized by formation of NHS esters on carboxylated graphene which was reacted with amino-modified ssDNA to form an amide bond. After identification and verification of the graphene type by X-ray photoelectron spectroscopy (XPS) and Raman spectroscopy, the different graphene transducer platforms were employed for the detection of DNA hybridization and DNA polymorphism by using electrochemical impedance spectroscopy (EIS). In this comparative study, the lowest LOD was obtained with ER-GO at 250 pM, followed by 3 nM for chemically reduced GO, 100 nM for GO, and 800 nM for graphite oxide. They later investigated other types of graphene materials consisting of

Table 3. Comparison of the most relevant studies of graphene-based biosensors for the detection of nucleic acids.

Analyte	Material	Technique	LOD	Sensitivity	Sensor additives	Ref.
DNA	rGO	Electrochemical	37 aM	0.1 fM–10 nM	PABSA–rGO nanocomposites	91
DNA	rGO	Electrochemical	5 aM	10 aM–10 pM	AuNP, HRP, carbon spheres	93
mRNA	GO	Fluorescence	2.1 fM	0.5 fM–50 pM	—	70
DNA	rGO	Electrochemical	32 fM	10 pM–0.1 μM	Polyaniline nanofibers	94
DNA HIV-1	rGO	Electrochemical	34 fM	10 pM–1 μM	AuNPs, PTCA[a]	96
DNA HIV-1	GO	Electrochemical	0.11 fM	1 fM–1 μM	—	121
DNA HIV-1	rGO	EIS	0.5 fM	1 fM–1 μM	PTCA[a]	97
DNA	Epitaxial graphene	Amperometry	20 fM	50 fM–1 μM	—	102
DNA	rGO	Triplex system (EIS, fluorescence, and FET)	Triplex system 10 fM; EIS 6.6 pM; flu. 100 pM and 1 nM; FET 1 nM and 2 nM	EIS: 10 fM–0.1 nM	AuNPs, Fc-PEI, mesoporous silica	99
mRNA	Graphene	Electrochemical	0.06 pM	0.1–70 pM	AuNPs, biotin, streptavidin-HRP	117
mRNA	GO	Fluorescence	100 pM	1 pM–5 nM	—	62
DNA	GO	Fluorescence	20 pM	20 pM–300 nM	Exonuclease III	71
DNA HIV-1	GO	Fluorescence	34 pM	0.1–3 nM	Luminol	73
DNA	GO	Fluorescence	4 pM	4–0.01 pmol	AuNPs	83
DNA	GO	Fluorescence imaging	IgG: 10 pM; DNA: 1 nM	G and C: 20 pM–100 μM; IgG: 10 pM–10 nM; DNA: 1 nM–1 μM	AgNPs	69

(*Continued*)

Table 3. (*Continued*)

Analyte	Material	Technique	LOD	Sensitivity	Sensor additives	Ref.
DNA	GO	Dls	1 pM	1 pM–10 nM	—	122
DNA	GO	Electrochemical	0.359 pM	1 pM–1 μM	BPPF6[b] in carbon paste	123
DNA	rGO	Electrochemical	72 pM	200 pM–500 nM	CTS/Fe_3O_4 microparticles; silver enhancer solution	95
DNA	rGO	Electrochemical	0.29 pM	1 pM–1 μM	MB[c], AuNPs, BPPF6[b]	92
DNA	GO	Electrochemical	0.169 pM	1 pM–1 μM	Polylysine	124
DNA	GO	Electrochemical	500 pM	50 pM–1.5 μM	—	125
DNA	GO	Electrochemical LAPS[a]	1 pM	1 pM–10 nM	—	126
DNA related to Alzheimer's disease	Graphene nanoribbons: single layer up to multilayer	EIS	50 nM for single layer, 6.6 pM for three and four layer, and 66 μM multilayer	30 pM–0.3 nM	FAM[d] dye	103
DNA	rGO	EIS	0.325 pM	1 μM–2.12 pM	Polyaniline nanowires	104
DNA	rGO	Voltammetry	8.33 pM	25 pM–1.25 nM	AuNPs; 1,10-phenanthroline cobalt	116
DNA	Graphene	Voltammetry	0.721 pM	1 pM–1 μM	MB[c], TiO_2 nanorods, chitosan	127
DNA	Graphene	Voltammetry	0.43 pM	1 pM–1 μM	Co_3O_4 nanorods, chitosan, MB[c]	128
DNA	Graphene	Voltammetry	15.8 pM	21.2 nM–21.2 pM	Prussian blue, chitosan	129
DNA	rGO	Voltammetry	0.035 pM	0.1 pM–10 nM	AuNP, adriamycin	115
ATP	GO	Fluorescence	1.54 nM	0–28.6 nM	—	67
DNA	GO	Fluorescence	1 nM	1 nM–1 mM	Silver nanoclusters	68

a Light-addressable potentiometric sensor (LAPS).

(*Continued*)

Table 3. (*Continued*)

Analyte	Material	Technique	LOD	Sensitivity	Sensor additives	Ref.
DNA Simian virus 40	GO	Fluorescence	14.3 nM	40–260 nM	FAM[d] dye	76
DNA SARS virus	GO	Fluorescence	100 nM	—	FAM[d] dye	80
DNA	GO	Fluorescence	12 nM	50–1500 nM	Quantum dots	82
DNA hepatitis B virus oligo-nucleotides	Graphene	Fluorescence	10.4 nM	50–2000 nM	CdTe QDs, glutathione	66
ATP	GO	Fluorescence	500 nM	500 nM–50 μM	FAM[d] dye	119
ATP	GO	Fluorescence	80 nM	0.5–100 μM	Upconverting nanoparticles	77
DNA	GO	Fluorescence	1 nM	0–400 nM	4-(1-pyrenylvinyl)-*N*-butyl-pyridinium bromide dye	130
DNA (Alzheimer's disease)	Graphene	Electrochemical	0.01 nM	0.01–10 nM	—	131
DNA (Alzheimer's disease)	rGO	EIS	Graphite oxide 800 nM; graphene oxide 100 nM; CR-GO 3 nM; ER-GO 250 pM	10 pM–1 μM	—	107
4 DNA bases (G, A, T, C)[(e)]	rGO	Electrochemical	G: 0.007 μM, A: 0.021 μM, T: 0.18 μM, C: 0.15 μM	G: 0.025–20 μM, A: 0.05–40 μM, T: 1.0–200 μM, C: 1.0–250 μM	Poly(alizarin red)	88

(*Continued*)

Table 3. (*Continued*)

Analyte	Material	Technique	LOD	Sensitivity	Sensor additives	Ref.
DNA	Graphene quantum dots	Electrochemical	100 nM	200 nM–500 nM	—	132
DNA	rGO	Electrochemical	42 nM	20 nM–700 nM	PEG	133
4 DNA bases (G, A, T, C)[e]	rGO	Electrochemical	0.2 μM	0.2–1 μM	AuNPs	89
4 DNA bases (G, A, T, C[e]); oligonucleotide of human influenza A(H1N1) virus	Graphene nanopores	Electrochemical	A: 50 mM, G: 4 mM, C: 100 mM, T: 100 mM; Influenza: 28 mM	*	—	90
DNA	Epitaxial graphene	Electrochemical	1 μg mL^{-1}	—	—	105
ATP	rGO	Impedance	15 nM	15 nM–4 mM	—	118
DNA	CVD graphene	FET	0.01 nM	10–500 nM	AuNPs	98
DNA	rGO	FET	200 nM	*	AuNPs	100
ATP	GO	Isothermal titration calorimetry	1 mM	*	FAM[d] dye	120

[a]PTCA: 3,4,9,10-perylene tetracarboxylic acid.
[b]BPPF6: 1-butylpyridinium hexafluorophosphate.
[c]MB: methylene blue.
[d]FAM: fluorescein, 6: carboxyfluorescein.
[e]G: guanine, A: adenine, T: thymine, C: cytosine.
*Only one concentration measured.

different numbers of 100 × 100 nm^2-sized graphene layers.[103] Using EIS, they found a lower LOD for triple- and four-layer graphene nanoribbons (6.6 pM), followed by single- and double-layered graphene nanoribbons (50 nM) and finally, MLG nanoribbons (66 μM).

It is evident when the literature is viewed as a whole while sorted by graphene type that rGO-based DNA sensors perform best when tested using electrochemical detection methods. From Table 3, it also appears that GO is perhaps a better choice for fluorescence-based detection methods for DNA biosensors. GO acts as a weak acid cation exchange resin due to its carboxylic groups located at the basal plane (edge sites) of the GO.[108] A simple ion exchange, typically with a dye, to form an energy or charge transfer complex for complexation with GO is a common explanation for the mechanism.[109,110] Additionally, GO is a highly suitable material for interaction with biomolecules as the carboxylic groups render the material soluble in aqueous solutions.

The sensitivity, that is, the ability of the biosensor to detect low DNA concentrations, is essential as is the selectivity and ability to detect a point mutation. With few exceptions, most sensors in this class detect in the nM range. Table 3 shows many graphene-based DNA biosensors, grouped by sensitivity. From this arrangement, one can see that electrochemical detection methods provide the best sensitivity. Additionally, it appears that rGO is the preferred type of graphene material, allowing for detection limits in the range of fM to aM, with graphene oxide also giving an excellent LOD in the pM to fM range. By comparison, CVD and epitaxial graphene do not provide the low limits of detection offered by rGO or even GO.

In order to meet ever-increasing demands for the detection of trace amounts of DNA, new strategies for enhanced detection and signal amplification are quickly evolving. Many past reports were based on the use of single or duplex DNA signal amplification strategies, although triplex sensing schemes are gaining more attention. The labels used in DNA biosensors are used as a storage reservoir for electrical charge. Multiple labels can be combined, often having different amplification mechanisms, to achieve excellent sensitivity. In such strategies, enzyme schemes are often combined with inorganic nanoparticles such as AuNPs. For example, in the case of one of the lowest reported LODs, Dong *et al.*[93] have developed a triplex amplification strategy, which enabled them to achieve an LOD of 5 aM with the combination of AuNPs, horseradish peroxidase (HRP), and functionalized carbon nanoparticles. This sensor was highly selective to various single-base and three-base mismatched sequences of DNA.

Another technique which provides ever-competitive sensitivity for DNA detection is EIS, where the electrochemical impedance is measured by applying an AC potential to an electrochemical cell and then measuring the current through the cell. EIS is an electrochemical detection technique often adopted to study biological events taking place at the interface between a surface and electrolyte, which can be applied to directly detect the DNA immobilization and hybridization without the addition of an electro-active indicator.[111–114] By adopting this method in combination with the high electrochemical activity of poly(*m*-aminobenzenesulfonic acid) (PABSA)–rGO nanocomposites, Yang *et al.*[91] contribute their exceptional sensitivity of 3.7×10^{-17} mol/L to both the detection method as well as the graphene nanocomposite contribution. Several other recent sensors combining rGO with various polymers[91,94] and aromatic hydrocarbons bearing carboxylic groups[96,97] have also proved to be highly sensitive, offering LODs in the range of fM. In particular, 3,4,9,10-perylene tetracarboxylic acid (PTCA) seems to enable the desired π–π stacking with graphene due to its carboxylic groups and π-conjugated structure. The PTCA has three distinct advantages making it an excellent additive for graphene-based sensors. First, the PTCA acts to separate the graphene sheets. It then decorates the graphene sheets with additional carboxylic groups, making the composite structure highly dispersible in aqueous solutions. Finally, the resulting PTCA–graphene structure provides many active sites for the immobilization of the desired probe DNA sequence. With the advancement of such sensor additives and improvement in detection schemes as described herein, graphenes could prove to be a leading sensor material in making graphene-based DNA biosensors competitive with other technologies.

To further increase sensitivity, many DNA–graphene biosensor systems employ the use of nanoparticles such as quantum dots,[66,82] upconverting nanoparticles,[77] or metal nanoparticles (most typically silver or gold),[68,69,83,89,93,95,96,98–100,115–117] with varying degrees of success for signal enhancement. Table 3 shows some recent graphene-based DNA biosensor systems where one column is dedicated to the various nanoparticle additives. AuNPs are considered to be biocompatible and highly stable. However, inconsistent signal amplification using metal nanoparticles remains a problem. They are often used in the immobilization layer to increase the quantity of DNA which is often functionalized with an amine group. The other benefit of AuNPs in such a sensor system is the enhanced signal provided by the plasmon resonance inherent in the properly engineered AuNPs. The adherence of such AuNPs effectively magnifies the hybridized signal, and overall, aims to provide enhanced sensitivity and a lower LOD. On a case by case basis, when sensors are developed with or without nanoparticle enhancers,

researchers do note an improvement, albeit typically not significant, in the sensor's performance. However, to date, only a few of the top performing sensors employ such sensor additives, but rather contribute the enhanced signal to other material additives or improved detection schemes.

Another area where graphene-based DNA biosensors have recently found moderate success is in the detection of adenosine-5'-triphosphate (ATP),[63,65–67,72,77,81,118–120] a nucleoside triphosphate used in cells as a coenzyme. Most biosensors in this category use carboxyfluorescein-tagged ATP, adsorbed onto GO, which quenches the fluorescence. Upon hybridization, the dye-labeled ATP molecule is released from the GO, and fluorescence is restored. From Table 3, one can see the LODs lie in the nM range. Application of some of the advanced techniques mentioned in this section could aid in the further reduction of the LOD for such biosensors.

Recently, graphene-based DNA biosensors have found application for highly sensitive virus detection[66,73,76,80,90,96,97,121] by employing specific recognition DNA elements. SARS,[80] Simian,[76] and Hepatitis B[66] viruses have been detected in the nM range. Exceptional sensitivity has been obtained in the detection of HIV virus,[73,96,97,121] with Hu *et al.*[96] reporting an LOD as low as 34 fM. It is worth noting that the authors also tested the same sensor system with[96] and without[97] the addition of AuNPs and found no discernible difference in the achieved LOD.

Although DNA has long been considered to be a strictly genetic information reservoir, there are a few biosensor systems that use DNA in the transducer to detect proteins and metal ions. These biosensors are discussed in Section 5.

4. Proteins

Biosensors for the detection of proteins are found in the literature with growing numbers. These are mostly developed as an immunosensor, that is, a device comprised of an antigen or antibody coupled to a signal transducer which detects the binding of the complementary species. Miniaturization and production of small compact biosensors with sensitive detection for diagnostic use is one main area of modern biochemical and biomedical research. Indeed, graphene has the potential to play a major role in future diagnostics. To date, the role of graphene materials in biosensors has been primarily to increase of the surface area of the transducer. This sensitive layer is often comprised of a hybrid or composite material, in combination with metal nanoparticles, ILs, or membranes made of Nafion or chitosan.

Due to the specific binding of an antibody to its antigen, biosensors based on this interaction are widely used for the specific detection of different

targets. The most common way is to immobilize antibodies onto a graphene sensor platform to form enzyme-linked immunosorbent assays (ELISA), which are more sensitive than conventional approaches. Another prominent way is the usage of dye-labeled antibodies or specific aptamers. The readout is performed by electrochemical methods such as differential pulse voltammetry (DPV), FETs, and impedance, or optical methods such as fluorescence or ECL. In such biosensors, mainly chemically and thermally rGO was used for electrochemical detection and GO for optical detection approaches. Optical biosensors employing fluorescence readout schemes seem to be more sensitive by an order of magnitude in comparison with electrochemical detection methods. This section highlights the different sensor strategies by providing examples of not only the most prominent protein analyte targets, such as cancer biomarkers, thrombin, but also single amino acids and immunoglobulins.

4.1. Cancer biomarkers

A major research field, which pushes the development of smaller and more sensitive immunosensors, is the detection of biomarkers. Their sensitive recognition is essential for early disease diagnosis and offers highly reliable predictions.[134,135] Therefore, many works investigate and optimize the detection of model markers, especially cancer biomarkers such as alpha-fetoprotein (AFP),[136–142] prostate-specific antigen (PSA),[143–147]cyclin A2,[148,149] phosphorylated p53,[150,151] carcinoembryonic antigen,[152–154] Integrin avb3,[155] or progastrin-releasing peptide.[156] Nearly all of the works combined a sandwich assay with electrochemical readout of the coupled enzymatic reaction.

A very representative electrochemical immunosensor was prepared by Yang *et al.*,[147] investigating the detection of PSA, an important tumor marker for clinical diagnosis of prostate cancer. In their work, thermally reduced GO was used in two ways (see Figure 8) to promote the sensitivity to a LOD of 1 pg mL^{-1}. On the one hand, it was applied as an electrode material for the immobilization of a primary antibody via π–π interactions of a linker molecule. On the other hand, it was used as a support to build up a label consisting of a secondary antibody, HRP, and a mediator thionine. The biosensor was prepared by incubating the electrode with PSA solutions of different concentrations, washing, incubating with the label, and washing again. The more PSA that was bound, the fewer labels that were attached to the electrode, resulting in a lower amperometric response against fixed H_2O_2 concentrations. This leads to a wide linear sensitivity of 0.002–10 ng mL^{-1}. The large surface-to-volume ratio (leading to a high enzyme loading of the label) and

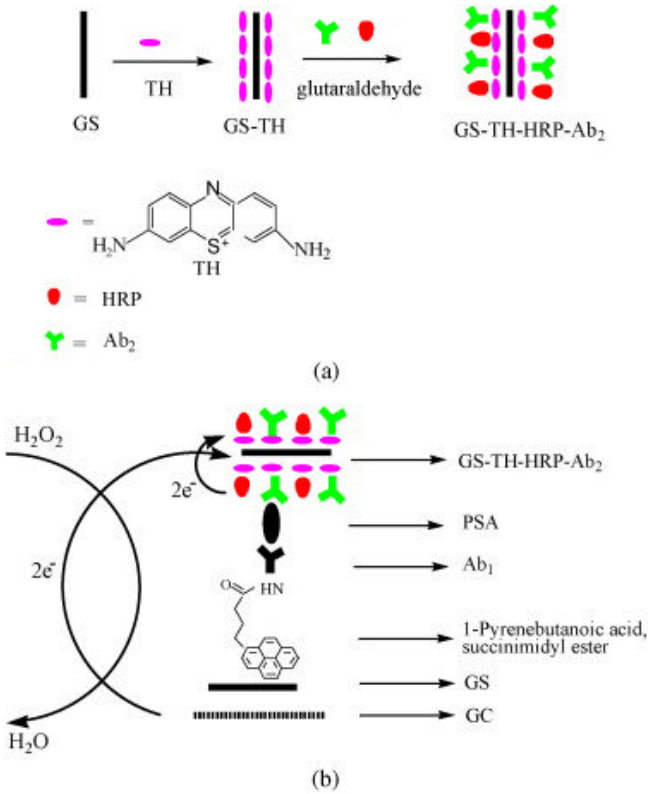

Figure 8. Schematic representation of preparation (a) and mechanism (b) of the graphene (GS)-based immunosensor for PSA. Reprinted from Ref. 147 with permission. Copyright © 2010 Elsevier.

the good conductivity of graphene are the main reasons for the improved sensitivity. To test interference and applicability, the immunosensor was tested toward human IgG, BSA, vitamin C, glucose, and human serum samples. Satisfactory test results were obtained in comparison with a commercial ELISA system.

Nearly same results in terms of sensitivity and LOD were obtained by Zeng *et al.*[136] for the detection of AFP, a widely used diagnostic biomarker for hepatocellular carcinoma.[157] The assay build-up and measurement principle were almost the same as for the PSA sensor, except for the support materials used for the electrode and the label. The electrode was first covered with chemically reduced GO and cyclodextrin while the label support consisted of mesoporous carbon covered with Pt nanoparticles. As seen in Table 4, there are many possible support materials for the label, which all lead to quite promising results competitive with conventional ELISAs. The main challenge

Table 4. Comparison of different support materials for labels in electrochemical immunosensors for AFP.[136]

Support material	LOD pg L^{-1}	Linear range ng mL^{-1}	Stability days	Ref.
Ag nanowire–graphene nanosheets	5	0.05–400	15	158
Ag-SiO_2	50	0.3–200	28	159
Mesoporous silica	500	1–90	30	160
Polyamidoaminic dendrimers	3000	5–375	28	161
Pt nanoparticles	1.7	0.005–20	30	162
Prussian blue-hydroxyapatite	9	0.02–8	7	163
Au–graphene nanosheets	50	0.1–200	20	164
Carbon nanospheres	20	0.05–6	—	165
SiO_2 nanoparticles	10	0.05–3	14	166
Au-CNTs	2.2	0.025–2	7	167
Pt-mesoporous carbon	1.5	0.002–10	22	136

in constructing good labels is to obtain a high loading of enzyme and secondary antibody onto a support material. Therefore not only AuNPs but also several carbon nanomaterials and their composites were demonstrated to be applicable.

Another promising amplification strategy for clinical screening of cancer biomarkers and point-of-care diagnostics was developed by Du *et al.* two years before.[142] Here, the primary AFP antibody was attached to a screen-printed carbon electrode, which was modified with thermally reduced GO and chitosan. The label was comprised of carbon nanospheres loaded with a secondary antibody and HRP. Using two carbon nanomaterials as a support for the antibody coupling also resulted in a quite low LOD of 0.02 ng mL^{-1} and a linear sensitivity up to 6 ng mL^{-1}. In contrast, measurements without graphene showed a seven fold decrease in detection signal. With this sensor approach, graphene-based biosensors became competitive with common ELISAs in terms of reproducibility and precision for the investigation of human serum samples.

A slightly different electrochemical approach for the detection of AFP without enzymes was developed by Huang *et al.*[139] Here, amine-functionalized rGO was drop-casted onto a carbon IL electrode, decorated with AuNPs and loaded with AFP antibodies. After incubation with the substrate, the formed antigen–antibody complex acted as an inert kinetic barrier for the electron transfer of the ferricyanide mediator. DPV measurements showed a decreasing current with increasing AFP concentration. Additionally, real blood samples were measured in concentrations in the range of ng mL^{-1}.

The detection of biomarkers is also possible via conductivity measurements, as was demonstrated by Zhang *et al.*[146] Their biosensor was built-up like a common sandwich assay as previously mentioned, with rGO as support and HRP bound to a secondary antibody. But instead of detecting only H_2O_2, AA was converted by the enzyme and led to a local pH shift at the graphene surface, resulting in a change of the conductivity of the graphene itself. Though PSA could be detected down to an incredible range of 4 fg mL^{-1} to 0.4 pg mL^{-1}, the sensor was highly unspecific. The conductivity of graphene is highly sensitive to any molecule adsorbing onto its surface. Operating such a sensor under real conditions could cause some problems due to unspecific binding.

A solution was given here in a recent study of Kim *et al.*[143] by implementing a FET, consisting of an electrically contacted layer of rGO, modified only with a PSA antibody. In addition, they presented an efficient scheme for the formation of homogeneous sensor layers due to the self-assembly of GO on a positively charged support with subsequent chemical reduction. To prevent unspecific binding, the modified rGO as well as the Au electrodes used for contacting were blocked. This enabled the specific binding of only the analyte with the immobilized antibodies and therefore the detection of PSA in real blood samples in the range of 0.1–10 ng mL^{-1}.

Another sensitive strategy which also is capable of detection of biomarkers in the range of pg mL^{-1}, is ECL.[137,145,152] Xu *et al.*[145] presented a well-composed sandwich ECL immunoassay for PSA, as seen below (Figure 9). An rGO–chitosan composite was again used as the electrode material to increase the loading of primary antibody, while using Au nanorods enabled a higher

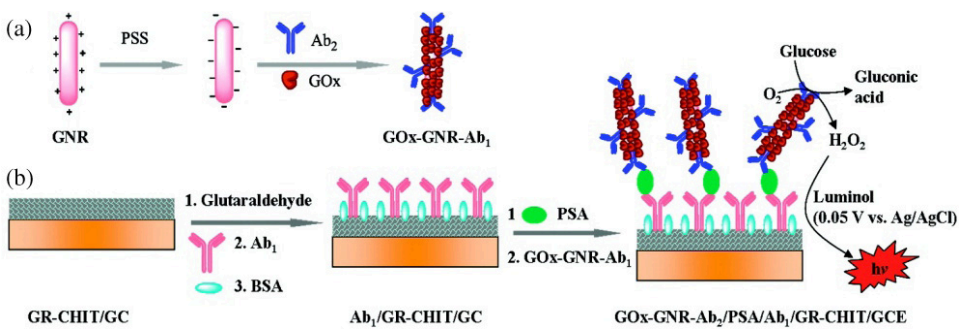

Figure 9. Modification procedure of gold nanorods (a) and ECL immunoassay of PSA with multiple amplification strategy based on a graphene composite-modified electrode (b). Reprinted from Ref. 145 with permission. Copyright © 2011 American Chemical Society.

concentration of antibodies and enzyme (GOx) to be loaded onto the label. However, in this case, the signal was generated by the ECL of luminol which led to comparable results with clinical assays having a sensitivity of 8 pg mL^{-1}.

To go one step further, Tu *et al.*[152] presented photoelectrochemical readout of the signal created by luminol for the detection of carcinoembryonic antigen, a tumor marker for colon cancer. The principle was nearly the same as that presented in Figure 9, apart from the addition of CdS quantum dots on the graphene electrode. After irradiation, the quantum dots induce a photocurrent, which allows the detection of the cancer marker down to 10 pg mL^{-1}. This concept can reduce the undesired background signal and requires simplified instrumentation for the electrical readout than would be needed for optical detection. An overview of the detection of important cancer biomarkers with graphene based sensors is given in Table 5.

4.2. Thrombin

In addition to the detection of cancer biomarkers, thrombin is an important analyte in molecular biology in terms of regulation of tumor growth, metastasis, and angiogenesis.[169] One of the most commonly used strategies for thrombin detection is based on aptamers, which are selected single-stranded oligonucleotides which bind with thrombin with excellent specificity.[170,171] The sensor principle is similar to the typical DNA detection scheme using graphene and has been previously explained in Sec. 3. The analyte in this case is a peptide, which binds to the fluorescently labeled aptamer. The pair is then released from the graphene, whereby fluorescence is restored (Figure 10). This was shown in the work of Chang *et al.*,[172] whereby simply using rGO and a FAM-labeled aptamer, they were able to detect thrombin down to an impressive LOD of 31.3 pM. Although the system led to good results in serum samples, the linear range was only in the region of pM. One major criticism was the poor long-term stability of the rGO suspensions. By simply applying the not reduced GO, it is possible to detect thrombin in concentrations ranging from 40 pM to 10 nM[119] or even higher (Table 6).[72,78,173,174]

There are also some approaches to detect thrombin electrochemically.[175–178] For example, an ELISA-like biosensor has been constructed by replacing primary and secondary antibody by the aptamer as was shown by Bai *et al.*[177] With their system, they were able to improve the sensitivity to an LOD of 11 pM and a wide linear range up to 45 nM, which are impressive results for electrochemical detection. Label-free biosensors showed comparable and even slightly better results.[175,176,178] For these aptasensors, an electrode was modified with rGO, and a thrombin binding aptamer was

Table 5. Summary of important cancer biomarkers detected with graphene-based biosensors.

Analyte	Material	Technique	LOD pg mL^{-1}	Linear range ng mL^{-1}	Sensor additives	Ref.
AFP	rGO	ECL	0.0002	0.0005–0.05	CdS, agarose	137
AFP	rGO	Fluorescence	150	up to 0.56	CdTe	140
AFP	rGO	CV	5.77	0.05–2	Thionine	141
AFP	rGO	SWV	20	0.05–6	HRP	142
AFP	rGO	DPV	1.5	0.002–10	PtNPs, HRP	136
AFP	rGO	DPV	0.5	0.05–400	HRP, Ag-nanowires	138
AFP	GO	DPV	100	1–250	AuNPs	139
PSA	rGO	FET	100	up to 10	APTMS, PDMS	143
PSA	Graphene	DPV	3.4	0.01–50	AuNPs, prussian blue, NiNPs, PEI	144
PSA	rGO	Amp	1	0.002–10	Thionine, HRP	147
PSA	rGO	ECL	8	0.01–8	Chitosan, GOx, glucose, luminol	145
Carcinoembryonic antigen	rGO	DPV	170	0.5–120	Nafion, methylene blue, AuNPs	153
Carcinoembryonic antigen	rGO	ECL	10	1–60	CdS, HRP, AuNPs, luminol	152
Carcinoembryonic antigen	rGO	CV	10	0.05–350	Prussian blue, HRP, AuNPs	154
Integrin avb3	GO	Fluorescence	10^5	up to 10,000	Pyrene	155
Phosphorylated p53	rGO	DPV	100	0.2–10	HRP, streptavidin, biotin, thionine	150
Phosphorylated p53	GO	DPV	0.01 nM	0.02–2 nM	HRP, thionine	151
Cyclin A2	GO	Fluorescence	0.5 nM	up to 3 nM	Fluorescein	149
Cyclin A2	rGO	Impedance	1.02 pM	—	Prussian blue, Tween 20, porphyrin derivative	148
HER2	rGO	FET	0.01 pM	up to 1 μM	AuNPs, APTES	168

immobilized on top. If the analyte now binds on the surface of the electrode, an electron transfer barrier for redox probes is formed and leads to a decrease in current with increasing thrombin concentrations. Here, one outstanding work of Wang *et al.*[175] achieved a sensitivity range on the level of fM. Readout via EIS without any redox probe was also possible.[176] The benefit of the

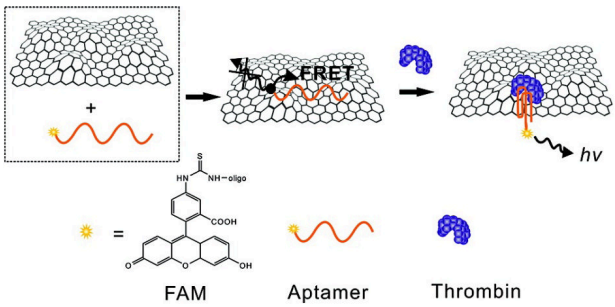

Figure 10. Schematic demonstration of a graphene fluorescence resonance energy transfer (FRET) aptasensor and the detection mechanism for thrombin. Reprinted from Ref. 172 with permission. Copyright © 2010 American Chemical Society.

Table 6. Comparison of different graphene-based sensor approaches for thrombin.

Material	Receptor	Technique	LOD pM	Linear range nM	Sensor additives	Ref.
rGO	Aptamer	Impedance	—	10–50	Prussian blue	176
rGO	Aptamer	DPV	450	up to 0.0001	Prussian blue	175
rGO	GOx, HRP	DPV	11	0.02–45	PtNP	177
rGO	Aptamer	DPV	6	0.01–50	Nafion, methylene blue	178
GO	DNA	Fluorescence	1000	—	Fluorescein[a]	72
GO	ssDNA	Fluorescence	—	up to 200	—	78
GO	Aptamer	Fluorescence	40	up to 10	Fluorescein	119
rGO	Aptamer	Fluorescence	31.3	0.062–0.187	Fluorescein	172

[a]Further sensor additives: exonuclease III, carboxy-X-rhodamine.

graphene in this sensor platform is explained by the greatly enhanced charge transfer of the carbon nanomaterial. Therefore, one main reason for the outstanding sensitivity could be the linkage of the aptamer to the electrode. In the work of Wang *et al.*, this was accomplished via covalent peptide bonding, whereas other studies only coupled the compounds via physical adsorption onto rGO[176] or thiol-gold molecules[178] which resulted in poorer sensitivity.

4.3. Amino acids

Aptamers can also be used for the detection of smaller peptides such as glutathione[179,180] or even single amino acids such as l-histidine,[181] l-tyrosine,[182]

and especially cysteine (Cys) (Table 7).[78,179–181,183–185] Cys has many vital biological functions and a wide range of physiological and pathophysiological effects.[186] For this category of biosensors, most works gain improved sensitivity by taking advantage of the high quenching efficiency of GO and DNA hybridization. Often dye-labeled ssDNA is used, which in the end binds to GO in the absence of Cys or is released in the presence of Cys (Figure 11) and leads to an increase in fluorescence intensity.

Here, Lin *et al.*[185] used a thiol-activated ssDNA, which is bound to Ag nanoparticles and is complementary to the dye-labeled strand. Cys then binds to the Ag surface and releases the previously bound ssDNA, which itself causes the release of the dye-labeled DNA from the GO. This leads to detection in the nM range. This was also achieved by Xie *et al.*[184] by using Ag^+ ions and a cytosine-rich DNA probe, which interacts with the ions in the absence of Cys. This system was also capable of detecting Ag^+ also in the range of nM. However, all of these approaches are based on metal/thiol interaction and are therefore not specific to different thiols. In real samples, one should always consider other biothiols which could interfere.[179] Measuring biothiols in general is still of great interest, as its level in plasma is a diagnostic tool and is related to diseases such as HIV.[187]

In a very recent work of Mei *et al.*,[69] they summarized the potential of the fluorescence "on/off" mechanism with GO for different groups of analytes, also showing its versatility (Figure 12). But instead of using GO as a quencher and an additional fluorophore coupled to a recognition element,

Table 7. Summary of different graphene-based approaches for the detection of various amino acids.

Analyte	Material	Receptor	Technique	LOD nM	Linear range μM	Sensor additives	Ref.
Cys	GO	ssDNA	Fluorescence	2	up to 1	AgNP	185
Cys	GO	ssDNA	Fluorescence	44	0.06–0.5	Fluorescein	184
Cys	GO	ssDNA	Fluorescence	60	up to 100	—	78
Cys, Glu	GO	ssDNA	Fluorescence	1	0.002–0.5	Fluorescein, Hg^{2+}	179
Cys, Glu, IgG	GO	Antibody	Fluorescence	0.02	0.0001–100	AgNPs	180
l-His	Graphene nanosheets	Thiolated DNA	CV	0.0001	0.00001–10000	AuNPs	181
l-Tyr	rGO	Hemin	CV	75	0.5–20	—	182

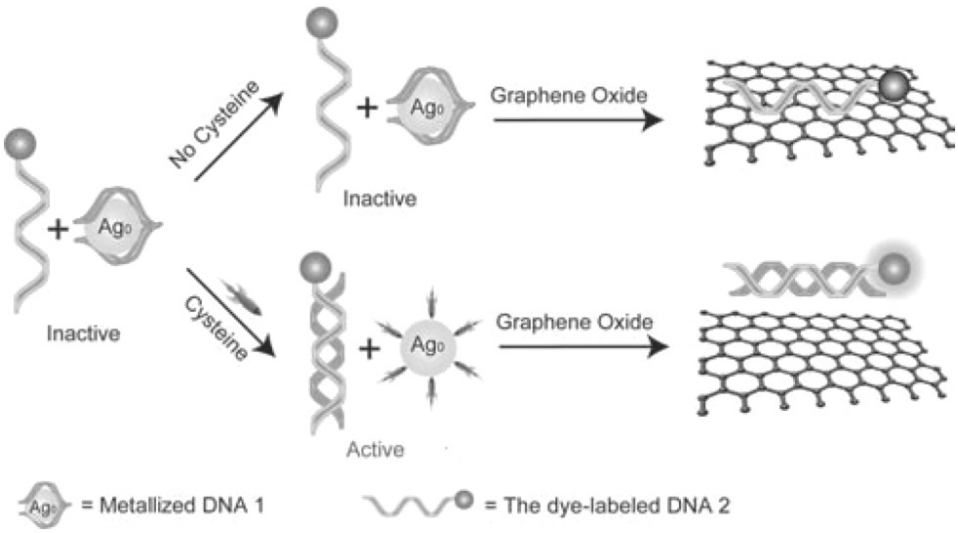

Figure 11. Schematic illustration of a turn-on fluorescent detection of cystein by using GO as quencher. Reprinted from Ref. 185 with permission. Copyright © 2011 WILEY-VCH Verlag GmbH & Co. KGaA, Weinheim.

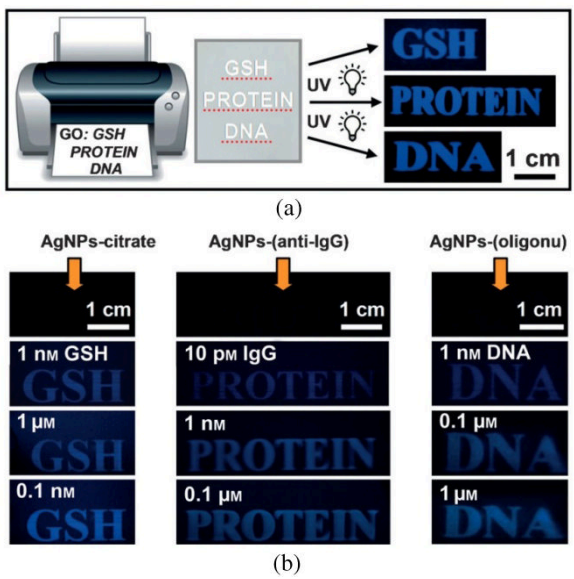

Figure 12. Inkjet printing of fluorescent GO nanosheets (a) and visual detection of glutathione, DNA, and IgG under a UV lamp (b). Reprinted from Ref. 180 with permission. Copyright © 2012 Wiley-VCH Verlag GmbH & Co. KGaA, Weinheim.

GO itself was utilized as fluorophore. It was treated with *n*-buylamine in order to form blue emitting nanosheets, which in turn were quenched by various functionalized Ag nanoparticles. By simply switching the recognition elements on the Ag nanoparticles, they achieved detection of glutathione, DNA, and immunoglobulin G (IgG) (as a model protein), in the range of pM. Also the sensor preparation where GO nanosheets are printed onto a non-fluorescent substrate seems quite applicable for future sensor applications. However, one should still consider here the low excitation wavelength of 350 nm, which could cause some problems in real biological samples in terms of high background signals.

4.4. Immunoglobulins

The detection of **immunoglobulins** is often performed in blood serum samples and the preferred sensor concepts on this field are ELISAs with electrochemical readout (Table 8).[188–190] This concept has been previously described and can be adopted by simply changing the recognition antibody. Additionally, there are other approaches such as the development of specific G-FETs with single graphene flakes (Figure 13).[191–193] In FET devices, electrical detection is used which exploits the change in conductivity that arises when molecules adsorb on the surface of the sensors. Benefits of FETs are label free and online detection, and also the possibility of miniaturization toward a nanoscale-size complete sensor. There are different strategies for the recognition element on graphene, either applying specific antibodies on AuNPs[193] or aptamers via π–π interaction of linker molecules.[191,192] All of these schemes realize selective detection in the nm range and are promising for the electrical detection of biomolecules. There are varying feasible explanations for the mechanism as to how analyte binding influences the conductivity of the graphene,[194,195] but none of them have been explicitly proven.

Finally, many other biosensor approaches with graphene for different protein analytes have been investigated, including model analytes such as BSA,[196] streptavidin,[197] or TATA-binding protein,[198] and also clinical and biological relevant substances such as platelet-derived growth factors,[177,199] lectins,[200] hemin[201] or vasopressin, neurohypophysial hormone.[202,203] There are also various enzyme assays with fluorescence readout, using graphene and phosphorylase D,[204] captase-3,[205] matrix metalloproteinase-2,[206,189] or lysozyme.[207] In these works, graphene (mostly GO and rGO) was again used as a support material, electrode surface, or quencher as described previously. The sensor concepts differ only slightly from those mentioned above.

Table 8. Summary of different graphene-based approaches for the detection of immunoglobulins.

Analyte	Material	Receptor	Technique	LOD	Linear range	Sensor additives	Ref.
IgE	Mechanically exfolliated graphene	Aptamer	FET	—	0.29–160 nM	—	191,192
IgG	GO	Antibody	Fluorescence	0.1 pM	0.001–100 nM	AgNPs	180
IgG	rGO	Antibody	DPV	0.5 fg mL^{-1}	10–500 ng mL^{-1}	Au nanoflowers	188
IgG	rGO	Antibody	DPV	50 pg mL^{-1}	0.1–200 ng mL^{-1}	PDDA, AuNPs, HRP	189
IgG	rGO	Antibody	FET	2 ng mL^{-1}	up to 0.02 mg mL^{-1}	AuNPs	193
IgG	rGO	Antibody	DPV	70 ng mL^{-1}	0.2–320 ng mL^{-1}	HRP, Cys, AuNPs	190

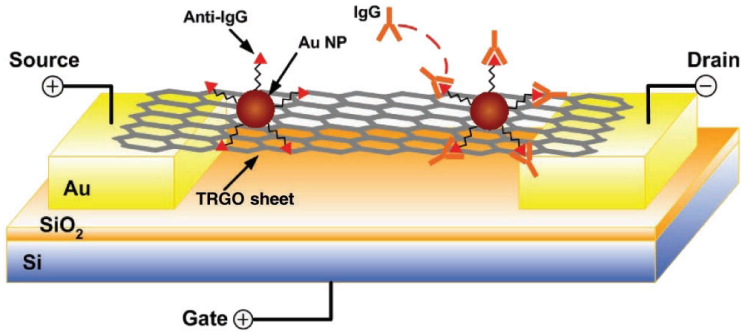

Figure 13. Schematic of the measurement setup using a G-FET for the detection of IgG. Reprinted from Ref. 193 with permission. Copyright © 2010 Wiley-VCH Verlag GmbH & Co. KGaA, Weinheim.

This section illustrates the versatility in graphene application for protein analytics. By immobilization of specific recognition elements such as enzymes, antibodies, or aptamers in combination with graphene, a broad spectrum of selective biosensors with impressive LODs were constructed. Many of the sensor strategies could be adapted for other biomarkers, target protein, or other immuno targets.

However, explanations as to why certain combinations of materials result in better sensitivity are lacking and descriptions of particular mechanisms with respect to the graphene are often missing. Major advantages are improved sensitivity, less expensive production, and smaller sensor device, which could enable better point-of-care diagnostics and aid in early disease recognition. However, to date, there is no commercial biosensor based on graphene, which could potentially replace the older and more laborious techniques.

5. Other Biologically Relevant Analytes

Aside from carbohydrates, nucleotides, and proteins, there are several approaches to detect smaller biomolecules such as lipids and biologically relevant substances such as pesticides, alcohols, single cations, anions, and also whole cells and viruses.

Cholesterol is an important lipid and its accumulation in blood is related to hypertension, arteriosclerosis, and heart disease.[208,209] Conventional methods such as spectroscopic, colorimetric, non-enzymatic, and other electrochemical approaches suffer from poor specificity and difficulty of analyte standardization.[210,211] Using a graphene electrode modified with cholesterol

oxidase (ChOx) enables electrochemical detection in the range of μM, whereas an additional decoration with PtNPs[212] or AuNPs[213,214] leads to more sensitivity.[215,216] Further attachment of cholesterol esterase (ChEt) enables the detection of cholesterol esters[212] (Figure 14). But, in principle, the concept is analogous to the electrochemical enzymatic detection of glucose, as described previously in Sec. 2. Metal nanoparticles enhance the conversion of H_2O_2 and their attachment to a graphene-modified electrode surface leads to more sensitive recognition. The readout of the H_2O_2 produced could also be realized via ECL with luminol, additionally catalyzed by the iron ions of hemin, which was attached to the graphene.[217] This resulted in an LOD of 0.06 μM, which is two orders of magnitude lower compared to the biosensors mentioned above.

Hydrogen peroxide is an important molecule in biological processes. It occurs as enzymatic by product of oxidases or as substrate of peroxidases.[218] Furthermore, it is an essential mediator in food, pharmaceutical, or clinical analyses.[219] Therefore, also a lot of sensor approaches which are using graphene materials are described. The sensor principles are almost the same as have been presented in Sec. 2.2 for the glucose sensors, except the usage of other enzymes. HRP is the most common enzyme to detect hydrogen peroxide.[220–234] The enzyme is adsorbed or immobilized on electrode surfaces together with GO or rGO. The working potential could be decreased from –400 mV vs SCE[222] by additional incorporation of metallic nanoparticles[220,224,225,231] to –200 mV vs Ag/AgCl, which makes these sensor more selective toward other electroactive substances such as AA, UA, or DA. The

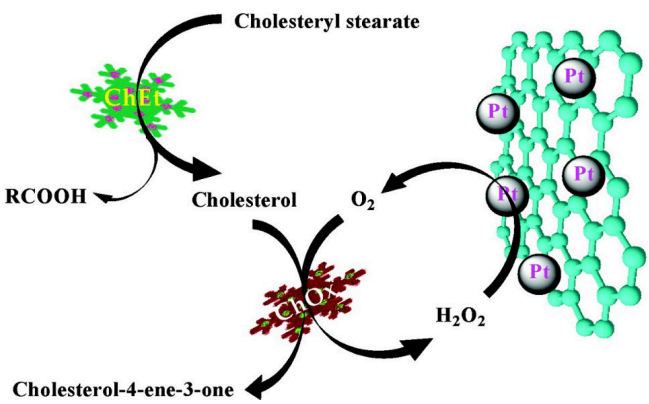

Figure 14. Scheme illustrating a biosensor for cholesterol ester based on PtNP-decorated graphene, ChEt, and ChOx. Reprinted from Ref. 212 with permission. Copyright © 2010 American Chemical Society.

selectivity could also be enhanced by applying perm-selective membranes which keep away potential interfering substances from the electrode surface. Nafion,[228] chatoyant,[232] or poly-lysine[223] have been used. The highest sensitivity, with an LOD of 10 nM is reported for a system comprising of rGO, HRP, AuNP, and thionine.[225] The linear change in the sensor signal ranges from 0.5×10^{-3} to 1.8 mM. Hemoglobin (Hb) is another biomolecule frequently used for amperometric detection of hydrogen peroxide.[235–242] One typical sensor layout is depicted in Figure 15.

The lowest LOD was obtained with a combination of platinum nanoparticles. It is reported to be 0.1 μm with a linear range from 0.01 to 1 mM. For sensing of hydrogen peroxide by amperometric transduction and with the use of graphene and an enzyme, it can be concluded that there is still a lot of work to do in order to decrease the sensitivity and to get higher selectivity. Most sensors reported so far cannot compete with luminescent probes which may have the additional benefit that they can be used for the detection of hydrogen peroxide in cellular analysis.[243]

The detection of alcohols is easily achievable by also simply changing the enzyme. The enzymatic detection of ethanol with alcohol dehydrogenase (ADH) always involves the sensitive recognition of the cofactor NADH. In conventional electrodes, the overpotential of NADH is greater than 0.6 V (vs Ag/AgCl),[244] which could lead to interference problems in real samples.[245] When graphene is implemented as an electrode material, rGO is typically used, as it enables oxidation of NADH at lower potentials and therefore leads to less cross sensitivity.

Many works investigated different sensor electrode additives such as Nafion,[246] chatoyant,[247] or methylene green[248] (Table 9). They yield good

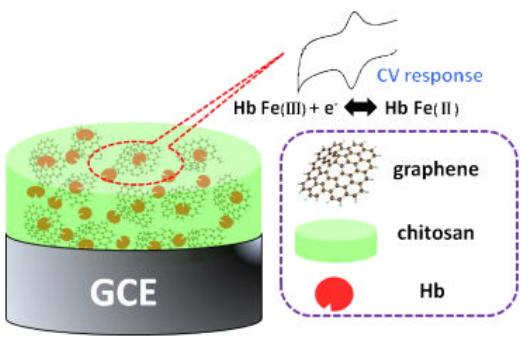

Figure 15. Principle of a hydrogen peroxide sensor with a composite of Hb, graphene and chitosan immobilized on a GC electrode.[242] Reprinted from Ref. 242 with permission. Copyright © 2010 Elsevier.

Table 9. Comparison of different sensor additives in graphene-based ethanol biosensors.

Sensor additives	LOD μM	Linear range mM	Technique	Working potential	Ref.
Nafion	25	0.2–21	Amp	0.5 V vs SCE	246
—	25	0.025–0.225	Amp	0.05 V vs SCE	249
Chitosan	5	0.025–0.2	Amp	0.45 V vs Ag/AgCl	247
Methylene green	500	0.5–11	Amp	0.1 V vs Ag/AgCl	248
$Ru(bpy)_3^{2+}$, BSA	0.1	0.001–2	ECL	0.2–1.3 V vs Ag/AgCl	250

results, even for common samples, such as wine or beer.[247] Simply casting ADH onto an rGO-modified electrode leads to sensitive detection in the range of μM, at a very low potential.[249] Like in other sensor approaches, the question here arises, as to whether complex graphene composites are even necessary at all, since they do not appear to drastically improve the sensitivity. By applying a ruthenium (II) complex to the biosensor, the detection of NADH could be performed again via ECL and was a slightly more sensitive than other approaches.[250]

Other biological compounds of interest which have been investigated with graphene-based biosensors are acetic acid,[105] DA,[105] UA,[105,251] glucosamine,[252] acetylcholine,[253]oxygen,[228,254] and clenbuterol.[255] Since all of them use similar strategies that were previously discussed, they will not be explained here again in detail. Again, rGO and GO are used mainly as an electrode, substrate, or label material due to their outstanding features. Biosensors with remarkable sensitivity and selectivity were prepared by simple attachment of enzymes, antibodies, or aptamers.

Besides the detection of biomolecules, there are also plenty of biosensor approaches with graphene used for improved recognition of biologically relevant compounds, especially pesticides, toxins, and other hazardous substances. The electrochemical detection of bisphenol A (BPA) was accomplished by a simple graphene-modified electrode with tyrosinase incorporated in chitosan at the surface.[256] BPA is extensively used in the preparation of epoxy resins and polycarbonate plastic. With this easy concept, it was even possible to detect traceamounts (nM) in real water samples, making this biosensor a real alternative to common laborious methods such as high-performance liquid chromatography mass spectrometry (HPLC-MS) or gas chromatography mass spectrometry (GC-MS). The same concept could also be applied for the detection of phenol[257,258] and catechol[259,260] in the range of μM. Environmental toxins are not always the result of industrial production, but can also be

produced by organisms such as pathogenic microbes. Ochratoxin A is one such toxin which can be detected using the same GO-based technique as was used for DNA detection. This simple method offers a platform to identify concentrations in the range of nM even in wine and food samples.[261] Here, a FAM-labeled aptamer binds to GO and is quenched in the absence of the analyte or is released when specific binding to the analyte occurs, restoring the fluorescence.

Another category of analytes of particular interest are organophosphates (OPs) such as carbaryl, chlorpyrifos, or paraoxon. These compounds are widely used as pesticides in agriculture, yet are harmful to human health, and therefore must be measured at trace levels.[262,263] Graphene-based acetylcholinesterase (AChE) electrochemical biosensors showed satisfactory results for pesticide analysis and are a good alternative to common techniques such as gas or liquid chromatography and mass spectroscopy,[262] which require extensive labor resources. The sensor approach makes use of the inhibition of the enzymatic reaction of AChE[264–267] or tyrosinase[256] and substrates such as thiocholine or catechol, respectively. OPs interfere with this reaction, which can be readout electrochemically with a graphene-modified electrode (Figure 16).

Differences in the biosensors for OP detection could only be found with respect to the electrode material. Here, composite materials such as rGO decorated with AuNPs,[264,267] PtNPs,[268] TiO_2,[265] and CdS[266] were used. These

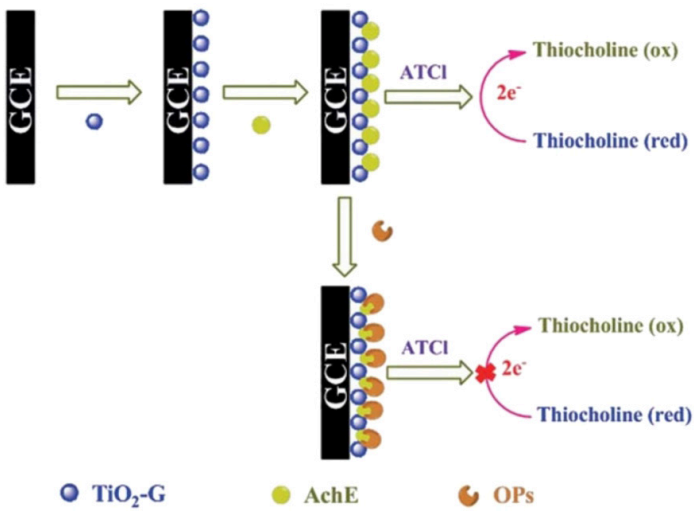

Figure 16. Schematic representation of biosensor fabrication with a modified GC electrode and detection principle for OPs. Reproduced from Ref. 265 with permission of The Royal Society of Chemistry.

additives are all intended to increase the charge transfer at the electrode. Since these studies investigated different compounds, they are not easily comparable. However, all of them resulted in detection below 1 ng mL^{-1} while several were able to detect as low as μg mL^{-1}, which are promising results for the detection of trace amounts of OPs.

In addition to small molecule detection, there are also approaches to detect even whole bacteria or image cells with techniques previously described in Sec. 3. *E.coli* bacteria were detected by attaching a specific antigen onto a CVD graphene FET and monitoring the change in conductivity when the bacteria are bound to the sensor surface.[269] Although the detection is not completely selective, and the sensing parameters are not suitable for a portable biosensor, this could still find application in assays for drug screening. Sulfate reducing bacteria (SRB) were detected by a common assay with specific antibodies where GO enhanced not only the potentiometric stripping analysis (PSA) but also the colometric detection.[270] GO sheets were labeled with secondary antibodies, which bind to target bacteria previously attached to the assay. In a further step, GO promotes the reduction of Ag(I) to Ag nanoparticles, which are needed for a further readout (Figure 17). In another study, they used an electrode covered with rGO covalently modified with aptamers for the specific capture of different cancer cell lines.[271] Only upon cell adhesion, the redox signals of a mediator decreased due to the formation of an inert barrier by the cells.

An optical readout was used for the detection of a rotavirus.[272] GO was used here as a transparent substrate material, which was further functionalized

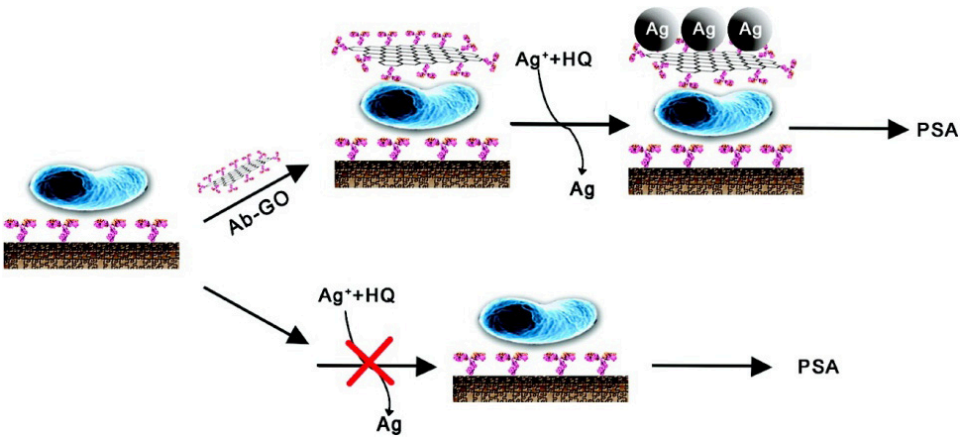

Figure 17. Schematic representation of a GO-based immunoassay combined with silver enhancement for the detection of SBR. Reprinted from Ref. 270 with permission. Copyright © 2010 American Chemical Society.

with antibodies via peptide bonding, and also served as fluorescent dye. A secondary antibody was labeled with AuNPs and through FRET, the fluorescence of GO was quenched. With this setup, they were able to selectively detect the virus to an LOD of 10^{-5} p.f.u. mL^{-1}, comparable to common ELISA technology.[273]

In a different optical approach, GO was applied as quencher of dye-labeled aptamers, as described previously in the DNA section. Pei *et al.*[196] were able to detect and distinguish between different proteins and also various cell types with the appropriate aptamer receptor. This again demonstrated the broad and easy adaptation of affinity-receptor-based applications for which GO can be used. The detection of cancer cells could be one interesting application for this setup and has already been demonstrated in a microfluidic system.[274]

Many heavy metal ions are a threat to the environment and also to human health. They require detection at trace levels, which usually requires sophisticated and expensive instruments such as inductively coupled plasma mass spectrometry (ICP-MS) or atomic absorption spectroscopy (AAS). Again, graphene-based affinity sensors are described as an inexpensive alternative, albeit less sensitive(Table 10). Thymine-rich and dye-labeled aptamers mainly served as receptor molecules for the detection of Hg^{2+}.[78,118,275,276] Again, their affinity to bind with GO led to fluorescence quenching, and respective recovery when the analyte interfered with this non-covalent binding, as previously described. This method was again shown to have great selectivity and high sensitivity up to LODs in the pM range. A slightly different strategy was used for the detection of Cu^{2+} [277,278] and Pb^{2+}.[279,280] Instead of using aptamers, DNAzymes with fluorescent dyes were applied. They also bind to GO via π-stacking; however, they are irreversibly cleaved in the presence of specific heavy metal ions.[281] Subsequently, the previously incorporated dye is released and fluorescence is again recovered (Figure 18). The sensitivity is comparable

Table 10. GO-based fluorescence "turn-on" biosensors for heavy metal ions.

Analyte	Receptor	LOD nM	Linear range nM	Attached dye	Ref.
Hg^{2+}	Aptamer	0.187	up to 0.623	FAM	276
Hg^{2+}	Aptamer	0.92	1–50	GO	275
Hg^{2+}	Aptamer	5.7	up to 10^4	Fluorescein	78
Cu^{2+}	DNAzyme	2	up to 250	GelRed	277
Cu^{2+}	DNAzyme	10	up to 90	FAM	278
Pb^{2+}	DNAzyme	0.5	up to 1.3×10^5	Cy-3	284
Pb^{2+}	DNAzyme	0.3	1–10	FAM	279

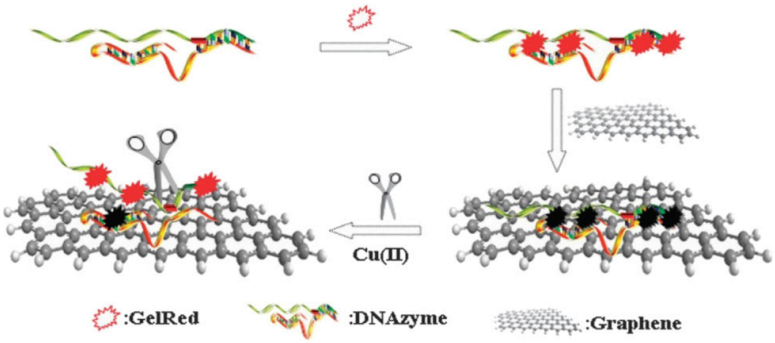

Figure 18. Schematic illustration of lable-free fluorescent detection of Cu^{2+} based on GO-quenched DNAzymes. Reproduced from Ref. 277 with permission of The Royal Society of Chemistry.

to the affinity sensors with aptamers, enabling the detection of different heavy metal ions, since highly selective DNAzymes have already been designed.[282,283]

In contrast to cations, only electrochemical methods are used for the detection of anions. In particular, nitrite (NO_2^-) is of general interest because it is used in large amounts as a preservative and fertilizing agent and has negative effects on human health.[285] In acidic medium, it is transformed into nitric oxide (NO), which has a high affinity to bind to heme proteins. Therefore, redox-active proteins such as myoglobin (Mb),[286,287] Hb,[288,289] or HRP[230] are attached to rGO-modified electrodes, often by embedding into a conductive polymer. These biosensors display excellent electrocatalytic reduction ability for NO, which offers the indirect determination of NO_2^-. Consequently, biosensors with Hb show more sensitivity than other receptors, which is explained through a better electron transfer of the heme group within the proteins to the electrode. As seen in Table 11, smaller proteins lead to a lower LOD. The same strategy was applied for analytes such as nitromethane,[280] trichloroacetic acid,[290] and chlorite,[291] leading to similar results.

6. Conclusions

The research discussed in this chapter shows that graphene can be used, at least in principle, in biosensors for the detection of glucose, DNA, various proteins, bacteria, metals, and even whole cells. Nevertheless, the advantages of including graphene in a biosensor scheme are not always readily apparent. The lack of a consistent preparation method for large-scale synthesis of well-defined graphene complicates the situation greatly. Further complicating matters, standards in material characterization are severely lacking, making a comparison of

Table 11. Electrochemical detection of NO_2^- using rGO-based biosensors with different receptor proteins.

Receptor	LOD μM	Linear range mM	Sensor additives[a]	Working potential	Ref.
Hemoglobin	0.04	0.0002–0.033	PDDA	–0.58 V vs SCE	289
Hemoglobin	0.18	0.0006–0.033	Chitosan	–0.25 V vs SCE	288
Myoglobin	10	0.05–2.5	TPA, Nafion	0.3 V vs SCE	287
Myoglobin	750	1.25–22.5	Nafion	–0.3 V vs SCE	286
HRP	19500	58.6–488.6	—	–0.8 V vs Ag/AgCl	137

[a]Tetrasodium 1,3,6,8-pyrenetetrasulfonic acid (TPA), poly(diallyldimethylammonium chloride) (PDDA).

the results from one sensor concept to the next very difficult, to say the least. This is viewed as a severe hindrance to the success of graphene-based biosensor development. A potential solution could be the total chemical synthesis of graphene. The group of Klaus Müllen successfully demonstrated the surface-mediated synthesis of nanographene and graphene nanoribbons.[292,293] The challenge hereby is the synthesis of larger flakes on insulating substrates.

In order to exploit all of the extraordinary properties of graphene at once, it would be necessary to produce such high quality material on insulating, flexible substrates. Graphene on its own has high sensitivity but without any selectivity at all. One possibility to introduce selectivity could be by chemical modification. First results have already been described. Another possibility is to design composite materials together with other nanomaterials. The functionality of graphene could also be expanded to other one-atom-thick, 2D atomic crystals, such as BN, $NbSe_2$, TaS_2, MoS_2, and many others. Investigation in this field has already begun, and it is expected that the first biosensors with such materials (or even a combination ora stack of different 2D crystals) will be reported soon.

For all of these optimistic and promising perceptions of graphene, there are three essential questions, which challenge biosensor technology that must seriously be discussed; these are: (i) Is there anything beyond a good paper? (ii) Will it be possible to produce more than one device? (iii) Does the market care? As of now, there are no convincing answers to these questions. Therefore, one should not expect biosensors based on graphene to appear on the market in the near future. Today, graphene-based biosensors cannot compete with existing biosensors, and may never be able to do so. One exception seems to be the detection of oligonucleotides using graphene-based biosensors. Electrochemical detection methods provide the best sensitivity when combined with rGO, with typical detection limits in the range of fM to aM. Although GO also yields excellent lower LOD in the pM to fM range, CVD

and epitaxial graphene do not provide the low LOD offered by rGO or even GO. Additionally, the immobilization of DNA onto graphene is relatively easy and understood. With the advancement of sensor additives, such as polymers and nanoparticles, and improvements in detection schemes, graphenes could prove to be a leading sensor material in making graphene-based DNA biosensors competitive with other technologies.

The most significant strides will not be made by imitating or improving well-established sensor technologies, but rather by focusing on exploiting the truly unique properties of carbon nanomaterials and in finding new applications and markets. Some of these properties include graphene's extremely high surface to volume ratio, together with its transparency, high conductivity, as well as its flexibility, which could lead to new miniaturized biosensors and sensor arrays having high sensitivity, long-term stability, multidetection capabilities, and ultrafast response.

References

1. *Editorial. Nat. Nanotechnol.* **2013**, *8*, 221.
2. Dreyer, D. R.; Ruoff, R. S.; Bielawski, C. W. *Angew. Chem. Int. Ed Engl.* **2010**, *49*, 9336–9344.
3. Stoller, M. D.; Park, S.; Zhu, Y.; An, J.; Ruoff, R. S. *Nano Lett.* **2008**, *8*, 3498–3502.
4. Lee, C.; Wei, X.; Kysar, J. W.; Hone, J. *Science* **2008**, *321*, 385–388.
5. Novoselov, K. S.; Geim, A. K.; Morozov, S. V.; Jiang, D.; Zhang, Y.; Dubonos, S. V.; Grigorieva, I. V.; Firsov, A. A. *Science* **2004**, *306*, 666–669.
6. Novoselov, K. S.; Fal′ko, V. I.; Colombo, L.; Gellert, P. R.; Schwab, M. G.; Kim, K. *Nature* **2012**, *490*, 192–200.
7. Kim, K. S.; Zhao, Y.; Jang, H.; Lee, S. Y.; Kim, J. M.; Kim, K. S.; Ahn, J.-H.; Kim, P.; Choi, J.-Y.; Hong, B. H. *Nature* **2009**, *457*, 706–710.
8. Emtsev, K. V.; Bostwick, A.; Horn, K.; Jobst, J.; Kellogg, G. L.; Ley, L.; McChesney, J. L.; Ohta, T.; Reshanov, S. A.; Röhrl, J.; Rotenberg, E.; Schmid, A. K.; Waldmann, D.; Weber, H. B.; Seyller, T. *Nat. Mater.* **2009**, *8*, 203–207.
9. Park, S.; Ruoff, R. S. *Nat. Nanotechnol.* **2009**, *4*, 217–224.
10. Dreyer, D. R.; Ruoff, R. S.; Bielawski, C. W. *Angew. Chem. Int. Ed.* **2010**, *49*, 9336–9344.
11. Ferrari, A. C.; Meyer, J. C.; Scardaci, V.; Casiraghi, C.; Lazzeri, M.; Mauri, F.; Piscanec, S.; Jiang, D.; Novoselov, K. S.; Roth, S.; Geim, A. K. *Phys. Rev. Lett.* **2006**, *97*, 187401.
12. Kochmann, S.; Hirsch, T.; Wolfbeis, O. S. *TrAC Trends Anal. Chem.* **2012**, *39*, 87–113.

13. Clark, L. C.; Lyons, C. *Ann. N. Y. Acad. Sci.* **1962**, *102*, 29–45.
14. Wang, J. *Electroanalysis*, **2001**, *13*, 983.
15. Hua, L.; Wu, X.; Wang, R. *The Analyst* **2012**, *137*, 5716.
16. Zheng, D.; Vashist, S. K.; Al-Rubeaan, K.; Luong, J. H. T.; Sheu, F.-S. *Talanta* **2012**, *99*, 22–28.
17. Mani, V.; Devadas, B.; Chen, S.-M. *Biosens. Bioelectron.* **2013**, *41*, 309–315.
18. Cai, C.-J.; Xu, M.-W.; Bao, S.-J.; Lei, C.; Jia, D.-Z. *RSC Adv.* **2012**, *2*, 8172–8178.
19. Jiang, Y.; Zhang, Q.; Li, F.; Niu L. *Sensors Actuators B Chem.* **2012**, *161*, 728–733.
20. Zhang, Q.; Wu, S.; Zhang, L.; Lu, J.; Verproot, F.; Liu, Y.; Xing, Z.; Li, J. Song, X.-M. *Biosens. Bioelectron.* **2011**, *26*, 2632–2637.
21. Yang, M. H.; Choi, B. G.; Park, H.; Hong, W. H.; Lee, S. Y.; Park, T. J. *Electroanalysis* **2010**, *22*, 1223–1228.
22. Yang, J.; Deng, S.; Lei, J.; Ju, H.; Gunasekaran, S. *Biosens. Bioelectron.* **2011**, *29*, 159–166.
23. Wang, K.; Liu, Q.; Guan, Q.-M.; Wu, J.; Li, H.-N.; Yan, J.-J. *Biosens. Bioelectron.* **2011**, *26*, 2252–2257.
24. Unnikrishnan, B.; Palanisamy, S.; Chen, S.-M. *Biosens. Bioelectron.* **2013**, *39*, 70–75.
25. Wu, P.; Shao, Q.; Hu, Y.; Jin, J.; Yin, Y.; Zhang, H.; Cai, C. *Electrochimica Acta* **2010**, *55*, 8606–8614.
26. Kang, X.; Wang, J.; Wu, H.; Aksay, I. A.; Liu, J.; Lin, Y. *Biosens. Bioelectron.* **2009**, *25*, 901–905.
27. Qiu, J.-D.; Huang, J.; Liang, R.-P. *Sensors Actuators B Chem.* **2011**, *160*, 287–294.
28. Zhang, S.; Tang, S.; Lei, J.; Dong, H.; Ju, H. *J. Electroanal. Chem.* **2011**, *656*, 285–288.
29. Palanisamy, S.; Vilian, A. E.; Chen, S.-M. *Int J Electrochem Sci* **2012**, *7*, 2153–2163.
30. Chen, Y.; Li, Y.; Sun, D.; Tian, D.; Zhang, J.; Zhu, J.-J. *J. Mater. Chem.* **2011**, *21*, 7604.
31. Liu, S.; Tian, J.; Wang, L.; Luo, Y.; Lu, W.; Sun, X. *Biosens. Bioelectron.* **2011**, *26*, 4491–4496.
32. Cheng, N. *Am. J. Anal. Chem.* **2012**, *03*, 312–319.
33. Zeng, Q.; Cheng, J.-S.; Liu, X.-F.; Bai, H.-T.; Jiang, J.-H. *Biosens. Bioelectron.* **2011**, *26*, 3456–3463.
34. Shi, J.; Zhang, H.; Snyder, A.; Wang, M.; Xie, J.; Marshall Porterfield, D.; Stanciu, L. A. *Biosens. Bioelectron.* **2012**, *38*, 314–320.
35. Claussen, J. C.; Kumar, A.; Jaroch, D. B.; Khawaja, M. H.; Hibbard, A. B.; Porterfield, D. M.; Fisher, T. S. *Adv. Funct. Mater.* **2012**, *22*, 3399–3405.

36. Guo, Y.; Han, Y.; Shuang, S.; Dong, C.; *J. Mater. Chem.* **2012**, *22*, 13166–13173.
37. Baby, T. T.; Aravind, S. S. J.; Arockiadoss, T.; Rakhi, R. B.; Ramaprabhu, S. *Sensors Actuators B Chem.* **2010**, *145*, 71–77.
38. Wu, H.; Wang, J.; Kang, X.; Wang, C.; Wang, D.; Liu, J.; Aksay, I. A.; Lin, Y. *Talanta* **2009**, *80*, 403–406.
39. Zhou, K.; Zhu, Y.; Yang, X; Li, C. *Electroanalysis* **2010**, *22*, 259–264.
40. Shan, C.; Yang, H.; Han, D.; Zhang, Q.; Ivaska, A.; Niu, L. *Biosens. Bioelectron.* **2010**, *25*, 1070–1074.
41. Zhang, Y.; Liu, S.; Wang, L.; Qin, X.; Tian, J.; Lu, W.; Chang, G.; Sun, X. *RSC Adv.* **2011**, *2*, 538–545.
42. Zhiguo, G.; Shuping, Y.; Zaijun, L.; Xiulan, S.; Guangli, W.; Yinjun, F.; Junkang, L. *Electrochimica Acta* **2011**, *56*, 9162–9167.
43. Kavitha, T.; Gopalan, A. I.; Lee, K.-P.; Park, S.-Y. *Carbon* **2012**, *50*, 2994–3000.
44. Norouzi, P.; Ganjali, H.; Larijani, B.; Ganjali, M. R.; Faridbod, F.; Zamani, H. A. *Int. J. Electrochem. Sci.* **2011**, *6*, 5189.
45. Gu, H.; Yu, Y.; Liu, X.; Ni, B.; Zhou, T.; Shi, G. *Biosens. Bioelectron.* **2012**, *32*, 118–126.
46. Ping, J.; Wang, Y.; Fan, K.; Wu, J.; Ying, Y. *Biosens. Bioelectron.* **2011**, *28*, 204–209.
47. Alwarappan, S.; Liu, C.; Kumar, A.; Li, C.-Z. *J. Phys. Chem. C* **2010**, *114*, 12920–12924.
48. Wang, Y.; Shao, Y.; Matson, D. W.; Li, J.; Lin, Y. *ACS Nano* **2010**, *4*, 1790–1798.
49. Alwarappan, S.; Boyapalle, S.; Kumar, A.; Li, C.-Z.; Mohapatra, S. *J. Phys. Chem. C* **2012**, *116*, 6556–6559.
50. Rao, C. N. R.; Sood, A. K.; Subrahmanyam, K. S.; Govindaraj, A. *Angew. Chem.* **2009**, *121*, 7890–7916.
51. Tang, D.; Li, Q.; Tang, J.; Su, B.; Chen, G. *Anal. Chim. Acta* **2011**, *686*, 144–149.
52. Chen, X.; Ye, H.; Wang, W.; Qiu, B.; Lin, Z.; Chen, G. *Electroanalysis* **2010**, *22*, 2347–2352.
53. Hummers, W. S.; Offeman, R. E. *J. Am. Chem. Soc.* **1958**, *80*, 1339–1339.
54. Lu, C.-H.; Yang, H.-H.; Zhu, C.-L.; Chen, X.; Chen, G.-N. *Angew. Chem. Int. Ed Engl.* **2009**, *48*, 4785–4787.
55. Manohar, S.; Mantz, A. R.; Bancroft, K. E.; Hui, C.-Y.; Jagota, A.; Vezenov, D. V. *Nano Lett.* **2008**, *8*, 4365–4372.
56. Varghese, N.; Mogera, U.; Govindaraj, A.; Das, A.; Maiti, P. K.; Sood, A. K.; Rao, C. N. R. *ChemPhysChem* **2009**, *10*, 206–210.

57. Liu, Z.; Robinson, J. T.; Sun, X.; Dai, H. *J. Am. Chem. Soc.* **2008**, *130*, 10876–10877.
58. Antony, S.; Grimme, J. *Phys. Chem. Chem. Phys.* **2008**, *10*, 2722–2729.
59. Gowtham, S.; Scheicher, R. H.; Ahuja, R.; Pandey, R.; Karna, S. P. *Phys. Rev. B* **2007**, *76*, 033401.
60. Ortmann, F.; Schmidt, W. G.; Bechstedt, F. *Phys. Rev. Lett.* **2005**, *95*, 186101.
61. Zhu, W.; Zhao, Z.; Li, Z.; Jiang, J.; Shen, G.; Yu, R. *J. Mater. Chem. B* **2013**, *1*, 361.
62. Yang, L.; Liu, C.; Ren, W.; Li, Z. *ACS Appl. Mater. Interfaces* **2012**, *4*, 6450–6453.
63. Zhu, W.; Zhao, Z.; Li, Z.; Jiang, J.; Shen, G.; Yu, R. *The Analyst*, **2012**, *137,* 5506.
64. Zhou, D.-M.; Xi, Q.; Liang, M.-F.; Chen, C.-H.; Tang, L.-J.; Jiang, J.-H.; *Biosens. Bioelectron.* **2013**, *41*, 359–365.
65. Tan, X.; Chen, T.; Xiong, X.; Mao, Y.; Zhu, G.; Yasun, E.; Li, C.; Zhu, Z.; Tan, W. *Anal. Chem.* **2012**, *84*, 8622–8627.
66. Zhang, C.; Xu, J.; Zhang, S.; Ji, X.; He, Z. *Chem. – Eur. J.* **2012**, *18*, 8296–8300.
67. Xing, X.-J.; Liu, X.-G.; Yue-He, Luo, Q.-Y.; Tang, H.-W.; Pang, D.-W. *Biosens. Bioelectron.* **2012**, *37*, 61–67.
68. Tao, Y.; Lin, Y.; Huang, Z.; Ren, J.; Qu, X. *The Analyst*, **2012**, *137*, 2588.
69. Mei, Q.; Zhang, Z. *Angew. Chem. Int. Ed.* **2012**, *51*, 5602–5606.
70. Dong, H.; Zhang, J.; Ju, H.; Lu, H.; Wang, S.; Jin, S.; Hao, K.; Du, H.; Zhang, X. *Anal. Chem.* **2012**, *84*, 4587–4593.
71. Zhao, X.-H.; Ma, Q.-J.; Wu, X.-X.; Zhu, X. *Anal. Chim. Acta* **2012**, *727*, 67–70.
72. Liu, X.; Aizen, R.; Freeman, R.; Yehezkeli, O.; Willner, I. *ACS Nano* **2012**, *6*, 3553–3563.
73. Luo, M.; Chen, X.; Zhou, G.; Xiang, X.; Chen, L.; Ji, X.; He, Z. *Chem. Commun.* **2012**, *48*, 1126.
74. Liu, M.; Zhao, H.; Chen, S.; Yu, H.; Quan, X. *J. Mater. Chem.* **2011**, *21*, 15266.
75. Liu, M.; Zhao, H.; Chen, S.; Yu, H.; Zhang, Y.; Quan, X. *Biosens. Bioelectron.*, **2011**, *26*, 4213–4216.
76. Wu, C.; Zhou, Y.; Miao, X.; Ling, L. *The Analyst* **2011**, *136*, 2106.
77. Liu, C.; Wang, Z.; Jia, H.; Li, Z. *Chem. Commun.* **2011**, *47*, 4661.
78. Zhang, M.; Yin, B.-C.; Tan, W.; Ye, B.-C. *Biosens. Bioelectron.* **2011**, *26*, 3260–3265.
79. Wu, W.; Hu, H.; Li, F.; Wang, L.; Gao, J.; Lu, J.; Fan, C. *Chem. Commun.* **2011**, *47*, 1201.

80. Jang, H.; Kim, Y.-K.; Kwon, H.-M.; Yeo, W.-S.; Kim, D.-E.; Min, D.-H. *Angew. Chem.* **2010**, *122*, 5839–5843.
81. Wang, Y.; Li, Z.; Hu, D.; Lin, C.-T.; Li, J.; Lin, Y. *J. Am. Chem. Soc.* **2010**, *132*, 9274–9276.
82. Dong, H.; Gao, W.; Yan, F.; Ji, H.; Ju, H. *Anal. Chem.* **2010**, *82*, 5511–5517.
83. Liu, F.; Choi, J. Y.; Seo, T. S. *Biosens. Bioelectron.* **2010**, *25*, 2361–2365.
84. Lu, C.-H.; Li, J.; Liu, J.-J.; Yang, H.-H.; Chen, X.; Chen, G.-N. *Chem. — Eur. J.* **2010**, *16*, 4889–4894.
85. He, S.; Song, B.; Li, D.; Zhu, C.; Qi, W.; Wen, Y.; Wang, L.; Song, S.; Fang, H.; Fan, C. *Adv. Funct. Mater.* **2010**, *20*, 453–459.
86. Drummond, T. G.; Hill, M. G.; Barton, J. K. *Nat. Biotechnol.*, **2003**, *21*, 1192–1199.
87. Zhou, M.; Zhai, Y.; Dong, S. *Anal. Chem.* **2009**, *81*, 5603–5613.
88. Ba, X.; Luo, L.; Ding, Y.; Zhang, Z.; Chu, Y.; Wang, B.; Ouyang, X. *Anal. Chim. Acta* **2012**, *752*, 94–100.
89. Du, M.; Yang, T.; Jiao, K. *J. Mater. Chem.* **2010**, *20*, 9253.
90. Merchant, C. A.; Healy, K.; Wanunu, M.; Ray, V.; Peterman, N.; Bartel, J.; Fischbein, M. D.; Venta, K.; Luo, Z.; Johnson, A. T. C.; Drndić, M. *Nano Lett.* **2010**, *10*, 2915–2921.
91. Yang, T.; Guan, Q.; Guo, X.; Meng, L.; Du, M.; Jiao, K. *Anal. Chem.* **2013**, *85*, 1358–1366.
92. Sun, W.; Qi, X.; Zhang, Y.; Yang, H.; Gao, H.; Chen, Y.; Sun, Z. *Electrochimica Acta* **2012**, *85*, 145–151.
93. Dong, H.; Zhu, Z.; Ju, H.; Yan, F. *Biosens. Bioelectron.* **2012**, *33*, 228–232.
94. Du, M.; Yang, T.; Li, X.; Jiao, K. *Talanta* **2012**, *88*, 439–444.
95. Lin, L.; Liu, Y.; Tang, L.; Li, J. *The Analyst* **2011**, *136*, 4732.
96. Hu, Y.; Hua, S.; Li, F.; Jiang, Y.; Bai, X.; Li, D.; Niu, L. *Biosens. Bioelectron.* **2011**, *26*, 4355–4361.
97. Hu, Y.; Li, F.; Bai, X.; Li, D.; Hua, S.; Wang, K.; Niu, L. *Chem. Commun.* **2011**, *47*, 1743.
98. Dong, X.; Shi, Y.; Huang, W.; Chen, P.; Li, L.-J. *Adv. Mater.* **2010**, *22*, 1649–1653.
99. Du, Y.; Guo, S.; Dong, S.; Wang, E. *Biomaterials* **2011**, *32*, 8584–8592.
100. Dong, X.; Huang, W.; Chen, P. *Nanoscale Res. Lett.* **2010**, *6*, 60.
101. Tang, Z.; Wu, H.; Cort, J. R.; Buchko, G. W.; Zhang, Y.; Shao, Y.; Aksay, I. A.; Liu, J.; Lin, Y. *Small* **2010**, *6*, 1205–1209.
102. Dubuisson, E.; Yang, Z.; Loh, K. P. *Anal. Chem.* **2011**, *83*, 2452–2460.
103. Bonanni A.; Pumera, M. *ACS Nano* **2011**, *5*, 2356–2361.
104. Bo, Y.; Yang, H.; Hu, Y.; Yao, T.; Huang, S. *Electrochimica Acta* **2011**, *56*, 2676–2681.

105. Lim, C. X.; Hoh, H. Y.; Ang, P. K.; Loh, K. P. *Anal. Chem.* **2010**, *82*, 7387–7393.
106. Dreyer, D. R.; Park, S.; Bielawski, C. W.; Ruoff, R. S. *Chem. Soc. Rev.* **2009**, *39*, 228–240.
107. Bonanni, A.; Ambrosi, A.; Pumera, M. *Chem. — Eur. J.* **2012**, *18*, 1668–1673.
108. Dikin, D. A.; Stankovich, S.; Zimney, E. J.; Piner, R. D.; Dommett, G. H. B.; Evmenenko, G.; Nguyen, S. T.; Ruoff, R. S. *Nature* **2007**, *448*, 457–460.
109. Liang, Y.; Wu, D.; Feng, X.; Müllen, K. *Adv. Mater.* **2009**, *21*, 1679–1683.
110. Xu, Y.; Bai, H.; Lu, G.; Li, C.; Shi, G. *J. Am. Chem. Soc.* **2008**, *130*, 5856–5857.
111. Meziane, D.; Barras, A.; Kromka, A.; Houdkova, J.; Boukherroub, R.; Szunerits, S. *Anal. Chem.* **2012**, *84*, 194–200.
112. Cai, H.; Xu, Y.; He, P.-G.; Fang, Y.-Z. *Electroanalysis* **2003**, *15*, 1864–1870.
113. Lee, T.-Y.; Shim, Y.-B. *Anal. Chem.* **2001**, *73*, 5629–5632.
114. K'Owino, I. O.; Sadik, O. A. *Electroanalysis* **2005**, *17*, 2101–2113.
115. Zhang, Y.; Jiang, W. *Electrochimica Acta* **2012**, *71*, 239–245.
116. Niu, S. ; Sun, J.; Nan, C.; Lin, J. *Sensors Actuators B Chem.* **2013**, *176*, 58–63.
117. Yin, H.; Zhou, Y.; Zhang, H.; Meng, X.; Ai, S. *Biosens. Bioelectron.* **2012**, *33*, 247–253.
118. Wang, L.; Xu, M.; Han, L.; Zhou, M.; Zhu, C.; Dong, S. *Anal. Chem.* **2012**, *84*, 7301–7307.
119. Wang, L.; Zhu, J.; Han, L.; Jin, L.; Zhu, C.; Wang, E.; Dong, S. *ACS Nano* **2012**, *6*, 6659–6666.
120. Huang, P.-J. J.; Kempaiah, R.; Liu, J. *J. Mater. Chem.* **2011**, *21*, 8991.
121. Hu, Y.; Li, F.; Han, D.; Wu, T.; Zhang, Q.; Niu, L.; Bao, Y. *Anal. Chim. Acta* **2012**, *753*, 82–89.
122. Tang, L.; Wang, Y.; Liu, Y.; Li, J. *ACS Nano* **2011**, *5*, 3817–3822.
123. Sun, W.; Qi, X.; Chen, Y.; Liu, S.; Gao, H. *Talanta* **2011**, *87*, 106–112.
124. Sun, W.; Zhang, Y.; Ju, X.; Li, G.; Gao, H.; Sun, Z. *Anal. Chim. Acta* **2012**, *752*, 39–44.
125. Bonanni, A.; Chua, C. K.; Zhao, G.; Sofer, Z.; Pumera, M. *ACS Nano* **2012**, *6*, 8546–8551.
126. Jia, Y.; Yin, X.-B.; Zhang, J.; Zhou, S.; Song, M.; Xing, K.-L. *The Analyst* **2012**, *137*, 5866.
127. Gao, H.; Sun, M.; Lin, C.; Wang, S. *Electroanalysis* **2012**, *24*, 2283–2290.
128. Qi, X.; Gao, H.; Zhang, Y.; Wang, X.; Chen, Y.; Sun, W. *Bioelectrochemistry Amst. Neth.* **2012**, *88*, 42–47.
129. Bo, Y.; Wang, W.; Qi, J.; Huang, S. *The Analyst* **2011**, *136*, 1946.
130. Balapanuru, J.; Yang, J.-X.; Xiao, S.; Bao, Q.; Jahan, M.; Polavarapu, L.; Wei, J.; Xu, Q.-H.; Loh, K. P. *Angew. Chem.* **2010**, *122*, 6699–6703.

131. Giovanni, M.; Bonanni, A.; Pumera, M. *The Analyst* **2012**, *137*, 580.
132. Zhao, J.; Chen, G.; Zhu, L.; Li, G. *Electrochem. Commun.* **2011**, *13*, 31–33.
133. Choi, B. G.; Park, H.; Yang, M. H.; Jung, Y. M.; Lee, S. Y.; Hong, W. H.; Park, T. J.; *Nanoscale* **2010**, *2*, 2692.
134. Kitano, H. *Science* **2002**, *295*, 1662–1664.
135. Srinivas, P. R.; Kramer, B. S.; Srivastava, S. *Lancet Oncol.* **2001**, *2*, 698–704.
136. Zeng, L.; Li, Q.; Tang, D.; Chen, G.; Wei, M. *Electrochimica Acta*, **2012**, *68*, 158–165.
137. Guo, Z.; Hao, T.; Duan, J.; Wang, S.; Wei, D. *Talanta* **2012**, *89*, 27–32.
138. Tang, J.; Tang, D.; Su, B.; Li, Q.; Qiu, B.; Chen, G. *Electrochimica Acta* **2011**, *56*, 8168–8175.
139. Huang, K.-J.; Niu, D.-J.; Sun, J.-Y.; Zhu, J.-J. *J. Electroanal. Chem.* **2011**, *656*, 72–77.
140. Liu, M.; Zhao, H.; Quan, X.; Chen, S.; Fan, X. *Chem. Commun.* **2010**, *46*, 7909.
141. Wei, Q.; Mao, K.; Wu, D.; Dai, Y.; Yang, J.; Du, B.; Yang, M.; Li, H. *Sensors Actuators B Chem.* **2010**, *149*, 314–318.
142. Du, D.; Zou, Z.; Shin, Y.; Wang, J.; Wu, H.; Engelhard, M. H.; Liu, J.; Aksay, I. A.; Lin, Y. *Anal. Chem.* **2010**, *82*, 2989–2995.
143. Kim, D.-J.; Sohn, I. Y.; Jung, J.-H.; Yoon, O. J.; Lee, N.-E.; Park, J.-S. *Biosens. Bioelectron.* **2013**, *41*, 621–626.
144. Han, J.; Zhuo, Y.; Chai, Y.; Yuan, R.; Zhang, W.; Zhu, Q. *Anal. Chim. Acta* **2012**, *746*, 70–76.
145. Xu, S.; Liu, Y.; Wang, T.; Li, J. *Anal. Chem.* **2011**, *83*, 3817–3823.
146. Zhang, B.; Cui, T. *Appl. Phys. Lett.* **2011**, *98*, 073116–073116–3.
147. Yang, M.; Javadi, A.; Li, H.; Gong, S. *Biosens. Bioelectron.* **2010**, *26*, 560–565.
148. Feng, L.; Wu, L.; Wang, J.; Ren, J.; Miyoshi, D.; Sugimoto, N.; Qu, X. *Adv. Mater.* **2012**, *24*, 125–131.
149. Wang, X.; Wang, C.; Qu, K.; Song, Y.; Ren, J.; Miyoshi, D.; Sugimoto, N.; Qu, X. *Adv. Funct. Mater.* **2010**, *20*, 3967–3971.
150. Xie, Y.; Chen, A.; Du, D.; Lin, Y. *Anal. Chim. Acta* **2011**, *699*, 44–48.
151. Du, D.; Wang, L.; Shao, Y.; Wang, J.; Engelhard, M. H.; Lin, Y. *Anal. Chem.* **2011**, *83*, 746–752.
152. Tu, W.; Wang, W.; Lei, J.; Deng, S.; Ju, H. *Chem. Commun.* **2012**, *48*, 6535.
153. Li, Y.; Yang, W.-K.; Fan, M.-Q.; Liu, A. *Anal. Sci.* **2011**, *27*, 727–727.
154. Zhong, Z.; Wu, W.; Wang, D.; Wang, D.; Shan, J.; Qing, Y.; Zhang, Z. *Biosens. Bioelectron.* **2010**, *25*, 2379–2383.
155. Wang, Z.; Huang, P.; Bhirde, A.; Jin, A.; Ma, Y.; Niu, G.; Neamati, N.; Chen, X. *Chem. Commun.* **2012**, *48*, 9768.
156. Zhuo, Y.; Chai, Y.-Q.; Yuan, R.; Mao, L.; Yuan, Y.-L.; Han, J. *Biosens. Bioelectron.* **2011**, *26*, 3838–3844.

157. Tamura, Y.; Yamagiwa, S.; Aoki, Y.; Kurita, S.; Suda, T.; Ohkoshi, S.; Nomoto, M.; Aoyagi, Y.; *Dig. Dis. Sci.* **2009**, *54*, 2530–2537.
158. Tang, J.; Tang, D.; Su, B.; Li, Q.; Qiu, B.; Chen, G. *Electrochimica Acta* **2011**, *56*, 8168–8175.
159. Tang, J.; Tang, D.; Su, B.; Li, Q.; Qiu, B.; Chen, G. *Electrochimica Acta*, **2011**, *56*, 3773–3780.
160. Lin, J.; Wei, Z.; Mao, C. *Biosens. Bioelectron.* **2011**, *29*, 40–45.
161. Giannetto, M.; Mori, L.; Mori, G.; Careri, M.; Mangia, A. *Sensors Actuators B Chem.* **2011**, *159*, 185–192.
162. Su, H.; Yuan, R.; Chai, Y.; Mao, L.; Zhuo, Y. *Biosens. Bioelectron.* **2011**, *26*, 4601–4604.
163. Dai, Y.; Cai, Y.; Zhao, Y.; Wu, D.; Liu, B.; Li, R.; Yang, M.; Wei, Q.; Du, B.; Li, H. *Biosens. Bioelectron.* **2011**, *28*, 112–116.
164. Liu, K.; Zhang, J.-J.; Wang, C.; Zhu, J.-J.; *Biosens. Bioelectron.* **2011**, *26*, 3627–3632.
165. Du, D.; Zou, Z.; Shin, Y.; Wang, J.; Wu, H.; Engelhard, M. H.; Liu, J.; Aksay, I. A.; Lin, Y. *Anal. Chem.* **2010**, *82*, 2989–2995.
166. Wu, Y.; Chen, C.; Liu, S. *Anal. Chem.* **2009**, *81*, 1600–1607.
167. Lai, G.; Yan, F.; Ju, H. *Anal. Chem.* **2009**, *81*, 9730–9736.
168. Myung, S.; Solanki, A.; Kim, C.; Park, J.; Kim, K. S.; Lee, K.-B. *Adv. Mater.* **2011**, *23*, 2221–2225.
169. Nierodzik, M. L.; Karpatkin, S. *Cancer Cell* **2006**, *10*, 355–362.
170. Xiao, Y.; Piorek, B. D.; Plaxco, K. W.; Heeger, A. J. *J. Am. Chem. Soc.* **2005**, *127*, 17990–17991.
171. Zhao, Q.; Lu, X.; Yuan, C.-G.; Li, X.-F.; Le, X. C. *Anal. Chem.* **2009**, *81*, 7484–7489.
172. Chang, H.; Tang, L.; Wang, Y.; Jiang, J.; Li, J. *Anal. Chem.* **2010**, *82*, 2341–2346.
173. Li, J.; Lu, C.-H.; Yao, Q.-H.; Zhang, X.-L.; Liu, J.-J.; Yang, H.-H.; Chen, G.-N. *Biosens. Bioelectron.* **2011**, *26*, 3894–3899.
174. Zhang, M.; Yin, B.-C.; Wang, X.-F.; Ye, B.-C. *Chem. Commun.* **2011**, *47*, 2399.
175. Wang, Y.; Xiao, Y.; Ma, X.; Li, N.; Yang, X. *Chem. Commun.* **2012**, *48*, 738.
176. Loo, A. H.; Bonanni, A.; Pumera, M. *Nanoscale* **2012**, *4*, 143.
177. Bai, L.; Yuan, R.; Chai, Y.; Zhuo, Y.; Yuan, Y.; Wang, Y. *Biomaterials* **2012**, *33*, 1090–1096.
178. Sun, T.; Wang, L.; Li, N.; Gan, X. *Bioprocess Biosyst. Eng.* **2011**, *34*, 1081–1085.
179. Gao, Y.; Li, Y.; Zou, X.; Huang, H.; Su, X. *Anal. Chim. Acta* **2012**, *731*, 68–74.

180. Mei, Q.; Zhang, Z. *Angew. Chem. Int. Ed.* **2012**, *51*, 5602–5606.
181. Liang, J.; Chen, Z.; Guo, L.; Li, L. *Chem. Commun.* **2011**, *47*, 5476.
182. Wei, J.; Qiu, J.; Li, L.; Ren, L.; Zhang, X.; Chaudhuri, J.; Wang, S. *Nanotechnology* **2012**, *23*, 335707.
183. Shi, Y.; Wu, J.; Sun, Y.; Zhang, Y.; Wen, Z.; Dai, H.; Wang, H.; Li, Z. *Biosens. Bioelectron.* **2012**, *38*, 31–36.
184. Xie, W. Y.; Huang, W. T.; Li, N. B.; Luo, H. Q. *Chem. Commun.* **2012**, *48*, 82.
185. Lin, Y.; Tao, Y.; Pu, F.; Ren, J.; Qu, X. *Adv. Funct. Mater.* **2011**, *21*, 4565–4572.
186. Song, Y.; Chen, Y.; Feng, L.; Ren, J.; Qu, X. *Chem. Commun.* **2011**, *47*, 4436–4438.
187. Staal, F. J.; Ela, S.; Roederer, M.; Anderson, M.; Herzenberg, L.; Herzenberg, L.; *The Lancet* **1992**, *339*, 909–912.
188. Liu, B.; Tang, D.; Tang, J.; Su, B.; Li, Q.; Chen, G. *The Analyst* **2011**, *136*, 2218.
189. Liu, K.; Zhang, J.-J.; Wang, C.; Zhu, J.-J. *Biosens. Bioelectron.* **2011**, *26*, 3627–3632.
190. Wang, G.; Huang, H.; Zhang, G.; Zhang, X.; Fang, B.; Wang, L. *Anal. Methods* **2010**, *2*, 1692.
191. Ohno, Y.; Maehashi, K.; Inoue, K.; Matsumoto, K. *Jpn. J. Appl. Phys.* **2011**, *50*, 070120.
192. Ohno, Y.; Maehashi, K.; Matsumoto, K. *J. Am. Chem. Soc.* **2010**, *132*, 18012–18013.
193. Mao, S.; Lu, G.; Yu, K.; Bo, Z.; Chen, J. *Adv. Mater.* **2010**, *22*, 3521–3526.
194. Ohno, Y.; Maehashi, K.; Yamashiro, Y.; Matsumoto, K. *Nano Lett.* **2009**, *9*, 3318–3322.
195. Shih, C.-J.; Paulus, G. L. C.; Wang, Q. H.; Jin, Z.; Blankschtein, D.; Strano, M. S. *Langmuir* **2012**, *28*, 8579–8586.
196. Pei, H.; Li, J.; Lv, M.; Wang, J.; Gao, J.; Lu, J.; Li, Y.; Huang, Q.; Hu, J.; Fan, C. *J. Am. Chem. Soc.* **2012**, *134*, 13843–13849.
197. Kasry, A.; Afzali, A. A.; Oida, S.; Han, S.-J.; Menges, B.; Tulevski, G. S. *Chem. Mater.* **2011**, *23*, 4879–4881.
198. Wang, J.; Zhao, W.-W.; Li, X.-R.; Xu, J.-J.; Chen, H.-Y. *Chem. Commun.* **2012**, *48*, 6429.
199. Qu, F.; Lu, H.; Yang, M.; Deng, C.; *Biosens. Bioelectron.* **2011**, *26*, 4810–4814.
200. Chen, Y.; Vedala, H.; Kotchey, G. P.; Audfray, A.; Cecioni, S.; Imberty, A.; Vidal, S.; Star, A. *ACS Nano* **2012**, *6*, 760–770.
201. Shi, Y.; Huang, W. T.; Luo, H. Q.; Li, N. B. *Chem. Commun.* **2011**, *47*, 4676.

202. Qin, H.; Liu, J.; Chen, C.; Wang, J.; Wang, E.; *Anal. Chim. Acta* **2012**, *712*, 127–131.
203. Du, Y.; Guo, S.; Qin, H.; Dong, S.; Wang, E. *Chem. Commun.* **2012**, *48*, 799.
204. Liu, S.-J.; Wen, Q.; Tang, L.-J.; Jiang, J.-H.; *Anal. Chem.* **2012**, *84*, 5944–5950.
205. Wang, H.; Zhang, Q.; Chu, X.; Chen, T.; Ge, J.; Yu, R. *Angew. Chem. Int. Ed.* **2011**, *50*, 7065–7069.
206. Feng, D.; Zhang, Y.; Feng, T.; Shi, W.; Li, X.; Ma, H. *Chem. Commun.* **2011**, *47*, 10680.
207. Chen, C.; Zhao, J.; Jiang, J.; Yu, R. *Talanta* **2012**, *101*, 357–361.
208. Arya, S. K.; Datta, M.; Malhotra, B. D. *Biosens. Bioelectron.* **2008**, *23*, 1083–1100.
209. Li, J.; Peng, T.; Peng, Y. *Electroanalysis* **2003**, *15*, 1031–1037.
210. Jiang, H.; Ju, H.; *Chem. Commun.* **2007**, *(4)*, 404–406.
211. Ekanayake, E. M. I. M.; Preethichandra, D. M. G.; Kaneto, K. *Biosens. Bioelectron.* **2007**, *23*, 107–113.
212. Dey, R. S.; Raj, C. R. *J. Phys. Chem. C* **2010**, *114*, 21427–21433.
213. Saini, D.; Chauhan, R.; Solanki, P. R.; Basu, T. *ISRN Nanotechnol.* **2012**, *2012*, 1–12.
214. Aravind, S. S. J.; Baby, T. T.; Arockiadoss, T.; Rakhi, R. B.; Ramaprabhu, S. *Thin Solid Films* **2011**, *519*, 5667–5672.
215. Manjunatha, R.; Shivappa Suresh, G.; Savio Melo, J.; D'Souza, S. F.; Venkatarangaiah Venkatesha, T. *Talanta* **2012**, *99*, 302–309.
216. Israr, M. Q.; Hasan, K.U.; Sadaf, J. R. *J. Biosens. Bioelectron.* **2011**, *02*, 109.
217. Zhang, M.; Yuan, R.; Chai, Y.; Chen, S.; Zhong, X.; Zhong, H.; Wang, C. *RSC Adv.* **2012**, *2*, 4639.
218. Banks, C. E.; Crossley, A.; Salter, C.; Wilkins, S. J.; Compton, R. G. *Angew. Chem. Int. Ed.* **2006**, *45*, 2533–2537.
219. Zhou, M.; Zhai, Y.; Dong, S. *Anal. Chem.* **2009**, *81*, 5603–5613.
220. Zhiguo, G.; Shuping, Y.; Zaijun, L.; Xiulan, S.; Guangli, W.; Yinjun, F.; Junkang, L. *Anal. Chim. Acta* **2011**, *701*, 75–80.
221. Zhang, Q.; Qiao, Y.; Hao, F.; Zhang, L.; Wu, S.; Li, Y.; Li, J.; Song, X.-M. *Chem. — Eur. J.* **2010**, *16*, 8133–8139.
222. Li, M.; Xu, S.; Tang, M.; Liu, L.; Gao, F.; Wang, Y. *Electrochimica Acta* **2011**, *56*, 1144–1149.
223. Shan, C.; Yang, H.; Han, D.; Zhang, Q.; Ivaska, A.; Niu, L. *Langmuir* **2009**, *25*, 12030–12033.
224. Sheng, Q.; Wang, M.; Zheng, J. *Sensors Actuators B Chem.* **2011**, *160*, 1070–1077.
225. Cui, Y.; Zhang, B.; Liu, B.; Chen, H.; Chen, G.; Tang, D. *Microchim. Acta* **2011**, *174*, 137–144.

226. Lu, Q.; Dong, X.; Li, L.-J.; Hu, X. *Talanta* **2010**, *82*, 1344–1348.
227. Feng, X.-M.; Li, R.-M.; Ma, Y.-W.; Chen, R.-F.; Shi, N.-E.; Fan, Q.-L.; Huang, W. *Adv. Funct. Mater.* **2011**, *21*, 2989–2996.
228. Zhang, L.; Cheng, H.; Zhang, H.; Qu, L. *Electrochimica Acta* **2012**, *65*, 122–126.
229. Zeng, Q.; Cheng, J.; Tang, L.; Liu, X.; Liu, Y.; Li, J.; Jiang, J. *Adv. Funct. Mater.* **2010**, *20*, 3366–3372.
230. Zhang, Q.; Qiao, Y.; Zhang, L.; Wu, S.; Zhou, H.; Xu, J.; Song, X.-M. *Electroanalysis* **2011**, *23*, 900–906.
231. Zhou, K.; Zhu, Y.; Yang, X.; Li, C. *Electroanalysis* **2011**, *23*, 862–869.
232. Zhou, K.; Zhu, Y.; Yang, X.; Luo, J.; Li, C.; Luan, S. *Electrochimica Acta* **2010**, *55*, 3055–3060.
233. Palanisamy, S.; Unnikrishnan, B.; Chen, S.-M. *Int J Electrochem Sci* **2012**, *7*, 7935–7947.
234. Wan, L.; Song, Y.; Zhu, H.; Wang, Y.; Wang, L. *Int J Electrochem Sci* **2011**, *6*, 4700–4713.
235. Huang, K.-J.; Miao, Y.-X.; Wang, L.; Gan, T.; Yu, M.; Wang, L.-L. *Process Biochem.* **2012**, *47*, 1171–1177.
236. Feng, X.; Li, R.; Hu, C.; Hou, W. *J. Electroanal. Chem.* **2011**, *657*, 28–33.
237. He, Y.; Zheng, J.; Li, K.; Sheng, Q.; Qiao, N. *Chin. J. Chem.* **2010**, *28*, 2507–2512.
238. He, Y.; Sheng, Q.; Zheng, J.; Wang, M.; Liu, B. *Electrochimica Acta* **2011**, *56*, 2471–2476.
239. Xu, J.; Liu, C.; Wu, Z. *Microchim. Acta* **2011**, *172*, 425–430.
240. Xu, X. X.; Zhang, J. X.; Guo, F.; Zheng, W.; Zhou, H. M.; Wang, B. L.; Zheng, Y. F.; Wang, Y. B.; Cheng, Y.; Lou, X.; Jang, B. Z. *Colloids Surf. B Biointerfaces* **2011**, *84*, 427–432.
241. Sun, A.; Sheng, Q.; Zheng, J. *Appl. Biochem. Biotechnol.* **2012**, *166*, 764–773.
242. Xu, H.; Dai, H.; Chen, G. *Talanta* **2010**, *81*, 334–338.
243. Schäferling, M.; Grögel, D. B. M.; Schreml, S. *Microchim. Acta* **2011**, *174*, 1–18.
244. Moiroux, J.; Elving, P. J. *Anal. Chem.* **1978**, *50*, 1056–1062.
245. Álvarez-González, M. I.; Saidman, S. B.; Lobo-Castañón, M. J.; Miranda-Ordieres, A. J.; Tuñón-Blanco, P. *Anal. Chem.* **2000**, *72*, 520–527.
246. Guo, K.; Qian, K.; Zhang, S.; Kong, J.; Yu, C.; Liu, B. *Talanta* **2011**, *85*, 1174–1179.
247. Shan, C.; Yang, H.; Han, D.; Zhang, Q.; Ivaska, A.; Niu, L. *Biosens. Bioelectron.* **2010**, *25*, 1504–1508.
248. Wang, X.; Wang, J.; Cheng, H.; Yu, P.; Ye, J.; Mao, L. *Langmuir* **2011**, *27*, 11180–11186.

249. Kumar, S. P.; Manjunatha, R.; Nethravathi, C.; Suresh, G. S.; Rajamathi, M.; Venkatesha, T. V. *Electroanalysis* **2011**, *23*, 842–849.
250. Gao, W.; Chen, Y.; Xi, S.; Lin, J.; Chen, Y.; Lin, Y.; Chen, Z. *Biosens. Bioelectron.* **2013**, *41*, 776–782.
251. Sun, Z.; Fu, H.; Deng, L.; Wang, J. *Anal. Chim. Acta* **2013**, *761*, 84–91.
252. Cheng, R.; Liu, Y.; Ou, S.; Pan, Y.; Zhang, S.; Chen, H.; Dai, L.; Qu, J. *Anal. Chem.* **2012**, *84*, 5641–5644.
253. Deng, S.; Lei, J.; Cheng, L.; Zhang, Y.; Ju, H.; *Biosens. Bioelectron.* **2011**, *26*, 4552–4558.
254. Wu, X.; Hu, Y.; Jin, J.; Zhou, N.; Wu, P.; Zhang, H.; Cai, C. *Anal. Chem.* **2010**, *82*, 3588–3596.
255. Bai, J.; Lai, Y.; Jiang, D.; Zeng, Y.; Xian, Y.; Xiao, F.; Zhang, N.; Hou, J.; Jin, L. *The Analyst* **2012**, *137*, 4349.
256. Wu, L.; Deng, D.; Jin, J.; Lu, X.; Chen, J. *Biosens. Bioelectron.* **2012**, *35*, 193–199.
257. Liu, F.; Piao, Y.; Choi, K. S.; Seo, S. T. *Carbon* **2012**, *50*, 123–133.
258. Zhang, Y.; Zhang, J.; Wu, H.; Guo, S.; Zhang, J. *J. Electroanal. Chem.* **2012**, *681*, 49–55.
259. Song, W.; Li, D.-W.; Li, Y.-T.; Li, Y.; Long, Y.-T. *Biosens. Bioelectron.* **2011**, *26*, 3181–3186.
260. Wei, L.; Borowiec, J.; Zhu, L.; Zhang, J. *Microchim. Acta* **2011**, *173*, 439–443.
261. Sheng, L.; Ren, J.; Miao, Y.; Wang, J.; Wang, E. *Biosens. Bioelectron.* **2011**, *26*, 3494–3499.
262. Chen P.-S.; Huang, S.-D. *Talanta* **2006**, *69*, 669–675.
263. Arduini, F.; Ricci, F.; Tuta, C. S.; Moscone, D.; Amine, A.; Palleschi, G. *Anal. Chim. Acta* **2006**, *580*, 155–162.
264. Liu, T.; Su, H.; Qu, X.; Ju, P.; Cui, L.; Ai, S. *Sensors Actuators B Chem.* **2011**, *160*, 1255–1261.
265. Wang, K.; Li, H.-N.; Wu, J.; Ju, C.; Yan, J.-J.; Liu, Q.; Qiu, B. *The Analyst* **2011**, *136*, 3349.
266. Wang, K.; Liu, Q.; Dai, L.; Yan, J.; Ju, C.; Qiu, B.; Wu, X. *Anal. Chim. Acta* **2011**, *695*, 84–88.
267. Wang, Y.; Zhang, S.; Du, D.; Shao, Y.; Li, Z.; Wang, J.; Engelhard, M. H.; Li, J.; Lin, Y. *J. Mater. Chem.* **2011**, *21*, 5319.
268. Liu, T.; Xu, M.; Yin, H.; Ai, S.; Qu, X.; Zong, S. *Microchim. Acta* **2011**, *175*, 129–135.
269. Huang, Y.; Dong, X.; Liu, Y.; Li, L.-J.; Chen, P. *J. Mater. Chem.* **2011**, *21*, 12358.
270. Wan, Y.; Wang, Y.; Wu, J.; Zhang, D. *Anal. Chem.* **2011**, *83*, 648–653.
271. Feng, L.; Chen, Y.; Ren, J.; Qu, X. *Biomaterials* **2011**, *32*, 2930–2937.

272. Jung, J. H.; Cheon, D. S.; Liu, F.; Lee, K. B.; Seo, T. S. *Angew. Chem. Int. Ed.* **2010**, *49*, 5708–5711.
273. Ajjampur, S. S. R.; Rajendran, P.; Ramani, S.; Banerjee, I.; Monica, B.; Sankaran, P.; Rosario, V. Arumugam, R.; Sarkar, R.; Ward, H.; Kang, G. *J. Med. Microbiol.* **2008**, *57*, 1364–1368.
274. Cao, L.; Cheng, L.; Zhang, Z.; Wang, Y.; Zhang, X.; Chen, H.; Liu, B.; Zhang, S.; Kong, J. *Lab. Chip* **2012**, *12*, 4864.
275. Li, M.; Zhou, X.; Ding, W.; Guo, S.; Wu, N. *Biosens. Bioelectron.* **2013**, *41*, 889–893.
276. Liu, X.; Miao, L.; Jiang, X.; Ma, Y.; Fan, Q.; Huang, W. *Chin. J. Chem.* **2011**, *29*, 1031–1035.
277. Liu, M.; Zhao, H.; Chen, S.; Yu, H.; Zhang, Y.; Quan, X. *Chem. Commun.*, **2011**, *47*, 7749.
278. Liu, M.; Zhao, H.; Chen, S.; Yu, H.; Zhang, Y.; Quan, X. *Biosens. Bioelectron.* **2011**, *26*, 4111–4116.
279. Zhao, X.-H.; Kong, R.-M.; Zhang, X.-B.; Meng, H.-M.; Liu, W.-N.; Tan, W.; Shen, G.-L.; Yu, R.-Q. *Anal. Chem.* **2011**, *83*, 5062–5066.
280. Wang, L.; Zhang, X.; Xiong, H.; Wang, S. *Biosens. Bioelectron.* **2010**, *26*, 991–995.
281. Yin, B.-C.; Ye, B.-C.; Tan, W.; Wang, H.; Xie, C.-C. *J. Am. Chem. Soc.* **2009**, *131*, 14624–14625.
282. Liu, J.; Lu, Y. *J. Am. Chem. Soc.* **2005**, *127*, 12677–12683.
283. Li, T.; Dong, S.; Wang, E. *Anal. Chem.* **2009**, *81*, 2144–2149.
284. Wen, Y.; Peng, C.; Li, D.; Zhuo, L.; He, S.; Wang, L.; Huang, Q.; Xu, Q.-H.; Fan, C. *Chem. Commun.* **2011**, *47*, 6278.
285. Kroupova, H.; Machova, J.; Piackova, V.; Blahova, J.; Dobsikova, R.; Novotny, L.; Svobodova, Z. *Ecotoxicol. Environ. Saf.* **2008**, *71*, 813–820.
286. Guo, C.; Sun, H.; Zhao, X. S. *Sensors Actuators B Chem.* **2012**, *164*, 82–89.
287. Yue, R.; Lu, Q.; Zhou, Y. *Biosens. Bioelectron.* **2011**, *26*, 4436–4441.
288. Liu, P.; Zhang, X.; Feng, L.; Xiong, H.; Wang, S. *Am J Biomed Sci* **2011**, *3*, 69–76.
289. Liu, K.; Zhang, J.; Yang, G.; Wang, C.; Zhu, J.-J. *Electrochem. Commun.* **2010**, *12*, 402–405.
290. Sun, W.; Guo, Y.; Li, T.; Ju, X.; Lou, J.; Ruan, C. *Electrochimica Acta* **2012**, *75*, 381–386.
291. Tu, W.; Lei, J.; Zhang, S.; Ju, H. *Chem. — Eur. J.* **2010**, *16*, 10771–10777.
292. Chen, L.; Hernandez, Y.; Feng, X.; Müllen, K. *Angew. Chem. Int. Ed.* **2012**, *51*, 7640–7654.
293. Cai, J.; Ruffieux, P.; Jaafar, R.; Bieri, M.; Braun, T.; Blankenburg, S.; Muoth, M.; Seitsonen, A. P.; Saleh, M.; Feng, X.; Müllen, K.; Fasel, R. *Nature* **2010**, *466*, 470–473.

This page intentionally left blank

Chapter 4

Graphene-Based Electrochemical Biosensor

Qian Zhang[*], *Ling Zhang*[†], *Yang Liu*[‡] *and Jinghong Li*[‡,§]

[*]*College of Chemistry, Liaoning University*
Shenyang 110036, China
[†]*College of Chemistry and Life Science, Shenyang Normal University*
Shenyang 110034, China
[‡]*Department of Chemistry, Beijing Key Laboratory for Analytical Methods and Instrumentation, Tsinghua University*
Beijing 100084, China

1. Introduction 148
2. Synthesis and Functionalization of Graphene 150
   2.1. Synthesis and characterization of graphene 150
   2.2. Functionalization of graphene 155
3. Electrochemical Properties of Graphene 158
4. Graphene-Based Electrochemical Enzymatic Biosensor 160
   4.1. The introduction of electrochemical enzymatic biosensor 160
   4.2. Organic molecular-modified graphene-based enzymatic biosensor 163
   4.3. Polymer-modified graphene-based enzymatic biosensor 166
   4.4. Inorganic nanoparticles-modified graphene-based enzymatic biosensor 171
   4.5. Biomolecular-modified graphene-based enzymatic biosensor 174
   4.6. Graphene–carbon nanotube-based enzymatic biosensor 176
   4.7. N-doped graphene-based enzymatic biosensor 178
5. Graphene-Based DNA Biosensor 179
6. Conclusions and Perspectives 181
Acknowledgments 182
References 182

[§]Corresponding author. E-mail: jhli@mail.tsinghua.edu.cn

1. Introduction

The name of electrochemical biosensors is applied to a molecular sensing device which intimately couples a biological recognition element to an electrode transducer.[1] Specific molecular recognition is a fundamental prerequisite, and the purpose of the electrode transducer is to convert the biological recognition event into a useful electrical signal, including the measurable current (amperometric), potential or charge accumulation (potentiometric), or altered conductive properties of a medium (conductometric).[2] Various techniques, such as cyclic voltammetry (CV), differential pulse voltammetry (DPV), square wave voltammetry (SWV), linear sweep voltammetry (LSV), anodic stripping voltammetry (ASV), amperometry, potentiometry, electrochemical impedance spectroscopy (EIS), are commonly utilized for the production of concentration-proportional signals.[3] Figure 1 is the schematic diagram that represents the concept of a biosensor.[1] As shown, the representation of an electrochemical biosensor mainly consists of three components: (i) the biological recognition element, (ii) the electrochemical transducer or the detector element, and (iii) the reader device. The biological recognition element can be enzymes, deoxyribonucleic acid (DNA), or microorganisms,

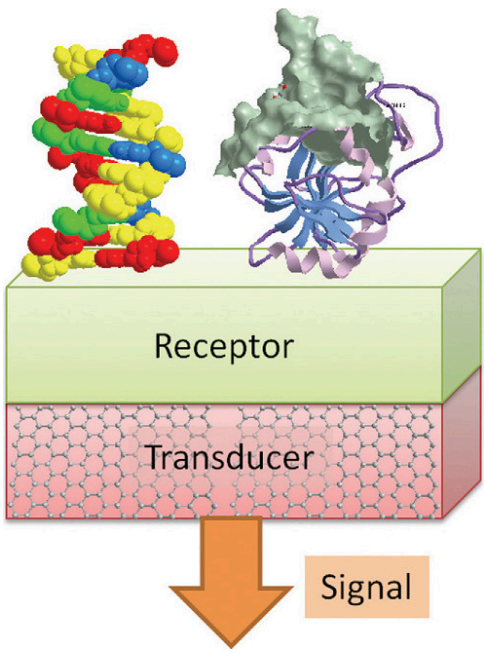

Figure 1. Scheme of a biosensor. The biosensor consists of a receptor layer, which consists of a biomolecule (*e.g.*, DNA or protein), and a transducer.[1]

etc., which recognizes the target analyte.[4] The role of the transducer is to convert chemical information into a measurable electrochemical signal. Compared with other types of biosensor, electrochemical biosensors offer several advantages related to their cost, simplicity, high sensitivity, and ease of miniaturization. Up to now, electrochemical biosensors have attracted great interest in the fields of environmental monitoring, clinical, biological, pharmaceutical, and biomolecular interactions.[5,6]

Since the performance of the biosensor highly depends on biological recognition systems connected to a suitable transducer, the key point for the construction of a good and reliable electrochemical biosensor lies on the kind of electrode material that constitutes the detection platform.[7] With the development of nanotechnology, the applications of nanomaterials in biosensors have advanced greatly. Carbonaceous nanomaterial might be the most widely used material in bioelectrocatalysis for sensing.[6,8] Because of the unique properties of carbonaceous nanomaterial, such as high surface area, acceptable biocompatibility, chemical and electrochemical stability, and good electrical conductivity, there has been an explosion of interest in utilization of such nanomaterials in fabrication of novel electrochemical biosensors.[9–11]

Graphene is a two-dimensional (2D) crystalline monolayer of the graphite structure, composed of carbon atoms arranged in a honeycombed network with six-membered rings.[12] The nature of graphene is described by analogy to a polycyclic aromatic hydrocarbon of quasi infinite size.[13] As the fundamental 2D carbon structure, graphene can be considered as the basic building block for graphitic allotropes of all other dimensionalities.[14] As shown in Figure 2, graphene can be wrapped to generate 0D buckyballs (fullerenes), rolled up to form 1D carbon nanotubes (CNTs), and stacked to produce 3D graphite.[14] Although it is considered as the basic component of different carbon forms, graphene exhibits distinctly different properties, such as large theoretical specific surface area of 2.6×10^3 m^2 g^{-1}, high thermal conductivity (3×10^3 W m^{-1} K^{-1}), high Young's modulus (1.06×10^3 GPa), high electron mobility, high quantum Hall effect, and massless Dirac fermions.[15–17] Moreover, the large delocalized π-electron system of graphene also endows it with excellent electrical conductivity. The electrical transfer rate could reach 1.5×10^4 cm^2 V^{-1} s^{-1} at room temperature. Except the unique structure and outstanding properties, a significant advantage of graphene over graphitic allotropes is that it can be synthesized by simple chemical methods from a very common and cheap raw material — graphite. This greatly promotes its wide application and also makes possible large-scale production of graphene at low cost. What is more, unlike CNT, graphene is a cleaner carbon material that does not contain residual metallic impurities, which come from the metal

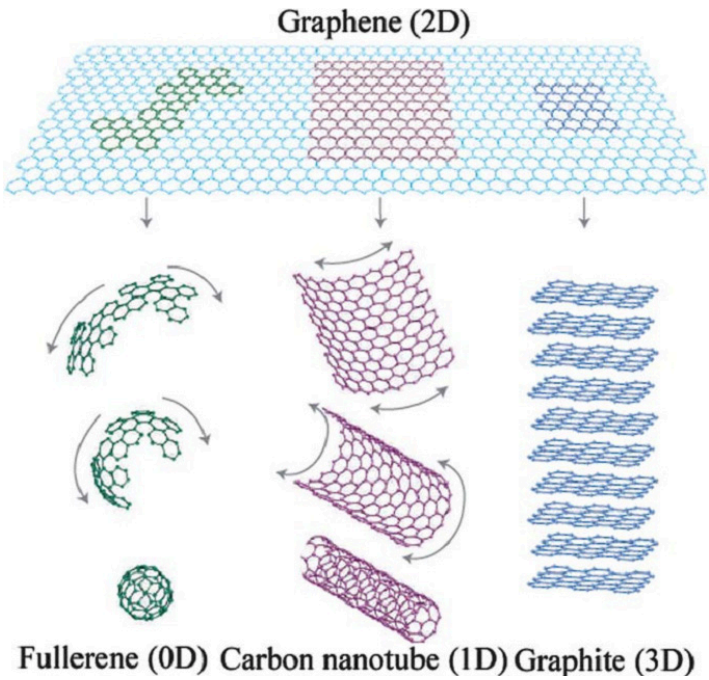

Figure 2. Graphene as the basic unit of 0D fullerene, 1D CNTs, and 3D graphite. Adapted from Ref. 14.

catalysts used in the synthesis of CNT. As a result of the advantages mentioned above, graphene can act as a promising candidate for electrocatalysis. Up to now, graphene and its derivative have been widely used to design and prepare graphene-oriented electrodes for a wide range of applications in electrochemistry.[18–22] Especially in the field of electrochemical biosensor, graphene has attracted tremendous attention and research interest.[11,23–25]

This chapter presents a general description of the synthesis, functionalization, and electrochemical properties of graphene. The developments and improvements in the electrochemical applications of graphene and its derivative in fabrication of enzyme and DNA biosensors are also discussed.

2. Synthesis and Functionalization of Graphene

2.1. Synthesis and characterization of graphene

The mass production of graphene with a stable structure and high quality is a crucial issue to the applications and fundamental research of graphene.[26] Up to now, several methods have been developed for the synthesis of graphene and its derivative. Briefly, the synthesis of graphene can be categorized into

three main approaches, such as the mechanical cleavage method, the chemical vapor deposition (CVD) method, and the chemical reduction of graphene oxide (GO).

The mechanical cleavage method was originally proposed by Novoselov *et al.* in 2004.[12] Based on breaking the van der Waals bonds that existed between the stacked graphene sheets (GSs) in graphite, graphene with remarkably high quality and stability under ambient conditions can be obtained by repeated peeling of highly oriented pyrolytic graphite (HOPG) (Figure 3).[26] This dry mechanical exfoliated method, which is also called scotch-tape method, is an efficient approach to produce graphene layer(s) with high quality for basic scientific research on optical and electronic properties and for selected applications, such as single-layer graphene in nanodevice. However, the yield of this method is extremely low and the process is difficult to control, thus making it unsuitable for application of electrochemistry, which often requires bulk quantities of graphene. Recently, it has been found that the exfoliation of graphite in surfactant/water solutions can efficiently produce single- or fewer-layered GSs with a honeycomb lattice.[27] The graphene that was obtained by liquid-phase exfoliated method consisted of 40% of sheets thinner than five layers and about 3% monolayers.

CVD is a simple approach that has shown promise for the production of defect-free graphene with large dimensions.[28] The nucleation and growth of

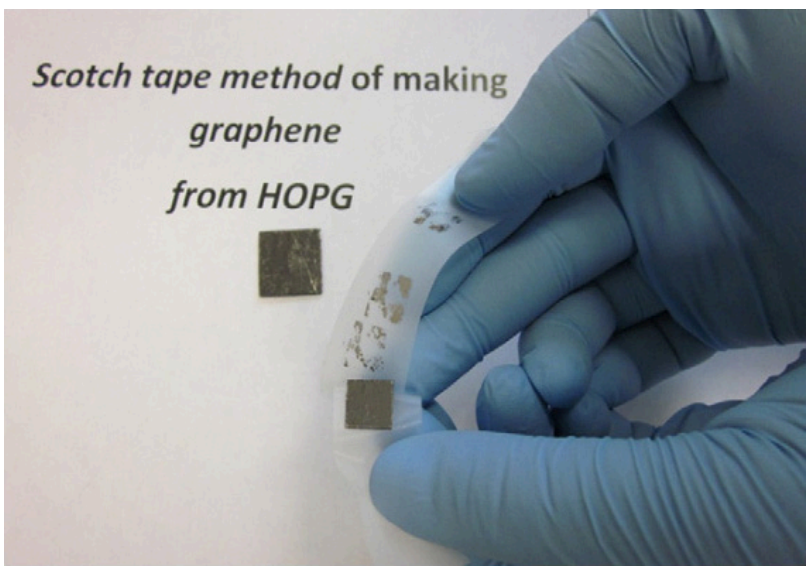

Figure 3. Mechanical exfoliation of graphene using scotch tape from highly oriented pyrolytic graphite (HOPG).[26]

graphene usually occur by exposure of the catalytic metal surface to a hydrocarbon gas under low pressure or ultrahigh vacuum conditions. Transition metals such as Cu, Co, Pt, Ir, Ru, and Ni are well-known catalysts for graphene growth.[29] The graphene films with multilayered structures fabricated on Ni substrates via CVD can be utilized for transparent electrodes in flexible, stretchable, and foldable electronics.[30] CVD epitaxial growth is another effective approach for the production of graphene.[31] As for this method, carbon was firstly dissolved into a nickel substrate, and then it was forced to precipitate out by cooling the metal substrate. The thickness and crystalline ordering of the as-formed graphene can be controlled by the adjustment of different experimental conditions, such as the cooling rate and concentration of carbon dissolved in the nickel substrate. Although CVD graphene can exhibit electrical transport properties similar to those of exfoliated graphene, such method has a disadvantage in terms of leaving the metallic impurities in the production inevitably. In order to eradicate the residual metallic impurities and obtain high-quality graphene, the improved substrate-free CVD strategy was reported in succession. It has been found that the graphene can also be prepared by thermal decomposition of hexagonal silicon carbide (SiC) wafer under ultrahigh vacuum conditions.[32] During this annealing process, the Si atoms on the top layer of SiC desorbed, thus making the C atoms remain on the surface and further reorganize and rebond to form epitaxial graphene layers. The thickness of graphene layers depends on the annealing time and temperature.

For the preparation of graphene of large quantities, the chemical synthesis of graphene from graphite to date is the most common and economical method. Such method is essentially based on the solution-based chemical reduction of GO. Graphene prepared by chemical synthesis method usually has abundant structural defects and functional groups due to the harsh oxidation conditions, which significantly differs from pristine graphene. However, it is well known that the existence of the defects and oxygen-bearing groups is advantageous for electrochemical applications. Therefore, this chapter will mainly focus on this kind of graphene.

As shown in Figure 4, the basic strategy of this chemical synthesis method involves three main steps.[33]

1. The preparation of graphite oxide from graphite.
   Graphite oxide is obtained via the oxidation of bulk graphite with strong mineral acids and oxidizing agents. For instance, based on the treatment of oxidant composed of potassium permanganate ($KMnO_4$) and sulfuric acid in Hummers method, graphite oxide could be produced from flake

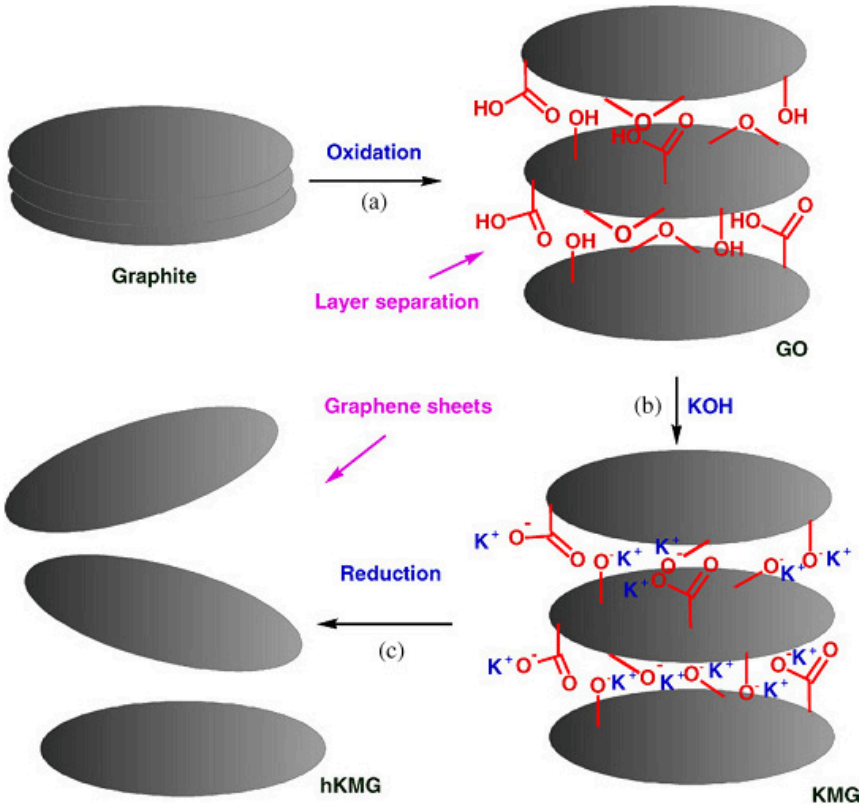

Figure 4. A simple route for the preparation of a homogeneous aqueous suspension of GSs from graphite stack.[33]

graphite.[34] Other oxidizing agents such as $KClO_3$ (or $NaClO_3$) and HNO_3 are also utilized in the Staudenmaier[35] or Brodie methods.[36] During this oxidative process, the delocalized electronic structure of graphite is ultimately disrupted, and a variety of oxygen-based chemical functionalities can be imparted onto the surface. It has been demonstrated that the C:O ratio between 2.1 and 2.9 retained the layer structure of graphite with larger and irregular spacing.

2. The preparation of GO.
   GO is mainly prepared based on the mechanical or thermal exfoliation of graphite oxide. For example, single-layer GO sheets can be produced by mechanical sonication of hydrophilic graphite oxide in water. It should be noticed that although the chemical composition (*i.e.*, surface functional group) of graphite oxide and GO is similar, their structures are quite different. GO is a sheet-like monolayer material, while graphite oxide is a

layered material that consists of GO sheets. Because of the intercalation of water molecules between the layers, the interlayer distance expanded from 6 to 12 Å depending on humidity.[37]

As an intermediate for the manufacture of graphene, GO sheets are hydrophilic, oxygenated graphene monolayer sheets. Using atomic force microscopy (AFM), it has been found that the thickness of single GO sheet obtained by exfoliation is around 1 nm. GO maintains the basic framework of graphene, but possesses many oxygen functional groups, such as hydroxyl and epoxy groups on the basal plane, and carboxy, carbonyl, phenol, lactone, and quinone groups located at the sheet edges.[38] Compared to graphene, GO exhibits high chemical and structural defects. The attachment of covalent oxygenated functional groups on GO greatly disrupts the sp^2-bonded graphitic structure, thus making GO electrically insulating. Moreover, GO is highly hydrophilic. It has been found that GO sheets exhibit negative charge when dispersed in water because of the ionization of the carboxylic acid and the phenolic hydroxyl groups. Owing to the electrostatic repulsion and its hydrophilicity, GO can be well soluble in water to yield clear, homogeneous, and stable dispersion consisting mostly of single-layered sheets at the concentrations up to 3 mg mL^{-1}.

3. Chemical reduction of GO.

   The reduction is an essential and final step to obtain graphene from GO. GO can be reduced via chemical, thermal, or electrochemical techniques.[39–42] According to the reduction method that was used, the products are typically referred to as chemically reduced graphene oxide (CRGO), thermally reduced graphene oxide (TRGO), or electrochemically reduced graphene oxide (ERGO). After reduction, some degree of oxygen-bearing groups of GO are eliminated and the π-electron conjugation within the aromatic system of graphite is partly restored. Determined by elemental analysis, the reduced GO can exhibit a high C:O ratio of over 10:1. However, due to the presence of defects in the lattice structure, graphene obtained from the reduction of GO sheets exhibits inferior electrical conductivity compared to pristine graphene. Moreover, because of the existence of lattice defects, graphene displays a wrinkled structure, which is different from the rippled structure that was observed in pristine graphene.

As for the preparation of CRGO, the common reducing agents include hydrazine monohydrate, sodium borohydride ($NaBH_4$), *p*-phenylene diamine, and hydroquinone.[43,44] Among these reducing agents, hydrazine monohydrate is the most frequently used reductant because of its strong reduction

activity. During the reduction process, most oxygen-containing functional groups of GO, such as ketones, carboxylic acids, and epoxy functional groups, can be well reduced by hydrazine, and the in-sheet conjugated structure can also be partially restored. However, due to the recovery of graphite domain on CRGO sheet, their hydrophobic property increased and the agglomeration of sheet happened. As a result, the production usually precipitated from the aqueous solution. The agglomeration can be limited by the addition of various stabilizing agents, such as polymers and surfactants, during the reduction process. Although hydrazine is an efficient organic reductant for the generation of CRGO, it is highly poisonous. Therefore, some alternative low-toxicity and environment-friendly reductants have been proposed. For instance, it has been reported that the reducing ability of L-ascorbic acid is similar to that of hydrazine.[45] Upon reduction with such biological reductant, the resulting graphene exhibited a highly graphitic structure and excellent electrical conductivity. The synthesis of hydrophilic graphene can even be achieved by the simple reduction of GO in tea solution.[46] Moreover, the green reduction of GO to graphene can also be carried out by the utilization of other eco-friendly technologies without any reductant, such as the electrochemical reduction and thermal reduction of GO. It has been reported that heat treatment is an efficient method for the deoxygenation of GO.[47] During the thermal reduction process, large amounts of oxygen-containing groups can be extruded as carbon dioxide. As for electrochemical reduction method, it has been reported that ionic liquids (ILs)-functionalized graphene could be simply originated from graphite anode immersed in a phase-separated mixture of water and imidazolium-based ILs.[48]

In order to characterize the morphology, structures, crystal structure, chemical compositions, and properties of the as-prepared graphene-based materials, various techniques have been proposed. The most frequently utilized techniques include AFM, transmission electron microscopy (TEM), scanning tunneling microscopy (STM), scanning electron microscopy (SEM), X-ray diffraction (XRD), X-ray photoelectron spectroscopy (XPS), and Raman spectroscopy, etc. Specific information on graphene characterization has been discussed in several reviews.[26,49,50]

2.2. Functionalization of graphene

Graphene is aromatic in nature. Pure graphene is hydrophobic and exhibits no solubility in most solvents. Especially during the reduction of GO without stabilizer, the reduction process removes most of the oxygen-containing functionalities of GO, making the as-formed hydrophobic GSs tend to

aggregate irreversibly back to graphite via π–π stacking interaction.[51] Such an event has greatly hindered the production, storage, and further processing of graphene. It is known that the lack of solubility of pure graphene in aqueous media has become a major technical barrier for many potential applications.[52] Especially in the field of bioelectrochemistry, it is known that a modified electrode can be well established through drop-casting, dip-coating, or spraying procedure only based on a stable suspension of the electrode material.[18] Therefore, the functionalization of graphene is of crucial importance because it can facilitate the formation of stable dispersions and stabilize graphene to avoid the undesired aggregation.[53] Moreover, the modification is also an effective strategy to enhance functionality of graphene, thus endowing the material with desired electronic, electrochemical properties, and biocompatibility. As a result, the graphene composites integrated of other moieties often offer better analytical characteristics than graphene alone. As shown in Figure 5, graphene has been reported to be functionalized with moieties such as small organic molecules, polymers, biosubstance, inorganic nanoparticles, and other type of carbon nanomaterials. The resulting graphene composites have been widely used for the fabrication of nanocomposites, supercapacitor devices, solar cells, memory devices, transistor device, biosensor, etc.[54–57]

For the functionalization of graphene, there are mainly three approaches: (i) covalent functionalization, (ii) non-covalent functionalization, and (iii) doping

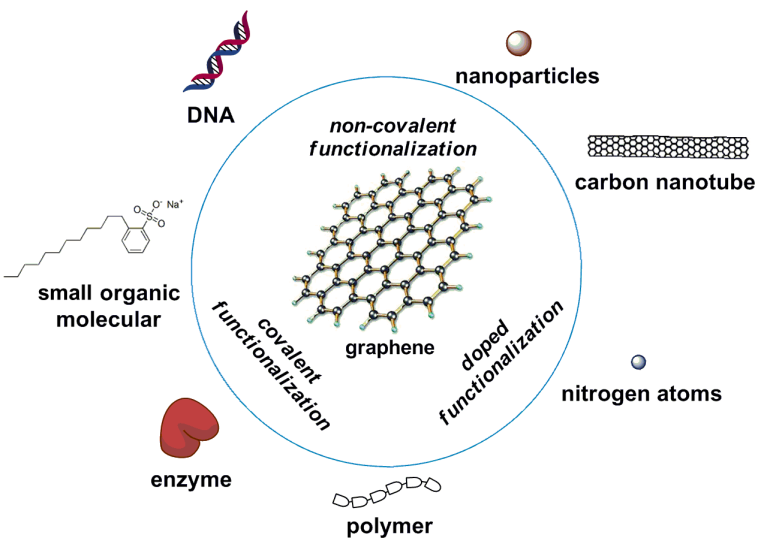

Figure 5. Schematic illustration of various functionalization methods of graphene.

functionalization. Covalent functionalization is a technique based on the modification of residual functionalities on graphene surfaces. During the reduction process of GO, it is very difficult to eliminate all the oxygen-containing functionalities. Therefore, the active oxygen functional groups remained at the sites of edges and defects can be further utilized to introduce surface functionality via covalent functionalization (Figure 6).[58] Such functionalization can be achieved by certain classes of reactions, including cycloadditions, click reactions, carbene insertion reactions, etc. The formation of covalent bonds via these reactions is associated with the breaking of sp^2 bonds on the basal plane of the GS. Therefore, although the covalent functionalization can improve the solubility and processability of graphene, it also adversely leads to the loss of electrical conductivity of the material.

Non-covalent functionalization is achieved by the interaction between graphene and polymer, surfactant, aromatic compounds and biomolecules such as DNA and peptides via hydrophobic, van der Waals, electrostatic, and π–π stacking forces.[59–62] Upon this treatment, the entire graphene surface can be generated with functional groups, which make the graphene water soluble or organic soluble for various further manipulation and applications. Moreover, unlike the covalent functionalization method, non-covalent functionalization

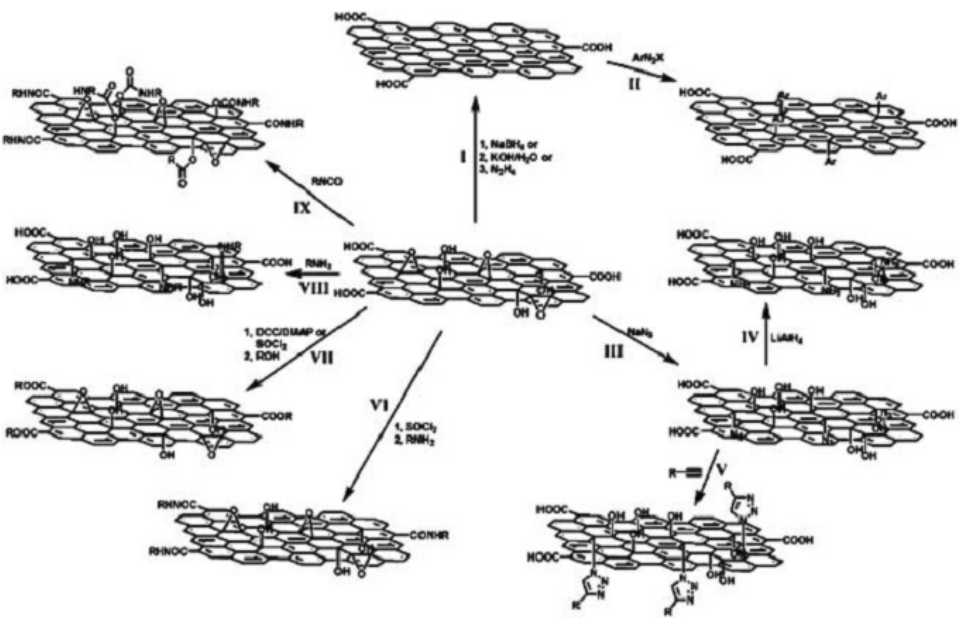

Figure 6. A schematic diagram of covalent functionalization chemistry for graphene or GO.[58]

technique does not destroy the extended π conjugation on the graphene surface, which can well preserve the natural structure and electrical properties of the material.

Chemical doping is an efficient approach to functionalize graphene intrinsically. Theoretical and experimental studies have shown that the substitution of carbon atoms in the honeycomb lattice of graphene by heteroatoms, such as nitrogen and boron, would disrupt sp^2 hybridization of carbon atoms, thus effectively tailoring the electronic properties.[63] For example, nitrogen doping can tune graphene from being a *p*-type to *n*-type semiconductor.[64] Recently, it has been found that the Fermi potential can be changed based on nitrogen doping, thus greatly improving the electron transfer efficiency of graphene and resulting in desirable properties for electrocatalysis.[65] Moreover, the chemical doping can enhance the biocompatibility of graphene. Recently, doping graphene has aroused great interest in the field of electrocatalysis and electrochemical biosensor.[66]

3. Electrochemical Properties of Graphene

Graphene and its derivatives have been considered as ideal materials for potential electronic and electrochemical applications because of their ultralarge surface area and excellent electrical conductivity. Graphene-based electrodes have shown excellent basic electrochemical behaviors, including wide potential windows, fast electron transfer rate, and good electrocatalytic activities for many redox reactions.[67] The fundamental electrochemical properties of graphene are comparable to that of edge-plane pyrolytic graphite. However, GSs are flexible as opposite to brittle graphite. Unlike highly oriented pyrolytic graphite, electrochemically active sites can be homogeneously distributed on a nanometer scale at graphene. Moreover, because of the flexibility of graphene, it can form open mesoporous structures on the surface of electrode, and provide large accessible surface areas for the electrocatalysis.

The electrochemical properties of graphene-based electrode are significantly better than those of other types of carbon electrodes. For instance, graphene exhibits a wide electrochemical potential window of 2.5 V in 0.1 M phosphate buffered saline (PBS) (pH 7.0), which is similar to that of graphite and glassy carbon (GC) electrodes, while the electrical resistance of graphene is much more lower than these two traditional carbon-based electrodes. In comparison to CNT, the advantages of graphene are apparent.[68,69] Firstly, unlike CNT, graphene is a kind of 2D carbon nanomaterial with high purity. Since graphene is mainly prepared from graphite, it does not contain any heterogeneous materials, such as metallic impurities that existed in CNT.[67] It has

been demonstrated that the transition metals, Fe, Ni, etc., that intercalated within the CNT are electrochemically active and dominate the electrochemistry of CNTs, which may lead to misleading conclusions. Therefore, graphene is much more suitable to act as a good platform for the electrochemical research of carbon materials.[24] In addition, serious toxicological effects have been found with CNTs due to the participation of metallic impurities in the redox activities of biomolecules. Thus, graphene is much more biocompatible than CNT because of the lack of metallic impurities. Secondly, it has been found that graphene exhibits superior electrochemical performance over CNTs due to a larger number of edges per mass of the material. The edges of GSs possess a variety of oxygen-containing groups. The electrochemical properties, especially the electron transfer, are greatly influenced by the concentration of surface oxide species presented onto the electrode. For instance, the increasing of the heterogeneous electron transfer rate constant of ferro/ferricyanide is responsible for carboxylic groups at electrodes modified by single-walled CNTs.[70] As for graphene, the basal plane is chemically inert, and the heterogeneous electron transfer rate from the basal plane of a GS is very close to zero, while the electron transfer rate constant of the edge plane of a GS is estimated to be 0.01 cms^{-1}.[71] Moreover, the existed oxygen-containing groups also played an important role for the adsorption and desorption of molecules, which take place before and after the electrochemical reaction. Thirdly, unlike CNT, graphene is the source material, which is mainly generated from inexpensive graphite via a simple method. The large-scale manufacturing of graphene at low cost greatly promotes its wide application in the field of biosensor.

The fundamental electrochemical properties of graphene have been investigated by the study of electrochemical responses of graphene-based electrodes toward different kinds of redox systems.[22] As determined from CV spectra, graphene-based electrode exhibits well-defined redox peaks toward various traditional redox probes.[72,73] The oxidative and reduction peak currents of the graphene-modified electrodes increase linearly with the square root of the scan rate, indicating that the redox processes are predominantly diffusion controlled. The peak-to-peak potential separations (ΔE_p) in CVs for $[Fe(CN)_6]/^{3-/4-}$ and $[Ru(NH_3)_6]^{3+/2+}$ are much more smaller than that observed on GC electrode, which are very close to the ideal quasi-reversible system on carbon electrodes. As is known, the peak-to-peak potential separation (ΔE_p) is related to the electron transfer coefficient. The low value of ΔE_p indicates that a fast electron transfer for a single-electron electrochemical reaction has been achieved on graphene.

The electrochemical behavior of representative redox species with different electron transfer properties, such as $[Fe(CN)_6]/^{3-/4-}$, $[Ru(NH_3)_6]^{3+/2+}$,

and $Fe^{3+/2+}$, have been investigated systematically on graphene electrodes.[74] $[Ru(NH_3)_6]^{3+/2+}$ is a simple outer-sphere redox couple that is relatively insensitive to the surface microstructure, surface oxides, and adsorbed monolayers on sp^2 carbon electrodes. The apparent electron transfer rate constants (k^0_{app}) of graphene and GC electrodes are $0.18\,cms^{-1}$ and $0.055\,cms^{-1}$ for $[Ru(NH_3)_6]^{3+/2+}$, respectively. As for $[Fe(CN)_6]/^{3-/4-}$, a redox couple which is "surface sensitive" but not "oxide sensitive", the k^0_{app} of graphene-modified electrode and GC electrode are estimated to be $0.49\,cms^{-1}$ and $0.029\,cms^{-1}$, respectively. Different from the above-mentioned two redox probes, $Fe^{3+/2+}$ is a traditional redox probe that is both "surface sensitive" and "oxide sensitive", which is sensitive to the surface carbon–oxygen functionalities, specifically surface carbonyl groups. The electron transfer rates for $Fe^{3+/2+}$ observed at the graphene-modified electrode are several orders of magnitude higher than that obtained at bare GC electrodes. The above-mentioned investigation indicates that graphene remarkably enhances the electron transfer in all the redox systems with respect to the bare GC electrode. The fast heterogeneous electron kinetics observed at graphene-based electrode can be ascribed to the unique electronic structure and the abundance of surface defects of graphene.[75] Besides the aforementioned traditional redox probes, graphene-based electrode could also be used for the detection of small molecules, such as ascorbic acid (AA) and dopamine (DA).[54,76]

4. Graphene-Based Electrochemical Enzymatic Biosensor

4.1. The introduction of electrochemical enzymatic biosensor

An electrochemical biosensor is a device that transforms chemical information into a useful electrochemical signal, in which the recognition system uses a biological sensing element. The most popular and up to now most reliable kind of biosensors are the electrochemical enzymatic biosensor, which combines the specificity of enzymatic reactions with electrochemical signal transduction.[77] Since the enzyme provides the selectivity for the sensor and catalyzes the formation of the electroactive product for detection, it is the most important component of the enzymatic biosensor.[78] The enzyme can be immobilized onto the surface of electrode through covalent bonding, cross-linking, or physical absorption.[79] Because of the low cost, ease of use, portability, and simplicity of construction and the exhibited excellent performances, such as high sensitivity and wide linear range, electrochemical enzymatic

biosensors hold a leading position among the presently available biosensor systems.

According to different mediators, the development of electrochemical biosensors can be historically divided into three generations: the first-, the second-, and the third-generation biosensors (Figure 7). The first-generation biosensors, which belonged to glucose biosensor, were firstly developed by Clark and Lyons in 1962.[80] In the structure of such biosensor, a glucose oxidase (GOD) enzyme is immobilized behind a semipermeable membrane at the surface of a Pt electrode. In this kind of biosensor, oxygen acts as the mediator to communicate electrons between the enzyme and the electrode.[81] Although the first-generation biosensors still take a significant portion in present commercial biosensors, they have many drawbacks, such as too high applied potential, the disturbance of O_2, and the complex fabricated processes.

With the aid of artificial mediator, which is small, soluble molecule capable of undergoing rapid and reversible redox reaction, the second-generation biosensors overcome some drawbacks of the first ones. The artificial mediator such as quinones, organic conducting salts, dyes, ruthenium complexes, ferrocene (Fc), and ferricyanide derivatives can react with the active center of the proteins and with the electrode surface, shuttling the electrons between the proteins and the electrode, which significantly reduce the applied potential. In order to eliminate the O_2 dependence, the artificial mediator-based biosensor exhibits much better sensor performance than the first-generation biosensor. Unfortunately, the redox mediators used in conjunction with redox proteins facilitate not only the electron transfer between electrode and proteins but also various interfering reactions.[82]

The first report on direct electron transfer was published in 1977 by Hill and Kuwana.[83,84] After that, the studies about the third-generation biosensors

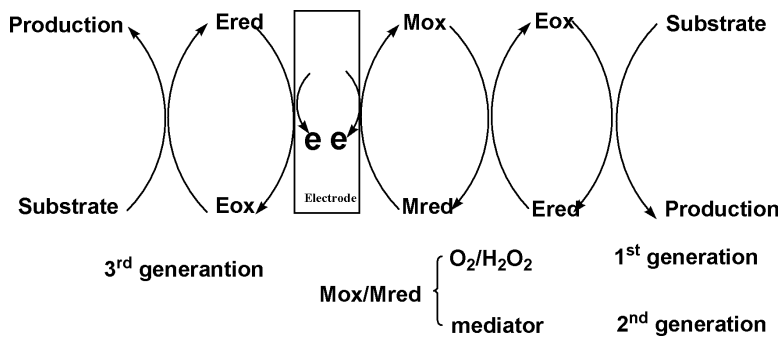

Figure 7. Schematic illustration of the mechanism of the electrochemical enzymatic biosensors.

have developed extensively. In the third-generation biosensors, the electron transfer avoids the absence of the "outside mediator" and could directly carry out between the electrode and the redox proteins.[85] The redox proteins themselves act as an electrocatalyst that facilitates the electron transfer between the electrode and the substrate molecule involving no mediator in this process. Unlike the mediator-based biosensor, direct electron transfer offers this kind of biosensors better sensor performance because of the following reasons. Firstly, they are able to work in a potential range closer to the redox potential of the proteins itself, and thus less exposed to interfering reactions. Secondly, some proteins and enzymes are natural catalyst and have superior selectivity and high affinity toward the substrates. Thirdly, the higher integration between the proteins or enzymes and the electrode surface can also improve the sensitivity of this kind of biosensor. Fourthly, the construction of biosensor based on direct electron transfer greatly simplifies the reaction system by eliminating the need for a chemical mediator. Another attractive feature of the systems based on direct electron transfer is that it can provide models for mechanism study of biological electron transport.

However, the achievement of direct electron transfer between redox proteins and electrodes was fairly difficult at normal electrode surface. For instance, at bare electrode, the native redox proteins do not easily undergo facile redox reactions due to deep burying of the electroactive prosthetic groups within the proteins structure, thus making the distance between the prosthetic group and the electrode surface too long for direct electron transfer. Thus, the most important thing for the design of the third-generation biosensor is to provide predefined electron transfer pathways interconnecting the redox site within the protein and the electrode surface based on electrode architectures. Moreover, it is also important for the immobilized redox enzymes to well keep their bioactivities and have a favorable orientation to facilitate the direct electron transfer between the active center of the biomolecule and the electrode surface.

Recently, it has been found that the performance of the third-generation biosensor depends strongly on the suitable electrode material that was utilized for the immobilization of proteins. Chemical modification of the electrode surface with suitable material of good biocompatibility can endow the enzyme/protein with good stability and appropriate orientation, thus further enhancing their direct electron transfer with the electrode surface.[86] Up to now, great efforts have been devoted to developing general, stable matrices for carrying active proteins in direct electrochemistry study and construction of the third-generation biosensors. Aiming at that, various new electrode materials have been exploited to achieve the direct electron transfer, such as

surfactant, polyelectrolyte, ILs, and inorganic nanomaterial.[87] In comparison with the organic membrane, the inorganic nanomaterials are more attractive because of their large surface area, good mechanical, chemical, and thermal stability.[88] Among these inorganic nanomaterials, carbonaceous nanomaterials as a promising host material for immobilization of proteins have gradually attracted attentions in the field of bioelectrochemistry.[89,90]

Since graphene possesses superior electrical properties and larger surface area than other kinds of carbonaceous nanomaterials, this kind of novel 2D material has attracted great interest and shown great potential for use in the third generation of biosensors. The graphene on the electrode surface can not only function as a "connecting arm" for attaching protein/enzymes to achieve the electron transfer reaction, but also act as a transducer for the enhancement of electrochemical response. However, the major technical barrier for the preparation of graphene-based biosensors is the lack of solubility of graphene in aqueous media. The hydrophobic property of graphene greatly impedes its interaction with hydrophilic redox enzymes and further limits its application. Moreover, pure graphene nanosheet is prone to form irreversible agglomerates or even restacks to form graphite in aqueous solution.[91] Since the individual sheet-like state of graphene is crucial to the electrochemical performances of graphene-based biosensor, the prevention of such aggregation is of particular importance.[92] Therefore, the functionalization of graphene becomes a critical step for its utilization in biosensor developments. Based on the suitable functionalization, various functional groups can be introduced onto the surface of graphene, which not only make the graphene to be more hydrophilic and biocompatible but also impart new functionality to graphene aiming at the improvement of the biosensor performance.

In the following sections, the applications of graphene and its derivatives in the enzymatic biosensing systems are described.

4.2. Organic molecular-modified graphene-based enzymatic biosensor

The modification of graphene with small organic molecule based on noncovalent method, which employs van der Waals force or π–π stacking interactions, is an efficient method to achieve the functionalization of graphene. For instance, the aromatic molecule tetrasodium 1,3,6,8-pyrenetetrasulfonic acid (TPA) can effectively exfoliate graphite into functionalized single-layer graphene nanoplatelet with good yield and hydrophilicity.[93] Using TPA-modified graphene as electrode material, Yue *et al.* fabricated a new type of nitrite electrochemical biosensor that consisted of single-layer graphene

nanoplatelet–myoglobin (Mb) composite film.[94] The hydrophilic and conductive graphene has been proved to be effective in providing a biocompatible microenvironment for Mb immobilization and a suitable electron transfer distance between the electroactive centers of redox protein and the electrode surface. Based on the direct electrochemistry of immobilized Mb, the biosensor exhibited good electrochemical response to nitrite with the linear range of 0.05–2.5 mM and the detection limit of 0.01 mM. The fabricated nitrite biosensor also showed high sensitivity and good stability.

Surfactant is a commonly used stabilizer for dispersing graphene. It has been found that the hydrophobic tail of surfactant can be adsorbed on the surface of graphene through hydrophobic interaction, while its hydrophilic head is oriented toward the aqueous phase. Due to the adsorbed surfactant molecular ions, the modified graphene is stabilized against reaggregation by electrostatic repulsion. Based on the surfactant-modified graphene, which is sodium dodecyl benzene sulfonate (SDBS)-functionalized GSs, Zeng *et al.* fabricated a self-assembled graphene–enzyme hierarchical nanostructures for electrochemical biosensing (Figure 8).[95] In their sensing platform, a common redox enzyme of horseradish peroxidase (HRP) was chosen as the model of bimolecular. Since the isoelectric point (pI) of HRP is around 8.8, it exhibits positively charged in physiological media. Because of the modification of SDBS, the functionalized GSs display oppositively negative charge under the same experimental condition. Then, based on the electrostatic interaction between these two moieties, SDBS–GSs can be easily assembled with HRP to form novel hierarchical nanostructures in aqueous solution. It has been found that the SDBS–GSs can not only provide large, open, and accessible 2D surfaces for tethering of the enzymes, but also provide "flexible distance" and restack by adapting to the dimensions of the biomolecules through electrostatic self-assembly, which is of great importance for retaining the native conformations of the guest enzymes. The electrochemical measurements revealed that the as-fabricated biosensor showed excellent electrocatalytic performance toward the reduction of H_2O_2 with fast response, wide linear range, high sensitivity, and good stability. These desirable electrochemical performances are attributed to excellent biocompatibility and superb electron transport efficiency of GSs, high HRP loading, and the synergistic catalytic effect of the HRP–GS bionanocomposites toward H_2O_2. Using surfactant hexadecyl trimethylammonium bromide (CTAB) together with graphene, Wen fabricated a highly sensitive nitric oxide (NO) biosensor.[96] The NO sensor was developed based on the immobilization of hemoglobin (Hb) on a graphene electrode modified by chitosan (CS) and CTAB hydrogel. The surfactant CTAB played an important role to disperse graphene and prevent the tendency toward graphene

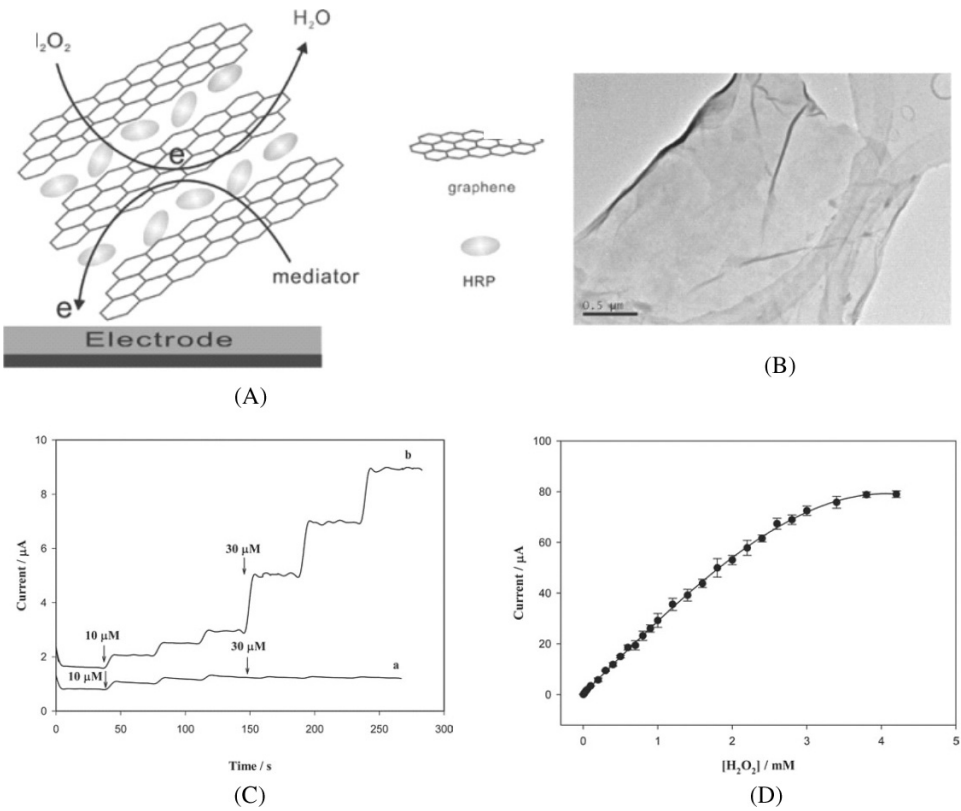

Figure 8. (A) Schematic representation of the self-assembled HRP–GSs hierarchical bionanocomposites on GC electrode and electron transfer process of the composites on the electrode surface. (B) TEM image of a single GS. (C) Dynamic amperometric response of the modified electrodes to successive additions of H_2O_2: GSs electrode (curve a) and HRP–GSs electrode (curve b) in a stirred 0.1 M PBS (pH 7.0) solution containing 1.0 mM hydroquinone. Applied potential was –80 mV versus SCE. Amperometric response of 10 μM H_2O_2 (30–130 s) and 30 μM H_2O_2 (from 140 s). (D) Calibration curve of the HRP–GSs electrode corresponding to amperometric response at –80 mV. Adapted from Ref. 95.

aggregation on the surface of GC electrode. The conductive graphene and the biocompatible CS greatly promoted the direct electron transfer between Hb and the underlying electrode. Therefore, the biosensor can achieve a limit of detection down to 6.75×10^{-9} M for quantitative NO analysis.

Lipid is a biocompatible organic molecule which can modify graphene similar to that of the surfactant. Liu *et al.* firstly fabricated a novel 1,2-dimyristoyl-*sn*-glycero-3-phospho-(1-rac-glycerol) phospholipid monolayer membrane-modified graphene (DMPG-G) for microperoxidase-11

(MP11) immobilization and subsequent direct electrochemistry and electrocatalysis.[97] The as-constructed DMPG-G-MP11-modified GC electrode exhibited a pair of well-defined quasi-reversible redox peaks of MP11 and showed high electrocatalytic activity toward H_2O_2.

Based on the reaction with oxygen-containing functionalities that existed on the chemical reduced graphene or GO, organic molecules can also be functionalized onto graphene via covalent modification. Using such method, Shan *et al.* firstly fabricated the IL-functionalized graphene by an epoxide ring-opening reaction between GO and 1-(3-aminopropyl)-3-methylimidazolium bromide ionic liquid (IL-NH_2).[98] Using a simple casting method, a novel ethanol biosensor with alcohol dehydrogenase (ADH)/IL-graphene/CS-modified electrode can be constructed. The resulting biosensor showed rapid and highly sensitive amperometric response to ethanol with a low detection limit (5 μM). Moreover, such proposed ethanol biosensor can also be used to determinate the ethanol concentrations in real samples. Zheng *et al.* synthesized a 3-aminopropyltriethoxysilane (APTES)-functionalized graphene via covalent modification.[99] The APTES modifier acted both as a dispersion agent for graphene and an amine surface modification agent for GC electrode and graphene. Using 1-ethyl-3-[3-dimethylaminopropyl] carbodiimide hydrochloride (EDC) as a cross-linking reagent, GOD can be further covalently bonded to graphene-functionalized electrode to fabricate GOD/APTES-graphene/GC electrode. The developed biosensor was further validated for detecting glucose in commercial artificial blood glucose linearity standards in the range 1.4–27.9 mM. Because of the covalent binding of GOD in the sensing platform, the biosensor exhibited excellent stability. When the biosensor was stored in a dry state at room temperature under ambient conditions, no decrease in the current response of the biosensor was found for the first three weeks and only a minor decrease of 12% was found in the next two weeks.

4.3. Polymer-modified graphene-based enzymatic biosensor

Polymers have been widely used in the areas of bioanalytical science due to their unique physical and chemical properties, which are helpful during the fabrication of electrochemical sensors and biosensors.[100] Polymer-modified electrode can be designed to have several functions, including diffusion control, reduction of interference, and mechanical protection of the sensing probe, which can greatly improve the sensitivity, selectivity, stability, and reproducibility of the electrode response to detect a variety of analytes.[101]

The development of polymer-functionalized graphene has opened a new and interesting area in materials science in recent years. Recently, researches

have made successful attempts for polymer–graphene composites.[102] These composite materials have shown considerable improvement in properties that cannot normally be achieved using conventional composites.[50] For instance, because of the formation of a conducting network by GSs in the polymer matrix, polymer–graphene composite exhibited superior electrical conductive properties compared to the neat polymer.[33] Therefore, the attractive features of polymer–graphene offer a great possibility for their novel applications in the field of electrochemical biosensor. Up to now, polymer–graphene related to biosensor applications have become an important topic in bioelectrochemistry. Surface modifications of graphene for the construction of biosensor have been carried out by different research groups with various polymers.

CS is a linear hydrophilic polysaccharide composed of $\beta(1\rightarrow4)$ linked glucosamine units together with some proportions of *N*-acetylglucosamine units. It is an attractive biocompatible, biodegradable, and non-toxic natural biopolymer that has been widely used for the fabrication of biosensor.[103,104] The utilization of CS in the sensing platform can increase film adherence and prevent the leakage of redox enzyme/protein on the basis of its high hydrophilicity and good film-forming ability.[105–108] The non-covalent dispersion method is the most common technique to prepare CS–graphene composite. This solution-based method generally involves the mixing of colloidal suspensions of GS with CS by simple stirring. Based on the CS–graphene composite synthesized by dispersion method, Kang *et al.* fabricated a GOD–graphene–CS-modified electrode for direct electrochemistry and glucose sensing (Figure 9).[109] CS played an important role in forming a well-dispersed graphene suspension and immobilizing the enzyme molecules. The GOD not only retained its bioactivity, but also exhibited a surface confined, reversible two-proton and two-electron transfer reaction, and exhibited a fast heterogeneous electron transfer rate with the rate constant (k_s) of 2.83 s^{-1}. As compared with other CNT-based biosensors, the CS–graphene-based biosensor exhibited a wider linearity range from 0.08 mM to 12 mM glucose with a detection limit of 0.02 mM and much higher sensitivity (37.93 μA mM^{-1} cm^{-2}).

By co-electrospinning the solution of polyvinyl alcohol (PVA), CS, GOD, and GO, Su *et al.* developed a novel biosensing platform, which was the PVA/CS/GOD/GO nanofibers-modified platinum (Pt) electrode (PVA/CS/GOD/GO/Pt electrode).[110] It has been found that the electrospun nanofibrous membrane on Pt electrode has very high porosity and large surface area, which can significantly reduce the diffusion resistance of substrates and then increase the response to electroactive species of modified electrodes. Due to the synergy effects of GO and electrospun polymer nanofibers, such biosensor exhibited good stability, reproducibility, and anti-interference

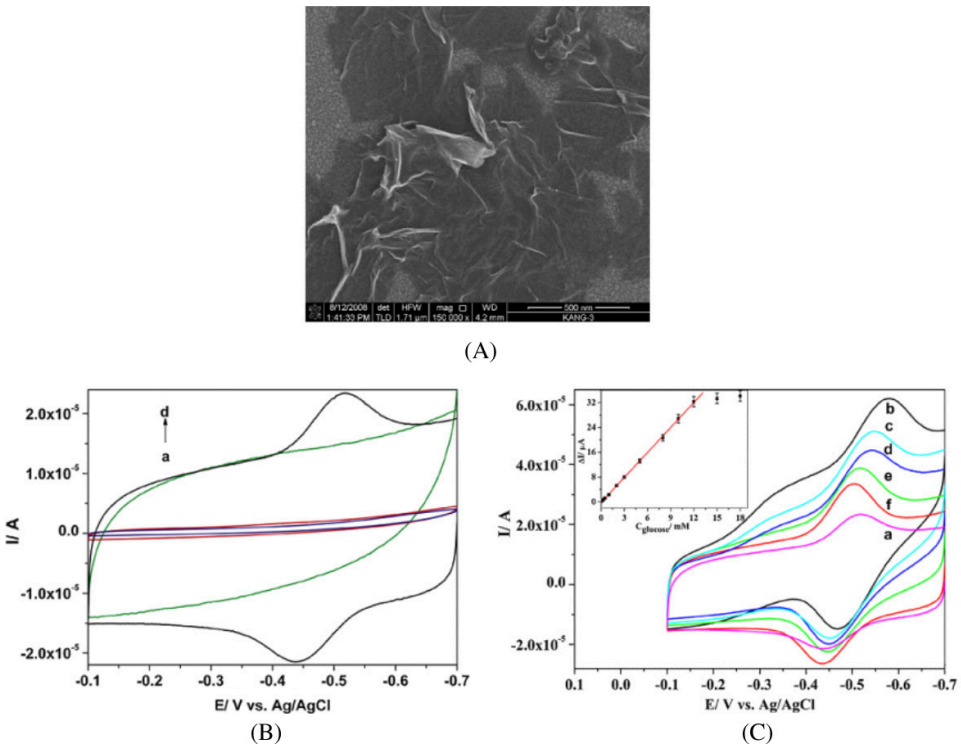

Figure 9. (A) SEM image of graphene–CS composite. (B) Cyclic voltammograms of the modified GCEs with (a–d) CS, GOD–CS, graphene– CS, and GOD–graphene–CS films in PBS with N_2 saturated at the scan rate of 100 mV s^{-1}. (C) Cyclic voltammograms of GOD–graphene–CS/GCE in PBS with 0.1 M KCl at a scan rate of 100 mV s^{-1} in the presence of different concentrations of glucose. (a) N_2 saturated without glucose, (b) O_2 saturated without glucose, and (c–f) with glucose of 3.0, 5.0, 8.0, and 10.0 mM. Adapted from Ref. 109.

capability. Moreover, such polymer — graphene-based biosensor can also be applied for the detection of glucose in real samples, such as human serum samples.

Recently, it has been found that CS can also act as an efficient reductant for the chemical reduction of GO. Liu *et al.* developed a green and environment-friendly route for preparation of well-stable graphene dispersion by the one-pot chemical reduction of GO with the use of CS as a reducing and stabilizing agent.[111] Graphene–GOD nanostructures was then fabricated on GC electrode through the electrostatic self-assembly between GOD and CS-functionalized graphene. The resulting biosensor exhibited good response to glucose. The linear detection range was estimated to be from 2 to 22 mM ($r = 0.9987$), and

the detection limit was estimated to be 20 μM at a signal-to-noise ratio of three. Based on the reactivity of the modified CS, other moieties can also be introduced onto graphene to fabricate functionalized graphene. Using a covalently modified method, Qiu *et al.* designed and synthesized a biocompatible and conductive Fc-branched CS.[112] The attachment of redox Fc group to CS matrix can effectively prevent the leakage of Fc from the matrix and improve the electrical conductivity of CS. Acted both as a stabilizer and modifier, this electroactive CS can not only improve the stability of GO, but also make GO exhibit a positive charge, which is more favorable for the further immobilization of negatively charged GOD without destructing its native structure and bioactivity. The resulting biosensors showed a linear response to glucose in the concentration range from 0.02 to 6.78 mM with a detection limit of 7.6 μM at a signal-to-noise ratio of three and exhibited a higher sensitivity of 10 μA $mM^{-1}cm^{-2}$.

Similar to that of CS, the commercial polymer Nafion, which is the product of copolymerization of perfluorosulfonate vinyl ether and tetrafluoroethylene, is often utilized to stabilize graphene via non-covalent dispersion method.[113–115] Chen *et al.* constructed a mediator-free H_2O_2 biosensor based on Nafion–graphene composites together with redox protein Hb.[116] According to the experimental result, the Hb–Nafion–graphene composite film-modified electrodes showed direct electrochemistry with a fast electron transfer rate of 6.63 s^{-1} and high electrocatalytic activity to the reduction of H_2O_2. The electrochemical performance of the resulting biosensor was much better than that of the similar biosensors based on the carbon nanofiber (CNF) and CNT. Toward the electrochemical reduction of H_2O_2, Nifion–graphene-based biosensor exhibited a high sensitivity of 412.7 mA $M^{-1}cm^{-2}$, a low detection limit of 2.0×10^{-7} M, and a small apparent Michaelis–Menten constant of 37 mM.

Another efficient approach to fabricate polymer–graphene is the non-covalent grafting of well-defined polymers to graphene via π–π stacking interaction. For instance, the attachment of conducting polymer poly (3,4-ethylenedioxy thiophene) (PEDOT) to graphene was recently reported.[117] The prepared G-PEDOT nanocomposite was of good biocompatibility, enhanced electric conductivity, and large specific surface area. The redox protein cytochrome c (Cyt c) embedded in G-PEDOT matrix displayed excellent direct electrochemistry and retained its biocatalytic activity toward the reduction of H_2O_2. The electrochemical signal of the biosensor showed a linear response to H_2O_2 in the concentration range from 5.0×10^{-7} to 4.0×10^{-4} M with a detection limit of 2.49×10^{-7} M.

The traditional *in situ* polymerization methods can be utilized for the production of polymer–graphene composites.[33] Such method generally involves mixing of graphene in neat monomer or a solution of monomer, followed

by polymerization in the presence of the dispersed graphene. Based on this method, Zhang *et al.* fabricated covalent bonded composites such as polymeric IL-modified graphene (poly(1-vinyl-3-butylimidazolium bromide)–graphene (denoted as poly(ViBuIm$^+$Br$^-$)-G)).[91] As shown in Figure 10, the GO was firstly prereduced. Then the IL monomer ViBuIm$^+$Br$^-$ was polymerized in the presence of graphene. The reduced GO can be activated using free radical initiators to open their π-bonds and participating in the polymerization of the monomer, thus generating the polymeric IL onto the nanosheet. Thereupon, the nanocomposites were further reduced by hydrazine to obtain the final poly(ViBuIm$^+$Br$^-$)-G. It has been reported that the polymeric IL plays a crucial

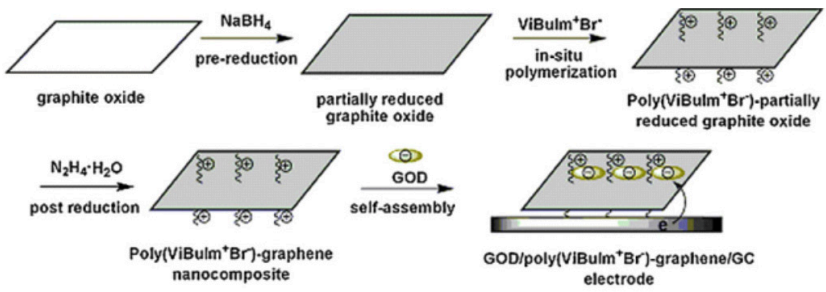

(A)

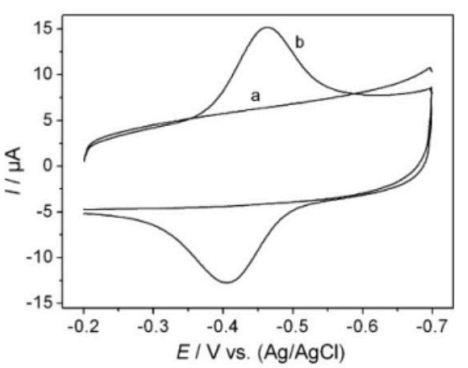

(B)

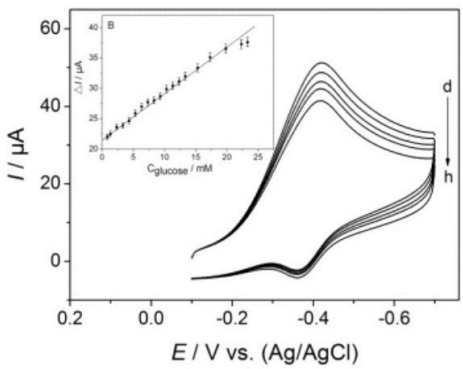

(C)

Figure 10. (A) Fabrication of GOD/poly(ViBuIm$^+$Br$^-$)–graphene/GC electrode and the direct electron transfer between GOD and GC electrode. (B) Cyclic voltammograms of poly(ViBuIm$^+$Br$^-$)–graphene/GC (a), GOD/poly(ViBuIm$^+$Br$^-$)–graphene/GC (b) electrodes in 0.1 M PBS (pH 6.5). Scan rate, 200 mV s^{-1}. (C) Cyclic voltammograms of GOD/poly(ViBuIm$^+$Br$^-$)–graphene/GC electrode in 0.1 M O_2-saturated PBS (pH 6.5) containing 2.3 mM (d), 3.3 mM (e), 4.3 mM (f), 5.3 mM (g), 7.3 mM (h) glucose, respectively, and plots of the electrocatalytic current (I_{cat}) versus glucose concentration for the GOD/poly(ViBuIm$^+$Br$^-$)–graphene/GC electrode (inset). Scan rate, 200 mV s^{-1}. Adapted from Ref. 91.

role in obtaining individual graphene nanosheets necessary for the enzymatic electrode. It not only well stabilizes graphene nanosheets but also acts as an efficient linker between the GOD and graphene. The experimental results demonstrate that the immobilized GOD on poly($ViBuIm^+Br^-$)-G exhibits a fast direct electron transfer at the GC electrode and perform very well for the electrocatalytic oxidation of glucose with good sensitivity and wide linear range.

Due to the existence of residual oxygen-containing functional groups on the surface of nanosheet, graphene prepared via chemical reduction method exhibits negative charge in aqueous solution, thus allowing positively charged polymer to non-covalently graft onto graphene based on electrostatic interaction. Based on this method, Liu *et al.* synthesized a functionalized graphene nanosheet (PDDA-G) with poly (diallyldimethylammonium chloride) (PDDA), which is a linear positively charged polyelectrolyte that has been found to be attractive for functionalizing nanomaterials.[118] By integrating PDDA-G, room temperature ionic liquid (RTIL) together with Hb, a novel mediator-free biosensor is thus constructed. Such biosensor can not only achieve the direct electrochemistry of Hb, but also exhibit excellent electrocatalytic activity for the detection of nitrate with a wide linear range from 0.2 to 32.6 μM and a low detection limit of 0.04 μM.

It is known that the layer-by-layer (LBL) technique provides a powerful strategy for construction of ordered thin polymer films with precise control of compositions, structures, and morphologies.[119] Since suitable polymer-modified graphene can exhibit specific surface charges, they can blend with various polyelectrolyte or biomolecules that have opposite surface charge through the LBL electrostatic interaction to form ordered membrane on electrode. Such membrane combines the excellent electrochemical properties of graphene and the versatility of LBL assembly, showing great promise in highly efficient biosensors. On the basis of this principle, Zeng *et al.* firstly synthesized negatively charged pyrene-grafted poly (acrylic acid) (PAA)-modified graphene via π–π stacking and van der Waals interactions.[120] Then they fabricated a bienzyme biosensing system for the detection of maltose based on the successive LBL assembly of polymer–graphene, GOD, and glucoamylase (GA). The detection limit and sensitivity of the as-fabricated biosensor for the detection of maltose were 1.37 mM (S/N = 3) and 0.00715 $\mu A\ mM^{-1}\ cm^{-2}$, respectively.

4.4. Inorganic nanoparticles-modified graphene-based enzymatic biosensor

Tremendous attention has been paid to nanoscale particles in recent years because of their intriguing properties and potential applications. Since these

nanomaterials often exhibit new interesting size-dependent physical and chemical properties that cannot be achieved by their bulk counterparts, they have found applications in various fields.[121] In the field of bioelectrochemistry, it has been found that inorganic nanoparticles can efficiently improve the stability and maintain the activity of biomolecules.[122] Moreover, due to the excellent conductivity and catalytic properties of inorganic nanoparticles, they are suitable electrode materials to act as electronic pathway between the redox centers in proteins and electrode surfaces, thus enhancing the direct electron transfer and increasing electrochemical reaction rate.[123]

Because of its unique structure, ultra-large surface area, and extraordinary properties, graphene is considered as promising nanoscale building block for the design and preparation of novel nanocomposites.[124,125] The recent research work demonstrate that the integration of inorganic particles with graphene may not only lead to the development of a broad new class of materials but also prevent the restack of GS at dry state, especially on the surface of the electrode. Acted as a spacer, the inorganic nanoparticles increase the distance between the GSs, thereby making both faces of graphene accessible. Recently, various inorganic nanoparticles, such as metals, metal oxides, and semiconducting nanoparticles, have been incorporated to graphene 2D structures aiming to achieve the synergistic effects of individual components or impart new functionality to graphene.[126–129] When utilized as an electrode material for the fabrication of biosensor, the inorganic nanoparticle–graphene composite has been found to provide the suitable microenvironment for the immobilized biomolecules to retain their biological activity with desired orientation.[126,130,131] Because of the enhancement of the electron transfer between the immobilized enzymes and electrode surfaces by synergic properties of the inorganic nanoparticles and graphene, the performance of nanocomposite-based electrochemical biosensor can be efficiently improved.[132–136]

Dey and Raj developed a bienzyme sensing platform based on Pt nanoparticle–graphene nanocomposite, enzymes cholesterol oxidase (ChOx) and cholesterol esterase (ChEt).[137] The scheme illustrating the biosensing of cholesterol ester with the Pt nanoparticle–graphene nanocomposite is shown in Figure 11. The graphene nanosheets were decorated with Pt nanoparticles by the *in situ* reduction of H_2PtCl_6 in aqueous solution. The Pt nanoparticle–graphene nanocomposite exhibited excellent electrocatalytic property. It has been found that the nanocomposite-modified electrode can efficiently catalyze the electrochemical oxidation of H_2O_2 at the potential of 0.4 V, which is more than 100 mV less positive with respect to the bulk Pt electrode. Based on the outstanding electrocatalytic property of the nanocomposite, the as-fabricated

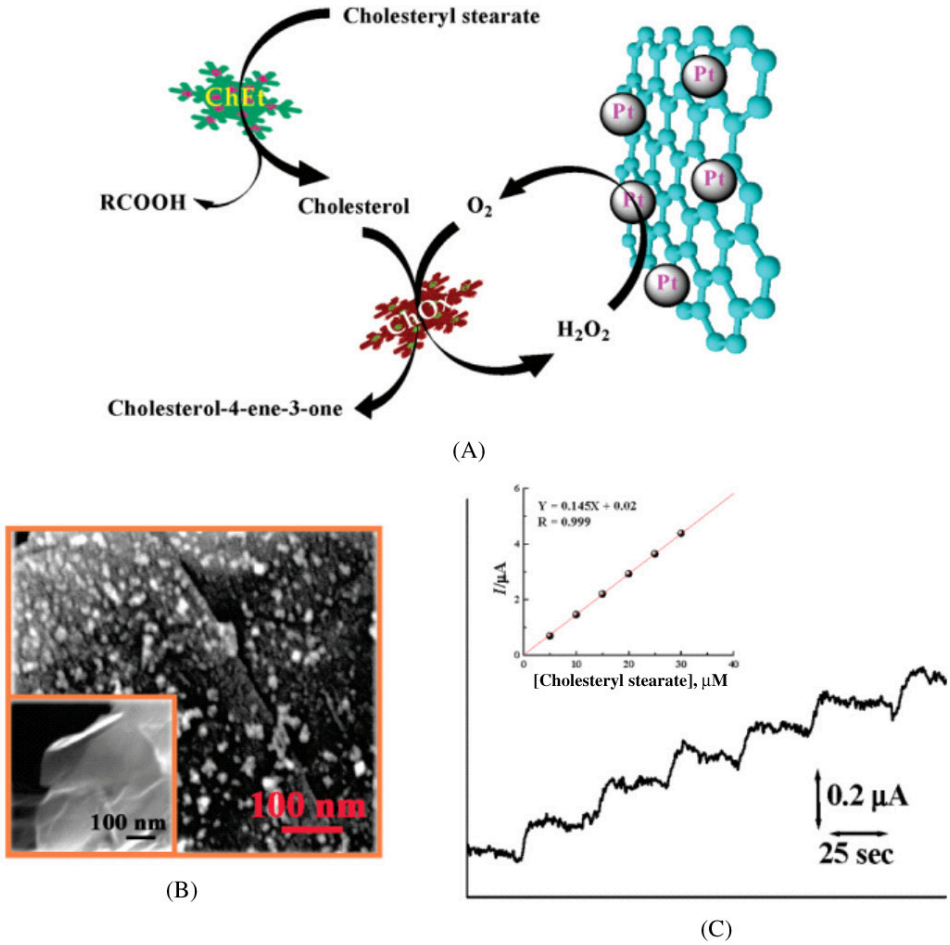

Figure 11. (A) Scheme illustrating the biosensing of cholesterol ester with the graphene nanosheets–Pt-based biosensor. (B) Field emission scanning electron microscopy (FESEM) image of Pt nanoparticle decorated graphene nanosheets. The image of the graphene nanosheets is shown in the inset. (C) Amperometric response of the cholesterol ester biosensors. Cholesteryl stearate (5 μM) was injected at regular intervals. Adapted from Ref. 137.

biosensor can linearly respond to cholesterol and cholesterol ester for a wide linear range with high sensitivity. The high sensitivity and low detection limit can be ascribed to the low background current and high electronic conductivity of graphene and good catalytic activity of the nanoparticles.

Semiconductor nanoparticle-modified graphene is also a good material for immobilizing biomolecules and fabricating the third-generation biosensors. Wang *et al.* firstly utilized CdS–graphene nanocomposite as a matrix for the GOD immobilization and construction of glucose biosensor.[138] In comparison

with the individual graphene and CdS nanocrystal, CdS–graphene nanocomposite exhibited excellent electron transfer properties for GOD with the rate constant of 5.9 s^{-1} due to the synergy effect of graphene and CdS nanoparticle. Based on the decrease of the electrocatalytic response of the reduced form of GOD to dissolved oxygen, a glucose sensor has been developed, which displays satisfactory analytical performance over a linear range from 2.0 to 16 mM along with good stability.

4.5. Biomolecular-modified graphene-based enzymatic biosensor

Functionalization of graphene with biomolecules, such as DNA or protein, is a promising strategy to fabricate 2D nanocomposite with better biocompatibility, solubility, and selectivity.[20,139,140] Up to now, various biomolecular-modified graphene has been utilized as electrode material for the construction of biosensors with excellent performance.[141] For instance, based on the biofunctionalization, DNA, which is a well-known natural biological macromolecule, has been incorporated into graphene-based electrochemical biosensors. Zhang *et al.* chemically reduced GO with hydrazine in the presence of freshly prepared single-stranded DNA (ssDNA) (Figure 12).[142] Due to the π–π stacking interactions between purine and pyrimidine bases of the ssDNA molecules and graphene, ssDNA could adsorb on the surface of the graphene to form a hydrophilic 2D nanocomposite during the chemical reduction procedure. The modified ssDNA can not only well stabilize graphene in aqueous solution but also endow it with negative charge. Thus, the positively charged HRP can be further self-assembled with ssDNA/GP on the surface of a GC via electrostatic interactions to form a novel modified electrode. A pair of large redox peaks of HRP with a formal potential of about –0.26 V (vs Ag/AgCl) in a pH 7.0 phosphate buffer solution were obtained at the modified electrode, demonstrating the direct electron transfer between the immobilized HRP and the electrode. The HRP coverage of the modified electrode was estimated to be 9.5×10^{-9} mol cm^{-2}, which was much more greater than loadings previously measured on other nanostructured electrodes. The ssDNA–graphene-based biosensor also exhibited good electrocatalytic performance toward H_2O_2, displaying a linear response from concentrations of 115.5 μM to 9.25 mM, with a detection limit of 39 μM.

Electrochemical biosensor can be directly obtained by the biofunctionalization of graphene with redox enzyme.[143–145] Based on such method, Manjunath *et al.* fabricated an amperometric bienzymatic cholesterol biosensor for total cholesterol determination.[146] In their sensing platform, ChOx

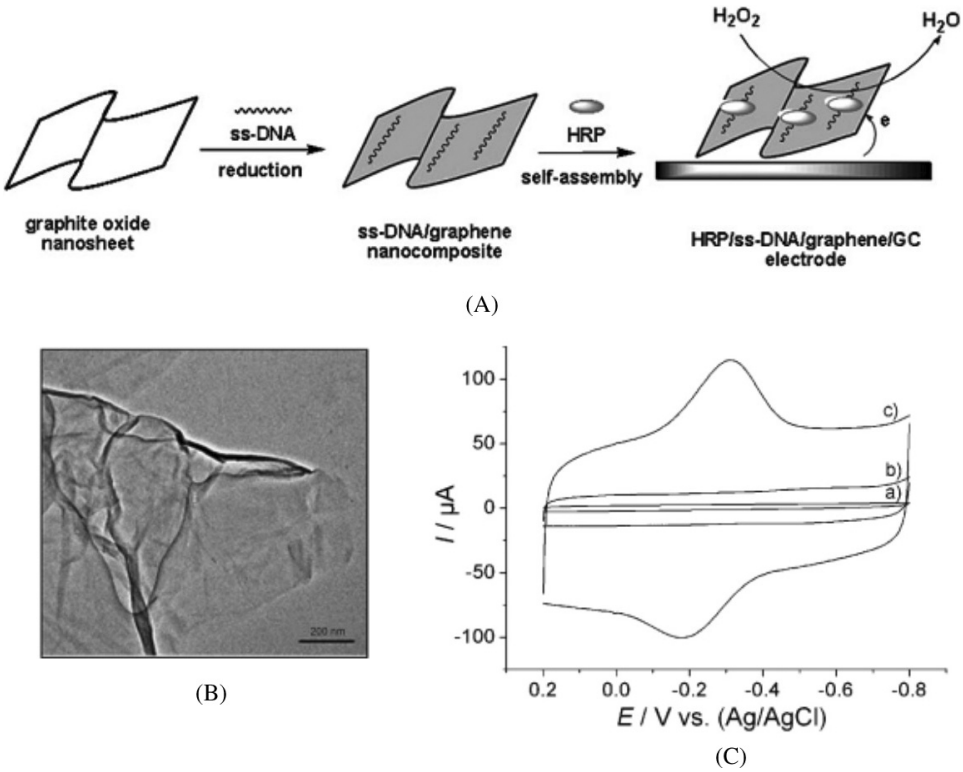

Figure 12. (A) Scheme of fabrication of HRP/ssDNA/graphene/GC electrode and the direct electron transfer between HRP and GC electrode. (B) TEM image of ssDNA/graphene. (C) Cyclic voltammograms of HRP/GC (a), ssDNA/graphene/GC (b), and HRP/ssDNA/graphene/GC (c) electrodes in 0.1 M PBS (pH 7.0). Scan rate, 200 mV s^{-1}. Adapted from Ref. 142.

and ChEt were immobilized onto functionalized graphene-modified graphite electrode through the covalent attachment between carboxyl acid groups of graphene and amines of enzymes. Due to the high conductivity and large surface area of graphene, the direct electron transfer between covalently immobilized ChOx and the surface of electrode can be achieved. The values of electron transfer coefficient (α) and electron transfer rate constant (k_s) were calculated to be 0.31 and 0.78 s^{-1}, respectively. As for the total cholesterol determination, the graphene-based bienzymatic biosensor exhibited linear range from 50 to 300 mM with a detection limit of 15 mM. It has also been found that the common interferents such as glucose, AA, and uric acid did not cause any interference because of the use of a low operating potential during the electroanalysis.

4.6. Graphene–carbon nanotube-based enzymatic biosensor

As the representatives of 1D and 2D nanostructures, CNT and graphene are mutually complementary in structure and properties.[147] For instance, the chemically reduced graphene usually has an electrical conductivity of about 100–200 Sm^{-1}, which is two orders of magnitude lower than conductive single-walled CNTs (usually 1×10^4 Sm^{-1}).[148] Therefore, one of the future trends is to integrate them into a hybrid structure that holds the promise of creating new potential for material research and applications. Recently, the combination of 1D CNT and 2D graphene to design hierarchically structured composites has been extensively studied in various electrochemical fields.[149] It has been found that the CNT in the obtained nanocomposite not only efficiently increases the basal spacing between graphene, which efficiently prevents the irreversible agglomerates of the nanosheet, but also bridges the defects for electron transfer between GSs, thus increasing electrolyte/electrode contact area and facilitating transportation of substrate and electron into the inner region of electrode. Therefore, the inclusion of CNT is expected to improve the unique potential of graphene as an electrode material for the construction of biosensor.[150]

Zhang *et al.* firstly constructed a third-generation biosensor based on graphene–multiwalled carbon nanotubes (GO-MWNTs). GO-MWNTs nanocomposite was explored based on the self-assembly of MWNTs and GO via π–π stacking interaction (Figure 13).[151] The hydrophilic GO can not only stabilize hydrophobic MWNTs to be well dispersed in aqueous solution but also endowed the composite with negative charge. Driven by the electrostatic interaction, positively charged HRP could then be immobilized onto GO-MWNTs at the surface of a GC electrode to form a HRP/GO-MWNTs/GC electrode under mild conditions. Since GO-MWNTs can well synergistically hybridize the different shapes and material properties of these two carbonaceous nanomaterials, such as the large surface area, high conductivity, and good biocompatibility, the immobilized HRP can exhibit enhanced direct electron transfer for the HRP-Fe(III)/Fe(II) redox center. Based on the direct electron transfer of the immobilized HRP, the GO-MWNTs-based biosensor exhibited excellent electrocatalytic behavior to the reduction of H_2O_2 with wide linear glucose response (3.5 to 293 μM), low detection limit (1.17 μM based on S/N = 3), high sensitivity (563.7 mA cm^{-2} M^{-1}), and high stability (response current –5% after 15 days).

Based on the direct electrochemistry of GOD at chemical reduced graphene oxide–multiwalled carbon nanotubes (ERGO-MWNTs) hybrid material-modified electrode, Mani *et al.* fabricated a biosensor for the detection of

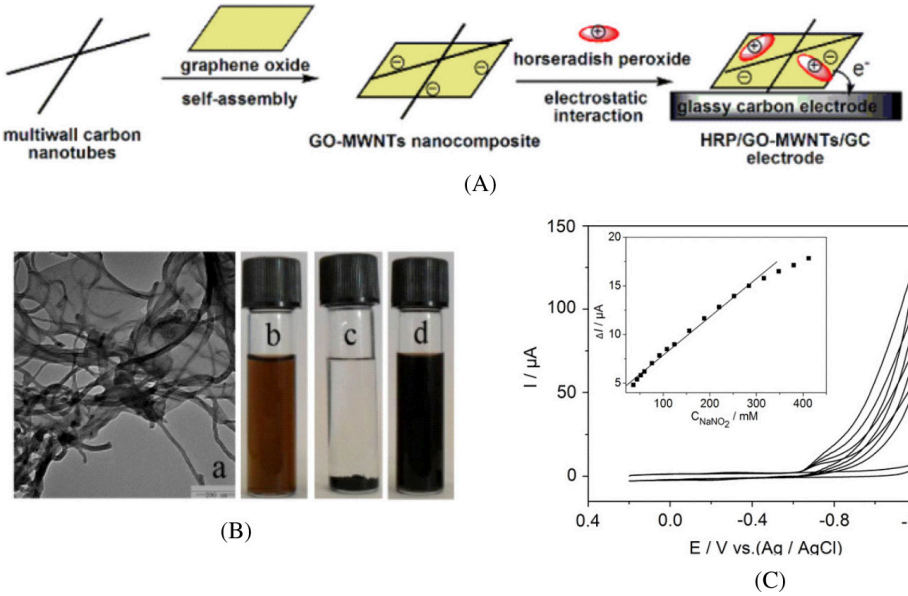

Figure 13. (A) Scheme of construction of HRP/GO-MWNTs/GC electrode and the direct electron transfer between the immobilized HRP and GC electrode. (B) TEM image of GO-MWNTs (a), photographs of GO (b), pristine MWNTs (c) and GO-MWNTs (d) in water. (C) Cyclic voltammograms of HRP/GO-MWNTs/GC electrode in 0.1 M PBS (pH 5.7) with 0 mM (a), 8 mM (b), 23 mM (c), 44 mM (d), 76 mM (e) $NaNO_2$ and plots of the increments of reduction peak current (ΔI) versus $NaNO_2$ concentration for the HRP/GO-MWNTs/GC electrode. Scan rate, 200 mV s^{-1}. Adapted from Ref. 151.

glucose.[152] The preparation of ERGO-MWNTs involved two steps. Similar to the above-mentioned self-assembly method, GO-MWNTs was firstly synthesized via non-covalent π–π stacking interaction. Then, GO-MWNTs were electrochemically reduced on GC electrode at the potential range from 0 to −1.5 V in PBS (pH 5.0). Due to the enhanced electron transfer promoted by MWNTs moiety in the hybrid, the electrochemical reduction of GO-MWNTs only required three cycles, which were much more smaller than that of the reduction of pristine GO (15 cycles). After that, GOD was well immobilized onto the ERGO-MWNT hybrid film; as a result direct electrochemistry of GOD has been achieved. Compared with that of pristine MWNTs, 2.1 fold higher peak current and very low peak to peak separation (ΔE_p) of 26 mV were observed at the hybrid film, demonstrating faster electron transfer between GOD and the modified electrode surface. Moreover, the modified electrode exhibited high electrocatalytic activity toward glucose determination

via oxygen consumption. The proposed biosensor exhibited low detection limit of 4.7 mM with wide linear range of 0.01–6.5 mM and acquired excellent storage and operational stabilities.

4.7. N-doped graphene-based enzymatic biosensor

The element doping is an effective strategy to modify the properties of graphene intrinsically. It has been demonstrated that doping graphene can tailor the electronic properties of graphene and bring out great application potential in many fields.[153,154] Since N atom contains one additional electron as compared to C, it can directly substitute C atoms in the graphitic lattice of graphene. It has been demonstrated that the N-doped graphene exhibited outstanding electronic properties that differ drastically from the undoped graphene. For example, N doping can generate significant changes in the electronic structure of graphene, which tunes the graphene from being a *p*-type to *n*-type semiconductor.[155] Moreover, doping graphene with heteroatom N has also shown to greatly improve the electrocatalytic activity due to the enrichment of free charge-carrier densities and enhancement of the electrical or thermal conductivities. For instance, N-doped graphene exhibited much higher electrocatalytic activity toward O_2 reduction and H_2O_2 reduction than graphene, and much higher durability and selectivity than the widely used and expensive Pt.[66] Besides the electrocatalytic activity, N doping also enhanced the biocompatibility of graphene, thus making it to be a desirable material for the construction of biosensor.

For the first time, Wang *et al.* constructed an N-doped graphene-based electrochemical biosensor for the determination of glucose (Figure 14).[65] The N-doped graphene was synthesized by a facile and fast methodology that was based on nitrogen plasma treatment of chemical reduced graphene. Such method is also tunable. The percentage of nitrogen doping could be regulated easily from 0.11 to 1.35% by controlling plasma exposure time. The as-prepared N-doped graphene displayed excellent electrocatalytic activity. As for the reduction of H_2O_2, the reduction peak of N-doped graphene electrode in cyclic voltammograms shifted 400 mV positively with 20 times current enhancement compared with a GC electrode. After immobilization with GOD, a pair of well-defined and quasi-reversible redox peaks corresponding to the direct electrochemistry of the redox enzyme can be obtained on the N-doped graphene electrode. Since the Fermi potential was changed and the electron transfer efficiency of N-doped graphene was enhanced via doping modification, the redox peak current obtained by N-doped graphene-based enzyme electrode was much more higher than that of observed at the undoped graphene one. Due to the excellent biocompatibility and conductivity of N-doped graphene,

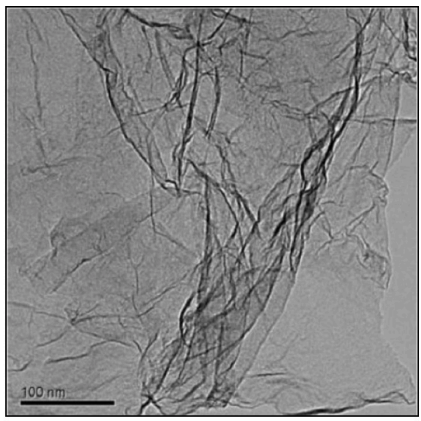

(A)

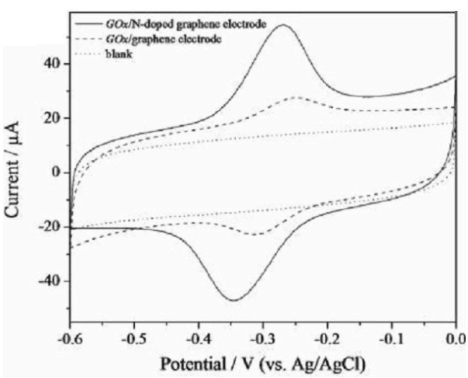

(B)

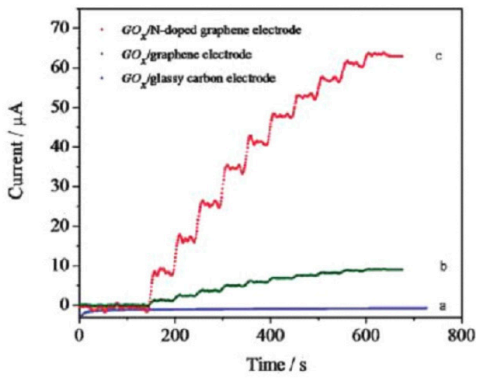

(C)

Figure 14. (A) TEM image of N-doped graphene. (B) Cyclic voltammograms of GOD immobilized on N-doped graphene electrode (solid line) and graphene electrode (dashed line) in N_2-saturated 0.1 M PBS solution (pH 7.0). Dotted line is for the background. Scan rate = 0.05 V s^{-1}. (C) Current–time curves for GOD immobilized on GCE (a), graphene electrode (b), and N-doped graphene electrode (c) at –0.15 V in 0.1 M PBS (pH 7.0) with successive addition of 0.1 mM glucose. Adapted from Ref. 65.

the N-doped graphene-based biosensor exhibited high sensitivity and selectivity, which can be used for glucose biosensing with concentrations as low as 0.01 mM in the presence of interferences such as uric acid and AA.

5. Graphene-Based DNA Biosensor

DNA plays an important role in the storage of genetic information and protein biosynthesis. The detection of sequence-specific DNA has grown rapidly because of its importance in many fields, such as genetics, pathology,

criminology, pharmacogenetics, food safety, and forensics.[156] It is highly desirable to develop DNA detection methods with high sensitivity and selectivity. Compared to the conventional methods developed for the analysis of specific DNA sequences, the electrochemical technique is attractive owing to its high sensitivity, rapid response, easy handling, possibility for real time, and low cost.[157] Nowadays, the electrochemical DNA biosensor has received much attention in the field of DNA sequence detection and has gradually become an important field in the study of molecular biology and biological research.[158] DNA electrochemical biosensors are analytical devices that result from the integration of a sequence-specific probe and an electrochemical signal transducer.[159] Among all kinds of electrochemical DNA sensors, the one based on the direct oxidation of DNA is the simplest.[10]

Because of its unique structure, good biocompatibility, and outstanding electrochemical properties, graphene has generated intense interest in DNA biosensing field. Zhou *et al.* fabricated an electrochemical DNA sensor based on CRGO.[160] It has been found that the anodic potentials of the four free bases (*i.e.*, guanine (G), adenine (A), thymine (T), and cytosine (C)) moved negatively with enhanced peak currents compared with GC and graphite/GC electrodes. The current signals of the four free bases of DNA on the CRGO/GC electrode are all separated efficiently, indicating that CRGO/GC can simultaneously detect four free bases. It has been speculated that the high density of edge-plane-like defective sites that existed on CRGO may be beneficial for accelerating electron transfer between the electrode and species in solution, thus facilitating the simultaneous detection of four free bases at the CRGO/GC. Moreover, CRGO/GC electrode can also efficiently separate the four DNA bases in both ssDNA and double-stranded DNA (dsDNA), which are more difficult to oxidize than free bases, without the need of a prehydrolysis step.

Ambrosi and Pumera reported a stacked graphene nanofibers (SGNFs)-based DNA biosensor for the electrochemical oxidation of DNA bases.[161] The schematic of GS orientation in MWNTs and SGNFs is shown in Figure 15. As for the electrochemical oxidation of DNA bases and ssDNA related to human influenza A(H1N1), the SGNFs-based biosensor exhibited superior electrochemical performance over MWNTs, edge plane pyrolytic graphite (EPPG), graphite microparticles (GMPs), and GC electrodes. For instance, the oxidation signals of all of the four free bases exhibited two to four times higher currents than that observed on CNT-based electrodes. This is attributed to the extraordinarily high number of electrochemically active graphene edges site that existed on the surfaces of SGNFs.

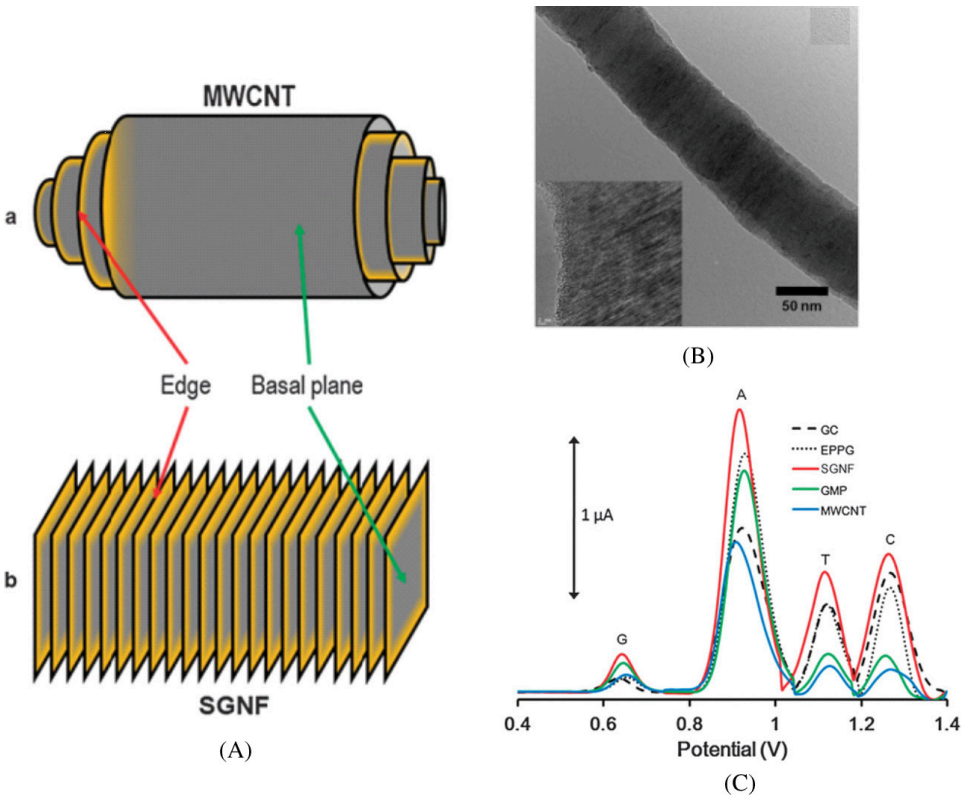

Figure 15. (A) Schematics of GS orientation in MWNTs (a) and SGNFs (b). The highly electroactive edge portion of the sheets is represented in yellow. (B) TEM images of SGNFs. Inset shows the high-resolution TEM of edge of SGNFs. (C) DPVs for a mixture of guanine, adenine, thymine, and cytosine at SGNF (red), GMP (green), and MWNT (blue) electrodes. For comparison, GC (black dashed) and EPPG (black dotted) electrode signals are also shown. Concentrations for the DNA bases: guanine, 4 mM; adenine, 50 mM; thymine and cytosine, 100 mM. Background electrolyte, 50 mM phosphate buffer, pH 7.4. Adapted from Ref. 161.

6. Conclusions and Perspectives

Considered as a "rising star" nanostructured carbon material, graphene has attracted intense interest since its discovery in 2004. Due to its unique properties, such as high surface area, high electrical conductivity, and good biocompatibility, graphene has received considerable interest for potential applications in the fields of bioelectrochemistry. This chapter has highlighted recent progress in the development of electrochemical biosensors based on graphene and graphene-based materials. The outstanding properties and the

unique 2D nature of graphene endow the material superior qualities as an electrode material of the biosensors. For instance, the large surface area of graphene enhances the surface loading of desired biomolecules, and the excellent conductivity is beneficial for enhancement of the electron transfer between biomolecules and the electrode surface. In most cases, the use of graphene can greatly improve the electrochemical performance of biosensors in comparison to other carbonaceous nanomaterial, such as CNT. Although graphene has conclusively been demonstrated to be a very promising material for electrocatalysis and construction of biosensor, there are still many challenges remaining. For example, it is still challenging to develop a reliable and scalable production method for the synthesis of mass-producing identical graphene. In addition, more efforts should also be put into understanding graphene's intrinsic characteristics as well as the underlying mechanisms of electron transfer between biomolecules and graphene, which will be helpful for rational design of better biosensors. Moreover, development of techniques for the functionalization of graphene as a sensing element is also of great value for their applications in biosensors. In general, graphene-based electrochemical biosensors show great promise for future applications in clinical diagnosis, health-care testing, and environmental monitoring.

Acknowledgments

This work was financially supported by National Basic Research Program of China (No. 2011CB935704, No. 2013CB934004), the National Natural Science Foundation of China (No. 21235004, No. 21128005, No. 20901035, No. 21327806, No. 21203126), Natural Science Foundation of Liaoning Province (No. 201202088, LJQ2013112), the European Union Seventh Framework Programme (FP7/2007–2013) under grant agreement No. 260600 ("GlycoHIT"), and Tsinghua University Initiative Scientific Research Program.

References

1. Pumera, M. *Mater. Today* **2011**, *14*, 308.
2. Zhu, Z. G.; Garcia, G. L.; Flewitt, A. J.; Xie, H.; Moussy, F.; Milne, W. I. *Sensors* **2012**, *12*, 5996.
3. Xu, Y. H.; Wang, E. K. *Electrochim. Acta* **2012**, *84*, 62.
4. Paleček, E.; Fojta, M.; Tomschik, M.; Wang, J. *Biosens. Bioelectron.* **1998**, *13*, 621.
5. Rivas, G. A.; Rubianes, M. D.; Rodríguez, M. C.; Ferreyra, N. F.; Luque, G. L.; Pedano, M. L.; Miscoria, S. A.; Parrado, C. *Talanta* **2007**, *74*, 291.

6. Wang, J.; Lin, Y. H. *Trac-Trend Anal. Chem.* **2008**, *27*, 619.
7. Zhang, S.; Wright, G.; Yang, Y. *Biosens. Bioelectron.* **2000**, *15*, 273.
8. Agüí, L.; Yáñez, S. P.; Pingarrón, J. M. *Anal. Chim. Acta* **2008**, *622*, 11.
9. Kochmann, S.; Hirsch, T.; Wolfbeis, O. S. *Trac-Trend Anal. Chem.* **2012**, *39*, 87.
10. Shao, Y. Y.; Wang, J.; Wu, H.; Liu, J.; Aksay, I. A.; Lin, Y. H. *Electroanalysis* **2010**, *22*, 1027.
11. Kuila, T.; Bose, S.; Khanra, P.; Mishrab, A. K.; Kim, N. H.; Lee, J. H. *Biosens. Bioelectron.* **2011**, *26*, 4637.
12. Novoselov, K. S.; Geim, A. K.; Morozov, S. V.; Jiang, D.; Zhang, Y.; Dubonos, S. V.; Grigorieva, I. V.; Firsov, A. A. *Science* **2004**, *306*, 666.
13. Geim, A. K. *Science* **2009**, *324*, 1530.
14. Geim, A. K.; Novoselov, K. S. *Nature Mater.* **2007**, *6*, 183.
15. Chae, H. K.; Perez, D. Y. S.; Kim, J. *Nature* **2004**, *427*, 523.
16. Schadler, L. S.; Giannaris, S. C.; Ajayan, P. M. *Appl. Phys. Lett.* **1998**, *73*, 3842.
17. Zhang, Y. B.; Tan, J. W.; Stormer, H. L.; Kim, P. *Nature* **2005**, *438*, 201.
18. Chen, D.; Li, J. H. *Chem. Rev.* **2012**, *112*, 6027.
19. Chen, D.; Tang, L. H.; Li, J. H. *Chem. Soc. Rev.* **2010**, *39*, 3157.
20. Wang, Y.; Li, Z. H.; Li, J. H.; Lin, Y. H. *Trends in Biotechnol.* **2011**, *29*, 205.
21. Tang, L. H.; Feng, H. B.; Cheng, J. S.; Li, J. H. *Chem. Commun.* **2010**, *46*, 5882.
22. Tang, L. H.; Wang, Y.; Liu, Y.; Li, J. H. *ACS Nano.* **2011**, *5*, 3817.
23. Jiang, H. J. *Small* **2011**, *7*, 2413.
24. Ratinac, K. R.; Yang, W. R.; Gooding, J. J.; Thordarson, P.; Braet, F.; Yun, A. S. *Electroanalysis* **2011**, *23*, 803.
25. Tang, L. H.; Chang, H. X.; Liu, Y.; Li, J. H. *Adv. Funct. Mater.* **2012**, *24*, 3083.
26. Singh, V.; Joung, D.; Zhai, L.; Das, S.; Khondaker, S. I.; Seal, S. *Prog. Mater. Sci.* **2011**, *56*, 1178.
27. Lotya, M.; Hernandez, Y.; King, P. J.; Smith, R. J.; Nicolosi, V.; Karlsson, L. S.; Blighe, F. M.; De, S.; Wang, Z.; McGovern, I. T.; Duesberg, G. S.; Coleman, J. N. *J. Am. Chem. Soc.* **2009**, *131*, 3611.
28. Coraux, J.; Ndiaye, A. T.; Busse, C.; Michely, T. *Nano Lett.* **2008**, *8*, 565.
29. Wintterlin, J.; Bocquet, M. L. *Surf. Sci.* **2009**, *603*, 1841.
30. Li, X.; Cai, W.; Colombo, L.; Ruoff, R. S. *Nano Lett.* **2009**, *9*, 4268.
31. Berger, C.; Song, Z. M.; Li, X. B.; Wu, X. S.; Brown, N.; Naud, C.; Mayou, D.; Li, T. B.; Hass, J.; Marchenkov, A. N.; Conrad, E. H.; First, P. N.; Heer, W. A. *Science* **2006**, *312*, 1191.
32. Zheng, M.; Takei, K.; Hsia, B.; Fang, H.; Zhang, X.; Ferralis, N.; Ko, H.; Chueh, Y. L.; Zhang, Y.; Maboudian, R.; Javey, A. *Appl. Phys. Lett.* **2010**, *96*, 063110.

33. Kuilla, T.; Bhadra, S.; Yao, D. H.; Kim, N. H.; Bose, S.; Lee, J. H. *Prog. Polym. Sci.* **2010**, *35*, 1350.
34. Hummers, W. S.; Offeman, R. E. *J. Am. Chem. Soc.* **1958**, *80*, 1339.
35. Staudenmaier, L. *Ber. Dtsch. Chem. Ges.* **1898**, *31*, 1481.
36. Brodie, B. C. *Ann. Chim. Phys.* **1860**, *59*, 466.
37. Xu, Y. X.; Shi, G. Q. *J. Mater. Chem.* **2011**, *21*, 3311.
38. Cai, M. Z.; Thorpe, D.; Adamson, D. H.; Schniepp, H. C. *J. Mater. Chem.* **2012**, *22*, 24992.
39. Zhu, C. Z.; Guo, S. J.; Fang, Y. X.; Dong, S. J. *ACS Nano.* **2010**, *4*, 2429.
40. Li, D.; Muller, M. B.; Gilije, S.; Kaner, R. B.; Wallace, G. G. *Nat. Nanotechnol.* **2008**, *3*, 101.
41. Cote, L. J.; Silva, R. C.; Huang, J. X. *J. Am. Chem. Soc.* **2009**, *131*, 11027.
42. Guo, H. L.; Wang, X. F.; Qian, Q. Y.; Wang, F. B.; Xia, X. H. *ACS Nano.* **2009**, *3*, 2653.
43. Li, D.; Muller, M. B.; Gilije, S.; Kaner, R. B.; Wallace, G. G. *Nat. Nanotechnol.* **2008**, *3*, 101.
44. Wang, G. X.; Yang, J.; Park, J.; Gou, X. L.; Wang, B.; Liu, H.; Yao, J. *J. Phys. Chem. C* **2008**, *112*, 8192.
45. Zhang, J.; Yang, H.; Shen, G.; Cheng, P.; Zhang, J.; Guo, S. *Chem. Commun.* **2010**, *46*, 1112.
46. Wang, Y.; Shi, Z.; Yin, J. *ACS Appl. Mater. Interf.* **2011**, *3*, 1127.
47. Schniepp, H. C.; Li, J. L.; McAllister, M. J.; Sai, H.; Herrera-Alonso, M.; Adamson, D. H.; Prud'homme, R. K.; Car, R.; Saville, D. A.; Aksay, I. A. *J. Phys. Chem. B* **2006**, *110*, 8535.
48. Liu, N.; Luo, F.; Wu, H. X.; Liu, Y. H.; Zhang, C.; Chen, J. *Adv. Funct. Mater.* **2008**, *18*, 1518.
49. Soldano, C.; Mahmood, A.; Dujardin, E. *Carbon* **2010**, *48*, 2127.
50. Potts, J. R.; Dreyer, D. R.; Bielawski, C. W.; Ruoff, R. S. *Polymer* **2011**, *52*, 5.
51. Huang, L. P.; Wu, B.; Yu, G.; Liu, Y. Q. *J. Mater. Chem.* **2011**, *21*, 919.
52. Kuila, T.; Bose, S.; Mishra, A. K.; Khanra, P.; Kim, N. H.; Lee, J. H. *Prog. Mater. Sci.* **2012**, *57*, 1061.
53. Liu, J. Q.; Tang, J. G.; Gooding, J. J. *J. Mater. Chem.* **2012**, *22*, 12435.
54. Wang, Y.; Li, Y. M.; Tang, L. H.; Lu, J.; Li, J. H. *Electrochem. Commun.* **2009**, *11*, 889.
55. Li, Y. M.; Tang, L. H.; Li, J. H. *Electrochem. Commun.* **2009**, *11*, 846.
56. Li, Y. M.; Lv, X. J.; Lu, J.; Li, J. H. *J. Phys. Chem. C* **2010**, *114*, 21770.
57. Cheng, J. S.; Tang, L. H.; Li, J. H. *J. Nanosci. Nanotechnol.* **2011**, *11*, 5159.
58. Loh, K. P.; Bao, Q. L.; Ang, P. K.; Yang, J. X. *J. Mater. Chem.* **2010**, *20*, 2277.
59. Patil, A. J.; Vickery, J. L.; Scott, T. B.; Mann, S. *Adv. Mater.* **2009**, *21*, 1.
60. Xu, Y. X.; Bai, H.; Lu, G. W.; Li, C.; Shi, G. Q. *J. Am. Chem. Soc.* **2008**, *130*, 5856.

61. Xu, Y. X.; Zhao, L.; Bai, H.; Hong, W. J.; Li, C.; Shi, G. Q. *J. Am. Chem. Soc.* **2009**, *131*, 13490.
62. Hao, R.; Qian, W.; Zhang, L. H.; Hou, Y. L. *Chem. Commun.* **2008**, 6576.
63. Chang, H. X.; Cheng, J. S.; Liu, X. Q.; Gao, J. F.; Li, J. H.; Tao, X. M.; Ding, F.; Zheng, Z. J. *Chem. Eur. J.* **2011**, *17*, 8896.
64. Ayala, P.; Arenal, R.; Rummeli, M.; Rubio, A.; Pichler, T. *Carbon* **2010**, *48*, 575.
65. Wang, Y.; Shao, Y. Y.; Matson, D. W.; Li, J. H.; Lin, Y. H. *ACS Nano* **2010**, *4*, 1790.
66. Shao, Y. Y.; Zhang, S.; Engelhard, M. H.; Li, G. S.; Shao, G. C.; Wang, Y.; Liu, J.; Aksay, I. A.; Lin, Y. H. *J. Mater. Chem.* **2010**, *20*, 7491.
67. Artiles, M. S.; Rout, C. S.; Fisher, T. S. *Adv. Drug Deliver. Rev.* **2011**, *63*, 1352.
68. Zhou, M.; Zhai, Y. M.; Dong, S. J. *Anal. Chem.* **2009**, *81*, 5603.
69. Liu, Q.; Shi, J. B.; Jiang, G. B. *Trac-Trend Anal. Chem.* **2012**, *37*, 1.
70. Chou, A.; Böcking, T.; Singh, N. K.; Gooding, J. J. *Chem. Commun.* **2005**, 842.
71. Pumera, M.; Ambrosi, A.; Bonanni, A.; Chng, E. L. K.; Poh, H. L. *Trac-Trend Anal. Chem.* **2010**, *29*, 954.
72. Yang, S. L.; Guo, D. Y.; Su, L.; Yu, P.; Li, D.; Ye, J. S.; Mao, L. Q. *Electrochem. Commun.* **2009**, *11*, 1912.
73. Lin, W. J.; Liao, C. S.; Jhang, J. H.; Tsai, Y. C. *Electrochem. Commun.* **2009**, *11*, 2153.
74. Tang, L. H.; Wang, Y.; Li, Y. M.; Feng, H. B.; Lu, J.; Li, J. H. *Adv. Funct. Mater.* **2009**, *19*, 2782.
75. McCreery, R. L. *Chem. Rev.* **2008**, *108*, 2646.
76. Alwarappan, S.; Erdem, A.; Liu, C.; Li, C. Z. *J. Phys. Chem. C* **2009**, *113*, 8853.
77. Niina J. Ronkainen; Halsall, H. B.; Heineman, W. R. *Chem. Soc. Rev.* **2010**, *39*, 1747.
78. Kotanen, C. N.; Moussy, F. G.; Carrara, S.; Elie, A. G. *Biosens. Bioelectron.* **2012**, *35*, 14.
79. Sassolas, A.; Blum, L. J.; Bouvier, B. D. L. *Biotechnol. Adv.* **2012**, *30*, 489.
80. Clark, L. C.; Lyons, C. *Ann. NY. Acad. Sci.* **1962**, *102*, 29.
81. Updike, S. J.; Hicks, G. P. *Nature* **1967**, *214*, 986.
82. Freire, R. S.; Pessoa, C. A.; Mello, L. D.; Kubota, L. T. *J. Braz. Chem. Soc.* **2003**, *14*, 230.
83. Eddowes, M. J.; Hill, H. A. O. *J. Chem. Soc. Chem. Commun.* **1977**, 71.
84. Yeh, P.; Kuwana, T. *Chem. Lett.* **1977**, 1145.
85. Karyakin, A. A. *Bioelectrochem.* **2012**, *88*, 70.
86. Gorton, L.; Lindgren, A.; Larsson, T.; Munteanu, F. D.; Ruzgas, T.; Gazaryan, I. *Anal. Chim. Acta* **1999**, *400*, 91.
87. Park, B.-W.; Yoon, D. Y.; Kim, D. S. *Biosens. Bioelectron.* **2010**, *26*, 1.
88. Li, H. H.; Liu, S. Q.; Dai, Z. H.; Bao, J. C.; Yang, X. D. *Sensors* **2009**, *9*, 8547.

89. Jacobs, C. B.; Peairs, M. J.; Venton, B. J. *Anal. Chim. Acta* **2010**, *662*, 105.
90. Ahammad, J. S.; Lee, J. J.; Rahman, M. A. *Sensors* **2009**, *9*, 2289.
91. Zhang, Q.; Wu, S. Y.; Zhang, L.; Lu, J.; Verproot, F.; Liu, Y.; Xing, Z. Q.; Li, J. H.; Song, X. M. *Biosens. Bioelectron.* **2011**, *26*, 2632.
92. Zhang, Q.; Qiao, Y.; Zhang, L.; Wu, S. Y.; Zhou, H.; Xu, J. W.; Song, X. M. *Electroanalysis* **2011**, *23*, 900.
93. Xu, Y. X.; Bai, H.; Lu, G. W.; Li, C.; Shi, G. Q. *J. Am. Chem. Soc.* **2008**, *130*, 5856.
94. Yue, R.; Lu, Q.; Zhou, Y. K. *Biosens. Bioelectron.* **2011**, *26*, 4436.
95. Zeng, Q.; Cheng, J. S.; Tang, L. H.; Liu, X. F.; Liu, Y. Z.; Li, J. H.; Jiang, J. H. *Adv. Funct. Mater.* **2010**, *20*, 3366.
96. Wen, W.; Chen, W.; Ren, Q. Q.; Hu, X. Y.; Xiong, H. Y.; Zhang, X. H.; Wang, S. F.; Zhao, Y. D. *Sensor Actuat. B-Chem* **2012**, *166–167*, 444.
97. Liu, J. Y.; Han, L.; Wang, T. S.; Hong, W.; Liu, Y. Q.; Wang, E. K. *Chem. Asian J.* **2012**, *7*, 2824.
98. Shan, C. S.; Yang, H. F.; Han, D. X.; Zhang, Q. X.; Ivaska, A.; Niu, L. *Biosens. Bioelectron.* **2010**, *25*, 1504.
99. Zheng, D.; Vashist, S. K.; Rubeaan, K. A.; Luong, J. H. T.; Sheu, F. S. *Talanta* **2012**, *99*, 22.
100. Moyo, M.; Okonkwo, J. O.; Agyei, N. M. *Sensors* **2012**, *12*, 923.
101. Teles, F. R. R.; Fonseca, L. P. *Mat. Sci. Eng. C* **2008**, *28*, 1530.
102. Stankovich, S.; Dikin, D. A.; Dommett, G. H. B.; Kohlhaas, K. M.; Zimney, E. J.; Stach, E. A.; Piner, R. D.; Nguyen, S. T.; Ruoff, R. S. *Nature.* **2006**, *442*, 282.
103. Xu, H. F.; Dai, H.; Chen, G. N. *Talanta* **2010**, *81*, 334.
104. Huang, K. J.; Miao, Y. X.; Wang, L.; Gan, T.; Yu, M.; Wang, L. L. *Process Biochem.* **2012**, *47*, 1171.
105. Wu, J. F.; Xu, M. Q.; Zhao, G. C. *Electrochem. Commun.* **2010**, *12*, 175.
106. Ruan, C. X.; Li, T. T.; Niu, Q. J.; Lu, M.; Lou, J.; Gao, W. M.; Sun, W. *Electrochim. Acta* **2012**, *64*, 183.
107. Wang, L.; Zhang, X. H.; Xiong, H. Y.; Wang, S. F. *Biosens. Bioelectron.* **2010**, *26*, 991.
108. Zhou, Y.; Liu, S.; Jiang, H. J.; Yang, H.; Chen, H. Y. *Electroanalysis* **2010**, *22*, 1323.
109. Kang, X. H.; Wang, J.; Wu, H.; Aksayc, I. A.; Liu, J.; Lin, Y. H. *Biosens. Bioelectron.* **2009**, *25*, 901.
110. Su, X. F.; Ren, J.; Meng, X. W.; Ren, X. L.; Tang, F. Q. *Analyst* **2013**, *138*, 1459.
111. Liu, S.; Tian, J. Q.; Wang, L.; Luo, Y. L.; Lu, W. B.; Sun, X. P. *Biosens. Bioelectron.* **2011**, *26*, 4491.
112. Qiu, J. D.; Huang, J.; Liang, R. P. *Sensor Actuat. B-Chem.* **2011**, *160*, 287.
113. Guo, H. C.; Sun, H.; Zhao, X. S. *Sensor Actuat. B-Chem.* **2012**, *164*, 82.

114. Zhang, L. L.; Cheng, H. H.; Zhang, H. M.; Qu, L. T. *Electrochim. Acta* **2012**, *65*, 122.
115. Li, H. J.; Chen, J.; Han, S.; Niu, W. X.; Liu, X. Q.; Xu, G. B. *Talanta* **2009**, *79* 165.
116. Chen, X.; Fu, C. L.; Yang, W. S. *Analyst* **2009**, *134*, 2135.
117. Wang, G. X.; Qian, Y.; Cao, X. X.; Xia, X. H. *Electrochem. Commun.* **2012**, *20*, 1.
118. Liu, K. P.; Zhang, J. J.; Yang, G. H.; Wang, C. M.; Zhu, J. J. *Electrochem. Commun.* **2010**, *12*, 402.
119. Shutava, T. G.; Kommireddy, D. S.; Lvov, Y. M. *J. Am. Chem. Soc.* **2006**, *128*, 9926.
120. Zeng, G. H.; Xing, Y.; Gao, J.; Wang, Z. Q.; Zhang, X. *Langmuir* **2010**, *26*, 15022.
121. You, C. C.; Chompoosor, A.; Rotello, V. M. *Nano Today* **2007**, *2*, 34.
122. Zhang, X. Q.; Guo, Q.; Cui, D. X. *Sensors* **2009**, *9*, 1033.
123. Guo, S. J.; Dong, S. J. *Trac-Trend Anal. Chem.* **2009**, *28*, 96.
124. Chen, Y.; Li, Y.; Sun, D.; Tian, D. B.; Zhang, J. R.; Zhu, J. J. *J. Mater. Chem.* **2011**, *21*, 7604.
125. Wang, Y.; Zhang, S.; Li, Z. H.; Wang, J.; Li, J. H.; Lin, Y. H. *J. Mater. Chem.* **2011**, *21*, 5319.
126. Wang, K.; Li, H. N.; Wu, J.; Ju, C.; Yan, J. J.; Liu, Q.; Qiu, B. J. *Analyst* **2011**, *136*, 3349.
127. Gu, Z.; Yang, S. P.; Zai, J. L.; Sun, X. L.; Guang, L. W.; Yin, J. F.; Jun, K. L. *Electrochim. Acta* **2011**, *56*, 9162.
128. Jang, H. D.; Kim, S. K.; Chang, H.; Roh, K. M.; Choi, J. W.; Huang, J. X. *Biosens. Bioelectron.* **2012**, *38*, 184.
129. Sun, J. Y.; Huang, K. J.; Zhao, S. F.; Fan, Y.; Wu, Z. W. *Bioelectrochem.* **2011**, *82*, 125.
130. Zhou, K. F.; Zhu, Y. H.; Yang, X. L.; Luo, J.; Li, C. Z.; Luanb, S. R. *Electrochim. Acta* **2010**, *55*, 3055.
131. Zhou, K. F.; Zhu, Y. H.; Yang, X. L.; Li, C. Z. *Electroanalysis* **2011**, *23*, 862.
132. Huang, K. J.; Niu, D. J.; Liu, X.; Wu, Z. W.; Fan, Y.; Chang, Y. F.; Wu, Y. Y. *Electrochim. Acta* **2011**, *56*, 2947.
133. Luo, Z. M.; Yuwen, L.; Han, Y. J.; Tian, J.; Zhu, X. R.; Weng, L. X.; Wang, L. H. *Biosens. Bioelectron.* **2012**, *36*, 179.
134. Feng, Q. L.; Liu, K. P.; Fu, J. J.; Zhang, Y. Z.; Zheng, Z. X.; Wang, C. M.; Du, Y. L.; Ye, W. C. *Electrochim. Acta* **2012**, *60*, 304.
135. Liu, T.; Su, H.; Qu, X.; Ju, P.; Cui, L.; Ai, S. *Sensor Actuat. B-Chem.* **2011**, *160*, 1255.
136. Sheng, Q. L.; Wang, M. Z.; Zheng, J. B. *Sensor Actuat. B-Chem.* **2011**, *160* 1070.
137. Dey, R. S.; Raj, C. R. *J. Phys. Chem. C* **2010**, *114*, 21427–21433.

138. Wang, K.; Liu, Q.; Guan, Q. M.; Wu, J.; Li, H. N.; Yan, J. J. *Biosens. Bioelectron.* **2011**, *26*, 2252.
139. Zhang, J. L.; Zhang, F.; Yang, H. J.; Huang, X. L.; Liu, H.; Zhang, J. Y.; Guo, S. W. *Langmuir* **2010**, *26*, 6083.
140. Liu, Y.; Yu, D. S.; Zeng, C.; Miao, Z. C.; Dai, L. M. *Langmuir* **2010**, *26*, 6158.
141. Sun, W.; Guo, Y. Q.; Li, T. T.; Ju, X. M.; Lou, J.; Ruan, C. X. *Electrochim. Acta* **2012**, *75*, 381.
142. Zhang, Q.; Qiao, Y.; Hao, F.; Zhang, L.; Wu, S. Y.; Li, Y.; Li, J. H.; Song, X. M. *Chem. Eur. J.* **2010**, *16*, 8133.
143. Alwarappan, S.; Liu, C.; Kumar, A.; Li, C. Z. *J. Phys. Chem. C* **2010**, *114*, 12920.
144. Wu, P.; Shao, Q.; Hu, Y. J.; Jin, J.; Yin, Y. J.; Zhang, H.; Cai, C. X. *Electrochim. Acta* **2010**, *55*, 8606.
145. Unnikrishnan, B.; Palanisamy, S.; Chen, S. M. *Biosens. Bioelectron.* **2013**, *39*, 70.
146. Manjunath, R.; Suresh, G. S.; Melo, J. S.; Souz, S. F. D.; Venkatesha, T. V. *Talanta* **2012**, *99*, 302.
147. Bai, L. J.; Yuan, R.; Chai, Y. Q.; Yuan, Y. L.; Wang, Y.; Xie, S. B. *Chem. Commun.* **2012**, *48*, 10972.
148. Cheng, Q.; Tang, J.; Ma, J.; Zhang, H.; Shiny, N.; Qin, L. C. *Phys. Chem. Chem. Phys.* **2011**, *13*, 17615.
149. Lee, S. H.; Lee, D. H.; Lee, W. J.; Kim, S. O. *Adv. Funct. Mater.* **2011**, *21*, 1338.
150. Chen, J. L.; Zheng, X. L.; Miao, F. J.; Zhang, J. N.; Cui, X. Q.; Zheng, W. T. *J. Appl. Electrochem.* **2012**, *42*, 875.
151. Zhang, Q.; Yang, S. J.; Zhang, J.; Zhang, L.; Kang, P. L.; Li, J. H.; Xu, J. W.; Zhou, H.; Song, X. M. *Nanotechnology* **2011**, *22*, 494010.
152. Mani, V.; Devadas, B.; Chen, S. M. *Biosens. Bioelectron.* **2013**, *41*, 309.
153. Panchakarla, L. S.; Govindaraj, A.; Rao, C. N. R. *Inorg Chim Acta* **2010**, *363*, 4163.
154. Wen, Z. H.; Cui, S. M.; Pu, H. H.; Mao, S.; Yu, K. H.; Fen, X. L.; Chen, J. H. *Adv. Mater.* **2011**, *23*, 5445.
155. Liu, H. T.; Liu, Y. Q.; Zhu, D. B. *J. Mater. Chem.* **2011**, *2011*, 3335.
156. Teles, F. R. R.; Fonseca, L. P. *Talanta* **2008**, *77*, 606.
157. Odenthal, K. J.; Gooding, J. J. *Analyst* **2007**, *132*, 603.
158. Lucarelli, F.; Tombelli, S.; Minunni, M.; Marrazza, G.; Mascini, M. *Anal. Chim. Acta* **2008**, *609*, 139.
159. Liu, A. L.; Wang, K.; Weng, S. H.; Lei, Y.; Lin, L. Q.; Chen, W.; Lin, X. H.; Chen, Y. Z. *Trac-Trend Anal. Chem.* **2012**, *37*, 101.
160. Zhou, M.; Zhai, Y. M.; Dong, S. J. *Anal. Chem.* **2009**, *81*, 5603.
161. Ambrosi, A.; Pumera, M. *Phys. Chem. Chem. Phys.* **2010**, *12*, 8943.

Chapter 5

Graphene and Carbon Nanotube-Based Nanomaterial: Application in Biomedical and Energy Research

Hemant Kumar, Debabrata Pramanik*, Santosh Mogurampelly*,[a], V. Vasumathi[†], Bidisha Nandy* and Prabal K. Maiti*,[‡]*

**Centre for Condensed Matter Theory, Department of Physics*
Indian Institute of Science, Bangalore 560012, India
[†]REQUIMTE, Department of Chemistry, University of Porto
Rua do Campo Alegre 687, 4168–007 Porto, Portugal

1. Introduction 190
2. Graphene–Nucleic Acid Composites 192
   2.1. Functionalization of graphene 192
   2.2. Adsorption of nucleic acids on graphene 193
   2.3. Biocompatibility of graphene 197
3. DNA–Carbon Nanotube Composite 197
   3.1. Structure and properties 198
   3.2. Influence of temperature on oligonucleotide adsorption 200
   3.3. Applications 202
      3.3.1. Solubilization and sorting of carbon nanotube 202
      3.3.2. DNA–CNT hybrid in sensing mechanism 202
      3.3.3. Supercapacitors 204
      3.3.4. Cellular delivery of DNA strands 204
4. Carbon Nanotube and Dendrimer Composite 206
   4.1. Covalent functionalization 207
      4.1.1. "Grafting to" approach 207
      4.1.2. "Grafting from" approach 209
   4.2. Non-covalent functionalization 211

[a] Present address: Department of Physics, University of Rome "La Sapienza", Ple A. Moro 2, 00185, Rome, Italy.
[‡] Corresponding author. E-mail: maiti@physics.iisc.ernet.in

5. Carbon Nanomaterials for Energy Conversion 213
5.1. Hydrogen storage 213
5.1.1. Historical development 216
5.1.2. Improving hydrogen storage by chemical functionalization 217
5.2. Blue energy 218
5.3. Voltage generation through flow 220
5.4. Energy-efficient nanoelectrical devices 222
5.4.1. Carbon nanotube-based FETs 223
5.4.2. Nanotubes and graphene as interconnectors 225
5.4.3. Flexible electronics: Thin film transistor 226
5.4.4. Photovoltaic devices 226
6. Conclusions and Outlook 227
Acknowledgments 229
References 229

1. Introduction

In the recent years, there have been growing interest in scientific communities in the field of carbon nanomaterials. Graphene, carbon nanotubes (CNTs), fullerene, nanoribbons, nanocone are the few known forms of carbon nanomaterials. Customizable physical and chemical properties via external sources make carbon nanomaterials a very suitable candidate for various nanodevices like chemical and biosensors, fuel cells, solar cells, batteries, *etc.* Among the various carbon nanomaterials, graphene and CNTs have attracted great attention for a wide variety of sectors.

Graphene is a free-standing two-dimensional monolayer of carbon atoms discovered nearly a decade ago by A. K. Geim and K. S. Novoselov for which they were awarded Nobel prize in physics in 2010. The crystal structure of graphene contains carbon atoms that are arranged into a honeycomb lattice. Graphene is found to have tremendous potential in various nanotechnological applications due to its extraordinary physiochemical, electronic, thermal, and mechanical properties. Graphene is a semi-metal with zero bandgap. The linear dispersion relation and zero rest mass of Dirac fermions in graphene are some of the very important properties. Numerous other important properties include a high mechanical strength (~1 TPa), large charge carrier mobility (~200,000 cm^2/Vs), high thermal conductivity (~5000 W/mK), very high sensitivity, excellent transport properties, extremely large specific surface area (2630 m^2/g), high optical transmittance, room temperature quantum Hall effect, *etc.*[1–3] Graphene has significant potential to use it in the biomedical

field also. Although graphene research has reached its peak in a short span of nine years, yet, more efforts are required to unravel its properties and applications. Writing in a review article in 2007, A. K. Geim speculated that *It has been just over two years since graphene was first reported, and despite remarkably rapid progress, only the very tip of the iceberg has been uncovered so far.*

CNTs are allotropes of carbon which are tubular in shape and made of graphite. The primary bonding in various carbon allotropes, such as graphite, carbon fibers, and nanotubes, is the sp^2 bonding between carbons. Despite the fact that primary bonding in graphite, carbon fibers, and nanotubes is the same, nanotubes differ from the other carbon forms by their unique morphology and defect structure. This cylindrical nanostructure can have a length-to-diameter ratio greater than 1,000,000 which is significantly larger than for any other material. Because of sp^2-bond, CNTs provide the strongest bonding in nature. In this one-dimensional nanostructure, each carbon atom is still threefold coordinated without any dangling bonds and this property makes CNT a popular building block for many prototype nanodevices like field-effect transistors (FETs), metallic wires, *etc.* CNTs are classified into two types, *viz.,* single walled carbon nanotubes (SWNT) and multiple walled carbon nanotubes (MWNT), which differ in the arrangement of their graphene cylinders. Various forms of carbon nanomaterials are shown in Figure 1. Similar to graphene, CNT has inherently high mechanical strength, electrical, and thermal conductivity. The huge applications landscape of CNTs include broad areas of nanoelectronics, energy storage, nanocomposites, sensors, field emission, biotechnology, and other miscellaneous fields.

This chapter aims to give a comprehensive overview of the recent developments on various important applications of graphene and CNT-based research. The organization of this chapter is as follows: In Section 2, we have

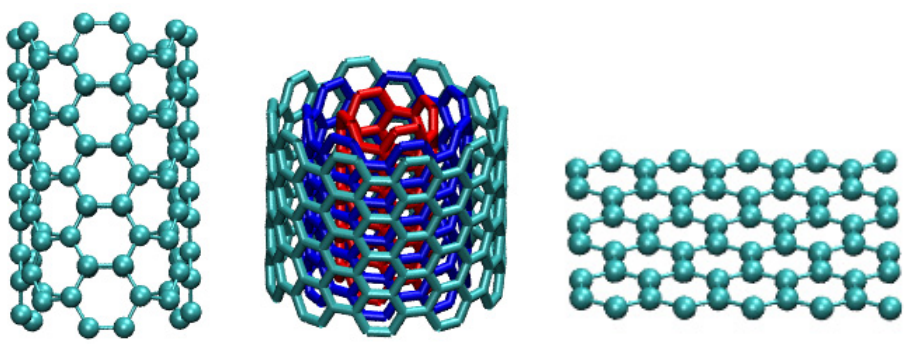

Figure 1. Various forms of carbon nanomaterials.

described the use of graphene in biomedical field, focusing on the interaction between small interfering ribonucleic acid (siRNA) and graphene. We discuss functionalization of graphene, biocompatibility of graphene for medical applications, and finally our simulation results of siRNA unzipping on graphene surface in detail. In Section 3, we discuss structural properties of DNA–CNT composite nanomaterial and some of their applications. Section 4 describes the functionalization of CNTs by dendrimer. This interaction has tremendous applications in various fields. This section also gives a detail overview as well as our simulation results on different approaches for functionalizing the CNT with dendrimer and their applicability. In section 5, we have described various applications of CNT and graphene in the field of hydrogen storage, energy harvesting, energy conversion devices along with nanoelectronics. We highlight the use of these materials in the field of efficient energy conservation.

2. Graphene–Nucleic Acid Composites

Applications of graphene ranges from engineering to medicine. Surface functionalization of graphene enhances its use in wide variety of applications in nanotechnology. Nucleic acids are found to adsorb on the surface of graphene in a specific way that opens gate for applications in bioengineering and medicine. However, a comprehensive understanding of the nucleic acid binding properties is required for such applications.

2.1. Functionalization of graphene

Functionalization of graphene is essential to enhance its scope of applicability in nanotechnology where graphene is to be interfaced with other moieties.[4,5] However, when graphene is functionalized, few important properties, such as electrical and mechanical properties, are modulated due to either change in carbon's hybridization state or dipole interaction or orbital hybridization with interfacing molecule.[6] Functionalization can be broadly divided into two main categories: (i) covalent and (ii) non-covalent functionalization.[7] Covalent functionalization involves either a direct covalent attachment of another atom to sp^2-hybridized carbon atom of graphene or substitution of carbon atom with other atom.[6] This introduces change of carbon hybridization from sp^2-to-sp^3 and causes disturbance in π-electron cloud. Therefore, there will be a considerable change in the electronic properties of graphene in covalent functionalization. Non-covalent functionalization can be achieved by several means, including van der Waals interaction, physisorption, *etc.*

In this case, the sp^2 network does not get affected but changes the doping density, electron-hole puddle, *etc.* Materials like inorganic nanostructures, polymers, biomaterials, metal organic frameworks, *etc.*, can be used as functionalizing agents to synthesize graphene composites. Specific method of functionalization and functionalizing material can be chosen depending on the application. For instance, soluble graphene layers are generated from the reaction of graphite fluoride with alkyl lithium reagents[8] via covalent functionalization of graphene with alkyl chains. Such covalently functionalized graphene is soluble in organic solvents such as carbon tetrachloride (CCl_4), dichloromethane (CH_2Cl_2), and tetrahydrofuran ($(CH_2)_4O$).[9,10]

2.2. Adsorption of nucleic acids on graphene

Recent experiments have demonstrated that graphene can be potentially used in DNA sequencing.[11–13] Therefore, basic understanding of the interaction of nucleic acids with graphene[14–17] is essential for such applications. Several attempts have been made to study the properties of nucleic acid interaction with graphene.[14,17–21] However, the interaction between graphene and siRNA/DNA has not been understood completely. siRNA molecules are a class of double stranded non-coding RNA which are typically 21 to 23 nucleotides in length. The properties of siRNA are actively being studied due to their potential influence on cell functionality and applications in medicine to achieve RNA interference (RNAi).[22–24]

Graphene is a partially hydrophobic molecule in the sense that its faces are highly hydrophobic whereas its edges can be hydrophilic in nature depending on the functionalization. Thus, graphene has the ability to pass through hydrophobic lipid bilayer and can also interact with the hydrophilic head groups. Dispersion interaction, including π–π stacking, serves as the major attractive interactions between the non-polar molecules.[25] The importance of dispersion interactions has been verified recently in analyzing the structure and energetics of the graphene–nucleobase complexes[26] and in studying the unzipping and translocation of siRNA with SWNT.[15,27]

In our recent work,[26] a very unusual phenomena of complete siRNA unzipping and binding on graphene substrate was reported as shown in Figure 2. siRNA unzips and binds to graphene and forms graphene–siRNA composite. siRNA unzipping is very important in the context of RNAi therapeutics where a short siRNA enters into cell and gets unzipped for further action. Understanding siRNA unzipping kinetics through graphene also offers an alternate route to nanopore-assisted unzipping where an electric field is applied to translocate (double-stranded) dsRNA/dsDNA. For the

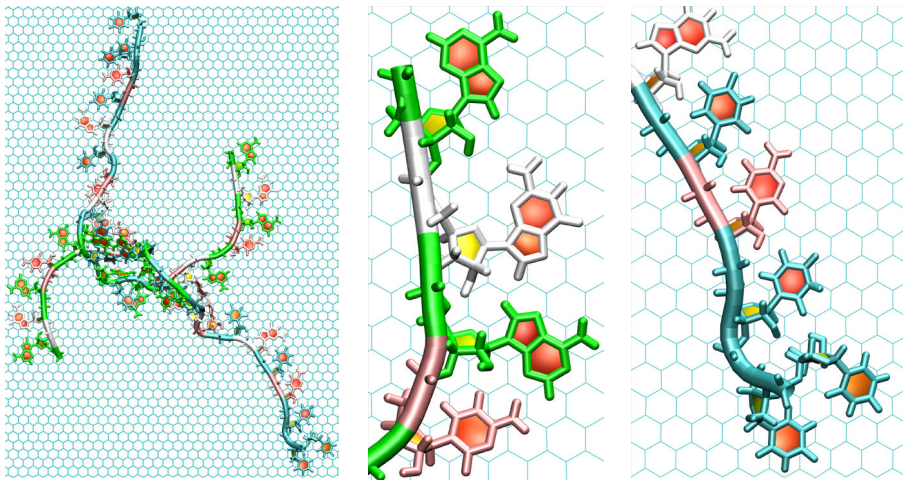

Figure 2. siRNA unzipping and binding on graphene: (a) Snapshot of siRNA on graphene after optimum binding, (b) and (c) shows the zoomed part of the completely unzipped siRNA strands whose bases are in π–π interaction with graphene. Reprinted from Ref. 26 with permission. Copyright © 2012 American Institute of Physics.

initiation of unzipping process on graphene, it takes almost 3 ns at 300 K and less than 1 ns at 340 K. Once the unzipping process is started, the strong van der Waals interaction between graphene and siRNA forces the rapid unzipping of siRNA. Unzipping time follows Arrhenius behavior and allows us to get an estimate of the energy barriers for the siRNA unzipping. Estimation of the unzipping time (τ) is performed from the unzipping probability distributions (f_{bb}) at three different temperatures as shown in Figure 3. The plot gives rise to τ = 9.8 ns, 8.4 ns, and 5.0 ns at temperatures 290 K, 300 K, and 340 K, respectively. Fit of unzipping time as a function of temperature to $\tau = \tau_0 e^{(E_a/k_{BT})}$ gives τ_0 to be 100.8 ps and the activation energy, E_a to be 2.637 kcal/mol or 0.114 eV. Plot of ln τ versus 1/T and the fit is shown in the inset of Figure. 3. The stable graphene–siRNA hybrid may also be used for efficient delivery of siRNA. The complex may penetrate the hydrophobic regions of the bilayer due to hydrophobicity of graphene. Inside the cell, the graphene–siRNA may remain as complex between graphene and two single stranded RNA (ssRNA) chains. One of the chains might easily dissociate from the complex whenever a competitive messenger RNA (mRNA) chain approaches the complex. This can silence the required gene. However, to be more effective and ease of forming graphene–siRNA composite, graphene and its

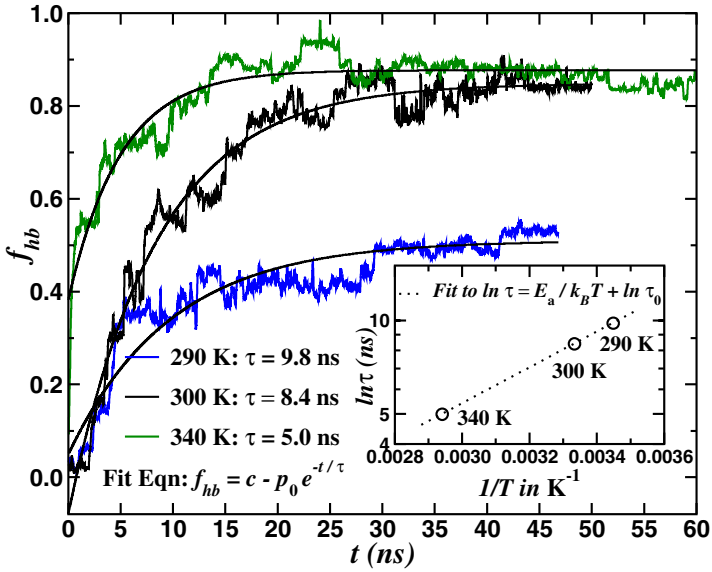

Figure 3. siRNA kinetics on graphene: Unzipping probability denoted by the fraction of broken WC H-bonds, f_{hb} as a function of time at different temperatures. Reprinted from Ref. 26 with permission. Copyright © 2012 American Institute of Physics.

derivatives such as graphene oxide (GO), reduced graphene oxide (rGO) can be functionalized. Recently, *in vivo* experiments showed that functionalized GO with polyethyleneimine (PEI) and polyethyleneglycol (PEG) is more effective to load siRNA and deliver it to reduce the expression of Stat3 gene in mice.[28] It is also shown that GO-PEI-PEG-siRNA composite is less toxic to the mice cell and offers high stability in physiological solutions. Another interesting observation is that dsDNA of same sequence as siRNA except thymine in place of uracil has less unzipping and less binding on graphene.[26] In Figure 4, we show the instantaneous snapshots of the graphene–dsDNA composite as dsDNA binds to graphene over nanosecond timescale. The binding kinetics follows same sequence as in the siRNA binding to graphene: unzipped base pairs at the two sticky ends first bind to the aromatic rings of the graphene sheet through π–π stacking. This binding helps unzipping of few more base pairs at both the ends which helps facilitate further binding and unzipping of the dsDNA. However, unzipping is far less as compared to the siRNA binding as can be seen from Figures 2 and 4. To get an understanding of this differential binding affinity of siRNA and dsDNA to graphene, we have also computed the binding energy of the siRNA–graphene

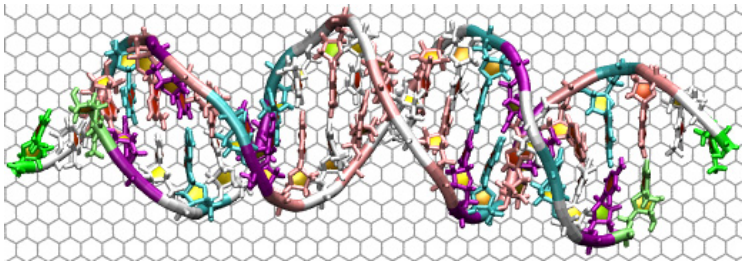

(a) 0 ns

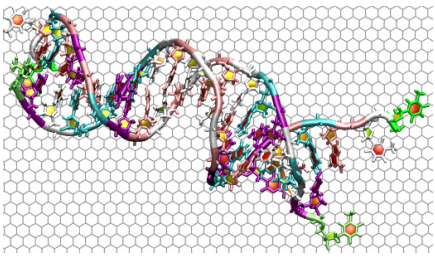

(b) 20 ns

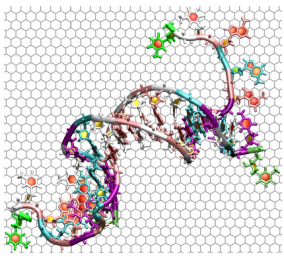

(c) 40 ns

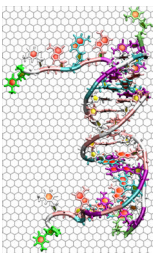

(d) 60 ns

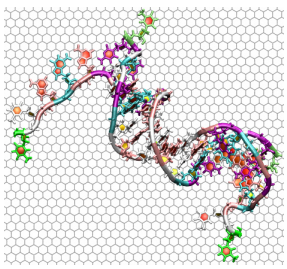

(e) 75 ns

Figure 4. Adsorption of dsDNA on graphene.

and dsDNA–graphene complex using dispersion corrected density functional theory (DFT) method (D-DFT) using ω B97XD/6-31G** method. It was found that graphene–uridine complex has stronger binding affinity in the order of −22.26 kcal/mol compared to the binding energy of the graphene–thymidine complex which is in the order of −20.30 kcal/mol.[26] The stronger binding of the uracil bases with graphene drives stronger unzipping of siRNA on graphene compared to dsDNA. Note that inclusion of sugar in the D-DFT calculation gives the interaction energy of nucleobases with graphene as *G*>*A*>*U*>*T*>*C*. This trend is in contrast to the binding energy trend of *G*>*A*>*C*>*T*>*U* when sugar is not included in the D-DFT calculation.[29]

This differential binding affinity of siRNA and dsDNA to graphene can have important application and could be used to detect or separate siRNA and dsDNA molecules.

2.3. Biocompatibility of graphene

Graphene and siRNA composite has to be biocompatible in order to be used in medical applications. Chemically unmodified graphene is known to be toxic to the cell environment.[30,31] To the best of our knowledge, so far there are no experimental studies on the biocompatibility of graphene–siRNA composite. However, recent experiments have demonstrated that chemically altered graphene sheets may be biocompatible to the cell.[32,33] *In vivo* experiments showed that PEG (polyetheleneglycol)ylated graphene is not toxic to mice cells at a dose of 20 mg/kg studied by blood biochemistry, histo-logical examinations, and hematological analysis.[33] These preliminary experimental studies of graphene biocompatibility suggests that a good choice of functionalization of graphene is non-toxic and therefore can be used in biomedical applications. However, much more *in vivo* studies are needed for a complete understanding of the biocompatibility of functionalized graphene for biomedical applications.

3. DNA–Carbon Nanotube Composite

DNA–carbon nanotube (DNA–CNT) composite nanomaterial has emerged to be very useful for various nanotechnological applications in recent years. Recent studies have shown that DNA and SWNT form a stable hybrid.[34–36] nanomaterial. This hybrid nanomaterial possesses many unique physical and electronic properties. It can be used in many applications such as chemical[37] and biomolecular[38] sensor, dispersion and sorting of SWNT,[39,40] cell delivery system,[41] sequencing of DNA.[42] To properly make use of this novel nanomaterial, we need to have a clear understanding about structure and different properties of this nanomaterial. This has led the scientists worldwide to study various microscopic properties of this hybrid structure. Lots of experimental and computational studies of DNA–CNT hybrid structure have been carried out in recent times. These studies have explored various properties about this hybrid structure like how DNA gets wrapped around CNT surface, binding mechanism, various wrapping conformations, influence of temperature on binding *etc.* In this section, we present various structures and properties of DNA–SWNT hybrid and highlight the potential applications of this novel nanomaterial.

3.1. Structure and properties

Recent experimental studies[40,43,44] using atomic force microscopy (AFM) on DNA–SWNT hybrid structure have reported a very interesting result about the hybrid structure. The AFM images Figure 5 have shown that there are bands on this hybrid structure with high and low regions in an alternating manner. These bands are spaced uniformly on the structure. This observation leads to speculation that the DNA strands wrapped helically on the SWNT surface and formed this hybrid structure. For getting better understanding of this structure, molecular dynamics (MD) studies have been performed with ssDNA and SWNT in the aqueous environment. MD studies[36,39,45] have revealed that the oligonucleotides are spontaneously adsorbed onto the CNT surface via π–π stacking and formed a stable structure at equilibrium condition. This binding interaction takes place between the aromatic nucleic bases and the CNT surface. The hydrophobic nucleic bases are adsorbed onto the CNT surface and the hydrophilic sugar phosphate backbone is exposed to the water environment. Thus, ssDNA–SWNT hybrid is made soluble in water and forms a stable structure.

The MD simulation is generally carried out at room temperature at ≈300 K. When the simulation of ssDNA and SWNT is performed, the

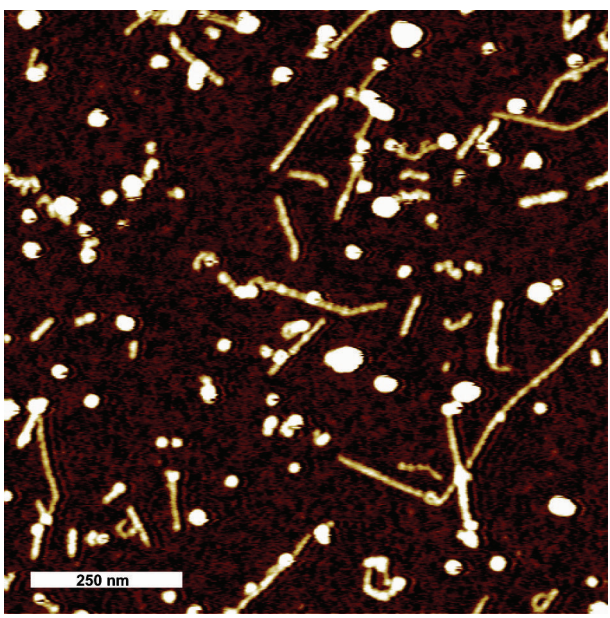

Figure 5. AFM images of CNT wrapped with oligonucleotides. Reprinted from Ref. 43 with permission. Copyright © 2008 American Chemical Society.

ssDNA wraps around the nanotube surface. During the course of hybrid structure formation, the system tries to reach an energetically favorable state as well as steady state in equilibrium conditions. Due to the existence of several low energy conformations of oligonucleotides, the ssDNA is trapped in one of the local energy minima during the simulation at room temperature. The final conformation not necessarily achieves the global energy minima after typical few tens nanosecond long MD simulations. Using replica exchange molecular dynamics (REMD),[46] this problem can be addressed more efficiently. In REMD simulation, a system traverse the whole conformational sample space. Recent REMD study for ssDNA–SWNT system has reported[47] that six different conformations exist for such hybrid structure. The free energies of these six conformations are shown in Figure 6. The figure shows that among six different conformations, the structure with U-looped shape is the energetically most favorable one. Thus, REMD study provides more deeper understanding and more elaborate pictures about the DNA–SWNT composite structure. Although there are numerous reports on

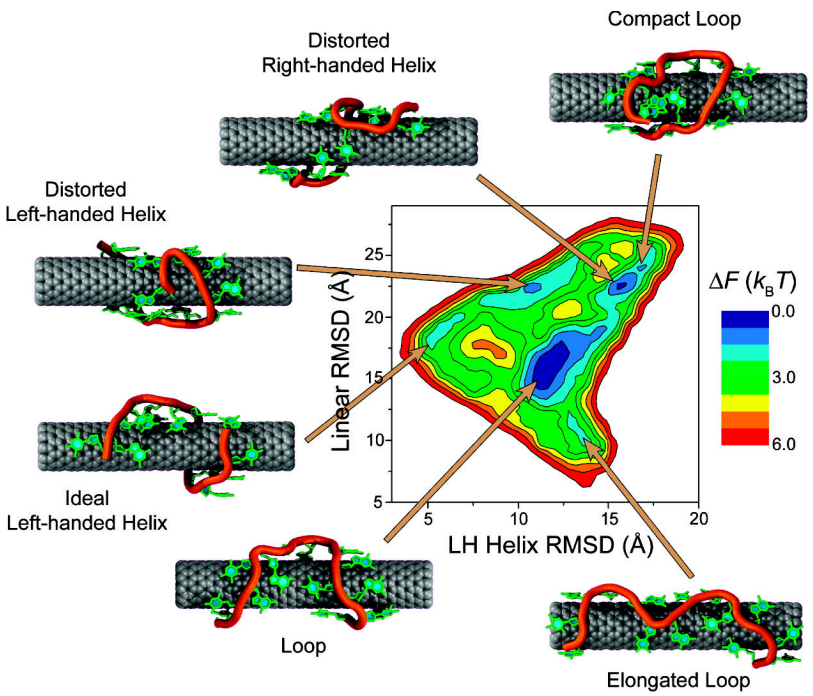

Figure 6. Six different free energy conformations of ssDNA (GT)–SWNT hybrid structure. Reprinted from Ref. 47 with permission. Copyright © 2009 American Chemical Society.

the structure of ssDNA–SWNT hybrid materials, very few studies exist on the structure of dsDNA–SWNT composite. Recently, we have studied the interaction of dsDNA and SWNT and have shown that unzipping of terminal base pairs leads to the complexation of dsDNA with SWNT.[15,16] REMD simulation on dsDNA–SWNT hybrid structure can also give valuable microscopic picture of the complex which is lacking at the moment.

3.2. Influence of temperature on oligonucleotide adsorption

We have already mentioned that MD study is very effective way to get a detailed microscopic picture of the binding mechanism between DNA and SWNT. The study shows that the hydrophobic nucleic bases of the DNA get adsorbed onto the nanotube surface whereas the hydrophilic phosphate backbone is exposed to the aqueous environment. The nucleic bases are adsorbed onto the CNT surface via π–π stacking interaction.

Mainly, there are two types of interactions between the DNA and CNT which play important role in the binding of ssDNA onto the nanotube surface. One is the base self-stacking and the other one is the spontaneous adsorption of the nucleic bases onto the CNT surface. Due to the self-stacking interaction among bases, the DNA strands are rigid and this rigidity opposes the spontaneous adsorption of the nucleic bases onto the CNT surface. So, the changing of system temperature has effect on the adsorption rate[48] of the oligonucleotide on the CNT surface. It is already known that when temperature rises above the room temperature, the DNA strands get melted.[49] A quantitative estimate of these two binding interactions can give valuable information about these two competing interactions. In Table 1, we give the energy values for these two interactions as has been calculated using *ab initio* MP2 and DFT method.[50,51]

The study shows that the energy for adsorption of the bases onto the CNT surface is higher than the self-stacking energy for nucleic bases.

When the temperature of this hybrid system is increased, the rise in temperature manifests two different effects on the spontaneous adsorption of the

Table 1. Quantitative estimation of self-stacking energy and adsorption energy for different nucleobases.[51]

Interaction type	Guanine (kcal/mol)	Adenine (kcal/mol)	Cytosine (kcal/mol)
Self-stacking energy	11.3	8.8	8.3
Adsorption energy	16	14	12

oligonucleotide onto the SWNT surface. One is the breaking of the base self-stacking which makes the polymer more flexible. Due to this structural flexibility of the polymer, the rate of spontaneous adsorption of the oligonucleotide onto the CNT surface is increased. As a result of temperature increase, more number of bases get stacked onto the CNT surface in a shorter time. Hence, the hybrid structure acquires an energetically favorable conformation and the binding energy of the system becomes maximum. The other effect of the temperature rising is that the base comes out of the kinetic trap which was there due to the existing barrier between neighboring hexagons of the CNT surface. This leads to movement of bases along the CNT surface more easily and the hybrid structure has better possibilities to acquire energetically more favorable state.

Since, at higher temperature there will be movement of the bases away from the CNT surface, we need to account for the base desorption[52] also. Figure 7a shows time evolution of different interaction energies between the polymer and the SWNT at three different temperatures. The plot shows that the rate of spontaneous adsorption of the bases onto the CNT surface increases with increase in temperature. At 363 K, the hybrid system acquires energetically favored state after 20 ns, whereas at 343 K, it reaches after 40 ns and for 293 K, the rate is very slow and ever after 50 ns, the system does not reach to the energetically favored state. Figure 7b shows the instantaneous snapshots of the wrapping conformations for SWNT and ssRNA(C) at three different temperatures.

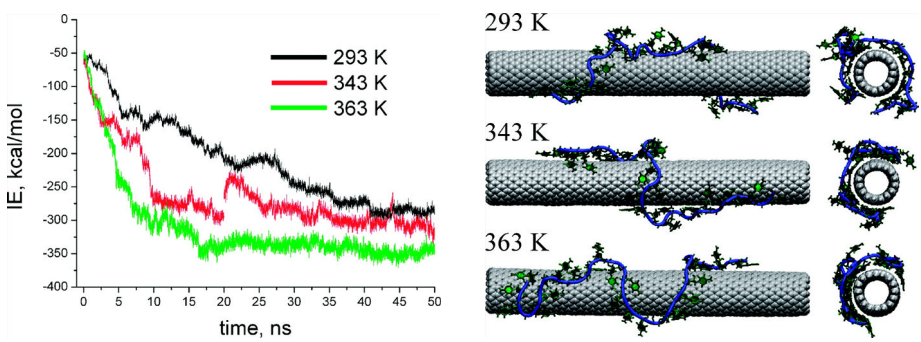

Figure 7. (a) Interaction energy vs time at three different temperatures. (b) Snapshots of ssRNA (C) –SWNT wrapped structures at three temperatures. Reprinted from Ref. 48 with permission. Copyright © 2011 American Chemical Society.

3.3. Applications

3.3.1. Solubilization and sorting of carbon nanotube

Laboratory synthesized CNT is found in bundle geometry with a mixture of various chiralities, diameter, and sizes. For a particular application, we need pristine CNTs with specific chiralities. Due to very low solubility strength of the CNT in both aqueous as well as non-aqueous solutions, the dispersion and sorting out of CNT from the bundle geometry is a big challenge to overcome.

Some external agents can tackle this problem by dispersing it from the bundle geometry. To accomplish this purpose, tremendous amount of work has been performed with many different polymers and various surfactants as dispersing agents. Recent experiments have reported that among various polymers and surfactants, DNA has the highest dispersion efficiency.[39] Among four different DNA oligonucleotides, poly(T) is the most effective dispersing agent with highest efficiency. Base self-stacking interaction is more in poly (A), poly(C) oligonucleotides compared to poly(T). So the dispersion efficiency of poly(A) and poly(C) is lower than poly(T).[39]

MD studies of model ssDNA and CNT systems in the aqueous environment have shown that the oligonucleotides of the ssDNA get helically adsorbed onto the SWNT surface.[53] The wrapping configurations are similar to those shown in Figures 6 and 7. This wrapping of nucleic bases around the CNT surface depends upon the sequence of oligonucleotides. A specific sequence of ssDNA binds around a specific chirality of nanotube surface.[54] As a result, specific ssDNA disperses and separates out CNTs of specific chirality. Nucleic bases of ssDNA carry negative charges in the aqueous environment. The hydrophobic nucleic bases are adsorbed onto the CNT surface due to the π–π interaction and the hydrophilic sugar phosphate backbone is exposed to the aqueous environment and form a stable structure.[55,56] Thus, CNT is made soluble in the aqueous solution. Using sonication method or the ion-exchange chromatography technique, the dispersed CNTs are separated out from the bundle geometry.

3.3.2. DNA–CNT hybrid in sensing mechanism

Recent progress in the field of nanomaterial has enriched the field of biological[57–59] and chemical[60–62] sensing system. CNTs have been found to be a very effective and ideal candidate to use in this field. CNTs are used to build FET as has been discussed in Ref.[63] The SWNT-FET is used as a sensor in chemical sensing. Recent studies[37] have reported that DNA can be used as a potential

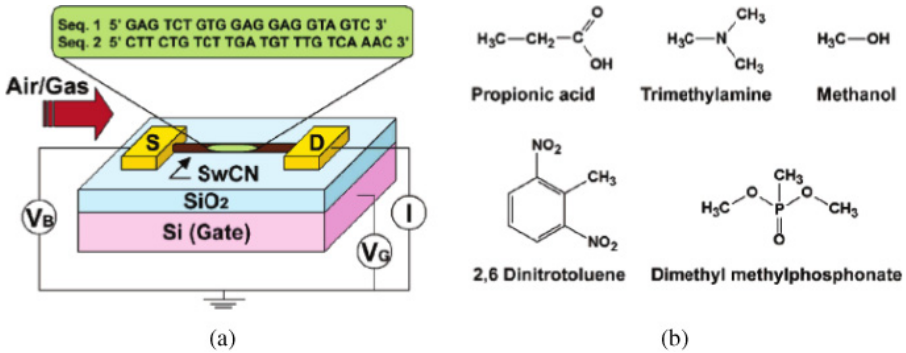

Figure 8. (a) Experimental setup of ssDNA-modified SWNT-FET. (b) Various odors used in the experiment. Reprinted from Ref. 37 with permission. Copyright © 2005 American Chemical Society.

Table 2. Experimentally measured values for various gas odors with bare SWNT-FET and DNA-modified SWNT-FET.

Odor	Vapor pressure (Torr)	Estimated concn(ppm)	Bare SWNT	$\%\Delta I/I$ SWNT + Seq 1	SWNT + Seq 2
Water	17.5	700	0 ± 10	0 ± 1	10 ± 1
Propionic acid	4	150	0 ± 1	17 ± 2	8 ± 1
TMA	500	20000	–9 ± 2	–20 ± 2	–30 ± 2
Methanol	100	4000	0 ± 1	–12 ± 2	–20 ± 2
DMMP	0.6	25	0 ± 1	–14 ± 2	–7 ± 2
DNT	1	40	0 ± 1	–14 ± 4	–4 ± 2

Source: Reprinted from Ref. 37 with permission. Copyright © 2005 American Chemical Society.

agent in this respect. The ssDNA bases bind to the SWNT surface and form a modified ssDNA-SWNT-FET. ssDNA-modified SWNT-FET as shown in Figure 8a shows change in conductance for different gas odors. But devices without ssDNA does not show detectable change to odors. Different gas odors used in the study are shown in Figure 8b. The conductance varies in sign and magnitude for different gas odors (see Table 2). It has been noticed that the response depends upon the DNA sequences also.

By varying the base sequences, the magnitude of conductance can be tuned accordingly. The response ability of the ssDNA-modified SWNT-FET is very quick and also it takes time in the order of seconds to recover at the initial state. It can be used in high security and safety purposes. Thus,

ssDNA-modified SWNT-FET turns out to be very useful with high detecting ability in sensing mechanism. SWNTs can also be used to characterize ssDNA bases by estimating binding energies or by translocating ssDNA through nanotube and measuring blockades of ionic current.

3.3.3. Supercapacitors

Electronic textile is a field of immense importance. As each individual CNT possesses very high mechanical and electronic properties, CNTs are used in this field of textile as a new device which will work as a storage of energy and can also function as an actuator.[64] But, increasing conductivity and electro-mechanical strength of the CNT fibers simultaneously is a big challenge. Large surface area is needed to increase the capacitance, whereas the mechanical strength of the composite fibers becomes lower due to large surface area. So, to circumvent this problem, some polymer binders are used to make the CNTs mechanically more stable. This also increases the surface area and also helps increase the transport of ions between the CNTs and electrolyte.[65,66] Studies have been performed with many polymer binders but satisfactory results are yet to achieve. Polymer binder enhances the conductivity but decreases the mechanical strength. Recent studies have been performed with DNA as a binding polymer with CNT fibers.[67] It has been reported that DNA with cross-linking appears to be a superior candidate for this purpose. DNA nucleic bases are adsorbed onto the surface of CNT via π–π interaction, the hydrophilic sugar phosphate backbone is exposed to the outer surface and thus makes the CNT soluble in the aqueous medium. This DNA–CNT hybrid structure is mechanically stable. This wrapped DNA–CNT hybrid structure is dispersed and separated out in the medium. Thus, this debundling of the CNT fibers from the assembled form increases the surface area which enhances the capacitance. As the DNA–CNT hybrid structure is separated out in the electrolyte, the positive counterions of the electrolyte condense around the DNA because of negatively charged bases. It enhances the ion-transport at the interface between the DNA–CNT hybrid and the electrolyte which effects the mechanical strain. Thus, DNA–CNT hybrid composite fibers can be used as supercapacitors with very high capacitance.[67]

3.3.4. Cellular delivery of DNA strands

In biomedical sciences, one of the most challenging problem is the delivery of DNA, RNA, or various other drug molecules to a specific targeted living

cell. These molecules which are transported inside the living cells,[16] also work as probes which can monitor the intracellular levels of molecules and ions. To accomplish these purposes, probe which targets a specific mRNA inside the living cells should be transported without any degradation. When a DNA-like probe is transported, it gets degraded by the cellular enzymes or digested by the cellular nuclease or it interacts with the other nucleic acid binding proteins. Again, this problem is intensified due to the long transportation time (sometimes for several hours). To overcome this, some delivery system is required which can protect and transport DNA/RNA or the drug molecules during transportation without any degradation.

In the recent times, many inorganic nanomaterials, such as nanotubes, nanoparticles, nanowires, *etc.*, are being used as a molecular transporter. These transporter occupies many interesting and very useful physical and chemical properties. Very few of them[68–76] offer a strong protection to the different types of cargo molecules. Among all the available molecular transporter, SWNT may be the most promising one. SWNT can transport with protection to a variety of cargo molecules to the target cells and it is effective in transportation to a wide range of living cell types.

To demonstrate that the SWNT protects various properties of the DNA probes,[41] a ssDNA oligonucleotide was used as a model sequence. Here, to perform the demonstration, SWNT was taken which was wrapped with ssDNA oligonucleotide. These oligonucleotides were with a repeated sequence of G–T nucleobases. Now, the aim was to determine the mobility of DNA which is bound to the SWNT and to check whether the mobility changes or not with respect to the free DNA. For this purpose, DNase I was used. It can cleave both ssDNA and dsDNA non-specifically. After treating both the GT–SWNT complex and the free DNA with DNase I, it was seen that the mobility for both the complex and the free DNA remains same. This demonstrates that the SWNT does not affect the inherent mobility of the bound DNA. To determine the effect of cleavage, the same model and protocol were used and the experiments were accomplished. The experiments show that the digestion in case of free DNA increased with time, whereas for GT–SWNT complex, there is no digestion. So, it demonstrates that SWNT protects the bound DNA from the DNase I cleavage.

While it is necessary that the DNA probes which are delivered into the cells should be protected from the enzymatic cleavage, it is also important that DNA probes should be functional when complexed with the SWNTs. By experimenting with specific DNA probes, SWNTs, manganese superoxide dismutase (MnSOD), polyT, and target cDNA, it is demonstrated that the functionality of the bound DNA is protected.

To test the ability of MnSOD probe–SWNTs to resist the nuclease cleavage *in vitro,* experiments were performed with both the free MnSOD and MnSOD probes–SWNT complex by adding one unit of DNase I endonuclease with both. The fluorescence intensity increases, if the probe gets digested by the DNase I, due to the separation of the donor dye molecules from the quencher. It shows little fluorescence for the probes–SWNT indicating little degradation, whereas a significant increase in fluorescence for the free MnSOD molecules indicate an increased degradation. These results demonstrate that the MnSOD probe–SWNT has the ability to resist the nuclease cleavage while delivered into the cells. Experiments[41] were performed to investigate how the free MnSOD and probe–SWNT interact, respectively, with ssDNA binding protein (SSB). It shows very little increase in fluorescence for probe–SWNT when interacting with the SSB which demonstrates that the probe may be well protected from the interference with the SSB. Thus, in comparison with the free DNA probes, SWNT-modified DNA probe possesses better transfection ability and intracellular biostability which opens up many ways to explore the basic genomic studies more rigorously.

4. Carbon Nanotube and Dendrimer Composite

Dendrimers and CNTs are two types of nanomaterials, which have met independently a large success within the scientific community.[77,78] Combining these two nanoscale objects either through covalent attachment or through non-covalent interaction can give rise to many exciting material properties which can have wide range of applications in physics, chemistry, biology, and materials science.[79–88]

Dendrimers,[89,90] first synthesized in 1985, are a class of hyperbranched polymers, constituted by the association of branched repetitive units and each level of branching units creates a hierarchy of structures called “generations”. The structure and dynamics of dendrimer are subjects of considerable interest[91–94] due to their versatile application in various fields ranging from catalysis, drug delivery, lubricants to sensors, and as nanoscale scaffold for molecular imprinting and molecular electronics. Unlike all other types of polymers (linear or branched), dendrimer synthesis offers high level control over the whole architecture, branching density surface functionality along with a high level of monodispersity.[95–97] Numerous terminal groups at the periphery facilitate further modification and can be covalently modified with some linear polymers or a broad range of functional groups, such as fluorophores, electroactive groups, perfluorinated moieties, and dyes.[95,96] On

the other hand, they can be used to entrap or stabilize various metals, metal oxides, and semiconducting/metallic nanoparticles.[97] Therefore, dendrimers are ideal materials for modification of CNTs.

In the recent past, two general strategies have been explored for functionalizing the CNT with dendrimer: (i) covalent functionalization of sp^2-hybridized carbons at the sidewalls and/or on the tips with dendrimers[98–100] and (ii) non-covalent functionalization through physical adsorption of dendrimers on CNT surface (*e.g.*, van der Waals interactions). In the following, we briefly discuss both the strategies.

4.1. Covalent functionalization

CNTs are functionalized by establishing strong covalent chemical bonds with the polymers.[101,102] Briefly, the chemical reactions can be performed at the sidewall site (sidewall functionalization) or at the defect sites (defect functionalization), usually localized on the tips. The covalent functionalization of CNTs with polymers helps to disperse the CNTs in a wide variety of solvents. Dispersion can be achieved even at a low degree of functionalization. There are mainly two different routes for the covalent attachment of polymer molecules to the surface of nanotubes, which are termed as "grafting to" and "grafting from" methods.

4.1.1. "Grafting to" approach

In the "grafting to" approach, the first step is the synthesis of a specific polymer with desired molecular weight and specific properties. This is followed by the modification of the end groups so that these polymers are reacted with the functional groups on surfaces of pristine or pre-treated CNTs[103–105] (see Figure 9). Usually, polymer chains with amino or hydroxyl moieties as terminal groups are attached through amidation or esterification reaction with the carboxylic acid groups or derivative acid chloride groups on CNTs surface.[106–110] Although the "grafting to" method has the limitation in the polymer growth by steric hindrance allowing a relatively low grafting density, it has been proved to be a facile and reliable approach for surface modification of nitrogen-containing CNTs.

In 2001, Sano *et al.*[112] reported the construction of star-shaped SWNTs using poly (amidoamine) (PAMAM) dendrimer with peripheral amine groups as a cross-linking reagent. Since the acid chloride groups were reactive at the open ends of SWNTs, this leads to divergent nanotubes from the core of the amine-terminated tenth-generation PAMAM dendrimer. They observed that

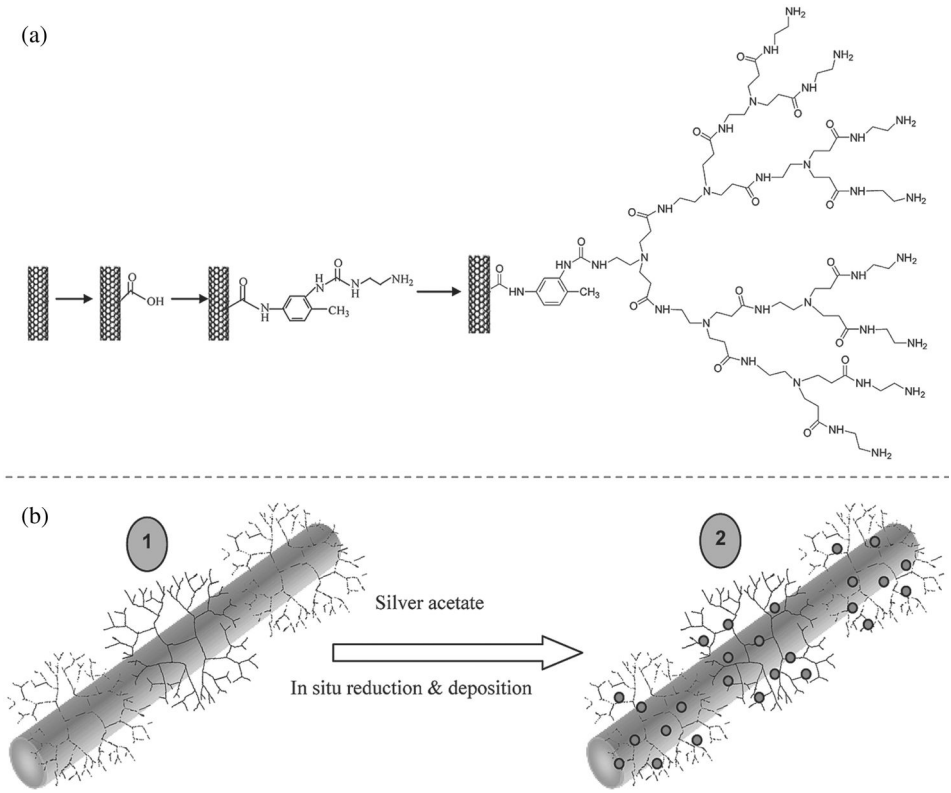

Figure 9. Synthesis of PAMAM dendron on MWNT with Ag (0) particles. Reprinted from Ref. 111 with permission. Copyright © 2008 American Chemical Society.

these interesting superstructure CNTs exhibited a peculiar response to electron beams.

Tao *et al.*[113] prepared fourth-generation hydroxyl-terminated PAMAM dendrons by sequential double Michael additions of methyl-acrylate to primary amines followed by amidation with excess ethylenediamine. Finally, the PAMAM dendrons are covalently linked to pre-functionalized MWNTs by esterification. To confirm the presence of dendrons on the surface of MWNTs, the silver nanoparticles were deposited on the surface of MWNTs (see Figure 9).

Similar PAMAM–CNT hybrid materials were also used for stabilizing CdTe quantum dots[114] or templating CdS quantum dots.[107] Later, the electro-catalytic activity of the PAMAM–CNT hybrid material with Pt–Ru nanoparticles composite electrode for methanol oxidation showed excellent performance. This implied that the resultant composite electrode can be used

in methanol fuel cells.[115] Further, the fourth-generation amine-terminated PAMAM-grafted MWNT-modified glass carbon electrodes are used for electrochemical determination of nitrite.[116] Beside these applications, CNT–dendrimer hybrid materials were also used in nanomedicine.[117–119] For instance, Shi *et al.*[120] reported functionalization of amine-terminated G5 PAMAM dendrimers with folic acid (FA) and fluorescein iso-thiocyanate (FI). Then, modified MWNTs with the multifunctional dendrimers via 1-ethyl-3-[3-dimethylaminopropyl] carbodiimide hydrochloride (EDC) coupling chemistry provided possibility for cancer cell targeting and imaging due to the covalently attached FA and FI on dendrimers. *In vitro* flow cy-tometry and confocal microscopy data showed that the formed composites can specifically target cancer cells that overexpress high-affinity FA receptors. Hence, these modified CNTs have potential applications in diagnosis and therapeutics.

Apart from the PAMAM–CNT hybrid materials, recently, Murugan *et al.*[98] has reported that the functionalized MWNT with amphiphilic poly (propy-leneimine) dendrimer carrying silver nanoparticles shows better dispersibility and antimicrobial activity.

4.1.2. "Grafting from" approach

The "grafting from" method involved the covalent immobilization of initiators or reactive groups onto the CNT substrate followed by *in situ* radical surface polymerization process to generate grafted polymer chain.[83,121,122] In contrast to "grafting to" approach, it allows high molecular weight polymers to be grafted from the CNT surface with quite high grafting density. Some well-known living polymerizations and polycondensations are utilized to graft a series of dendrimers from the pre-functionalized CNTs.

Cao *et al.*[123] prepared and reported the hyperbranched PAMAM-modified MWNTs (MWNT–PAMAM) through a divergent methodology. Lots of active amino groups of MWNT–PAMAM can be further functionalized by reacting with the FI which showed strong photoluminescent properties.

The step-by-step method of grafting PAMAM dendrimers from the SWNTs has been reported by Campidelli *et al.*[83] on the surface of SWNTs. The amino groups were anchored by 1,3-dipolar cycloaddition which is shown in Figure 10. After that, the second generation of PAMAM dendrons from the functionalized SWNT surface has been obtained by the Michael addition of methyl acrylate to the surface amino group and amidation of terminal ester groups with ethylenediamine. The resulting nanoconjugates of porphyrins-terminated dendrons were expected to harvest light to give more

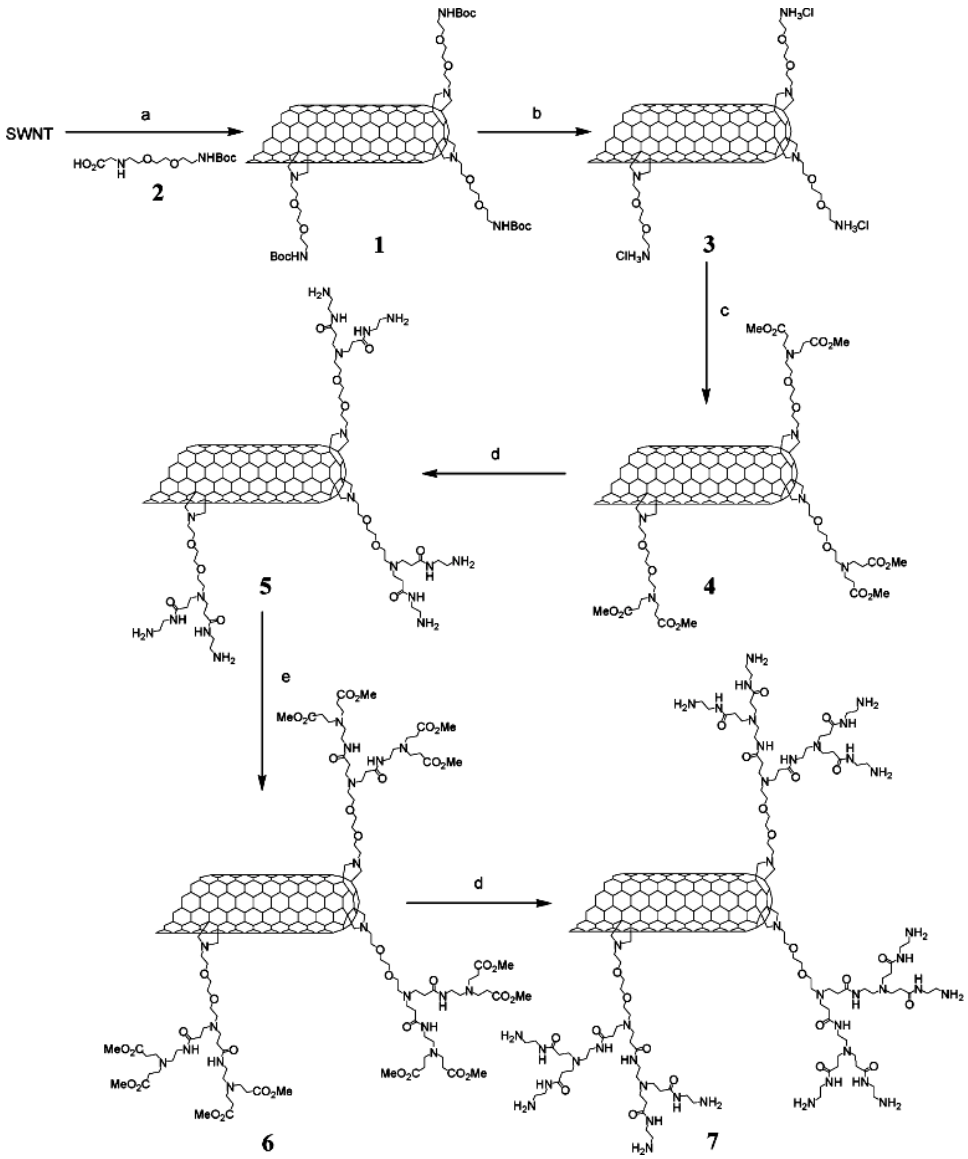

Figure 10. Schematic representation of modification of MWNTs with PAMAM dendrimer via grafting from method. Reprinted from Ref. 83 with permission. Copyright © 2006 American Chemical Society.

efficient electron transfers. In addition, positively charged tetra-alkyl ammonium salts of PAMAM dendrons were used as the efficient vectors for siRNA delivery.[124] In the similar way, SWNTs with dendritic PAMAM were modified and the anisotropic microsize fibers were obtained by reactive spinning using

the functionalized SWNTs as filler in thermosetting epoxy.[125] The fibers showed high tensile strength and Young's modulus, which was correlative with the alignment of modified SWNTs. The nanohybrids of PAMAM-modified MWNTs with silver nanoparticles showed strong antimicrobial effects.[111] Using the similar method, Pan *et al.*[126,127] prepared amine-terminated PAMAM dendrimers–CNT hybrid materials and investigated their application in gene delivery by conjugation with FI-labeled antisense c-myc oligonucleotides. The composites with dendrimers of generation five exhibited maximal transfection efficiency and inhibition effects on tumor cells.

Recently, palladium nanoparticles (PdNPs) encapsulated on PAMAM–MWNTs hybrid material were synthesized and used to fabricate modified electrodes.[128] The modified electrode gave very good catalytic activity and also showed good promise for the fast detection of oxalic acid (OA) concentration.[128] This sensor based on this modified electrode was used to detect the level of OA concentration in spinach with good success.

4.2. Non-covalent functionalization

Non-covalent functionalization of CNTs involves van der Waals, hydrophobic, or π–π interactions between CNTs and polymers. In this context, dendrimers are physically adsorbed on the surface of the CNTs and some dendrimers could also be used to modify the pristine CNTs by other physical interactions like physical entanglement or van der Waals interactions, *etc.* Further, oxidized CNTs are functionalized by dendrimers via electrostatic adsorption or hydrogen-bonding interactions.

This non-covalent functionalization is particularly advantageous because it does not perturb the electronic structure of CNTs.

The electrochemical sensors consisting of an electrode loaded with PAMAM–MWNTs and Pt nanoparticles (PtNPs) were developed. Here, PAMAM dendrimers have been used as protectors/stabilizers of metal/metal compound nanoparticles, including PtNPs and their binders on MWNTs.[84,129] These sensing systems show good stability and electrocatalytic activity, which can be used in variety of applications as sensors. Encapsulation of Au nanoparticles within generation six (G6) amine-terminated PAMAM dendrimers on the surface of MWNTs via electrostatic interaction was reported by Her-rero *et al.*[81] (see Figure 11). Lihuan Xu *et al.*[130] proposed a novel amperometric glucose biosensor. The fabrication of the sensor was based on layer-by-layer (LbL) adsorption of glucose oxidase (GOx) and dendrimer-encapsulated Pt nanoparticles (Pt-DENs) on MWNTs. This LbL assembly is achieved through electrostatic adsorption.

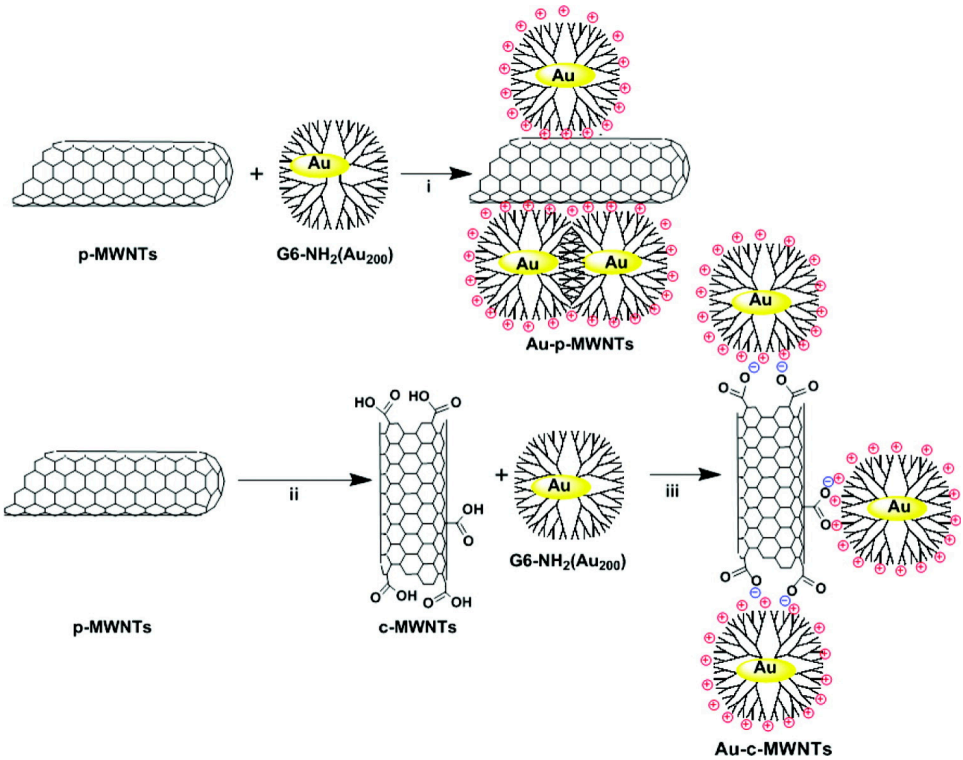

Figure 11. Schematic representation of adsorption of dendrimer-encapsulated Au nanoparticles on the surface of pristine or oxidized MWNTs. Reprinted from Ref. 81 with permission. Copyright © 2010 American Chemical Society.

Understanding the basic mechanism of interaction between CNT and dendrimer is crucial for potential application in biomedical and other fields. Recently, we have studied the complexation of non-toxic, oxygen-core poly(propyl ether imine) (PETIM) dendrimers with SWNT experimentally.[131] The wrapping of the PETIM dendrimer onto SWNT was monitored by the quenching of the inherent fluorescence of the dendrimer as well as change in the electrical resistance of the complex. The experiment was followed by all atom MD simulations to provide a microscopic picture of the dendrimer–nanotube complex. The complexation was achieved through charge transfer and hydrophobic interactions, aided by multitude of oxygen, nitrogen, and *n*-propyl moieties of the dendrimer. Subsequently, we have also studied the microscopic picture of the CNT–PAMAM dendrimer and CNT–PETIM dendrimer complexes for different generations at high (non-protonated case) and neutral pH (protonated case) using all atom MD simulations.[132]

The instantaneous snapshots for the case of PAMAM–CNT and PETIM–CNT complexes at different generations are shown in Figures 12 and 13, respectively. There is a strong van der Waals interaction between the CNT and the dendrimer mediated by the charge transfer between them. The simulation results demonstrated that the size of the G3 PAMAM/G4 PETIM dendrimer is enough to wrap the nanotube of length 36 Å and diameter 7.5 Å. Further, it was observed that the nanotube–PAMAM dendrimer complexes are more stable than the nanotube–PETIM dendrimer complexes but there is no significant change in the charge of the nanotube. This variation could be due to the difference in the chemical nature of the branches of the two dendrimers. It is possible that a hydrogen bond can form in the case of PAMAM dendrimers and the free lone pair electrons present in oxygen may not transfer to the nanotube. However, for PETIM dendrimers, there is no possibility of forming a hydrogen bond and hence more electrons from the lone pair present in oxygen atoms may transfer to the nanotube. Hence, the nanotube–PAMAM dendrimer complexes can be used as efficient carriers for drug delivery as well as siRNA delivery platform. There are indication that the nanotube–PETIM dendrimer complexes can also be used as efficient photoactive surfaces in photovoltaic devices.

5. Carbon Nanomaterials for Energy Conversion

Tunable band gap with excellent electron mobility makes CNTs a much sought after candidate in the field of nanoelectronics for the fabrication of various nanodevices such as FETs, electrochemical sensors, photovoltaic devices, *etc.* In this section, we will give a brief summary of how carbon nanomaterials can be used for energy conversion.

5.1. Hydrogen storage

Decreasing fossil fuel reserve and growing environmental concern have forced us to think for the alternative energy sources. Being highly efficient and pollution free on combustion, hydrogen has been proposed to be ideal replacement of fossil fuels. In the recent years, many technological advances have been made in the field of hydrogen fuel but many more advancements are required before hydrogen can be used for general fuel purposes. Current limitations include inadequate technology to store hydrogen at ambient conditions at low cost for using hydrogen as fuel. So it is necessary to explore new approaches to store hydrogen. At ambient temperature and pressure, hydrogen exists in the form of gas. So the most appropriate way to store

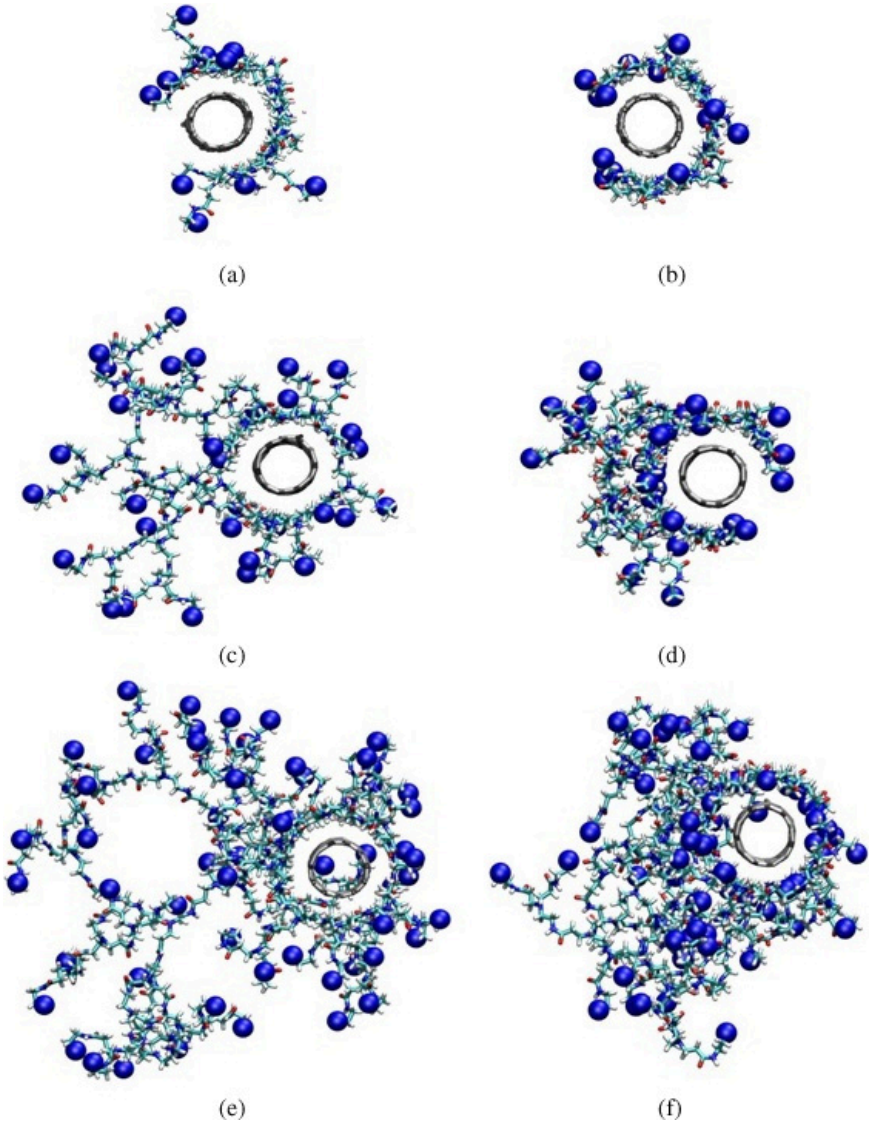

Figure 12. Equilibrated snapshot of the nanotube–PAMAM dendrimer complexes: nanotube with (a) protonated (b) non-protonated dendrimer of generation two, (c) protonated (d) non-protonated dendrimer of generation three, (e) protonated and (f) non-protonated dendrimer of generation four. Reproduced from Ref. 132 with permission of the Royal Society of Chemistry.

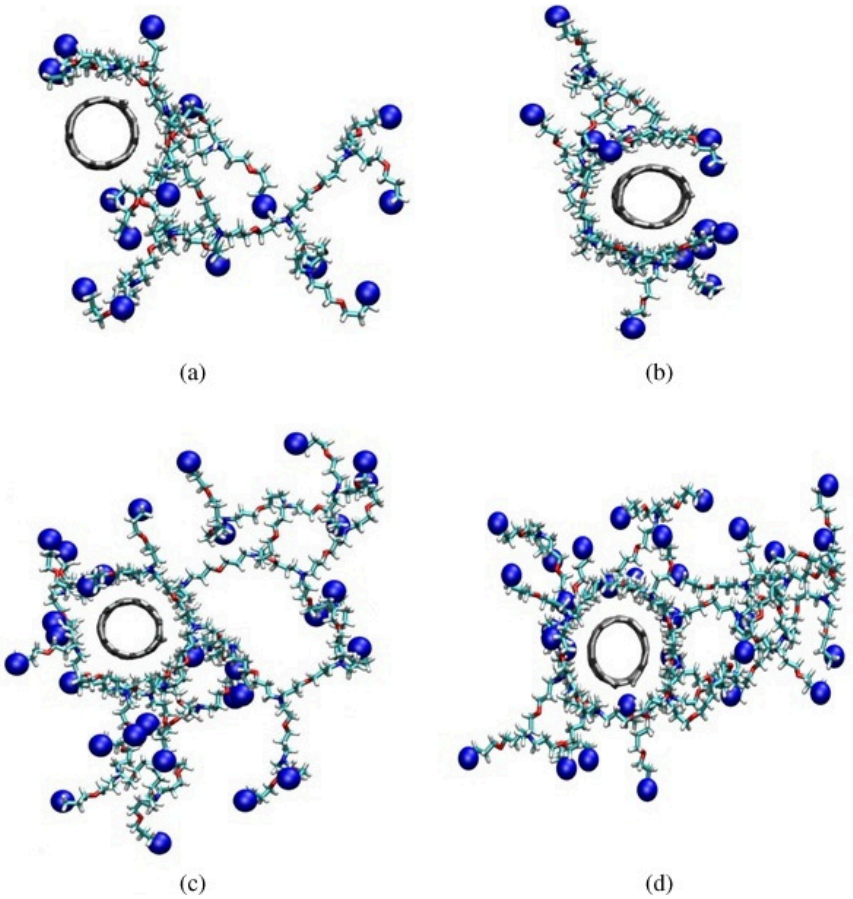

Figure 13. Instantaneous snapshots of the nanotube–PETIM dendrimer complexes: nanotube with (a) protonated (b) non-protonated dendrimer of generation three, (c) protonated and (d) non-protonated dendrimer of generation four. Reproduced from Ref. 132 with permission of the Royal Society of Chemistry.

hydrogen is in gas form. And the best storage media or material should be one which is capable of adsorbing and releasing large quantities of hydrogen gas easily and reliably. In addition to high storage capacity, another most indispensable requirement for hydrogen storage material is reversibility. SWNTs have been shown to be excellent hydrogen storage material. Hydrogen storage through both physisorption and chemisorption mechanism has been proposed.[133–135] Due to their large surface area with comparatively small mass, SWNTs have high potential to be considered as high capacity hydrogen storage materials. Theoretical calculations demonstrate that they can store hydrogen up to 7.7 wt.%,[136] as every carbon atom in

CNTs chemiosorps one hydrogen atom. Further enhancement in the storage capacity was suggested by the subsequent physisorption of hydrogen over hydrogenated SWNTs. Most of the experimental studies[137–140] so far have focused on the physisorption of molecular hydrogen. The interaction energy between the hydrogen and CNTs critically depends on the nanotube size and influences the storage and release capacity. Among a wide range of CNT sizes, only a small fraction of the CNT surface would be suitable for hydrogen storage. Experimentalists are yet to achieve theoretically predicated storage capacities, mostly due to the lack of control in preparing SWNTs as a hydrogen storage medium.

5.1.1. Historical development

In 1997, Dillon *et al.*[135] at National Renewable Energy Laboratory (NREL) experimentally demonstrated hydrogen storage capacity of highly impure sample of SWNT to be 0.1 to 0.2 wt.% at 133 K. Based on these finding, they extrapolated adsorptivity of pure SWNT sample to be 4.5% to 10% weight and predicated that nanotube of diameter between 16Å to 20Å will have adsorptivity close to targeted value of 6.5 wt.%. Later Ye. *et al.*[140] showed that almost one hydrogen atom can be adsorbed per carbon atom on crystalline carbon ropes at temperature 80 K and pressure close to 12 MPa. Subsequently, Chen *et al.*[141] observed that MWNTs doped with Li or K can have hydrogen uptake of around 20 wt.% and 14 wt.%, respectively, at ambient pressure condition. Although K-doped MWNTs are capable of adsorbing hydrogen at ambient temperature (298 K), they are very unstable at this temperature. This was followed by Liu *et al.*[142] observation where they demonstrated hydrogen adsorptivity of SWNT, synthesized by semicontinuous arc discharge method, to be around 4.5 wt.% at room temperature and modestly high pressure. Despite the initial encouraging experimental and theoretical reports of feasible hydrogen adsorption, adsorptivity of SWNT has yet to be accepted globally. Different research groups across the world have different observations about the adsorptivity and these results turn out to be not very reproducible.

Recently, it was pointed out by Liu *et al.*[143] that initial measurements of hydrogen storage properties of CNTs were performed using the apparatus built up for measuring metal hydrides. This could have significant influences on the reported measurement as there are distinct differences between these two experiments related to CNTs and metal hydrides. In the experiment involving CNTs, the amount of the CNTs used is much less than that of metal hydrides. This is due to the low packing density and small sample chamber

volume of CNTs. Because of small chamber volume, precision measurement of sample volume as well pressure measurement is a challenge. These errors along with the temperature fluctuation in the small volume can be attributed to be the main reason behind the disagreement between reports among various groups. Liu *et al.*,[143] performed an experiment by specifically designing Seivelt apparatus for CNT measurement and studied the adsorptivity of various types of CNT samples and concluded that maximum adsorptivity of 1.7% by weight can be achieved at room temperature.

Another form of the carbon nanomaterials, graphene, also has been studied for hydrogen storage potential. Due to the possibility of adsorption on both sides of surface and flexible nature of sheets, graphene has added advantage for the hydrogen storage over CNTs. From *ab initio* simulations,[144] it was predicated that up to 8 wt.% adsorptivity can be achieved for graphene sheets. Experimentally, graphene has been shown to adsorb 3.2 wt.% hydrogen and its reversibility of thermal annealing.

Although there are various theoretical predictions and experimental reports of hydrogen storage capability of carbon nanomaterials, ultimate goal to have 6.5 wt.% adsorption capacity at room temperature, to be able to use hydrogen for practical application, is yet to be reached. It has been suggested that storage capacity of graphene can be further enhanced by chemical functionalization.[145]

5.1.2. Improving hydrogen storage by chemical functionalization

Carbon nanomaterials have lower adsorption capacity for hydrogen. One way to improve the hydrogen adsorption capacity of CNTs/graphene is fine tuning their interaction by chemical doping with alkali metal atoms such as Li and K. It was shown in Ref. 141 that each Li atom adsorbed on the graphene surface can take up to four H_2, leading to adsorptivity of more than 10 wt.%. Enhanced adsorptivity of K-doped graphene has also been established. Other class of material which has been shown to be useful to functionalize the graphene for optimized carbon–hydrogen interaction is transition metal,[144–148] including Sc, Ti, and V. Several first principle calculations[146] have established that adsorption capacity up to 7% can be achieved for Ti-decorated graphene which can adsorb up to four H_2 molecule per Ti atom. In another study, it was predicated[147] that an ethylene–titanium complex can hold up to 10 H_2 molecules, further increasing the adsorption capacity. However, due to large cohesive energy, transition metals have a tendency to form clusters, hence reducing their storage capacity. A number of measures can be taken to circumvent the problem, for instance applying strain on the graphene sheet or

decorating with another atom such as Ca.[149] Studies have suggested[149] up to 5 wt.% adsorption capacity of Ca-decorated graphene sheets with almost negligible clustering of Ca atoms. In order to improve further, it has been also suggested to use GO and attach transition metal atoms such as Ti on the epoxy and hydroxide bonds.

5.2. Blue energy

When sea water with higher ionic concentration is mixed with the fresh water with lower ionic concentration, entropy of the system increases.[150] This increase in entropy can release energy which can be utilized to generate electrical energy from the thermal energy of the mixed liquids. A rough estimate[150] of the energy extraction can be made using heuristic thermodynamic argument: When V_1 volume of pure water is mixed irreversibly with V_2 volume of sea water with osmotic concentration of C_2, resulting solution will have osmotic concentration of $C_2V_2/(V_1 + V_2)$. Assuming the ions in the sea water as gas particles with initial C_2V_2 number of moles, change in entropy due to isothermal expansion from volume V_2 to volume $V_1 + V_2$ is $\Delta S = C_2V_2RIn(1 + V_1/V_2)$, R being the gas constant. Assuming expansion to be reversible at constant temperature, energy released will be $\Delta W = T\Delta S$. Since the volume V_2 (of sea) is much larger as compared to V_1, ΔS can be approximated to be $\Delta S = C_2RV_1$ and hence $\Delta W = RTC_2V_1$; taking the sea water concentration equal to 0.5 osmole/liter will give energy of 2.24 kJ for each liter of fresh water mixed with 1L of sea water. This concept can be utilized to extract energy from the mixing of sea water with river water. Estimation suggests that sufficient energy to fulfill the global usage of electricity can be extracted from this renewable source of energy if optimal device for the energy conversion can be designed. Presently, there exists various technologies to extract the energy from the controlled mixing of different salinity solutions like pressure retarded osmosis[151,152] (PRO): based on semipermeable membrane to create pressure head utilizing osmotic pressure difference; reverse electrodialysis[153]: based on selective ion membrane; hydroelectric piles[154]: based on acidic and basic membrane. Main drawback of membrane-based technique is higher membrane cost and short lifetime of membrane due to fouling. Due to these limitations, industrial utilization of these techniques is yet to happen.

Recently, Brogioli[155] has proposed a device design for the energy extraction from the salinity difference, based on the electrochemical double layer (EDL) capacitor technology using nanoporous carbon electrode. The device consists of two activated carbon electrodes immersed in salt water chamber which is periodically flushed with fresh water. Due to large surface area

of nanoporous carbon electrode, EDL capacitor with huge capacitance is formed close to electrode surface. When this salt solution is mixed with the fresh water, EDL diffuses and counterions move away from the electrode surface, increasing electrostatic energy of the system. This additional energy can be extracted in the form of electrical energy by converting free energy of mixing into usable electrical energy. To extract energy from the capacitor, a four-phase cycle, which consists of systematic charging of capacitor, mixing of fresh water, subsequent discharge of external capacitor, and energy extraction, was suggested. It was shown that this device can extract power of the order of 1.6 kJ/L of fresh water. In the further development, Roij *et al.*[156] proposed Carnot cycle equivalent of this cycle to further improve the efficiency of this device. To achieve better efficiency, Brogioli *et al.*[157] designed a larger version of the device. New design consists of carbon electrodes kept parallel instead of side by side as in earlier design to each other to reduce internal resistance of device. A schematic diagram of this flow cell device is shown in Figure 14.

In this device, carbon electrodes are first brought into contact with the salt water and charged with external capacitor operating at a certain fixed voltage V_0. As soon as electrodes are connected with the external capacitor, electrons start flowing through external circuit and equal and opposite charges are developed on both the electrodes. As these carbon electrodes are in contact with salt water, electric double layer with excess opposite charges are created on each electrode until potential across flow cell V_{cell} is equal to

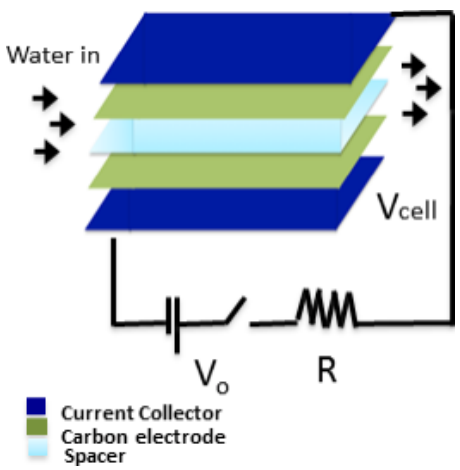

Figure 14. Schematic diagram for the energy extraction from the salinity difference of sea water and salt water using EDl capacitor principle. External capacitor provides constant voltage while *R* represents load.

the potential of external capacitor V_0. At this point of time, fresh water flushed through the cell causes the expansion in the diffuse layer of ions. As ions move away from the electrode surfaces, cell potential V_{cell} increases which leads to the charging of external capacitor. External capacitor can be discharged to V_0 via external load to use the energy.

Principle behind the EDL capacitor-based flow cell can be understood in terms of Gouy–Chapman–Stern (GCS) theory.[157] According to this theory, EDL near an electrode with constant surface charge density σ can be described by combination of two layers: (i) stern layer and (ii) diffuse layer. Potential V_s at the Stern layer is given by

$$V_s = \frac{\sigma}{C_s}, \tag{1}$$

where C_s is the capacity of Stern layer. For monovalent ionic solution like NaCl (which constitutes large ionic part of sea water), diffuse layer potential V_d is given by

$$V_d = 2V_{T_a} \sinh(\alpha\sigma\lambda_d), \tag{2}$$

where V_T is equal to k_B/e, e being electronic charge, $\alpha = 1/(2\varepsilon V_T)$ and λ_d is the Debye screening length related to ionic concentration c by the relation

$$\lambda_d = \frac{1}{\sqrt{8\pi\lambda_B c N_A}}, \tag{3}$$

where λ_B is the Bjerrum length of water, N_A is the Avogadro number. According to GCS theory, potential at double layer is given by the sum of two potential $V_s + V_d$. Since each fuel cell consists of two EDLs hence

$$V_{cell} = 2(V_s + V_d) \tag{4}$$

From Eqs. (2)–(4), we see that as ionic concentration c decreases (upon mixing the fresh water in salt water), cell potential V_{cell} increases.

5.3. Voltage generation through flow

Filling of water inside cavity of CNT has drawn considerable attention due to potential application of this system for nanotechnological devices.

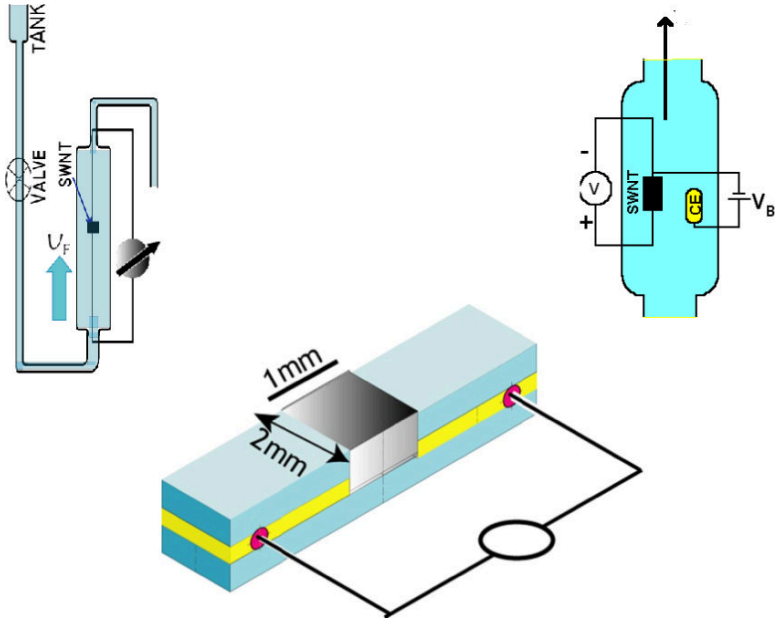

Figure 15. Schematic diagram for the CNT-based flow sensor and the value of induced voltage for different flow velocities. Induced voltage varies logarithmically on the flow velocity.

In 2003, Ghosh *et al.*[158] reported that flow of liquids through SWNT bundle induces voltage across SWNT in the flow direction. In the experiment, SWNT bundle produced from electric arc discharge, with an average diameter of 1.5 nm was inserted between two metal electrodes. To avoid any turbulence effect, sensor was kept away from the inlet of flow chamber. Schematic of the experimental setup to get induced voltage with flow velocity is shown in Figure 15. It was shown that value of the voltage generated depends logarithmically on the flow velocity over six orders of magnitude. This observation highlights the application of CNTs not only as a flow sensor but also as energy harvesting device. Soon after this report, similar experiment was performed[160] with MWNTs. It was found that aligned MWNTs can generate up to 15 times more voltage than SWNTs. In another study, it was shown[161] that semiconducting nanotubes produce three times more voltage than the metallic nanotubes. Presence of ions can considerably change the value of voltage depending on the concentration and type of ions. Yuan *et al.*,[162] using *ab initio* simulation showed that for the very narrow CNT where all dipoles are aligned along the nanotube axis, voltage is generated due to induced polarization. Although, there have been various experimental reports for flow-induced voltage generation across nanotube

ends, values of reported voltages is always < 10 mV. For efficient practical applications, values of the voltage generated need to be enhanced. Dhiman *et al.*[163] showed that an order of magnitude more voltage can be obtained by flowing HCl solution over stacked graphene sheets. Specific power output from their experiment was reported to be 175 W/m^2 for the flow velocity of 0.01 m/s.

5.4. Energy-efficient nanoelectrical devices

In the last few decades, electronics industry has grown exceptionally. Electronic devices are being used in computing, communications, automation, and almost all aspects of human life. At present, most of the power consumption in the electronic and computing industry depends on the energy usage of integrated circuits (ICs). Hence, there is growing incentives to develop low power and energy-efficient technology. Shrinking device size leads to improved energy efficiency and speed of the operation. Miniaturization of silicon-based FET devices is continuously taking place in order to make more efficient devices. However, there are technological barriers and physical limitations to continue the scaling of devices.

When device size is of order of nanometer, quantum mechanical phenomenons such as tunneling[164] becomes very important consideration. Due to quantum tunneling, leakage current is increased which in turn not only leads to over power consumption but also undermines the function of transistor as a switch.[165] Scaling of device also leads to reduction in the size of metallic contact wire which causes higher resistance and slower performances of the device. To overcome these challenges, efforts to develop alternate technologies are being made worldwide. One of the most promising technology, which is being developed in the recent years, is using the carbon nanomaterials such as aligned CNT array or graphene ribbons for device fabrication.

Various forms of carbon nanomaterials such as SWNT, graphene, and graphene nanoribbons possess the fascinating physical and electrical properties which can be used to overcome many above-stated challenges in the electronic device industry. Due to one-dimensional and defect-free structure of the CNTs, scattering of electrons by defects or phonon is absent in these materials. This leads to much lower electrical resistivity and very long[166] mean free path (100 nm) as compared to conventional materials even at room temperature. Detailed comparison of the relevant properties of carbon nanomaterials with the conventional materials is given in Table 3. These superior properties of nanosized carbon allotrope can be exploited in various

Table 3. Comparison of the different properties which are relevant to IC designs of carbon nanomaterial with Si and Cu.[165]

Property	SWNT	MWNT	Graphene	(Ribbon)	Si	Cu
Mean free path (nm)	10^3	10^4	10^3	—	30	40
Temp coeff. of resistance ($\times 10^{-3}$/K)	< 1.1	−1.37	−1.47	—	—	4
Max. current density	$>10^9$	$>10^9$	$>10^8$	—	—	10^7
Mobility *(cm²/Vs)*	$> 10^4$	—	$>10^4$	—	1400	—
Melting point (K)	3800	—	—	—	1687	1367

ways to design energy-efficient electronic devices. We will discuss below areas where applications of carbon nanomaterials are expected to make the difference.

5.4.1. Carbon nanotube-based FETs

In 1998, CNT-based FET was first created by replacing the channel with CNT in conventional FET. In this prototype device, silicon wafer-covered SiO_2 films and noble metal electrode was first fabricated[63] using lithography and then SWNT was placed in between two electrodes which acts as transistor channel. Electrodes acts as source and drain while silicon wafer act as gate. A schematic diagram of the device is shown in Figure 16. These FETs are shown to have 10,000 times higher current flow in on state than off state. A characteristic curve for the carbon nanotube field effect transistor (CNFET) is shown in Figure 17. Due to unique electrical and physical properties of CNTs, in addition to high carrier mobility and scattering free mean path, CNFET has much more advantages[167] over conventional FETs. Due to small diameter of CNTs, optimum coupling between gate can be achieved which leads to strong control of gate voltage over channel potential. Absence of dangling bonds and smooth surface further helps to avoid "short channel effect" which in turn help to have better gate control over channel. Another advantage of CNFET is the lower capacitance and lower operating voltage.

In CNFETs, metals like Au, Ti, Al, and Pd are used as electrodes. Due to different work function of metals and CNTs, charge transfer happens at the interface which leads to formation of energy barrier[168,169] known as "Schottky Barrier". Depending on the relative work function of metal and CNT, only one type of carrier transport in the channel is permitted, in

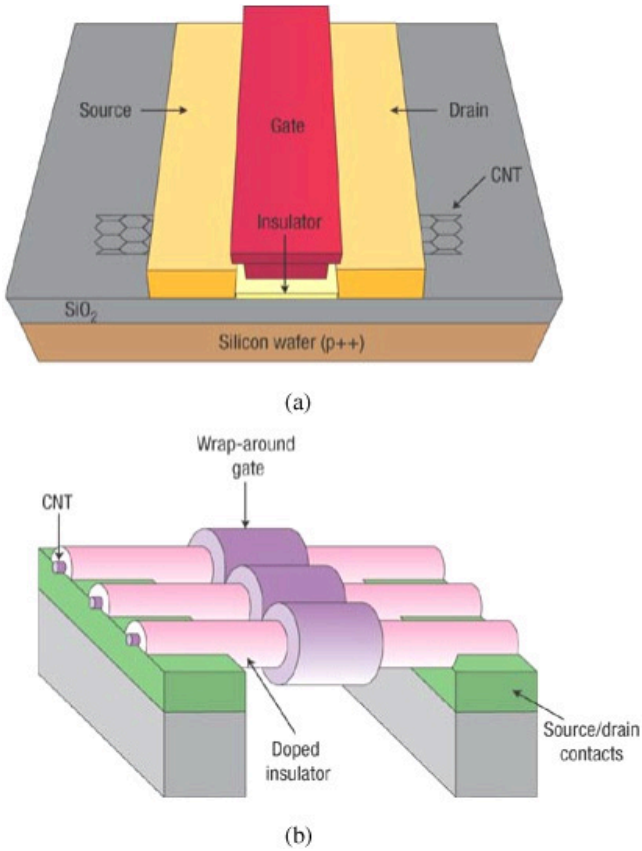

Figure 16. Schematic diagram for the CNT-based FET. (a) "Top gate CNFET," (b) "wrap around gated CNFET" have been shown. Reprinted from Ref. 167 with permission. Copyright © 2007 Macmillan Publishers Ltd.

presence of this Schottky barrier.[170] For example, metal Pd, with high work function, will create low height barrier, and will allow the transport of holes only and electron will face high barrier at the interface. These Schottky barrier affects the performance of FET in on and off state. However, it is possible to screen the Schottky barrier and get conventional MOSFET-like transport behavior. Two ways gating, where one gate is used near contact to diminish the Schottky barrier while other central gate is used to control the channel, has been shown to eliminate ambipolar[169] behavior and leakage current. Atoms or molecules which are adsrobed on the CNT surface through a charge-transfer mechanism can also be used for chemical doping. By doing selective chemical doping to the regions near the contacts of the CNFET and using a central gate for switching, one can achieve a bulk-like behavior.

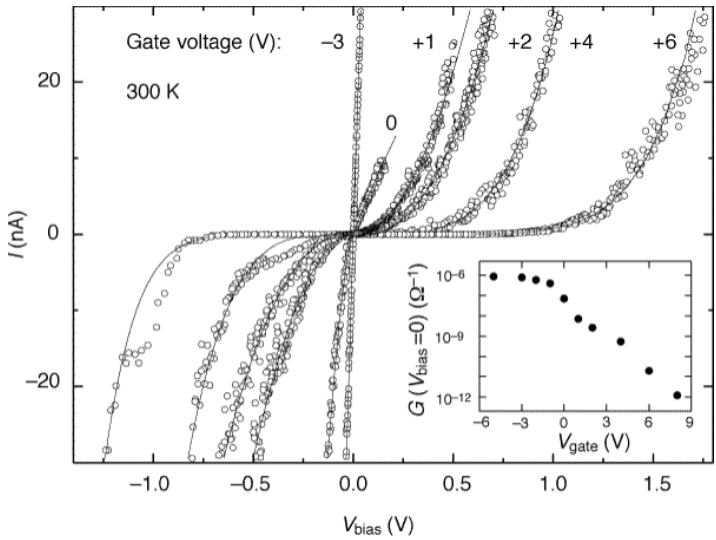

Figure 17. Performance characteristic curve for the SWNT-based FET. Reprinted from Ref. 63 with permission. Copyright 1998 Macmillan Publishers Ltd.

5.4.2. Nanotubes and graphene as interconnectors

One of the major challenge in the high-speed IC technology is to have suitable interconnector. Currently, in most advanced IC technology, power consumption associated with interconnects is around 50% of total power consumption.[171] With continuous scaling of device, problems such as delay in signal along the interconnects and electro migration have become more pronounced. When dimension of the conventional interconnects such as copper is reduced from 100 nm to 50 nm, resistivity is significantly increased due to increased electron scattering[172] at boundaries which cause signal delay. Another challenge of copper interconnects at nanoscale device comes from increased Joule heating and electromigration which in turn limits the maximum allowed current density. This implies need for the alternative materials for interconnects.

Graphene and CNTs are known to have very high electron conductivity and long mean free paths. Metallic graphene ribbons have been shown to outperform[173,174] copper wire with interconnect width of 8 nm. Theoretical calculation[174,175] has shown to have smaller signal delay when doped graphene nanoribbon is used as global wire. Further, graphene nanoribbons have order of magnitude higher maximum allowed current density than the copper. Chen *et al.*[176] has demonstrated integration of graphene interconnects using standard complementary metal-oxide-semiconductor (CMOS) technology and shown that this device can operate up to frequency 1.3 GHz.

Signal delay in graphene nanoribbon and CNT was shown[165] to be much lower as compared to conventional metal interconnects such as copper. For global interconnect, most of CNT and graphene nanoribbon have been shown[165,177] to give lower latency. Interconnect with graphene nanoribbon and CNT not only gives lower signal delay but also consumes much less power due to low electrical resistance.

5.4.3. Flexible electronics: Thin film transistor

In the recent years, significant progress has been made in nanotube-based transistor and devices but commercial-level application is yet to be realized due to difficulty in nanoscale fabrication. Main challenge[178] with the nanotubes-based device fabrication is to have deterministic assembly, development of scalable fabrication process, minimal device to device variation, and placement of objects with nanoscale accuracy. On the other hand, solution deposition of semiconductor-rich SWNT networks presents a highly promising path for the realization of high performance thin-film transistors (TFTs) flexible electronic applications.[179,180] Flexible electronics has applications[178] in wide variety of areas such as flexible circuits, flexible displays, flexible solar cells, implantable medical devices, skin-like sensors, and conformable RFID (radio-frequency identification) tags. The most significant advantages of using SWNT for TFTs is that the SWNT thin films can be prepared using solution-based room temperature processing and their ease of fabrication with conventional lithography methods. Compared to other competing technologies like organic semiconductors, the nanotube-based thin films offer much better carrier mobility. Although much progress has been made, future research should aim to have uniform device performance with precise control over threshold voltage, further lowering of the I_{off}, without sacrificing I_{on}.

5.4.4. Photovoltaic devices

In addition to electronic device applications, carbon nanomaterials also have shown to possess excellent properties suitable for photovoltaic applications. Chemical stability, high electron conductivity, mechanical flexibility, and earth abundance of carbon make carbon nanomaterial a potential candidate for low cost and efficient solar cell applications. Fullerene has been extensively used for electron transport material in organic photovoltaic (OPV) due to its strong electron acceptor characteristic. First fullerene-based photovoltaic cell was reported[181,182] from the bilayer heterojunction *of poly*[2-*methoxy*-5-(2'-*ethylhexyloxy*)-*p-phenylenevinylene*] (MEH-PPV) and $C_{60,}$ where MEH-PPV

acts as a donor while C_{60}' acts as an acceptor. Soon after, different donor molecules have been used. However, efficiency of the bilayer hetero junction-based device is very low in the range of 0.05% mainly due to availability of limited surface area of the bilayer hetero junction. In the subsequent attempts to improve the efficiency, Wudl group functionalized C_{60} to derive a new form of fullerene ([6–6]*phenyl-*C_{61}*-butyricacidmethylester*) (PCBM) to improve its solubility[183] in organic solvents. Later, PCBM and MEV-PPV were combined to get interconnected bulk heterojucntion with large junction area. OPVs based on this heterojunction had much more improved efficiency[184] of 2.9%. Since then, PCBM is one of the mostly used material for fulleren's-based OPVs.

Not only the fullerene, CNTs are also gaining considerable attention for OPVs due to its optical and electrical properties.[185] In the beginning, CNTs were used with conjugated polymer poly 3-octyl thiophene (P3OT) as an active layer in OPVs. Although these devices showed large open circuit voltage of 0.75 V, efficiency of these devices was reported[186] to be very low in the range of 0.063%. In further attempts[187] to improve the efficiency, SWNTs and MWNTs were mixed with poly 3-hexathiophene(P3HT):PCBM active layer and 100% increase in the short circuit current was reported. It has also been shown that incorporation of CNTs in various layers of OPVs[188,189] (anode, hole transport layer, cathode, heterojuction active layer) also adds to the efficiency of OPVs. CNTs have also been used in dye-sensitized solar cells[190] and photoelectrochemical solar cells. Efficiency of 4.5% was achieved[191] when CNTs were incorporated in TiO_2 nanoparticle matrix. In another approach, presence of direct band gap in semiconductor nanotubes has been exploited for photovoltaic cells by using them as an active layer. However, this approach suffers from the difficulty of achieving CNT based p–n junction due to unstable n-type doping of CNTs. This challenge can be overcome by using n-type fullerene or by using n-type silicon wafer to create p–n junction. Wu *et al.* designed a thin film solar cell[192] by creating a p–n junction of double-walled CNT and n-type silicon wafer with efficiency of 1%. Optimizing Si–CNT interface has also been shown to improve the efficiency to 7%. Future works continue to improve various approaches and we can hope to have carbon nanomaterial-based solar cells to be used in day to day life soon.

6. Conclusions and Outlook

The unique physicochemical properties of CNTs and graphene make them promising candidates for use in many different fields, including biomedical, electronics, energy storage, *etc.* This chapter gives an overview as to how graphene can be used in biomedicine for the delivery of siRNA for the treatment

of cancer by synthesizing graphene–siRNA composite. Functionalization of graphene enhances the scope and biocompatibility of graphene in the cell environment. However, more efforts are required for a complete understanding of the delivery mechanism and toxic effects in this exciting field. We have also shown different binding mechanism and kinetics for the dsDNA–graphene complex and attributed this difference to the different binding affinity of uracil and thymine to graphene. This chapter also reviews our current understanding of the CNT–DNA hybrid structure which has many other potential applications. In this area, both experiments and simulation have given us valuable information about the structure and thermodynamics of CNT–DNA complexation. MD studies have explored that ssDNA nucleic bases are adsorbed onto the CNT surface and formed a stable structure via π–π stacking interaction between bases and nanotube surface and the hydrophilic phosphate backbone is exposed to the aqueous environment. Further studies using REMD on ssDNA–SWNT hybrid system have reported that there are six different conformations with one as global minima. To study the temperature effect on the binding of nucleic bases with CNT, MD simulations were performed at different temperatures. It has been observed that with increasing temperature, the base self-stacking breaks and the polymer becomes more flexible. As a result, the rate of spontaneous adsorption of oligonucleotides onto the CNT surface increases. Thus, the hybrid system reaches to an energetically more favorable conformation in a comparatively shorter time. This hybrid structure possesses many useful physical and electronic properties. Due to these excellent properties, it is used in a variety of fields in nanotechnology. Unlike ssDNA–CNT hybrid, dsDNA–CNT hybrid has received less attention theoretically and much more work is required in this field to gain a deeper understanding about the microscopic picture of the dsDNA–CNT hybrid. Modification of CNTs with dendrimers has also attracted lots of attention because dendrimers show great advantages in solubilizing CNTs. Because of their globular architecture and the presence of large number of terminal groups, dendrimers facilitate further functionalization and enable the resultant nanohybrids to have many interesting and useful properties. The novel CNT–dendrimer-based nanoconjugates are potentially applicable in various fields, namely, mechanical engineering materials, nanocatalysts, fuel cells, nanomedicine, and sensors, *etc.*, and hence, there should be further interdisciplinary research in this area. We have also highlighted how graphene and CNTs have huge potential in the field of energy harvesting and energy storage devices. Importance of carbon nanomaterials in fast and efficient electronic devices is discussed in detail. However, to make this a reality, significant practical challenges need to be overcome.

Acknowledgments

We tank Department of Science and Technology (DST) and Department of Biotechnology (DBT), India for financial support.

References

1. Novoselov, K.; Geim, A.; Morozov, S.; Jiang, D.; Zhang, Y.; Dubonos, S.; Grigorieva, I.; Firsov, A. *Science* **2004**, *306*, 666–669.
2. Meyer, J. C.; Geim, A. K.; Katsnelson, M. I.; Novoselov, K. S.; Booth, T. J.; Roth, S. *Nature* **2007**, *446*, 60–63.
3. Geim, A. K.; Novoselov, K. S. *Nat. Mater.* **2007**, *6*, 183–191.
4. Stankovich, S.; Dikin, D. A.; Dommett, G. H. B.; Kohlhaas, K. M.; Zimney, E. J.; Stach, E. A.; Piner, R. D.; Nguyen, S. T.; Ruoff, R. S. *Nature* **2006**, *442*, 282–286.
5. Huang, X.; Qi, X.; Boey, F.; Zhang, H. *Chem. Soc. Rev.* **2012**, *41*, 666–686.
6. Sreeprasad, T. S.; Berry, V. *Small* **2013**, *9*, 341–350.
7. Georgakilas, V.; Otyepka, M.; Bourlinos, A. B.; Chandra, V.; Kim, N.; Kemp, K. C.; Hobza, P.; Zboril, R.; Kim, K. S. *Chem. Rev.* **2012**, *112*, 6156–6214.
8. Worsley, K. A.; Ramesh, P.; Mandal, S. K.; Niyogi, S.; Itkis, M. E.; Haddon, R. C. *Chem. Phys. Lett.* **2007**, *445*, 51–56.
9. Subrahmanyam, K. S.; Vivekchand, S. R. C.; Govindaraj, A.; Rao, C. N. R. *J. Mater. Chem.* **2008**, *18*, 1517–1523.
10. Rao, C. N. R.; Sood, A. K.; Subrahmanyam, K. S.; Govindaraj, A. *Angew. Chem. Int. Ed.* **2009**, *48*, 7752–7777.
11. Garaj, S.; Hubbard, W.; Reina, A.; Kong, J.; Branton, D.; Golovchenko, J. A. *Nature* **2010**, *467*, 190–193.
12. Schneider, G. F.; Kowalczyk, S. W.; Calado, V. E.; Pandraud, G.; Zandbergen, H. W.; Vandersypen, L. M. K.; Dekker, C. *Nano Lett.* **2010**, *10*, 3163–3167.
13. Merchant, C. A.; Healy, K.; Wanunu, M.; Ray, V.; Peterman, N.; Bartel, J.; Fischbein, M. D.; Venta, K.; Luo, Z.; Johnson, A. T. C.; Drndic, M. *Nano Lett.* **2010**, *10*, 2915–2921.
14. Varghese, N.; Mogera, U.; Govindaraj, A.; Das, A.; Maiti, P. K.; Sood, A. K.; Rao, C. N. R. *Chem. Phys. Chem.* **2009**, *10*, 206–210.
15. Santosh, M.; Panigrahi, S.; Bhattacharyya, D.; Sood, A. K.; Maiti, P. K. *J. Chem. Phys.* **2012**, *136*, 065106.
16. Nandy, B.; Santosh, M.; Maiti, P. K. *J. Biosci.* **2012**, *37*, 457–474.
17. Umadevi, D.; Sastry, G. N. J. *Phys. Chem. Lett.* **2011**, *2*, 1572–1576.
18. Mohanty, N.; Berry, V. *Nano Lett.* **2008**, *8*, 4469–4476.
19. Zhao, X. *J. Phys. Chem. C* **2011**, *115*, 6181–6189.

20. Lu, C.-H.; Zhu, C.-L.; Li, J.; Liu, J.-J.; Chen, X.; Yang, H.-H. *Chem. Commun.* **2010**, *46*, 3116–3118.
21. Lv, W.; Guo, M.; Liang, M.-H.; Jin, F.-M.; Cui, L.; Zhi, L.; Yang, Q.-H. *J. Mater. Chem.* **2010**, *20*, 6668–6673.
22. Napoli, C.; Lemieux, C.; Jorgensen, R. *Plant Cell* **1990**, *2*, 279–289.
23. Fire, A.; Xu, S. Q.; Montgomery, M. K.; Kostas, S. A.; Driver, S. E.; Mello, C. C. *Nature* **1998**, *391*, 806–811.
24. Couzin, J. *Science* **2002**, *298*, 2296–2297.
25. Paton, R. S.; Goodman, J. M. *J. Chem. Inf. Mod.* **2009**, *49*, 944–955.
26. Mogurampelly, S.; Panigrahi, S.; Bhattacharyya, D.; Sood, A. K.; Maiti, P. K. *J. Chem. Phys.* **2012**, *137*, 054903.
27. Mogurampelly, S.; Maiti, P. K. *J. Chem. Phys.* **2013**, *138*, 034901.
28. Yin, D.; Li, Y.; Lin, H.; Guo, B.; Du, Y.; Li, X.; Jia, H.; Zhao, X.; Tang, J.; Zhang, L. *Nanotechnology* **2013**, *24*, 105102.
29. Das, A.; Sood, A. K.; Maiti, P. K.; Das, M.; Varadarajan, R.; Rao, C. N. R. *Chem. Phys. Lett.* **2008**, *453*, 266–273.
30. Zhang, Y.; Ali, S. F.; Dervishi, E.; Xu, Y.; Li, Z.; Casciano, D.; Biris, A. S. *ACS Nano* **2010**, *4*, 3181–3186.
31. Feng, L.; Liu, Z. *Nanomedicine* **2011**, *6*, 317–324.
32. Chen, H.; Mueller, M. B.; Gilmore, K. J.; Wallace, G. G.; Li, D. *Adv. Mater.* **2008**, *20*, 3557+.
33. Yang, K.; Wan, J.; Zhang, S.; Zhang, Y.; Lee, S.-T.; Liu, Z. *Acs Nano* **2011**, *5*, 516–522.
34. Lu, G.; Maragakis, P.; Kaxiras, E. *Nano Lett.* **2005**, *5*, 897–900.
35. Zhao, X.; Johnson, J. K. *J. Am. Chem. Soc.* **2007**, *129*, 10438–10445.
36. Manohar, S.; Tang, T.; Jagota, A. *J. Phys. Chem. C* **2007**, *111*, 17835–17845.
37. Staii, C.; Johnson, A. *Nano Lett.* **2005**, *5*, 1774–1778.
38. Jeng, E.; Moll, A.; Roy, A.; Gastala, J.; Strano, M. *Nano Lett.* **2006**, *6*, 371–375.
39. Zheng, M.; Jagota, A.; Semke, E.; Diner, B.; Mclean, R.; Lustig, S.; Richardson, R.; Tassi, N. *Nat. Mater.* **2003**, *2*, 338–342.
40. Zheng, M.; Jagota, A.; Strano, M.; Santos, A.; Barone, P.; Chou, S.; Diner, B.; Dresselhaus, M.; McLean, R.; Onoa, G.; Samsonidze, G.; Semke, E.; Usrey, M.; Walls, D. *Science* **2003**, *302*, 1545–1548.
41. Wu, Y.; Phillips, J. A.; Liu, H.; Yang, R.; Tan, W. *ACS Nano* **2008**, *2*, 2023–2028.
42. Meng, S.; Maragakis, P.; Papaloukas, C.; Kaxiras, E. *Nano Lett.* **2007**, *7*, 45–50.
43. Campbell, J. F.; Tessmer, I.; Thorp, H. H.; Erie, D. A. *J. Am. Chem. Soc.* **2008**, *130*, 10648–10655.

44. Jin, H.; Jeng, E. S.; Heller, D. A.; Jena, P. V.; Kirmse, R.; Lan-gowski, J.; Strano, M. S. *Macromolecules* **2007**, *40*, 6731–6739.
45. Johnson, R. R.; Johnson, A. T. C.; Klein, M. L. *Nano Lett.* **2008**, *8*, 69–75.
46. Mitsutake, A.; Sugita, Y.; Okamoto, Y. *Biopolymers* **2001**, *60*, 96–123.
47. Johnson, R. R.; Kohlmeyer, A.; Johnson, A. T. C.; Klein, M. L. *Nano Lett.* **2009**, *9*, 537–541.
48. Karachevtsev, M. V.; Karachevtsev, V. A. *J. Phys. Chem. B* **2011**, *115*, 9271–9279.
49. Petruska, J.; Goodman, M. F.; Boosalis, M. S.; Sowers, L. C.; Cheong, C.; Tinoco, I. *Proc. Natl. Acad. Sci. USA.* **1988**, *85*, 6252–6256.
50. Sponer, J.; Leszczynski, J.; Hobza, P. *Biopolymers* **2001**, *61*, 3–31.
51. Stepanian, S. G.; Karachevtsev, M. V.; Glamazda, A. Y.; Karachevtsev, V. A.; Adamowicz, L. *J. Phys. Chem. A* **2009**, *113*, 3621–3629.
52. Tang, B.; Xu, H. *Macromolecules* **1999,** *32*, 2569–2576. 2nd East Asian Polymer Conference, Hong Kong, Hong Kong, Jan 12–16, **1999**.
53. Roxbury, D.; Tu, X.; Zheng, M.; Jagota, A. *Langmuir* **2011**, *27*, 8282–8293.
54. Tu, X.; Manohar, S.; Jagota, A.; Zheng, M. *Nature* **2009**, *460*, 250–253.
55. Roxbury, D.; Mittal, J.; Jagota, A. *Nano Lett.* **2012**, *12*, 1464–1469.
56. Roxbury, D.; Jagota, A.; Mittal, J. *J. Am. Chem. Soc.* **2011**, *133*, 13545–13550.
57. Tang, X.; Bansaruntip, S.; Nakayama, N.; Yenilmez, E.; Chang, Y.-L.; Wang, Q. *Nano Lett.* **2006**, *6*, 1632–1636.
58. Wang, J. *Electroanal.* **2005**, *17*, 7–14.
59. Star, A.; Tu, E.; Niemann, J.; Gabriel, J.; Joiner, C.; Valcke, C. *Proc. Natl. Acad. Sci. USA.* **2006**, *103*, 921–926.
60. Johnson, A. T. C.; Staii, C.; Chen, M.; Khamis, S.; Johnson, R.; Klein, M. L.; Gelperin, A. *Semicond. Sci. Tech.* **2006**, *21*, S17–S21.
61. Johnson, A. T. C.; Staii, C.; Chen, M.; Khamis, S.; Johnson, R.; Klein, M. L.; Gelperin, A. *Phys. Status Solidi. B* **2006**, *243*, 3252–3256. 20th International Winterschool/Euroconference on Electronic Properties of Novel Materials, Kirchberg, Austria, Mar 04–11, **2006**.
62. Chen, C.-L.; Yang, C.-F.; Agarwal, V.; Kim, T.; Sonkusale, S.; Bus-naina, A.; Chen, M.; Dokmeci, M. R. *Nanotechnology* **2010**, *21*, 095504.
63. Tans, S.; Verschueren, A.; Dekker, C. *Nature* **1998**, *393*, 49–52.
64. Badaire, S.; Pichot, V.; Zakri, C.; Poulin, P.; Launois, P.; Vavro, J.; Guthy, C.; Chen, M.; Fischer, J. *J. Appl. Phys.* **2004**, *96*, 7509–7513.
65. Baughman, R.; Cui, C.; Zakhidov, A.; Iqbal, Z.; Barisci, J.; Spinks, G.; Wallace, G.; Mazzoldi, A.; De Rossi, D.; Rinzler, A.; Jaschinski, O.; Roth, S.; Kertesz, M. *Science* **1999**, *284*, 1340–1344.
66. Bhalla, V.; Bajpai, R.; Bharadwaj, L. *EMBO Rep.* **2003**, *4*, 442–445.
67. Shin, S. R.; Lee, C. K.; So, I.; Jeon, J.-H.; Kang, T. M.; Kee, C.; Kim, S. I.; Spinks, G. M.; Wallace, G. G.; Kim, S. J. *Adv. Mater.* **2008**, *20*, 466+.

68. Kwon, N. H.; Beaux, M. F.; II, Ebert, C.; Wang, L.; Lassiter, B. E.; Park, Y. H.; McIlroy, D. N.; Hovde, C. J.; Bohach, G. A. *Nano Lett.* **2007**, *7*, 2718–2723.
69. Hampton, T. *JAMA-J. Am. Med. Assoc.* **2007**, *298*, 505.
70. Heller, D.; Jeng, E.; Yeung, T.; Martinez, B.; Moll, A.; Gastala, J.; Strano, M. *Science* **2006**, *311*, 508–511.
71. Kam, N.; O'Connell, M.; Wisdom, J.; Dai, H. *Proc. Natl. Acad. Sci. USA.* **2005**, *102*, 11600–11605.
72. Cai, D.; Mataraza, J.; Qin, Z.; Huang, Z.; Huang, J.; Chiles, T.; Car-nahan, D.; Kempa, K.; Ren, Z. *Nat. Methods* **2005**, *2*, 449–454.
73. Chen, C.; Liu, Y.; Wu, C.; Yeh, C.; Su, M.; Wu, Y. *Adv. Mater.* **2005**, *17*, 404+.
74. Cui, X.; Yu, S.; Li, L.; Li, K.; Yu, B. *Adv. Mater.* **2004**, *16*, 1109+.
75. He, X.; Wang, K.; Tan, W.; Liu, B.; Lin, X.; He, C.; Li, D.; Huang, S.; Li, J. *J. Am. Chem. Soc.* **2003**, *125*, 7168–7169.
76. Li, J.; Fang, X.; Schuster, S.; Tan, W. *Angew. Chem. Int. Edit.* **2000**, *39*, 1049+.
77. Caminade, A.-M.; Majoral, J.-P.; *Chem. Soc. Rev.* **2010**, *39*, 2034–2047.
78. Sun, J.-T.; Hong, C.-Y.; Pan, C.-Y. *Polym. Chem.* **2011**, *2*, 998–1007.
79. Neelgund, G. M.; Oki, A. *Appl. Catal. B-Environ* **2011**, *110*, 99–107.
80. Murugan, E.; Vimala, G. *J. Colloid. Interf. Sci.* **2013**, *396*, 101–111.
81. Herrero, M. A.; Guerra, J.; Myers, V. S.; Victoria Gomez, M.; Crooks, R. M.; Prato, M. *ACS Nano* **2010**, *4*, 905–912.
82. Guerra, J.; Antonia Herrero, M.; Carrion, B.; Perez-Martinez, F. C.; Lucio, M.; Rubio, N.; Meneghetti, M.; Prato, M.; Cena, V.; Vazquez, E. *Carbon* **2012**, *50*, 2832–2844.
83. Campidelli, S.; Sooambar, C.; Diz, E. L.; Ehli, C.; Guldi, D. M.; Prato, M. *J. Am. Chem. Soc.* **2006**, *128*, 12544–12552.
84. Siriviriyanun, A.; Imae, T. *Phys. Chem. Chem. Phys.* **2013**, *15*, 4921–4929.
85. Qin, W.; Yang, K.; Tang, H.; Tan, L.; Xie, Q.; Ma, M.; Zhang, Y.; Yao, S. *Colloid Surface B* **2011**, *84*, 206–213.
86. Huang, P.; Lin, J.; Yang, D.; Zhang, C.; Li, Z.; Cui, D. *J. Control. Release* **2011**, *152*, E33–E34. 1st Symposium on Innovative Polymers for Controlled Delivery, Suzhou, People's Rep. China, Sep 14–17, **2010**.
87. Nandy, B.; Maiti, P. K. *J. Phys. Chem. B* **2011**, *115*, 217–230.
88. Vasumathi, V.; Maiti, P. K. *Macromolecules* **2010**, *43*, 8264–8274.
89. Tomalia, D.; Baker, H.; Dewald, J.; Hall, M.; Kallos, G.; Martin, S.; Roeck, J.; Ryder, J.; Smith, P. *Polym. J.* **1985**, *17*, 117–132.
90. Newkome, G. R.; Shreiner, C. D. *Polymer* **2008**, *49*, 1–173.
91. Maiti, P. K.; Cagin, T.; Wang, G.; Goddard, W. *Macromolecules* **2004**, *37*, 6236–6254.
92. Maiti, P. K.; Cagin, T.; Lin, S.; Goddard, W. *Macromolecules* **2005**, *38*, 979–991.
93. Maiti, P. K.; Messina, R. *Macromolecules* **2008**, *41*, 5002–5006.

94. Maiti, P. K.; Li, Y.; Cagin, T.; Goddard, W. A.; III, *J. Chem. Phys.* **2009**, *130*, 144902.
95. Rolland, O.; Turrin, C.-O.; Caminade, A.-M.; Majoral, J.-P. *New J. Chem.* **2009**, *33*, 1809–1824.
96. Grayson, S.; Frechet, J. *Chem. Rev.* **2001**, *101*, 3819–3867.
97. Astruc, D.; Boisselier, E.; Ornelas, C. *Chem. Rev.* **2010**, *110*, 1857–1959.
98. Murugan, E.; Vimala, G. *J. Colloid. Interf. Sci.* **2011**, *357*, 354–365.
99. Ma, J.; Deng, S.; Cheng, X.; Wei, W.; Hu, A. *J. Polym. Sci. A1* **2011**, *49*, 3951–3959.
100. Siriviriyanun, A.; Imae, T.; Motojime, S. *Sci. Adv. Mater.* **2013**, *5*, 1–6.
101. Liu, P. *Eur. Polym. J.* **2005**, *41*, 2693–2703.
102. Spitalsky, Z.; Tasis, D.; Papagelis, K.; Galiotis, C. *Prog. Polym. Sci.* **2010**, *35*, 357–401.
103. You, Y.-Z.; Hong, C.-Y.; Pan, C.-Y. *Macromol. Rapid Comm.* **2006**, *27*, 2001–2006.
104. You, Y.-Z.; Hong, C.-Y.; Pan, C.-Y. *Adv. Funct. Mater.* **2007**, *17*, 2470–2477.
105. Sun, L.; Warren, G. L.; O'Reilly, J. Y.; Everett, W. N.; Lee, S. M.; Davis, D.; Lagoudas, D.; Sue, H. J. *Carbon* **2008**, *46*, 320–328.
106. Feng, Q.-P.; Xie, X.-M.; Liu, Y.-T.; Zhao, W.; Gao, Y.-F. *J. Appl. Polym. Sci.* **2007**, *106*, 2413–2421.
107. Hwang, S.; Moorefield, C.; Wang, P.; Jeong, K.; Cheng, S.; Kotta, K.; Newkome, G. *J. Am. Chem. Soc.* **2006**, *128*, 7505–7509.
108. Zeng, Y.-L.; Huang, Y.-F.; Jiang, J.-H.; Zhang, X.-B.; Tang, C.-R.; Shen, G.-L.; Yu, R.-Q. *Electochem. Commun.* **2007**, *9*, 185–190.
109. Shen, Y.; Xu, Q.; Gao, H.; Zhu, N. *Eelectrochem. Commun.* **2009**, *11*, 1329–1332.
110. Zhu, N.; Gao, H.; Xu, Q.; Lin, Y.; Su, L.; Mao, L. *Biosens. Bioelectron.* **2010**, *25*, 1498–1503.
111. Yuan, W.; Jiang, G.; Che, J.; Qi, X.; Xu, R.; Chang, M. W.; Chen, Y.; Lim, S. Y.; Dai, J.; Chan-Park, M. B.; *J. Phys. Chem. C* **2008**, *112*, 18754–18759.
112. Sano, M.; Kamino, A.; Shinkai, S. *Angew. Chem. Int. Edit.* **2001**, *40*, 4661+.
113. Tao, L.; Chen, G.; Mantovani, G.; York, S.; Haddleton, D. M. *Chem. Commun.* **2006**, *(47)*, 4949–4951.
114. Zeng, Y.; Tang, C.; Wang, H.; Jiang, J.; Tian, M.; Shen, G.; Yu, R. *Spectrochim. Acta A* **2008**, *70*, 966–972.
115. Maiyalagan, T. *J. Solid. State. Electr.* **2009**, *13*, 1561–1566. 5th Chianti Electrochemistry Meeting 2008, Siena, Italy, Jul 08–13, **2008**.
116. Zhu, N.; Xu, Q.; Li, S.; Gao, H. *Electochem. Commun.* **2009**, *11*, 2308–2311.
117. Singh, R.; Pantarotto, D.; McCarthy, D.; Chaloin, O.; Hoebeke, J.; Par-tidos, C.; Briand, J.; Prato, M.; Bianco, A.; Kostarelos, K. *J. Am. Chem. Soc.* **2005**, *127*, 4388–4396.

118. Welsher, K.; Liu, Z.; Daranciang, D.; Dai, H. *Nano Lett.* **2008**, *8*, 586–590.
119. Shao, N.; Lu, S.; Wickstrom, E.; Panchapakesan, B. *Nanotechnology* **2007**, *18*, 315101.
120. Shi, X.; Wang, S. H.; Shen, M.; Antwerp, M. E.; Chen, X.; Li, C.; Petersen, E. J.; Huang, Q.; Jr., Weber, W. J.; Jr., Baker, J. R. *Biomacromolecules* **2009**, *10*, 1744–1750.
121. Hong, C.; You, Y.; Pan, C. *Chem. Mater.* **2005**, *17*, 2247–2254.
122. Zhao, G.; Li, Y.; Wang, J.; Zhu, H. *Appl. Microbiol. Biot.* **2011**, *91*, 591–601.
123. Cao, L.; Yang, W.; Yang, J.; Wang, C.; Fu, S. *Chem. Lett.* **2004**, *33*, 490–491.
124. Antonia Herrero, M.; Toma, F. M.; Al-Jamal, K. T.; Kostarelos, K.; Bianco, A.; Da Ros, T.; Bano, F.; Casalis, L.; Scoles, G.; Prato, M. *J. Am. Chem. Soc.* **2009**, *131*, 9843–9848.
125. Che, J.; Yuan, W.; Jiang, G.; Dai, J.; Lim, S. Y.; Chan-Park, M. B.; *Chem. Mater.* **2009**, *21*, 1471–1479.
126. Pan, B.; Cui, D.; Gao, F.; He, R. *Nanotechnology* **2006**, *17*, 2483–2489.
127. Pan, B.; Cui, D.; Xu, P.; Ozkan, C.; Feng, G.; Ozkan, M.; Huang, T.; Chu, B.; Li, Q.; He, R.; Hu, G. *Nanotechnology* **2009**, *20*, 125101.
128. Ahmar, H.; Fakhari, A. R.; Nabid, M. R.; Rezaei, S. J. T.; Bide, Y. *Sensor Actuat. B-Chem.* **2012**, *171*, 611–618.
129. Vijayaraghavan, G.; Stevenson, K. J. *Langmuir* **2007**, *23*, 5279–5282.
130. Xu, L.; Zhu, Y.; Tang, L.; Yang, X.; Li, C. *Electroanal.* **2007**, *19*, 717–722.
131. Jayamurugan, G.; Vasu, K. S.; Rajesh Kumar, Y. B. R. D. S.; Vasumathi, V.; Maiti, P. K.; Sood, A. K.; Jayaraman, N. *J. Chem. Phys.* **2011**, *134* , 104507.
132. Vasumathi, V.; Pramanik, D.; Sood, A. K.; Maiti, P. K. *Soft. Matter.* **2013**, *9*, 1372–1380.
133. Ye, Y.; Ahn, C. C.; Witham, C.; Fultz, B.; Liu, J.; Rinzler, A. G.; Colbert, D.; Smith, K. A.; Smalley, R. E. *Appl. Phys. Lett.* **1999**, *74*, 2307–2309.
134. Chan, S.-P.; Chen, G.; Gong, X. G.; Liu, Z.-F. *Phys. Rev. Lett.* **2001**, *87*, 205502.
135. Dillon, A.; Jones, K.; Bekkedahl, T.; Kiang, C.; Bethune, D.; Heben, M. *Nature* **1997**, *386*, 377–379.
136. Li, J.; Furuta, T.; Goto, H.; Ohashi, T.; Fujiwara, Y.; Yip, S. *J. Chem. Phys.* **2003**, *119*, 2376–2385.
137. Rzepka, M.; Lamp, P.; de la Casa-Lillo, M. *J. Phys. Chem. B* **1998**, *102*, 10894–10898.
138. Ahn, C.; Ye, Y.; Ratnakumar, B.; Witham, C.; Bowman, R.; Fultz, B. *Appl. Phys. Lett.* **1998**, *73*, 3378–3380.
139. Fan, Y.; Liao, B.; Liu, M.; Wei, Y.; Lu, M.; Cheng, H. *Carbon* **1999**, *37*, 1649–1652.

140. Ye, Y.; Ahn, C.; Witham, C.; Fultz, B.; Liu, J.; Rinzler, A.; Colbert, D.; Smith, K.; Smalley, R. *Appl. Phys. Lett.* **1999**, *74*, 2307–2309.
141. Chen, P.; Wu, X.; Lin, J.; Tan, K. *Science* **1999**, *285*, 91–93.
142. Liu, C.; Fan, Y.; Liu, M.; Cong, H.; Cheng, H.; Dresselhaus, M. *Science* **1999**, *286*, 1127–1129.
143. Liu, C.; Chen, Y.; Wu, C.-Z.; Xu, S.-T.; Cheng, H.-M. *Carbon* **2010**, *48*, 452–455.
144. Dimitrakakis, G. K.; Tylianakis, E.; Froudakis, G. E. *Nano Lett.* **2008**, *8*, 3166–3170.
145. Tozzini,V.; Pellegrini, V. *Phys. Chem. Chem. Phys.* **2013**, *15*, 80–89.
146. Durgun, E.; Ciraci, S.; Yildirim, T. *Phys. Rev. B* **2008**, *77*, 085405.
147. Durgun, E.; Ciraci, S.; Zhou, W.; Yildirim, T. *Phys. Rev. Lett.* **2006**, *97*, 226102.
148. Du, A.; Zhu, Z.; Smith, S. C. *J. Am. Chem. Soc.* **2010**, *132*, 2876+.
149. Lee, H.; Ihm, J.; Cohen, M. L.; Louie, S. G. *Nano Lett.* **2010**, *10*, 793–798.
150. Norman, R. *Science* **1974**, *186*, 350–352.
151. Loeb, S. *Science* **1975**, *189*, 654–655.
152. Levenspi, O.; Nevers, N. *Science* **1974**, *183*, 157–160.
153. Weinstein, J.; Leitz, F. *Science* **1976**, *191*, 557–559.
154. Pattle, R. *Nature* **1954**, *174*, 660.
155. Brogioli, D. *Phys. Rev. Lett.* **2009**, *103*, 058501.
156. Boon, N.; van Roij, R. *Mol. Phys.* **2011**, *109*, 1229–1241.
157. Brogioli, D.; Zhao, R.; Biesheuvel, P. M. *Energ. Environ. Sci.* **2011**, *4*, 772–777.
158. Ghosh, S.; Sood, A.; Kumar, N. *Science* **2003**, *299*, 1042–1044.
159. Ghosh, S.; Sood, A. K.; Ramaswamy, S.; Kumar, N. *Phys. Rev. B* **2004**, *70*, 205423.
160. Liu, J.; Dai, L.; Baur, J. W. *J. Appl. Phys.* **2007**, *101*, 064312.
161. Lee, S. H.; Kim, D.; Kim, S.; Han, C.-S. *Appl. Phys. Lett.* **2011**, *99*, 104103.
162. Yuan, Q.; Zhao, Y.-P. *J. Am. Chem. Soc.* **2009**, *131*, 6374+.
163. Dhiman, P.; Yavari, F.; Mi, X.; Gullapalli, H.; Shi, Y.; Ajayan, P. M.; Koratkar, N. *Nano Lett.* **2011**, *11*, 3123–3127.
164. Martel, R.; Schmidt, T.; Shea, H. R.; Hertel, T.; Avouris, P. *Appl. Phys. Lett.* **1998**, *73*, 2447–2449.
165. Li, H.; Xu, C.; Srivastava, N.; Banerjee, K. *IEEE T. Electron. Dev.* **2009**, *56*, 1799–1821.
166. Naeemi, A.; Meindl, J. *Electron Dev. Lett. IEEE* **2007**, *28*, 428–431.
167. Avouris, P.; Chen, Z.; Perebeinos, V. *Nat. Nanotechnol.* **2007**, *2*, 605–615.
168. Leonard, F.; Tersoff, J. *Phys. Rev. Lett.* **2000**, *84*, 4693–4696.

169. Martel, R.; Derycke, V.; Lavoie, C.; Appenzeller, J.; Chan, K.; Ter-soff, J.; Avouris, P. *Phys. Rev. Lett.* **2001**, *87*, 256805.
170. Chen, Z.; Appenzeller, J.; Knoch, J.; Lin, Y.; Avouris, P. *Nano Lett.* **2005**, *5*, 1497–1502.
171. Magen, N.; Kolodny, A.; Weiser, U.; Shamir, N. In *Proceedings of the 2004 international workshop on System Level Interconnect Prediction*, SLIP '04, New York, USA, 7–13, ACM, **2004**.
172. Rossnagel, S.; Kuan, T. *J. Vac. Sci. Technol. B.* **2004**, *22*, 240–247.
173. Palacios, T.; Hsu, A.; Wang, H. *IEEE Commun. Mag.* **2010**, *48*, 122–128.
174. Naeemi, A.; Meindl, J. D. *IEEE T. Electron. Dev.* **2009**, *56*, 1822–1833.
175. Chen, C.; Rosenblatt, S.; Bolotin, K. I.; Kalb, W.; Kim, P.; Kymis-sis, I. Stormer, H. L.; Heinz, T. F.; Hone, J. *Nat. Nanotechnol.* **2009**, *4*, 861–867.
176. Chen, X.; Akinwande, D.; Lee, K.-J.; Close, G. F.; Yasuda, S.; Paul, B. C.; Fujita, S.; Kong, J.; Wong, H. S. P. *IEEE T. Electron. Dev.* **2010**, *57*, 3137–3143.
177. Lin, Y. M.; Dimitrakopoulos, C.; Jenkins, K. A.; Farmer, D. B.; Chiu, H. Y.; Grill, A.; Avouris, P. *Science* **2010**, *327*, 662.
178. Park, S.; Vosguerichian, M.; Bao, Z. *Nanoscale* **2013**, *5*, 1727–1752.
179. Cao, Q.; Kim, H.-S.; Pimparkar, N.; Kulkarni, J. P.; Wang, C.; Shim, M.; Roy, K.; Alam, M. A.; Rogers, J. A. *Nature* **2008**, *454*, 495–U4.
180. Bradley, K.; Gabriel, J.; Gruner, G. *Nano Lett.* **2003**, *3*, 1353–1355.
181. Sariciftci, N.; Smilowitz, L.; Heeger, A.; Wudl, F. *Science* **1992**, *258*, 1474–1476.
182. Sariciftci, N. S.; Braun, D.; Zhang, C.; Srdanov, V. I.; Heeger, A. J.; Stucky, G.; Wudl, F. *Appl. Phys. Lett.* **1993**, *62*, 585–587.
183. Hummelen, J. C.; Knight, B. W.; LePeq, F.; Wudl, F.; Yao, J.; Wilkins, C. L. *J. Org. Chem.* **1995**, *60*, 532–538.
184. Yu, G.; Gao, J.; Hummelen, J. C.; Wudl, F.; Heeger, A. J. *Science* **1995**, *270*, 1789–1791.
185. Jariwala, D.; Sangwan, V. K.; Lauhon, L. J.; Marks, T. J.; Hersam, M. C. *Chem. Soc. Rev.* **2013**, *42*, 2824–2860.
186. Kymakis, E.; Alexandrou, I.; Amaratunga, G. A. J. *J. Appl. Phys.* **2003**, *93*, 1764–1768.
187. Berson, S.; deBettignies, R.; Bailly, S.; Guillerez, S.; Jousselme, B. *Adv. Funct. Mater.* **2007**, *17*, 3363–3370.
188. Geng, J.; Zeng, T. *J. Am. Chem. Soc.* **2006**, *128*, 16827–16833.
189. Ren, S.; Bernardi, M.; Lunt, R. R.; Bulovic, V.; Grossman, J. C.; Gradeak, S. *Nano Lett.* **2011**, *11*, 5316–5321.
190. Oregan, B.; Gratzel, M. *Nature* **1991**, *353*, 737–740.
191. Hwa Jung, K.; Hong, J. S.; Vittal, R.; Kim, K.-J. *Chem. Lett.* **2002**, *31*, 864–865.
192. Wei, J.; Jia, Y.; Shu, Q.; Gu, Z.; Wang, K.; Zhuang, D.; Zhang, G.; Wang, Z.; Luo, J.; Cao, A.; Wu, D. *Nano Lett.* **2007**, *7*, 2317–2321.

Cumulative Index of Volumes 5 and 6

Adsorption on and reactivity of CNT and graphene, Vol. 5:40–42
  chemisorption on CNT and graphene
    gases, Vol. 5:83–97
    liquids, Vol. 5:97–99
    solids, Vol. 5:99–122
  effects of interactions with nanotubes on IR spectra of small molecules, Vol. 5:59
  nitrogen-containing species on carbon surface, Vol. 5:126
  oxygen-containing species, Vol. 5:125
  physisorption on CNTs and graphene, Vol. 5:54–55
    gases, Vol. 5:55–66
    liquids, Vol. 5:66–77
    solids, Vol. 5:77–83
  reactivity on CNTs and graphene, Vol. 5:122
    bioreactivity and degradability of CNTs and graphene, Vol. 5:153–160
    catalysis, Vol. 5:128–150
    gas sensors, Vol. 5:150–153
    main advantages offered by CNT or CNF supports, Vol. 5:129
    nanostructured carbon materials, surface chemistry of, Vol. 5:124–128
  structure and adsorption sites, Vol. 5:42
    graphene and few layer graphene (FLG), Vol. 5:42–49
AEPA (2-aminoethylphosphonic acid), Vol. 5:79
Amperometric glucose biosensors
  with detection of H_2O_2, Vol. 6:93–101
  with direct electron transfer, Vol. 6:88–93
APTES (3-aminopropyltriethoxysilane), Vol. 5:79
Atomic collapse on graphene, Vol. 5:14–16

Bilayer-graphene, Vol. 5:8
Biocompatibility of graphene, Vol. 6:197
Bioreactivity and degradability of CNTs and graphene, Vol. 5:153–160
  biodegradability and toxicity, Vol. 5:158
  biosensors, Vol. 5:155–156
  drug delivery, Vol. 5:156–158
Biosensor applications, graphene for, Vol. 6:83–87
  biosensors for glucose, Vol. 6:87–88
    amperometric glucose biosensors with detection of H_2O_2, Vol. 6:93–101

amperometric glucose biosensors with direct electron transfer, Vol. 6:88–93
mass-sensitive glucose biosensors, Vol. 6:101–102
nucleic acids, Vol. 6:103–112
proteins, Vol. 6:112–113
amino acids, Vol. 6:119–122
cancer biomarkers, Vol. 6:113–117
immunoglobulins, Vol. 6:122–124
thrombin, Vol. 6:117–119

Cancer biomarkers, Vol. 6:113–117
Carbon
elastic properties of several allotropes, Vol. 5:17
graphene as allotropes of. *See* Graphene
Carbon adatoms, Vol. 5:23–24
defects with, Vol. 5:24
Carbon nanofibers (CNFs), Vol. 5:122
characteristics of, Vol. 5:123
Carbon nanostructures, Vol. 5:4
Carbon nanotubes (CNT), Vol. 5:40
characteristics of, Vol. 5:123
physisorption and chemisorption
common features characterizing, Vol. 5:55
difference between, Vol. 5:54
presence of defects, Vol. 5:51–54
molecular orbitals (MO), Vol. 5:53
non-hexagonal rings, Vol. 5:52
rehybridization, Vol. 5:50
side view of nanotube structure, Vol. 5:52
structure
and adsorption sites of, Vol. 5:49–54
and its specific uses, Vol. 5:40–41
toxicity of, Vol. 5:158–160
Carbon vacancies, Vol. 5:21–23
defects in graphene, Vol. 5:21–23
double vacancies, Vol. 5:22
single vacancy, Vol. 5:21
Chemisorption on CNT and graphene
gases, Vol. 5:83–97
on CNTs, Vol. 5:83–84
effect of dopants on graphene, Vol. 5:93–97
effect of dopants on with CNTs, Vol. 5:84–87
on graphene, Vol. 5:87–93
liquids, Vol. 5:97–99
hydrogen chemisorption on, Vol. 5:98
solids, Vol. 5:99–122
adsorption of other metals, metalloids, and non-metals, Vol. 5:115–116
alkali metals, Vol. 5:99–101
alkaline-earth metals, Vol. 5:102
clusters, Vol. 5:109
d-metals, Vol. 5:102–103
gold clusters, Vol. 5:114–115
platinum clusters, Vol. 5:109–114
polymers, Vol. 5:116–122
single metal atoms, Vol. 5:103–109
CNT. *See* Carbon nanotubes (CNT)
CNT and graphene, adsorption on and reactivity of, Vol. 5:40–42
chemisorption on CNT and graphene
gases, Vol. 5:83–97
liquids, Vol. 5:97–99
solids, Vol. 5:99–122

effects of interactions with nanotubes on IR spectra of small molecules, Vol. 5:59
nitrogen-containing species on carbon surface, Vol. 5:126
oxygen-containing species, Vol. 5:125
physisorption on CNTs and graphene, Vol. 5:54–55
gases, Vol. 5:55–66
liquids, Vol. 5:66–77
solids, Vol. 5:77–83
reactivity on CNTs and graphene, Vol. 5:122
bioreactivity and degradability of CNTs and graphene, Vol. 5:153–160
catalysis, Vol. 5:128–150
gas sensors, Vol. 5:150–153
main advantages offered by CNT or CNF supports, Vol. 5:129
nanostructured carbon materials, surface chemistry of, Vol. 5:124–128
structure and adsorption sites, Vol. 5:42
graphene and FLG, Vol. 5:42–49
Covalent functionalization of graphene in dispersions, Vol. 5:199–201
dienophiles addition, Vol. 5:201–204
free radical addition, Vol. 5:201

Defects in graphene, Vol. 5:45
atomic scale properties of, Vol. 5:29
carbon adatoms, Vol. 5:23–24
with carbon adatoms, Vol. 5:24, 46
carbon vacancies, Vol. 5:21–23
double vacancies, Vol. 5:22
single vacancy, Vol. 5:21
compendium of formation and migration energies, Vol. 5:20
dislocation-like defects, Vol. 5:48–49
divacancy, Vol. 5:46
doping of graphene, Vol. 5:28
edge configuration and types of edge defects, Vol. 5:44–45
in edges of graphene layer, Vol. 5:49
effect of defects on properties of graphene, Vol. 5:27–30
extrinsic, Vol. 5:45
foreign adatoms, Vol. 5:47
grain boundaries, Vol. 5:26–27
grain boundary loops, Vol. 5:24–25
intrinsic, Vol. 5:22, Vol. 5:45
mechanical properties of, Vol. 5:30
monovacancy, Vol. 5:46
noncarbon adatoms and substitutional impurities, Vol. 5:25–26
one-dimensional defects, Vol. 5:48–49
point defects, Vol. 5:46–48
single and multiple vacancies, Vol. 5:46
Stone–Wales defects, Vol. 5:18, 21, 46
structural defects in, Vol. 5:19–21
ways of connecting graphene sheets, Vol. 5:48
Dendrimer composite, carbon nanotube and, Vol. 6:206–207
covalent functionalization, Vol. 6:207–211
non-covalent functionalization, Vol. 6:211–213

Dirac point, Vol. 5:15
DNA biosensor, graphene-based, Vol. 6:179–181
DNA–carbon nanotube composite, Vol. 6:197
  applications, Vol. 6:202–206
  influence of temperature on oligonucleotide adsorption, Vol. 6:200–201
  structure and properties, Vol. 6:198–200

Energy conversion, carbon nanomaterials for, Vol. 6:213
  blue energy, Vol. 6:218–220
  energy-efficient nanoelectrical devices, Vol. 6:222–227
  hydrogen storage, Vol. 6:213–218
  voltage generation through flow, Vol. 6:220–222
Energy storage applications
  graphene-based materials for, Vol. 6:2–4
  nanomaterials (graphene-based) for energy conversion and storage, Vol. 6:51–52
Enzymatic biosensor
  graphene-based electrochemical, Vol. 6:160–163
  graphene–carbon nanotube-based, Vol. 6:176–178
  inorganic nanoparticles-modified graphene-based, Vol. 6:171–174
  organic molecular-modified graphene-based, Vol. 6:163–166
  polymer-modified graphene-based, Vol. 6:166–171

Few-layer graphene (FLG), Vol. 5:42
  characteristics of, Vol. 5:123
  structure and adsorption sites, Vol. 5:42–49
FLG. *See* Few-layer graphene (FLG)
Fullerenes, Vol. 5:2, 4

Glucose, biosensors for, Vol. 6:87–88
Grain boundaries, Vol. 5:26–27, 30
  atomic structure in graphene, Vol. 5:28
Grain boundary loops (GBL), Vol. 5:24–25
  atomic configurations of, Vol. 5:25
Granular activated carbon (GAC), Vol. 5:74
Graphene
  adsorption on and reactivity of. *See* Carbon nanotubes and graphene, adsorption on and reactivity of
  adsorption sites of, Vol. 5:47
  AFM nanoindentation of monolayer graphene membrane, Vol. 5:18
  application of, Vol. 6:11–15
  characteristics of, Vol. 5:123
  characterization of, Vol. 6:6
    morphological characterization, Vol. 6:6–9
    structural characterization, Vol. 6:9–11
  defects in, Vol. 5:see defects in graphene
  dirac fermions, Vol. 5:10, 11
  in dispersions
    chemical manipulation of, Vol. 5:186–187
    covalent functionalization of, Vol. 5:199–204
    phonon dispersion at zero stress, Vol. 5:19
  edge shape, Vol. 5:43, 44
    configurations, Vol. 5:43
  elastic properties of, Vol. 5:16–19
    monolayer graphene, experiment vs theory, Vol. 5:18
  electronic properties of, Vol. 5:8
    atomic collapse on graphene, Vol. 5:14–16

band structure, Vol. 5:5–8
chirality and quantum hall effect, Vol. 5:10–11
few-layered graphene, Vol. 5:8–10
Klein tunneling in graphene, Vol. 5:11–14
energy dispersion, Vol. 5:6
intrinsic defects in, Vol. 5:22
isolation, Vol. 5:2. *See also* *Micromechanical cleavage*
magnetism in, Vol. 5:30
miscellaneous applications of, Vol. 5:210–212
physisorption and chemisorption
common features characterizing, Vol. 5:55
difference between, Vol. 5:54
quantum electrodynamics (QED), Vol. 5:10
quantum hall effect (QHE), Vol. 5:11
staking orders in, Vol. 5:8
effect of, Vol. 5:9
structural defects in, Vol. 5:19–21
atomic scale properties of, Vol. 5:29
carbon adatoms, Vol. 5:23–24
carbon vacancies, Vol. 5:21–23
compendium of formation and migration energies, Vol. 5:20
doping of graphene, Vol. 5:28
effect of defects on properties of graphene, Vol. 5:27–30
grain boundaries, Vol. 5:26–27
grain boundary loops, Vol. 5:24–25
mechanical properties of, Vol. 5:30
noncarbon adatoms and substitutional impurities, Vol. 5:25–26
Stone–Wales defects, Vol. 5:18, 21
structure, Vol. 5:2, 3
and adsorption sites, Vol. 5:42–49
electronic structure of, Vol. 5:6
and its specific uses, Vol. 5:40–41
lattice vectors of graphene unit cell, Vol. 5:5
synthesis of. *See* Synthesis of graphene
three adsorption sites of, Vol. 5:47
topology of defective, Vol. 5:48
toxicity of, Vol. 5:158–160
Graphene and carbon nanotube-based nanomaterial, Vol. 6:190–191
biocompatibility of graphene, Vol. 6:197
carbon nanomaterials for energy conversion, Vol. 6:213
blue energy, Vol. 6:218–220
energy-efficient nanoelectrical devices, Vol. 6:222–227
hydrogen storage, Vol. 6:213–218
voltage generation through flow, Vol. 6:220–222
carbon nanotube and dendrimer composite, Vol. 6:206–207
covalent functionalization, Vol. 6:207–211
non-covalent functionalization, Vol. 6:211–213
DNA–carbon nanotube composite, Vol. 6:197
applications, Vol. 6:202–206
influence of temperature on oligonucleotide adsorption, Vol. 6:200–201

structure and properties, Vol. 6:198–200
Graphene-based composites, Vol. 6:66
for lithium ion batteries, Vol. 6:68–73
for oxygen reduction reaction, Vol. 6:66–68
for supercapacitors, Vol. 6:74–75
Graphene-based electrochemical biosensor, Vol. 6:148–150
biomolecular-modified graphene-based enzymatic biosensor, Vol. 6:174–175
electrochemical properties of graphene, Vol. 6:158–160
functionalization of graphene, Vol. 6:155–158
graphene-based DNA biosensor, Vol. 6:179–181
graphene-based electrochemical enzymatic biosensor, Vol. 6:160–163
graphene–carbon nanotube-based enzymatic biosensor, Vol. 6:176–178
inorganic nanoparticles-modified graphene-based enzymatic biosensor, Vol. 6:171–174
N-doped graphene-based enzymatic biosensor, Vol. 6:178–179
organic molecular-modified graphene-based enzymatic biosensor, Vol. 6:163–166
polymer-modified graphene-based enzymatic biosensor, Vol. 6:166–171
synthesis and characterization of graphene, Vol. 6:150–155
Graphene-based materials for energy storage applications, Vol. 6:2–4
Graphene-based supercapacitor, Vol. 6:15
applications of, Vol. 6:40
emergency management, Vol. 6:41
public transport, Vol. 6:41
starter for fuel-efficient stop–start systems, Vol. 6:40–41
graphene/conducting polymer composite supercapacitor, Vol. 6:32–40
metal nanoparticle/oxide-decorated graphene supercapacitor, Vol. 6:25–31
reduced graphene oxide (rGO) supercapacitor, Vol. 6:16–21
surface-modified graphene supercapacitor, Vol. 6:21–25
Graphene composites, Vol. 5:204–206
graphene/inorganic material composites, Vol. 5:208
graphene/polymer composites, Vol. 5:206–207
synthesis of graphene–inorganic nanocomposites, Vol. 5:209–210
synthesis of graphene/polymer composites, Vol. 5:207–208
Graphene–nucleic acid composites, Vol. 6:192
adsorption of nucleic acids on graphene, Vol. 6:193–197
functionalization of graphene, Vol. 6:192–193
Graphenium, Vol. 5:3
Graphite, Vol. 5:2, 4

High-Angle Annular Dark-Field (HAADF) mode, Vol. 5:79
Highly ordered pyrolytic graphite (HOPG), Vol. 5:65
High-Resolution Transmission Electron Microscopy (HRTEM), Vol. 5:79

Janus graphene, Vol. 5:77
static water contact angle measurements in fabrication procedures of, Vol. 5:78

Klein paradox, Vol. 5:11, 12

Liquid-phase exfoliated graphene
non-ultrasonication techniques
ball-milling production, Vol. 5:193
intercalation compounds, Vol. 5:190
ionics compounds, Vol. 5:191–193
supercritical fluids, Vol. 5:194
unzipping of carbon nanotubes, Vol. 5:194–195
ultrasonication of graphite, Vol. 5:187–188
graphene dispersions in organic solvents, Vol. 5:188–189
graphene dispersions in surfactant solutions, Vol. 5:190
Liquid-phase synthesis of graphene, Vol. 6:52–53
from expanded graphite, Vol. 6:53–55
from graphite oxide, Vol. 6:56–57

Mass-sensitive glucose biosensors, Vol. 6:101–102
Mermin–Wagner theorem, Vol. 5:6–7
Micromechanical cleavage, Vol. 5:2, 3
Multiwalled CNTs (MWCNTs), Vol. 5:59, 60–62, 74–75

Nanomaterials (graphene-based) for energy conversion and storage, Vol. 6:51–52
Nanostructured carbon materials, surface chemistry of, Vol. 5:124–128
Nanostructures from liquid-phase exfoliated graphene, Vol. 5:195
deformation, folding, and stabilization, Vol. 5:196
ultrasonication of graphite
tiopronin as antioxidant molecule, Vol. 5:196–197
Vol. 5:transformation of few-layer graphene into MWNTs, Vol. 5:197–199
Nanotubes, Vol. 5:2, 4
Natural organic matter (NOM), Vol. 5:67, 74
N-doped graphene-based enzymatic biosensor, Vol. 6:178–179
Nitrogen-doped graphene, Vol. 6:57–59
applications of
lithium ion batteries, Vol. 6:64–65
oxygen reduction reaction of fuel cells, Vol. 6:61–63
synthesis of, Vol. 6:59–61
Nitrogen-doped graphene (N-graphene), Vol. 5:80–81
Noncarbon adatoms and substitutional impurities, Vol. 5:25–26

Physisorption on CNTs and graphene, Vol. 5:54–55
adsorption energies, Vol. 5:86–87
debundling of CNTs by physisorption of polymer, Vol. 5:82
gases, Vol. 5:55–66
chemical vapor deposition (CVD) synthesis, Vol. 5:65
on CNTs bundles, Vol. 5:59–62
effects of interactions with nanotubes on IR spectra of small molecules, Vol. 5:59
on graphene, Vol. 5:62–66

HOMO and LUMO orbitals, Vol. 5:65
on individual CNTs, Vol. 5:55–59
mechanism to fix and remove gaseous CO_2 molecules, Vol. 5:64
proposed microscopic mechanism for hydrogen storage, Vol. 5:63
liquids, Vol. 5:66–77
adsorption curves for SWCNTs and MWCNTs, Vol. 5:75
adsorption of water on CNTs and graphene, Vol. 5:68–71
on CNTs and graphene of ions and molecules from Vol. 5:solution, 73–77
of ionic liquids on graphene and CNTs, Vol. 5:71–73
liquid–solid surface interaction, Vol. 5:66
of liquids on doped CNTs and graphene, Vol. 5:77
non-covalent functionalization of PILs, Vol. 5:72
pi-pi interactions and hydrogen bonding between bisphenol A and graphene, Vol. 5:76
resistivities, Vol. 5:70
surface wetting phenomenon, Vol. 5:67
water adsorbed in SWCNTs, Vol. 5:69
"wettability" for solid phase, Vol. 5:66
molecular modeling of ideal stilbenoid dendrimer, Vol. 5:82
of noble gases, Vol. 5:57
solids, Vol. 5:77–83
metals and semiconductors, Vol. 5:77–79
of metals and semiconductors on doped CNTs or graphene, Vol. 5:80–81
polymer adsorption on doped graphene or CNTs, Vol. 5:82–83
of polymers, Vol. 5:81–82
Poly(methyl methacrylate) (PMMA)-mediated transfer approach, Vol. 5:77
Projector Augmented-Wave (PAW) method, Vol. 5:78

Relativistic charge carriers, Vol. 5:14

Single-walled CNTs (SWCNTs), Vol. 5:56, 57, 58, 60, 74–75, 97–98
front and side views of most favorable binding geometries, Vol. 5:89
optimized structures of pristine, Co-doped, Rh-doped, and Ir-doped, Vol. 5:88
Stone–Wales defects, Vol. 5:18, 21, 46
Supercapacitors
graphene-based, Vol. 6:15
applications of, Vol. 6:40–41
graphene/conducting polymer composite supercapacitor, Vol. 6:32–40
metal nanoparticle/oxide-decorated graphene supercapacitor, Vol. 6:25–31
rGO supercapacitor, Vol. 6:16–21
surface-modified graphene supercapacitor, Vol. 6:21–25
graphene-based composites for, Vol. 6:74–75
Surface wetting phenomenon, Vol. 5:67

Synthesis of graphene, Vol. 6:4–6
liquid-phase, Vol. 6:52–53
from expanded graphite, Vol. 6:53–55
from graphite oxide, Vol. 6:56–57

Thermodynamic characteristics of thermal desorption of hydrogen, Vol. 5:220–223
HREELS/LEED data on thermal desorption of hydrogen from hydrogenated graphene on SiC substrate, Vol. 5:239–242
hydrogen desorption in hydrogenated mono- and bilayer epitaxial graphene samples, Vol. 5:230–233
on hydrogen thermal desorption from theoretical and experimental graphanes, Vol. 5:226–228
intercalation of solid H_2 into hydrogenated graphite nanofibers, relevance to the hydrogen on-board storage problem, Vol. 5:250–253
PES and ARPES data on dehydrogenation of graphene/SiC samples, Vol. 5:245–246
Raman spectroscopy data on thermal desorption of hydrogen from hydrogenated graphene flakes, Vol. 5:235–237
Raman spectroscopy data on thermal desorption of hydrogen from hydrogenated graphene layers on SiO_2 substrate, Vol. 5:242–244
STM and STS data on reversible hydrogenation of epitaxial graphene and graphite surfaces, Vol. 5:237–239
TDS and STM data on HOPG treated by deuterium, Vol. 5:244–245
TDS and STM data on HOPG treated by hydrogen, Vol. 5:246–250
on theoretical graphanes (CH), Vol. 5:223
thermodynamic probability of existence of hydrogenated graphenes–graphanes possessing, Vol. 5:228–230
3D graphite crystal, Vol. 5:2
Trilayer graphene, lattice structure of, Vol. 5:43

"Wettability" for solid phase, Vol. 5:66